



UNIL | Université de Lausanne

Unicentre

CH-1015 Lausanne

<http://serval.unil.ch>

Year : 2022

Resolving coupled physical processes in porous rocks: From linear quasi-static and dynamic phenomena to non-linear instabilities

Alkhimenkov Yury

Alkhimenkov Yury, 2022, Resolving coupled physical processes in porous rocks: From linear quasi-static and dynamic phenomena to non-linear instabilities

Originally published at : Thesis, University of Lausanne

Posted at the University of Lausanne Open Archive <http://serval.unil.ch>

Document URN : urn:nbn:ch:serval-BIB_3FE39219D1424

Droits d'auteur

L'Université de Lausanne attire expressément l'attention des utilisateurs sur le fait que tous les documents publiés dans l'Archive SERVAL sont protégés par le droit d'auteur, conformément à la loi fédérale sur le droit d'auteur et les droits voisins (LDA). A ce titre, il est indispensable d'obtenir le consentement préalable de l'auteur et/ou de l'éditeur avant toute utilisation d'une oeuvre ou d'une partie d'une oeuvre ne relevant pas d'une utilisation à des fins personnelles au sens de la LDA (art. 19, al. 1 lettre a). A défaut, tout contrevenant s'expose aux sanctions prévues par cette loi. Nous déclinons toute responsabilité en la matière.

Copyright

The University of Lausanne expressly draws the attention of users to the fact that all documents published in the SERVAL Archive are protected by copyright in accordance with federal law on copyright and similar rights (LDA). Accordingly it is indispensable to obtain prior consent from the author and/or publisher before any use of a work or part of a work for purposes other than personal use within the meaning of LDA (art. 19, para. 1 letter a). Failure to do so will expose offenders to the sanctions laid down by this law. We accept no liability in this respect.

Faculté des géosciences et de l'environnement
Institut des sciences de la Terre

Resolving coupled physical processes in porous rocks: From linear quasi-static and dynamic phenomena to non-linear instabilities

Thèse de doctorat

Présentée à la
Faculté des géosciences et de l'environnement
de l'Université de Lausanne
par

Yury Alkhimenkov

Diplôme (M.Sc., avec Distinction) en Géophysique Appliquée
Swiss Federal Institute of Technology Zürich, Zürich, Switzerland

Diplôme (M.Sc., avec Distinction) en Géophysique Appliquée
Delft University of Technology, Delft, Netherlands

Diplôme (M.Sc., avec Distinction) en Géophysique Appliquée
RWTH Aachen University, Aachen, Germany

Diplôme (M.Sc.) en Exploration Sismique
Lomonosov Moscow State University, Moscow, Russia

Jury

Prof. Marie-Elodie Perga	Université de Lausanne	Présidente du jury
Dr. Beatriz Quintal	Université de Lausanne	Directrice de thèse
Prof. Yury Y. Podladchikov	Université de Lausanne	Co-directeur de thèse
Prof. Stefan M. Schmalholz	Université de Lausanne	Expert interne
Prof. Holger Steeb	University of Stuttgart	Expert externe
Prof. Taras Gerya	ETH Zürich	Expert externe

Lausanne, 2022

IMPRIMATUR

Vu le rapport présenté par le jury d'examen, composé de

Présidente de la séance publique :	Mme la Professeure Marie-Elodie Perga
Présidente du colloque :	Mme la Professeure Marie-Elodie Perga
Directrice de thèse :	Mme la Professeure Beatriz Quintal
Co-directeur de thèse :	M. le Professeur Yury Y. Podladchikov
Expert interne :	M. le Professeur Stefan Schmalholz
Expert externe :	M. le Professeur Holger Steeb
Expert externe :	M. le Professeur Taras Gerya

Le Doyen de la Faculté des géosciences et de l'environnement autorise l'impression de la thèse de

Monsieur Yury ALKHIMENKOV

*Titulaire d'un
Joint Master's in Applied Geophysics
de Swiss Federal Institute of Technology Zurich -
Delft University of Technology - RWTH Aachen University et d'un
Master in Seismic Exploration
de Lomonosov Moscow State University*

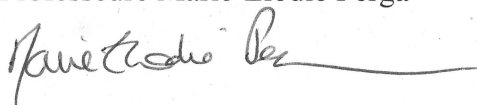
intitulée

RESOLVING COUPLED PHYSICAL PROCESSES IN POROUS ROCKS: FROM LINEAR QUASI-STATIC AND DYNAMIC PHENOMENA TO NON-LINEAR INSTABILITIES

Lausanne, le 04 mai 2022

Pour le Doyen de la Faculté des géosciences et de
l'environnement

Professeure Marie-Elodie Perga



Acknowledgements

My personal acknowledgements goes to my supervisors: Beatriz Quintal and Yury Y. Podladchikov. Thank you for your support and freedom during my stay at the university of Lausanne, thank you for sharing your experience and knowledge! What a journey it has been!

Swiss National Science Foundation (SNSF) is gratefully acknowledged for financial support through the project number 172691.

Contents

Acknowledgements	i
List of figures	ix
List of tables	xxi
Résumé	xxiii
Abstract	xxv
Curriculum Vitae and Research Output list	xxvii
1 Introduction	1
1.1 Coupling physical phenomena	1
1.2 Coupled physics at the micro-scale (or pore scale)	2
1.3 Coupled physics at the macro-scale	4
1.4 Objectives, outline and contributions	7
1.4.1 Objectives	7
1.4.2 Outline	7
1.4.3 Contributions	8
2 Frequency-dependent attenuation and dispersion caused by squirt flow: Three-dimensional numerical study	11
2.1 Introduction	12
2.2 A brief overview of the physics	13
2.2.1 Low frequencies	14
2.2.2 High frequencies	14
2.2.3 Intermediate frequencies	14
2.3 Numerical methodology	15
2.4 Analytical solution of Collet and Gurevich (2016)	16
2.5 Results	18
2.5.1 $P_f = 0$ model	20
2.5.2 <i>Big pore</i> model	21
2.5.3 <i>Small pore</i> model	24
2.5.4 Modified frame	26
2.5.5 Numerical results for different crack aspect ratios	29
2.6 Discussion	31
2.7 Conclusions	34
2.8 Appendix A: Boundary conditions	35
2.9 Appendix B: Rotation of a fourth-rank tensor: HTI versus VTI	37
3 Azimuth-, angle- and frequency-dependent seismic velocities of cracked rocks due to squirt flow	39
3.1 Introduction	40
3.2 Numerical methodology	41
3.3 Numerical model	43
3.4 Results	44
3.4.1 Dry stiffness moduli	44
3.4.2 Fluid pressure fields	45
3.4.3 Dispersion and attenuation	46
3.4.4 Quantitative analysis of the frequency-dependent anisotropy	48
3.5 Discussion	51

3.5.1	Elastic anisotropy	51
3.5.2	Comparison with previous works	52
3.5.3	A qualitative comparison against analytical models	52
3.6	Conclusions	53
3.7	Appendix A: Boundary conditions for c_{ij} off-diagonal components	54
3.8	Appendix B: Thomsen-type anisotropic parameters	54
3.9	Appendix C: The universal elastic anisotropy index parameter	55
4	An accurate analytical model for squirt flow in anisotropic porous rocks — Part 1: Classical geometry	57
4.1	Introduction	58
4.1.1	Importance of validating analytical models against numerical simulations	59
4.1.2	Seismic attenuation and dispersion due to squirt flow	60
4.2	The analytical model	61
4.2.1	General expressions	62
4.2.2	General expressions for our geometry	63
4.2.3	Calculation of the model compliance	64
4.2.4	Calculation of the frequency-dependent crack stiffness	68
4.2.5	Relaxation of the crack stiffness	69
4.2.6	Summary	76
4.3	Validation against three-dimensional numerical solutions	78
4.3.1	Big pore model	79
4.3.2	Big pore model with the finite thickness crack	80
4.3.3	Modified frame of the Big pore model with finite thickness crack	80
4.3.4	Modified frame of the Small pore model	81
4.4	Discussion	81
4.4.1	The key features making our model accurate	81
4.4.2	The effect of the finite volume of the stiff pore	83
4.4.3	The importance of pore connectivity and elastic interactions	84
4.4.4	The correctness of expression 4.19 for the normal crack compliance	85
4.4.5	The choice of the model	85
4.4.6	A standard linear solid as an analytical model	86
4.5	Conclusions	87
4.6	Appendix A: Numerical methodology	87
4.7	Appendix B: Analytical model of Collet and Gurevich (2016)	89
5	An accurate analytical model for squirt flow in anisotropic porous rocks — Part 2: Complex geometry	93
5.1	Introduction	94
5.2	Numerical analysis	95
5.2.1	Fractions of the torus	95
5.2.2	Spherical pores	98
5.3	Analytical model	100
5.3.1	General expressions	100
5.3.2	Step 1: Dry model compliances	101
5.3.3	Step 2: Relaxation of the crack stiffness	105
5.3.4	Step 3: Stiffness of the fully saturated model	107
5.4	Validation: comparison against three-dimensional numerical solutions	107
5.5	Discussion	107
5.6	Conclusion	109
5.7	Appendix A: Fluid pressure diffusion in a crack	109
6	Resolving wave propagation in anisotropic poroelastic media using graphical processing units (GPUs)	111
6.1	Introduction	112
6.2	Elastodynamic Biot's equations in isotropic media	114
6.2.1	Constitutive equations	114
6.2.2	Dynamic equations	116
6.3	Dimensional analysis of the elastodynamic Biot's equations	116

6.3.1	Dispersion analysis of the elastodynamic Biot's equations	118
6.4	Numerical implementation of the elastodynamic Biot's equations	124
6.4.1	The first order elastodynamic Biot's equations with a volumetric-deviatoric split	124
6.4.2	Discretization	124
6.4.3	Stiffness of Biot's equations	125
6.4.4	Von Neumann stability analysis	126
6.4.5	Sources, initial and boundary conditions	128
6.5	Multi-GPU implementation	129
6.5.1	Computing systems	129
6.5.2	Code implementation on a single GPU	129
6.5.3	The multi-GPU code implementation	129
6.5.4	Performance benchmark	131
6.5.5	Validation of the numerical solver	134
6.6	Numerical experiments	136
6.6.1	Wave propagation in 2D poroelastic media	136
6.6.2	Wave propagation in 3D anisotropic poroelastic media	138
6.7	Conclusions	138
6.8	Appendix A: Equations describing a single phase continuum material	144
6.8.1	Stress-strain relations	144
6.8.2	Dynamic equations	145
6.9	Appendix B: Poroelastic parameters	145
6.10	Appendix C: An alternative dimensional analysis of Biot's equations	145
6.11	Appendix D: Elastodynamic Biot's equations for anisotropic media	147
6.11.1	Arbitrary anisotropic media	147
6.11.2	Orthorhombic media	147
6.12	Appendix E: Discretization of Biot's equations	149
6.13	Appendix F: The GPU architecture	150
7	Stability of discrete schemes of Biot's poroelastic equations	153
7.1	Introduction	154
7.2	Theory	155
7.2.1	Basic theory for von Neumann stability analysis	156
7.3	Discrete schemes of the linear damped wave equation	156
7.3.1	The damped linear wave equation	156
7.3.2	The discrete system of equations	158
7.3.3	The explicit scheme	158
7.3.4	The implicit and implicit-explicit schemes	160
7.3.5	Summary to the CFL conditions of the linear damped wave equation	160
7.3.6	Back propagation of the damped linear wave equation	162
7.4	Discrete schemes of dimensionless Biot's poroelastic equations	162
7.4.1	Example 1	167
7.4.2	Example 2	170
7.5	Discrete schemes of dimensional Biot's poroelastic equations	173
7.5.1	Numerical examples	175
7.6	Summary	177
7.7	Discussion	178
7.7.1	Comparison with previous works	178
7.8	Conclusions	179
7.9	Appendix A: The dimensional damped linear wave equation	180
7.10	Appendix B: Dimensional analysis of the elastodynamic Biot's equations	181
7.11	Appendix C: The amplification matrices for different schemes for Example 1	185

8	Non-linear instabilities, strain localization and spontaneous earthquake nucleation	187
8.1	Introduction	188
8.2	The pseudo-transient method	190
8.2.1	The damped wave equation	190
8.2.2	The double damped wave equation	193
8.3	Non-linear instabilities	196
8.3.1	Plasticity	196
8.3.2	The theory of spontaneous earthquake nucleation	197
8.4	Conclusions	199
9	Perspectives	201
9.1	Conclusions	201
9.2	Outlook	202
	Bibliography	223
A	Appendix A: Squirt flow in cracks with rough walls	225
A.1	Introduction	226
A.2	Methodology	227
A.2.1	Mathematical formulation	227
A.2.2	Numerical upscaling	229
A.2.3	Local energy dissipation	230
A.3	Results	230
A.3.1	Cracks with binary aperture distribution	231
A.3.2	Cracks with more intricate rough walls	235
A.3.3	Cracks with contact areas	237
A.4	Discussion	239
A.5	Conclusions	240
A.6	Acknowledgments	241
A.7	Appendix	241
A.7.1	Reduced Reynolds number	241
A.7.2	REV boundary effects	241
A.7.3	Hydraulic aperture	242
B	Appendix B: Fast and efficient MATLAB-based MPM solver (fMPMM-solver v1.1)	245
B.1	Introduction	246
B.2	Overview of the Material Point Method (MPM)	247
B.2.1	A Material Point Method implementation	247
B.2.2	Domain-based material point method variants	249
B.3	MATLAB-based MPM implementation	250
B.3.1	Rate formulation and elasto-plasticity	250
B.3.2	Structure of the MPM solver	251
B.3.3	Vectorisation	252
B.3.4	Initial settings and adaptive time step	258
B.4	Results	258
B.4.1	Validation of the solver and numerical efficiency	259
B.4.2	Computational performance	264
B.5	Discussion	267
B.6	Conclusions	269
B.7	Appendix A: Acronyms	270
B.8	Appendix B: fMPMM-solver Variables	271

C Appendix C: An explicit GPU-based material point method solver for elastoplastic problems (ep2-3De v1.0)	273
C.1 Introduction	274
C.2 Numerical implementation	275
C.2.1 Governing equations	275
C.2.2 Rate formulation	276
C.2.3 Elastoplastic deformation	277
C.3 GIMPM implementation under a GPU architecture	279
C.3.1 Implementation on a graphical processing unit (GPU)	279
C.3.2 The multi-GPU code implementation	280
C.3.3 Available computational resources	283
C.3.4 Measuring computational performance on a GPU	284
C.4 Results	284
C.4.1 Model 1	285
C.4.2 Model 2	287
C.4.3 Model 2b: homogeneous and heterogeneous slumps	294
C.5 Discussion	297
C.5.1 GIMPM suitability	297
C.5.2 Collapse limitation	297
C.5.3 Performance	298
C.5.4 Slumping mechanics	298
C.5.5 Local damping coefficient	298
C.5.6 Code portability	299
C.6 Conclusions	299
C.7 Appendix A: GIMPM basis functions and derivatives	300
C.8 Appendix B: Gaussian random cohesion fields	301
C.9 Appendix C: Volumetric locking and damping corrections	301
C.10 Appendix E: Heterogeneities for the peak cohesion field	303

List of Figures

1.1	Conceptual representation of rock structure at the micro-scale.	2
1.2	A conceptual model of a rock and a slice of a sandstone.	3
1.3	Big torus	4
1.4	Snapshots of different fields from a numerical simulation of propagating waves in two-dimensional media.	5
1.5	Numerical simulation of propagating waves in three-dimensional media.	5
1.6	Earthquake	6
2.1	Sketch	19
2.2	The element's size distribution for the $P_f = 0$ model (Figure 2.2): (left) Full model and (right) Zoomed in part of the model showing elements in the crack (element size 0.00025 – 0.00015 m) and in the surrounding grain material (element size 0.038 – 0.008 m). The element's size is the smallest inside the crack and growing toward the walls of the model domain.	21
2.3	Numerical and analytical results for the model with fluid pressure equal to zero at the edge ($P_f = 0$) (Figure 2.1b): (up) Real part of the C_{33} component and (down) dimensionless attenuation for the C_{33} component. Each red circle corresponds to a numerical calculation.	22
2.4	Snapshots of the fluid pressure P_f in the fracture at three different frequencies for the $P_f = 0$ model: Lf - low frequency (relaxed state), Fc - intermediate frequency (close to the characteristic frequency) and HF - high frequency (unrelaxed state).	22
2.5	Numerical results for the real part of C_{mn} components for the <i>big pore</i> model (Figure 2.1c, 2.1d) using five direct tests.	24
2.6	Sketch illustrating the calculation of normal and tangential compliances of the crack for Workflows A and B. S_r^{VTI} denotes the compliance tensor, which is the inverse of the corresponding stiffness tensor. i.e., $S_r^{VTI} = (C_r^{VTI})^{-1}$, for $r = 1, 2, 3$. The resulting Z_n and Z_t are used to calculate the analytical solution for corresponding models (Figure 2.1).	25
2.7	Numerical and analytical results for the <i>big pore</i> model (Figure 2.1(c-d)): (a) Real part of the C_{33} component, (b) dimensionless attenuation for the C_{33} component. Each red circle corresponds to one test. The maximum of the attenuation curve (Analytical solution with Workflow A, blue curve) is exactly the same as in the numerical result by a chance because the comparison between the analytical solution and numerical result for the modified frame exhibit discrepancy; it is explained in the text.	25
2.8	Snapshots of the fluid pressure P_f in the fracture at three different frequencies for the <i>big pore</i> model: Lf - low frequency (relaxed state), Fc - intermediate frequency (close to the characteristic frequency) and HF - high frequency (unrelaxed state).	26
2.9	Numerical and analytical results for the <i>small pore</i> model (Figure 2.1(e-f)): (a) Real part of the C_{33} component and (b) dimensionless attenuation for the C_{33} component.	27
2.10	Snapshots of the fluid pressure P in the fracture at three different frequencies for the <i>small pore</i> model: Lf - low frequency (relaxed state), Fc - intermediate frequency (close to the characteristic frequency) and HF - high frequency (unrelaxed state).	27
2.11	Numerical and analytical results for the <i>modified frame big pore</i> model: (up) Real part of the C_{33} component and (down) dimensionless attenuation for the C_{33} component. Each rhombus corresponds to a numerical calculation. Crack aspect ratio is 0.0025.	28
2.12	Numerical results and the <i>modified frame big pore</i> , the <i>modified frame small pore</i> models and corresponding saturated models: (up) Real part of the C_{33} component and (down) dimensionless attenuation for the C_{33} component. Each red circle or rhombus correspond to a numerical calculation.	29

2.13	Numerical results for the <i>big pore</i> model (Figure 2.1(c-d)) and the $P_f = 0$ model (with fluid pressure equal to zero at the edge of the cylinder) (Figure 2.1(a-b)), cracks with different aspect ratios of 0.0025; 0.005; 0.01: (up) Real part of the C_{33} component and (down) dimensionless attenuation for the C_{33} component.	30
2.14	Sketch illustrating that the two-step homogenization approach produces the C_2^{VTI} stiffness tensor which is approximately equal to the case if we embed the crack and the stiff pore (disconnected) into the grain material.	32
3.1	Sketch illustrating two flat cylinders representing two cracks. The blue region represents the pore space saturated with a fluid and the transparent gray area corresponds to the solid grain material. In the first model, the two cracks are disconnected as illustrated by the upper right sketch. In the second model, the two cracks are connected as illustrated by the lower right sketch.	43
3.2	Sketch illustrating the element's size distribution for the model with connected cracks. The element's size in the crack is $5 \times 10^{-5} - 1 \times 10^{-3}$ m, and in the surrounding grain material it is $2.4 \times 10^{-3} - 1.6 \times 10^{-2}$ m. The element's size distribution for the model with disconnected cracks is the same.	45
3.3	Snapshots of the fluid pressure P_f in the cracks at three different frequencies: LF – the low-frequency limit (corresponds to 10^1 Hz, relaxed state), Fc – intermediate frequency snapshot (corresponds to 10^4 Hz, close to the characteristic frequency) and HF – the high-frequency limit (corresponds to $10^{6.5}$ Hz, unrelaxed state).	46
3.4	Numerical results for the connected (C) and disconnected (D) crack models: real part of the c_{ij} components versus frequency (a–c), dimensionless inverse quality factor of the c_{ij} components versus frequency (d–f). Each symbol corresponds to the test result of one numerical simulation and lines correspond to linear interpolation between discrete numerical results.	47
3.5	P-wave phase velocity versus phase angle in the $Y-Z$ plane (a) and the $X-Z$ plane (b). Curves $10^1-10^{6.5}$ denote the frequency of the P wave for the model with connected cracks. (D) denotes the P wave for the model with disconnected cracks.	49
3.6	SV-wave phase velocity versus phase angle in the $Y-Z$ plane (a) and the $X-Z$ plane (b). Curves $10^1 - 10^{6.5}$ denote the frequency of the P wave for the model with connected cracks. (D) denotes the P wave for the model with disconnected cracks.	49
3.7	SH-wave phase velocity versus phase angle in the $Y-Z$ plane (a) and the $X-Z$ plane (b). Curves $10^1 - 10^{6.5}$ denote the frequency of the P wave for the model with connected cracks. (D) denotes the P wave for the model with disconnected cracks.	49
3.8	Thomsen-type anisotropic parameters in the $Y-Z$ (a) and $X-Z$ (b) planes.	50
3.9	The universal elastic anisotropy index measure A^U versus frequency (a) and the anisotropy measures in bulk and shear (A^{bulk} and A^{shear}) (b). These plots show that the overall anisotropy of the model increases in the low frequencies due to fluid flow.	51
4.1	Workflow to (i) benchmark published analytical models and (ii) ensure the quality of future models.	59
4.2	Raw synchrotron radiation X-ray tomographic microscopy image of dry Berea sandstone. One slice of the total data cube with 1024^3 voxels [from <i>Madonna et al.</i> (2013)].	60
4.3	The development of the present analytical model.	61
4.4	(a) Sketch illustrating the Big pore model: a flat cylinder representing a crack whose edge is connected to a torus representing a stiff isometric pore. (b) A vertical slice across half of the model. r is the minor radius of the torus ($d_{Mn} = 2r$ is the minor diameter of the torus), $d_{Mj} = r + b$ is the major radius of the torus.	62
4.5	Cartoon illustrating the different model configurations used to obtain the corresponding compliance matrices.	63
4.6	Sketch illustrating the configurations of our model that corresponds to the high- and low-frequency limits obtained from the numerical calculations for the $[C_{33}^*]_{\text{sat}}$ component (properties in Tables 5.1 and 5.2).	65
4.7	Sketch illustrating the workflow for calculating analytically different components of the compliance matrix for the model with interconnected isometric pore and crack.	68

4.8	Sketch illustrating the simplifications made in analytical models via applied boundary conditions (a vertical slice of the two models shown in Figure 4.4). Panels a) and c) — boundary conditions applied to the walls of the model. Panels b) and d) — boundary conditions applied to the walls of the crack. Panel e) shows the numerical result; note, that the high-frequency slope of the attenuation curve is substantially different if the crack is connected to an actual pore.	70
4.9	The real part of the frequency-dependent fluid bulk modulus K_f^* and the dimensionless attenuation calculated using different expressions for the Big pore model with $\alpha = 0.005$	74
4.10	The real part of the frequency-dependent fluid bulk modulus K_f^* and the dimensionless attenuation calculated using different expressions for the Big pore model with $\alpha = 0.005$	75
4.11	The real part of the frequency-dependent fluid bulk modulus K_f^* and the dimensionless attenuation calculated using different expressions for the Small pore model with $\alpha = 0.0025$	76
4.12	Numerical and analytical results for the Big pore model (Figure 4.4) with a crack aspect ratio $\alpha = 0.0025$: (a) Real part of the $[C_{33}^*]_{\text{sat}}$ component and (b) dimensionless attenuation for the $[C_{33}^*]_{\text{sat}}$ component. On the right, snapshots of the fluid pressure P_f at three different frequencies : LF - low frequency limit (relaxed state), Fc - intermediate frequency (close to the characteristic frequency) and HF - high frequency limit (unrelaxed state). The spatial dimension of the snapshots are not-to-scale and their colors representing the fluid pressure P_f correspond to a downward displacement (compression) of 10^{-8}m applied to the top boundary of the model. The inset represents the cross section of half of the model.	79
4.13	Numerical and analytical results for the Big pore model with the crack aspect ratio $\alpha = 0.005$ (i.e., finite thickness crack): (a) Real part of the $[C_{33}^*]_{\text{sat}}$ component and (b) dimensionless attenuation for the $[C_{33}^*]_{\text{sat}}$ component. Here the crack aperture is two times larger than in the model with aspect ratio of $\alpha = 0.0025$ (Figure 4.12). The inset represents the cross section of half of the model.	80
4.14	Numerical and analytical results for the modified frame of the Big pore model with the crack aspect ratio $\alpha = 0.005$ (i.e., finite thickness crack): (a) Real part of the $[C_{33}^*]^{\text{MF}}$ component and (b) dimensionless attenuation for the $[C_{33}^*]^{\text{MF}}$ component. The inset represents the cross section of half of the model.	81
4.15	Numerical and analytical results for the modified frame of the Small pore model with the crack aspect ratio $\alpha = 0.0025$: (a) Real part of the $[C_{33}^*]^{\text{MF}}$ component and (b) dimensionless attenuation for the $[C_{33}^*]^{\text{MF}}$ component. The inset represents the cross section of half of the model.	82
4.16	A slice of the three-dimensional models illustrating the effect of elastic interactions on the $[C_{33}^*]_{\text{dry}}$ component. (a) The isometric pore is connected to the crack representing a unified interconnected pore space, (b) the isometric pore and crack are disconnected but close and (c) disconnected and far from each other.	84
4.17	Sketch illustrating the pore space (dry) of the Big pore model with two different crack apertures — h (left) and $50h$ (right).	85
4.18	Numerical and analytical results for the big pore model with the crack aspect ratio $\alpha = 0.025$: (a) Real part of the $[C_{33}^*]_{\text{sat}}$ component and (b) dimensionless attenuation for the $[C_{33}^*]_{\text{sat}}$ component.	86
4.19	The element's size distribution for the Big pore model. The element's size in the crack is $\approx 6 \times 10^{-4}$ m, and in the surrounding grain material it is $7.2 \times 10^{-3} - 4 \times 10^{-2}$ m. The element's size distribution for the other models is similar. The total number of elements is $1.5 \times 10^6 - 5 \times 10^6$ depending on the model configuration, e.g., Big/Small pore or full/half/quarter of a model was used.	88
4.20	Sketch illustrating the calculation of normal and tangential compliances of the crack for workflows A and B. S_r^{VTI} denotes the compliance tensor, which is the inverse of the corresponding stiffness tensor, i.e., $S_r^{VTI} = (C_r^{VTI})^{-1}$, for $r = 1, 2, 3$. The resulting Z_n and Z_t are used to calculate the analytical solution for corresponding models.	91
5.1	Sketch illustrating the the model geometry of a crack connected to a fraction of a torus. The displacement boundary condition $u = 10^{-8} \times \exp(i\omega t)$ applied to the top side of the model to calculate the C_{33} component of the effective stiffness matrix (Voigt notation).	95
5.2	(a) $P_f = 0$ model, (b) 1/9 torus model, (c) 4/9 torus model, (d) 6/9 torus model, (e) 8/9 torus model, (f) the Big torus model. Results of numerical simulations for the real part of the C_{33} component (g) and dimensionless attenuation for the C_{33} component (h). The crack aspect ratio is $\alpha = 0.02$	97

5.3	(a) the Big torus model, (b) 4 spheres model, (c) 2 spheres model, (d) 1 sphere model model. Results of numerical simulations for the Real part of the C_{33} component (e) and dimensionless attenuation for the C_{33} component (f). The crack aspect ratio $\alpha = 0.01$	99
5.4	Sketch of the development of the present analytical model.	101
5.5	Sketch illustrating the workflow on calculating analytically the stiffness moduli for different configurations of interconnected isometric pores and cracks.	104
5.6	Sketch illustrating the definition of the squirt flow length l_{sq} for different geometries.	106
5.7	Numerical and analytical results for the Big torus, 4 spheres and 1 sphere models. The crack aspect ratio $\alpha = 0.01$: (a) Real part of the $[C_{33}^*(\omega)]_{sat}$ component and (b) dimensionless attenuation for the $[C_{33}^*(\omega)]_{sat}$ component. On the right, geometries of the pore-space are shown.	108
5.8	Numerical results for the Big torus model, the Big torus plus the sphere in the center, and the crack with the sphere in the center. The crack aspect ratio $\alpha = 0.01$: (a) Real part of the $[C_{33}^*(\omega)]_{sat}$ component and (b) dimensionless attenuation for the $[C_{33}^*(\omega)]_{sat}$ component. On the right, geometries of the pore-space are shown.	108
5.9	Numerical and analytical results for the 8/9 torus model: (a) Real part of the $[C_{33}^*(\omega)]_{sat}$ component and (b) dimensionless attenuation for the $[C_{33}^*(\omega)]_{sat}$ component. On the right, geometries of the pore-space are shown.	110
6.1	Phase velocities and the corresponding inverse quality factors $1/Q$ obtained via the dispersion analysis. (a) Dispersion relations for the non-dimensional elastodynamic Biot's equations, \tilde{V}_1 is the wave of the first kind (non-dimensional), \tilde{V}_2 is the wave of the second kind (non-dimensional). (b) Dispersion relations for the dimensional elastodynamic Biot's equations. V_1 <i>dim</i> and V_2 <i>dim</i> correspond to dimensional velocities, V_1 <i>non-dim</i> and V_2 <i>non-dim</i> correspond to non-dimensional velocities, which were re-scaled by the dimensional characteristic velocity V_d and the transformation frequency ω^* . ω_c is the Biot's characteristic frequency. The material parameters are those from Table 6.3.	121
6.2	The inverse quality factors $1/Q$ of the the wave of the first kind. (a) $1/Q$ for the non-dimensional elastodynamic Biot's equations having different viscosities and permeabilities, all collapsed into one curve. (b) $1/Q$ for the dimensional elastodynamic Biot's equations for the same data set of viscosities and permeabilities. The material parameters are those from Table 6.3, except for viscosities and permeabilities.	122
6.3	Non-dimensional phase velocities (\tilde{V}_1 and \tilde{V}_2) and the corresponding quality factors ($1/Q_1$ and $1/Q_2$) as a function of the non-dimensional Biot-Willis coefficient α and the non-dimensional angular frequency ω . The material parameters are those from Table 6.3.	122
6.4	Non-dimensional phase velocities (\tilde{V}_1 and \tilde{V}_2) and the corresponding quality factors ($1/Q_1$ and $1/Q_2$) as a function of the non-dimensional parameter ρ_{ft} and the non-dimensional angular frequency ω . The material parameters are those from Table 6.3.	123
6.5	A sketch representing (a) the finite volume, where the solid particle velocities preserve mass balance and (b) the spatial positions of different fields in the X-Z plane. Darcy's fluxes obey the same behavior.	125
6.6	The von Neumann stability analysis for the elastodynamic Biot's equations (7.94)-(7.95) as a function of $\eta_k = \eta/k$ and porosity ϕ . Panel (a) corresponds to the $\chi = 0$ scheme and panel (b) corresponds to the $\chi = 1/2$ scheme. The stability of the $\chi = 1$ scheme is identical to that one of the $\chi = 1/2$ scheme. The material parameters are those from Table 6.3.	127
6.7	The one dimensional code using the proposed scheme with $\chi = 1/2$ in MATLAB. The initial condition of the Gaussian form is set to the fluid pressure. <code>zeta_ij</code> are the matrix coefficients ζ_{ij} in equation (8.8), <code>vrrho_ij</code> are the matrix coefficients ρ_{ij} in equation (6.47), <code>etaf_k</code> corresponds to η/k , <code>chi</code> corresponds to χ , <code>lamx</code> stands for l_x , <code>stress_xx</code> stands for $\bar{\sigma}_{xx}$, <code>Prf</code> stands for p_f , <code>Qx</code> stands for q_x^D , <code>Vx</code> stands for v_x^s	128
6.8	Time loop computations for (a) a single GPU CUDA C code and (b) a multi-GPUs CUDA C code implementation. <code>compute_StressPrf</code> corresponds to the update of all stresses $\bar{\sigma}_{ij}$ and fluid pressure p_f . <code>update_QV</code> corresponds to the update of velocities v_i^s and Darcy fluxes q_i^D . <code>swap(. . .)</code> stands for a pointer swap of Darcy's fluxes between old and new values.	130

6.9	Schematic representation of a domain decomposition on four GPUs. First, the computation of the boundary points (1) of the local domains using streams is performed, then the computation of the inner points (2) of the local domains is carried out together with the non-blocking MPI messages to exchange the boundary values (represented by red boundary lines) among neighboring GPU units.	131
6.10	The Nvidia visual profiler (nvvp) output for various GPU code implementations: (a) single GPU (without computation/communication overlap), (b) multi-GPUs (without computation/communication overlap) and (c) multi-GPUs (with computation/communication overlap). All implementations share the same compute_StressPrf kernel. The update_QV kernel is (a) executed once per time step updating both boundary and inner points, (b) executed once per time step and followed by internal boundary exchange using MPI, (c) executed in a serial fashion, first updating the boundary points, then internal boundary exchange occurs using MPI while the inner points are asynchronously computed in the second call of the update_QV kernel. The computation/communication overlap referred to as computational split involves 48, 16 and 16 grid cells in x-, y- and z- directions, respectively.	132
6.11	The effective memory throughput as a function of the number of threads per blocks (in x-, y- and z- direction). The MTP of all simulations ($MTP_{\text{effective}}$) are normalized by MTP_{ref} (corresponds to Block (32,2,16)). The bold color corresponds to thread-block combinations of 512 threads out of the 1024 available.	133
6.12	The memory access efficiency as a function of the allocated on-chip DRAM memory. The blue curve corresponds to the “ideal” memory copy efficiency (copying two 3D arrays without performing any calculations), red and yellow curves represent the memory copy efficiency involving all the physics, which is on average 90% of the “ideal” memory copy efficiency.	133
6.13	The impact of the boundary width on the memory access efficiency. All the performance results are normalized by MTP_{ref} of the non-MPI code implementation.	134
6.14	The MPI weak scaling tests of the anisotropic Biot 3D implementation. We show the parallel efficiency of the two Nvidia hardware accelerators, the 1-8 Tesla V100 32 GB NVlink GPUs (Volta) and the 1-128 Titan X 12 GB GPUs (Maxwell). All the performance results are normalized by the single-MPI code performance.	134
6.15	A comparison between numerically calculated dimensional phase velocities (up) and $1/Q$ (down) against an analytical solution of Biot’s equations. Each red circle corresponds to a numerical simulation. The phase velocity V_1 is normalized by the velocity in the high frequency limit V_1^{HF} and the dimensional angular frequency ω^d is normalized against Biot’s frequency ω_c . The material parameters are those from Table 6.3.	135
6.16	The truncation error magnitudes of the numerically estimated velocities. (a) the low frequency source and (b) f_c of the source is close to the frequency of $1/Q_1$ maximum. The material parameters are those from Table 6.3.	136
6.17	Numerical simulation of a propagating waves. (a), (c), (e) show the total pressure field \bar{p} , (v), (d), (f) show the particle-velocity field V_x . Plots (a) and (b) correspond to the poro-acoustic medium, (c) and (d) correspond to the poro-elastic medium (low frequency regime) and (e), (f) correspond to the poro-elastic medium (high frequency regime). The total physical simulation time is approximately $t = 9 \cdot 10^{-4}$ seconds. The material properties are those of an isotropic sandstone (Table 6.4).	140
6.18	Snapshots showing particle-velocity fields V_x and V_z in the epoxy-glass medium (Table 6.4). Panels (a) and (b) correspond to the inviscid medium ($\eta = 0$), panels (c) and (d) correspond to the viscid medium ($\eta \neq 0$). The total physical simulation time is $t = 7.061 \cdot 10^{-04}$ seconds.	141
6.19	Snapshots showing particle-velocity fields V_x and V_z in the sandstone-VTI medium (Table 6.4). Panels (a) and (b) correspond to the inviscid medium ($\eta = 0$), panels (c) and (d) correspond to the viscid medium ($\eta \neq 0$). The total physical simulation time is $t = 6.15 \cdot 10^{-04}$ seconds.	142
6.20	Snapshots showing the total solid particle velocity field $V = V_x + V_y + V_z$ in the medium having the properties of the glass-epoxy (Table 6.4). The velocity field is projected into $X - Z$ and $Y - Z$ slices. Red and blue isosurfaces denote the wave amplitudes of ± 0.4 . The anisotropic nature of the model is clearly visible due to the non-symmetric velocity field pattern. The total physical simulation time is $6.8 \cdot 10^{-4}$ seconds.	143

6.21	Snapshots showing the solid particle velocity field V_x in the medium having the properties of the glass-epoxy (Table 6.4). Panel (a) shows V_x of the same model as in Figure 6.20, red and blue isosurfaces denote the wave amplitudes of ± 0.4 , the total physical simulation time is $6.8 \cdot 10^{-4}$ seconds. Panel (b) shows V_x of the 100 times smaller model, which corresponds to the high frequency regime, The total physical simulation time is $6.8 \cdot 10^{-6}$ seconds. Red and blue isosurfaces denote the wave amplitudes of ± 3.0	143
6.22	Schematic chip representation for both the central processing unit (CPU) and graphical processing unit (GPU) architectures. The GPU architecture consist of thousands of arithmetic and logical units (ALU). On the CPU, most of the on-chip space is devoted to controlling units and cache memory, while the number of ALUs is significantly reduced.	151
7.1	Snapshots of the velocity wave fields of DWE (7.14). Panel (a) shows one propagating wave, which corresponds to the wave propagation regime of DWE. Panel (b) shows a diffusive mode, which corresponds to the diffusive regime of DWE. We apply a Gaussian distribution to the pressure p at the center of the model as an initial condition.	159
7.2	The CFL condition Δt as a function of Δx for the explicit scheme ($\chi = 0$) (red curve), its wave equation limit ($\Delta x \ll 1$) (blue curve), its parabolic limit (black curve), the standard wave equation (dashed green curve), the diffusive equation (dashed brown curve) and the parabolic limit (dashed light blue curve).	161
7.3	The CFL condition Δt as a function of Δx for the explicit scheme ($\chi = 0$) (red curve), the implicit-explicit scheme ($\chi = 0.5$) (black curve), the implicit scheme ($\chi = 1$) (blue curve), the standard wave equation (dashed green curve), the diffusive equation (dashed brown curve) and the parabolic limit (dashed light blue curve).	161
7.4	The eigenvalues $\lambda_{1,2}$ of the amplification matrix F for the three discrete schemes as a function of r (7.6). (a) - explicit scheme ($\chi = 0$), (b) - implicit-explicit scheme ($\chi = 0.5$) and (c) implicit scheme ($\chi = 1$). The x -axis in panels (a) and (b) is linear while the x -axis in panel (c) is logarithmic.	163
7.5	The CFL conditions of DWE for positive (a) and negative (b) Δt as a function of Δx for the three schemes — the explicit scheme ($\chi = 0$) (red curve), the implicit-explicit scheme ($\chi = 0.5$) (black curve), the implicit scheme ($\chi = 1$) (blue curve).	164
7.6	Snapshots of the solid velocity wavefields of the dimensionless Biot's poroelastic equations (7.28)-(7.29). Panel (a) shows two propagating waves V_1 and V_2 , which corresponds to the wave propagation regime for V_2 . Panel (b) shows one propagating wave V_1 and a diffusive mode, which corresponds to V_2 . The initial condition is given to the fluid pressure p_f of a Gaussian shape. The material parameters are $\zeta_{12} = 1/8$, $\zeta_{22} = 1/4$, $\varrho_{12} = 1/4$, $\varrho_{22} = 1/2$	166
7.7	A sketch representing the spatial locations of the field variables of Biot's equations in a staggered mesh.	167
7.8	The restrictions on Δt arising from the roots $\gamma_{1,4}$ as a function of Δx for Biot's and modified DWE equations considering explicit, implicit-explicit and implicit schemes for the Darcy's flux. $\lambda_1 = 1$ and $\lambda_3 = 1$ correspond to the positive roots.	170
7.9	The restrictions on Δt arising from the roots $\gamma_{1,4}$ as a function of Δx for Biot's and DWE equations. $\lambda_1 = 1$ and $\lambda_3 = 1$ correspond to the positive roots of (7.57) for positive Δt	172
7.10	Snapshots of the solid velocity and fluid pressure wavefields of the dimensionless Biot's poroelastic equations (7.28)-(7.29) and for the diffusion equation. Panel (a) shows one propagating wave V_1 and a diffusive mode, which corresponds to V_2 . Panel (b) shows the fluid pressure field of Biot's equations (solid blue) and of the diffusion equation (dashed red). The initial condition is given to the fluid pressure p_f of a Gaussian shape. The material parameters are $\zeta_{12} = 1/8$, $\zeta_{22} = 1/4$, $\varrho_{12} = 1/4$, $\varrho_{22} = 1/2$	173
7.11	Number of iterations before the numerical instabilities appeared in the 1D numerical solution of Biot's equations. Each blue square corresponds to the numerical simulation. The material and numerical parameters are given in Table 7.4.	176
7.12	The the solid velocity wave field V_x after 850 time steps. The material and numerical parameters are given in Table 7.4.	177
8.1	The triggering front of seismic events due to fluid injection at a borehole at Soultz, France [from <i>Shapiro and Dinske</i> (2009)].	189
8.2	The dynamic rupture model: final slip magnitude [from <i>Ulrich et al.</i> (2019)].	189

8.3	The conceptual model of fluid-induced seismicity mechanism. Panel (a) shows the reservoir surrounding the fault, panel (b) shows the poroelastic spring–poro-slider model of a fault [from <i>Alghannam and Juanes (2020)</i>].	190
8.4	(a and b) The decay rate for residuals with different wavenumbers corresponding to different damping parameters for single (a) and double (b) damped wave equations. A total cell number of 100 is used for both cases. A larger absolute value of the decay rate ($\lambda\Delta t$) implies a faster the convergence process. (c and d). A comparison of the numerical and analytical processes via different damping parameters for single (c) and double (d) damped wave equations. An accuracy of 10^{-12} is used for both cases in terms of convergence criteria.	194
8.5	The solution (8.14) plotted for $L_{Lc} = 30$ and $L_{Lc} = 10$	195
8.6	The strain localization of a poro-elasto-plastic medium under shear loading (total pressure). The resolution of the simulation is $10,000 \times 10,000 = 100,000,000$ grid cells.	196
8.7	The fluid pressure snapshots of a poro-elasto-plastic medium under shear loading: 2-D fields (left) and 1-D diagonal cross sections (right).	197
8.8	The conceptual model of the seismic event nucleation. Panel (a) shows the displacement field corresponding to a stress drop in the model representing the focal mechanism. Panel (b) shows the fractal shear bands developed during the evolution of the stress field. Panel (c) shown the stress evolution in the model as time evolves. The 3-D moment tensor source type figure (beach-ball) in panel (a) is grabbed from <i>Tape and Tape (2012)</i>	198
A.1	a) Numerical model consisting of two perpendicular and hydraulically interconnected cracks of $200 \times 200 \times h \mu m^3$ embedded in a cubic non-porous solid elastic background of $210 \times 210 \times 210 \mu m^3$. b) Mesh of the numerical model coloured according to the side length of each tetrahedral element. The inset of panel b shows the meshing inside the cracks only.	228
A.2	Example of one model having two hydraulically interconnected cracks with a binary aperture distribution, i.e., only two apertures of $h_{min} = 0.3 \mu m$ (5% of crack area) and of $h_{max} = 2.7 \mu m$ (95% of crack area) are present. The distribution of the minimum aperture zones is uncorrelated.	231
A.3	Aperture distributions employed in the model of Figure A.2 containing two identical and perpendicular cracks with binary apertures: $h_{min} = 0.3 \mu m$ (varying from 2.5% to 50% of crack areas) and $h_{max} = 2.7 \mu m$ (for the remaining percentage of crack wall areas). In addition, the apertures between parenthesis correspond to the crack conditions after an increase of the confining pressure described in Section 3.3.	231
A.4	Real part of the P-wave modulus $Re(H)$ and attenuation $1/Q_p$ as functions of frequency for the interconnected cracks presented in Figure A.3 and for pairs of interconnected planar cracks with aperture of 0.3 or 2.7 μm . In addition, P-wave modulus at low- and high-frequency limits following <i>Gassmann (1951)</i> and <i>Mavko and Jizba (1991)</i> approaches, respectively, are shown in dotted lines for the planar crack models having 0.3 μm (red dotted lines) and 2.7 μm (black dotted lines) of aperture.	232
A.5	Local contribution $1/q_n$ (Eq. 7) to the total attenuation $1/Q$ at $f_{c1} = 10$ Hz (left) and $f_{c2} = 10^4$ Hz (right) in two horizontal slices (xy -planes), at $z=0 \mu m$ (top) and $z=1.05 \mu m$ (middle), for the binary model of Figure A.3 having 5% of h_{min} . At the bottom, the sum of the $1/q_n$ for each horizontal slice within the crack is plotted for both frequencies.	233
A.6	Sum of the local attenuation contribution $1/q_n$ for each horizontal slice within the horizontal crack at six frequencies (top) and the total attenuation (blue solid line) with the volumetric integration of $1/q_n$ only inside aperture h_{min} (blue circles) as a function of frequency (bottom) for the binary model having 5% of h_{min}	234
A.7	Arithmetic mean, harmonic mean and hydraulic apertures for binary model having from 5% to 70% of h_{min} in their apertures. Also $h_{min}=0.3 \mu m$ and $h_{max}=2.7 \mu m$ are plotted in dashed lines for reference (top). Seismic attenuation ($1/Q_p$) for the binary models of Figure A.3 at the characteristic frequencies as functions of h_{min} (bottom).	235
A.8	Real part of the P-wave modulus and attenuation for binary models having 5%, 10% and 50% of h_{min} (solid lines) and the ones corresponding to planar crack models having their equivalent hydraulic apertures, that is $h_H=2.31 \mu m$, $h_H=2.04 \mu m$ and $h_H=0.55 \mu m$, respectively (dashed lines).	236
A.9	Aperture of cracks having rough walls with uncorrelated (Model A) and correlated (Model B) distributions of zones of minimum aperture $h_{min} = 0.3 \mu m$ (white zones). In addition, the apertures between parenthesis correspond to the crack conditions after an uniform reduction in the apertures that emulates an increase of the confining pressure.	237

A.10	Real part of the P-wave modulus and attenuation as functions of frequency for the interconnected cracks presented in Figure A.9 and for interconnected planar cracks having the minimum, the mechanical and the hydraulic apertures of the Models A and B.	237
A.11	Real part of the P-wave modulus and attenuation as functions of frequency for the interconnected cracks presented in Figure A.3 having 5% and 10% of contact area density (CAD) and for interconnected planar cracks having their equivalent hydraulic apertures. Same curves of those models with binary aperture before the emulated confining pressure increment are also included.	238
A.12	Real part of the P-wave modulus and attenuation as functions of frequency for the interconnected cracks presented in Figure A.9 having 20% of contact areas and for interconnected plane cracks having their hydraulic apertures. Same curves of Models A and B before the emulated confining pressure increment are also included.	239
A.13	Model composed by four RUCs as the one presented in Figure A.1 having two planar cracks with $2.7 \mu\text{m}$ of aperture.	242
A.14	Real part of the P-wave modulus $\text{Re}(H)$ and attenuation $1/Q_p$ as functions of frequency for two models composed by one and four RUCs (as the one presented in Figure A.13) having planar cracks with $2.7 \mu\text{m}$ of aperture.	243
B.1	Typical calculation cycle of a MPM solver for a homogeneous velocity field, inspired by <i>Dunatunga and Kamrin</i> (2017). a) The continuum (orange) is discretized into a set of Lagrangian material points (red dots), at which state variables or properties (e.g., mass, stress, and velocity) are defined. The latter are mapped to an Eulerian finite element mesh made of nodes (blue square). b) Momentum equations are solved at the nodes and, the solution is explicitly advanced forward in time. c) The nodal solutions are interpolated back to the material points and, their properties are updated.	248
B.2	Nodal connectivities of a) standard MPM, b) GIMPm and c) CPDI2q variants. The material point's location is marked by the blue cross. Note that for sMPM (and similarly BSMMPM) the particle domain does not exist, unlike GIMPm or CPDI2q (the blue square enclosing the material point). Nodes associated with the material point are denoted by filled blue squares, and the element number appears in green in the centre of the element. For sMPM and GIMPm, the connectivity array between the material point and the element is $p2e$ and, the array between the material point and its associated nodes is $p2N$. For CPDI2q, the connectivity array between the corners (filled red circles) of the quadrilateral domain of the material point and the element is $c2e$ and, the array between the corners and their associated nodes is $c2N$	249
B.3	Workflow of the explicit GIMPm solver and the calls to functions within a calculation cycle. The role of each function is described in the text.	251
B.4	Code Fragment 1 shows the vectorised solution to the calculation of the basis functions and their derivatives within <code>SdS.m</code> . Table B.3 lists the variables used.	254
B.5	Code Fragment 2 shows the vectorised solution to the nodal projection of material point quantities (e.g., mass and momentum) within the local function <code>p2Nsolve.m</code> . The core of the vectorization process is the extensive use of the built-in function of MATLAB [®] <code>accumarray()</code> , for which we detail the main features in the text. Table B.3 lists the variables used.	255
B.6	a) Wall-clock time to solve for a matrix multiplication between a multidimensional array and a vector with an increasing number of the third dimension with a double arithmetic precision and, b) number of floating point operations per second (flops) for single and double arithmetic precisions. The continuous line represents the averages value whereas the shaded area denotes the standard deviation.	256
B.7	Code Fragment 3 shows the vectorised solution for the interpolation of nodal solutions to material points with a double mapping procedure (or MUSL) within the function <code>mapN2p.m</code>	257
B.8	Initial geometry of the column.	259
B.9	a) Convergence of the error: a limit is reached at error $\approx 2 \cdot 10^{-6}$ for the explicit solver, whereas the quasi-static solution still converges. This was already demonstrated in <i>Bardenhagen and Kober</i> (2004) as an error saturation due to the explicit scheme, i.e., the equilibrium is never resolved. b) The stress σ_{yy} along the y -axis predicted at the deformed position y_p by the CPDI2q variant is in good agreements with the analytical solution for a refined mesh.	260

B.10	Wall-clock time for cpGIMPM (vectorised and iterative solutions) and the CPDI2q solution with respect to the total number of material points n_p . There is no significant differences between CPDI2q and cpGIMPM variants regarding the wall-clock time. The iterative implementation is also much slower than the vectorised implementation.	260
B.11	Initial geometry for the cantilever beam problem; the free end material point appears in red where a red cross marks its centre.	261
B.12	Vertical deflection Δu for the cantilever beam problem. The black markers denote the solutions of <i>Sadeghirad et al.</i> (2011) (circles for CPDI and squares for FEM). The line colour indicates the MPM variant (blue for CPDI and red for cpGIMP), solid lines refer to a linear elastic solid, whereas dashed lines refer to a neo-Hookean solid. Δu corresponds to the vertical displacement of the bottom material point at the free end of the beam (the red cross in Fig. B.11).	261
B.13	Finite deformation of the material point domain and vertical Cauchy stress σ_{yy} for CPDI, i.e., a) & b), and for cpGIMPM, i.e., c) & d). The CPDI variant gives a better and contiguous description of the material point's domain and a slightly smoother stress field, compared to the cpGIMPM variant, which is based on the stretch part of the deformation gradient.	262
B.14	Initial geometry for the slump problem from <i>Huang et al.</i> (2015). Roller boundary conditions are imposed on the left and right of the domain while a no-slip condition is enforced at the base of the material.	263
B.15	MPM solution to the elasto-plastic slump. The red lines indicate the numerical solution of <i>Huang et al.</i> (2015) and, the coloured points indicate the second invariant of the accumulated plastic strain ϵ_{II} obtained by the CPDI solver. An intense shear zone progressively develops backwards from the toe of the slope, resulting in a circular failure mode.	264
B.16	Initial geometry for the elasto-plastic collapse (<i>Huang et al.</i> , 2015). Roller boundaries are imposed on the left and right boundaries of the computational domain while a no-slip condition is enforced at the bottom of the domain. The aluminium-bar assemblage has dimensions of $l_0 \times h_0$ and is discretized by $n_{pe} = 4$ material points per initially populated element.	264
B.17	Final geometry of the collapse: in the intact region (horizontal displacement $u_x < 1$ mm), the material points are coloured in green, whereas in the deformed region (horizontal displacement $u_x > 1$ mm), they are coloured in red and indicate plastic deformations of the initial mass. The transition between the deformed and undeformed region marks the failure surface of the material. Experimental results of (<i>Bui et al.</i> , 2008) are depicted by the blue dotted lines. The computational domain is discretized by a background mesh made of 320×48 quadrilateral elements with $n_p = 4$ per initially populated element, i.e., a total $n_p = 12'800$ material points discretize the aluminium assemblage.	265
B.18	Number of floating point operation per seconds (flops) with respect to the total number of material point n_p for the vectorised implementation. The discontinuous lines refer to the functions of the solver, whereas the continuous line refer to the solver. A peak performance of 900 Mflops is reached by the solver for $n_p > 1000$ and, a residual performance of 600 Mflops is further resolved for an increasing n_p	266
B.19	Number of iterations per second with respect to the total number of material point n_p . The greatest performance gain is reached around $n_p = 1000$, which is related to the peak performance of the solver (see Fig. B.18). The gains corresponding to the peak and residual performances are 46 and 28 respectively.	266
C.1	Drucker-Prager yield surface in the $(\sigma_m - \tau)$ space. The yield surface is made of a shear line segment (in red) and a tensile line segment (in blue).	278
C.2	Schematic chip representation for both the central processing unit (CPU) and the graphical processing unit (GPU) architecture (<i>Nvidia</i> , 2007). The latter is made of thousands of arithmetic logical units (ALUs). The CPU architecture is primarily dedicated to controlling units and cache memory, and the physical space allowed for ALUs is considerably reduced compared to a GPU architecture.	280
C.3	Multifunctional workflow: 1) usage of MATLAB for data initialization, compilation and postprocessing activities and 2) system calls to a performant compiled language such as C (CPU-based) and CUDA C (GPU-based) for heavy calculations. Here, I/O stands for input/output, and the colouring (red or green) specifies which one is active, i.e., I/O means data only are transferred to the GPU (or CPU) for further calculation activities.	280

C.4	Specific workflow for the source code running of the GPU, t_{end} is a user-defined time that controls the total time of the simulation, and the operator $*$ stands for the pointer object, as in the C language. It should be noted that a vast majority of operations within kernels are performed on pointers.	281
C.5	Initial configuration for the granular collapse numerical model. The blue surrounding frame depicts the computational domain, i.e., the background Eulerian mesh, and the red volume is the granular material, which is discretized by 8 material points. The total number of background elements n_{el} depends on the number of elements in the x - direction $n_{el,x}$ used to discretize the granular material.	285
C.6	Final geometry of the granular collapse for three-dimensional configuration of our GPU-based explicit GIMPM implementation ep3De v1.0. The green region (i.e., the intact region) is defined by the L_2 -norm of the material point displacement $u_p = \ \mathbf{u}_p\ _2 \leq 0.5$ mm, whereas the red region (i.e., the deformed region) is defined by $u_p = \ \mathbf{u}_p\ _2 > 0.5$ mm. The experiment of <i>Bui et al.</i> (2008) is indicated by the blue dashed line (i.e., the free surface) and the blue dotted line (i.e., the failure surface).	286
C.7	Equivalent plastic strain ϵ_{eqv}^p for the final configuration of the granular collapse. The principal feature of a granular collapse can be observed, i.e., a backward propagation of plastic deformation along a principal failure surface.	286
C.8	Final geometry of the granular collapse for the plane-strain configuration for our GPU-based explicit GIMPM implementation ep2De v1.0. The numerical solution and the experimental results are in good agreement. Some differences are more pronounced when compared with the numerical results obtained under a three-dimensional configuration.	287
C.9	Equivalent plastic strain ϵ_{eqv}^p for the final configuration of the granular collapse. The dashed red rectangle denotes the location of the zoomed-in region in Fig. C.10 (a). One can observe more complex plastic strain localizations compared to the numerical results obtained in Fig. C.7 for a three-dimensional configuration with a coarser background mesh resolution.	288
C.10	(a) ϵ_{eqv}^p for the zoomed-in area in Fig. C.9. A shallow granular flow clearly appears, as suggested by the higher values of ϵ_{eqv}^p . This supports evidence of shallower granular avalanches during collapses. Deeper structures, which result in lower accumulated plastic strains, probably highlight slower deformation modes along well-defined and persistent shear bands. (b) ϵ_{eqv}^p for a coarser background mesh resolution, which demonstrates the influence of the mesh resolution over shear bands.	288
C.11	Geometry for the earth slump. The number of elements in the y -direction $n_{el,y}$ and the width of the problem l_y are variable. This allows us to increase (or decrease) the number of both elements and material points without decreasing the mesh resolution. The parameter n controls the dimension of the domain and the number of elements along the y -direction. The wall-clock time depends only on the total number of elements, nodes and material points and is not influenced by the mesh resolution.	288
C.12	a) Effective memory throughput MTP_{eff} of the solver ep2-3De v1.0 for double-arithmetic precision. One can see the on-chip memory limit, as both the RTX 2080 ti and V100 cannot resolve the same number of material points as the RTX 3090. b) GPU on-chip memory load increases with the number of material points n_{mp} , which demonstrates, as expected, one of the GPU's hardware limits.	290
C.13	a) Wall-clock time reported for various computing architectures (GPUs and CPU). The differences in the maximal number of material points n_{mp} are due to the on-chip memory limit. A significant difference in terms of wall-clock time is observed between the CPU and GPUs, even for the low-entry consumer electronic GTX 1650, i.e., a performance gain of $\approx 10\times$. b) Performance gains of GPUs relative to the CPU, i.e., $1\times$ as a baseline. We add the CPU and the GTX 1650 wall-clock time for an easier comparison.	291
C.14	Domain partition of the material points amongst 8 GPUs. Combined with an overlap of 8 elements along the y -direction, material points can moderately move while still residing within the same GPU during the whole simulation.	292
C.15	Wall-clock time for 1, 2, 4 and 8 Tesla V100 GPUs.	292
C.16	Sum across the GPUs involved of the MTP_{eff} . We roughly report a weak scaling between the number of GPUs and the overall effective memory throughput.	293
C.17	Wall-clock time reported for up to 128 Geforce GTX Titan X GPUs and up to $n_{mp} \approx 9.75 \cdot 10^8$	293

C.18	MTP _{eff} sum across the GPUs involved.	293
C.19	Displacement field obtained after $t = 15$ s for a homogeneous peak cohesion field. One can see an overall homogenous displacement field with some of the first-order characteristics of a slump, i.e., a rotational displacement with a compression zone at the toe, a transition zone delimited by one principal shear zone and a major scarp at the top of the material.	294
C.20	Displacement field obtained after $t = 15$ s for a heterogeneous peak cohesion field with a Gaussian covariance function.	295
C.21	Heterogeneous cohesion field with an exponential covariance function: time evolution of the equivalent plastic strain ϵ_{eqv}^p . Similar to Fig. C.27, heterogeneous behaviour is observed. However, the exponential covariance function results in an even more complex pattern of strain localization, i.e., minor and major scarps develop at the top. The crown-like structure of the slump becomes even more heterogeneous.	296
C.22	Displacement field obtained after $t = 15$ s for a heterogeneous peak cohesion field with an exponential covariance function.	297
C.23	a) Numerical solution without any volumetric locking strategy and b) numerical solution with the proposed volumetric locking strategy. For both cases, no damping is introduced.	302
C.24	Non-smooth pressure field due to volumetric locking. The typical check-board pattern of volumetric locking can be observed where the material has yielded, i.e., the shear band.	302
C.25	Smoother pressure field when volumetric locking is mitigated with the proposed solution.	303
C.26	Homogeneous cohesion field: time evolution of the equivalent plastic strain ϵ_{eqv}^p . Its evolution is rather homogeneous, and the overall plastic behaviour is free of any heterogeneities. Some of the first-order characteristics are observed, i.e., a principal shear zone and a compression zone at the toe of the slump.	304
C.27	Heterogeneous cohesion field with a Gaussian covariance function: time evolution of the equivalent plastic strain ϵ_{eqv}^p . Unlike Fig. C.26, heterogeneous behaviour is observed, i.e., the appearance of a second shear zone highlights a more complex deformation pattern. Moreover, a crown-like structure starts to develop at the top of the material, where an initial weak zone is located.	305
C.28	Heterogeneous cohesion field with an exponential covariance function: time evolution of the equivalent plastic strain ϵ_{eqv}^p . Similar to Fig. C.27, heterogeneous behaviour is observed. However, the exponential covariance function results in an even more complex pattern of strain localization, i.e., minor and major scarps develop at the top. The crown-like structure of the slump becomes even more heterogeneous.	306

List of Tables

2.1	The material properties used for all numerical simulations.	20
2.2	Geometrical properties for $P_f = 0$ model, <i>Big pore</i> model and <i>Small pore</i> model. Major radius — the distance from the center of the tube to the center of the torus. Minor radius — the radius of the tube.	20
3.1	Material properties of the numerical model.	44
4.1	Geometrical properties for the Big pore model and the Small pore model. Major radius — the distance from the center of the tube to the center of the torus. Minor radius — the radius of the tube (our isometric pore).	78
4.2	Material properties used in all models.	78
5.1	Geometrical properties for the Big pore model. Major radius — the distance from the center of the tube to the center of the torus. Minor radius — the radius of the tube (our isometric pore). The volume of the fractions of the torus for models (1/9 torus, 4/9 torus, 6/9 torus, 8/9 torus) correspond to the fractions (1/9, 4/9, 6/9, 8/9) of the Big torus model, respectively.	96
5.2	Material properties used in all models.	96
5.3	Geometrical properties for the 1, 2, 4 spheres models and the Big torus model with crack aspect ratio $\alpha = 0.01$	98
6.1	List of Principal Notation	114
6.2	Shorthand notations	115
6.3	Poroelastic properties of carbonate.	120
6.4	Properties of anisotropic poroelastic rocks used for numerical simulations. VTI corresponds to a vertical transverse isotropic medium.	137
7.1	List of Principal Notation	162
7.2	Summary of CFL conditions for different schemes in Example 1	169
7.3	Summary of CFL conditions for different schemes in Example 2	172
7.4	Material parameters of a sandstone.	174
7.5	List of Principal Notation	182
A.1	Material properties of the models.	229
A.2	Apertures for crack models presented in Figure A.9	236
A.3	Apertures for crack binary models with contact areas	238
A.4	Apertures for crack models with contact areas presented in Figure A.9	239
B.1	Efficiency comparison of the Julia implementation of <i>Sinaie et al.</i> (2017), and the MATLAB-based implementation for the two elastic disk impact problems.	267
B.2	Acronyms used throughout the manuscript	270
B.3	Variables of the structure arrays for the mesh <code>meD</code> and the material point <code>mpD</code> used in Code Fragment 1 & 2 shown in Figs. B.4 & B.5. <code>nDF</code> stores the local and global number of degrees of freedom, i.e., $nDF = [nNe, nN*DoF]$. The constant <code>nstr</code> is the number of stress components, according to the standard definition of the Cauchy stress tensor using the Voigt notation, e.g., $\sigma_p = (\sigma_{xx}, \sigma_{yy}, \sigma_{xy})$	272

C.1	List of the graphical processing units (GPUs) used throughout this study. We also report the peak memory throughput, i.e., MTP_{peak} , measured thanks to the routine <code>bandwidthTest.cu</code> provided by Nvidia alongside with the CUDA toolkit. When compared with the effective memory throughput MTP_{eff} , one can estimate the possible gain of an additional optimization of the algorithm. This is particularly useful when estimating the level of optimization of a GPU-based implementation.	283
C.2	List of the graphical processing units (GPUs) used for multi-GPU simulations.	284
C.3	Parameters used in Models 1 a & b for the granular collapse. $n_{el,i}$ is the number of elements to discretize the granular material along the i -th direction, n_{el} and n_{no} are the total number of elements and nodes of the background mesh, n_{pe} is the number of material points per element and n_{mp} is the total number of material points. Note that the mesh resolution is $\Delta x = \Delta y = \Delta z = 2.5$ mm.	285
C.4	Material properties shared by both Models 2a & 2b.	289
C.5	Geometrical and material properties for Models 2a & 2b. The correlation length vector is $\boldsymbol{\lambda} = (\lambda_x, \lambda_y, \lambda_z) = (2.5, 2.5, 2.5)$ m for both Gaussian and exponential isotropic covariance functions. The grid spacing is always constant in Models 2a & 2b, i.e., $\Delta z = \Delta y = \Delta x = 0.8$ m	290

Résumé

La majorité des processus physiques sur Terre sont couplés. Un processus physique peut en induire un autre, ce qui est le cas d'une onde se propageant dans une roche poreuse saturée de fluide, ce qui induit un écoulement de fluide. Dans un milieu biphasique, l'interaction entre les phases solides et fluides conduit à des effets physiques qui ne sont pas observés dans un milieu monophasique. Ainsi, une description satisfaisante de systèmes physiques complexes nécessite un traitement particulier.

L'application des théories décrivant les processus physiques couplés dans les roches poreuses fracturées est d'une grande importance dans les scénarios impliquant la séquestration géologique du CO_2 , l'élimination des déchets nucléaires, l'exploration et la production d'énergie géothermique et les hydrocarbures. Le développement de méthodes géophysiques non invasives de détection et de surveillance de ces formations géologiques est crucial. La recherche scientifique vise à faire progresser la description quantitative et qualitative des processus physiques couplés dans les roches poreuses. Conformément à ces objectifs, les contributions présentées ici sont réparties dans quatre disciplines différentes : la micromécanique, la géophysique, la mécanique computationnelle et la poroélasticité computationnelle, et la théorie des instabilités non linéaires. Différentes méthodes analytiques et numériques sont utilisées pour résoudre la physique aux micro- et macro-échelles. Cela comprend l'étude des processus linéaires quasi-statiques et dynamiques. Ce travail de recherche contient également des résultats basés sur la théorie des processus physiques non linéaires.

À l'échelle microscopique (ou à l'échelle des pores), une roche est constituée de grains, de pores et de fractures individuels. De petites déformations causées par une onde sismique se propageant à travers la roche induisent des gradients de pression dans les fractures conformes. En conséquence, un écoulement de fluide (appelé "écoulement de jet") a lieu jusqu'à ce que la pression interstitielle s'équilibre. En raison de la viscosité du fluide et du frottement visqueux associé, un tel écoulement de fluide provoque une forte dissipation d'énergie. Des simulations numériques tridimensionnelles de l'écoulement de jet à l'aide d'une approche par éléments finis sont effectuées et les résultats sont comparés à un modèle analytique publié. À partir de cette comparaison, de nombreuses limitations de la solution analytique publiée sont quantifiées et décrites. Par la suite, un nouveau modèle analytique pour la dispersion sismique et l'atténuation associées à l'écoulement de jet est présenté pour une géométrie de pores qui a été classiquement utilisée pour expliquer ce mécanisme d'expulsion de l'eau. Ensuite, ce modèle analytique est étendu pour traiter des géométries plus complexes de l'espace poreux, beaucoup plus représentatives de celle d'une roche. Les paramètres clés de l'espace poreux qui contrôlent la fréquence caractéristique (à laquelle se produit le maximum d'atténuation) sont redéfinis. De plus, des expressions analytiques pour calculer les propriétés de rigidité effective d'un modèle de roche, dont l'espace poreux est décrit par une fracture reliée à un pore ou à plusieurs pores, sont fournies.

À l'échelle macroscopique, une roche poreuse peut être décrite par un ensemble de propriétés macroscopiques, par exemple, les modules élastiques effectifs, la perméabilité, etc. Les équations de Biot décrivent un système couplé hydro-mécaniquement et établissent la théorie largement reconnue de la poroélasticité. Le milieu biphasique est représenté par une matrice poreuse solide élastique saturée d'un fluide visqueux compressible. La réponse dynamique d'un tel milieu biphasique et isotrope se traduit par deux ondes longitudinales et une onde de cisaillement, comme prédit par Yakov Frenkel. La modélisation numérique efficace et précise des équations de la poroélasticité de Biot nécessite la connaissance des conditions exactes de stabilité. Cette recherche présente les résultats de l'analyse de stabilité de von Neumann des équations de Biot discrétisées et de l'équation d'onde amortie linéaire discrétisée. Les conditions exactes de stabilité pour un certain nombre de schémas implicites et explicites sont dérivées. De plus, un solveur numérique d'unités de traitement multi-graphiques (GPU) est développé pour résoudre les équations élastodynamiques anisotropes de Biot afin de simuler, en quelques secondes, des champs d'ondes pour des domaines spatiaux impliquant plus de 4,5 milliards de mailles. Une analyse dimensionnelle complète est présentée, réduisant ainsi le nombre de paramètres matériels nécessaires pour les expériences numériques de dix à quatre. Une analyse de dispersion en fonction de paramètres adimensionnels est effectuée, conduisant à des relations de dispersion simples et transparentes. La haute efficacité de notre implémentation numérique la rend facilement accessible pour étudier des scénarios tridimensionnels et à haute résolution d'applications pratiques.

Dans le cadre de la théorie des instabilités non linéaires, une nouvelle théorie de la nucléation sismique est présentée. La rhéologie visco-plastique ou élasto-plastique la plus simple permet de modéliser la nucléation sismique spontanée. En augmentant lentement la contrainte dans le milieu, elle atteint la limite plastique, produisant ainsi la localisation de la déformation et entraînant le développement lent de bandes de cisaillement fractales. Au fil du temps, ces dernières se développent spontanément et des chutes de contrainte se produisent dans le milieu. Une chute de contrainte correspond à un nouveau modèle particulier de localisation de déformation, qui agit alors comme source sismique et déclenche la propagation des ondes sismiques. Cette nouvelle approche de modélisation est basée sur des lois de conservation sans aucune relation constitutive dérivée expérimentalement.

Mots clefs : Roches poreuses, atténuation, squirt flow, poroélasticité, GPU, propagation des ondes, localisation des déformations.

Abstract

The majority of the physical processes on the Earth are coupled. A physical process might induce a different one, which is the case of a wave propagating in a fluid-saturated porous rock and inducing fluid flow. In a two-phase medium, the interaction between solid and fluid phases leads to physical effects, that are not observed in a single-phase medium. Thus, a successful description of complex physical systems requires special treatment.

The applications of theories describing coupled physical processes in cracked porous rocks are of great importance in scenarios involving CO_2 geological sequestration, nuclear waste disposal, the exploration and production of geothermal energy, and hydrocarbons. Developing non-invasive geophysical detection and monitoring methods for these geological formations is crucial. Scientific research aims to advance the quantitative and qualitative description of coupled physical processes in porous rocks. In line with these objectives, the contributions presented here are distributed across four different disciplines: micromechanics, geophysics, computational mechanics and computational poroelasticity, and the theory of non-linear instabilities. Different analytical and numerical methods are used to resolve the physics at the micro- and macro-scales. It includes the study of linear quasi-static and dynamic processes. This research work also contains some results based on the theory of non-linear physical processes.

At the micro-scale (or pore-scale), a rock consists of individual grains, pores, and cracks. Small deformations caused by a passing seismic wave propagating through the rock induce pressure gradients in compliant cracks. As a result, fluid flow (so-called squirt flow) takes place until the pore pressure equilibrates. Due to the fluid viscosity and the associated viscous friction, such fluid flow causes strong energy dissipation. Three-dimensional numerical simulations of squirt flow using a finite-element approach are performed and the results are compared against a published analytical model. From this comparison, many limitations of the published analytical solution are quantified and described. Subsequently, a new analytical model for squirt flow associated seismic dispersion and attenuation is presented for a pore geometry that has been classically used to explain squirt flow. Then, this analytical model is extended to deal with more complex geometries of the pore space, which are much more closely representative of that of a rock. The key parameters of the pore space which control the characteristic frequency (at which the maximum of attenuation occurs) are re-defined. Additionally, closed-form analytical expressions to calculate the effective stiffness properties of a rock model whose pore space is described by a crack connected to a pore or multiple pores are provided.

At the macro-scale, a porous rock can be described by a set of macroscopic properties, e.g., effective elastic moduli, permeability, etc. Biot's equations describe a hydro-mechanically coupled system and establish the widely recognized theory of poroelasticity. The two-phase medium is represented by an elastic solid porous matrix saturated with a compressible viscous fluid. The dynamic response of such an isotropic two-phase medium results in two longitudinal waves and one shear wave, as predicted by Yakov Frenkel. The efficient and accurate numerical modeling of Biot's equations of poroelasticity requires the knowledge of the exact stability conditions. This research presents the results of the von Neumann stability analysis of the discretized Biot's equations and the discretized linear damped wave equation. The exact stability conditions for several implicit and explicit schemes are derived. Additionally, a multi-graphical processing units (GPU) numerical solver is developed to resolve the anisotropic elastodynamic Biot's equations to simulate, in a few seconds, wave fields for spatial domains involving more than 4.5 billion grid cells. A comprehensive dimensional analysis is presented reducing the number of material parameters needed for the numerical experiments from ten to four. A dispersion analysis as a function of dimensionless parameters is performed leading to simple and transparent dispersion relations. The high efficiency of our numerical implementation makes it readily accessible to investigate three-dimensional and high-resolution scenarios of practical applications.

As a part of the theory of non-linear instabilities, a new theory for earthquake nucleation is presented. The simplest visco-plastic or elasto-plastic rheology allows us to model spontaneous earthquake nucleation. By slowly increasing the stress in the medium, it reaches the yield surface, strain localization occurs resulting in the slow development of fractal shear bands. As time evolves, shear bands grow spontaneously, and stress drops take place in the medium. A stress drop corresponds to a particular new strain localization pattern which acts as

seismic source and triggers seismic wave propagation. This new modeling approach is based on conservation laws without any experimentally derived constitutive relations.

Key words: Porous rocks, attenuation, squirt flow, poroelasticity, GPU, wave propagation, strain localization.

Curriculum Vitae

Personal information

Yury Alkhimenkov

Geophysicist

alkhimenkov.yury@gmail.com | Skype: alkhimenkov.yury

Personal Website: <https://sites.google.com/view/yury-alkhimenkov/>

Google Scholar: https://scholar.google.ru/citations?user=Sx_8GPoAAAAJ&hl=en

ResearchGate: https://www.researchgate.net/profile/Yury_Alkhimenkov

ORCID: <http://orcid.org/0000-0002-6529-9256>

Objective

Main interests are 3D GPU-based numerical modeling, e.g., dynamic and quasi-static response of two-phase (poroelastic) media; pressure-dependent plasticity in rocks; seismic attenuation and dispersion at different scales (numerical modeling and analytical models).

Co-authored 10 published peer reviewed articles, q1 and q2 (6 as the first author), 3 more articles are under preparation.

Education

- 03/2018 – 05/2022 **University of Lausanne** (Lausanne, Switzerland)
Ph.D. in Geophysics
Supervisors: Beatriz Quintal, Yury Y. Podladchikov
- 09/2015 – 09/2017 **IDEA League, Joint Master's in Applied Geophysics**
Swiss Federal Institute of Technology in Zurich (Zurich, Switzerland)
MSc (with honors) in Applied Geophysics
Delft University of Technology (Delft, Netherlands)
MSc (with honors) in Applied Geophysics
RWTH Aachen University (Aachen, Germany)
MSc (with honors) in Applied Geophysics
Supervisors: Joeri Brackenhoff, Kees Wapenaar
- 09/2013 – 08/2015 **Lomonosov Moscow State University** (Russia), GPA: 4.8/5.0
MSc in Seismic Exploration
Supervisor: Irina Bayuk
- 09/2009 – 08/2013 **Lomonosov Moscow State University** (Russia), GPA: 4.8/5.0
BSc (with honors) in Geophysics
Supervisor: Irina Bayuk

Work Experience

- 03/2018 – Present Research/Teaching Assistant, University of Lausanne (Lausanne, Switzerland)
Supervisors: Beatriz Quintal
- 12/2014 – 7/2015 RN-Exploration (Moscow, Russia), Geophysicist, 23rd Licensing Round in the Barents Sea; Responsible for AVO/AVA, attribute analysis, velocity model building, well tie and presentations; Used Landmark DS Geophysics and Hampson-Russell software
- 01/2014 – 12/2014 IPERAS - Institute of Physics of the Earth of the Russian Academy of Sciences (Moscow, Russia), Lead Engineer & Research Geophysicist, Responsible for rock physics modeling using Effective Medium Theory. Supervisor: Irina Bayuk.

Institutional responsibilities and teaching activities

Teaching Assistant in the annual *field work*, responsible for ground-penetrating radar course.

Teaching Assistant in the *numerical modeling course*, the lecturer is Ludovic Räss.

Research Assistant: writing articles, collaborating with researches, participating in the conferences.

Individual scientific reviewing activities

Reviewing articles for peer-reviewed journals:

Journal of Geophysical Research: Solid Earth (Wiley) – 1 article
Geophysics (Society of Exploration Geophysicists) – 4 articles
Geophysical Journal International (Oxford University Press) – 2 articles
Frontiers in Earth Science – 1 article

Memberships in scientific societies

European Geosciences Union (EGU), Society of Exploration Geophysicists (SEG), European Association of Geoscientists and Engineers (EAGE), Society for Industrial and Applied Mathematics (SIAM)

Prizes, Awards, Fellowships

12/2021	Swiss National Science Foundation fellowship for young outstanding scientists (90,000 CHF)
09/2015	IDEA League Scholarship Award, Sponsored by Royal Dutch Shell (€50,000)
09/2015	Regional Student Paper Contest Winner; Society of Petroleum Engineers https://www.spe.org/en/students/contest/winners/
06/2014	Best Scientific Presentation, Russian Academy of Sciences
02/2014	Chevron Award

Personal skills

English: Full professional proficiency; Russian: Native

Working knowledge of: Matlab, CUDA C, Maple, FORTRAN90, LaTeX and Microsoft Office applications;
Basic knowledge: Python, ProMAX, Hampson-Russell software, Landmark DS software, Petrel 2015.

Special Courses/Certifications

9/2017	Concepts and Applications in 3D Seismic Imaging, Biondo L. Biondi, SEG (USA)
06/2015	Understanding Seismic Anisotropy in Exploration and Exploitation: Hands On, Leon Thomsen, the 77th EAGE Conference & Exhibition 2015 (Madrid, Spain)
04/2015	Seismic Data Management & Decision Space, Landmark, Halliburton (Moscow, Russia)
08/2014-10/2014	IELTS Preparation Course, Education First (Oxford, UK)
08/2015-03/2018	Weekly Private 1-on-1 English Lessons with www.SchoolOf2.us (online)

Research output list

Publications in peer-reviewed scientific journals resulting from my PhD

- 10 **Alkhimenkov, Y.**, Quintal, B. An accurate analytical model for squirt flow in anisotropic porous rocks - Part 2: Complex geometry. *Geophysics*. (Submitted)
- 9 **Alkhimenkov, Y.**, & Quintal, B. (2022). An accurate analytical model for squirt flow in anisotropic porous rocks - Part 1: Classical geometry. *Geophysics*, 87(2), MR85-MR103.
- 8 Wyser E., **Alkhimenkov Y.**, Jaboyedoff M., Podladchikov Y.Y. (2021) An explicit GPU-based material point method solver for elastoplastic problems (ep2-3De v1.0). *Geoscientific Model Development (GMD)*.
- 7 Wang, L. H., Yarushina, V., **Alkhimenkov, Y.**, & Podladchikov, Y. (2021). Physics-inspired pseudo-transient method and its application in modelling focused fluid flow with geological complexity. *Geophysical Journal International*.
- 6 **Alkhimenkov, Y.**, Räss, L., Khakimova, L., Quintal, B., & Podladchikov, Y. (2021). Resolving wave propagation in anisotropic poroelastic media using graphical processing units (GPUs). *Journal of Geophysical Research: Solid Earth*, e2020JB021175.
<https://agupubs.onlinelibrary.wiley.com/doi/full/10.1029/2020JB021175>
- 5 **Alkhimenkov, Y.**, Khakimova, L., & Podladchikov, Y. Y. (2021). Stability of discrete schemes of Biot's poroelastic equations. *Geophysical Journal International*, 225(1), 354-377.
<https://doi.org/10.1093/gji/ggaa584>
- 4 Wyser, E., **Alkhimenkov, Y.**, Jaboyedoff, M., & Podladchikov, Y. Y. (2020). A fast and efficient MATLAB-based MPM solver: fMPMM-solver v1. 1. *Geoscientific Model Development*, 13(12), 6265-6284.
<https://doi.org/10.5194/gmd-13-6265-2020>
- 3 **Alkhimenkov, Y.**, Caspari, E., Lissa, S., & Quintal, B. (2020). Azimuth-, angle- and frequency-dependent seismic velocities of cracked rocks due to squirt flow. *Solid Earth*, 11(3), 855-871.
<https://doi.org/10.5194/se-11-855-2020>
- 2 Lissa, S., Barbosa, N. D., Caspari, E., **Alkhimenkov, Y.**, & Quintal, B. (2020). Squirt flow in cracks with rough walls. *Journal of Geophysical Research: Solid Earth*, 125(4), e2019JB019235.
<https://agupubs.onlinelibrary.wiley.com/doi/full/10.1029/2019JB019235>
- 1 **Alkhimenkov, Y.**, Caspari, E., Gurevich, B., Barbosa, N. D., Glubokovskikh, S., Hunziker, J., & Quintal, B. (2020). Frequency-dependent attenuation and dispersion caused by squirt flow: Three-dimensional numerical study. *Geophysics*, 85(3), MR129-MR145.
<https://library.seg.org/doi/10.1190/geo2019-0519.1>

Peer-reviewed conference proceedings

- **Alkhimenkov, Y.**, Khakimova, L., Raess, L., Quintal, B., & Podladchikov, Y. High-Resolution Numerical Simulation of Biot's Poroelastic Equations Using Multiple GPUs. (2021, June). In 2021 The Platform for Advanced Scientific Computing (PASC) Conference, University of Geneva, Geneva.
- **Alkhimenkov, Y.**, Quintal, B., & Podladchikov, Y. (2021, June). Numerical implementation of Biot's equations on graphical processing units. In Biot-Bazant Conference 2021.
- **Alkhimenkov, Y.**, Quintal, B., & Podladchikov, Y. (2021, June). Resolving Dynamic and Quasi-Static Physics in 3D Poroelastic Media using GPUs. SIAM Conference on Mathematical & Computational Issues in Geosciences.
- **Alkhimenkov, Y.**, Caspari, E., Lissa, S., & Quintal, B. (2021, December). Three-Dimensional Numerical Study of Frequency-Dependent Anisotropy of Cracked Rocks Due to Squirt Flow. In 82nd EAGE Annual Conference & Exhibition (Vol. 2020, No. 1, pp. 1-5). European Association of Geoscientists & Engineers.
- **Alkhimenkov, Y.**, Khakimova, L., Raess, L., Quintal, B., & Podladchikov, Y. (2021, December). Parallel Numerical Modeling of Poroelastic Wave Propagation Using Multiple NVIDIA Volta GPUs. In 82nd EAGE Annual Conference & Exhibition (Vol. 2020, No. 1, pp. 1-5).
- Bayuk, I., **Alkhimenkov, Y.**, & Barbosa, N. D. (2020). Seismic reflectivity and attenuation in viscoelastic fractured zones associated with Krauklis waves. In SEG Technical Program Expanded Abstracts 2020 (pp. 2590-2594). Society of Exploration Geophysicists.
- **Alkhimenkov, Y.**, Caspari, E., Barbosa, N. D., Glubokovskikh, S., Gurevich, B., & Quintal, B. (2019). Numerical study of dispersion and attenuation caused by squirt flow. In SEG Technical Program Expanded Abstracts 2019 (pp. 3563-3567). Society of Exploration Geophysicists.
- **Alkhimenkov, Y.**, & Bayuk, I. (2018). Stiffness tensor dispersion and seismic attenuation in fractured rocks modeled using the T-matrix approach and Krauklis Wave theory. In SEG Technical Program Expanded Abstracts 2018 (pp. 3542-3546). Society of Exploration Geophysicists.
- **Alkhimenkov, Y.**, Brackenhoff, J., Slob, E., Wapenaar, K. (2018). Q-factor Estimation and Redatuming in a Lossy Medium Using the Marchenko Equation. At the 80th EAGE Conference and Exhibition 2018.
- **Alkhimenkov, Y.** and Bayuk, I. (2017). Unified Effective Medium Theory for Cracked Porous Rocks: Theory and

Contributions to conferences

- **Alkhimenkov, Y.**, Quintal, B., & Podladchikov, Y. (2021, April). Fluid-total pressure partitioning in shear banding poro-visco-elasto-plastic media. In EGU General Assembly Conference Abstracts (pp. EGU21-15459).
- **Alkhimenkov, Y.**, Khakimova, L., Raess, L., Quintal, B., & Podladchikov, Y. (2020, May). GPU-based solution of Biot's elastodynamic equations to account for fluid pressure diffusion. In EGU General Assembly Conference Abstracts (p. 10287).
- Lissa, S., Barbosa, N. D., Caspari, E., **Alkhimenkov, Y.**, & Quintal, B. (2020, May). Seismic attenuation and velocity dispersion due to squirt flow in cracks with rough walls. In EGU General Assembly Conference Abstracts (p. 1424).
- Khakimova, L., **Alkhimenkov, Y.**, Cheremisin, A., & Podladchikov, Y. (2020, May). Modelling of nonlinear processes in deforming and reacting porous saturated rocks: different regimes for reaction front propagation. In EGU General Assembly Conference Abstracts (p. 19684).
- **Alkhimenkov, Y.**, Quintal, B., & Podladchikov, Y. (2019, January). GPU accelerated simulation of the elastodynamic Biot's equations. In Geophysical Research Abstracts (Vol. 21).

Outreach activities

Participation in the international science-art competition and exhibition in Lausanne [FIGURE 1.A.] in 2019 and in 2020.

Other artefacts with documented use

MSc Thesis - **TU Delft**:

Redatuming and Quantifying Attenuation from Reflection Data using the Marchenko Equation: A Novel Approach to Quantify Q-factor and Seismic Upscaling.

Supervisors: J. Brackenhoff and K. Wapenaar

<https://repository.tudelft.nl/islandora/search/Alkhimenkov?collection=education>

Unpublished work

Three articles are under preparation.

Chapter 1

Introduction

We know the age of the universe (*Ade et al.*, 2016) and it is widely accepted that the universe is expanding. Several accurate experimental studies, modeling studies and theories exist to support the two statements above. The Solar System is represented by the Sun and planets and other objects that orbit it. The third planet away from the Sun is the Earth and, as far as we know, the Earth is the only one that supports life. The evolution of successful biological populations based on organic compounds has resulted in a huge variety of organisms on the Earth. Particularly, some organisms reached certain level of evolution, the humans (or *Homo sapiens*), that resulted in the development of advanced culture, language, science and other complex social mechanisms. By "We" in the first sentence of this paragraph I meant humans. One amazing role of humanity is the scientific research and, thrilled to be part of this, my present thesis is devoted to the scientific development of new knowledge.

1.1 Coupling physical phenomena

The majority of the physical processes on the Earth are coupled. For example, seismic wave propagation in fluid saturated porous rocks cause wave-induced fluid flow. Therefore, a successful description of complex physical systems requires a special treatment. The purpose of this scientific research is to advance the quantitative and qualitative description of coupled physical processes in porous rocks. The contributions presented here are distributed across four different disciplines: micromechanics (*Eshelby*, 1957; *Nemat-Nasser and Hori*, 2013; *Kachanov and Sevostianov*, 2018), geophysics (*Mavko and Nur*, 1975; *O'Connell and Budiansky*, 1978), computational mechanics and computational poroelasticity (*Charney et al.*, 1950; *Harlow and Welch*, 1965; *Virieux*, 1986; *Frenkel*, 1944; *Biot*, 1962a) and the theory of non-linear instabilities (e.g., bifurcation theory) which are useful to describe spontaneous earthquake nucleation (*Poincaré*, 1885; *Rudnicki and Rice*, 1975; *Poliakov et al.*, 1994; *Sulem and Vardoulakis*, 1995; *Holzapfel*, 2000; *Yabuno*, 2021). I used different analytical and numerical methods in my research. I start my scientific journey from linear quasi-static and dynamic processes. Such linear approximations are, in principle, able to capture the key features of the studied phenomena. Then, I move on to non-linear physical processes and bifurcation theory. This is the most complex and advanced concept to describe coupled physical processes. Furthermore, this theory may have certain predictive power, which makes it highly attractive.

I divide my research into four branches (i-iv). The first two branches are denoted to study the coupled physical processes at the pore scale, the scale of individual grains and pores. It includes the (i) static and (ii) quasi-static response of a porous rock. The second two branches are denoted to study the coupled physical processes at the macro scale, by using derived equations for homogenized physical fields. It includes the modeling of (iii) wave propagation in fluid saturated porous rocks and the modeling of (iv) a non-linear quasi-static response resulting in strain localization. The strain localization is represented by fractal shear bands. A conceptual representation of the micro- and macro-scales is shown in Figure 1.1. Below, I provide a more detailed description of the four branches of my research.

Three main concepts were largely taken into account in my work: **coupling**, **averaging** and **resolving**:

Coupling stands for the coupled physical processes in complex systems. A porous rock saturated with a fluid is an example of such a system. A physical process taking place in the system might induce a different physical

process as it is the case of wave propagating in a fluid saturated rock and inducing pressure diffusion in the fluid.

Averaging denotes the two different features:

- Averaging of material parameters, averaged over a particular scale of interest.
- Averaging of physical fields to define a set of equations, which describe the physics at a particular scale of interest.

Resolving stands for tackling high spatial and temporal resolution in numerical solutions. We aim to be able to quantify all the important characteristics of the relevant fields during the modeling. If the goal is to obtain averaged quantities, then we calculate volume averages of those fields over the highly resolved spatial domains.

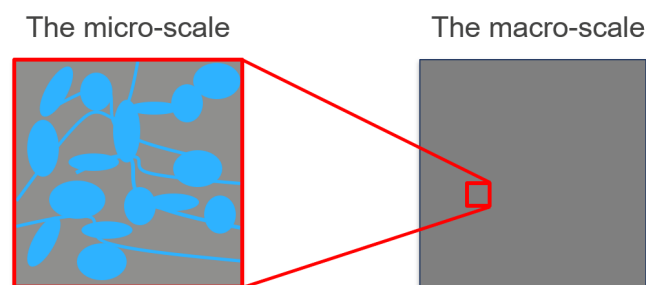


Figure 1.1: (a) Conceptual representation of rock structure at the micro- and macro-scales.

1.2 Coupled physics at the micro-scale (or pore scale)

At the micro-scale (or pore scale), a rock consists of individual grains, pores and cracks. The rock is heterogeneous at multiple scales (and at the micro-scale as well), thus any deformation applied to the rock will cause heterogeneous stress and strain distribution within its volume. If the rock is fluid saturated, an appropriate coupling between solid and fluid phases is needed.

Let us consider a particular setup of a fluid saturated cracked porous rock. Cracks are much more compliant than isotropic pores. Small deformations caused by a passing seismic wave propagating through the rock induce pressure gradients in compliant cracks. As a result, fluid flow (so called squirt flow) takes place until the pore pressure equilibrates. Due to the fluid viscosity and associated viscous friction, such fluid flow causes strong energy dissipation (*Mavko and Nur, 1975; O'Connell and Budiansky, 1978; Mavko and Jizba, 1991; Dvorkin et al., 1995; Pride et al., 2004; Gurevich et al., 2010; Müller et al., 2010*). This phenomenon results in significant dispersion and attenuation of seismic waves. Figure 1.2 shows a slice of a three-dimensional X-ray image of a rock (a) and the conceptual model of a rock (b) where an isotropic pore (torus) is connected to a crack (flat cylinder). Here this conceptual model is used to study the squirt flow numerically and analytically.

I study static and quasi-static processes the rock model. To accurately describe the elastic and visco-elastic properties of the model (Figure 1.2b), one needs (a) the static elastic moduli of the interconnected pore and crack and (b) and accurate description of the visco-elastic rock stiffness due to the fluid flow in the crack. The static elastic moduli can be calculated by applying a displacement boundary condition of the form u to a certain wall of the three-dimensional model (u is the displacement). Similarly, the visco-elastic moduli can be calculated by applying the displacement boundary condition of the form $u = 10^{-8} \times e^{i\omega t}$, where i is the imaginary unit, ω is the angular frequency and t is time.

One measure of seismic P-wave attenuation is defined as the so-called inverse quality factor $1/Q(\omega) = \text{Im}(M(\omega))/\text{Re}(M(\omega))$ (O'Connell and Budiansky, 1978), where $\omega = 2\pi f$ is the angular frequency (f is the frequency) and $M = K + 4/3G$ is the complex-valued P-wave modulus, K and G are the bulk and shear moduli, respectively.

We recall a brief overview of the physics based on previous analytical studies (Mavko and Jizba, 1991) with some additional information obtained from numerical simulations (Quintal et al., 2019; Alkhimenkov et al., 2020a,b; Lissa et al., 2020). In the physics of squirt flow, the cause of energy dissipation is fluid pressure diffusion at the pore scale. An idealized rock model can be parameterized by three components: solid elastic matrix, isometric pores and thin compliant cracks. Pores and cracks are interconnected and saturated with a fluid. A passing seismic wave deforms the compliant cracks more than the stiff pores, which causes fluid pressure gradients in the cracks. This results in fluid pressure diffusion, sometimes referred to as local fluid flow or squirt flow, which strongly depends on the frequency of the propagating wave.

At low-frequencies, the fluid pressure becomes uniform throughout the pore space because there is enough time for it to equilibrate (Figure 1.3). This is called relaxed state. The effective elastic properties can be calculated by using Gassmann's equations (Gassmann, 1951) given that the elastic moduli of the dry frame are known. At low-frequencies, $1/Q$ is proportional to $\approx \omega^1$ according to numerical simulations for simple geometries (Alkhimenkov et al., 2020a). At intermediate frequencies, the fluid pressure gradients are at their maximum, which corresponds to the attenuation peak. The frequency at which the attenuation is at its maximum is called the characteristic frequency ω_c . At high frequencies, there is no time for fluid to flow or fluid pressure to diffuse between cracks and pores; cracks behave as hydraulically isolated from pores. This is called unrelaxed state. The slope of the high-frequency asymptote of the attenuation curve depends on the pore geometry (Alkhimenkov et al., 2020a,b). If the pore space is represented by a penny shaped crack connected to a toroidal pore, then $1/Q$ at high-frequencies is proportional to $\approx \omega^{-1/2}$.

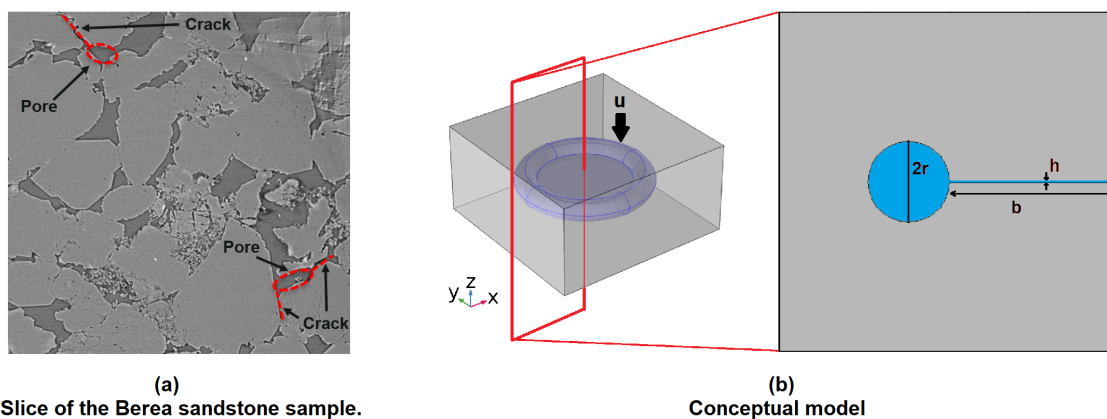


Figure 1.2: (a) A conceptual model of a rock and (b) a slice of a sandstone.

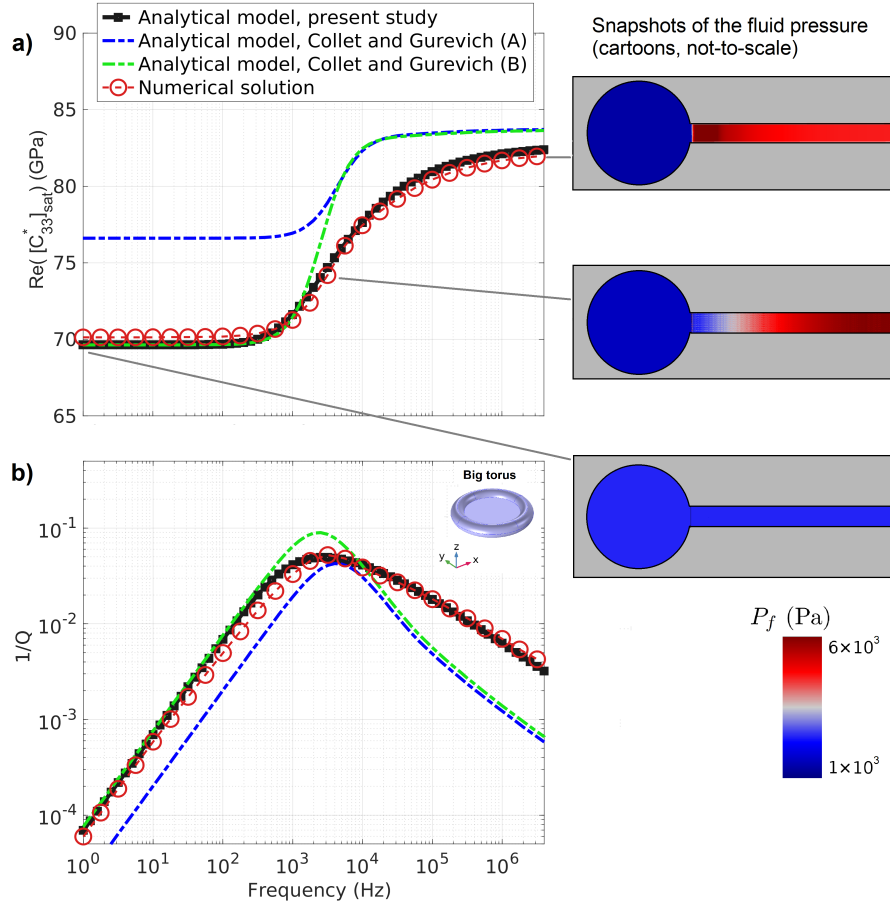


Figure 1.3: Numerical and analytical results for the Big pore model with a crack aspect ratio $\alpha = 0.005$: (a) Real part of the $[C_{33}^*]_{\text{sat}}$ component and (b) dimensionless attenuation for the $[C_{33}^*]_{\text{sat}}$ component. On the right, snapshots of the fluid pressure P_f at three different frequencies : LF - low frequency limit (relaxed state), Fc - intermediate frequency (close to the characteristic frequency) and HF - high frequency limit (unrelaxed state). The spatial dimension of the snapshots are not-to-scale and their colors representing the fluid pressure P_f correspond to a downward displacement (compression) of $u = 10^{-8} \times e^{i\omega t}$ m applied to the top boundary of the model.

1.3 Coupled physics at the macro-scale

At the macro-scale, a porous rock can be described by a set of macroscopic properties, e.g., effective (averaged) elastic moduli, permeability etc. Such properties can be measured and/or calculated numerically and analytically for a particular representative elementary volume (REV). Furthermore, a special set of equations should be used to model the coupled physics at the governing scale of interest.

Let us consider a porous rock saturated with a fluid. A set of equations describing such a hydro-mechanically (HM) coupled system is governed by Biot's equations (*Biot*, 1956b,a, 1962a,b), which establish the widely recognized theory of poroelasticity. The two-phase medium is represented by an elastic solid matrix (skeleton) saturated with a compressible viscous fluid. The dynamic response of such an isotropic two phase medium results in two longitudinal waves (Figure 1.4) and one shear wave, as predicted by Frenkel (*Frenkel*, 1944). The wave of the first kind is a true longitudinal P wave (primary wave or fast P-wave) where the solid matrix motion and the fluid particle velocity are in-phase. The wave of the second kind (slow P-wave) is a highly attenuated wave where the solid matrix motion and the fluid particle velocity are out-of-phase. Depending on the medium's properties, the slow wave may propagate as a longitudinal wave (Figure 1.5b), or it may diffuse and attenuate

quickly (Figure 1.5a). The fluid diffusion process exhibit a much larger characteristic time scale then the wave propagation process, therefore, a special numerical scheme is needed to resolve both processes simultaneously.

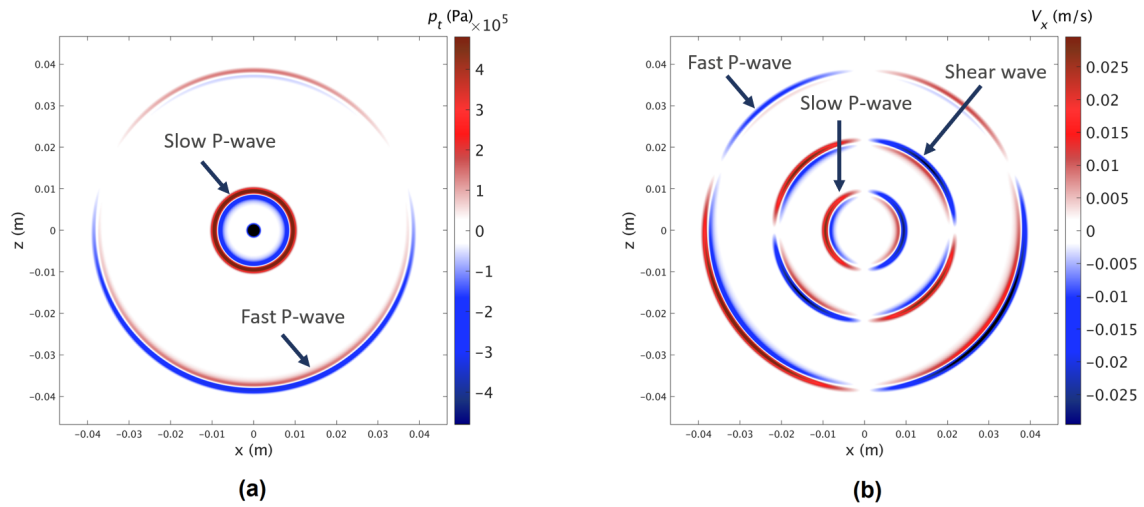


Figure 1.4: Snapshots of different fields from a numerical simulation of propagating waves in two-dimensional isotropic poroelastic media. Panel (a) shows the total pressure field where the fast P-wave and the slow P-wave are indicated. Panel (b) shows the velocity field in the x -direction, where the fast P-wave, shear wave and slow P-wave are visible.

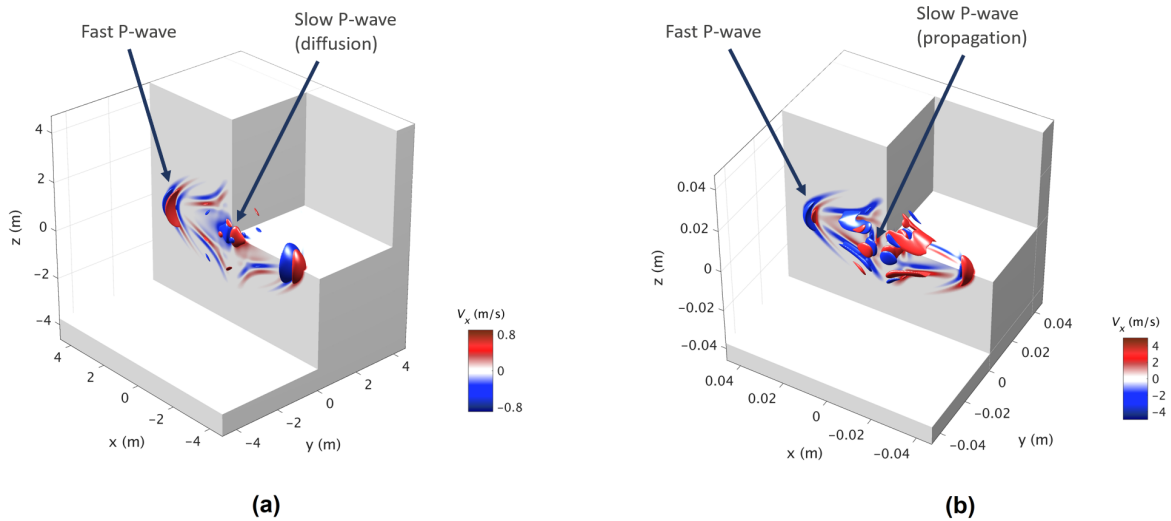


Figure 1.5: Snapshots of the velocity field in x -direction from a numerical simulation of propagating waves in three-dimensional anisotropic poroelastic media. Panels (a-b) show the velocity field. The slow P-wave behaves as a diffusion mode (a) and as a true propagating wave (b).

Non-linear instabilities and spontaneous earthquake nucleation

Earthquakes are seismic events that are caused in the Earth's subsurface either by natural processes (e.g. tectonic activity) or by anthropogenic activities (e.g. fluid injection). A lot of research has been done on the mechanism of seismic triggering events, but the physics behind earthquake nucleation is still poorly understood. The limitations in knowledge are associated with (i) oversimplified physics in analytical models and numerical simulations, which only describe a subset of features of the seismic cycle, (ii) usually one- or two-dimensional modeling studies bounded by the lack of computing power, (iii) lack of fully coupled physical models resolving thermo-hydro-mechanical interactions. All these limitations result in little predictive power of the current models.

We propose a new mechanism of earthquake nucleation (Figure 1.6), considering an elasto-plastic rheology, where the plasticity is implemented using a pressure-dependent Coulomb yield theory. So far in 2D, we apply a pure shear boundary condition and slowly increase shear stress in the simulation. At some point, the stress reaches the Coulomb yield surface and then local strain localizations start to develop (Minakov and Yarushina, 2021) resulting in fractal shear bands (Figure 1.6b). The evolution of the strain localizations is spontaneous and cannot be rigorously predicted. Per one load increment, only local new strain localisation appears which results in stress drop (Figure 1.6c). This new strain localisation can be visible in the anti-symmetric displacement field (Figure 1.6a), which corresponds to the initial condition for the earthquake nucleation. This triggering mechanism is similar to a particular double-couple (DC) moment tensor source, typically observed in real earthquakes. Real earthquakes may also include more complicated processes with non-DC components which can be analysed with seismic full moment tensors (e.g., Alvizuri et al. (2018)). Our new numerical algorithm simulates the quasi-static loading and wave propagation mechanics simultaneously and can be further extended to capture a more complex rheology. Furthermore, follow up studies will be performed in 3D.

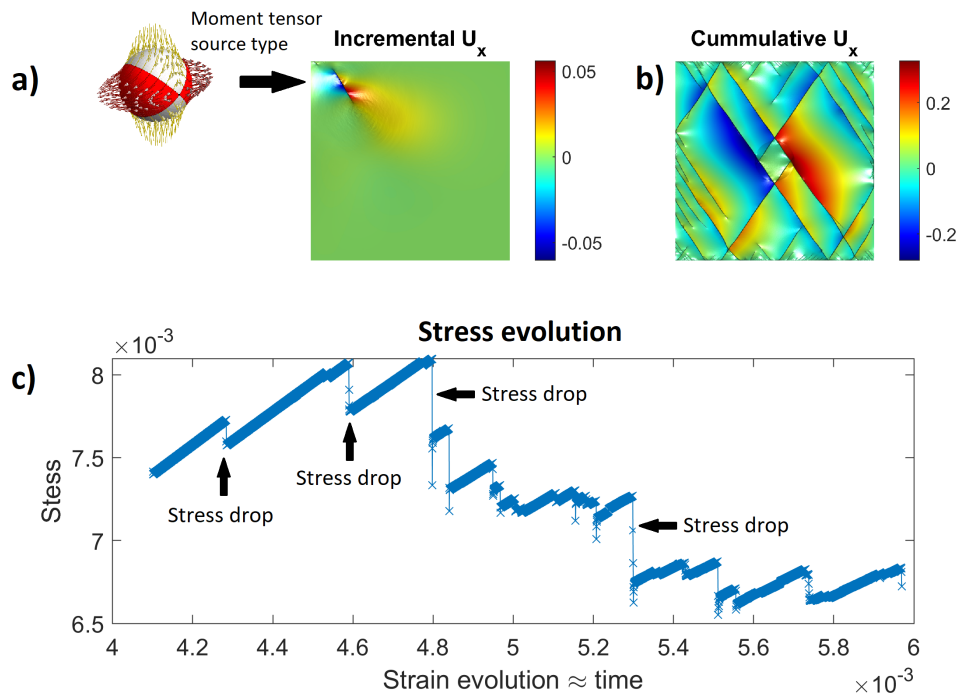


Figure 1.6: Conceptual model of spontaneous earthquake nucleation. Panel (a) illustrates the displacement field corresponding to a stress drop; this displacement field represents the focal mechanism. Panel (b) illustrates the fractal strain localization pattern of the displacement field developed during the cumulative evolution of the strain field. Panel (c) shows the stress evolution in the model with time. The inset in panel (a) represents the moment tensor source. All quantities are dimensionless.

1.4 Objectives, outline and contributions

1.4.1 Objectives

Development of methods

The global objective of this thesis is to study and resolve a range of coupled physics using analytical and numerical techniques.

For this, I develop the following algorithms:

- The development and validation of a finite-element numerical solver to calculate the effective visco-elastic properties of a hydro-mechanically coupled system at the pore scale.
- The development and validation of an analytical model for seismic dispersion and attenuation due to fluid flow at the pore scale (squirt flow) for various geometries.
- The development and validation of high-performance algorithms based on graphical processing units for wave propagation in poroelastic media.
- The development of high-performance algorithms based on graphical processing units for non-linear elasto-plastic, visco-plastic, visco-elasto-plastic and poro-elasto-plastic rheologies.
- The development of a high-performance algorithm based on graphical processing units to simultaneously simulate quasi-static and dynamic responses to model spontaneous earthquake nucleation.

1.4.2 Outline

The thesis is structured as follows:

Micro-scale

- In **Chapter 2**, we present a three-dimensional numerical study of fluid flow at the pore scale (squirt flow) resulting in seismic dispersion and attenuation. We compare our inherently accurate three-dimensional numerical solution against a published analytical model for a simple pore geometry and a range of scenarios. As a result, we observe significant discrepancies which reveal and delineate the limitations of the analytical model.
- **Chapter 3** presents a three-dimensional numerical study of fluid flow at the pore scale (squirt flow) for a different pore geometry (two intersecting cracks) with a particular focus on azimuth-, angle- and frequency-dependent behavior of seismic waves. Among our conclusions, we show that even in such a simple pore geometry, the velocity anisotropy and other seismic characteristics are complex. Therefore, seismic data cannot provide us exclusive characterization of the pore space without additional prior information.
- In **Chapter 4**, we present a new analytical model for fluid flow at the pore scale (squirt flow). This model is validated against a three-dimensional numerical solution for a simple pore geometry that has been classically used to explain squirt flow. Our analytical model provides very accurate predictions for the attenuation and dispersion of the moduli across the whole frequency range.
- In **Chapter 5**, we extend the developed analytical model for a more complex geometry of the pore space. This model is validated against a three-dimensional numerical solution for different pore geometries and provide accurate results for attenuation and dispersion.

Macro-scale

- In **Chapter 6**, we developed a multi- graphical processing units (GPU) numerical application to resolve the anisotropic elastodynamic Biot's equations that relies on a conservative numerical scheme to simulate, in a few seconds, wave fields for spatial domains involving more than 1.5 billion grid cells. We present a comprehensive dimensional analysis reducing the number of material parameters needed for the numerical experiments from ten to four. Finally, we present several numerical modeling experiments, including a three-dimensional simulation of fluid injection into a poroelastic medium.
- In **Chapter 7**, we perform the von Neumann stability analysis of the discretized Biot's equations. We use an explicit scheme for the wave propagation and different implicit and explicit schemes for Darcy's flux. We derive the exact stability conditions for all the considered schemes. The obtained stability conditions for the discretized Biot's equations were verified numerically in one-, two- and three-dimensions.
- In **Chapter 8**, we present a physically based model of a spontaneous earthquake nucleation. This includes modeling of the visco-elasto-plastic behavior of rocks and more complex rheologies. We propose an implementation which simultaneously simulates both, the quasi-static loading and dynamic wave propagation.

In **Appendix A**, I include the article by *Lissa et al. (2020)*. This scientific article describes the squirt flow in cracks with rough surfaces.

In **Appendix B**, I include the article by *Wyser et al. (2020a)*. We present an efficient MATLAB-based implementation of the material point method (MPM) and its most recent variants.

In **Appendix C**, I include the article by *Wyser et al. (2021a)*. We propose an explicit GPU-based solver (including a multi-GPU implementation) within the material point method (MPM) framework on a single graphics processing unit (GPU) to resolve elastoplastic problems under two- and three-dimensional configurations (i.e., granular collapses and slumping mechanics).

1.4.3 Contributions

I have contributed as a leading author in the project presented in Chapters 2-8, and as a co-author in the projects presented in Appendices A-C. I have written the main chapters and created all the figures included in these chapters based on selected results obtained from my research. All the co-authors contributed with ideas, corrections, suggestions and improvements to the readability and clarity of the results. My contributions in each chapter are given below.

- In **Chapter 2**, I used the finite element solver presented by Beatriz Quintal (*Quintal et al., 2019*). I have extended the solver to deal with anisotropic materials (vertical transverse isotropy and orthorhombic symmetries) and I have implemented the boundary conditions for the direct relaxation tests to compute all components of the stiffness matrix. I have implemented in Matlab the existing analytical model by *Collet and Gurevich (2016)*.
- In **Chapter 3**, I have presented two scalar parameters which can be used to measure the anisotropy strength of a model with any elastic symmetry in bulk and shear. I have written Matlab codes for the calculation of the anisotropy measures in bulk and shear.
- In **Chapters 4 and 5**, I have developed the new analytical models for seismic dispersion and attenuation due to squirt flow for various geometries. I have written symbolic Maple and Matlab codes.
- In **Chapter 6**, I have developed a multi- graphical processing units (GPU) numerical solver to resolve the anisotropic elastodynamic Biot's equations that relies on a conservative numerical scheme to simulate, in a few seconds, wave fields for spatial domains involving more than 1.5 billion grid cells. I have used previous open access results by Ludovic Räss during the development phase. I have written symbolic

Maple, Matlab and GPU-based (CUDA C) solvers.

- In **Chapter 7**, I have performed the von Neumann stability analysis of the discretized Biot's equations. I have written symbolic Maple, Matlab and GPU-based (CUDA C) solvers. Together with Lyudmila Khakimova and Yury Podladchikov, I have performed the von Neumann stability analysis of the discretized damped wave equation.
- In **Chapter 8**, together with Yury Podladchikov, I have performed a physically based model of a spontaneous earthquake nucleation in visco-plastic medium. Then, I have performed a physically based model of a spontaneous earthquake nucleation in elasto-plastic medium. Together with Ivan Utkin, I have extended the rheology to visco-elasto-plastic. I have written the solver which simultaneously simulates both, the quasi-static loading and dynamic wave propagation. This solver is used to simulate spontaneous earthquake nucleation.
- In **Appendix A**, I have contributed with ideas, corrections, suggestions and improvements to the readability and clarity of the results. I provided Matlab scripts to calculate the effective elastic properties of fluid saturated porous media using Gassmann's equations.
- In **Appendix B and C**, I helped Emmanuel Wyser to write the original manuscript and to develop the Matlab and GPU-based solvers.

Chapter 2

Frequency-dependent attenuation and dispersion caused by squirt flow: Three-dimensional numerical study

Yury Alkhimenkov, Eva Caspari, Boris Gurevic, Nicolás D. Barbosa, Stanislav Glubokovskikh, Jürg Hunziker and
Beatriz Quintal

Published¹ in *Geophysics*.

¹Alkhimenkov, Y. et al. (2020). Frequency-dependent attenuation and dispersion caused by squirt flow: Three-dimensional numerical study. *Geophysics*, **85**(3), MR129-MR145, doi:10.1190/geo2019-0519.1

Abstract

Seismic waves may exhibit significant dispersion and attenuation in reservoir rocks due to pore-scale fluid flow. Fluid flow at the microscopic scale is referred to as squirt flow and occurs in very compliant pores, such as grain contacts or microcracks, that are connected to other stiffer pores. We perform 3D numerical simulations of squirt flow using a finite element approach. Our 3D numerical models consist of a pore space embedded into a solid grain material. The pore space is represented by a flat cylinder (a compliant crack) whose edge is connected with a torus (a stiff pore). Grains are described as a linear isotropic elastic material while the fluid phase is described by the quasistatic linearized compressible Navier-Stokes momentum equation. We obtain the frequency-dependent effective stiffness of a porous medium and calculate dispersion and attenuation due to fluid flow from a compliant crack to a stiff pore. We compare our numerical results against a published analytical solution for squirt flow and analyze the effects of its assumptions. Previous interpretation of the squirt flow phenomenon based mainly on analytical solutions is verified and some new physical effects are identified. The numerical and analytical solutions agree only for the simplest model in which the edge of the crack is subjected to zero fluid pressure boundary condition while the stiff pore is absent. For the more realistic model that includes the stiff pore, significant discrepancies are observed. We identify two important aspects that need improvement in the analytical solution: the calculation of the frame stiffness moduli and the frequency dependence of attenuation and dispersion at intermediate frequencies.

2.1 Introduction

Seismic methods are widely used for detection and characterization of fluid-saturated porous rocks (Yan *et al.*, 2019). Many studies show that a passing wave loses energy propagating through fluid-saturated rocks (Mavko and Jizba, 1991; Dvorkin *et al.*, 1995; Pride *et al.*, 2004; Müller *et al.*, 2008; Gurevich *et al.*, 2010; Müller *et al.*, 2010; Pimienta *et al.*, 2015a,b). There are several phenomena responsible for energy loss associated with the pore fluid (Müller *et al.*, 2010): e.g. wave-induced fluid flow in partially saturated rocks and in fractures at the mesoscopic scale, and squirt flow in cracks or in grain-to-grain contacts at the pore scale. Rocks are heterogeneous at all scales and can be described with respect to a particular scale: the wavelength scale, the mesoscopic scale and the pore scale. The wavelength scale obviously refers to the wavelength of a propagating wave; the mesoscopic scale is much larger than the size of individual grains and pores but smaller than the wavelength; the pore scale is of the size of individual grains, pores and micro-cracks. Here, we identify fractures as discontinuities at the mesoscopic scale and cracks as discontinuities at the pore scale.

At the wavelength scale, so-called global flow occurs due to fluid pressure gradients between peaks and troughs of a passing wave (Biot, 1956b, 1962b). At the mesoscopic scale, fluid pressure gradients occur at scales much larger than the pore-scale but smaller than the wavelength of a propagating wave: for example, flow may occur between fractures and the porous background of the rock (Brajanovski *et al.*, 2005; Masson *et al.*, 2006; Masson and Pride, 2007; Rubino *et al.*, 2014; Grab *et al.*, 2017). This wave-induced fluid flow in fractures at the mesoscopic scale can be described using the theory of Biot (1956b, 1962b) assuming heterogeneous material properties (i.e., soft, highly permeable fractures and stiff, low-permeability rock matrix). Analytical solutions for mesoscopic heterogeneities of specific geometries were developed, for example, by White *et al.* (1975), White (1975), Pride and Berryman (2003a,b) and Pride *et al.* (2004).

Fluid flow in cracks at the pore scale (squirt flow) occurs between cracks and pores of different stiffness, sizes and orientations. Such flow is believed to be significant at ultrasonic and sonic frequencies (Mavko and Nur, 1975) and also at seismic frequencies (Mavko *et al.*, 2009; Müller *et al.*, 2010). Several experimental studies confirmed the importance of squirt flow at different frequency ranges (Mayr and Burkhardt, 2006; Mikhailsevitch *et al.*, 2015; Subramaniyan *et al.*, 2015; Pimienta *et al.*, 2015a,b; Chapman *et al.*, 2019). An overview of early theoretical studies on squirt flow is given by Jones (1986).

Simple analytical solutions for squirt flow exist and are based on interconnected pores with different aspect ratios (O'Connell and Budiansky, 1977; Palmer and Traviolia, 1980), on the connection of a compliant crack and a stiff pore (Murphy *et al.*, 1986; Mukerji and Mavko, 1994; Dvorkin *et al.*, 1995; Pride *et al.*, 2004; Gurevich *et al.*, 2010) or on the connection of small aspect ratio cracks and spheroidal pores (Xu, 1998; Chapman *et al.*, 2002;

Chapman, 2003; Jakobsen and Chapman, 2009). In real rocks, examples of compliant pores are microcracks and grain contacts. The low- and high-frequency limits of the stiffness moduli in such media when saturated with a liquid are reasonably well understood (Gassmann, 1951; Mavko and Jizba, 1991; Mavko et al., 2009; Gurevich et al., 2009a). On the other hand, the frequency-dependent behavior of velocity and attenuation at intermediate frequencies is not fully understood. Numerically, squirt flow can be studied by simulating the coupled fluid-solid deformation at the pore scale which is a difficult exercise from a computational point of view. A few numerical approaches appeared in the literature (Zhang and Toksöz, 2012; Quintal et al., 2016, 2019; Das et al., 2019). The very recent study by Das et al. (2019) simulates the coupled fluid-solid deformation at the pore scale, including inertial and non-linear terms in the Navier-Stokes equation.

The wavelength of a passing wave is much larger than the size of individual cracks and pores, therefore, wave propagation is controlled by effective rock properties. Squirt flow is frequency dependent, thus effective frequency-dependent stiffness moduli represent volume averaged rock properties. This is called upscaling (going from the microscale to larger scales through averaging). We calculate the effective stiffness tensor over a representative elementary volume and analyze the corresponding stiffness moduli dispersion and attenuation. Our numerical simulation is based on the approach proposed by Quintal et al. (2016, 2019). This numerical approach describes the rock matrix properties using Hooke's law and the fluid flow using the quasi-static linearised compressible Navier-Stokes momentum equation, and then, through volume averaging, calculates the effective viscoelastic stiffness tensor. We compare our numerical results with those of an analytical solution for squirt flow in anisotropic media (Collet and Gurevich, 2016). We choose this particular analytical solution because it uses very specific material properties (e.g., pore-space geometry, elastic properties of the background medium, crack compliances, porosity, fluid viscosity) without adjusted abstract parameters, so that the direct comparison with the numerical results is possible. The aim of this work is to (1) numerically evaluate the energy loss caused by squirt flow at the pore scale for a specific 3D pore geometry (a torus connected to a crack), (2) compare the numerical results against a published analytical solution to examine the assumptions made during the derivation of this analytical solution. Our conclusions can be also applied to the analytical solution for squirt flow in isotropic media proposed by Gurevich et al. (2010).

The paper is organized as follows. First, we briefly describe the physics behind the squirt flow mechanism. We then describe the theory and methodology of the numerical solution. After, we briefly explain the analytical solution by Collet and Gurevich (2016). Next, we show the numerical results and the comparison with the analytical solution. Finally, we discuss the results and draw some conclusions.

2.2 A brief overview of the physics

Squirt flow causes seismic wave dispersion and attenuation due to the energy dissipation caused by fluid pressure diffusion at the pore scale. Assume that the pore space consists of big isometric pores and cracks with low aspect ratios, pores and cracks are fully saturated with a liquid. Cracks are much more compliant than isometric pores, therefore, a passing wave induces pressure gradients in compliant cracks. These pressure gradients force fluid to move between compliant cracks and stiff isometric pores until the pore pressure equilibrates. Due to the fluid's viscosity and associated viscous friction, this mechanism causes strong energy dissipation. Some useful definitions: "rock matrix" or "porous background" refer to grains and pores, "frame" refers to grains, pores and cracks, "modified frame" refers to grains, pores and cracks saturated with a liquid while pores are dry.

2.2.1 Low frequencies

In the low frequency regime, the fluid pressure has enough time to equilibrate during a half-cycle of the wave and become uniform throughout the pore space, therefore, Gassmann's equations are valid (Gassmann, 1951). This is called relaxed state. Only a few parameters are needed to calculate the effective properties of the rock in the low frequency limit: the bulk modulus of the grains, the bulk modulus of the drained frame, the bulk modulus of the fluid and total porosity. Then, isotropic or anisotropic Gassmann's equations can be used to calculate the effective elastic moduli of the saturated medium. Typically, the relative volume of cracks is very small (i.e., two orders of magnitude smaller compared to the volume of the stiff pores), therefore, in Gassmann's equations only the porosity of the stiff pores can be used instead of the total porosity (Mavko and Jizba, 1991; Gurevich et al., 2010).

2.2.2 High frequencies

In the high frequency regime, the fluid pressure does not equilibrate between cracks and stiff pores during a half-wave cycle. Furthermore, for cracks with very low aspect ratios saturated with a liquid, the normal crack compliance is equal to zero (but not the tangential compliance). Therefore, cracks become stiffer with respect to normal deformation. In other words, cracks behave as hydraulically isolated and are stiffened by the liquid. This is called unrelaxed state. The fluid in the cracks is assumed to be part of the frame material (Mavko and Jizba, 1991).

Isotropic or anisotropic Gassmann's equations can be used to calculate the effective elastic moduli of the saturated medium, but the frame moduli are stiffer compared to those at the low frequency because the normal crack compliance is negligible. Gassmann's equations are still valid because the pore pressure is uniform in all stiff pores. Thus, the effective elastic moduli are different in the high frequency regime from those in the low frequency regime.

2.2.3 Intermediate frequencies

At intermediate frequencies a quantitative description of the physics becomes more complicated. Roughly, during the transition from a relaxed state to an unrelaxed state, the pressurized fluid stiffens the cracks as frequency increases. Therefore, this frequency-dependent stiffening phenomenon also stiffens the effective stiffness moduli. This non-linear stiffening effect is difficult to model analytically. The present numerical study sheds some light on this problem and provides a quantitative description on the frequency-dependent behavior of the moduli dispersion and attenuation.

Mathematical formulation

We consider that at the pore scale, a rock is composed by a solid phase (grains) and a fluid-saturated pore space. Grains are described as a linear isotropic elastic material for which the conservation of momentum is

$$\nabla \cdot \boldsymbol{\sigma} = 0, \tag{2.1}$$

where $\boldsymbol{\sigma}$ is the stress tensor, $\nabla \cdot$ denotes the divergence operator acting on a tensor field $\boldsymbol{\sigma}$. The stress-strain relation is written as

$$\boldsymbol{\sigma} = \mathbf{C} : \boldsymbol{\epsilon}, \tag{2.2}$$

where $\boldsymbol{\epsilon}$ is the strain tensor, \mathbf{C} is the 4-th rank stiffness tensor and \cdot denotes the double dot product. For an isotropic material, the components of the stiffness tensor can be fully described by the bulk K and shear μ moduli.

The fluid phase is described by the quasi-static linearised compressible Navier-Stokes momentum equation (Landau and Lifshitz, 1959a):

$$-\nabla p + \eta \nabla^2 \mathbf{v} + \frac{1}{3} \eta \nabla (\nabla \cdot \mathbf{v}) = 0, \quad (2.3)$$

where \mathbf{v} is the particle velocity, p is the pressure and η is the shear viscosity and ∇ denotes the nabla operator acting on vector v and scalar p fields. Equation 4.54 is valid for the laminar flow of a Newtonian fluid (i.e., low Reynolds numbers Re , $Re < 1$).

2.3 Numerical methodology

For the numerical simulation we solve the conservation of momentum equation 4.52 in the frequency domain for both solid and fluid phases and the generalized stress-strain relation resulting from combining equations 4.53 and 4.54 (Quintal *et al.*, 2016, 2019). Thus, the stress-strain relation in the temporal-frequency domain is (in index form):

$$\sigma_{ij} = \lambda e \delta_{ij} + 2\mu \epsilon_{ij} + i\omega \left(2\eta \epsilon_{ij} - \frac{2}{3} \eta e \delta_{ij} \right), \quad (2.4)$$

where ϵ_{ij} are the components of the strain tensor,

$$\epsilon_{ij} = \frac{1}{2} \left(\frac{\partial u_i}{\partial x_j} + \frac{\partial u_j}{\partial x_i} \right), \quad (2.5)$$

e is the trace of the strain tensor, λ and μ are the Lamé parameters, u_i denotes the displacement in the i -th direction, δ_{ij} is the Kronecker delta and ω is the angular frequency.

Equations 4.52 and 2.4 are implemented into a finite-element solver. In the domain of the model representing a solid material, equation 2.4 reduces to Hooke's law (equation 4.53) by setting the shear viscosity η to zero. Similarly, in the domain of the model representing a compressible viscous fluid, the shear modulus μ is set to zero and hence equations 2.4 and 4.52 reduce to the linearised compressible Navier-Stokes equation (equation 4.54). An advantage of the proposed formulation is the natural coupling between the solid and fluid displacements at the boundaries between subdomains (Quintal *et al.*, 2016). In our simulation the energy dissipation is caused only by fluid pressure diffusion since inertial effects are neglected.

The whole domain is discretized using an unstructured mesh with tetrahedral elements. A direct PARDISO solver (Schenk and Gärtner, 2004) is used for solving a linear system of equations. For all models, the total number of elements ranges from 4.3×10^6 to 6.3×10^6 . The total number of degrees of freedom is 17×10^6 or more. The simulation is performed for 13 – 25 different frequencies (depending on the model) from 1 Hz to 10^6 Hz. For each frequency, the solver uses approximately 0.9 TB of RAM memory. Under a 100% performance of 32 Intel dual-socket E5-2683 v4 2.1GHz cores, two hours of calculations are needed for each frequency.

Direct relaxation tests are performed for numerically computing the five independent components of the effective stiffness tensor. Only five components are needed because the symmetry of the proposed geometry is transversely isotropic with the vertical axis of symmetry (VTI) (the model's geometry is explained below). For simplicity purposes, we use Voigt notation for the stress, strain, stiffness and compliance tensors. For the normal compression test in the vertical z direction (C_{33} component) the boundary conditions are: at the top boundary

a vertical displacement is assigned of the form $u_3 = 10^{-6} \times \exp(i\omega t)$, at the bottom the vertical displacement is set to zero, at the side boundaries the normal displacement is set to zero. For the xy shear test (C_{66} component), the top boundary is assigned a displacement in x-direction of the form $u_1 = 10^{-6} \times \exp(i\omega t)$, at the bottom all displacements are set to zero, at the side boundaries displacements in y- and z- directions are set to zero. Equivalent sets of boundary conditions are applied to obtain the relationships between the other stress and strain components and, hence, the C_{11} , C_{44} components. For the $C_{13}(\omega)$ component, a mixed direct test is used, the corresponding boundary conditions are given in Appendix 3.7. The initial conditions for displacements are set to zero. The resulting stress and strains are averaged over the entire spatial domain for each frequency. Then, the complex valued $C_{ij}(\omega)$ component is calculated for each frequency. For example,

$$C_{33}(\omega) = \frac{\langle \sigma_3(\omega) \rangle}{\langle \epsilon_3(\omega) \rangle}, \quad (2.6)$$

where $\langle \cdot \rangle$ represents the volume averaging over the sample volume. Equation 4.56 is valid because all our models exhibit VTI symmetry. We calculate $C_{11}(\omega)$, $C_{22}(\omega)$, $C_{44}(\omega)$, $C_{66}(\omega)$, $C_{12}(\omega) = C_{11}(\omega) - 2C_{66}(\omega)$ components in the same way. The inverse quality factor is calculated as (O'Connell and Budiansky, 1978)

$$\frac{1}{Q_{ij}(\omega)} = \frac{\text{Im}\{C_{ij}(\omega)\}}{\text{Re}\{C_{ij}(\omega)\}}. \quad (2.7)$$

2.4 Analytical solution of Collet and Gurevich (2016)

In this study, we compare the results of our numerical simulation against an anisotropic version of the squirt flow analytical solution of Gurevich *et al.* (2010) proposed by Collet and Gurevich (2016). These squirt flow solutions combine the pore pressure relaxation model of Murphy *et al.* (1986) with the discontinuity tensor formulation of Sayers and Kachanov (1995). Collet and Gurevich (2016) consider a double-porosity medium with aligned identical cracks embedded in a hypothetical background rock matrix made up of grains and stiff pores only (see also Pervukhina *et al.* (2010)). This anisotropic squirt flow solution, contrary to our numerical method, assumes (A) an isotropic rock matrix embedding the cracks (we extend that assumption to a rock with a transversely isotropic background) and (B) a smaller crack aspect ratio, in the range of $10^{-3} - 10^{-5}$ (we show that the crack aspect ratio can be larger).

In the Collet and Gurevich (2016) model, low- and high-frequency limits are expected to be consistent with Gassmann's and Mavko-Jizba (Mavko and Jizba, 1991) equations, respectively, and the frequency dependence is controlled by a frequency dependent effective fluid bulk modulus $K_f^*(\omega)$ of the fluid filling the crack (Gurevich *et al.*, 2010). The crack is fully described in terms of normal and tangential compliances, Z_n and Z_t , respectively (Kachanov, 1993; Schoenberg and Sayers, 1995; Sayers and Kachanov, 1995). They consider the so-called modified frame in which only the cracks are filled with fluid, whereas the stiffer pores are empty (Mavko and Jizba, 1991). In the low-frequency limit, the relaxed moduli of the modified frame are equal to the rock dry moduli (which means that $Z_n^{mf} = Z_n$); while in the high-frequency limit, the fluid in the cracks stiffens the frame and the unrelaxed moduli of the modified frame are equal to the dry moduli of the rock without a compliant porosity (which means that $Z_n^{mf} = 0$, i.e., without a crack) (Mavko and Jizba, 1991; Berryman, 2007; Gurevich *et al.*, 2009a).

In the analytical solution of Collet and Gurevich (2016), the frequency dependent compliance tensor of the modified frame is written as (for a horizontal transversely isotropic (HTI) medium) (Kachanov, 1993; Schoenberg and Sayers, 1995; Sayers and Kachanov, 1995):

$$S_{mn}^{MF}(\omega) = S_{mn}^b + \Delta S_{mn}^{MF}(\omega), \quad (2.8)$$

where S_{mn}^b is the compliance tensor of the rock matrix, and $\Delta S_{mn}^{MF}(\omega)$ is the additional compliance due to the crack (Schoenberg and Helbig, 1997):

$$\Delta S_{mn}^{MF}(\omega) = \begin{bmatrix} Z_n^{MF}(\omega) & 0 & 0 & 0 & 0 & 0 \\ 0 & 0 & 0 & 0 & 0 & 0 \\ 0 & 0 & 0 & 0 & 0 & 0 \\ 0 & 0 & 0 & 0 & 0 & 0 \\ 0 & 0 & 0 & 0 & Z_t & 0 \\ 0 & 0 & 0 & 0 & 0 & Z_t \end{bmatrix}. \quad (2.9)$$

The frequency-dependent normal fracture compliance is

$$Z_n^{MF}(\omega) = \frac{Z_n}{1 + \frac{Z_n}{\phi_c(1/K_f^*(\omega) - \beta_{mf})}}, \quad (2.10)$$

where ϕ_c is the compliant porosity (crack porosity), Z_n is the normal compliance of the crack and β_{mf} is the compressibility of the modified frame (the arithmetic average). Equation 4.60 differs slightly from the corresponding equation in Collet and Gurevich (2016) which erroneously contained the compressibility of the grain material β_g instead of β_{mf} . However, our calculation shows that the corresponding error has a very small effect on the effective properties: adding or subtracting 30% from β_{mf} in equation 4.60 leads to less than 5% effect on the effective properties.

Gurevich et al. (2010) showed that the stiffness of the crack can be described using a frequency-dependent fluid bulk modulus $K_f^*(\omega)$:

$$K_f^*(\omega) = \left[1 - \frac{2J_1(ka)}{kaJ_0(ka)} \right] K_f, \quad (2.11)$$

where J_ξ is Bessel function of the first kind ($\xi = 0$ or $\xi = 1$ correspond to the zero- or first-order Bessel function), K_f is the fluid bulk modulus, a is the radius of the crack, k is the wavenumber of the pressure wave:

$$ka = \frac{1}{\alpha} \left(-\frac{3i\omega\eta}{K_f} \right)^{1/2}, \quad (2.12)$$

α is the aspect ratio of the crack (thickness h divided by diameter: $h/(2a)$) and η is the viscosity of the fluid. Equations 4.61-4.62 were obtained by imposing a zero fluid pressure boundary condition ($P_f = 0$) at the edge of the cylindrical crack (Gurevich et al., 2010).

The frequency-dependent stiffness tensor of the fluid saturated medium is given by the anisotropic Gassmann's equation (Gassmann, 1951):

$$C_{mn}^{sat}(\omega) = C_{mn}^{MF}(\omega) + \alpha_m \alpha_n M \quad (2.13)$$

$$\alpha_m = 1 - \left(\sum_{n=1}^3 C_{mn}^{MF} \right) \beta_g / 3 \quad (2.14)$$

for $m = 1, 2, 3$ and $\alpha_4 = \alpha_5 = \alpha_6 = 0$, and where

$$M = \left(\varphi \beta_f + (1 - \varphi) \beta_g - K^* \beta_g^2 \right)^{-1}, \quad (2.15)$$

$$K^* = \frac{1}{9} \sum_{m=1}^3 \sum_{n=1}^3 C_{mn}^{MF}(\omega), \quad (2.16)$$

φ is the total porosity of the medium without the compliant porosity (which is neglected because the compliant porosity is two or more orders of magnitude lower than the stiff pore's porosity), K^* is the generalized bulk modulus of the modified frame, β_f is the compressibility of the fluid, α_m is the Biot-Willis coefficient, β_g is the compressibility of the grain material. The effective transversely isotropic stiffness matrix can be written for horizontal (HTI) and vertical (VTI) symmetry axis (see Appendix 2.9). The resulting VTI stiffness matrix is used to compare the analytical solution with results from numerical simulations.

2.5 Results

We model coupled solid-fluid deformation at the pore scale. In this study, we consider three 3D numerical models consisting of a pore space embedded in an elastic solid grain material. The pore spaces are:

- i) a flat cylinder (crack), whose edge (or tip of the crack) is subjected to zero fluid pressure boundary condition ($P_f = 0$ model, Figure 2.1a, 2.1b),
- ii) a flat cylinder whose edge is connected to a big torus (*big pore* model, Figure 2.1c, 2.1d),
- iii) a flat cylinder whose edge is connected to a small torus (*small pore* model, Figure 2.1e, 2.1f).

Topologically a flat cylinder whose edge is connected to a big/small torus represents one domain. Geometrical properties are shown in Table 5.1. The model geometry i) with zero fluid pressure boundary condition is chosen because it represents the analytical solution of *Collet and Gurevich* (2016). Originally, the model geometry in ii) and iii) was proposed by *Murphy et al.* (1986). Then, this was modified by *Gurevich et al.* (2010), *Collet and Gurevich* (2016) to the pore geometry in i), where the shape of the stiff pores is irrelevant (which means that a torus is a possible choice). Each of these three 3D numerical models highlights different physical aspects of the squirt flow mechanism. The employed fluid properties are those of glycerol and the grain material has properties of quartz (Table 5.2). As shown in Table 5.1, the crack diameter is 20 cm and the crack thickness is 0.05 cm, therefore, the crack aspect ratio is $0.5/200 = 0.0025$. The model geometry is scalable, i.e, if all geometrical parameters are divided or multiplied by any number, the numerical results will be the same. The results are controlled by the dimensionless aspect ratio.

The mesh is coarse in the solid domain, finer in the torus and the finest in the flat cylinder representing the crack. Due to the model's symmetry and RAM memory limitations, the simulations are performed on a quarter of the model (Figure 2.1b, 2.1d and 2.1f), a cuboid (grain material) whose size is $(0.2 \times 0.2 \times 0.2)\text{m}^3$. In all simulations, the grain is described as a linear elastic solid material (equations 4.52 and 4.53) and the fluid is described as a compressible Newtonian fluid (equation 4.54).

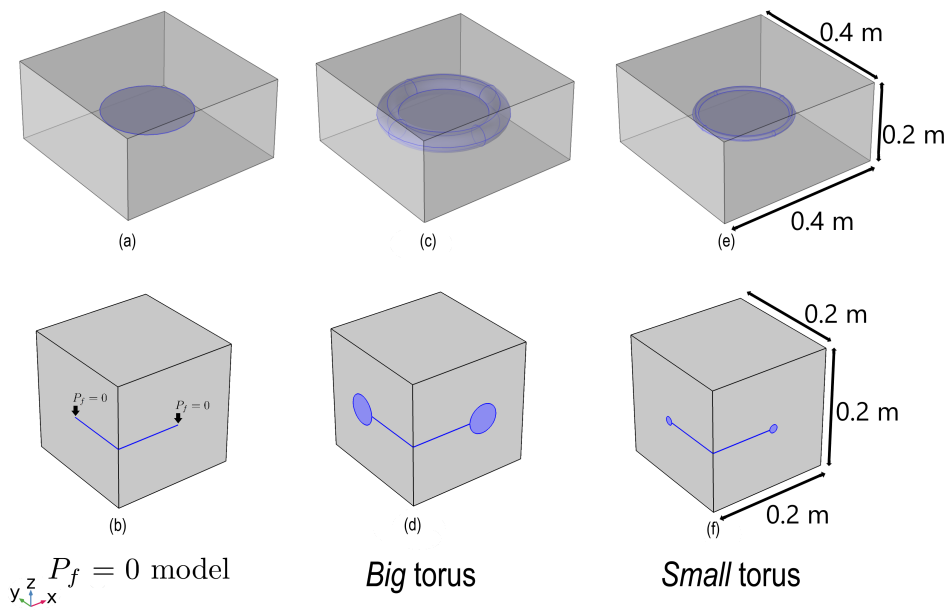


Figure 2.1: $P_f = 0$ model: (A) Sketch illustrating a flat cylinder representing a crack with fluid pressure equal to zero at the edge. The blue region represents the pore space saturated with a fluid, the transparent gray area corresponds to the solid grain material. (B) Sketch showing a quarter of the model. *Big pore* model: (C) Sketch illustrating a flat cylinder representing a crack whose edge is connected to a torus representing a stiff pore. The blue region represents the pore space saturated with a fluid, the transparent gray area corresponds to the solid grain material. (D) Sketch showing a quarter of the model. *Small pore* model: (E) Sketch illustrating a flat cylinder representing a crack whose edge is connected to a small torus representing a stiff pore. The blue region represents the pore space saturated with a fluid, the transparent gray area corresponds to the solid grain material. (F) Sketch showing a quarter of the model.

Table 2.1: The material properties used for all numerical simulations.

Material parameter	Solid	Fluid
Bulk modulus K	36 GPa	4.3 GPa
Shear modulus μ	44 GPa	0 GPa
Shear viscosity η	0 Pa·S	1.414 Pa·S

Table 2.2: Geometrical properties for $P_f = 0$ model, *Big pore* model and *Small pore* model. Major radius — the distance from the center of the tube to the center of the torus. Minor radius — the radius of the tube.

Geometrical parameter	$P_f = 0$ model	<i>Big pore</i> model	<i>Small pore</i> model
Crack radius	0.1 m	0.1 m	0.1 m
Crack thickness	0.0005 m	0.0005 m	0.0005 m
Crack aspect ratio	0.0025	0.0025	0.0025
Major radius of torus	—	0.124 m	0.1067 m
Minor radius of torus	—	0.024 m	0.0067 m
Total porosity	$\approx 4.9 \cdot 10^{-4}$	0.045	0.0034
Crack porosity	$\approx 4.9 \cdot 10^{-4}$	$\approx 4.9 \cdot 10^{-4}$	$\approx 4.9 \cdot 10^{-4}$

2.5.1 $P_f = 0$ model

a) Numerical solution

We consider a 3D numerical model of a flat cylinder embedded in the grain material (Figure 2.1a, 2.1b). Besides the boundary conditions applied to the external walls of the cubic model, the tip of the crack is subjected to a zero fluid pressure boundary condition ($P_f = 0$). This specific boundary condition corresponds to that of the analytical solution proposed by *Collet and Gurevich* (2016). By applying this $P_f = 0$ boundary condition, we simulate the conditions where the crack is filled with the liquid, whereas a virtual stiff pore acts as a sink for the fluid flow from the crack but, at the same time, has the grain material properties. The total porosity of the model is equal to the crack porosity. The proposed geometry belongs to the vertical transverse isotropic (VTI) symmetry class. Figure 2.2 shows the whole model domain discretization using an unstructured mesh with tetrahedral elements. The colors represent the element's size. The mesh is coarse in the grain (the elements sizes are 0.038 – 0.008 m) and the finest in the cylinder (the elements sizes are 0.00025 – 0.00015 m). Because the fluid flow and, thus, the dissipation take place inside the crack, a fine, regular mesh is compulsory there, while in the grain material, the mesh can be much coarser. The corresponding numerical results are shown in Figure 2.3.

b) Analytical solution

To obtain the results from the anisotropic squirt flow model of *Collet and Gurevich* (2016), a crack embedded into an isotropic background (grain material) can be described in terms of the normal and tangential compliances of the crack Z_n and Z_t , respectively. These parameters are calculated numerically using the following approach: the dry crack is embedded into the isotropic solid grain material and the effective compliance tensor is calculated numerically (S_{crack}^{VTI} compliance tensor). Then, we calculate the difference between the S_{crack}^{VTI} and the grain material S_{grain}^{VTI} compliance tensors. In the resulting compliance matrix, only the $S(3,3)$, $S(4,4)$ and $S(5,5)$ components are non-negligible. Thus, $Z_n = S(3,3)$ and $Z_t = S(4,4) = S(5,5)$. Using equations 4.58-6.100, the effective stiffness tensor is calculated, which then is transformed from HTI to VTI symmetry.

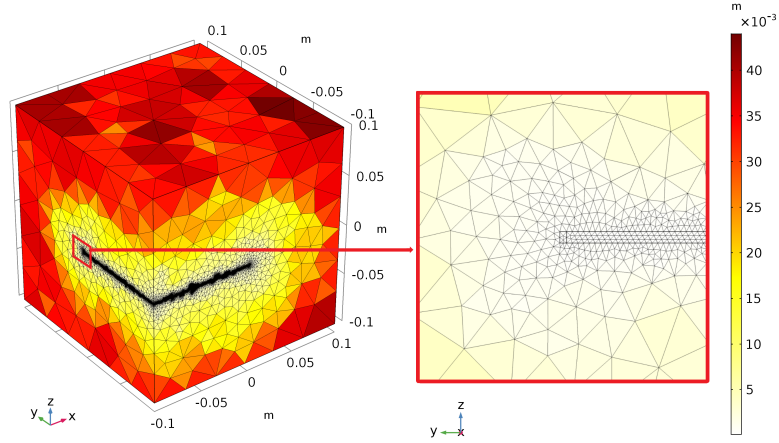


Figure 2.2: The element's size distribution for the $P_f = 0$ model (Figure 2.2): (left) Full model and (right) Zoomed in part of the model showing elements in the crack (element size 0.00025 – 0.00015 m) and in the surrounding grain material (element size 0.038 – 0.008 m). The element's size is the smallest inside the crack and growing toward the walls of the model domain.

c) Comparison

Only the results for C_{33} component are shown in Figure 2.3 because the other components are constant with frequency, except C_{13} , which varies slightly. The analytical and numerical results are in a very good agreement including the low- and high-frequency limits, the frequency dependence of the dispersion and attenuation curves at intermediate frequencies and the left and right asymptotes of the attenuation curve (Figure 2.3). This comparison shows that our numerical result is correct and can be used to simulate more complicated models. Furthermore, such a good agreement indicates that our numerical solution fulfills the conditions (A)-(B) of the analytical solution.

Figure 2.4 shows snapshots of the fluid pressure P_f in the crack at three different frequencies. In the relaxed state, there is enough time for pressure equilibration between the crack and zero fluid pressure at the crack tip (because of the $P_f = 0$ boundary condition) (Figure 2.4, LF). Therefore, the fluid in the crack does not impose any stiffening to the crack. The stiffness of the crack is the same as if it was dry (thus, the $P_f = 0$ model is not consistent with Gassmann equations in the low frequency limit). At intermediate frequencies, there is a large pressure gradient in the crack, which corresponds to the maximum attenuation (Figure 2.4, Fc). In the unrelaxed state, there is no equilibration between the fluid pressure inside the crack and zero fluid pressure at the tip of the crack (Figure 2.4, HF). Therefore, the crack behaves as hydraulically isolated and the fluid highly stiffens the crack, so that the normal compliance of the crack approaches zero (tangential compliance is not zero).

2.5.2 Big pore model

a) Numerical solution

We consider a 3D numerical model of a flat cylinder whose edge is connected with a big torus (Figure 2.1b, 2.1c). The flat cylinder representing a crack has the same radius and thickness as in the $P_f = 0$ model. The torus represents a much stiffer pore. The torus and the crack are embedded into a cuboid of grain material and are fully saturated with a liquid. The proposed geometry belongs to the vertical transverse isotropic (VTI) symmetry class. Numerical results for the C_{mn} components using five direct tests are shown in Figure 2.5. From this figure, only the C_{33} component seems to be frequency-dependent but the C_{13} component is also slightly frequency dependent.

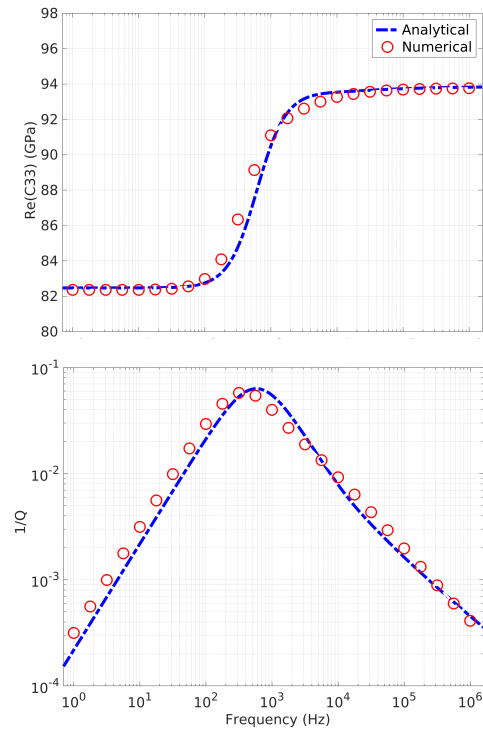


Figure 2.3: Numerical and analytical results for the model with fluid pressure equal to zero at the edge ($P_f = 0$) (Figure 2.1b): (up) Real part of the C_{33} component and (down) dimensionless attenuation for the C_{33} component. Each red circle corresponds to a numerical calculation.

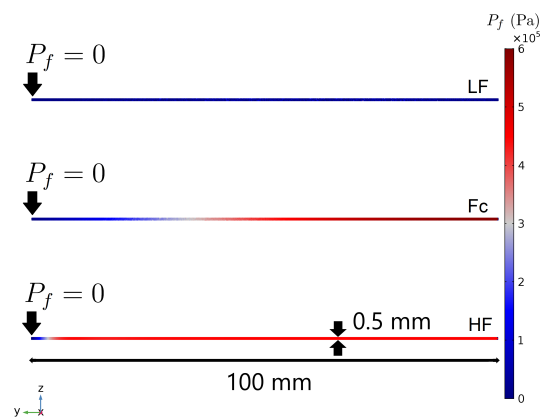


Figure 2.4: Snapshots of the fluid pressure P_f in the fracture at three different frequencies for the $P_f = 0$ model: Lf - low frequency (relaxed state), Fc - intermediate frequency (close to the characteristic frequency) and HF - high frequency (unrelaxed state).

b) Extended analytical solution

For the comparison between the analytical solution and the numerical results, all stiffness properties of the dry medium are calculated numerically (or are the same as in the numerical simulation) and used as input to the analytical solution. To obtain the corresponding results from the analytical solution, normal Z_n and tangential Z_t compliances of the crack are needed. To obtain Z_n and Z_t we numerically calculate several (homogenized) elastic stiffness tensors of a dry medium (Figure 2.6): a torus embedded into the solid grain material (C_1^{VTI} stiffness tensor); a crack embedded into a medium described by the C_1^{VTI} stiffness tensor (C_2^{VTI} stiffness tensor); a torus connected with a crack embedded into an isotropic solid grain material (C_3^{VTI} stiffness tensor). Then, all C^{VTI} stiffness tensors are inverted to the corresponding compliance tensors S^{VTI} . For obtaining Z_n and Z_t there are at least two possible workflows.

Workflow A: We calculate Z_n and Z_t using the difference between the S_1^{VTI} compliance tensor and the S_2^{VTI} compliance tensor (Figure 2.6). In this case, we first homogenize the torus (and obtain C_1^{VTI}) and, then embed the crack into this homogenized material C_1^{VTI} . Thus, Z_n and Z_t do not account for the fact that the crack is connected with the stiffer pore which implies a different geometry from the one shown in Figure 2.1c and 2.1d for calculating the stiffness tensor of the dry material. This approach is used by *Collet and Gurevich* (2016).

Workflow B: We calculate the normal and tangential compliances using the difference between the S_1^{VTI} compliance tensor and the S_3^{VTI} compliance tensor (Figure 2.6). In this case, we also first homogenize the torus but, then embed the crack connected to the torus into the solid grain material. Thus, the C_3^{VTI} stiffness tensor corresponds to the dry stiffness tensor of the model, so the difference $S_1^{VTI} - S_3^{VTI}$ gives the correct compliances Z_n and Z_t for the dry model (using the homogenized material C_1^{VTI}). These compliances Z_n and Z_t approximately correspond to the crack embedded into the C_1^{VTI} material and have a total effective radius equal to the radius of the crack itself plus the additional minor diameter of the torus. This approach is similar to the one used in *Gurevich et al.* (2009a).

The generalization of *Collet and Gurevich* (2016) to an anisotropic porous background is straightforward because the principal symmetry axis of the torus (stiff pore), embedded into the grain material is, the same as, that of the crack and the torus embedded into the grain material, and the corresponding frame stiffnesses are described by the same equations 4.58-4.59. Thus, we are able to fulfill the condition (A) for anisotropy of the rock matrix. Moreover, according to *Collet and Gurevich* (2016), the assumption $Z_n^{mf} = 0$ in the high frequency limit holds only for cracks with aspect ratio lower than 0.001. However, we have already seen in our numerical results in Figure 2.3 (for an aspect ratio of 0.0025) that this assumption also holds for cracks with larger aspect ratios (up to 0.005). Therefore, we conclude that our extended numerical simulation fulfills the conditions (A)-(B) of the analytical solution of *Collet and Gurevich* (2016).

Using equations 4.58-6.100 the complex-valued stiffness tensor is calculated for Workflows A and B. The difference between these two solutions is due to the different Z_n and Z_t parameters which are used in equations 4.58-6.100.

c) Comparison

Figure 2.7 shows results for the C_{33} complex-valued component of the stiffness tensor obtained from the numerical simulation and from the analytical solution with two different sets of normal and tangential compliances derived from Workflows A and B (Figure 2.6). The dispersion curves show that in the high-frequency limit the two analytical solutions and the numerical result are in reasonably good agreement. In the low-frequency regime, the dispersion curve predicted by the analytical result with Workflow A is much stiffer compared to the numerical result. This is because the calculation of Z_n and Z_t involved the strong assumptions described above. The attenuation curve from Workflow A shows, only by chance, a good match with the numerical result except for the asymptotic behavior in the high-frequency regime. In the low-frequency regime, the analytical result with Workflow B is close to the numerical dispersion curve: a difference around 2 GPa because parameters Z_n and Z_t cannot fully describe the elastic behavior of a crack. In this case, the C_{13} component is affected and causes this difference in the anisotropic Gassmann's equations. The attenuation curve predicted by the analytical solution with Workflow B is different from the numerical result: the characteristic frequency is shifted to the left and the maximum attenuation is approximately twice that of the numerical results.

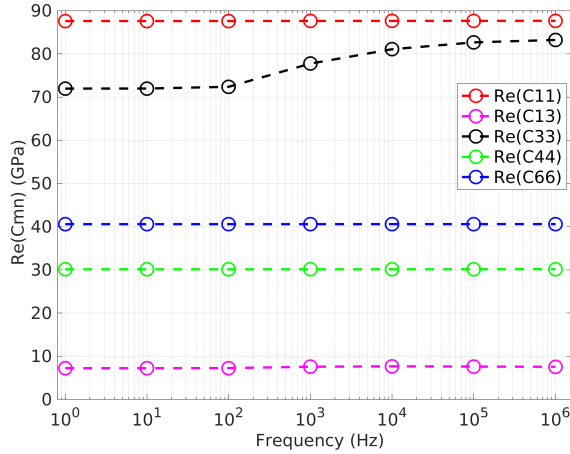


Figure 2.5: Numerical results for the real part of C_{mn} components for the *big pore* model (Figure 2.1c, 2.1d) using five direct tests.

Figure 2.8 shows snapshots of the fluid pressure P_f in the fracture and the stiff pore at three different frequencies. In the relaxed state, the fluid pressure is equilibrated throughout the pore domain (Figure 2.8, LF). At intermediate frequencies, there is a large pressure gradient in the crack, which corresponds to the maximum attenuation (Figure 2.8, Fc). In the unrelaxed state, there is no pressure equilibration between the fluid pressure inside the crack and the fluid pressure inside the torus (Figure 2.8, HF). In the relaxed state (Figure 2.8, LF), the pore pressure inside the stiff pore is slightly increased compared to the unrelaxed state (Figure 2.8, HF). That is due to a finite volume of the stiff pore. Though the crack porosity is several orders of magnitude lower than the stiff pore porosity, such a little volume of fluid still slightly increases the pore pressure inside the stiff pore in the relaxed state.

Little numerical artifacts (red points) can be seen in the torus in the low and intermediate frequencies (Figure 2.8, LF and Fc); this is due to the fact that the mesh is not very fine inside the torus. Due to RAM memory limitations, it is difficult to significantly increase the resolution inside the torus but the simulation has been run for several different mesh distributions and element sizes converging to the same output results. The limits of the dispersion curve were also verified: the low-frequency limit was verified by running dry elastic simulations and adding fluid using the Gassmann's equations; the high-frequency limit was verified by running elastic simulations and thus representing fluid as an elastic material. The Kramers-Kronig relation was also used to verify the consistency of the numerical results: the attenuation curve was reproduced from the dispersion curve using the Kramers-Kronig relation. Thus, we conclude that these artifacts are local and do not affect our results and our results are accurate. There are also some little boundary effects resulting in minor artifacts in the crack (artifacts appear near the walls of the cube) which have negligible effects on our numerical results. The snapshots of fluid pressure are from a diagonal slice in the xy -plane in order to avoid boundary effects.

2.5.3 *Small pore* model

a) Numerical solution

We consider the same model as in the previous section (*big pore* model) but now the volume of the torus is smaller (Figure 2.1e, 2.1f). The flat cylinder (representing a crack) has the same radius and thickness as in the $P_f = 0$ and *big pore* models. The torus and the crack are embedded into a cuboid of grain material. The proposed geometry belongs to the vertical transverse isotropic (VTI) symmetry class. Our numerical results for the C_{33} component are shown in Figure 2.9.

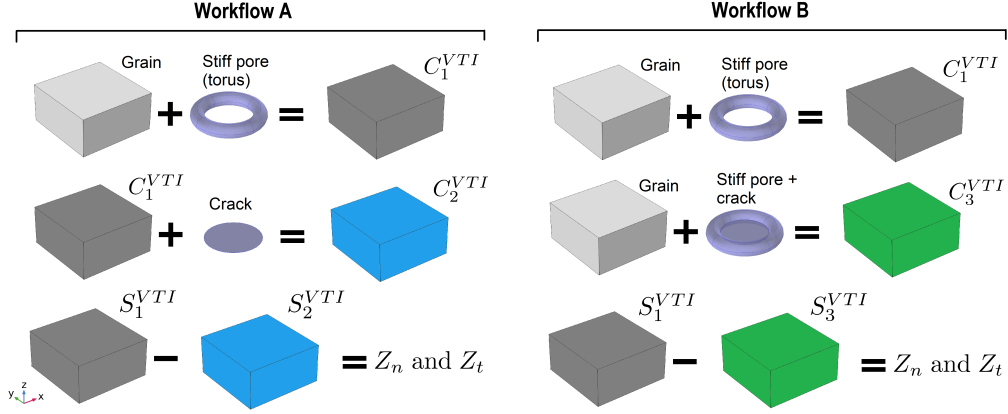


Figure 2.6: Sketch illustrating the calculation of normal and tangential compliances of the crack for Workflows A and B. S_r^{VTI} denotes the compliance tensor, which is the inverse of the corresponding stiffness tensor. i.e., $S_r^{VTI} = (C_r^{VTI})^{-1}$, for $r = 1, 2, 3$. The resulting Z_n and Z_t are used to calculate the analytical solution for corresponding models (Figure 2.1).

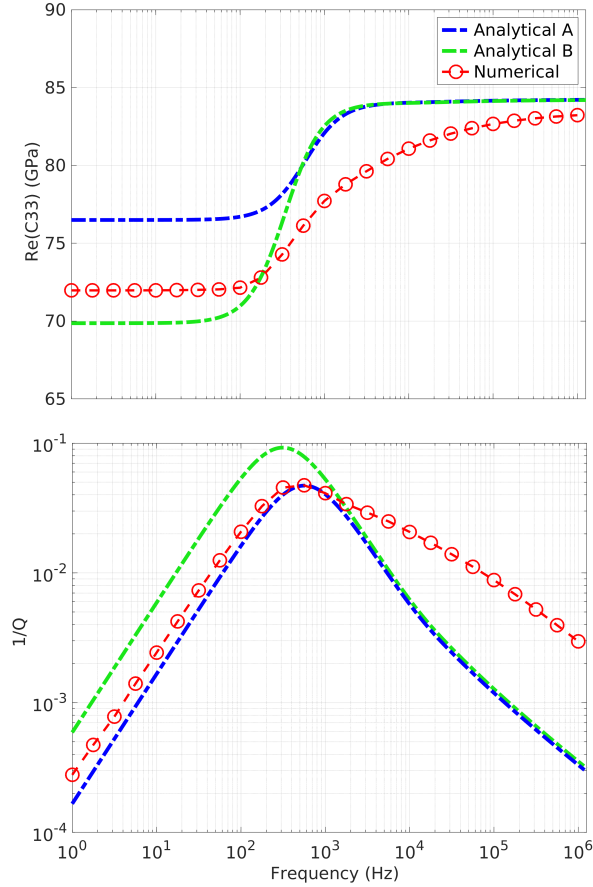


Figure 2.7: Numerical and analytical results for the *big pore* model (Figure 2.1(c-d)): (a) Real part of the C_{33} component, (b) dimensionless attenuation for the C_{33} component. Each red circle corresponds to one test. The maximum of the attenuation curve (Analytical solution with Workflow A, blue curve) is exactly the same as in the numerical result by a chance because the comparison between the analytical solution and numerical result for the modified frame exhibit discrepancy; it is explained in the text.

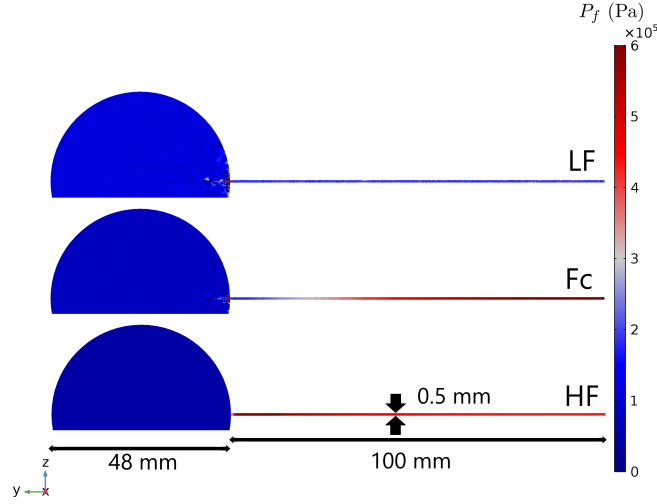


Figure 2.8: Snapshots of the fluid pressure P_f in the fracture at three different frequencies for the *big pore* model: Lf - low frequency (relaxed state), Fc - intermediate frequency (close to the characteristic frequency) and HF - high frequency (unrelaxed state).

b) Extended analytical solution

To obtain the results from the analytical solution, Z_n and Z_t are calculated using the same extended analytical solution as in the *big pore* model. Then, using equations 4.58-6.100 the complex-valued stiffness tensor is calculated for the output of the Workflows A and B (Figure 2.6).

c) Comparison

Figure 2.9 shows the results for the C_{33} complex-valued component of the stiffness tensor obtained from the numerical simulations and from the analytical solution with two different sets of normal and tangential compliances derived from the Workflows A and B. The dispersion and attenuation are small in this model, therefore, the two analytical solutions show an apparent better agreement than for the *big pore* model (Figure 2.7). However, the relative difference between the analytical and numerical results is comparable to those for the *big pore* model. Here, both analytical solutions predict much higher attenuation compared to the numerical result.

Figure 2.10 shows snapshots of the fluid pressure P_f in the fracture and in the stiff pore at three different frequencies. The only geometrical difference between this *small pore* model and *big pore* model is that the torus is smaller. The volume of the small torus is only approximately six times bigger than the crack volume, therefore, the fluid pressure gradient equilibrates faster and a larger value of the fluid pressure is observed in the relaxed state than that in the *big pore* model (Figure 2.8, LF). The characteristic frequency is higher and the overall dissipation is lower. The numerical artifacts observed in these snapshots have negligible effect on our numerical solution as explained above.

2.5.4 Modified frame

As mentioned before, the modified frame is a virtual rock, in which only the crack is filled with fluid, whereas the stiffer pore is empty (Mavko and Jizba, 1991). In the low-frequency limit, the relaxed moduli of the modified frame are equal to the rock dry moduli. In the high-frequency limit, the fluid-saturated crack stiffens the frame and the unrelaxed moduli of the modified frame are equal to the dry moduli of the rock without a compliant porosity (i.e., without a crack).

Considering the *big pore* model (Figure 2.1c, 2.1d), the torus is dry whereas the crack is filled with a compressible Newtonian fluid (glycerol). This configuration corresponds to the modified frame. Because the torus is dry, this configuration implies $P_f = 0$ boundary condition at the edge of the crack. The main difference between this

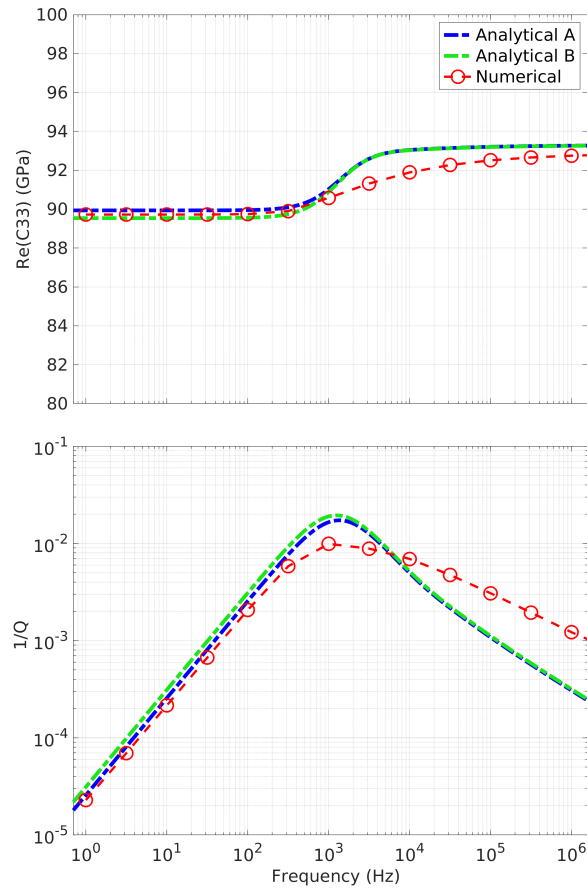


Figure 2.9: Numerical and analytical results for the *small pore* model (Figure 2.1(e-f)): (a) Real part of the C_{33} component and (b) dimensionless attenuation for the C_{33} component.

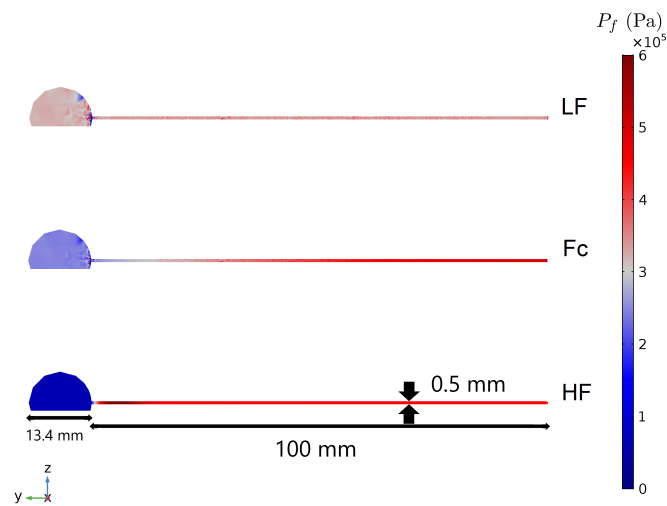


Figure 2.10: Snapshots of the fluid pressure P in the fracture at three different frequencies for the *small pore* model: Lf - low frequency (relaxed state), Fc - intermediate frequency (close to the characteristic frequency) and HF - high frequency (unrelaxed state).

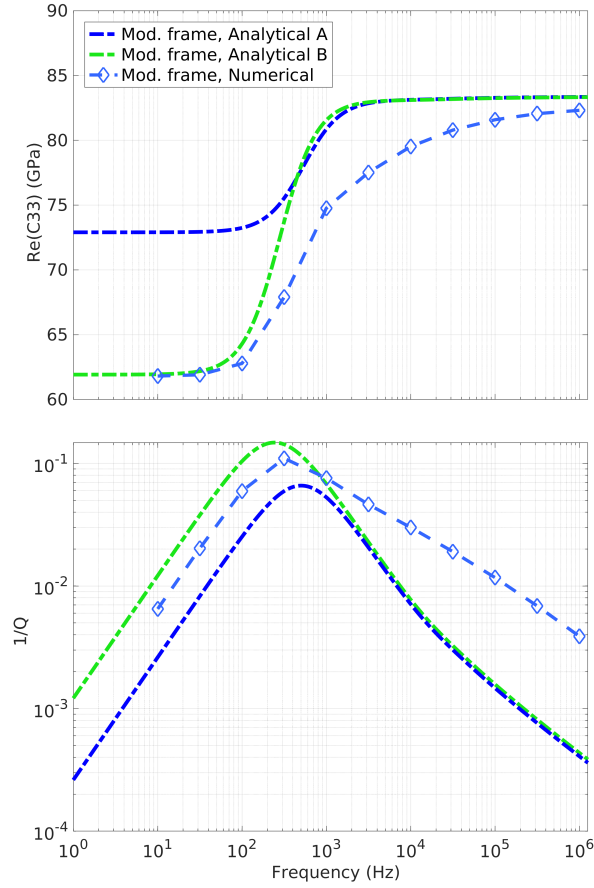


Figure 2.11: Numerical and analytical results for the *modified frame big pore* model: (up) Real part of the C_{33} component and (down) dimensionless attenuation for the C_{33} component. Each rhombus corresponds to a numerical calculation. Crack aspect ratio is 0.0025.

modified frame model and the $P_f = 0$ model (Figure 2.1a, 2.1b) is the actual presence of the torus which affects the effective properties of the model.

To compare the numerical results with the analytical solution, Z_n and Z_t are calculated for Workflows A and B. Then, using equations 4.58-4.63 the complex-valued stiffness tensor $C_{mn}^{MF}(\omega)$ is calculated. In these analytical solutions we do not use Gassmann equation to saturate the medium because the stiff pore is dry (equation 4.63 becomes $C_{mn}^{sat}(\omega) = C_{mn}^{MF}(\omega)$). Figure 2.11 shows results for the C_{33} complex-valued component of the stiffness tensor obtained from the numerical result and from the analytical solution with two different sets of normal and tangential compliances derived from Workflows A and B. The dispersion curves show that in the high frequency limit the two analytical and the numerical solutions are in a very good agreement and the analytical solution with Workflow B also shows a good fit in the low frequency regime. However, the frequency dependences of the dispersion and attenuation curves obtained via the numerical simulation have a completely different shape compared to both analytical solutions. More specifically, the maximum amplitude of the attenuation peak and the right slope of the attenuation curve are different compared to both analytical solutions. The previous very good fit of the attenuation magnitude between the analytical solution with Workflow A and the numerical result for the saturated case (Figure 2.7) is coincidental. This becomes apparent by the mismatch of the attenuation curves for the corresponding modified frame between the analytical solution with Workflow A and the numerical solution shown in Figure 2.11. In Figure 2.7, this discrepancy was coincidentally corrected by applying the anisotropic Gassmann equation to the analytical model with Workflow A.

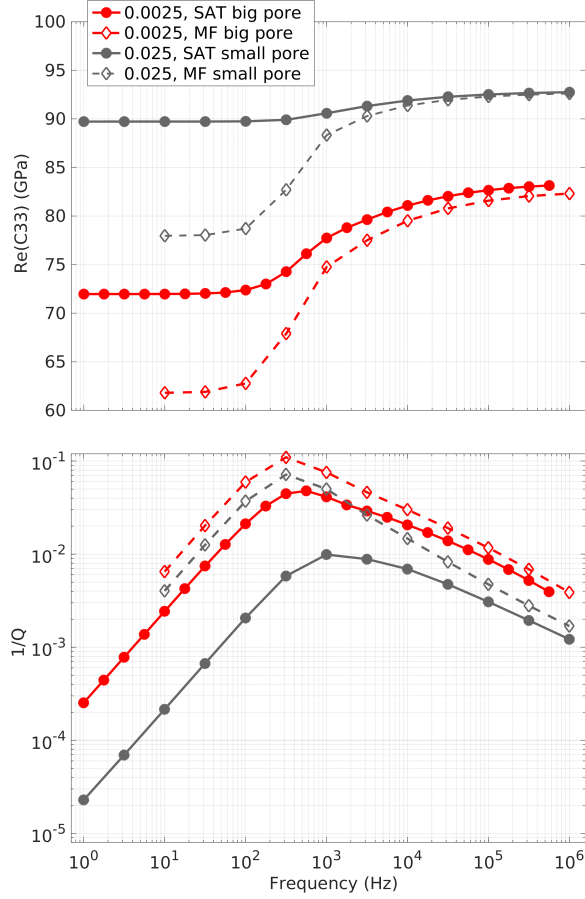


Figure 2.12: Numerical results and the *modified frame big pore*, the *modified frame small pore* models and corresponding saturated models: (up) Real part of the C_{33} component and (down) dimensionless attenuation for the C_{33} component. Each red circle or rhombus correspond to a numerical calculation.

Comparison to full saturation

Figure 2.12 shows numerical results for four models: the *modified frame* model for the *big pore* model, the corresponding fully saturated *big pore* model, the *modified frame* model for the *small pore* model, the corresponding fully saturated *small pore* model. Basically, the difference between the dashed and solid curves is due to the presence of the fluid in a big or small torus. The right slope of the attenuation curves of the *modified frame* models is approximately the same independently of the size of the torus. The same behavior follows for the saturated cases: the right slope of the attenuation curves of saturated models is approximately the same independently of the size of the torus.

2.5.5 Numerical results for different crack aspect ratios

We consider the fully-saturated *big pore* model and change the aspect ratio of the crack. In other words, we keep the same length of the crack but increase its aperture. Figure 2.13 shows results for the C_{33} complex-valued component of the stiffness tensor obtained from the numerical simulation with aspect ratios of 0.0025, 0.005 and 0.01. For comparison, we also show results for the C_{33} complex-valued component of the $P_f = 0$ model. According to Figure 2.13, the frequency dependence of the dispersion and attenuation curves for those three aspect ratios is the same. The shift in the characteristic frequency is controlled by the aspect ratio of the crack. The attenuation magnitude is the same at those three characteristic frequencies.

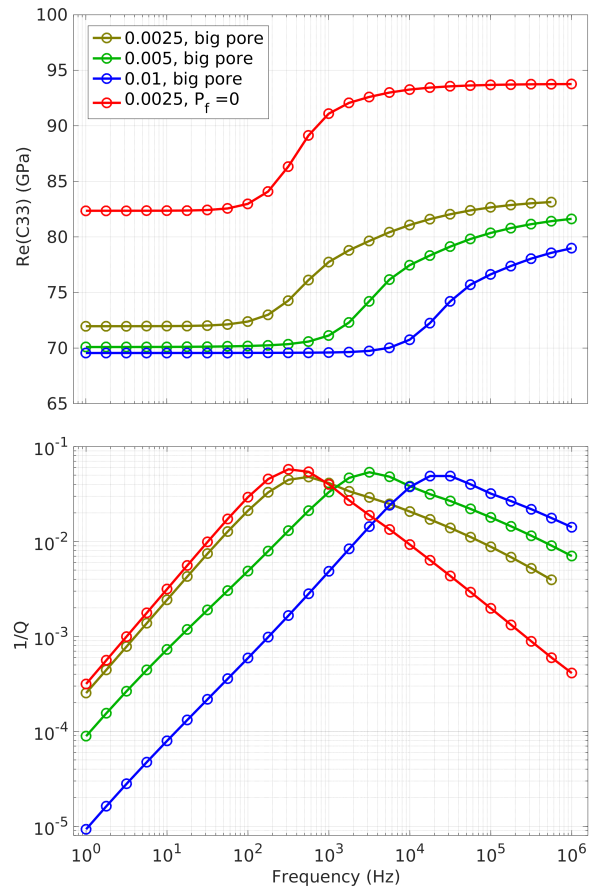


Figure 2.13: Numerical results for the *big pore* model (Figure 2.1(c-d)) and the $P_f = 0$ model (with fluid pressure equal to zero at the edge of the cylinder) (Figure 2.1(a-b)), cracks with different aspect ratios of 0.0025; 0.005; 0.01: (up) Real part of the C_{33} component and (down) dimensionless attenuation for the C_{33} component.

2.6 Discussion

There are two main sources of strong discrepancies between the numerical results and the analytical solution. First, the calculation of the frame stiffness moduli in the analytical solution considers the pores and cracks as being disconnected. Second, the frequency dependence of attenuation and dispersion at intermediate frequencies in the analytical solution is based on several strong assumptions and shows significant discrepancies compared to the numerical results. The first one could be improved in the current analytical squirt flow solutions by using a more complete approach for calculating the frame moduli. The second one is more difficult and unclear how to implement via an analytical solution. Another observation from this study is the frequency dependence of the C_{13} component of the frame moduli, which is difficult to take into account in the analytical solution but, in general, the effect is of minor importance.

We showed that the analytical solution of *Collet and Gurevich (2016)* is accurate only for the $P_f = 0$ model where the stiff porosity is zero, but it does not approximate accurately the results for models with non-zero stiff porosity. Despite all of the discrepancies between the analytical solution and numerical results, this analytical solution is probably the best for such an analysis because it uses specific material and geometrical properties without any fitting parameters.

Design and calculation of the modified frame and dry frame moduli

One of the most important outcomes of this numerical study is the adequate calculation of the double porosity frame moduli. By double porosity we mean that the pore space consists of two types of pores: the stiff isometric pore and the compliant crack. Furthermore, the pore and the crack are connected. The analytical solution by *Collet and Gurevich (2016)* is based on the two-step homogenization approach: they consider a rock matrix (grains and a pore) and then embed a crack into that rock matrix using the normal and tangential compliances of the crack. This corresponds to our Workflow A (Figure 2.6). Roughly, this workflow gives the frame moduli accounting for the crack and the stiff pore as being not connected (i.e., as if the crack and the pore are embedded simultaneously into the grain material but disconnected and far from each other, so the elastic interactions are very small, see Figure 2.14). Hence, this workflow significantly overestimates the stiffness of the frame material and significantly underestimates dispersion and the overall attenuation (Figure 2.7). In this case, there is a controversial issue: *Gurevich et al. (2010)* and *Collet and Gurevich (2016)* study the effect of fluid flow between the crack and the stiff pore and, at the same time, they use the frame moduli of disconnected cracks and pores. Workflow B shows a better prediction of the low- and high-frequency limits of the dispersion curve and the overall attenuation but significantly overestimates the maximum attenuation (due to amplification of the imaginary part of $Z_n^{MF}(\omega)$ if we connect the crack and the stiff pore). Quantitatively, Z_n in Workflow B is two times larger than Z_n in Workflow A, which is only due to the connectivity effect of the crack and the pore. Thus, any change in the geometry of the pore space will immediately affect the stiffness of the rock and the fluid-flow properties, thus these properties are strongly coupled.

The two-step homogenization approach for calculating the effective elastic properties of cracked-porous rocks can be used considering a mesoscopic scenario. In this scenario, the cracks are at least two orders of magnitude larger than the pores, therefore, the two-step homogenization approach might work quite well (i.e., the torus connected to the crack makes no sense at a mesoscopic scale since cracks or fractures are much larger than the pores). Such double porosity media with mesoscopic cracks were studied by *Galvin and Gurevich (2009)*, *Gurevich et al. (2009b)* and *Guo et al. (2017a,b)*.

Collet and Gurevich (2016) assumed that the crack can be accurately described by the two parameters: normal and tangential compliances Z_n and Z_t (however, we show that the C_{13} component is also different). This approach is known as the linear-slip theory (*Schoenberg and Sayers, 1995*). There are several solutions which link the crack compliances Z_n and Z_t with crack geometry and the stiffness of the background medium (*Walsh, 1965; Kachanov, 1993*). Some insights into these theories are given by *Bakulin et al. (2000a,b)*. Note, that the linear-slip theory leads to the so-called non-interactive approximation (*Sevostianov and Kachanov, 1999; Kachanov and Sevostianov, 2018*), which assumes that different cracks (or cracks and surrounding pores) do not interact with each other; for higher porosity — more complicated effective methods should be used as it is shown in the numerical study by *Saenger et al. (2004)*.

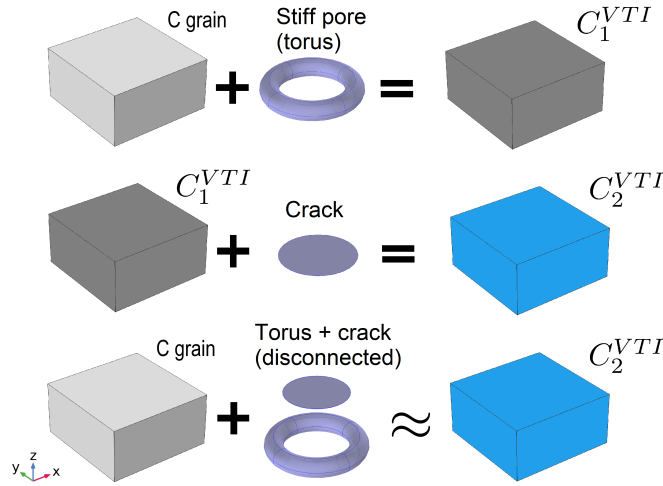


Figure 2.14: Sketch illustrating that the two-step homogenization approach produces the C_2^{VTI} stiffness tensor which is approximately equal to the case if we embed the crack and the stiff pore (disconnected) into the grain material.

The effect of connectivity of the pore space is usually not taken into account properly in analytical solutions due to theoretical difficulties (as far as we know there is no general analytical solution of this problem) and due to the fact that the information about the connectivity of the pore space in real rocks is usually unknown. However, there are several solutions to this problem, for example, by introducing an additional "pore space connectivity" parameter. This parameter can be inverted by linking the effective properties predicted by the analytical solution to a given real data set (Bayuk *et al.*, 2007; Alkhimenkov and Bayuk, 2017).

Frequency-dependent fluid bulk modulus

Gurevich *et al.* (2010) showed that the stiffness of the crack in relaxed and unrelaxed states can be described by the frequency dependent fluid bulk modulus $K_f^*(\omega)$. Our numerical results confirmed that this is true if the crack having $P_f = 0$ boundary condition at the edge is embedded into the grain material whereas the torus is replaced by the grain material. This occurs because the Gurevich *et al.* (2010) solution for the frequency-dependent fluid bulk modulus simply applies boundary conditions to the walls of the crack and does not take into account the stiffness of the pore space surrounding the crack. Our numerical simulation of the modified frame clearly shows that, once we include a small volume (0.3%) of the dry stiff pore connected to the crack, the frequency-dependence of the effective properties changes completely (Figure 2.11). However, it is very difficult to fully solve that coupled elasticity-fluid flow problem analytically.

The slopes of the high frequency asymptote of the attenuation curve in the numerical and analytical solutions are different (ω^{-1} for the analytical solution versus $\omega^{-1/2}$ for the numerical solution). In both numerical models, the *big pore* and the *small pore* models, the frequency range over which attenuation is significant broadens compared to the analytical solution due to the different asymptotic behavior of the attenuation curve in the high frequency regime. It is interesting that the $\omega^{-1/2}$ power law also describes the high frequency asymptote of the attenuation curves due to flow between stiff pores and mesoscopic cracks (that is, cracks much larger than pores but still smaller than the wavelength) (Galvin and Gurevich, 2009; Guo *et al.*, 2017a).

C_{13} component of the frame moduli

Our numerical simulations show that the C_{13} component of the modified frame (the *big pore* model) is frequency dependent. Furthermore, the crack connected to the torus can not be accurately described by only two parameters in the compliance domain: Z_n and Z_t . Equation 2.17 shows the difference in the compliance domain $\Delta S_{mn} = S_1^{VTI} - S_3^{VTI}$, which is used to calculate Z_n and Z_t in Workflow B (Figure 2.6). It can be seen that $\Delta S_{33} = 4.251 \cdot 10^{-12}$ and $\Delta S_{44} = \Delta S_{55} = 7.680 \cdot 10^{-12}$ are the actual Z_n and Z_t parameters in the Workflow B. But $\Delta S_{13} = 0.486 \cdot 10^{-12}$ is still significant. Hence, if we ignore the non-negligible off-diagonal elements, the corresponding C_{13} in the stiffness domain diverges from the correct numerical C_{13} by approximately 4.5 GPa. This affects the analytical model in two ways. First, the difference between the low and high frequency limits of the C_{13} component of the modified frame is approximately 4.5 GPa in the *big pore* model, so the modified frame C_{13} component gradually increases with frequency during the transition from the low to the high frequency. Second, in the generalized Gassmann's equation (equation 6.100), the calculation of K^* involves the C_{13} component four times (because $C_{13} = C_{23} = C_{31} = C_{32}$), which leads to more than 15 GPa overestimation of the correct K^* (thus, K^* is also frequency dependent). Therefore, if we neglect the frequency dependence of the C_{13} component, the generalized bulk modulus of the frame will become significantly different from the actual value. It is clearly visible in Figure 2.7 where the low-frequency limit of the analytical solution with Workflow B does not match the numerical result because this analytical solution is saturated using Gassmann's equations. On the other hand, the low-frequency limit of the modified frame for the analytical solution with Workflow B is in excellent agreement with the numerical result because the stiff pore is dry and the C_{13} component effects vanish (Figure 2.11). For the *big pore* model,

$$\Delta S_{mn}^{big\ pore} = S_1^{VTI} - S_3^{VTI} = 10^{-12} \cdot \begin{bmatrix} 0.034 & -0.037 & 0.486 & 0 & 0 & 0 \\ -0.037 & 0.034 & 0.486 & 0 & 0 & 0 \\ 0.486 & 0.486 & 4.251 & 0 & 0 & 0 \\ 0 & 0 & 0 & 7.680 & 0 & 0 \\ 0 & 0 & 0 & 0 & 7.680 & 0 \\ 0 & 0 & 0 & 0 & 0 & 0.018 \end{bmatrix}. \quad (2.17)$$

For the *small pore* model,

$$\Delta S_{mn}^{small\ pore} = S_1^{VTI} - S_3^{VTI} = 10^{-12} \cdot \begin{bmatrix} 0.004 & -0.0001 & 0.009 & 0 & 0 & 0 \\ -0.0001 & 0.004 & 0.009 & 0 & 0 & 0 \\ 0.009 & 0.009 & 2.244 & 0 & 0 & 0 \\ 0 & 0 & 0 & 3.109 & 0 & 0 \\ 0 & 0 & 0 & 0 & 3.109 & 0 \\ 0 & 0 & 0 & 0 & 0 & 0.010 \end{bmatrix}. \quad (2.18)$$

For the *small pore* model, the C_{13} component is almost the same as for the $P_f = 0$ model and does not change significantly over the frequency range. Equation 3.7 shows the difference in the compliance domain $\Delta S_{mn} = S_1^{VTI} - S_3^{VTI}$, which is used to calculate Z_n and Z_t in Workflow B (see Figure 2.6). It can be seen that $\Delta S_{33} = 2.244 \cdot 10^{-12}$ and $\Delta S_{44} = \Delta S_{55} = 3.109 \cdot 10^{-12}$ are the actual Z_n and Z_t parameters in Workflow B. $\Delta S_{13} = 0.009 \cdot 10^{-12}$ is negligible.

In summary, the crack compliance in the $P_f = 0$ model and in the *small pore* model can be accurately described by only the two parameters: Z_n and Z_t . But, in the *big pore* model, the crack compliance can not be described by only Z_n and Z_t , the C_{13} component is also important.

Fluid pressure field as a function of frequency

One of the key parameters in the squirt flow mechanism is the ratio between the non-compliant and compliant pore volumes. In the *big pore* model, the ratio of non-compliant (torus) to compliant (crack) porosity is $0.045/(4.9 \cdot 10^{-4}) \approx 92$. Therefore, only a little increase in the fluid pressure is expected in the big torus at low frequencies. In the big torus, the fluid pressure is $\approx 1 \cdot 10^5$ Pa in the low-frequency limit (10^0 Hz); the fluid pressure is $\approx 0.435 \cdot 10^5$ Pa in the high frequency limit (10^6 Hz). Thus, the increase in fluid pressure is of about 2.3 times. The applied boundary conditions are for displacement (10^{-6} m) and the fluid pressure values are given for the P-wave modulus test in z -direction (i.e. for C_{33} component).

In the *small pore* model, the ratio of non-compliant to compliant porosity is $0.0034/(4.9 \cdot 10^{-4}) \approx 7$. Thus, a significantly increase in fluid pressure in the torus is expected in the low frequency regime, compared to the high frequency limit, because the difference between non-compliant and compliant porosity is small (less than one order of magnitude). In the small torus, the fluid pressure is $\approx 3.3 \cdot 10^5$ Pa in the low-frequency limit (10^0 Hz); the fluid pressure is $\approx 0.58 \cdot 10^5$ Pa in the high-frequency limit (10^6 Hz). Thus, the increase in the fluid pressure is of about 5.7 times.

2.7 Conclusions

We have calculated numerically the frequency dependence of the effective stiffness properties of a fluid-saturated porous medium caused by squirt flow. Our 3D numerical models consist of a pore space embedded into a solid grain material. The pore space is represented by a flat cylinder, representing a crack, whose edge is connected with a torus, representing a stiff isometric pore. Grains were described as a linear isotropic elastic material while the fluid phase filling the pore space was described by the quasistatic linearized compressible Navier-Stokes momentum equation.

We compared the numerical results to a published analytical solution for squirt flow. The numerical and analytical solutions agree only for the simplest model: the edge of the crack is subjected to zero fluid pressure boundary condition while the stiff pore is absent. For this model, low- and high-frequency limits of the dispersion and attenuation curves, intermediate-frequency behavior and all asymptotes are in a very good agreement between the numerical and analytical solutions. However, the considered model is not realistic.

For the model with a stiff pore modeled as a torus, there are significant differences between numerical and analytical solutions: (1) the maximum attenuation predicted by the analytical model is significantly under- or over- estimated, depending on the frame moduli calculation in the analytical model; (2) the transition from the low to high frequencies is much sharper compared to the numerical results; (3) the slopes of the high-frequency asymptote of the attenuation curve in the numerical and analytical solutions are different (ω^{-1} for the analytical solution versus $\omega^{-1/2}$ for the numerical solution). The maximum magnitude of attenuation predicted by the analytical solution is under- or over- estimated significantly (depending on how the frame moduli are calculated in the analytical model) compared to the numerical results.

Our analysis suggests that there are two main sources of discrepancies between the numerical results and the analytical solution. First, the calculation of the frame stiffness moduli in the analytical solution does not take into account the fact that pores and cracks are connected, as it assumes a porous background and in the next step embeds cracks into this homogenized medium. The numerical results show that this two-step homogenization approach corresponds to the double-porosity media where crack and pores are disconnected, which contradicts the concept of fluid flow in the analytical solution. Second, the frequency dependence of the attenuation and dispersion at intermediate frequencies in the analytical solution is based on several strong assumptions: the analytical model assumes that the frequency dependence is controlled only by the fluid flow in the crack while the numerical results show that the frequency dependence is affected also by surrounding stiff pores connected to the crack. Further research should involve the modification of the analytical solution to include more adequate frame moduli calculation of the double-porosity model, more adequate modeling of the flow between compliant and stiff pores, and a more realistic geometry of the pore space.

Acknowledgments

This research is funded by the Swiss National Science Foundation, project number 172691. Yury Alkhimenkov thanks Holger Steeb for fruitful discussions regarding the numerical simulations and Yury Podladchikov for fruitful discussions regarding the Bessel functions. We thank Yves Guéguen, Erik Saenger and an anonymous reviewer for their constructive comments which helped us to improve the manuscript.

2.8 Appendix A: Boundary conditions

Let us consider a cuboid with volume $V = (0, Lx) \times (0, Ly) \times (0, Lz)$ and Γ its boundary $\Gamma = \Gamma^{xz0} \cup \Gamma^{xzL} \cup \Gamma^{yz0} \cup \Gamma^{yzL} \cup \Gamma^{xy0} \cup \Gamma^{xyL}$, where, for example, Γ^{xz0} represents a xz plane with zero coordinate and, e.g., Γ^{xzL} represents a xz plane with Ly coordinate. There are six planes in total. Because we are dealing with a VTI medium, only five independent components of the stiffness tensor are needed. Three kinds of tests were applied: a normal compression relaxation test, a simple shear test and one mixed test for the C_{13} component. The general approach is the following: we apply displacement boundary conditions for a certain frequency. Then, we calculate the volume average stress and strain fields over the whole model domain using the following equations for a given frequency ω :

$$\langle \epsilon_{ij} \rangle = \frac{1}{V} \int_V \epsilon_{ij}(\mathbf{x}) dV, \quad (2.19)$$

where V is a model domain and

$$\langle \sigma_{ij} \rangle = \frac{1}{V} \int_V \sigma_{ij}(\mathbf{x}) dV. \quad (2.20)$$

Volume averaged stress $\langle \sigma_{ij} \rangle$ and strain $\langle \epsilon_{ij} \rangle$ fields are related via the Hooke's law

$$\langle \sigma_{ij} \rangle = C_{ijkl} \langle \epsilon_{kl} \rangle, \quad (2.21)$$

which is the $C_{ijkl} = C_{mnn}$ component of the stiffness matrix. Thus, we need several tests to obtain a relation between different $\langle \sigma_{ij} \rangle$ and $\langle \epsilon_{kl} \rangle$.

Normal compression relaxation test

Normal compression relaxation test is needed to calculate $M = \lambda + 2\mu$ component of the stiffness tensor.

For the C_{33} component ($\langle \sigma_3 \rangle = C_{33} \cdot \langle \epsilon_3 \rangle$):

Γ^{xyL} is set to $u_{zz} = \Delta u$; u_{xx}, u_{yy} are free

Γ^{xy0} is set to $u_{zz} = 0$; u_{xx}, u_{yy} are free

Γ^{xz0} and Γ^{xzL} are set to $u_{yy} = 0$; u_{zz}, u_{xx} are free

Γ^{yz0} and Γ^{yzL} are set to $u_{xx} = 0$; u_{zz}, u_{yy} are free,

where $\Delta u = 10^{-6}$. The same relaxation tests are used to calculate C_{11} and C_{22} components.

Simple shear relaxation test

Simple shear relaxation test is needed to calculate shear modulus μ component of the stiffness tensor. For the C_{55} (xz) component ($\langle\sigma_5\rangle = C_{55} \cdot \langle\epsilon_5\rangle$):

Γ^{xyL} is set to $u_{xx} = \Delta u$; u_{zz}, u_{yy} are free
 Γ^{xy0} is set to $u_{zz} = 0$; $u_{xx} = 0, u_{yy} = 0$
 Γ^{xz0} and Γ^{xzL} are set to $u_{yy} = 0$; $u_{zz} = 0, u_{xx}$ is free
 Γ^{yz0} and Γ^{yzL} are set to $u_{yy} = 0$; $u_{zz} = 0, u_{xx}$ is free

The same type of relaxation tests are used to calculate C_{44} and C_{66} components.

C_{13} mixed test

The mixed test for C_{13} component can be easily derived from the anisotropic stress-strain relation (Hooke's law) (similar to the 2D approach by *Carcione et al.* (2011)).

Γ^{xyL} is set to $u_{zz} = \Delta u$; u_{xx}, u_{yy} are free
 Γ^{xzL} is set to $u_{yy} = \Delta u$; u_{zz}, u_{xx} are free
 Γ^{xy0} is set to $u_{zz} = 0$; u_{xx}, u_{yy} are free
 Γ^{xz0} is set to $u_{yy} = 0$; u_{xx}, u_{zz} are free
 Γ^{xz0} and Γ^{xyL} are set to $u_{yy} = 0$; u_{zz}, u_{xx} are free
 Γ^{yz0} and Γ^{yzL} are set to $u_{xx} = 0$; u_{zz}, u_{yy} are free

Then, using the following equations

$$C_{13} = \frac{\langle\sigma_2\rangle \cdot C_{33} - \langle\sigma_3\rangle \cdot C_{22}}{\langle\sigma_3\rangle - \langle\sigma_2\rangle}, \quad (2.22)$$

or

$$C_{13} = \frac{\langle\sigma_2\rangle}{\langle\epsilon_2\rangle} - C_{22}, \quad (2.23)$$

the C_{13} component is calculated (C_{33} and $C_{22} = C_{11}$ are taken from the direct tests). Equations 2.22 and 3.11 are found from the Hooke's Law considering non-zero strains in y - and z directions and, then, solving a system of two equations analytically.

Direct test approach

The direct test approach for calculating effective stiffness moduli can be used when the model's symmetry is known, which is the case in our modeling. According to the stress-strain relation (equation 2.21), C_{mn} components are calculated via

$$C_{mn} = \frac{\langle\sigma_m\rangle}{\langle\epsilon_n\rangle}. \quad (2.24)$$

We are dealing with a VTI medium, only five independent components of the stiffness tensor are needed. Thus, we need two normal compression relaxation tests for C_{11} and C_{33} components (because $C_{11} = C_{22}$), two simple shear relaxation tests for C_{55} and C_{66} components (because $C_{44} = C_{55}$) and one mixed direct test for the C_{13} component

2.9 Appendix B: Rotation of a fourth-rank tensor: HTI versus VTI

The stiffness matrix of a transversely isotropic medium with a vertical symmetry axis (VTI) is (in Voigt notation) (*Tsvankin, 2012*)

$$C_{mn}^{VTI} = \begin{bmatrix} C_{11}^{VTI} & C_{11}^{VTI} - 2C_{66}^{VTI} & C_{13}^{VTI} & 0 & 0 & 0 \\ C_{11}^{VTI} - 2C_{66}^{VTI} & C_{11}^{VTI} & C_{13}^{VTI} & 0 & 0 & 0 \\ C_{13}^{VTI} & C_{13}^{VTI} & C_{33}^{VTI} & 0 & 0 & 0 \\ 0 & 0 & 0 & C_{44}^{VTI} & 0 & 0 \\ 0 & 0 & 0 & 0 & C_{44}^{VTI} & 0 \\ 0 & 0 & 0 & 0 & 0 & C_{66}^{VTI} \end{bmatrix}, \quad (2.25)$$

where the superscript $(\cdot)^{VTI}$ means that the component belongs to VTI media. In this study, all numerical simulations are performed in VTI media. The analytical solution of *Collet and Gurevich (2016)* is developed for horizontal transverse isotropy media (HTI). The stiffness matrix of HTI media with the symmetry axis along x direction is:

$$C_{mn}^{HTI} = \begin{bmatrix} C_{11}^{HTI} & C_{13}^{HTI} & C_{13}^{HTI} & 0 & 0 & 0 \\ C_{13}^{HTI} & C_{33}^{HTI} & C_{33}^{HTI} - 2C_{44}^{HTI} & 0 & 0 & 0 \\ C_{13}^{HTI} & C_{33}^{HTI} - 2C_{44}^{HTI} & C_{33}^{HTI} & 0 & 0 & 0 \\ 0 & 0 & 0 & C_{44}^{HTI} & 0 & 0 \\ 0 & 0 & 0 & 0 & C_{66}^{HTI} & 0 \\ 0 & 0 & 0 & 0 & 0 & C_{66}^{HTI} \end{bmatrix}, \quad (2.26)$$

where the superscript $(\cdot)^{HTI}$ means that the component belongs to HTI media. Generally speaking, the 4-th rank stiffness tensor in Euclidean space can be rotated using Euler angles. Fortunately, both VTI and HTI symmetry classes belong to a transversely isotropic (TI) medium, which has a single axis of rotational symmetry (*Fedorov, 1968*). Therefore, the transformation from HTI media to VTI, and vice versa, doesn't require any sophisticated operations. Thus, the transformation from the VTI stiffness matrix to the HTI stiffness matrix, and vice versa, can be done by interchanging the indices 1 and 3 and slightly modifying the structure of the stiffness matrix. The recipe is the following: 1) using the analytical solution of *Collet and Gurevich (2016)*, calculate the resulting stiffness matrix which is of a HTI symmetry (equation 2.26) and 2) construct the VTI stiffness matrix using the components of the HTI stiffness matrix from step 1) by the following rule:

$$C_{mn}^{VTI} = \begin{bmatrix} C_{33}^{HTI} & C_{33}^{HTI} - 2C_{44}^{HTI} & C_{13}^{HTI} & 0 & 0 & 0 \\ C_{33}^{HTI} - 2C_{44}^{HTI} & C_{33}^{HTI} & C_{13}^{HTI} & 0 & 0 & 0 \\ C_{13}^{HTI} & C_{13}^{HTI} & C_{11}^{HTI} & 0 & 0 & 0 \\ 0 & 0 & 0 & C_{66}^{HTI} & 0 & 0 \\ 0 & 0 & 0 & 0 & C_{66}^{HTI} & 0 \\ 0 & 0 & 0 & 0 & 0 & C_{44}^{HTI} \end{bmatrix} \quad (2.27)$$

The resulting stiffness matrix (equation 2.27) corresponds to VTI media but all components are those from the HTI stiffness matrix (equation 2.26).

Chapter 3

Azimuth-, angle- and frequency-dependent seismic velocities of cracked rocks due to squirt flow

Yury Alkhimenkov, Eva Caspari, Simon Lissa and Beatriz Quintal

Published¹ in *Solid Earth*.

¹Alkhimenkov, Y. et al. (2020). Azimuth-, angle- and frequency-dependent seismic velocities of cracked rocks due to squirt flow. *Solid Earth*, 11(3), 855-871, doi:10.5194/se-11-855-2020

Abstract

Understanding the properties of cracked rocks is of great importance in scenarios involving CO_2 geological sequestration, nuclear waste disposal, geothermal energy, and hydrocarbon exploration and production. Developing noninvasive detecting and monitoring methods for such geological formations is crucial. Many studies show that seismic waves exhibit strong dispersion and attenuation across a broad frequency range due to fluid flow at the pore scale known as squirt flow. Nevertheless, how and to what extent squirt flow affects seismic waves is still a matter of investigation. To fully understand its angle- and frequency-dependent behavior for specific geometries, appropriate numerical simulations are needed. We perform a three-dimensional numerical study of the fluid–solid deformation at the pore scale based on coupled Lamé–Navier and Navier–Stokes linear quasistatic equations. We show that seismic wave velocities exhibit strong azimuth-, angle- and frequency-dependent behavior due to squirt flow between interconnected cracks. Furthermore, the overall anisotropy of a medium mainly increases due to squirt flow, but in some specific planes the anisotropy can locally decrease. We analyze the Thomsen-type anisotropic parameters and adopt another scalar parameter which can be used to measure the anisotropy strength of a model with any elastic symmetry. This work significantly clarifies the impact of squirt flow on seismic wave anisotropy in three dimensions and can potentially be used to improve the geophysical monitoring and surveying of fluid-filled cracked porous zones in the subsurface.

3.1 Introduction

Wave propagation is controlled by the effective rock properties. Wave velocity and attenuation can be estimated from seismic data in scenarios such as seismic exploration, seismology, borehole measurements and tomography. Rock physics could then be used to estimate different rock properties, such as mineral composition, elastic moduli, the presence of a fluid, and pore space connectivity (and hence permeability) from seismic measurements. Thus, investigation of how cracks and fluids affect seismic properties has many practical applications. In activities including nuclear waste disposal, CO_2 geological sequestration, hydrocarbon exploration and production, geothermal energy production, and seismotectonics, a quantification of the fluid content, porosity and permeability of rocks are of great interest. All these activities can benefit from rock physics studies, and that is why cracked rocks have been under intensive studies during the last decades.

Cracks and grain-scale discontinuities are the key rock parameters which control effective elastic and hydraulic properties of such rocks. Many studies show that seismic waves exhibit significant dispersion and attenuation in cracked porous rocks due to pore-scale fluid flow (O'Connell and Budiansky, 1977; Dvorkin *et al.*, 1995; Gurevich *et al.*, 2010; Müller *et al.*, 2010). Furthermore, cracks cause significant seismic wave anisotropy (Schoenberg and Sayers, 1995; Sayers and Kachanov, 1995; Sayers, 2002; Chapman, 2003; Maultzsch *et al.*, 2003; Tsvankin and Grechka, 2011).

Fluid flow due to a passing wave may happen at different scales: at the wavelength scale, at the mesoscopic scale and at the pore scale (Müller *et al.*, 2010). Biot's theory (Biot, 1962b) describes the so-called global flow at the wavelength scale, but its overall effect on a passing wave at seismic frequencies is usually much smaller than that of fluid flow at the mesoscopic and pore scales (Pride *et al.*, 2004). The mesoscopic scale is that much larger than the pore-scale but smaller than the wavelength. At this scale, studies are performed in the framework of Biot theory, assuming heterogeneous rock properties. One can define fractures as discontinuities at the mesoscopic scale and cracks as discontinuities at the pore scale. There are several analytical and numerical studies on the effect of wave-induced fluid flow between mesoscopic fractures and a porous rock background and between interconnected fractures using Biot's equations (Brajanovski *et al.*, 2005; Rubino *et al.*, 2013; Quintal *et al.*, 2014; Masson and Pride, 2014; Grab *et al.*, 2017; Hunziker *et al.*, 2018; Caspari *et al.*, 2019) as well as on the comparison between the numerical and analytical results (Guo *et al.*, 2017b, 2018a). Experimental studies of synthetic rock samples showed the impact of fluid-saturated fractures on seismic velocities (Amalokwu *et al.*, 2016; Tillotson *et al.*, 2012, 2014). The resulting frequency-dependent anisotropy was analyzed by Carcione *et al.* (2013), Rubino *et al.* (2017) and Barbosa *et al.* (2017). The last two also considered fracture-to-fracture flow, in addition to fracture-to-background flow.

At the pore scale, a passing wave induces fluid pressure gradients which occur between interconnected cracks, as well as between cracks and stiffer pores. Such pressure gradients force fluid to move between different cracks and pores until the pore pressure equilibrates throughout the connected pore space. This phenomenon, known as squirt flow (*Mavko and Nur, 1975*), causes strong energy dissipation due to the viscosity of the fluid and the associated viscous friction. Several experimental studies confirmed the importance of squirt flow at different frequency ranges (*Mayr and Burkhardt, 2006; Best et al., 2007; Adelinet et al., 2010; Mikhaltsevitch et al., 2015; Pimienta et al., 2015b; Subramaniyan et al., 2015; Chapman et al., 2019*). There are several analytical solutions for squirt flow (*O’Connell and Budiansky, 1977; Dvorkin et al., 1995; Chapman et al., 2002; Guéguen and Sarout, 2009, 2011; Gurevich et al., 2010*), which are based on simplified pore geometries and many physical assumptions.

Dispersion and attenuation caused by squirt flow can be simulated numerically by solving the coupled fluid–solid deformation at the pore scale using Lamé–Navier and Navier–Stokes equations with appropriate boundary conditions and then calculating effective frequency-dependent viscoelastic properties. During the last decades, many studies used numerical methods to solve mechanical problems (*Andrä et al., 2013a,b; Saxena and Mavko, 2016*). Recently, some numerical studies appeared in the geophysical literature aiming to solve the coupled fluid–solid deformation and hence studying dispersion and attenuation caused by squirt flow (*Zhang et al., 2010; Zhang and Toksöz, 2012; Quintal et al., 2016, 2019; Das et al., 2019; Alkhimenkov et al., 2020a*). *Das et al.* (2019) numerically simulated a fully coupled fluid–solid interaction at the pore scale for digital rock samples. They modeled the pore fluids as Newtonian fluids using the Navier–Stokes equation with appropriate coupling between both the solid and liquid phases, accounting for inertial effects. *Quintal et al.* (2016, 2019) simplified the Navier–Stokes equations by neglecting the inertial term and hence used the linearized quasistatic Navier–Stokes equation.

We numerically simulate squirt flow in three dimensions and calculate frequency-dependent effective stiffness moduli using the finite-element method to solve the quasistatic Lamé–Navier equations coupled to the linearized quasistatic Navier–Stokes equations (*Quintal et al., 2016, 2019; Alkhimenkov et al., 2020a*). We apply an oscillatory deformation to certain boundaries of the numerical model, and, assuming that the wavelength is much larger than the size of individual cracks, we calculate the volume-average stress and strain fields and the resulting effective stiffness moduli. Then, we calculate the associated azimuth-, angle- and frequency-dependent seismic velocities by solving the Christoffel equation. The main goal of this study is to analyze seismic anisotropy due to squirt flow in three dimensions since the previous numerical studies of seismic anisotropy were performed only in two dimensions and in the framework of Biot’s theory (*Rubino et al., 2017; Barbosa et al., 2017*).

This paper is organized as follows. First, we briefly describe the numerical methodology. Then, we describe the numerical model and show the numerical results – frequency-dependent effective stiffness moduli. After, by solving the Christoffel equation, we evaluate the angle-, azimuth- and frequency dependent velocities of the model. Lastly, we quantify the anisotropy strength of the models analyzing the conventional Thomsen-type anisotropy parameters and also by adopting another scalar parameter.

3.2 Numerical methodology

We consider that at the pore scale, a rock is composed of a solid material (grains) and a fluid-saturated pore space (cracks). The numerical methodology is described by *Quintal et al.* (2016, 2019) and *Alkhimenkov et al.* (2020a), and here we briefly outline the main equations. The solid phase is described as a linear isotropic elastic material for which the conservation of momentum is (e.g., *Landau and Lifshitz, 1959b* and *Nemat-Nasser and Hori, 2013*)

$$\nabla \cdot \boldsymbol{\sigma} = 0, \tag{3.1}$$

where “ $\nabla \cdot$ ” denotes the divergence operator acting on the stress tensor $\boldsymbol{\sigma}$. The infinitesimal stress–strain relation for an elastic material can be written as

$$\begin{aligned} \boldsymbol{\sigma} = & \left(K - \frac{2}{3}\mu \right) \text{tr} \left(\frac{1}{2} \left((\nabla \otimes \vec{u}) + (\nabla \otimes \vec{u})^T \right) \right) \mathbf{I}_2 \\ & + 2\mu \left(\frac{1}{2} \left((\nabla \otimes \vec{u}) + (\nabla \otimes \vec{u})^T \right) \right), \end{aligned} \quad (3.2)$$

where \mathbf{I}_2 is the second-order identity tensor, tr is the trace operator, “ \otimes ” defines the tensor product, the superscript “ T ” corresponds to the transpose operator, \vec{u} is the displacement vector, and K and μ are respectively the bulk and shear moduli.

The fluid phase is described by the quasistatic linearized compressible Navier–Stokes momentum equation (Landau and Lifshitz, 1959a):

$$-\nabla p + \eta \nabla^2 \vec{v} + \frac{1}{3} \eta \nabla (\nabla \cdot \vec{v}) = 0, \quad (3.3)$$

where \vec{v} is the particle velocity, p is the fluid pressure and η is the shear viscosity. Equation (4.54) is valid for the laminar flow of a Newtonian fluid. In the finite-element numerical solver, Eqs. (4.53)–(4.54) are combined in the space–frequency domain

$$\sigma_{ij} = \lambda e \delta_{ij} + 2\mu \epsilon_{ij} + i\omega \left(2\eta \epsilon_{ij} - \frac{2}{3} \eta e \delta_{ij} \right), \quad (3.4)$$

where ϵ_{ij} represents the components of the strain tensor $\epsilon_{ij} = 0.5(u_{i,j} + u_{j,i})$, e is the trace of the strain tensor, λ and μ are the Lamé parameters, u_i is the displacement in the i th direction, δ_{ij} is the Kronecker delta, i is the imaginary unit, and ω is the angular frequency. In the domain representing a solid material, Eq. (4.55) reduces to Eq. (4.53) by setting the shear viscosity η to zero. In the domain representing compressible viscous fluid, Eq. (4.54) is recovered by setting the shear modulus μ to zero. The solid and fluid displacements are described by the same variable, and thus they are naturally coupled at the boundaries between subdomains (Quintal *et al.*, 2016, 2019). In the simulations, the energy dissipation is caused only by fluid pressure diffusion, since inertial terms are neglected.

The COMSOL Multiphysics partial differential equation module is used for implementing Eqs. (4.52) and (4.55) (displacement–stress formulation) in a weak form. Our numerical results can be fully reproduced by using any open-access software which includes mesh generation and finite-element implementation with a corresponding solver for a linear system of equations. The whole spatial domain is discretized using an unstructured mesh with tetrahedral elements. A direct PARDISO solver (Schenk and Gärtner, 2004) is used for solving the linear system of equations. Direct relaxation tests are performed to compute all components of the stiffness matrix (in Voigt notation) c_{ij} . The basic idea of the direct relaxation tests is that a displacement boundary condition of the form $u = 10^{-6} \times \exp(i\omega t)$ is applied to a certain external wall of the model and in a certain direction, while at other walls of the model the displacements are set to zero or let free to change. In the direct tests that we perform, only one component of the stiffness matrix c_{ij} can be directly calculated after one numerical simulation. A detailed description of the boundary conditions is given in Alkhimenkov *et al.* (2020a). The initial conditions for displacements are set to zero. The resulting stress and strains are averaged over the spatial domain for each frequency. Then, the complex-valued $c_{ii}(\omega)$ components (diagonal) are calculated for each frequency (in Voigt notation, no index summation):

$$c_{ii}(\omega) = \frac{\langle \sigma_i(\omega) \rangle}{\langle \epsilon_i(\omega) \rangle}, \quad (3.5)$$

where $\langle \cdot \rangle$ represents the volume averaging over the sample volume. For calculating the P-wave modulus ($ii = 11, 22, 33$), a harmonic displacement on the i direction is applied perpendicularly to a wall of the model. At the other walls of the model, the normal component of the displacement is set to zero. For calculating shear components of the stiffness matrix ($ii = 44, 55, 66$), the boundary conditions applied are those of a simple shear test. For the $c_{12}(\omega)$, $c_{13}(\omega)$ and $c_{23}(\omega)$ components (off-diagonal), mixed direct tests are needed, and the corresponding boundary conditions are given in Appendix 3.7. The corresponding inverse quality factor is

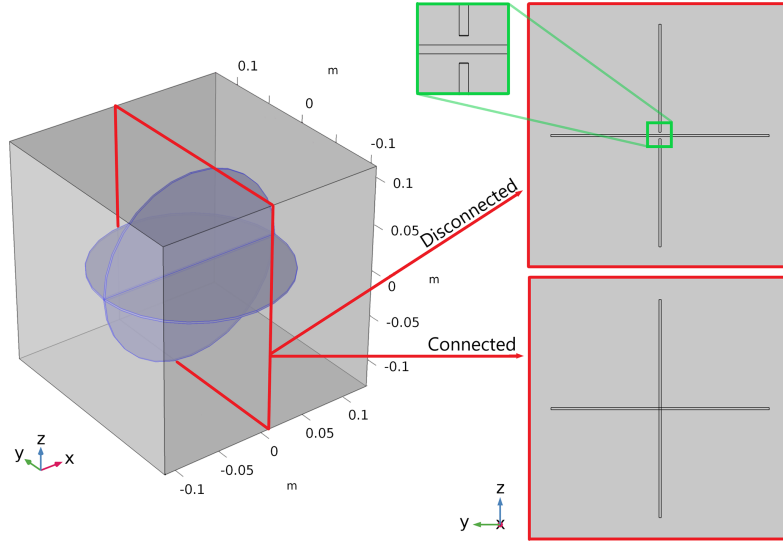


Figure 3.1: Sketch illustrating two flat cylinders representing two cracks. The blue region represents the pore space saturated with a fluid and the transparent gray area corresponds to the solid grain material. In the first model, the two cracks are disconnected as illustrated by the upper right sketch. In the second model, the two cracks are connected as illustrated by the lower right sketch.

(O'Connell and Budiansky, 1978)

$$\frac{1}{Q_{ij}(\omega)} = \frac{\text{Im}(c_{ij}(\omega))}{\text{Re}(c_{ij}(\omega))}. \quad (3.6)$$

Note that usually the inverse quality factor is used as a measure of attenuation (O'Connell and Budiansky, 1978). In this study, we show the inverse quality factor for each component of the stiffness tensor, even though the ratio $\text{Im}(c_{ij}(\omega))/\text{Re}(c_{ij}(\omega))$ does not represent attenuation of any corresponding wave mode for some components.

3.3 Numerical model

Two 3D numerical models are constructed, which consist of a pore space embedded into an elastic solid grain material (Fig. 3.1). The solid grain material is represented by a cuboid whose size is $(0.24 \times 0.24 \times 0.24) \text{ m}^3$. The pore space consists of two perpendicular cracks represented by thin cylinders of 0.002 m thickness, 0.1 m radius (i.e., the aspect ratio is thickness divided by diameter – 0.01) and fully saturated with a liquid. In the first model, the two cracks are disconnected, while, in the second model, the two cracks are connected (cross sections in Fig. 3.1). The employed liquid properties are those of glycerol, and the grain material has properties of quartz (Table 5.2).

A fine, regular mesh is used inside the crack to accurately account for dissipation, while in the grain material the mesh is coarser (Fig. 3.2). The total number of elements is 3.3×10^6 . The simulation is performed for 12 different frequencies from 10^1 to $10^{6.5}$ Hz for each of the nine components of the stiffness matrix (c_{11} , c_{22} , c_{33} , c_{12} , c_{13} , c_{23} , c_{44} , c_{55} , c_{66}). For each frequency, the solver uses approximately 0.95 TB (terabytes) of RAM memory and takes approximately 2.5 h on 32 Intel dual-socket E5-2683 v4 2.1 GHz (1024 GB RAM) cores.

One crack embedded into an isotropic background induces a transverse isotropy (five independent components of the stiffness tensor, e.g., Mavko et al., 2009). If the crack is parallel to the x - y plane, then the symmetry is vertical and the medium exhibits vertical transverse isotropy – VTI symmetry. If the crack is parallel to the x - z plane, then the symmetry is horizontal and the medium exhibits horizontal transverse isotropy – HTI symmetry. If two cracks, perpendicular to each other, are embedded into an isotropic material and the crack compliances are different, then the medium exhibits orthorhombic symmetry (nine independent components

Table 3.1: Material properties of the numerical model.

Material property	Quartz	Glycerol	Air
Bulk modulus K	36 GPa	4.3 GPa	1.01×10^{-4} GPa
Shear modulus μ	44 GPa	–	–
Shear viscosity η	–	1.414 Pa s^{-1}	$1.695 \times 10^{-5} \text{ Pa s}^{-1}$

of the stiffness tensor). If the crack compliances are the same, then the medium symmetry is tetragonal (six independent components of the stiffness tensor); some authors attribute this geometry to a special case of orthorhombic symmetry (e.g., *Bakulin et al.*, 2000b), while tetragonal and orthorhombic symmetry classes are different. On the other hand, one can argue that an orthorhombic medium (created by two perpendicular sets of cracks) degenerates into a tetragonal medium if the crack compliances are the same.

The symmetry of the saturated numerical model with connected cracks is tetragonal (Fig. 3.1), because the crack compliances are the same. Thus, there are only six independent components of the stiffness tensor. We will see that the symmetry of the saturated numerical model with disconnected cracks is orthorhombic, because one crack is stiffer than the other one due to its separation into two parts. However, the difference between c_{22} and c_{33} stiffness components is less than 0.3 %, thus the divergence from the tetragonal symmetry is negligible, and therefore this model is considered tetragonal as well.

3.4 Results

3.4.1 Dry stiffness moduli

Let us first consider the geometry shown in Fig. 3.1 with a pore space filled with air (i.e., dry). We perform nine relaxation tests to calculate the full stiffness tensor for each of the two models with connected and disconnected cracks. The resulting effective stiffness moduli for the model with connected cracks are (in Voigt notation)

$$c_{ij}^{\text{Con}} = \begin{bmatrix} 93.53 & 4.65 & 4.65 & 0 & 0 & 0 \\ 4.65 & 63.91 & 5.46 & 0 & 0 & 0 \\ 4.65 & 5.46 & 63.91 & 0 & 0 & 0 \\ 0 & 0 & 0 & 31.62 & 0 & 0 \\ 0 & 0 & 0 & 0 & 35.16 & 0 \\ 0 & 0 & 0 & 0 & 0 & 35.16 \end{bmatrix} \text{ (GPa)}. \quad (3.7)$$

For the model with disconnected cracks, the effective stiffness moduli are (in Voigt notation)

$$c_{ij}^{\text{Dis}} = \begin{bmatrix} 93.55 & 4.92 & 4.60 & 0 & 0 & 0 \\ 4.92 & 69.21 & 4.40 & 0 & 0 & 0 \\ 4.60 & 4.40 & 64.06 & 0 & 0 & 0 \\ 0 & 0 & 0 & 31.95 & 0 & 0 \\ 0 & 0 & 0 & 0 & 35.16 & 0 \\ 0 & 0 & 0 & 0 & 0 & 36.96 \end{bmatrix} \text{ (GPa)}. \quad (3.8)$$

The effective stiffness moduli of the two models are different. Zero values are written if the value is below 0.0002 GPa (i.e., up to numerical precision). The c_{ij}^{Con} stiffness matrix precisely belongs to the tetragonal symmetry class, while the c_{ij}^{Dis} stiffness matrix has all diagonal components different from each other; thus, it represents the orthorhombic symmetry class. The largest difference between c_{ij}^{Con} and c_{ij}^{Dis} is in the c_{22} component; i.e., $\Delta c_{22} = c_{22}^{\text{Dis}} - c_{22}^{\text{Con}} = 5.3 \text{ GPa}$. That is a significant difference and it is only due to the vertical crack separation. There are two different features which must be clearly separated. (1) The effect of crack intersection without changing the crack geometry on the effective elastic properties. In this case, the crack intersection is achieved by changing the spatial position of the cracks. *Grechka and Kachanov* (2006) studied

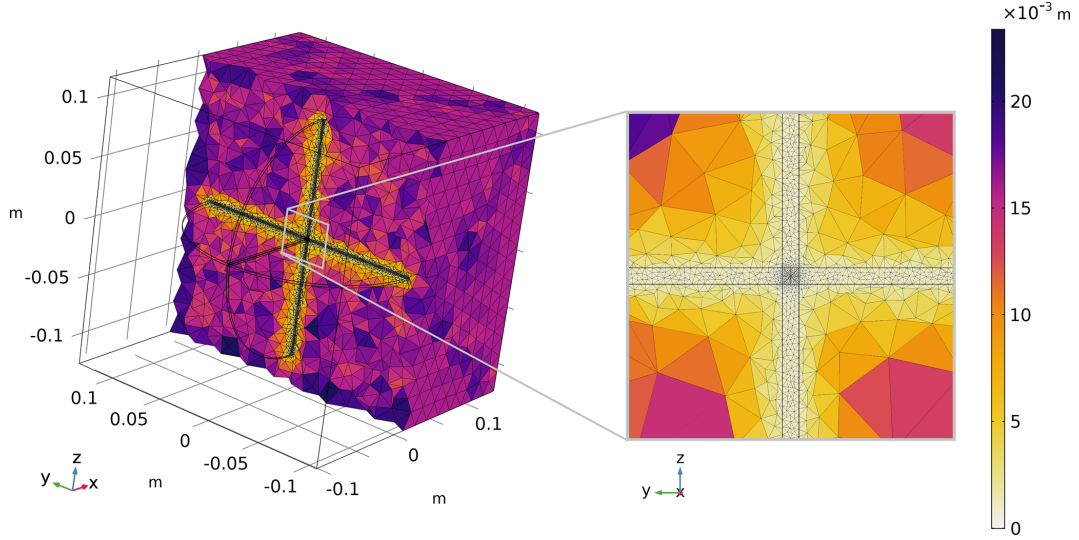


Figure 3.2: Sketch illustrating the element's size distribution for the model with connected cracks. The element's size in the crack is $5 \times 10^{-5} - 1 \times 10^{-3}$ m, and in the surrounding grain material it is $2.4 \times 10^{-3} - 1.6 \times 10^{-2}$ m. The element's size distribution for the model with disconnected cracks is the same.

numerically the effect of crack intersection without changing the crack geometry. They concluded that crack intersection has a very little impact on the effective elastic moduli. (2) The effect of the crack partition into two “halves” on the effective elastic properties. In this case, the partitioned crack has a long, thin contact area across the whole diameter (Fig. 3.1). It is well known that the contact areas inside a crack significantly reduce crack compliance (Trofimov *et al.*, 2017; Kachanov and Sevostianov, 2018; Markov *et al.*, 2019; Lissa *et al.*, 2019). Comparing Eqs. (3.7) and (3.8), we also observe that the thin contact area significantly reduces the crack compliance: the effective dry moduli of the model with disconnected cracks are much higher compared to the model with connected cracks. An intuitive explanation is the following: if crack surfaces have not been changed by changing the spatial position of the cracks in the volume, the effect of crack intersection is negligible (Grechka and Kachanov, 2006); if the crack surfaces have been changed – as we did in the present study by partitioning the vertical crack into two pieces (and introducing a thin additional contact area) – the effective elastic moduli would become much stiffer compared to the model where the crack surfaces have not been changed.

3.4.2 Fluid pressure fields

Here and later on we deal only with a liquid-saturated pore space. The liquid has properties of glycerol (Table 5.2). A direct P-wave modulus test is performed to calculate dispersion and attenuation for the c_{33} component. (A harmonic displacement is applied to the top wall of the model in the z direction, while the normal component of the displacement is set to zero on all the other walls.) Figure 3.3 shows snapshots of the fluid pressure P_f in the cracks at three different frequencies, in the vertical middle slice of the model (the y - z plane, red frame in Fig. 3.1a). For the model with connected cracks, at low frequencies, there is enough time for pressure equilibration between the cracks; thus, the pore pressure is uniform throughout the pore space (Fig. 3.3, LF (connected)). This is called the relaxed state. At intermediate frequencies, there is a large pressure gradient in the cracks, which corresponds to the maximum attenuation due to squirt flow between cracks (Fig. 3.3, Fc (connected)). At high frequencies, there is no time for fluid to move; hence, there is no fluid pressure equilibration between the vertical and horizontal cracks (Fig. 3.3, HF (connected)). This is called the unrelaxed state. Therefore, at high frequencies, the connected cracks behave as hydraulically isolated and the fluid highly stiffens the crack.

In the model with disconnected cracks, the fluid pressure in the cracks is the same in all three regimes, which corresponds to the unrelaxed state in the model with connected cracks. The unrelaxed state can be interpreted as the elastic limit because there is no fluid flow between the cracks, and the effective properties of the two models (connected and disconnected cracks) are the same, as will be shown in the next subsection.

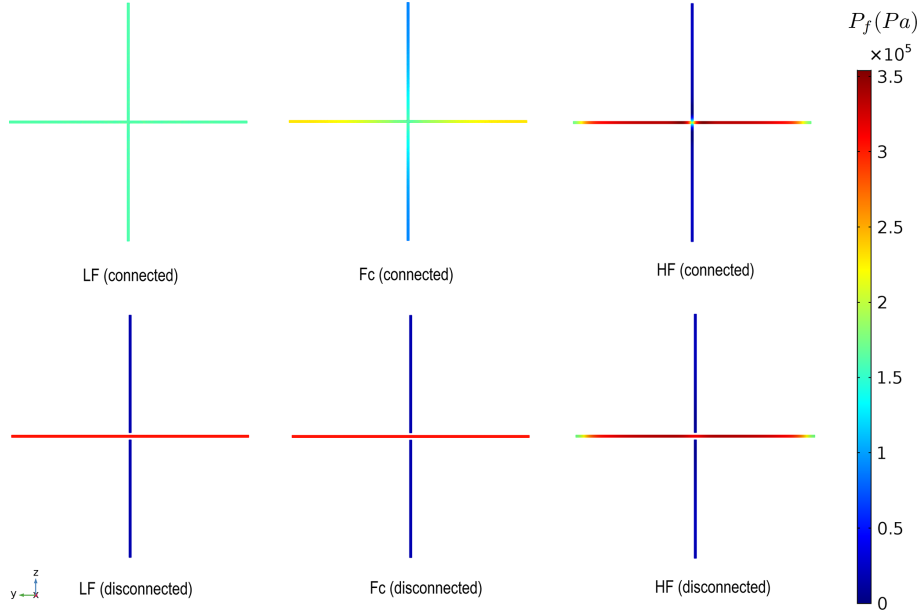


Figure 3.3: Snapshots of the fluid pressure P_f in the cracks at three different frequencies: LF – the low-frequency limit (corresponds to 10^1 Hz, relaxed state), Fc – intermediate frequency snapshot (corresponds to 10^4 Hz, close to the characteristic frequency) and HF – the high-frequency limit (corresponds to $10^{6.5}$ Hz, unrelaxed state).

3.4.3 Dispersion and attenuation

Elastic moduli

Figure 3.4 shows the numerical results for the complex-valued frequency-dependent components of the stiffness matrix $c_{ij}(\omega)$ (in Voigt notation) for the models with connected and disconnected cracks filled with glycerol. In the model with connected cracks, the real part of the c_{ij} component and the corresponding inverse quality factor (Eq. 4.57) curves show strong frequency-dependent behavior of the c_{22} , c_{33} and c_{23} components (Fig. 3.4a and c). The inverse quality factor and dispersion of the c_{22} and c_{33} components coincide because the geometrical properties of the two cracks are the same (Fig. 3.4a) and the model is symmetric. The c_{11} component is nondispersive and exhibits zero attenuation. The dispersion of the c_{44} , c_{55} and c_{66} components is negligible and these components also exhibit negligible attenuation (Fig. 3.4b). The c_{12} and c_{13} components are nondispersive, the c_{23} component exhibits strong negative dispersion and a negative inverse quality factor peak is shifted towards high frequencies compared to that of the c_{22} and c_{33} components. A similar phenomenon has been reported by *Guo et al.* (2017b) in the context of two-dimensional simulations. The c_{23} component does not correspond to a wave mode alone; it is always used together with c_{22} and/or c_{33} components. Therefore, no wave will gain energy. This negative inverse quality factor sign for the c_{23} component was also verified using Kramers–Kronig relations. In other words, different components of the stiffness tensor might have positive or negative values of the ratio $\text{Im}(c_{23})/\text{Re}(c_{23})$ but, when we calculate the velocity and the inverse quality factor of a wave, the cumulative effect of all c_{ij} components must be physical and no negative attenuation will be observed.

Note that the width of the inverse quality factor peak (at half amplitude) for the components c_{22} and c_{33} has a 1.5 order of magnitude (Fig. 3.4a and 3.4c). It means that attenuation and dispersion due to squirt flow play a significant role over a broad frequency range even for cracks with a single aspect ratio.

In the model with disconnected cracks, all components of the stiffness tensor $c_{ij}(\omega)$ (Fig. 3.4a and 3.4c) are constant across the whole frequency range and exhibit zero inverse quality factor. Furthermore, all components are approximately equal to the high-frequency values of the model with connected cracks. This is expected in the unrelaxed state because the connected cracks behave as hydraulically isolated with respect to fluid flow. A very small discrepancy between the two models at high frequencies is associated with the vertical crack partition (two thin regions of pore space replaced with stiffer grain material).

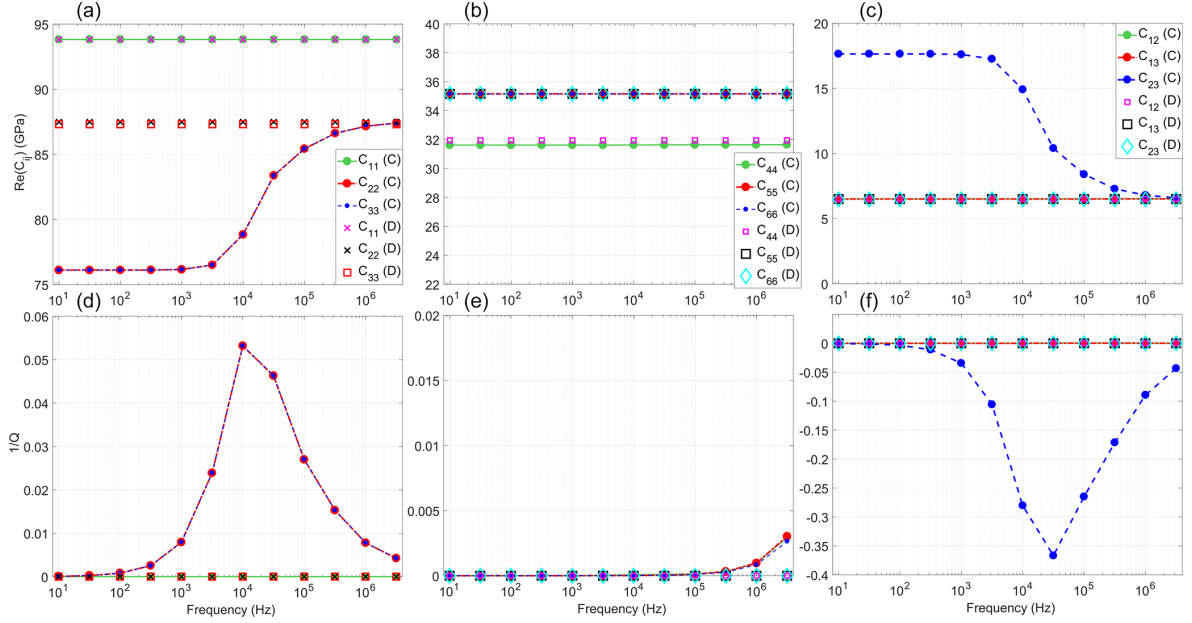


Figure 3.4: Numerical results for the connected (C) and disconnected (D) crack models: real part of the c_{ij} components versus frequency (a–c), dimensionless inverse quality factor of the c_{ij} components versus frequency (d–f). Each symbol corresponds to the test result of one numerical simulation and lines correspond to linear interpolation between discrete numerical results.

P- and S-wave velocities

Figure 3.5 shows the P-wave (primary wave) phase velocity as a function of the phase angle of the numerical model with connected and disconnected cracks (Fig. 3.1), where the zero phase angle corresponds to the vertical wave propagation (along z axis). The P- and S-wave phase velocities are calculated by solving the Christoffel equation, which represents an eigenvalue problem relating the stiffness components c_{ij} , the phase velocities of plane waves that propagate in the medium and the polarization of the waves (Fedorov, 1968; Tsvankin, 2012). Considering the plane Y – Z , the P-wave velocity is the same for phase angles of 0 and 90°; it changes with frequency only for phase angles between 0 and 90° and is maximal in the high-frequency limit at phase angle of $\theta = 90(\pm 90)^\circ$ (Fig. 3.5a). Furthermore, in the high-frequency limit the P-wave phase velocity coincides for the models with connected and disconnected cracks. As frequency decreases, the P-wave velocity decreases, and at 10^4 Hz the P-wave velocity is almost angle independent (yellow curve, Fig. 3.5a). It is interesting that this “local” isotropy corresponds to the maximum attenuation of the c_{22} and c_{33} components (Fig. 3.4). As frequency further decreases, the P-wave velocity decreases and stays nearly unchanged for the frequencies below $10^{3.5}$ Hz. In the X – Z plane, the P-wave phase velocity is the same for the models with connected and disconnected cracks in the high-frequency limit (Fig. 3.5b). For the model with connected cracks, as frequency decreases, the P-wave velocity decreases, reaching its minimum at low frequencies (10^1 – $10^{3.5}$ Hz).

Figures 3.6–3.7 show the quasi-shear (SV) and the pure shear (SH) phase velocities as functions of the phase angle of the numerical models with connected and disconnected cracks (Fig. 3.1). The SV wave velocity is strongly frequency dependent in both the X – Z and Y – Z planes. The SH wave exhibits some frequency-dependent behavior in the X – Z plane and is angle and frequency independent in the Y – Z plane. It is interesting that the SV waves in two different planes have different velocities at 0 and 90° phase angles, which is due to their different wave polarization. The SV wave in the Y – Z plane has the same polarization as the SH wave in the X – Z plane; their velocities are equivalent at the 0 and 90° phase angles. The same conclusion is valid for the SV wave in the X – Z plane and the SH wave in the Y – Z plane. A slight discrepancy (around 0.5%) between the SV wave velocities for the disconnected crack model (Fig. 3.6, dashed red line) and the high-frequency velocity for the connected crack model (Fig. 3.6, green line) at phase angles of 0, 90 and 180° is due to the crack separation.

Due to the symmetry of the model, the behaviors of the P-, SV-, SH-wave phase velocities in the X – Z and X – Y planes are identical; thus, the results in the X – Y plane are not shown here.

3.4.4 Quantitative analysis of the frequency-dependent anisotropy

First, we quantify the Thomsen-type anisotropic parameters (Thomsen, 1986) for orthorhombic media (Tsvankin, 1997; Bakulin et al., 2000a). Then, we quantify the universal elastic anisotropy index (Ranganathan and Ostoja-Starzewski, 2008) and the two parameters which define the anisotropy strength in bulk and shear modes. All these anisotropy measures highlight different frequency-dependent features of the models. Our results shown in Fig. 3.4 (frequency-dependent elastic moduli) are used as input to quantify these anisotropy measures.

Thomsen-type parameters

Thomsen-type anisotropic parameters (ϵ , δ , γ) describe the P-wave anisotropy – ϵ , the shape of the P-wave phase velocity at different phase angles – δ and the S-wave anisotropy – γ : each set of three parameters corresponds to one plane. Thus, for our model symmetry, there are two different planes – $Y-Z$ and $X-Z$ (because the $X-Z$ plane is equivalent to the $X-Y$ plane). In this study, we refer to Thomsen parameters $|\epsilon|, |\delta|, |\gamma| \in [0, 0.1]$ as to weak elastic anisotropy ($|\cdot|$ corresponds to the absolute value), $|\epsilon|, |\delta|, |\gamma| \in [0.1, 0.15]$ as moderate elastic anisotropy and $|\epsilon|, |\delta|, |\gamma| \in [0.15, +\infty]$ as strong elastic anisotropy. The choice of these intervals is based on the divergence between the exact and approximate (by using Thomsen parameters) equations for the P-wave phase velocities in cracked media.

Figure 3.8 shows the Thomsen-type anisotropy parameters in the $Y-Z$ and $X-Z$ planes (formulas are given in Appendix 3.8). In the high-frequency limit, all anisotropy parameters are the same for both models with connected and disconnected cracks. Furthermore, for the model with disconnected cracks, all anisotropy parameters are frequency independent, because the stiffness tensor is frequency independent. For the model with connected cracks, several anisotropy parameters are frequency dependent due to squirt flow.

In the $Y-Z$ plane, parameters ϵ^{YZ} and γ^{YZ} are zero for both models. The parameter δ^{YZ} is frequency dependent and controls the shape of the P-wave phase velocity between 0 and 90°. In the high-frequency limit, δ^{YZ} exhibits the maximum negative value which corresponds to strong elastic anisotropy. As frequency decreases, δ^{YZ} also decreases reaching a zero value around 10^4 Hz, and then δ^{YZ} increases reaching its positive maximum at low frequencies, which corresponds to weak elastic anisotropy; the positive maximum is approximately one-third of the absolute value of its negative maximum. It is interesting that δ^{YZ} changes sign from negative to positive, which is indeed observed in the P-wave velocity behavior (Fig. 3.5a) as P-wave velocity changes polarity with frequency. This was also observed by Barbosa et al. (2017) in the framework of Biot's theory. This polarity change has a fully mechanical nature. In the high-frequency limit, cracks behave as hydraulically isolated and fluid highly stiffens the normal compliance of the cracks (not tangential). As frequency decreases, fluid started to flow from more compliant to stiffer cracks as a response to the applied displacement boundary condition. $\delta^{(yz)} = 0$ corresponds to zero anisotropy; the numerator of δ^{YZ} is $[c_{23}(\omega) + c_{44}(\omega)]^2 - [c_{33}(\omega) - c_{44}(\omega)]^2$ (see Appendix 3.8). Therefore, for zero anisotropy, $c_{23}(\omega) + c_{44}(\omega)$ must be equal to $c_{33}(\omega) - c_{44}(\omega)$. The function $c_{44}(\omega)$ is constant across the whole frequency range, $c_{23}(\omega)$ is strictly decreasing with frequency and $c_{33}(\omega)$ is strictly increasing with frequency (Fig. 3.4). At a certain frequency (here it is at $\sim 10^4$ Hz), the c_{33} and c_{23} components are in such a combination that $c_{23}(10^4) + c_{44}(10^4) \approx c_{33}(10^4) - c_{44}(10^4)$, so $\delta^{YZ} = 0$, and the P-wave velocity in the $Y-Z$ plane behaves as in a fully isotropic media.

In the $X-Z$ plane, ϵ^{XZ} and δ^{XZ} are frequency dependent in the model with connected cracks. ϵ^{XZ} exhibits moderate elastic anisotropy at low frequencies, while δ^{XZ} exhibits moderate elastic anisotropy at high frequencies. Other parameters are frequency independent and exhibit certain nonzero values from weak to moderate elastic anisotropy.

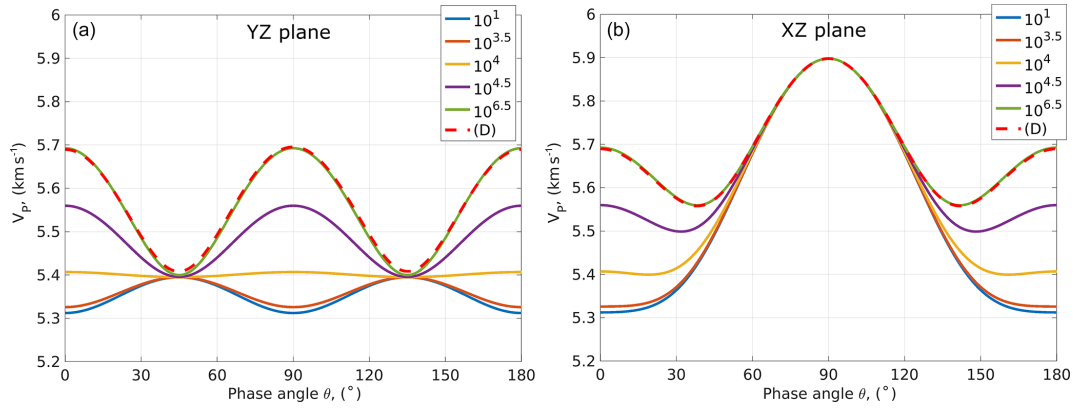


Figure 3.5: P-wave phase velocity versus phase angle in the Y - Z plane (a) and the X - Z plane (b). Curves 10^1 – $10^{6.5}$ denote the frequency of the P wave for the model with connected cracks. (D) denotes the P wave for the model with disconnected cracks.

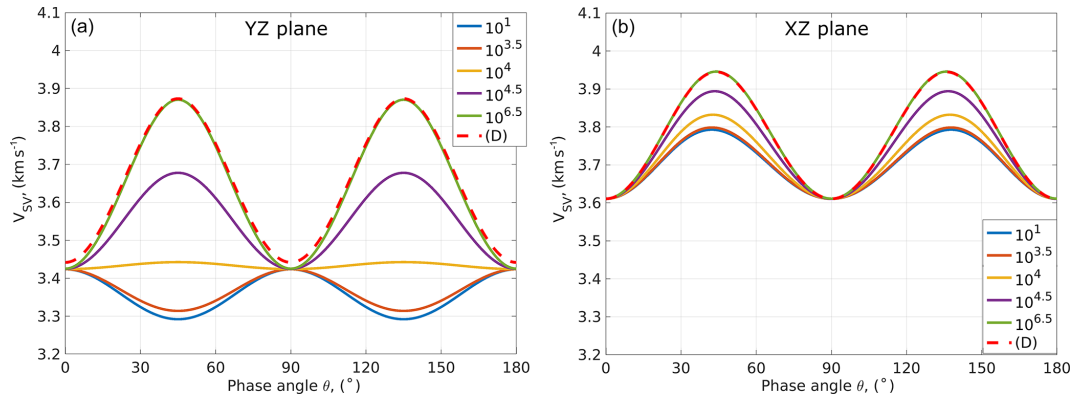


Figure 3.6: SV-wave phase velocity versus phase angle in the Y - Z plane (a) and the X - Z plane (b). Curves 10^1 – $10^{6.5}$ denote the frequency of the P wave for the model with connected cracks. (D) denotes the P wave for the model with disconnected cracks.

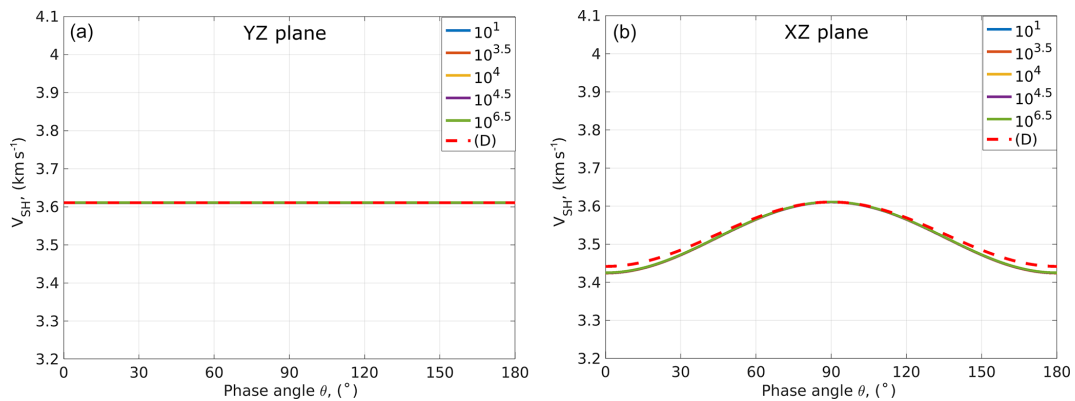


Figure 3.7: SH-wave phase velocity versus phase angle in the Y - Z plane (a) and the X - Z plane (b). Curves 10^1 – $10^{6.5}$ denote the frequency of the P wave for the model with connected cracks. (D) denotes the P wave for the model with disconnected cracks.

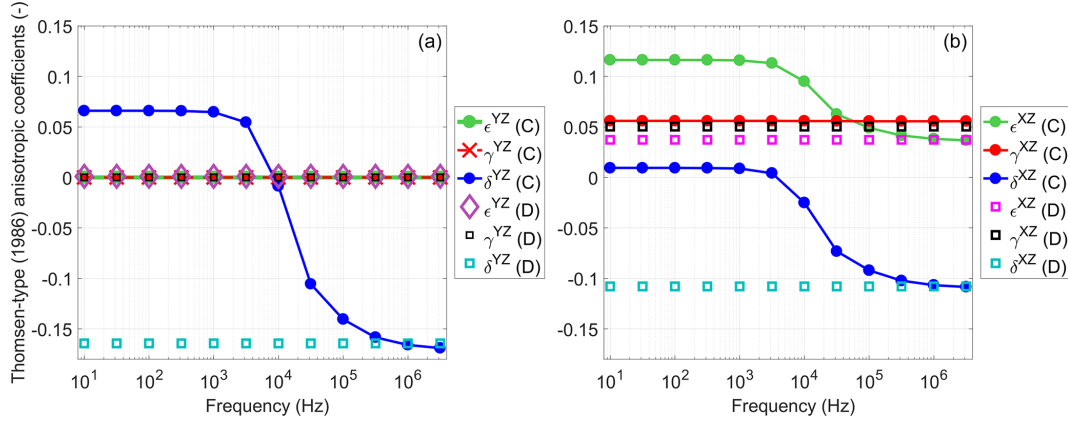


Figure 3.8: Thomsen-type anisotropic parameters in the Y–Z (a) and X–Z (b) planes.

The universal elastic anisotropy index

The universal elastic anisotropy index A^U (Ranganathan and Ostoja-Starzewski, 2008) is widely used to measure the anisotropy strength in crystallography, engineering and materials science. This parameter is designed to evaluate the anisotropy strength of crystals having any elastic symmetry class (Ranganathan and Ostoja-Starzewski, 2008). Since A^U is a scalar, it gives a simple and fast identification of the overall anisotropy strength of a model. $A^U = 0$ corresponds to zero anisotropy of a model, while the discrepancy of A^U from zero defines the anisotropy strength and accounts for both the shear and the bulk contributions simultaneously. In analogy to the universal elastic anisotropy index, two other parameters are adopted which define the anisotropy strength in bulk A^{bulk} and in shear A^{shear} . As far as we are concerned, these parameters have not been widely used in earth sciences: only a few studies were found. *Almqvist and Mainprice (2017)* applied the universal elastic anisotropy index and two similar parameters for bulk and shear to study seismic properties and anisotropy of the continental crust. *Kube and De Jong (2016)*, *Duffy (2018)* and *Vieira et al. (2019)* applied A^U to quantify the elastic anisotropy of polycrystals. A brief review of these anisotropic measures and all necessary equations for their calculation are provided in Appendix 3.9.

Figure 3.9 shows the universal elastic anisotropy index A^U and the anisotropy measures in bulk $A^{\text{bulk}}(\omega)$ and shear A^{shear} . For the model with disconnected cracks, A^U is constant and frequency independent (Fig. 3.9, black line). Because A^U has a certain small value (about 0.058), the model with disconnected cracks exhibits a certain small anisotropy. For the model with connected cracks, A^U in the high-frequency limit is almost the same as for the model with disconnected cracks (Fig. 3.9, red line). (The nature of the discrepancy is related to the region containing the crack intersection.) For the model with connected cracks, the overall anisotropy slightly decreases towards lower frequencies until $10^{4.3}$ Hz, reaching its minimum of 0.048 (Fig. 3.9, red line). This local minimum indeed corresponds to the c_{23} attenuation peak (Fig. 3.4c). Then, still towards lower frequencies, $A^U(\omega)$ increases reaching its maximum of 0.083 at frequencies below 10^3 Hz (Fig. 3.9, red line). Thus, the overall anisotropy of the model mainly increases due to squirt flow between the cracks, so the crack connectivity increases the overall anisotropy of the model towards low frequencies.

The anisotropy measure in bulk A^{bulk} is constant and frequency independent for the models with connected and disconnected cracks (Fig. 3.9b). It means that fluid flow does not affect bulk properties of the model or the anisotropy strength in bulk. On the other hand, the anisotropy measure in shear $A^{\text{shear}}(\omega)$ basically reproduces the behavior of the universal elastic anisotropy index measure A^U . Therefore, one can conclude that the fluid flow changes anisotropy in shear mode but not in bulk mode.

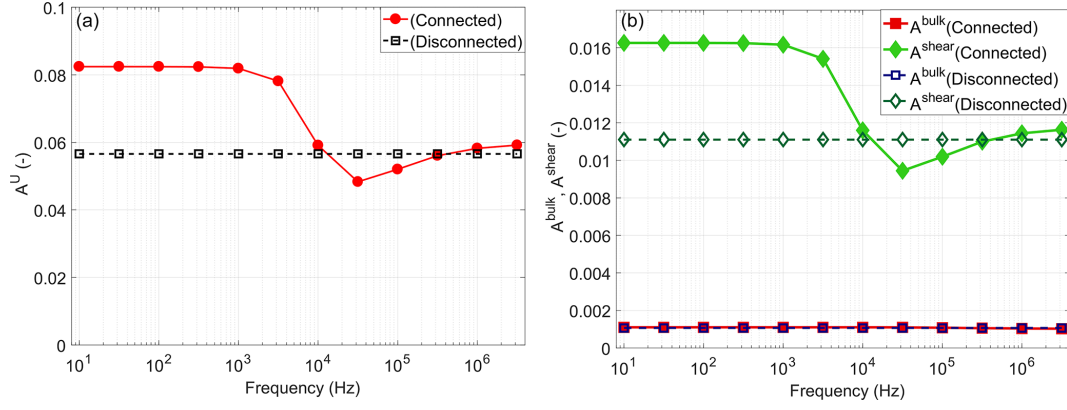


Figure 3.9: The universal elastic anisotropy index measure A^U versus frequency **(a)** and the anisotropy measures in bulk and shear (A^{bulk} and A^{shear}) **(b)**. These plots show that the overall anisotropy of the model increases in the low frequencies due to fluid flow.

3.5 Discussion

3.5.1 Elastic anisotropy

Thomsen-type anisotropic parameters provide a very detailed description of the velocity anisotropy in different planes. Most importantly, only a limited number of the stiffness tensor coefficients are needed to calculate ϵ , δ and γ in each plane. Thus, Thomsen parameters can be used to quantify the medium anisotropy using seismic data. On the other hand, when all components of the stiffness tensor are known and the model's symmetry is low, it is difficult to analyze the overall anisotropy due to a large number of Thomsen parameters. For example, if the model exhibits orthorhombic symmetry, one should analyze nine Thomsen anisotropic parameters (three in each plane). Due to a large number of Thomsen parameters in this study, it is difficult to evaluate whether the overall medium's anisotropy is increasing or decreasing with frequency and how far the current model is from the closest isotropy. Thus, in addition to (or instead of) the Thomsen-type anisotropic parameters, the universal elastic anisotropy index can be used. The universal elastic anisotropy index A^U and the related measures in bulk, A^{bulk} , and shear, A^{shear} , provide the overall description of the anisotropy strength regardless of the model's complexity. The calculation of these parameters is as simple as the calculation of the Thomsen parameters. An obvious disadvantage of the universal elastic anisotropy index (and related measures) is that it requires knowledge of the full stiffness tensor. Thus, this anisotropic measure can be useful to evaluate results of numerical simulations of laboratory experiments and for measuring the anisotropy of single crystals.

The analysis of two sets of anisotropic measures shows that (i) the overall anisotropy of the model with connected cracks (Fig. 3.1) mainly increases due to squirt flow towards low frequencies with a slight local decrease at intermediate frequencies (Fig. 3.9a); (ii) in the $Y-Z$ plane, the magnitude of the “delta” anisotropy parameter decreases, reaches zero, and then increases again (reaching approximately one-third of its high-frequency value) towards low frequencies (Fig. 3.8a, blue curve); and (iii) in the $X-Z$ plane, the “delta” anisotropy parameter decreases towards low frequencies (Fig. 3.8b, blue curve), while the “epsilon” anisotropy parameter increases (Fig. 3.8b, green curve).

3.5.2 Comparison with previous works

In this study, we numerically solve a coupled fluid–solid deformation problem at the pore scale. If we consider the mesoscopic scale scenario and use Biot’s (1941) equations, the fluid flow effects on the effective moduli are equivalent to that of the coupled elastic Stokes equations (as in the present study), as it was shown by *Quintal et al.* (2016). The frequency-dependent anisotropy due to fluid flow at the mesoscopic scale for orthogonal fracture sets with different degrees of connectivity was numerically studied by *Rubino et al.* (2017), but their study was limited to two dimensions. The main conclusion of *Rubino et al.* (2017) is that the anisotropy decreases with fracture connectivity in the seismic frequency band due to fluid flow between connected fractures. The Y – Z plane in the present 3D numerical model is reasonably equivalent to the 2D numerical model of *Rubino et al.* (2017) as well as the physical mechanism under consideration. The results of *Rubino et al.* (2017) are reflected in Fig. 3.5 of this study. However, a more in-depth analysis shows that the anisotropy in the Y – Z plane decreases, reaches zero and then increases again towards low frequencies due to squirt flow (Fig. 3.5a, green, yellow and blue curves, respectively). Moreover, our present study shows that the overall anisotropy of the model with cracks of finite length actually increases due to fluid flow between interconnected cracks (Figs. 3.8, 3.9). This conclusion is not universal and is valid only for a specific set of model parameters.

Barbosa et al. (2017) performed a more detailed study of seismic anisotropy for a similar fracture geometry in two dimensions, as in the study of *Rubino et al.* (2017), specifying that the decrease in anisotropy is described by the anisotropy parameter δ while ϵ is zero. Furthermore, they observed a polarity change of the P-wave phase velocity behavior with frequency. In the present study, the “delta” anisotropy parameter in the Y – Z plane is more pronounced in the low-frequency limit (Fig. 3.5a, blue curve) compared to the work of *Barbosa et al.* (2017) due to different material properties and the three-dimensional nature of the present model configuration.

In summary, fluid flow effects on seismic anisotropy are nonlinear with a possible increase or decrease in the elastic anisotropy at different frequencies. These two extreme cases, the maximum negative and the maximum positive δ parameter (and hence P-wave velocity) in the Y – Z plane, correspond to the relaxed and unrelaxed states. In other words, seismic anisotropy may behave completely different in different scenarios; therefore, more studies should be performed, especially with the sensitivity analysis of model parameters.

3.5.3 A qualitative comparison against analytical models

Numerical simulations are useful but analytical models are especially attractive since they help us to better understand the physics and do not require sophisticated numerical simulations. The limitations of the analytical solutions are restricted to simple pore space geometry, and some assumptions related to physics are needed to derive the closed form analytical formulas. Such a comparison of the numerical results against an analytical solution has been performed by *Alkhimenkov et al.* (2020a) for a different pore space geometry. Unfortunately, there is no analytical solution for the present study considering a periodic distribution of intersecting cracks in three dimensions. But the qualitative comparison of the low- and high-frequency limits (which correspond to relaxed and unrelaxed states) is possible (*Mavko and Jizba*, 1991). Several analytical studies show that the anisotropy (described by Thompson’s parameters) is, in general, more pronounced at high frequencies than at low frequencies (*Guéguen and Sarout*, 2009, 2011). In the relaxed state, one can calculate the effective dry elastic moduli and use Gassmann’s equations to obtain the effective moduli of the saturated medium. In the unrelaxed state, one can calculate the effective elastic moduli by restricting fluid flow (by using zero displacement boundary conditions in the crack intersections). The low- and high-frequency limits for elastic moduli have been calculated using these semi-analytical approaches, and numerical results have been reproduced.

3.6 Conclusions

We have numerically calculated the frequency-dependent elastic moduli of a fluid-saturated porous medium caused by squirt flow. The considered 3D numerical models consist of two perpendicular connected or disconnected cracks embedded in a solid grain material. Cracks are represented by very flat cylinders filled with a fluid. Grains are described as a linear isotropic elastic material, while the fluid phase is described by the quasistatic linearized compressible Navier–Stokes momentum equation.

We showed that seismic velocities are azimuth, angle and frequency dependent due to squirt flow between connected cracks. The resulting elastic frequency-dependent anisotropy was analyzed by using the Thomsen-type anisotropic parameters and the universal elastic anisotropy index. The latter is a scalar parameter which can be used to analyze the overall anisotropy of the model and its divergence from the closest isotropy. We showed that the seismic anisotropy may locally decrease as well as increase due to squirt flow in one specific plane. However, the overall anisotropy of the model mainly increases due to squirt flow between the cracks towards low frequencies. In the model with disconnected cracks, no fluid flow occurs, and thus the effective properties of the model correspond to the elastic limit. The elastic limit is equivalent to the high-frequency limit for the model with connected cracks. Seismic velocities are only azimuth and angle dependent as for a fully elastic material, and they are independent of frequency. In summary, squirt flow does affect effective mechanical properties of cracked rocks and thus seismic velocity anisotropy. Given that seismic anisotropy variations with frequency are very sensitive to the pore space geometry and material properties, it is difficult to make a general prediction. According to our study, the effective frequency-dependent response of a cracked medium is different in different planes. The local response (in a certain plane) is controlled by crack orientation, which is the key parameter. The magnitude of the frequency-dependent response (i.e., the dispersion and attenuation) is controlled by crack compliances, crack porosity and their fluid content. (Dry or liquid-saturation conditions will cause completely different behavior.) Most importantly, crack porosity is a very important parameter in fluid-saturated rocks (contrary to dry rocks) since it defines the volume of fluid which may flow due to wave propagation, causing wave attenuation and dispersion.

Acknowledgments

This research is funded by the Swiss National Science Foundation, project number 172691. Yury Alkhimenkov thanks Germán Rubino (CONICET, Centro Atómico Bariloche, Argentina) for fruitful discussions on the frequency-dependent anisotropy due to fluid flow, Nicolás D. Barbosa (University of Geneva, Switzerland) for fruitful discussions regarding the polarity change of the P-wave velocity with frequency and Irina Bayuk (Russian Academy of Sciences, Russia) for enlightening discussions regarding the fourth-rank tensor averaging and the elastic symmetry classes.

Author contributions

YA performed the numerical simulations and wrote the article. The idea of this project was first inspired by the paper by *Rubino et al. (2017)*. A detailed project was planned by YA and BQ. EC, SL and BQ provided many ideas and suggestions which influenced the project path and helped writing the article.

3.7 Appendix A: Boundary conditions for c_{ij} off-diagonal components

Let us consider a cuboid, volume $V = (0, Lx) \times (0, Ly) \times (0, Lz)$ and Γ its boundary, $\Gamma = \Gamma^{xz0} \cup \Gamma^{xzL} \cup \Gamma^{yz0} \cup \Gamma^{yzL} \cup \Gamma^{xy0} \cup \Gamma^{xyL}$, where Γ^{xz0} represents an x - z with zero coordinate, Γ^{xzL} represents an x - z with Ly coordinate, etc. There are six planes in total.

The mixed test for the c_{13} component can be derived from the anisotropic stress-strain relation (Hooke's law) (similarly to the c_{13} component in a VTI medium; *Alkhimenkov et al.*, 2020a); Γ^{xyL} is set to $u_{zz} = \Delta u$; u_{xx} and u_{yy} are free;

Γ^{yzL} is set to $u_{xx} = \Delta u$; and u_{zz} and u_{yy} are free,

where $\Delta u = 10^{-6}$. In the other four planes, the normal component of the displacement is set to zero and other components are free. The stress-strain relation for the $\langle \sigma_1 \rangle$ stress component is

$$\langle \sigma_1 \rangle = c_{11} \langle \epsilon_1 \rangle + c_{12} \langle \epsilon_2 \rangle + c_{13} \langle \epsilon_3 \rangle. \quad (3.9)$$

Using the abovementioned boundary conditions and setting $\langle \epsilon_2 \rangle = 0$, Eq. (3.9) becomes

$$\langle \sigma_1 \rangle = c_{11} \langle \epsilon_1 \rangle + c_{13} \langle \epsilon_3 \rangle. \quad (3.10)$$

Equation (3.10) can be solved for the c_{13} component; the solution is

$$c_{13} = \frac{\langle \sigma_1 \rangle}{\langle \epsilon_1 \rangle} - c_{11}. \quad (3.11)$$

Equation (3.11) is used to calculate the c_{13} component (c_{11} is taken from the direct tests).

The mixed test for the c_{23} (in this numerical model, the c_{23} is dispersive) component again can be derived from the anisotropic stress-strain relation (Hooke's law) (similarly to the previous test). Γ^{xyL} is set to $u_{zz} = \Delta u$; u_{xx}, u_{yy} are free;

Γ^{xzL} is set to $u_{yy} = \Delta u$; and u_{zz} and u_{xx} are free.

In the other four planes, the normal component of the displacement is set to zero, other components are free. Then, using the following equation

$$c_{23} = \frac{\langle \sigma_2 \rangle}{\langle \epsilon_2 \rangle} - c_{22}, \quad (3.12)$$

the c_{23} component is calculated (c_{22} is taken from the direct test). Equations (3.11)–(3.12) are found from Hooke's law considering nonzero strains in the x and z (in y and z) directions and then solving a system of two equations analytically.

3.8 Appendix B: Thomsen-type anisotropic parameters

Thomsen-type anisotropic parameters (*Thomsen*, 1986) are widely used in the applied geophysics community. Thomsen weak anisotropy parameters were originally developed for vertical transverse isotropic media (*Thomsen*, 1986). A natural extension of these parameters to orthorhombic media was suggested by *Tsvankin* (1997) and *Bakulin et al.* (2000a). These parameters correspond to the anisotropy of the compression and shear waves in orthorhombic media in different Cartesian propagation planes. In the Y - Z plane, Thomsen-type anisotropic parameters are

$$\begin{aligned} \epsilon^{(YZ)}(\omega) &= \frac{c_{22}(\omega) - c_{33}(\omega)}{2c_{33}(\omega)}, \quad \gamma^{(YZ)}(\omega) \\ &= \frac{c_{66}(\omega) - c_{55}(\omega)}{2c_{55}(\omega)}, \end{aligned} \quad (3.13)$$

and

$$\delta^{(YZ)}(\omega) = \frac{[c_{23}(\omega) + c_{44}(\omega)]^2 - [c_{33}(\omega) - c_{44}(\omega)]^2}{2c_{33}(\omega) [c_{33}(\omega) - c_{44}(\omega)]}. \quad (3.14)$$

In the X - Z plane, Thomsen-type anisotropic parameters are

$$\begin{aligned} \epsilon^{(XZ)}(\omega) &= \frac{c_{11}(\omega) - c_{33}(\omega)}{2c_{33}(\omega)}, \quad \gamma^{(XZ)}(\omega) \\ &= \frac{c_{66}(\omega) - c_{44}(\omega)}{2c_{44}(\omega)}, \end{aligned} \quad (3.15)$$

and

$$\delta^{(XZ)}(\omega) = \frac{[c_{13}(\omega) + c_{55}(\omega)]^2 - [c_{33}(\omega) - c_{55}(\omega)]^2}{2c_{33}(\omega) [c_{33}(\omega) - c_{55}(\omega)]}. \quad (3.16)$$

3.9 Appendix C: The universal elastic anisotropy index parameter

Assuming that one deals with an anisotropic frequency-dependent effective fourth-rank stiffness tensor \mathbf{C} (might be frequency dependent $\mathbf{C} \Rightarrow \mathbf{C}(\omega)$), a compliance tensor is defined as $\mathbf{S}(\omega) = \mathbf{C}(\omega)^{-1}$. Then, for each frequency, the effective single orientation fourth-rank stiffness and compliance tensors are uniformly distributed and the isotropic stiffness and compliance tensors are calculated. Averaging the single orientation stiffness tensor belongs to the Voigt assumption, which is the theoretical maximum value of the isotropic elastic moduli. On the other hand, averaging the single orientation compliance tensor belongs to the Reuss assumption which is the theoretical minimum value of the isotropic elastic moduli. The resulting isotropic tensors can be expressed in terms of the spherical and deviatoric parts corresponding to bulk K and shear moduli μ :

$$\mathbf{C}^V(\omega) = 3K^V \mathbf{J} + 2\mu^V \mathbf{D} \quad (3.17)$$

and

$$\mathbf{S}^R(\omega) = \frac{1}{3K^R} \mathbf{J} + \frac{1}{2\mu^R} \mathbf{D}, \quad (3.18)$$

where the superscripts “V” and “R” correspond to Voigt and Reuss estimates, respectively. \mathbf{J} and \mathbf{D} are the spherical (volumetric) and deviatoric parts of the symmetric unit fourth-order tensor.

The double contraction of the scalar product (quadruple contraction) of Eqs. (3.17) and (3.18) gives

$$\mathbf{C}^V(\omega) :: \mathbf{S}^R(\omega) = \frac{K^V(\omega)}{K^R(\omega)} + 5 \frac{\mu^V(\omega)}{\mu^R(\omega)}. \quad (3.19)$$

If the effective stiffness tensor is isotropic, then $\mathbf{C}^V(\omega) = (\mathbf{S}^R(\omega))^{-1}$ and $K^V/K^R = \mu^V/\mu^R = 1$. Therefore, when the effective stiffness tensor is isotropic, the value of Eq. 3.19 equals to 6 and this value increases when the effective stiffness tensor becomes anisotropic. Thus, the universal elastic anisotropy index measure A^U is defined as (Ranganathan and Ostoja-Starzewski, 2008):

$$A^U(\omega) = \frac{K^V(\omega)}{K^R(\omega)} + 5 \frac{\mu^V(\omega)}{\mu^R(\omega)} - 6 \geq 0, \quad (3.20)$$

In geophysics, the separation of the elastic anisotropy measure in bulk and shear modes is necessary because rocks might exhibit different frequency dependencies due to bulk and shear deformations. Therefore, in analogy to the universal elastic anisotropy index measure A^U , the anisotropy measures in bulk $A^{\text{bulk}}(\omega)$ and shear

$A^{\text{shear}}(\omega)$ can be defined as

$$A^{\text{bulk}}(\omega) = \frac{K^{\text{V}}(\omega)}{K^{\text{R}}(\omega)} - 1 \quad (3.21)$$

and

$$A^{\text{shear}}(\omega) = \frac{G^{\text{V}}(\omega)}{G^{\text{R}}(\omega)} - 1. \quad (3.22)$$

These two parameters, $A^{\text{bulk}}(\omega)$ and $A^{\text{shear}}(\omega)$, obey the same interpretation as the universal elastic anisotropy index measure: $A^{\text{bulk}} = 0$ ($A^{\text{shear}} = 0$) corresponds to zero bulk (shear) anisotropy of the model, while the discrepancy of A^{bulk} (A^{shear}) from zero anisotropy defines the anisotropy strength in bulk (shear). The Voigt and Reuss estimates (K^{V} , K^{R} , μ^{V} and μ^{R}) can be calculated via simple algebraic formulas for different symmetry classes which can be found elsewhere, e.g., in *Ravindran et al.* (1998) for orthorhombic symmetry, in *Feng et al.* (2012) for tetragonal symmetry and in *Duffy* (2018) for cubic symmetry. Thus, for orthorhombic symmetry (lowest possible symmetry created by two perpendicular sets of cracks embedded into an isotropic material), the Voigt and Reuss bulk moduli are (written for the components of stiffness (compliance) matrices c_{ij} (s_{ij}), in Voigt notation)

$$K^{\text{V}} = \frac{1}{9} [(c_{11} + c_{22} + c_{33}) + 2(c_{12} + c_{13} + c_{23})] \quad (3.23)$$

and

$$K^{\text{R}} = [(s_{11} + s_{22} + s_{33}) + 2(s_{12} + s_{13} + s_{23})]^{-1}. \quad (3.24)$$

Similarly, the Voigt and Reuss shear moduli are (in Voigt notation)

$$\mu^{\text{V}} = \frac{1}{15} [(c_{11} + c_{22} + c_{33} - c_{12} - c_{13} - c_{23}) + 3(c_{44} + c_{55} + c_{66})] \quad (3.25)$$

and

$$\mu^{\text{R}} = 15 [4(s_{11} + s_{22} + s_{33} - s_{12} - s_{13} - s_{23}) + 3(s_{44} + s_{55} + s_{66})]^{-1}. \quad (3.26)$$

Equations (3.23)–(3.26) are valid for orthorhombic symmetry and for higher symmetries: tetragonal, transverse isotropy and cubic. Thus, for evaluating the universal elastic anisotropy index A^{U} and the anisotropy measures in bulk $A^{\text{bulk}}(\omega)$ and shear $A^{\text{shear}}(\omega)$, one can use Eqs. (3.23)–(3.26) to calculate the Voigt and Reuss estimates (K^{V} , K^{R} , μ^{V} and μ^{R}) and then calculate A^{U} using Eq. (3.20) and $A^{\text{bulk}}(\omega)$ and $A^{\text{shear}}(\omega)$ using Eqs. (3.21) and (3.22), respectively.

Chapter 4

An accurate analytical model for squirt flow in anisotropic porous rocks — Part 1: Classical geometry

Yury Alkhimenkov and Beatriz Quintal

Accepted ¹ in *Geophysics*.

¹Alkhimenkov, Y. and Quintal B. (2021). An accurate analytical model for squirt flow in anisotropic porous rocks — Part 1: Classical geometry. *Geophysics* (accepted).

Abstract

Seismic wave propagation in porous rocks that are saturated with a liquid exhibits significant dispersion and attenuation due to fluid flow at the pore scale, so-called squirt flow. This phenomenon takes place in compliant flat pores such as microcracks and grain contacts that are connected to stiffer isometric pores. Accurate quantitative description is crucial for inverting rock and fluid properties from seismic attributes such as attenuation. Up to now, many analytical models for squirt flow were proposed based on simplified geometries of the pore space. These models were either not compared with a numerical solution or showed poor accuracy. We present a new analytical model for squirt flow which is validated against a three-dimensional numerical solution for a simple pore geometry that has been classically used to explain squirt flow; that is why we refer to it as classical geometry. The pore space is represented by a flat cylindrical (penny-shaped) pore whose curved edge is fully connected to a toroidal (stiff) pore. Compared with correct numerical solutions, our analytical model provides very accurate predictions for the attenuation and dispersion across the whole frequency range. This includes correct low- and high-frequency limits of the stiffness modulus, the characteristic frequency, and the shape of the dispersion and attenuation curves. In a companion paper (Part 2), we extend our analytical model to more complex pore geometries. We provide as supplementary material Matlab and symbolic Maple routines to reproduce our main results.

4.1 Introduction

Wave propagation in fluid-saturated porous rocks exhibits energy loss, or attenuation, and velocity dispersion. Most of the attenuation and dispersion of seismic waves in such rocks are usually due to fluid flow taking place at various scales. At the pore scale, this energy loss is referred to as squirt flow (*Mavko and Nur, 1975; Mavko and Jizba, 1991; Dvorkin et al., 1995; Pride et al., 2004; Gurevich et al., 2010; Müller et al., 2010; Pimienta et al., 2015a,b*). Squirt flow occurs between interconnected pores due to different shapes or different orientations (*Mavko et al., 2009; Müller et al., 2010*). Many analytical models describing squirt flow have been suggested. These models explore squirt flow between interconnected compliant cracks (*O'Connell and Budiansky, 1977; Palmer and Traviolia, 1980*), between compliant cracks and stiff pores (*Murphy et al., 1986; Mukerji and Mavko, 1994; Dvorkin et al., 1995; Pride et al., 2004; Gurevich et al., 2010; Collet and Gurevich, 2016*) and between cracks and spheroidal pores (*Xu, 1998; Chapman et al., 2002; Chapman, 2003; Jakobsen and Chapman, 2009*). In real rocks, examples of compliant pores, which here are simply referred to as cracks, are microcracks and grain contacts. An overview of early theoretical studies on squirt flow is given by *Jones (1986)*. Several experimental studies confirmed the importance of squirt flow at different frequency ranges, including seismic frequencies (*Mayr and Burkhardt, 2006; Adelinet et al., 2010; Mikhaltsevitch et al., 2015; Subramaniyan et al., 2015; Pimienta et al., 2015a,b; Chapman et al., 2019; Borgomano et al., 2019*).

Numerically, squirt flow can be modeled by solving a set of equations describing coupled fluid-solid deformation (*Zhang et al., 2010; Zhang and Toksöz, 2012; Quintal et al., 2016, 2019; Das et al., 2019; Alkhimenkov et al., 2020a,b; Lissa et al., 2020, 2021*). *Quintal et al. (2016, 2019)* proposed a simplified numerical solution based on the linearized quasistatic Navier-Stokes equation. *Alkhimenkov et al. (2020a)* benchmarked this numerical solution using a published analytical model (*Collet and Gurevich, 2016*) under a specific scenario, while identifying and quantifying the causes of inaccuracies due to the assumptions used in the analytical model for scenarios corresponding to the described pore geometry. Guided by the numerical simulations presented in *Alkhimenkov et al. (2020a)*, we develop an analytical model for squirt flow which allows us to accurately calculate the corresponding seismic dispersion and attenuation. This model does not have any fitting parameters and is in a very good agreement with three-dimensional numerical solutions across a wide frequency band. This article (Part 1) is focused on describing the analytical model for the classical geometry used in many previous studies: a penny shaped crack surrounded by a toroidal pore (*Murphy et al., 1986; Gurevich et al., 2010; Collet and Gurevich, 2016*). In a companion article (Part 2), we propose an analytical model for more complex geometries and investigate in further details the characteristic frequency of attenuation due to squirt flow. We provide Matlab and symbolic Maple routines to allow the reader to reproduce our main results and/or to obtain results for other material properties and pore sizes. The routines archive (v1.0) is available from a permanent DOI repository (Zenodo) at http://doi.org/link_removed (last access: 11 November 2021).

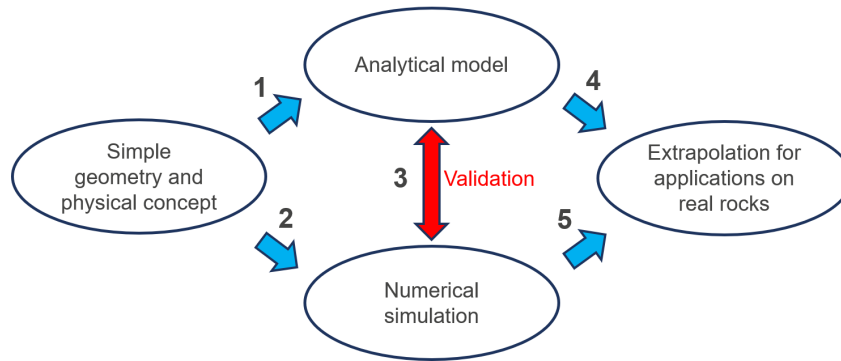


Figure 4.1: Workflow to (i) benchmark published analytical models and (ii) ensure the quality of future models.

4.1.1 Importance of validating analytical models against numerical simulations

Rock physics relies on models that quantitatively describe certain physical concepts with predictive power. For squirt flow, all the models presented in the literature quantitatively describe the dispersion and attenuation based on many assumptions. Only recently, computational advances made it possible to directly compare analytical models against three-dimensional numerical solutions. As a result, it has been shown that certain analytical models are not accurate because some of their assumptions are not fulfilled even for idealized geometries (Alkhimenkov *et al.*, 2020a).

We propose a simple and logical workflow which will make it possible to (i) benchmark published analytical models and (ii) ensure the quality of future models (Figure 4.1). There are five key steps. For a given physical concept, an analytical model for a simple geometry is considered (step 1). The solution can also be calculated numerically for the same simple geometry (step 2). The results predicted by the analytical model are benchmarked through the comparison with the numerical solution (step 3). If the analytical model can adequately describe the physics for a simple geometry, it then could be extrapolated for real rocks (step 4). This can be done by finding key parameters of the analytical models. If the analytical model for a simple geometry cannot describe the key features of the exact numerical solution for the same simple geometry, then this model shouldn't be applied to real rocks.

Up to now, "validation" of analytical models involved only steps 1 and 4. However, step 4 does not appropriately validate the analytical model because of obvious differences in corresponding geometries. Furthermore, other physical mechanisms, which were not accounted for in the analytical model, could have an important effect on the laboratory results. Indeed, "validation" against laboratory results usually require a number of fitting parameters. Therefore, validating analytical models against inherently accurate three-dimensional numerical simulations based on exact same model geometry and same physical mechanisms is of primary importance. Using a numerical solution helps to better understand the involved physical mechanism by evaluating the effect of key parameters as well as to improve the analytical model by testing assumptions.

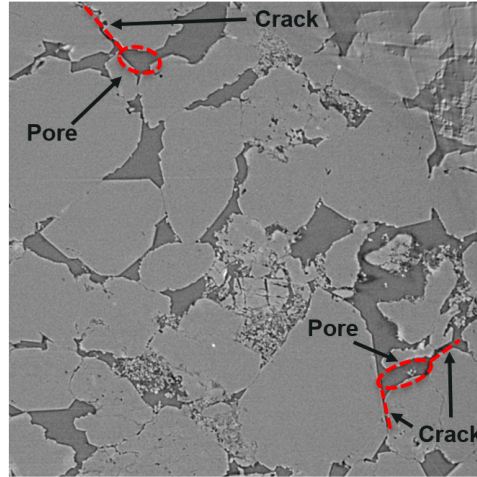


Figure 4.2: Raw synchrotron radiation X-ray tomographic microscopy image of dry Berea sandstone. One slice of the total data cube with 1024^3 voxels [from *Madonna et al.* (2013)].

4.1.2 Seismic attenuation and dispersion due to squirt flow

One measure of seismic P-wave attenuation is the so-called inverse quality factor $1/Q(\omega) = \text{Im}(M(\omega))/\text{Re}(M(\omega))$ (*O'Connell and Budiansky*, 1978), where $\omega = 2\pi f$ is the angular frequency (f is the frequency) and $M = K + 4/3G$ is the complex-valued P-wave modulus, K and G are the bulk and shear moduli, respectively. Throughout the article, by attenuation we imply the inverse quality factor.

We recall a brief overview of the physics based on previous analytical studies (*Mavko and Jizba*, 1991) with some additional information obtained from numerical simulations (*Quintal et al.*, 2019; *Alkhimenkov et al.*, 2020a,b; *Lissa et al.*, 2020). In the physics of squirt flow, the cause of energy dissipation is fluid pressure diffusion at the pore scale. An idealized rock model can be parameterized by three components: solid elastic matrix, isometric pores and thin compliant cracks (Figure 4.2). Pores and cracks are interconnected and saturated with a fluid. A passing seismic wave deforms the compliant cracks more than the stiff pores, which causes fluid pressure gradients in the cracks. This results in fluid pressure diffusion, sometimes referred to as local fluid flow or squirt flow, which strongly depends on the frequency of the propagating wave.

At low-frequencies, the fluid pressure becomes uniform throughout the pore space because there is enough time for it to equilibrate. This is called relaxed state. The effective elastic properties can be calculated by using Gassmann's equations (*Gassmann*, 1951) given that the elastic moduli of the dry frame are known. At low-frequencies, $1/Q$ is proportional to $\approx \omega^1$ according to numerical simulations for simple geometries (*Alkhimenkov et al.*, 2020a). At intermediate frequencies, the fluid pressure gradients are at their maximum, which corresponds to the attenuation peak. The frequency at which the attenuation is at its maximum is called the characteristic frequency ω_c . At high frequencies, there is no time for fluid to flow or fluid pressure to diffuse between cracks and pores; cracks behave as hydraulically isolated from pores. This is called unrelaxed state. The slope of the high-frequency asymptote of the attenuation curve depends on the pore geometry (*Alkhimenkov et al.*, 2020a,b). If the pore space is represented by a penny shaped crack connected to a toroidal pore, then $1/Q$ at high-frequencies is proportional to $\approx \omega^{-1/2}$. An evaluation of the high-frequency asymptote of $1/Q$ for more complex geometries is presented in the Part 2 of the present study.

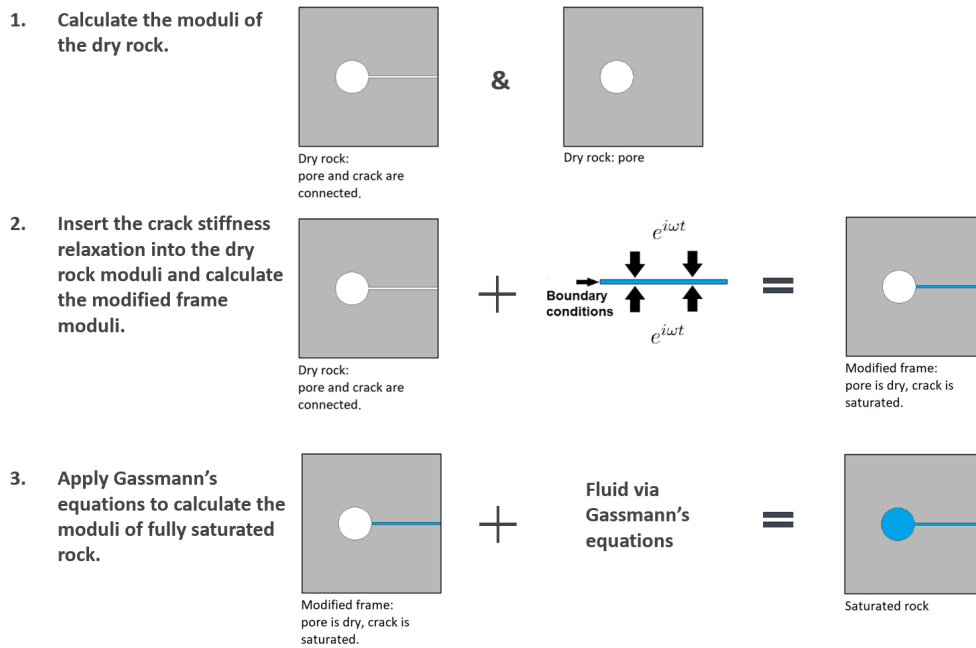


Figure 4.3: The development of the present analytical model.

4.2 The analytical model

An analytical model for seismic attenuation and dispersion caused by squirt flow should, at least, accurately determine three key features: the low- and high-frequency limits for the elastic moduli and the characteristic frequency. To calculate the low-frequency limit, one needs the correct dry moduli of the rock and then use Gassmann's equations to obtain the moduli in the case of saturation with a fluid. To calculate the high-frequency limit, one needs the dry moduli of the rock where the crack normal compliance is zero and again use Gassmann's equations to obtain the moduli of the saturated rock. The characteristic frequency is directly related to the aspect ratio of compliant cracks and can be reasonably estimated. If these three parameters are determined, the dispersion and attenuation curves can be plotted using, for example, a standard linear solid (SLS) rheology. The disadvantage of the SLS model is that the resulting $1/Q$ is a symmetric curve if plotted in a bi-logarithmic scale, which is usually not the case for attenuation caused by squirt flow (Alkhimenkov *et al.*, 2020a,b; Lissa *et al.*, 2020).

The analytical model that we present here features the key components of previous analytical models for squirt flow (e.g., Dvorkin and Nur (1993); Mukerji and Mavko (1994); Dvorkin *et al.* (1995); Gurevich *et al.* (2010); Glubokovskikh *et al.* (2016); Collet and Gurevich (2016)) but with several key modifications which make it accurate. The main building block of our analytical model is the so-called modified frame, which was originally introduced by Mavko and Jizba (1991). The modified frame represents a rock configuration where cracks are saturated with a fluid, whereas the isometric pores are dry. The development of our analytical model is shown in Figure 5.4. First, we calculate the moduli of the dry rock for two configurations: the dry rock containing the torus connected to the crack and the dry rock containing the torus connected to the crack with zero normal compliance (step 1, Figure 5.4). Then, we calculate the relaxation of the crack stiffness due to fluid pressure diffusion and obtain accurate values of the frequency-dependent moduli of the modified frame (step 2, Figure 5.4). Finally, we use Gassmann's equations to obtain the frequency-dependent moduli of the fully saturated medium (step 3, Figure 5.4).

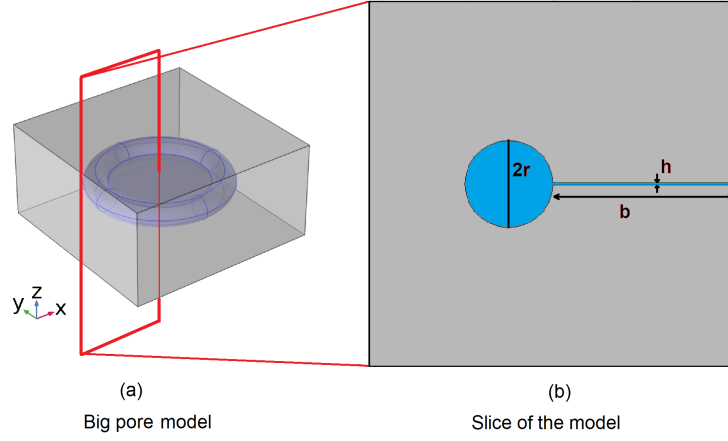


Figure 4.4: (a) Sketch illustrating the Big pore model: a flat cylinder representing a crack whose edge is connected to a torus representing a stiff isometric pore. (b) A vertical slice across half of the model. r is the minor radius of the torus ($d_{Mn} = 2r$ is the minor diameter of the torus), $d_{Mj} = r + b$ is the major radius of the torus.

4.2.1 General expressions

Let us consider the classical model for squirt flow presented in Figure 4.4, assuming a representative volume element (RVE) (for clarity, later in this article we will show slices of half of the models as in Figure 4.4b). The stiff isometric pore is represented by a torus and the penny-shaped crack is represented by a flat cylinder. The embedding medium consists of an elastic grain material described by a compliance tensor S_{ijkl}^g . The m -th inclusion (interconnected isometric pore and crack) is represented by a compliance contribution tensor \mathbf{H} with components H_{ijkl}^m . The relation for the overall strain ϵ_{ij} can be written as

$$\epsilon_{ij} = S_{ijkl}^g \sigma_{kl} + \Delta\epsilon_{ij} = S_{ijkl}^g \sigma_{kl} + \sum_m H_{ijkl}^m \sigma_{kl}, \quad (4.1)$$

where σ_{kl} represents remotely applied stresses, $\Delta\epsilon_{ij}$ represents the extra strain due to the presence of the inclusion described by the \mathbf{H} -tensor. The components of the effective compliance tensor of a three-dimensional medium with inclusion(s) are

$$S_{ijkl}^* = S_{ijkl}^g + \sum_m H_{ijkl}^m. \quad (4.2)$$

The expression 4.2 is exact and valid for a finite and infinitely extended RVE (*Nemat-Nasser and Hori, 2013*). The main assumption is that the grain material and inclusions are elastic and homogeneous. The compliance tensors can be complex functions of frequency (*Hashin, 1970*). In three-dimensions, the \mathbf{H} -tensors can be calculated exactly for ellipsoids by using the Eshelby result; in two-dimensions, exact results are known for several geometries (*Kachanov and Sevostianov, 2018*). In our particular case, in equations 4.1 and 4.2 $m = 1$ since we have only one inclusion. For our pore space geometry (Figure 4.4), no closed form expression of this \mathbf{H} -tensor exist, thus, we derive an approximation.

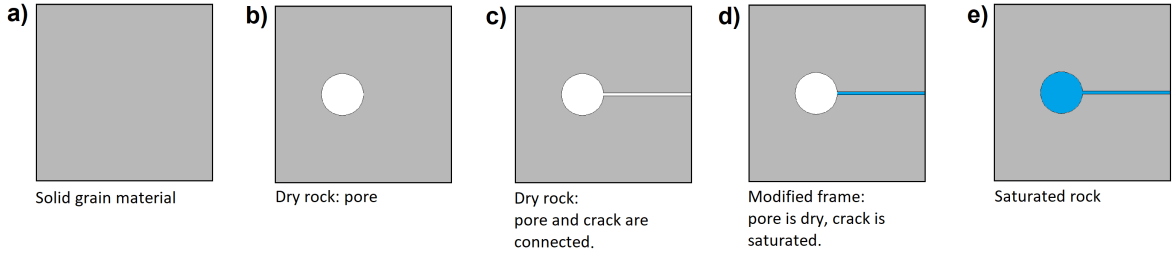


Figure 4.5: Cartoon illustrating the different model configurations used to obtain the corresponding compliance matrices.

4.2.2 General expressions for our geometry

The key components of our model are illustrated in Figure 4.5. The effective compliance tensor with components S_{ijkl}^* for the dry model represented in Figure 4.5c can be written similarly to expression 4.2 (in Voigt notation),

$$[S_{mn}^*]_{\text{dry}} = S_{mn}^g + [H_{mn}]_{\text{dry}}. \quad (4.3)$$

The effective frequency-dependent compliance tensor with components $S_{ijkl}^*(\omega)$ for the fluid-saturated model is (Figure 4.5e)

$$[S_{mn}^*(\omega)]_{\text{sat}} = S_{mn}^g + [H_{mn}(\omega)]_{\text{sat}}. \quad (4.4)$$

The corresponding effective stiffness matrix for the saturated model is

$$[C_{mn}^*(\omega)]_{\text{sat}} = [S_{mn}^*(\omega)]_{\text{sat}}^{-1}. \quad (4.5)$$

The compliance matrix of an elastic grain material S_{mn}^g is frequency independent. We also introduce the compliance contribution matrix of the dry torus $[H_{mn}^{\text{tp}}]_{\text{dry}}$ and the compliance contribution matrix $[H_{mn}(\omega)]^{\text{MF}}$ of an inclusion represented by a dry torus connected to a crack saturated with a fluid (this compliance contribution can be used to obtain the moduli of the modified frame). By using expressions 4.3-4.5, several configurations of the model (illustrated in Figure 4.5) can be evaluated. For example, the effective compliance tensor for the dry model containing only the torus (Figure 4.5b) $[S_{mn}^*]^{\text{tp}}$ is

$$[S_{mn}^*]^{\text{tp}} = S_{mn}^g + [H_{mn}^{\text{tp}}]_{\text{dry}}. \quad (4.6)$$

The effective compliance matrix for the modified frame model (Figure 4.5d) is

$$[S_{mn}^*(\omega)]^{\text{MF}} = S_{mn}^g + [H_{mn}(\omega)]^{\text{MF}}. \quad (4.7)$$

Finally, the effective compliance matrix for the fluid-saturated model $[S_{mn}^*(\omega)]_{\text{sat}}$ can be calculated by applying anisotropic Gassmann's equations to expression 4.7 for each frequency. The result will be equivalent to that obtained via expression 4.4.

Some remarks

To calculate the resulting effective moduli, one needs to find the frequency-dependent compliance contribution matrix $[H_{mn}(\omega)]_{\text{sat}}$ of a saturated pore space represented by a torus connected to a flat cylinder (see expression 4.4). Equivalently, instead of finding $[H_{mn}(\omega)]_{\text{sat}}$ directly, we can find $[S_{mn}^*(\omega)]^{\text{MF}}$ and then obtain $[H_{mn}(\omega)]_{\text{sat}}$. Let's assume that a torus and a flat cylinder are disconnected and far from each other. We can represent the **H**-tensor in the form

$$[H_{mn}]_{\text{dry}} = [H_{mn}^{\text{tp}}]_{\text{dry}} + [H_{mn}^{\text{cr}}]_{\text{dry}}, \quad (4.8)$$

where $[H_{mn}^{\text{tp}}]_{\text{dry}}$ and $[H_{mn}^{\text{cr}}]_{\text{dry}}$ represent the compliance contribution matrices of the dry torus and the dry crack, respectively. The compliance contribution matrix for the modified frame (dry torus and saturated crack with a frequency-dependent fluid bulk modulus) is

$$[H_{mn}(\omega)]^{\text{MF}} = [H_{mn}^{\text{tp}}]_{\text{dry}} + [H_{mn}^{\text{cr}}(\omega)]_{\text{sat}}, \quad (4.9)$$

where the compliance contribution matrix of the torus $[H_{mn}^{\text{tp}}]_{\text{dry}}$ is frequency-independent but the compliance contribution matrix of the crack $[H_{mn}^{\text{cr}}(\omega)]_{\text{sat}}$ is frequency-dependent. However, the expressions 4.8 and 4.9 are accurate only when the torus and the crack are not connected and far from each other, so that there is no elastic interactions. Since we are working with a model where the torus and the crack are interconnected, the expressions 4.8 and 4.9 are not valid as illustrated by *Alkhimenkov et al. (2020a)*. The compliance contribution matrix $[H_{mn}(\omega)]^{\text{MF}}$ should be calculated differently, such as in the procedure that we describe below.

4.2.3 Calculation of the model compliance

The overall dispersion and attenuation magnitudes of the modified frame (and hence, of the fully saturated model) are controlled by the elastic bounds: the low-frequency limit — the dry moduli of the model containing the interconnected torus and crack (Figure 4.5c), and the high-frequency limit — the dry moduli of the model containing the torus while the crack normal compliance is zero (Figure 4.5b). The corresponding values of the dispersion are illustrated in Figure 4.6. These low- and high-frequency values can be taken from different sources:

- i) These values can be estimated from the laboratory measurements by measuring the low- and high-pressure rock moduli, this procedure is described in many studies, e.g., (*Gurevich et al., 2010*). We do not examine nor use this approach here.
- ii) The second option is to calculate the low- and high-frequency moduli of a dry model numerically.
- iii) The third option is to calculate the low- and high-frequency moduli of a dry model analytically.

If the analytical methods are properly used, then the resulting moduli are equivalent to that ones obtained numerically. In this study, we adopt the dry moduli calculated numerically and we provide the workflow to calculate the dry moduli analytically; the numerical and analytical approaches provide us identical results.

One of the most important outcomes of this study is the adequate calculation of the effective elastic moduli of the interconnected pore space using an analytical approach. The pore space consists of two interconnected cavities: the stiff isometric pore (torus) and the compliant crack (flat cylinder). The correct values for the elastic moduli are obtained numerically for several configurations and shown in Figure 4.6. Details on the numerical solutions and applied boundary conditions are given in Appendix 4.6. These correct values are used to benchmark the model compliance obtained analytically. The analytical expressions are provided below.

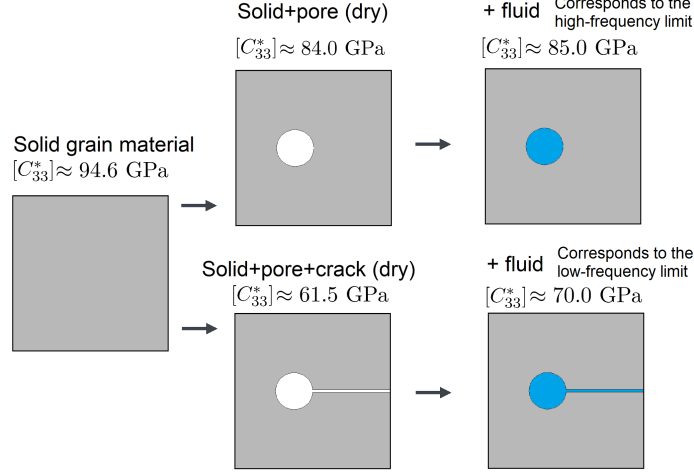


Figure 4.6: Sketch illustrating the configurations of our model that corresponds to the high- and low-frequency limits obtained from the numerical calculations for the $[C_{33}^*]_{\text{sat}}$ component (properties in Tables 5.1 and 5.2).

Analytical expressions

To derive the compliance contribution matrix of the interconnected torus and crack $[H_{mn}]_{\text{dry}}$, we employ the conventional approach used in micromechanics to construct the property contribution matrix of complex geometries (e.g., intersecting cracks, inclusions of “irregular” shapes), see chapters 4.3 and 4.4 in *Kachanov and Sevostianov* (2018). Several different techniques exist, which can be used separately or in combinations. Here, we adopt the following method: by using the results of three-dimensional numerical simulations for the interconnected torus and crack, we find the structure of the compliance contribution matrix, its principal directions and the key geometrical characteristics of inclusions which control the compliance contribution matrix. Then, we construct the compliance contribution matrix of the interconnected torus and crack $[H_{mn}]_{\text{dry}}$ by using the known property contribution tensors for simple geometries (in our case, the crack, the torus and spheroid). It turns out, that all components of the $[H_{mn}]_{\text{dry}}$ are controlled by the torus except for $[H_{33}]_{\text{dry}}$, $[H_{44}]_{\text{dry}}$ and $[H_{55}]_{\text{dry}}$. This is simple to understand because the compliance contribution matrix of the crack is described by the two components only (*Schoenberg and Douma*, 1988; *Schoenberg and Helbig*, 1997); thus, the only non-zero components are $[H_{33}^{\text{cr}}]_{\text{dry}}$, $[H_{44}^{\text{cr}}]_{\text{dry}} \equiv [H_{55}^{\text{cr}}]_{\text{dry}}$. However, the crack is connected to the torus, therefore, the theory for cracks embedded into a homogenous material by *Schoenberg and Douma* (1988); *Schoenberg and Helbig* (1997) cannot be used here to calculate $[H_{33}^{\text{cr}}]_{\text{dry}}$, $[H_{44}^{\text{cr}}]_{\text{dry}}$, $[H_{55}^{\text{cr}}]_{\text{dry}}$. Instead, from the numerical experiments we find that the $[H_{33}]_{\text{dry}}$, $[H_{44}]_{\text{dry}}$ and $[H_{55}]_{\text{dry}}$ components of the compliance contribution matrix of the interconnected torus and crack are the same as for a spheroid $[H_{mn}^{\text{Ecr}}]_{\text{dry}}$. From now on, we refer to this spheroid as the extended crack. The shape of the extended crack is such that it works as an envelope for the torus as shown in Figure 4.7. Thus, we employ $[H_{33}^{\text{Ecr}}]_{\text{dry}}$, $[H_{44}^{\text{Ecr}}]_{\text{dry}}$, $[H_{55}^{\text{Ecr}}]_{\text{dry}}$ components to the contribution matrix of the interconnected torus and crack $[H_{mn}]_{\text{dry}}$. This approach provide us with a very good approximation of the compliance contribution matrix for this particular geometry — the interconnected torus and crack. A detailed workflow is given below (see also Figure 4.7).

i) The compliance contribution matrix of the dry torus $[H_{mn}^{\text{tp}}]_{\text{dry}}$ should be calculated as

$$[H_{mn}^{\text{tp}}]_{\text{dry}} = \begin{bmatrix} [H_{11}^{\text{tp}}]_{\text{dry}} & [H_{12}^{\text{tp}}]_{\text{dry}} & [H_{13}^{\text{tp}}]_{\text{dry}} & 0 & 0 & 0 \\ [H_{21}^{\text{tp}}]_{\text{dry}} & [H_{22}^{\text{tp}}]_{\text{dry}} & [H_{23}^{\text{tp}}]_{\text{dry}} & 0 & 0 & 0 \\ [H_{31}^{\text{tp}}]_{\text{dry}} & [H_{32}^{\text{tp}}]_{\text{dry}} & [H_{33}^{\text{tp}}]_{\text{dry}} & 0 & 0 & 0 \\ 0 & 0 & 0 & [H_{44}^{\text{tp}}]_{\text{dry}} & 0 & 0 \\ 0 & 0 & 0 & 0 & [H_{55}^{\text{tp}}]_{\text{dry}} & 0 \\ 0 & 0 & 0 & 0 & 0 & [H_{66}^{\text{tp}}]_{\text{dry}} \end{bmatrix}. \quad (4.10)$$

ii) The compliance contribution matrix of the extended dry crack is calculated $[H_{mn}^{\text{Ecr}}]_{\text{dry}}$. The diameter of the extended crack is equal to the diameter of the crack ($2b$) plus an extension corresponding to twice the minor diameter of the torus ($4r$), as shown in Figure 4.7. In other words, the projection of the pore space containing the crack and torus and the projection of the extended crack model onto the xy -plane are the same. The thickness of the extended crack is such as the extended crack is a spheroidal envelope for the torus as shown in Figure 4.7. For our particular geometry, the thickness of the extended crack is approximately twice the minor diameter of the torus, $d_{Mn} = 2r$ (see Figure 4.7 and Figure 4.4 for geometrical parameters).

iii) The compliance contribution matrix of the interconnected torus and crack $[H_{mn}]_{\text{dry}}$ is thus constructed by using the obtained components of $[H_{mn}^{\text{tp}}]_{\text{dry}}$ and $[H_{mn}^{\text{Ecr}}]_{\text{dry}}$:

$$[H_{mn}]_{\text{dry}} = \begin{bmatrix} [H_{11}^{\text{tp}}]_{\text{dry}} & [H_{12}^{\text{tp}}]_{\text{dry}} & [H_{13}^{\text{tp}}]_{\text{dry}} & 0 & 0 & 0 \\ [H_{21}^{\text{tp}}]_{\text{dry}} & [H_{22}^{\text{tp}}]_{\text{dry}} & [H_{23}^{\text{tp}}]_{\text{dry}} & 0 & 0 & 0 \\ [H_{31}^{\text{tp}}]_{\text{dry}} & [H_{32}^{\text{tp}}]_{\text{dry}} & [H_{33}^{\text{Ecr}}]_{\text{dry}} & 0 & 0 & 0 \\ 0 & 0 & 0 & [H_{44}^{\text{Ecr}}]_{\text{dry}} & 0 & 0 \\ 0 & 0 & 0 & 0 & [H_{55}^{\text{Ecr}}]_{\text{dry}} & 0 \\ 0 & 0 & 0 & 0 & 0 & [H_{66}^{\text{tp}}]_{\text{dry}} \end{bmatrix}. \quad (4.11)$$

The components $[H_{13}^{\text{tp}}]_{\text{dry}}$ and $[H_{23}^{\text{tp}}]_{\text{dry}}$, and corresponding symmetric components, could also be replaced by $[H_{13}^{\text{Ecr}}]_{\text{dry}}$ and $[H_{23}^{\text{Ecr}}]_{\text{dry}}$ (which may improve the accuracy) but this effect is of minor importance, thus, we do not explore it in more details. The components $[H_{33}^{\text{tp}}]_{\text{dry}}$, $[H_{44}^{\text{tp}}]_{\text{dry}}$ and $[H_{55}^{\text{tp}}]_{\text{dry}}$ representing the torus are replaced by the components representing the extended crack $[H_{33}^{\text{Ecr}}]_{\text{dry}}$, $[H_{44}^{\text{Ecr}}]_{\text{dry}}$ and $[H_{55}^{\text{Ecr}}]_{\text{dry}}$. The compliance contribution matrices of a torus and extended crack (spheroid) can be calculated analytically as described in chapters 4.3 and 4.2 of *Kachanov and Sevostianov* (2018) (and references therein).

The compliance contribution matrix of the modified frame is

$$[H_{mn}(\omega)]^{\text{MF}} = \begin{bmatrix} [H_{11}^{\text{tp}}]_{\text{dry}} & [H_{12}^{\text{tp}}]_{\text{dry}} & [H_{13}^{\text{tp}}]_{\text{dry}} & 0 & 0 & 0 \\ [H_{21}^{\text{tp}}]_{\text{dry}} & [H_{22}^{\text{tp}}]_{\text{dry}} & [H_{23}^{\text{tp}}]_{\text{dry}} & 0 & 0 & 0 \\ [H_{31}^{\text{tp}}]_{\text{dry}} & [H_{32}^{\text{tp}}]_{\text{dry}} & [H_{33}^{\text{Ecr}}(\omega)]^{\text{MF}} & 0 & 0 & 0 \\ 0 & 0 & 0 & [H_{44}^{\text{Ecr}}]_{\text{dry}} & 0 & 0 \\ 0 & 0 & 0 & 0 & [H_{55}^{\text{Ecr}}]_{\text{dry}} & 0 \\ 0 & 0 & 0 & 0 & 0 & [H_{66}^{\text{tp}}]_{\text{dry}} \end{bmatrix}. \quad (4.12)$$

The only difference between the matrices in equation 4.11 and equation 4.12 is the component $[H_{33}^{\text{Ecr}}(\omega)]^{\text{MF}}$. Since the fluid flow takes place in the crack only when the displacement boundary condition in the vertical (z)

direction is applied, the component $[H_{33}^{\text{Ecr}}(\omega)]^{\text{MF}}$ is the only frequency-dependent component. This statement is also supported by the numerical simulations by *Alkhimenkov et al.* (2020a). The component $[H_{13}^{\text{Ecr}}(\omega)]^{\text{MF}}$ might also exhibit some dispersion but the magnitude is negligibly small (*Alkhimenkov et al.*, 2020a). The limits of $[H_{33}^{\text{Ecr}}(\omega)]^{\text{MF}}$ are

$$\lim_{\omega \rightarrow +\infty} [H_{33}^{\text{Ecr}}(\omega)]^{\text{MF}} = [H_{33}^{\text{tp}}]_{\text{dry}}, \quad (4.13)$$

and

$$\lim_{\omega \rightarrow +0} [H_{33}^{\text{Ecr}}(\omega)]^{\text{MF}} = [H_{33}^{\text{Ecr}}]_{\text{dry}}. \quad (4.14)$$

To separate the contribution of the torus, which is a constant value across a full frequency band, from the contribution of the extended crack compliance, which is frequency dependent, we introduce

$$[H'_{mn}(\omega)]^{\text{MF}} = [H_{mn}(\omega)]^{\text{MF}} - [H_{mn}^{\text{tp}}]_{\text{dry}} = \begin{bmatrix} 0 & 0 & 0 & 0 & 0 & 0 \\ 0 & 0 & 0 & 0 & 0 & 0 \\ 0 & 0 & [H'_{33}(\omega)]^{\text{MF}} & 0 & 0 & 0 \\ 0 & 0 & 0 & [H'_{44}]_{\text{dry}}^{\text{MF}} & 0 & 0 \\ 0 & 0 & 0 & 0 & [H'_{55}]_{\text{dry}}^{\text{MF}} & 0 \\ 0 & 0 & 0 & 0 & 0 & 0 \end{bmatrix}. \quad (4.15)$$

Expression 4.15 has the same structure as the compliance contribution matrix of a crack written in terms of normal and tangential compliances Z_n and Z_t . The limits of $[H'_{33}(\omega)]^{\text{MF}}$ are

$$\lim_{\omega \rightarrow +\infty} [H'_{33}(\omega)]^{\text{MF}} = 0, \quad (4.16)$$

and

$$\lim_{\omega \rightarrow +0} [H'_{33}(\omega)]^{\text{MF}} = [H_{33}^{\text{Ecr}}]_{\text{dry}} - [H_{33}^{\text{tp}}]_{\text{dry}} \equiv Z_n, \quad (4.17)$$

where for simplicity we introduce the apparent normal crack compliance Z_n . The apparent tangential crack compliance is $Z_t = [H'_{44}]_{\text{dry}}^{\text{MF}} \equiv [H'_{55}]_{\text{dry}}^{\text{MF}}$. Even though the structure of the matrices is the same, the absolute values of the components in equation 4.15 are calculated differently from the formulas for Z_n and Z_t suggested for cracks embedded into a homogenous material by *Schoenberg and Douma* (1988); *Schoenberg and Helbig* (1997). The effective compliance matrix for the modified frame can be calculated using the equation 4.7 as

$$[S_{mn}^*(\omega)]^{\text{MF}} = S_{mn}^g + [H_{mn}^{\text{tp}}]_{\text{dry}} + [H'_{mn}(\omega)]^{\text{MF}}. \quad (4.18)$$

Finally, the effective compliance moduli of a fully saturated model $[S_{mn}^*(\omega)]$ can be obtained by saturating the modified frame $[S_{mn}^*(\omega)]^{\text{MF}}$ with a fluid using Gassmann's equations. The expression 4.18 is the main result of this study and is valid for any geometry of the pore space if the appropriate compliance contribution matrices are used.

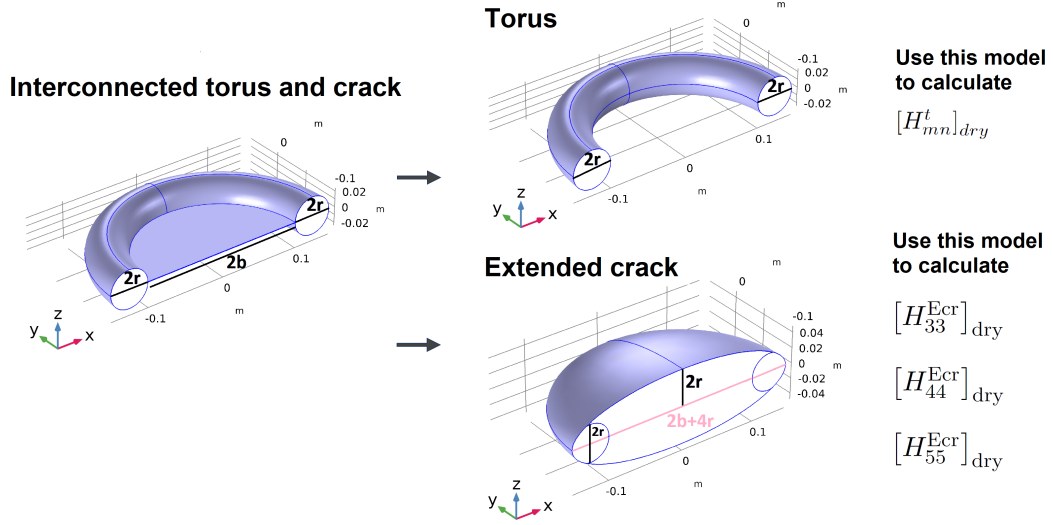


Figure 4.7: Sketch illustrating the workflow for calculating analytically different components of the compliance matrix for the model with interconnected isometric pore and crack.

4.2.4 Calculation of the frequency-dependent crack stiffness

To derive the frequency-dependent component of the contribution matrix $[H'_{33}(\omega)]^{\text{MF}}$ (i.e. the normal crack compliance), we note that the thin crack is adequately described by two parameters (as in equation 4.15), then we use anisotropic Gassmann's equations to calculate the moduli considering the crack saturated. The derivation is simple, requires only algebraic manipulations which are cumbersome, thus we refer to the supplementary material for the full derivation (Maple script). The resulting expression is

$$[H'_{33}(\omega)]^{\text{MF}} = \frac{(K_g - K_f^*(\omega)) \phi_c Z_n}{(K_g - K_f^*(\omega)) \phi_c + K_f^*(\omega) K_g Z_n}, \quad (4.19)$$

where ϕ_c is the compliant porosity (crack porosity), Z_n is the normal compliance of the crack (see expression 4.17) and K_g is the bulk modulus of the solid grains. If a crack cannot be described by two parameters (for example, the $[H'_{13}]^{\text{MF}}_{\text{dry}}$ component is also affected), then one can use our Maple script (supplementary material) with already derived equations for the general (anisotropic) form of the solid background and the property contribution matrix of the inclusion, e.g., crack. The expression for the frequency-dependent bulk modulus of the fluid $K_f^*(\omega)$ will be given below.

Extension for cracks with finite thickness

If the crack thickness is not so small, so that the aspect ratio is larger than 0.0025 then the limit given in 4.16 is not equal to zero. A small non-zero value of Z_n^{fth} will be present,

$$\lim_{\omega \rightarrow +\infty} [H'_{33}(\omega)]^{\text{MF}} = Z_n^{fth}. \quad (4.20)$$

and the normal crack compliance becomes

$$Z_n^f = Z_n - Z_n^{fth} \quad (4.21)$$

In this case, the only modification that is needed is a slight change in expression 4.19 by including the additional compliance Z_n^{fth}

$$\left[H'_{33} \right]^{MF} = \frac{(K_g - K_f^*(\omega)) \phi_c Z_n^f}{(K_g - K_f^*(\omega)) \phi_c + K_f^*(\omega) K_g Z_n^f} + Z_n^{fth}. \quad (4.22)$$

4.2.5 Relaxation of the crack stiffness

In the analytical model, the relaxation of the crack stiffness due to fluid pressure diffusion controls the frequency-dependence of the effective elastic moduli of the medium. The relaxation of the crack stiffness can be modeled via the relaxation of the fluid bulk modulus $K_f^*(\omega)$ in the crack. In several previous studies, the task is reduced to solving the problem for a crack only by applying boundary conditions directly to the crack walls and to the tip of the crack (e.g., *Murphy et al.* (1986)). Then, the derived expression for $K_f^*(\omega)$ is treated as the crack stiffness. Unfortunately, applying boundary conditions to the crack walls and to the crack tip produces a different result compared to applying the boundary conditions directly to the walls of the model. For illustration, we show the models considering zero fluid pressure at the crack tip and the Big pore model, with the corresponding results of numerical simulations (Figure 4.8).

In the rock physics literature, the relaxation of fluid pressure was derived by solving an equation for fluid pressure distribution p in the flat cylinder (crack) under sinusoidal loading $\Delta h e^{i\omega t}$ applied to the walls of the crack, Δh is the displacement of the crack walls (e.g., *Murphy et al.* (1986); *Dvorkin and Nur* (1993)). Then, by integrating the fluid pressure p over the thickness and area of the crack, the frequency-dependent fluid bulk modulus $K_f^*(\omega)$ was determined. In the mechanics literature, similar problems were solved in time domain for different visco-elastic materials (e.g., *Chalhoub and Kelly* (1990); *Tsai and Lee* (1998)). All the solutions are very similar for the same geometries and applied boundary conditions with slight differences depending on the approximations done during the derivation.

We use symbolic environment Maple to derive a general structure of the solutions for the frequency-dependent fluid bulk modulus $K_f^*(\omega)$. We start with the known approach by applying the boundary conditions to the walls of the crack (*Murphy et al.*, 1986; *Tsai and Lee*, 1998). But afterwards we modify the resulting solution by taking into account the heterogeneous stress field induced by the torus. In Cartesian coordinates, the expression for fluid pressure under the compression strain ϵ_c applied to the walls of the crack is

$$\frac{\partial^2 p}{\partial x^2} + \frac{\partial^2 p}{\partial y^2} - k^2 p = -k^2 K_f \epsilon_c, \quad (4.23)$$

where k is a parameter a function of the applied strain and rheology of the crack (e.g., *Tsai and Lee* (1998)). In polar coordinates, the expression for fluid pressure becomes

$$\frac{\partial^2 p}{\partial r^2} + \frac{1}{r} \frac{\partial p}{\partial r} - k^2 p = -k^2 K_f \epsilon_c \quad (4.24)$$

The stiffness of the crack H can be expressed via the surface integral over the crack area S for the averaged vertical stress $\bar{\sigma}_{zz}$,

$$H = - \left[\int_S \bar{\sigma}_{zz} dS \right] / (S \epsilon_c), \quad \bar{\sigma}_{zz} = \left[\int_h \sigma_{zz} dh \right] / h. \quad (4.25)$$

If the crack rheology represents a pure fluid, then $H \equiv K_f$. Similar equations were considered in the previous studies by *Murphy et al.* (1986); *Chalhoub and Kelly* (1990).

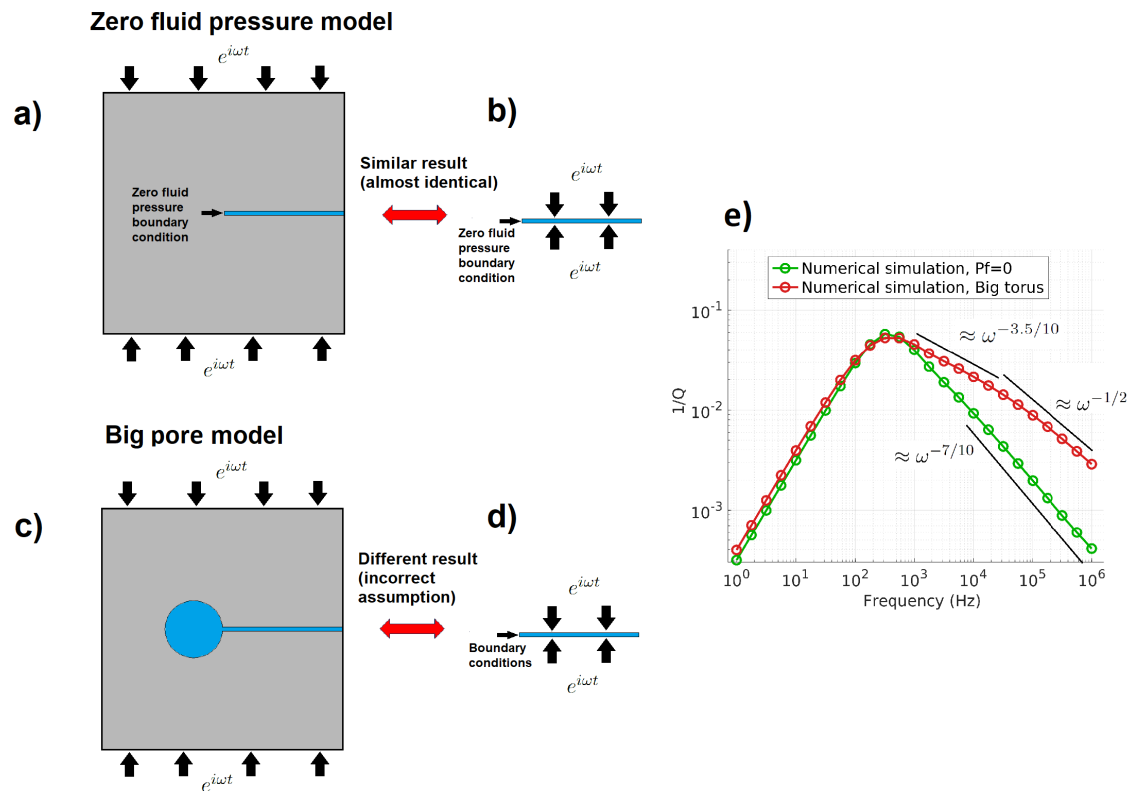


Figure 4.8: Sketch illustrating the simplifications made in analytical models via applied boundary conditions (a vertical slice of the two models shown in Figure 4.4). Panels a) and c) — boundary conditions applied to the walls of the model. Panels b) and d) — boundary conditions applied to the walls of the crack. Panel e) shows the numerical result; note, that the high-frequency slope of the attenuation curve is substantially different if the crack is connected to an actual pore.

Zero fluid pressure at the crack tip

In the modified frame configuration, the crack is connected to the dry isometric pore, which corresponds to zero fluid pressure boundary condition at the edge of the crack. This configuration was studied by *Chalhoub and Kelly* (1990); *Tsai and Lee* (1998). The solution for $K_f^*(\omega)$ treating the crack as a flat cylinder is

$$K_f^*(\omega) = K_f + \frac{4}{3}i\omega\eta - \frac{\left(K_f - \frac{2}{5}i\omega\eta\right)^2}{\left(K_f + \frac{4}{3}i\omega\eta\right) \frac{\bar{k}_1 J_0(\bar{k}_1)}{J_1(\bar{k}_1)} - i\omega\eta}, \quad (4.26)$$

where η is a fluid dynamic viscosity, J_0 and J_1 are the are the Bessel functions of the first kind of order 0 and 1, respectively, and \bar{k}_1 is defined as

$$\bar{k}_1 = \frac{1}{\alpha} \sqrt{3i\omega\eta / \left(K_f + \frac{4}{3}i\omega\eta\right)}, \quad (4.27)$$

where $\alpha = h/(2b)$ is the crack aspect ratio. A different expression for $K_f^*(\omega)$ was provided by *Chalhoub and Kelly* (1990)

$$K_f^*(\omega) = K_f \left[1 - \frac{2J_1(\bar{k}_2)}{\bar{k}_2 J_0(\bar{k}_2)} \right], \quad (4.28)$$

where \bar{k}_2 is

$$\bar{k}_2 = \frac{1}{\alpha} \sqrt{-3i\omega\eta / K_f}. \quad (4.29)$$

It was pointed out by *Tsai and Lee* (1998) that the solution 4.28 is similar to 4.26 for Poisson ratio = 0.5 but different if Poisson ratio ≤ 0.5 (the solution 4.26 matches numerical solutions for Poisson ratio ≤ 0.5). Thus, for fluids (Poisson ratio = 0.5) either solution 4.26 or 4.28 can be used (Figure 4.9). The expression 4.28 was used by *Gurevich et al.* (2010); *Collet and Gurevich* (2016) for the relaxation of the fluid bulk modulus of the modified frame.

Non-zero fluid pressure at the crack tip

In this configuration, the crack is connected to the saturated isometric pore meaning that the fluid pressure in such a pore will increase due to the fluid flow from the crack (see *Murphy et al.* (1986) for the precise boundary conditions). In this case, during the relaxation of the fluid bulk modulus, the fluid “feels” the finite volume of the isometric pore. The solution of 4.25 for this boundary condition is (*Murphy et al.*, 1986)

$$K_f^*(\omega) = K_f \left[1 - \frac{2V_{por} J_1(\bar{k}_2)}{2V_{cr} J_1(\bar{k}_2) + \bar{k}_3 V_{por} J_0(\bar{k}_2)} \right] \quad (4.30)$$

V_{por} is the volume of the stiff pore and $V_{cr} = \pi h b^2$ is the volume of the compliant crack. The geometrical parameters h , b and r are given in Table 5.1. For a torus, V_{por} is calculated as $V_{por} = 2\pi^2(b+r)r^2$. Under the assumption of $V_{por} \rightarrow \infty$, the expression 4.30 reduces to expression 4.28 (it can be seen from expression 4.30 by removing terms with $1/V_{por}$). The low-frequency limit of K_f^* calculated using equation 4.30 is

$$\lim_{\omega \rightarrow 0} K_f^* = \frac{V_{cr} K_f}{V_{cr} + V_{por}}. \quad (4.31)$$

Note, that the shape of the curves in expressions 4.26, 4.28 and 4.30 is the same (Figure 4.9a), which means that for the Big pore model solutions 4.26, 4.28 and 4.30 are equivalent. In other words, the volume of the Big pore is so large compare to the volume of the crack, that zero fluid pressure boundary condition provides us a good approximation. The low-frequency limit $K_f^* \neq 0$ (but close to 0) in equation 4.30 compared to expressions for zero fluid pressure boundary condition at the edge of the crack (expressions 4.26, 4.28 where $K_f^* = 0$). The

high-frequency limit of the K_f^* is

$$\lim_{\omega \rightarrow \infty} K_f^* = \left(1 + 2 \left(\frac{\cos(ka + \pi/4)}{\sin(ka + \pi/4)} \right) \frac{1}{ka} \right) K_f. \quad (4.32)$$

This high-frequency limit (Eq. 4.32) also applies to expression 4.28 for $K_f^*(\omega)$.

Modification of the relaxation of the fluid bulk modulus for the classical geometry

Alkhimenkov et al. (2020a) showed that the $[C_{33}^*(\omega)]_{\text{sat}}$ component obtained via the analytical model by using $K_f^*(\omega)$ (Eq. 4.28) is in agreement with the numerical simulation for zero fluid pressure at the crack tip and no stiff pore (Figure 4.8). It means that if the background material is homogeneous, the relaxation of the fluid bulk modulus is not affected (or the effect is negligible) by the surrounding homogeneous grains. In other words, applying boundary conditions to the walls of the crack or to the walls of the model produces similar results in this special case of no stiff pore (Figure 4.8ab). But this configuration is not realistic. For a more realistic scenario, when a stiff pore is present (Figure 4.8c), the $[C_{33}^*(\omega)]_{\text{sat}}$ component obtained via the analytical model by using $K_f^*(\omega)$ obtained analytically for the configuration shown in Figure 4.8a diverges from the numerical result (*Alkhimenkov et al.*, 2020a). This disagreement is due to the presence of the isometric pore connected to the crack, which changes the stress field in the model. Because of the modified stress field, the fluid flow is also affected and the boundary conditions applied to the wall of the crack are no longer accurate (Figure 4.8cd). According to numerical solutions for the models where a torus is connected to a crack, the high-frequency slopes of the dispersion and attenuation curves are substantially different from those obtained via solution for the crack only having a zero fluid pressure boundary condition at the tip (Eq. 4.28) (Figure 4.8e). A similar observation has been pointed out by *Solazzi et al.* (2021) for partially saturated cracks.

By analyzing the numerical results, we find that the $1/Q$ at high-frequencies is proportional to $\approx \omega^{-1/2}$ for the classical geometry (the crack connected to the toroidal pore). However, the solutions for $K_f^*(\omega)$ (expressions 4.26, 4.28 and 4.30) and the resulting $1/Q$ exhibit different behavior at high-frequencies compare to the numerical solutions. Therefore, we derive an approximation to the relaxation of the fluid bulk modulus $K_f^*(\omega)$ for the classical geometry by simply using the solution 4.30 with a modified high-frequency asymptote. For that, we use a special form of a branching function. The concept of a branching function is simple and allows us to find an accurate approximation for a given cumbersome exact solution (*Pride et al.*, 1993; *Johnson*, 2001). A branching function is designed such that it satisfies the Kramers–Kronig relations, thus can be used to approximate seismic attenuation and dispersion curves. To construct the branching function, one needs to know the low- and high-frequency limits along with the low- and high-frequency asymptotes of the exact solution. We use the following branching function,

$$K_f^*(\omega) = K_f - (K_f - y \cdot K_f^{LF}) / (1 - \zeta + \zeta \sqrt{1 + i\omega\tau/\zeta^2}), \quad (4.33)$$

where $y = 0$ for the solution considering zero fluid pressure at the crack tip or $y = 1$ for the solution considering non-zero fluid pressure boundary condition at the crack tip. In equation 4.33, K_f corresponds to the high frequency limit of the exact solution (which is exactly the fluid bulk modulus), K_f^{LF} (if $y = 1$) or 0 (if $y = 0$) correspond to the low frequency limit of the exact solution 4.30 or 4.26, respectively. The two parameters ζ and τ control the shape of the branching function. The recipe to construct the branching function is the following:

i) We extract several parameters of the solution 4.30 for $K_f^*(\omega)$: the low- and high-frequency limits of $K_f^*(\omega)$, the low-frequency asymptote of $1/Q_{K_f^*} = \text{Im}(K_f^*(\omega)) / \text{Re}(K_f^*(\omega))$ and the characteristic frequency f_c^{crack} of $1/Q_{K_f^*}$ (at the maximum of $1/Q_{K_f^*}$). This gives us four parameters.

ii) We construct the branching function 4.33 with $y = 1$ to approximate the solution 4.30 using the known parameters obtained in i) but with the modified high-frequency asymptote being proportional to $\approx \omega^{-1/2}$. There are only four parameters in the branching function 4.33. The last relation to close the system of equations is that the intersection of low- and high-frequency asymptotes of the branching function coincides with the characteristic frequency f_c^{crack} obtained in i). The resulting modified solution is shown in Figure 4.9 (black squares).

iii) The final modified solution for $K_f^*(\omega)$ is obtained from the step ii) by setting $y = 0$ in the expression 4.33. This step is needed to obtain the solution for the zero fluid pressure boundary condition at the crack tip since our analytical model is based on the modified frame (Figure 5.4).

The calculations in steps i), ii) and iii) are simple, require only algebraic manipulations but they are cumbersome, thus we refer to the supplementary material for the full derivation (Maple script). The resulting expressions for the branching function are given below.

By setting $y = 0$ in expression 4.33 (corresponding to zero fluid pressure at the crack tip), the frequency-dependent bulk modulus of the fluid $K_f^*(\omega)$ becomes

$$K_f^*(\omega) = K_f - K_f / (1 - \zeta + \zeta \sqrt{1 + i\omega\tau/\zeta^2}), \quad (4.34)$$

where the parameter τ is calculated as

$$\tau = \frac{3}{4} \frac{\eta}{K_f} \frac{\zeta}{\alpha^2}, \quad (4.35)$$

and the parameter ζ is calculated as

$$\zeta = \frac{128}{27} \frac{K_f}{\eta^3} \frac{(K_f^{LF})^2}{(f_c^{crack})^3} \alpha^6, \quad (4.36)$$

with f_c^{crack} given by

$$f_c^{crack} = \frac{4}{\sqrt{3}} \frac{\sqrt{K_f \cdot K_f^{LF}}}{\eta} \alpha^2. \quad (4.37)$$

The parameter f_c^{crack} determines the characteristic frequency of $K_f^*(\omega)$. The apparent fluid bulk modulus at low frequencies K_f^{LF} is

$$K_f^{LF} = \frac{V_{cr} K_f}{V_{cr} + V_{por}}, \quad (4.38)$$

The low-frequency asymptote of the K_f^* calculated using equation 4.33 is

$$\lim_{\omega \rightarrow 0} K_f^* = \frac{(K_f - K_f^{LF})\tau}{K_f^{LF}\zeta} \omega. \quad (4.39)$$

The high-frequency asymptote of the K_f^* calculated using equation 4.33 is

$$\lim_{\omega \rightarrow \infty} K_f^* = \frac{(K_f - K_f^{LF})\sqrt{2}}{2K_f\sqrt{\tau}} \frac{1}{\omega^2}. \quad (4.40)$$

It is possible that for some specific parameters that expressions 4.34-4.38 lose their accuracy. In this case, one can modify the expressions 4.34-4.38 using the Maple symbolic environment to improve the accuracy. We do not explore in detail the accuracy of the boundary conditions for the crack tip proposed by *Murphy et al.* (1986) (the solution 4.30), different boundary conditions may slightly modify the expression 4.30 and the derived modification of this solution 4.34-4.38.

Note that the branching function of the form 4.33 was used to approximate cumbersome exact solutions in different contexts by many authors (*Pride et al.*, 1993; *Johnson*, 2001). Note that 4.33 is designed to approximate solutions in the stiffness. A similar branching functions exists to approximate solutions in the compliance, which is more suitable for some applications (*Gurevich et al.*, 2009b).

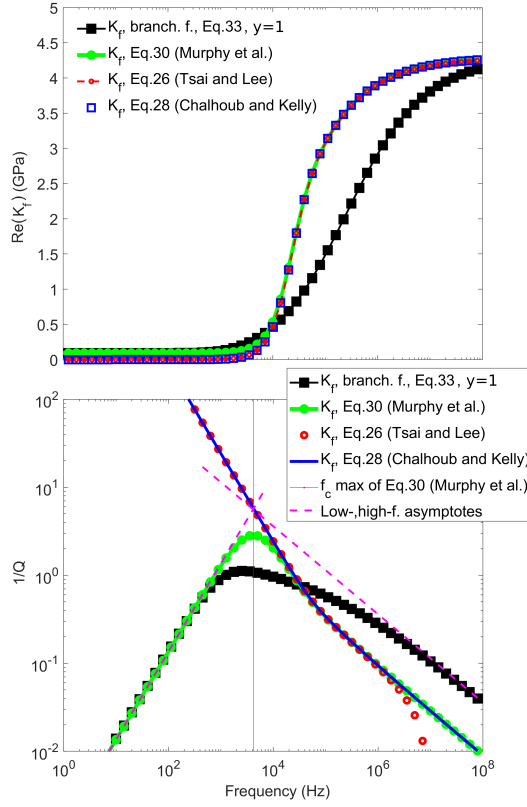


Figure 4.9: The real part of the frequency-dependent fluid bulk modulus K_f^* and the dimensionless attenuation calculated using different expressions for the Big pore model with $\alpha = 0.005$.

Big pore model

Figure 4.9 shows the real part of the frequency-dependent fluid bulk modulus K_f^* and the dimensionless attenuation calculated using different expressions for the Big pore model with $\alpha = 0.005$. Since the volume of the big pore is large, the expressions for K_f^* 4.26 and 4.28 reduce to expression 4.30. Note, that $1/Q$ of K_f^* of Eq. 4.26 and 4.28 is the same as for 4.30 for frequencies larger than the characteristic frequency but tend to infinity for frequencies lower than the characteristic frequency because $K_f^* \rightarrow 0$ as $\omega \rightarrow 0$. K_f^* calculated via the branching function 4.33 ($y = 1$) is identical to 4.30 except for the high frequency asymptote. Note, that asymptotes of the branching function intersect at the characteristic frequency of K_f^* calculated via equation 4.30.

Figure 4.10 is similar to Figure 4.9 but K_f^* calculated via the equation 4.34 is shown together with the numerical solution. The numerical solution was obtained from the simulations for the modified frame of the Big pore model ($\alpha = 0.005$), and then inverting for K_f^* via the analytical formulas 4.18 and 4.19. K_f^* calculated via equation 4.34 is in agreement with the numerical solution (note, that there are no fitting parameters in equation 4.34).

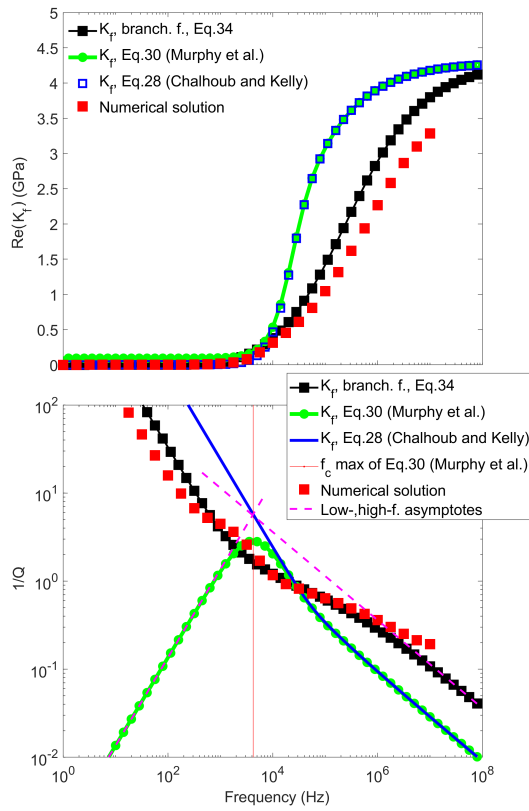


Figure 4.10: The real part of the frequency-dependent fluid bulk modulus K_f^* and the dimensionless attenuation calculated using different expressions for the Big pore model with $\alpha = 0.005$.

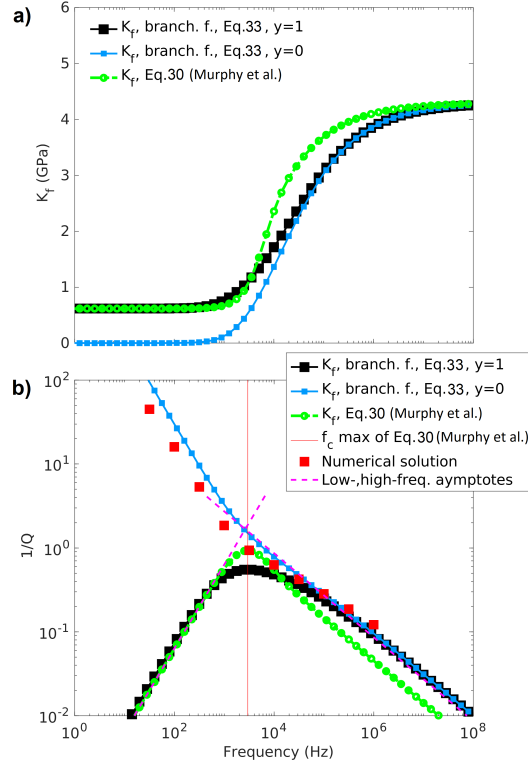


Figure 4.11: The real part of the frequency-dependent fluid bulk modulus K_f^* and the dimensionless attenuation calculated using different expressions for the Small pore model with $\alpha = 0.0025$.

Small pore model

Figure 4.11 shows the real part of the frequency-dependent fluid bulk modulus K_f^* and the dimensionless attenuation calculated using different formulas for the Small pore model with $\alpha = 0.0025$. The branching function with $y = 0$ (equation 4.33 or, equivalent, equation 4.34) corresponds to the configuration with zero fluid pressure at crack tip (which is used in the present analytical model for the modified frame). At low frequencies, K_f^* calculated via the branching function 4.33 ($y = 0$) and the solution 4.30 are not equal to zero because the volume of the Small pore is only slightly larger than the volume of the crack. $1/Q$ calculated via the the branching function with $y = 0$ (equation 4.33 or equation 4.34) is in agreement with the numerical solution.

4.2.6 Summary

Our analytical model requires (i) the calculation of the effective compliance matrix of the modified frame (expression 4.18), (ii) the calculation of the frequency dependent component $\left[H'_{33}\right]^{MF}$ (expression 4.19), which represents the frequency-dependent crack stiffness, (iii) the calculation of the effective stiffness moduli of a fully saturated model by applying Gassmann's equations (Gassmann, 1951). If the low- and high-frequency limits of the dry model are known, then the step (i) can be skipped; the frequency dependent component $\left[H'_{33}\right]^{MF}$ (expression 4.19) provides the transition from low- to high-frequencies (step (ii)).

(i) The modified frame

Our analytical model requires the calculation of effective compliance matrix of the modified frame (expression 4.18),

$$[S_{mn}^*(\omega)]^{\text{MF}} = S_{mn}^g + [H_{mn}^{\text{tp}}]_{\text{dry}} + [H'_{mn}(\omega)]^{\text{MF}}, \quad (4.41)$$

where S_{mn}^g is the compliance matrix of the solid grain material, $[H_{mn}^{\text{tp}}]_{\text{dry}}$ is the compliance contribution matrix of the isometric pore (torus) and $[H'_{mn}(\omega)]^{\text{MF}}$ is the additional compliance contribution matrix of the crack connected to the torus. The compliance contribution matrices of a torus $[H_{mn}^{\text{tp}}]_{\text{dry}}$ and extended crack (ellipsoid) $[H_{mn}^{\text{Ecr}}]_{\text{dry}}$ can be calculated analytically using expressions from e.g., *Kachanov and Sevostianov (2018)*. Then, following the workflow presented in Figure 4.7, the $[H'_{mn}(\omega)]^{\text{MF}}$ can be calculated as $[H'_{mn}(\omega)]^{\text{MF}} = [H_{mn}(\omega)]^{\text{MF}} - [H_{mn}^{\text{tp}}]_{\text{dry}}$ (see formula 4.15 for details), where $[H_{mn}(\omega)]^{\text{MF}}$ is constructed by expression 4.12 using the already obtained $[H_{mn}^{\text{tp}}]_{\text{dry}}$ and $[H_{mn}^{\text{Ecr}}]_{\text{dry}}$.

(ii) The frequency-dependent crack stiffness

The $[H'_{33}]^{\text{MF}}$ component is calculated by

$$[H'_{33}(\omega)]^{\text{MF}} = \frac{(K_g - K_f^*(\omega)) \phi_c Z_n}{(K_g - K_f^*(\omega)) \phi_c + K_f^*(\omega) K_g Z_n}, \quad (4.42)$$

where ϕ_c is the compliant porosity (crack porosity), Z_n is the apparent normal compliance of the crack (see expression 4.17) and K_g is the bulk modulus of the solid grains. The expression for the frequency-dependent bulk modulus of the fluid $K_f^*(\omega)$ can be calculated by using equation 4.34. For cracks of finite thickness, equation 4.22 should be used instead of equation 4.42.

(iii) The moduli of a fully saturated model

Finally, the effective stiffness moduli of a fully saturated model $[C_{mn}^*(\omega)]_{\text{sat}}$ can be obtained by using anisotropic Gassmann's equations (*Gassmann, 1951*) at each frequency to $[S_{mn}^*(\omega)]^{\text{MF}}$:

$$[C_{mn}^*(\omega)]_{\text{sat}} = \left([S_{mn}^*(\omega)]^{\text{MF}} \right)^{-1} + \alpha_m \alpha_n M, \quad (4.43)$$

$$\alpha_m = 1 - \left(\sum_{n=1}^3 C_{mn}^{\text{MF}} \right) / K_g / 3, \quad (4.44)$$

for $m = 1, 2, 3$ and $\alpha_4 = \alpha_5 = \alpha_6 = 0$, and where

$$M = \left(\phi / K_f + (1 - \phi) / K_g - K^* / K_g^2 \right)^{-1}, \quad (4.45)$$

$$K^* = \frac{1}{9} \sum_{m=1}^3 \sum_{n=1}^3 C_{mn}^{\text{MF}}(\omega), \quad (4.46)$$

where ϕ is the total porosity of the medium without the compliant porosity (which is neglected because the

compliant porosity is usually two or more orders of magnitude lower than the stiff pore's porosity), K^* is the generalized bulk modulus of the modified frame and α_m is the Biot-Willis coefficient.

4.3 Validation against three-dimensional numerical solutions

For the validation, we consider several 3-D models consisting of a pore space embedded in an elastic solid grain material. The numerical methodology is described in Appendix A and was introduced by *Quintal et al.* (2016, 2019); the boundary conditions for the direct relaxation tests to compute all components of the stiffness matrix are described in *Alkhimenkov et al.* (2020a,b). The models considered are the following:

- i) The saturated Big pore model with crack aspect ratio $\alpha = 0.0025$. This is the model that was shown in Figure 4.4.
- ii) The saturated Big pore model with finite thickness crack (aspect ratio $\alpha = 0.005$).
- iii) The modified frame of the Big pore model with finite thickness crack (aspect ratio $\alpha = 0.005$).
- iv) The modified frame of the Small pore model with crack aspect ratio $\alpha = 0.0025$. Here the isometric pore represented by the torus is small.

The geometrical properties of the models with crack aspect ratio $\alpha = 0.0025$ are shown in Table 5.1 and the material parameters are shown in Table 5.2. The model geometry is scalable; i.e., if all geometric parameters of the models are divided or multiplied by any number, the results will be the same.

Table 4.1: Geometrical properties for the Big pore model and the Small pore model. Major radius — the distance from the center of the tube to the center of the torus. Minor radius — the radius of the tube (our isometric pore).

Geometrical parameter	Big pore model	Small pore model
Flat cylinder (crack) radius, b	0.1 m	0.1 m
Flat cylinder (crack) thickness, h	0.0005 m	0.0005 m
Crack aspect ratio, $\alpha = h/(2b)$	0.0025	0.0025
Major radius of torus, $b + r$	0.124 m	0.1067 m
Minor radius of torus, r	0.024 m	0.0067 m
Total porosity	0.045	0.0034
Crack porosity	$\approx 4.9 \cdot 10^{-4}$	$\approx 4.9 \cdot 10^{-4}$

Table 4.2: Material properties used in all models.

Material parameter	Solid	Fluid
Bulk modulus K	36 GPa	4.3 GPa
Shear modulus μ	44 GPa	0 GPa
Shear viscosity η	0 Pa·s	1.414 Pa·s

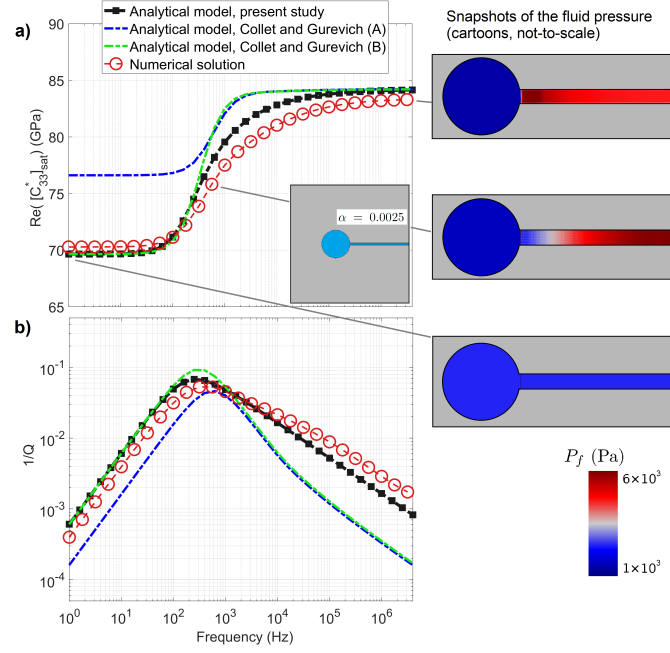


Figure 4.12: Numerical and analytical results for the Big pore model (Figure 4.4) with a crack aspect ratio $\alpha = 0.0025$: (a) Real part of the $[C_{33}^*]_{\text{sat}}$ component and (b) dimensionless attenuation for the $[C_{33}^*]_{\text{sat}}$ component. On the right, snapshots of the fluid pressure P_f at three different frequencies : LF - low frequency limit (relaxed state), Fc - intermediate frequency (close to the characteristic frequency) and HF - high frequency limit (unrelaxed state). The spatial dimension of the snapshots are not-to-scale and their colors representing the fluid pressure P_f correspond to a downward displacement (compression) of 10^{-8} m applied to the top boundary of the model. The inset represents the cross section of half of the model.

4.3.1 Big pore model

Figure 4.12 shows results for the $[C_{33}^*]_{\text{sat}}$ complex-valued component of the stiffness matrix obtained using the present analytical model, the model of *Collet and Gurevich* (2016) with two different sets of normal and tangential compliances (see Appendix 4.7 and *Alkhimenkov et al.* (2020a) for more details) and the numerical solution for the model shown in Figure 4.4. The model A of *Collet and Gurevich* (2016) doesn't take into account the connectivity of the crack and pore gives stiffer moduli of the rock at low frequencies compared to the correct moduli. The model B of *Collet and Gurevich* (2016) takes into account the connectivity of the crack and pore using the modification introduced by *Alkhimenkov et al.* (2020a) and gives correct moduli of the rock at low frequencies. The aspect ratio is $\alpha = 0.0025$ which corresponds to the limit where the crack aperture is small enough so that at high-frequencies the fluid stiffens the crack to the point that $Z_n = 0$. Our analytical model is in good agreement with the numerical solution. For the big pore model, f_c^{crack} (equation 4.37) is almost identical to the characteristic frequency f_c of the fully saturated model.

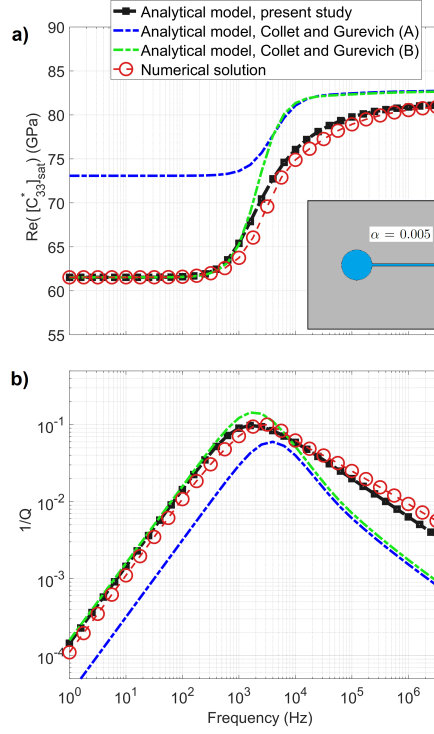


Figure 4.13: Numerical and analytical results for the Big pore model with the crack aspect ratio $\alpha = 0.005$ (i.e., finite thickness crack): (a) Real part of the $[C_{33}^*]_{\text{sat}}$ component and (b) dimensionless attenuation for the $[C_{33}^*]_{\text{sat}}$ component. Here the crack aperture is two times larger than in the model with aspect ratio of $\alpha = 0.0025$ (Figure 4.12). The inset represents the cross section of half of the model.

4.3.2 Big pore model with the finite thickness crack

Figure 4.13 shows results for the $[C_{33}^*]_{\text{sat}}$ complex-valued component of the stiffness matrix obtained from the our analytical model, the models A and B of *Collet and Gurevich* (2016) and from the numerical simulation. The aspect ratio here is $\alpha = 0.005$. The high frequency limit of the $[C_{33}^*]_{\text{sat}}$ slightly lower due to the increased crack aperture and, thus, compliance. Our present analytical model takes into account the non-zero value of Z_n corresponding to larger aspect ratios showing a good agreement with numerical solutions.

4.3.3 Modified frame of the Big pore model with finite thickness crack

We also validate the extension of the analytical model to finite thickness crack against a modified frame configuration. Figure 4.14 shows results for the $[C_{33}^*]_{\text{MF}}$ complex-valued component of the stiffness matrix obtained from the present analytical model, the models A and B of *Collet and Gurevich* (2016) and from the numerical simulation. In this case, dispersion and attenuation is much stronger than in Figure 4.13 because the fluid in the crack can freely flow into the empty pore without experiencing any difficulties due to the finite volume of the torus that would otherwise result in an increase in fluid pressure at low frequencies. Our analytical model is in good agreement with numerical solutions confirming that it can adequately describe the frequency-dependence of the modified frame.

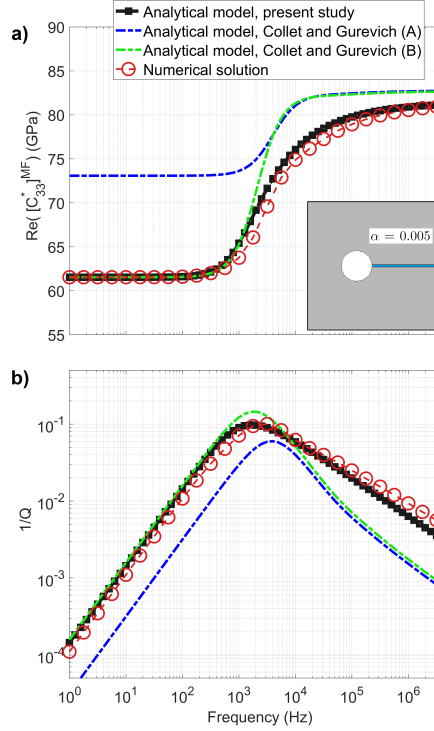


Figure 4.14: Numerical and analytical results for the modified frame of the Big pore model with the crack aspect ratio $\alpha = 0.005$ (i.e., finite thickness crack): (a) Real part of the $[C_{33}^*]^{MF}$ component and (b) dimensionless attenuation for the $[C_{33}^*]^{MF}$ component. The inset represents the cross section of half of the model.

4.3.4 Modified frame of the Small pore model

We also apply our analytical model to a different pore space configuration — Small pore model (Table 5.1). In this configuration, the volume of the torus is small, thus dispersion and attenuation are also small. But the modified frame of the Small pore model shows significant dispersion and attenuation (Figure 4.15). We consider an aspect ratio $\alpha = 0.0025$. The result from our analytical model is in a good agreement with the numerical solutions.

4.4 Discussion

4.4.1 The key features making our model accurate

There are two key features which make the present analytical model very accurate. The first one is the correct calculation of the model compliances. We provide the workflow to obtain the effective compliance matrix which takes into account the connectivity of the stiff pore and the compliant crack; it provides the correct values of the low and high frequency limits of the stiffness moduli. The second feature is the accurate description of the relaxation of the compliant crack due to fluid pressure diffusion; it gives the correct shape of the dispersion and attenuation curves across the whole frequency range.

The usual treatment of the pore and crack as being disconnected when calculating the model compliance provides inaccurate predictions of the overall attenuation and dispersion. The error of the low frequency limit of the dispersion curve can be as large as 100% of the crack compliance, as it can be seen in Figure 4.12 (blue curve, analytical model A of *Collet and Gurevich* (2016)). However, once the workflow for calculating the model compliance takes into account the connectivity of the pore and crack, the low and high frequency limits of the dispersion curve become accurate (green curve, modification of analytical model of *Collet and Gurevich* (2016)).

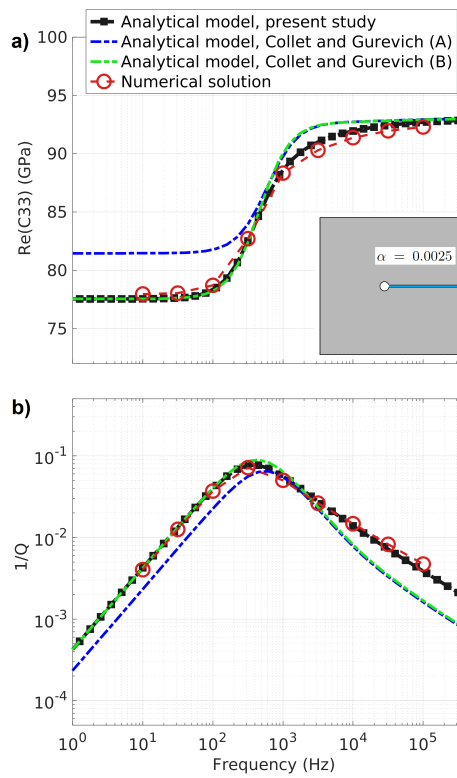


Figure 4.15: Numerical and analytical results for the modified frame of the Small pore model with the crack aspect ratio $\alpha = 0.0025$: (a) Real part of the $[C_{33}^*]^{MF}$ component and (b) dimensionless attenuation for the $[C_{33}^*]^{MF}$ component. The inset represents the cross section of half of the model.

The modification of the analytical model of *Collet and Gurevich* (2016) (model B) was provided by *Alkhimenkov et al.* (2020a) (Appendix 4.7). Our analytical model is based on the property contribution tensors which provides a general approach for calculating the moduli and can be extended for more complex geometries of the pore space (equation 4.41). The presented workflow (Figure 4.7) to construct the property contribution tensor of the interconnected pore and crack provides the correct values of the low and high frequency limits of the dispersion curve (Figures 4.12-4.15).

Small deformations caused by the wave propagation compress the compliant crack and cause fluid pressure diffusion or squirt flow. The fluid pressure distribution in the crack is significantly affected by the inhomogeneous stress field introduced by the isometric pore (especially at frequencies higher than the characteristic frequency). The stiffening effect of the fluid in the crack is substantially different for homogeneous and heterogeneous stress field distributions surrounding the crack (see Figure 4.8). Thus, we had to modify the expression for the relaxation of the crack stiffness for this specific geometry of the pore space represented by the interconnected torus and crack. This modification depends on the shape of the pore space and is explored in more details in Part 2 of this study. The popular idea of considering certain viscoelastic moduli describing the stiffening effect of fluid is, in general, imprecise. The stiffness of the fluid can be replaced by viscoelastic moduli only for particular pore space geometries, as we show in the present and follow up studies.

4.4.2 The effect of the finite volume of the stiff pore

The volume of the isometric (stiff) pore V_{por} has a key influence on the magnitude of the dispersion and attenuation. If this volume is significantly larger than the volume of a compliant crack V_{cr} (i.e. by two orders of magnitude or more), then the fluid in the crack does not “feel” that the volume of the isometric pore is finite. In other words, in the low-frequency limit the normal crack compliance of the saturated model is the same as if it was dry. This can be seen in Figure 4.10, where in the low frequency limit K_f^* approaches zero.

On the other hand, if the volume of an isometric pore is similar to the volume of a compliant crack (or just an order of magnitude larger), then the fluid in the crack does “feel” that the volume of the isometric pore is finite and the resulting dispersion and attenuation are reduced. At low-frequencies fluid flow from the crack into the isometric pore significantly increases fluid pressure in the stiff pore. As a result, in the low-frequency limit the normal crack compliance has a finite non-zero value. This can be seen in Figure 4.11 (Small pore model) where in the low frequency limit K_f^* approaches ≈ 0.6 GPa. The resulting attenuation and dispersion are very small (*Alkhimenkov et al.*, 2020a).

The expression 4.31 gives an estimate of $K_f^*(\omega)$ for the case where the fluid flow in the crack “feels” the finite volume of the isometric pore, the low frequency limit of $K_f^*(\omega)$ is

$$K_f^{LF} = \frac{V_{cr} K_f}{V_{cr} + V_{por}}. \quad (4.47)$$

The resulting value of K_f^{LF} can be used in expression 4.19 to calculate the normal fracture compliance

$$Z_n^{LF} = \frac{(K_g - K_f^{LF}) \phi_c Z_n}{(K_g - K_f^{LF}) \phi_c + K_f^{LF} K_g Z_n}, \quad (4.48)$$

The value Z_n^{LF} gives the quantitative answer to the question: “how strong will be the stiffening effect of the crack at low frequencies?”

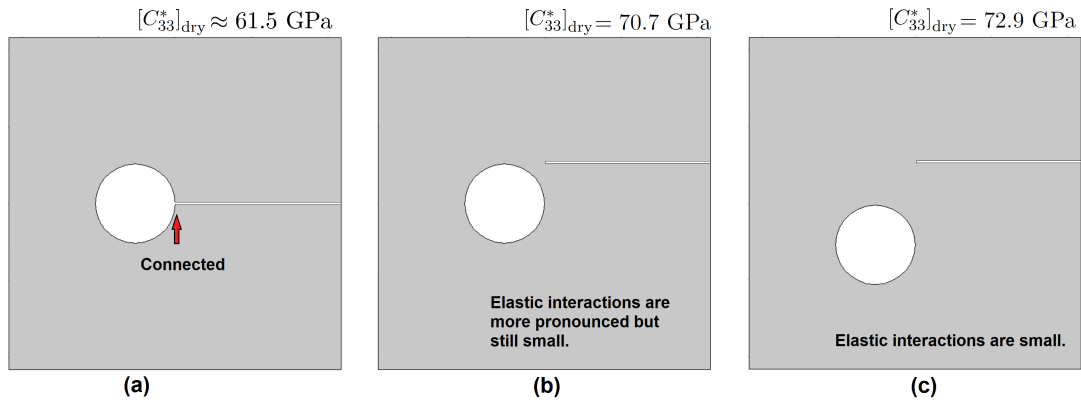


Figure 4.16: A slice of the three-dimensional models illustrating the effect of elastic interactions on the $[C_{33}^*]_{\text{dry}}$ component. (a) The isometric pore is connected to the crack representing a unified interconnected pore space, (b) the isometric pore and crack are disconnected but close and (c) disconnected and far from each other.

4.4.3 The importance of pore connectivity and elastic interactions

Elastic interaction is a very popular topic in mechanics as well as in rock physics. When the concentration of cracks or pores is small, the elastic interactions are also small and can be ignored. In this case, for calculating the effective elastic moduli one can use methods which do not take into account elastic interactions (so-called non-interactive approximation of effective medium theory); these methods usually provide exact results for simple pore geometries. When the concentration of cracks or pores is increased, the elastic interactions take place and affect the effective elastic properties. Exact results are possible only for a limited number of configurations, usually for two-body problems. For many-body problems many approximations exist. The effect of pore connectivity, however, is a distinct subject with a distinct contribution.

Figure 4.16 shows a slice equivalent to that in Figure 4.4 with the three pore configurations: the torus and the crack are connected, the torus and the crack are disconnected but close to each other, and the torus and the crack are disconnected and a bit further from each other. On top of each subplot, the effective stiffness component $[C_{33}^*]_{\text{dry}}$ calculated numerically (with properties given in Tables 5.1 and 5.2) is shown. Roughly, the pore is reducing the $[C_{33}^*]_{\text{dry}}$ component of the solid grain material by 10.6 GPa (from 94.6 GPa to 84 GPa) (Figure 4.6). Then, embedding the crack connected to the pore is further reducing the $[C_{33}^*]_{\text{dry}}$ component by 22.5 GPa (from 84 GPa to 61.5 GPa). Conversely, if the crack is not connected to the pore, the reduction of the $[C_{33}^*]_{\text{dry}}$ component is only 11 GPa (from 84 GPa to 73 GPa), thus the “connectivity” costs 11.5 GPa. The “connectivity” cost to the stiffness of the model (11.5 GPa) is five times bigger than the effect of elastic interactions (2 GPa) shown in Figure 4.16. This example shows that the first order effect to the effective elastic properties is due to the connectivity of the pores and cracks. The effect of elastic interactions on the effective elastic properties is of secondary importance and can be considered only when interconnectivity is taken into account. Roughly, interconnectivity significantly increases the “apparent” crack density in such a way that the surface of the crack together with its invisible continuation into the isometric pore control the effective elastic properties. Such “apparent” crack density can be two or even more times bigger than the crack density of the cracks only. Unfortunately, elastic interactions are very popular in research articles but interconnectivity is usually ignored.

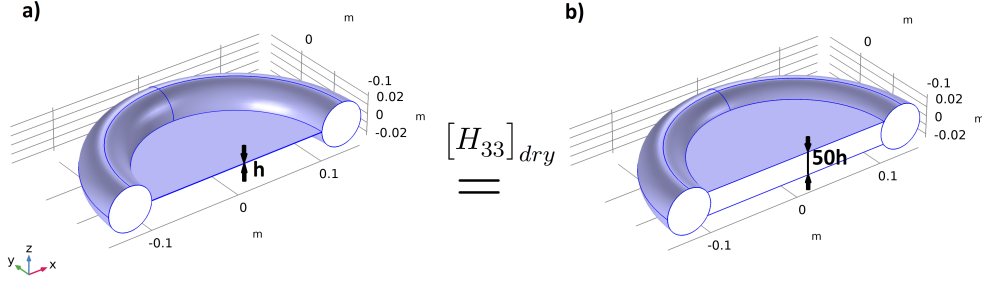


Figure 4.17: Sketch illustrating the pore space (dry) of the Big pore model with two different crack apertures — h (left) and $50h$ (right).

4.4.4 The correctness of expression 4.19 for the normal crack compliance

The expression 4.19 is equivalent to the expression derived before (e.g., Gurevich (2003)):

$$Z_n^{\text{sat}} = \frac{Z_n}{1 + \frac{Z_n}{\phi_c(1/K_f - 1/K_g)}}, \quad (4.49)$$

where Z_n^{sat} is the normal crack compliance of the saturated crack, K_f can be replaced by $K_f^*(\omega)$ (e.g., Collet and Gurevich (2016)). The expression 4.19 (or 4.49) is exact for the following configuration: a thin crack embedded into a solid grain material; the crack compliance is described by the only two parameters Z_n and Z_t . Then, we apply anisotropic Gassmann's equation to calculate the moduli considering the crack saturated. The result of Gassmann's equations is the only modification of Z_n , which becomes Z_n^{sat} .

In the present framework, we use Gassmann's equations in two ways. First, we use them to saturate the crack while the stiff pore remains dry. This violates the assumptions for the applicability of Gassmann's equations (because the model is three-phase: grains, dry stiff pore and crack saturated with a fluid). Second, we apply Gassmann's equations to the modified frame to calculate the moduli of the fully saturated model. Since the modified frame is heterogeneous, this also violates the assumptions for the applicability of Gassmann's equations. However, numerical solutions show that the present analytical model is very accurate for the modified frame as well as for the fully saturated pore space. One explanation for such accuracy is that the pore space is correctly partitioned into the stiff pore and compliant crack. The stiff pore acts as a "storage" volume for the fluid and doesn't contribute directly to the overall attenuation; the fluid pressure is approximately uniform at each frequency. The fluid flow in the compliant crack is responsible for the overall attenuation of the model.

In the low-frequency limit, the expression 4.19 gives the normal crack compliance Z_n of the dry crack. In this case, we apply anisotropic Gassmann's equations to saturate the model where the pore and the crack are present; this procedure is correct without regard to the pore space structure. If in the anisotropic Gassmann's equations we use the whole porosity (stiff pore and crack porosities), then the result is exact in the low-frequency limit.

4.4.5 The choice of the model

Figure 4.17 shows the Big torus model with the crack aperture h on the left and the crack aperture $50h$ on the right. Surprisingly, the $[C_{33}^*]_{\text{dry}}$ component of the effective elastic moduli of the dry model is the same for both models. This means that the torus surrounding cracks controls the stiffness because it is connected to the whole circumference of the crack. The components of the stiffness matrix $[H_{33}]_{\text{dry}}$, $[H_{44}]_{\text{dry}}$ and $[H_{55}]_{\text{dry}}$ are controlled by the torus only. This geometry cannot represent the rock pore space adequately since cracks do control the stiffness in real rocks. That's why in Part 2 we explore more complex pore space geometries where isometric stiff pores are rather spherical and the crack circumference is only partially connected to stiff pores.

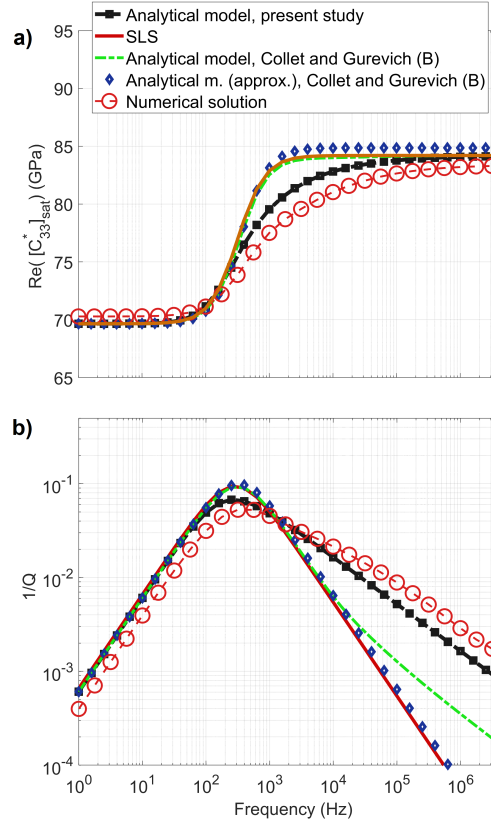


Figure 4.18: Numerical and analytical results for the big pore model with the crack aspect ratio $\alpha = 0.025$: (a) Real part of the $[C_{33}^*]_{\text{sat}}$ component and (b) dimensionless attenuation for the $[C_{33}^*]_{\text{sat}}$ component.

4.4.6 A standard linear solid as an analytical model

The standard linear solid (SLS) rheology for the $[C_{33}^*(\omega)]_{\text{sat}}$ component can be written as

$$[C_{33}^*(\omega)]_{\text{sat}} = \frac{[C_{33}^*]_{\text{sat}}^{LF} + i [C_{33}^*]_{\text{sat}}^{HF} (\omega/\omega_c)}{1 + i (\omega/\omega_c)}, \quad (4.50)$$

where $[C_{33}^*]_{\text{sat}}^{LF}$ and $[C_{33}^*]_{\text{sat}}^{HF}$ are the effective moduli of the saturated model at low- and high-frequency limits, respectively and ω_c is the characteristic frequency (*Mavko et al., 2020*). Thus, only three input parameters are needed to calculate dispersion and attenuation. Figure 4.18 shows results for the $[C_{33}^*(\omega)]_{\text{sat}}$ complex-valued component of the stiffness matrix obtained with the present analytical model, with the SLS model, with the modified model of *Collet and Gurevich* (2016) (model B, with correct limits), with the approximation of the modified model of *Collet and Gurevich* (2016) (model B) and with the numerical solution. Note, that model of *Collet and Gurevich* (2016) is the same as the model of *Gurevich et al.* (2010) but for anisotropic media (all cracks with the same orientation). *Gurevich et al.* (2010) proposed an approximation for the relaxation of the fluid bulk modulus $K_f^*(\omega)$ (Eq. 4.28),

$$K_f^*(\omega) = -(\bar{k}_2)^2 K_f / 8 \quad (4.51)$$

If this approximation 4.51 is used for $K_f^*(\omega)$ in the modified model of *Collet and Gurevich* (2016) (model B), then it becomes identical to the SLS result across all frequencies (Figure 4.18). In other words, SLS is almost identical to the model of *Collet and Gurevich* (2016), thus a single expression 4.50 can be used to obtain the same dispersion and attenuation curves. A similar observation is given in *Carcione and Gurevich* (2011) for an isotropic squirt flow model of *Gurevich et al.* (2010).

4.5 Conclusions

We have developed an analytical model for seismic attenuation and dispersion in a fluid-saturated porous medium caused by squirt flow. We used the classical pore space geometry used in many previous studies, a penny-shaped crack surrounded by a toroidal stiff pore. Our model can be applied to very thin cracks as well as to cracks with finite thicknesses. We compared our analytical model with three-dimensional numerical solutions. The analytical and numerical results are in a very good agreement for all considered relative sizes of pores and cracks. Our analytical model features several key differences compared with previously published analytical models making it much more accurate. First, we provide an approach to calculate the elastic moduli of interconnected pore and crack. We showed that ignoring the inter-connectivity of cracks and pores in the calculation of the model compliance leads to inaccurate predictions of low- and high- frequency limits of the moduli dispersion. Second, we derived a good approximation for the relaxation of the crack stiffness due to fluid pressure diffusion, which makes our model accurate for the whole frequency band. Furthermore, we showed that the crack stiffness is significantly affected by the surrounding heterogeneities. Thus, precise expressions for the crack stiffness are possible only for specific pore geometries.

Acknowledgments

This research is funded by the Swiss National Science Foundation, project number 172691.

4.6 Appendix A: Numerical methodology

The numerical methodology we use for validation of the analytical models is described by *Quintal et al.* (2019) and *Alkhimenkov et al.* (2020a,b), here we briefly outline the main equations. We consider that a model is composed by a solid material (grains) and a pore space saturated with a fluid. The solid phase is described as a linear isotropic elastic material for which the conservation of momentum is (e.g., *Landau and Lifshitz* (1959b) and *Nemat-Nasser and Hori* (2013)).

$$\nabla \cdot \boldsymbol{\sigma} = 0, \quad (4.52)$$

where “ $\nabla \cdot$ ” stands for the divergence operator acting on the stress tensor $\boldsymbol{\sigma}$. The infinitesimal stress-strain relation for an isotropic elastic material can be written as

$$\boldsymbol{\sigma} = (K - \frac{2}{3}\mu) \mathbf{tr} \left(\frac{1}{2} ((\nabla \otimes \mathbf{u}) + (\nabla \otimes \mathbf{u})^T) \right) \mathbf{I}_2 + 2\mu \left(\frac{1}{2} ((\nabla \otimes \mathbf{u}) + (\nabla \otimes \mathbf{u})^T) \right), \quad (4.53)$$

where \mathbf{I}_2 is the second order identity tensor, \mathbf{tr} is the trace operator, “ \otimes ” denotes the tensor product, the superscript “ T ” corresponds to the transpose operator, \mathbf{u} is the displacement vector, K and μ are the bulk and shear moduli, respectively. The fluid phase is described by the quasi-static linearised compressible Navier-Stokes momentum equation (*Landau and Lifshitz*, 1959a):

$$-\nabla p + \eta \nabla^2 \mathbf{v} + \frac{1}{3} \eta \nabla (\nabla \cdot \mathbf{v}) = 0, \quad (4.54)$$

where \mathbf{v} is the particle velocity, p is the fluid pressure and η is the shear viscosity. Equation (4.54) is valid for the laminar flow of a Newtonian fluid. In the numerical solver, equations (4.53)-(4.54) are written in the space-frequency domain as

$$\sigma_{ij} = \lambda e \delta_{ij} + 2\mu \epsilon_{ij} + i\omega \left(2\eta \epsilon_{ij} - \frac{2}{3} \eta e \delta_{ij} \right), \quad (4.55)$$

where ϵ_{ij} are the components of the strain tensor $\epsilon_{ij} = 0.5(u_{i,j} + u_{j,i})$, e is the trace of the strain tensor, λ and μ are the Lamé parameters, u_i is the displacement in the i -th direction, δ_{ij} is the Kronecker delta, i is the imaginary unit and ω is the angular frequency. Equations (4.52) and (4.55) are implemented into a

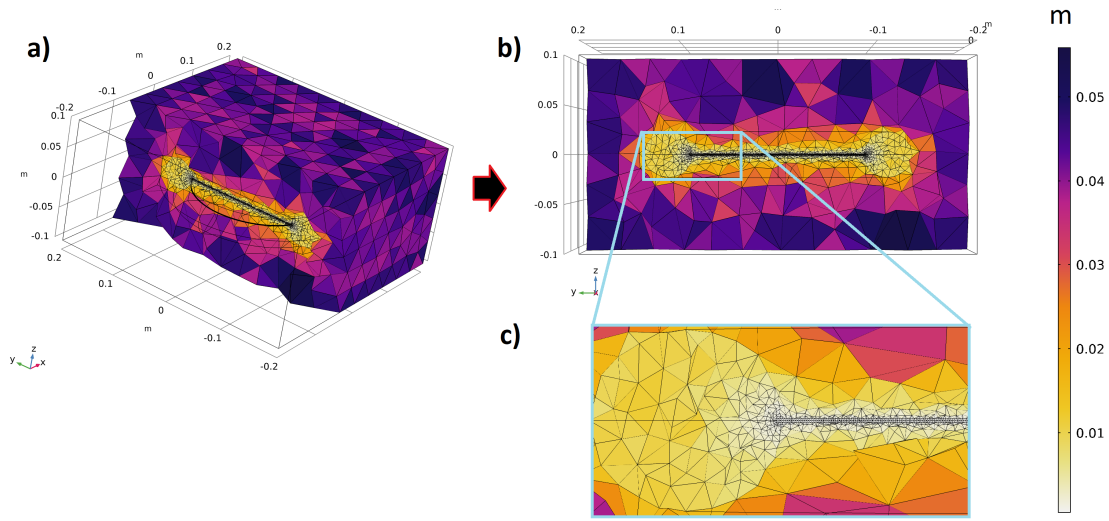


Figure 4.19: The element's size distribution for the Big pore model. The element's size in the crack is $\approx 6 \times 10^{-4}$ m, and in the surrounding grain material it is $7.2 \times 10^{-3} - 4 \times 10^{-2}$ m. The element's size distribution for the other models is similar. The total number of elements is $1.5 \times 10^6 - 5 \times 10^6$ depending on the model configuration, e.g., Big/Small pore or full/half/quarter of a model was used.

finite-element solver. In the domain representing a solid material, the equation (4.55) reduces to equation (4.53) by setting the shear viscosity η to zero. In the domain representing compressible viscous fluid, equation (4.54) is recovered by setting the shear modulus μ to zero. The solid and fluid displacements are described by the same variable and, thus, naturally coupled at the boundaries between subdomains (Quintal *et al.*, 2016, 2019). The numerical model is discretized using an unstructured mesh with tetrahedral elements (Figure 4.19). A direct PARDISO solver (Schenk and Gärtner, 2004) is used for solving the linear system of equations.

Direct relaxation tests are performed to compute all components of the stiffness matrix C_{ij} (Voigt notation) by applying a displacement boundary condition of the form $u = 10^{-8} \times \exp(i\omega t)$ to a certain external wall of the model and in a certain direction, while at other walls of the model, the displacements are set to zero or let free to change. In the direct tests that we perform, only one component of the stiffness matrix c_{ij} can be directly calculated after one numerical simulation. A detailed description of the boundary conditions is given in Alkhimenkov *et al.* (2020a,b). The resulting stress and strains are averaged over the spatial domain for each frequency. Then, the complex valued $C_{ii}(\omega)$ components (diagonal) are calculated for each frequency (in Voigt notation, no index summation):

$$C_{ii}(\omega) = \frac{\langle \sigma_i(\omega) \rangle}{\langle \epsilon_i(\omega) \rangle}, \quad (4.56)$$

where $\langle \cdot \rangle$ represents the volume averaging over the sample volume. For calculating the P-wave modulus ($ii = 11, 22, 33$), a harmonic displacement on the i direction is applied perpendicularly to a wall of the model. At the other walls of the model, the normal component of the displacement is set to zero. For calculating shear components of the stiffness matrix ($ii = 44, 55, 66$), the boundary conditions applied are those of a simple shear test. For the $C_{12}(\omega)$, $C_{13}(\omega)$ and $C_{23}(\omega)$ components (off-diagonal), mixed direct tests are performed. The corresponding inverse quality factor is (O'Connell and Budiansky, 1978)

$$\frac{1}{Q_{ij}(\omega)} = \frac{\text{Im}(C_{ij}(\omega))}{\text{Re}(C_{ij}(\omega))}, \quad (4.57)$$

which is used as a measure of attenuation (O'Connell and Budiansky, 1978). In the simulations, the energy

dissipation is caused by fluid pressure diffusion. The viscous shear relaxation in the fluid (O'Connell and Budiansky, 1977) is negligible in our study.

4.7 Appendix B: Analytical model of Collet and Gurevich (2016)

We compare the results of our numerical simulation against an anisotropic version of the squirt flow analytical solution of Gurevich *et al.* (2010) proposed by Collet and Gurevich (2016). Here we use the formulation presented by Alkhimenkov *et al.* (2020a). Collet and Gurevich (2016) consider a double-porosity medium with aligned identical cracks embedded in a hypothetical background rock matrix made up of grains and stiff pores only. The crack is fully described in terms of normal and tangential compliances Z_n and Z_t , respectively (Kachanov, 1993; Schoenberg and Sayers, 1995; Sayers and Kachanov, 1995). They consider the so-called modified frame in which only the cracks are filled with fluid, whereas the stiffer pores are empty (Mavko and Jizba, 1991). In the low frequency limit, the relaxed moduli of the modified frame are equal to the rock dry moduli (which means that $Z_n^{\text{MF}} = Z_n$); while in the high frequency limit, the fluid in the cracks stiffens the frame and the unrelaxed moduli of the modified frame are equal to the dry moduli of the rock without a compliant porosity (which means that $Z_n^{\text{MF}} = 0$) (Mavko and Jizba, 1991).

In the analytical solution of Collet and Gurevich (2016), the frequency dependent compliance tensor of the modified frame is written as (for a vertical transversely isotropic (VTI) medium)

$$S_{mn}^{\text{MF}}(\omega) = S_{mn}^b + \Delta S_{mn}^{\text{MF}}(\omega), \quad (4.58)$$

where S_{mn}^b is the compliance tensor of the rock matrix, and $\Delta S_{mn}^{\text{MF}}(\omega)$ is the additional compliance due to the crack (Schoenberg and Helbig, 1997):

$$\Delta S_{mn}^{\text{MF}}(\omega) = \begin{bmatrix} 0 & 0 & 0 & 0 & 0 & 0 \\ 0 & 0 & 0 & 0 & 0 & 0 \\ 0 & 0 & Z_n^{\text{MF}}(\omega) & 0 & 0 & 0 \\ 0 & 0 & 0 & Z_t & 0 & 0 \\ 0 & 0 & 0 & 0 & Z_t & 0 \\ 0 & 0 & 0 & 0 & 0 & 0 \end{bmatrix}. \quad (4.59)$$

The frequency-dependent normal fracture compliance is

$$Z_n^{\text{MF}}(\omega) = \frac{Z_n}{1 + \frac{Z_n}{\phi_c(1/K_f^*(\omega) - 1/K_g)}}, \quad (4.60)$$

where ϕ_c is the compliant porosity (crack porosity), Z_n is the normal compliance of the crack. Gurevich *et al.* (2010) proposed that the stiffness of the crack can be described using a frequency-dependent fluid bulk modulus $K_f^*(\omega)$:

$$K_f^*(\omega) = \left[1 - \frac{2J_1(ka)}{kaJ_0(ka)} \right] K_f, \quad (4.61)$$

where J_ξ is Bessel function of the first kind ($\xi = 0$ or $\xi = 1$ correspond to the zero or first order Bessel function), K_f is the fluid bulk modulus, a is the radius of the crack, k is the wavenumber of the pressure wave:

$$ka = \frac{1}{\alpha} \left(-\frac{3i\omega\eta}{K_f} \right)^{1/2}, \quad (4.62)$$

α is the aspect ratio of the crack (crack thickness divided by diameter) and η is the viscosity of the fluid. Equations (4.61)-(4.62) were obtained by imposing a zero fluid pressure boundary condition ($P_f = 0$) at the edge of the cylindrical crack (Gurevich *et al.*, 2010). The frequency-dependent stiffness tensor of the fluid saturated

medium is given by the anisotropic Gassmann's equation (Gassmann, 1951):

$$C_{mn}^{\text{sat}}(\omega) = C_{mn}^{\text{MF}}(\omega) + \alpha_m \alpha_n M, \quad (4.63)$$

$$\alpha_m = 1 - \left(\sum_{n=1}^3 C_{mn}^{\text{MF}} \right) \beta_g / 3, \quad (4.64)$$

for $m = 1, 2, 3$ and $\alpha_4 = \alpha_5 = \alpha_6 = 0$, and where

$$M = \left(\phi \beta_f + (1 - \phi) \beta_g - K^* \beta_g^2 \right)^{-1}, \quad (4.65)$$

$$K^* = \frac{1}{9} \sum_{m=1}^3 \sum_{n=1}^3 C_{mn}^{\text{MF}}(\omega), \quad (4.66)$$

ϕ is the total porosity of the medium without the compliant porosity, K^* is the generalized bulk modulus of the modified frame, β_f is the compressibility of the fluid, α_m is the Biot-Willis coefficient, β_g is the compressibility of the grain material.

For the comparison between the analytical solution and the numerical results, all stiffness properties of the dry medium are calculated numerically (or are the same as in the numerical simulation) and used as input to the analytical solution. In order to obtain the normal Z_n and tangential Z_t compliances of the crack we numerically calculate several (homogenized) elastic stiffness tensors of a dry medium (Figure 4.20): a torus embedded into the solid grain material (C_1^{VTI} stiffness tensor); a crack embedded into a medium described by the C_1^{VTI} stiffness tensor (C_2^{VTI} stiffness tensor); a torus connected with a crack embedded into the solid grain material (C_3^{VTI} stiffness tensor). Then, all C^{VTI} stiffness tensors are inverted to the corresponding compliance tensors S^{VTI} . For obtaining Z_n and Z_t there are two options:

Workflow A) Z_n and Z_t are calculated using the difference between the S_1^{VTI} compliance tensor and the S_2^{VTI} compliance tensor (Figure 4.20). In this case, we first homogenize the torus (and obtain C_1^{VTI}) and then, embed the crack into this homogenized material C_1^{VTI} . Thus, Z_n and Z_t do not take into account the fact that the crack is connected with the stiffer pore. This approach is used by *Collet and Gurevich* (2016).

Workflow B) Z_n and Z_t are calculated using the difference between the S_1^{VTI} compliance tensor and the S_3^{VTI} compliance tensor (Figure 4.20). In this case, we also first homogenize the torus but then, embed the crack connected to the torus into the solid grain material. Thus, the C_3^{VTI} stiffness tensor corresponds to the dry stiffness tensor of the model, so the difference $S_1^{VTI} - S_3^{VTI}$ gives the correct compliances Z_n and Z_t for the dry model (using the the homogenized material C_1^{VTI}).

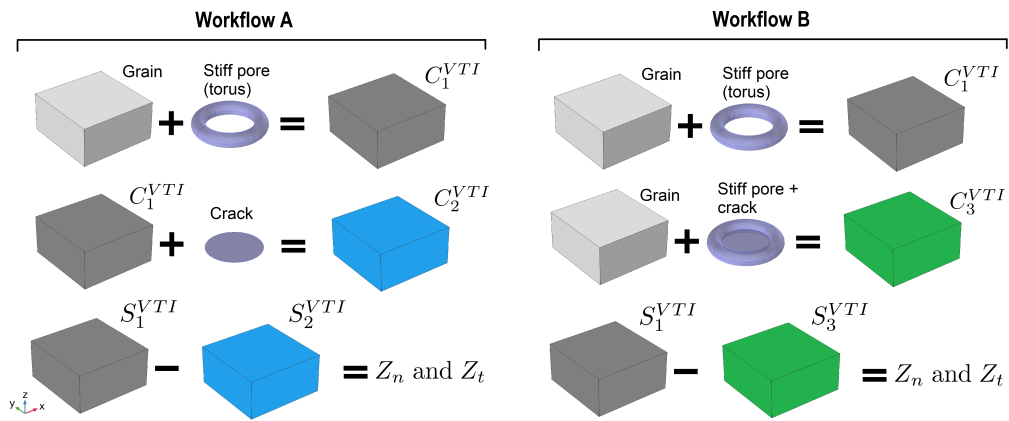


Figure 4.20: Sketch illustrating the calculation of normal and tangential compliances of the crack for workflows A and B. S_r^{VTI} denotes the compliance tensor, which is the inverse of the corresponding stiffness tensor, i.e., $S_r^{VTI} = (C_r^{VTI})^{-1}$, for $r = 1, 2, 3$. The resulting Z_n and Z_t are used to calculate the analytical solution for corresponding models.

Chapter 5

An accurate analytical model for squirt flow in anisotropic porous rocks — Part 2: Complex geometry

Yury Alkhimenkov and Beatriz Quintal

Under review¹ in *Geophysics*.

¹Alkhimenkov, Y. and Quintal B. An accurate analytical model for squirt flow in anisotropic porous rocks — Part 2: Complex geometry. *Geophysics* (under review).

Abstract

Seismic wave propagation exhibits strong attenuation and velocity dispersion in cracked porous rocks saturated with a fluid. The main cause of such a energy dissipation is the fluid flow at the pore space, so called squirt flow. Squirt flow takes place between interconnected pores and cracks. The corresponding theory can be used to characterize cracked porous rocks in subsurface with non-invasive seismic methods. We extend the analytical model for a classical pore geometry presented in our article Part 1 to more complex geometries of the pore space, where the crack edge is partially connected to multiple pores. This pore geometry is much more closely representative of that of a rock than the classical geometry where the crack edge is fully connected to a toroidal pore. We propose an approach to calculate the model compliance taking into account the interconnectivity of the crack and pores. We show that the crack aspect ratio does not control the characteristic frequency of squirt flow. We redefine a squirt flow length parameter which takes into account the geometrical configuration of the multiple connections between a crack and the surrounding pores. This configuration will control the geometric flow pattern and thus the diffusion length scale or, in other words, the characteristic frequency. We validate the analytical model against inherently accurate three-dimensional numerical solutions based on the exact same model geometries. The analytical and numerical results are in good agreement for a range of different pore geometries.

5.1 Introduction

A passing seismic wave cause small deformations in rocks. Since rocks are heterogeneous at any scale, such deformations cause heterogeneous strain field distribution in the rock. If rock is fluid saturated, such heterogeneous strain field cause fluid flow until the fluid pressure equilibrates (Müller *et al.*, 2010). The fluid flow can take place at different scales. At the pore scale, such fluid flow is called squirt flow and is known to cause strong wave energy dissipation and velocity dispersion. Many analytical models were suggested to quantify the squirt flow effect on propagating waves, e.g., squirt flow between interconnected pores (O'Connell and Budiansky, 1977; Palmer and Traviolia, 1980), between interconnected compliant cracks and stiff pores (Murphy *et al.*, 1986; Mukerji and Mavko, 1994; Dvorkin *et al.*, 1995; Pride *et al.*, 2004; Gurevich *et al.*, 2010) and between interconnected small aspect ratio cracks and spheroidal pores (Xu, 1998; Chapman *et al.*, 2002; Chapman, 2003; Jakobsen and Chapman, 2009). In real rocks, examples of compliant pores are microcracks and grain contacts.

Several numerical approaches were proposed to study squirt flow (Zhang *et al.*, 2010; Zhang and Toksöz, 2012; Quintal *et al.*, 2016, 2019; Das *et al.*, 2019). Recently, a number of three-dimensional numerical studies were conducted for several pore space geometries (Alkhimenkov *et al.*, 2020a,b; Lissa *et al.*, 2020). Lissa *et al.* (2021) studied frequency-dependent attenuation caused by squirt flow in a pore geometry of a real rock derived from three-dimensional images based on micro-computed X-ray tomography. Alkhimenkov *et al.* (2020a) compared accurate numerical solutions against a published analytical model for squirt flow (Collet and Gurevich, 2016) for the exact same classical pore geometry and showed that significant discrepancies exist. The classical pore geometry consists of a penny-shaped (circular) crack fully connected to a surrounding toroidal stiff pore. Recently, Alkhimenkov and Quintal (2021), in Part 1 of this study, proposed a new analytical model which is in a good agreement with an accurate three-dimensional numerical simulation for the classical pore geometry.

In this contribution, we extend the analytical model presented in Part 1 (Alkhimenkov and Quintal, 2021) to more complex geometries of the pore space, where the crack is only partially connected to one or more spherical pores. For that, we propose a new approach to calculate the model compliances for more complex geometries. We show that the fluid flow directions and the squirt flow characteristic frequency change dramatically compared to the classical pore geometry. To take this into account, we present another parameter to characterize the characteristic frequency of the squirt flow. We also derive another solution for the crack stiffness relaxation. We validate all the results against accurate three-dimensional numerical simulations based on exact same model geometry. We provide Matlab and (symbolic) Maple routines to allow the reader to reproduce our main results and/or to obtain results for other material properties and pore sizes.

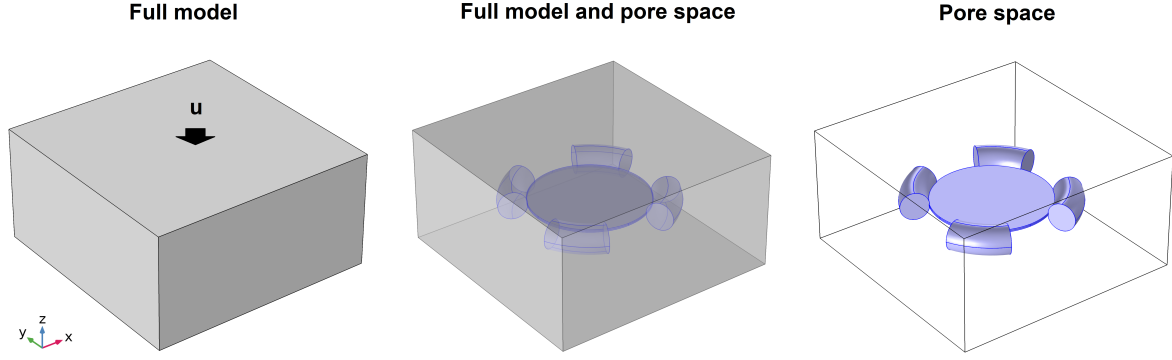


Figure 5.1: Sketch illustrating the the model geometry of a crack connected to a fraction of a torus. The displacement boundary condition $u = 10^{-8} \times \exp(i\omega t)$ applied to the top side of the model to calculate the C_{33} component of the effective stiffness matrix (Voigt notation).

5.2 Numerical analysis

For the numerical analysis, we explore several three-dimensional numerical models consisting of a pore space saturated with a fluid embedded in an elastic solid grain material. The numerical method is described in *Quintal et al. (2016, 2019)*. The solid grains are described as a linear isotropic elastic material, the fluid phase is described by the quasi-static linearised compressible Navier-Stokes momentum equation. To obtain all components of the stiffness matrix C_{ij} (Voigt notation), we perform the direct relaxation tests by applying a displacement boundary condition of the form $u = 10^{-8} \times \exp(i\omega t)$ to a certain external wall of the model, where $\omega = 2\pi f$ is the angular frequency, f is frequency, t is time, i is an imaginary unit (Figure 5.1). A detailed description of the applied boundary conditions are given in *Alkhimenkov et al. (2020a,b)*. The models are given below:

- i) The model with a crack connected to the fractions of the torus (crack aspect ratio $\alpha = 0.02$).
- ii) The model with a crack partially connected to spherical pores (crack aspect ratio $\alpha = 0.01$).

The material parameters used in all models are shown in Table 5.2. The elastic solid grain material is represented by a rectangular cuboid with the dimensions of $0.4 \times 0.4 \times 0.2\text{m}$ in all simulations. The geometrical properties of the pore space are given in the corresponding sections. The geometry in all models is scalable; i.e., the numerical solution remains unchanged, if all the geometrical properties are re-scaled by any fraction. An illustration of the model with a crack connected to fractions amounting to $4/9$ of a torus is given in Figure 5.1. Other models use the same rectangular cuboid with different pore space geometries.

5.2.1 Fractions of the torus

Alkhimenkov et al. (2020a) performed a three-dimensional numerical study of the stiffness moduli dispersion due to squirt flow for a classical geometry, a crack (flat cylinder) connected to a pore (torus). The numerical results of the effective stiffness modulus $[C_{33}^*(\omega)]_{\text{sat}}$ (Voigt notation) showed that the slopes of the high-frequency asymptote of the attenuation curve is proportional to $\approx \omega^{-1/2}$ whereas a published analytical model (*Collet and Gurevich, 2016*) suggests $\approx \omega^{-1}$. However, the reason of such an asymptote of the attenuation curve ($\approx \omega^{-1/2}$) remained unexplored. To further investigate the shape of the dimensionless attenuation $1/Q$ for different geometries, we present the results for a crack connected to fractions of the Big torus model (Figure 5.2). They include the fluid pressure snapshots at different frequencies (low-frequency — 10 Hz, high-frequency — 5.6×10^6 Hz, and the characteristic frequency), the $[C_{33}^*(\omega)]_{\text{sat}}$ complex-valued component of the stiffness matrix and dimensionless attenuation ($1/Q$).

The fluid pressure snapshots of a model corresponding to the configuration where a zero fluid pressure boundary condition is applied to the edge of the crack (representing a pore having an infinite volume while the pore is absent are shown for comparison (Alkhimenkov *et al.*, 2020a). The geometrical properties of the model with crack aspect ratio $\alpha = 0.02$ are shown in Table 5.1. Figure 5.2 provides us with several insights into the physics of squirt flow and the shape of the attenuation and dispersion curves, as described below.

At low frequencies, the fluid pressure is low and uniform in all the models representing so-called relaxed state (Figure 5.2a-f). One can observe, that the fluid pressure at the low frequency is the highest for the 1/9 torus model (Figure 5.2b), the fluid pressure magnitude is reducing as the volume of the pore is increasing (Figure 5.2c-f) and is the lowest for the $P_f = 0$ model. This trend shows that the volume of the stiff pore has a significant impact on the overall attenuation magnitude, as it can be seen in Figure 5.2h.

At the characteristic frequency, the fluid pressure is high at the center of the crack but low close to the edge of the crack. This configuration corresponds to the maximum gradients of the fluid pressure in the crack. Thus, the crack stiffness is high at the crack center but low at the edge; except for the 1/9 torus model, where the crack stiffness is high at the crack edge opposite to the pore. The transition from the low frequency limit to the characteristic frequency is approximately the same in all the models (Figure 5.2a-f), that's why the behavior of the attenuation curve $1/Q$ and its asymptote is the same in all models for frequencies below the characteristic frequency (Figure 5.2h).

At high frequencies, the fluid pressure snapshots are different in all the models (Figure 5.2a-f) as well as the shapes of the attenuation curves $1/Q$ (Figure 5.2h). One can observe a regions of a high fluid pressure close to partially connected pores (pointed as "anomaly" in Figures 5.2b-f). For the Big torus model, the fluid pressure anomaly is present along the whole circumference ("red ring" in Figure 5.2f). However, there is no such anomaly in the $P_f = 0$ model (high freq. in Figure 5.2a), explaining why this model is in agreement with the analytical model of Collet and Gurevich (2016); Alkhimenkov *et al.* (2020a). These high pressure anomalies are responsible for different shapes of the attenuation curves $1/Q$ at high frequencies in the considered models (Figure 5.2h).

The characteristic frequency shifts to lower values as the fraction of the torus reduces (Figure 5.2h). However, the characteristic frequency of the 1/9 torus model is about one order of magnitude lower compare to the Big torus model. Note, that the crack aspect ratio is the same in all simulations which means that the crack aspect ratio does not control the characteristic frequency of squirt flow as it was believed until now. Instead, a different parameter control the characteristic frequency of squirt flow, which is explored in the next sections.

Table 5.1: Geometrical properties for the Big pore model. Major radius — the distance from the center of the tube to the center of the torus. Minor radius — the radius of the tube (our isometric pore). The volume of the fractions of the torus for models (1/9 torus, 4/9 torus, 6/9 torus, 8/9 torus) correspond to the fractions (1/9, 4/9, 6/9, 8/9) of the Big torus model, respectively.

Geometrical parameter	Big pore model
Flat cylinder (crack) radius, b	0.1 m
Flat cylinder (crack) thickness, h	0.004 m
Crack aspect ratio, $\alpha = h/(2b)$	0.02
Major radius of torus, $b + r$	0.124 m
Minor radius of torus, r	0.024 m
Total porosity	≈ 0.0478
Crack porosity	≈ 0.0039

Table 5.2: Material properties used in all models.

Material parameter	Solid	Fluid
Solid bulk modulus K	36 GPa	4.3 GPa
Solid shear modulus μ	44 GPa	0 GPa
Fluid shear viscosity η	0 Pa·s	1.414 Pa·s

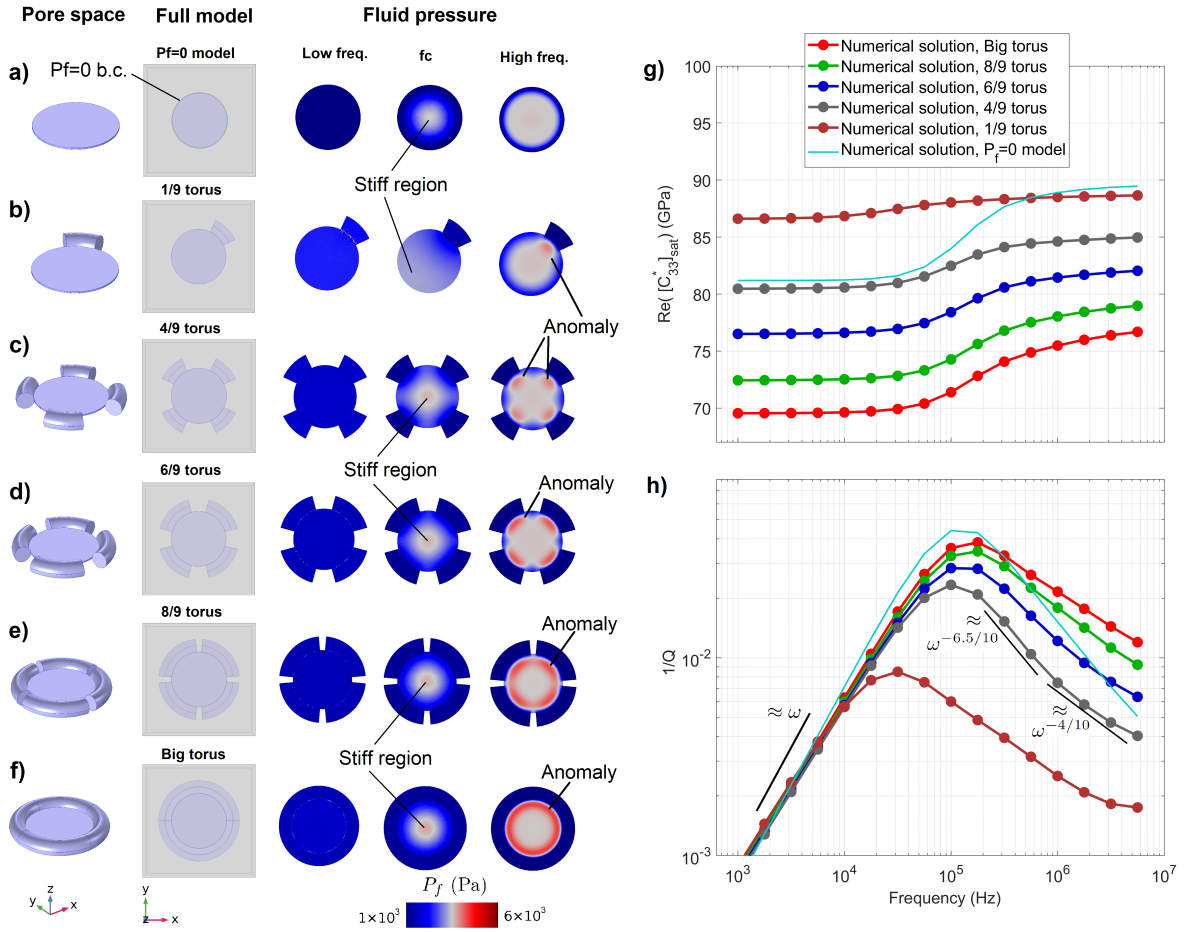


Figure 5.2: (a) $P_f = 0$ model, (b) 1/9 torus model, (c) 4/9 torus model, (d) 6/9 torus model, (e) 8/9 torus model, (f) the Big torus model. Results of numerical simulations for the real part of the C_{33} component (g) and dimensionless attenuation for the C_{33} component (h). The crack aspect ratio is $\alpha = 0.02$.

5.2.2 Spherical pores

To further understand which parameters control the characteristic frequency f_c of squirt flow and to what extent the pore shape affects the shape of the dispersion and attenuation curves, we present numerical results for models with a crack partially connected to spherical pores (Figure 5.3). The geometrical properties of this set of models with crack aspect ratio $\alpha = 0.01$ is shown in Table 5.3.

At low frequencies, the fluid pressure is low and uniform in all the models (Figure 5.3a-d), similar to the model with a crack connected to fractions of the torus (Figure 5.2). The fluid pressure magnitude is the lowest in the 4 spheres model (Figure 5.2b) and increases in the 1 and 2 spheres model (Figure 5.2c-d). Obviously, the 4 spheres model has the largest volume of the stiff pores compare to other models, thus there is enough volume to store the fluid flowing from the crack resulting in low fluid pressure. The Big torus model with crack aspect ratio $\alpha = 0.01$ has approximately the same volume of the stiff pores as the 2 spheres model, however, the attenuation peak (and the cumulative attenuation) of the Big torus model is the greatest among other models. It means that the volume of the stiff pores and the model compliances are the key parameters determining the attenuation magnitudes. The difference between the dry moduli of the interconnected crack and pore and the moduli of the interconnected dry pore and saturated crack (i.e., modified frame) define the attenuation magnitude. This difference is the largest for the Big torus model, that's why the attenuation is also the largest. The volume of the stiff pores is another important parameter, which controls the attenuation magnitude — the volume should be sufficiently large, two orders of magnitude larger than the crack volume (*Alkhimenkov et al., 2020a*), to keep the fluid pressure low in the pore at low frequencies.

At the characteristic frequency, the fluid pressure is high at the center of the crack (Figure 5.3) similar to the previous model (Figure 5.2). The shape of the central region of the high fluid pressure in the crack is slightly different in all models. Nevertheless, the shape of the attenuation curve $1/Q$ at low frequencies is the same in all models (Figure 5.3f).

At high frequencies, the fluid pressure snapshots (Figure 5.3a-d) and the shape of the attenuation curve $1/Q$ (Figure 5.3f) exhibit similar behavior compared to that of the fraction of the torus models (Figure 5.2f). The shape of the attenuation curve of the Big torus model with $\alpha = 0.01$ (Figure 5.3a-f) is the same as in the Big torus model with $\alpha = 0.02$ (Figure 5.2h); the “ring” anomaly of fluid pressure at high frequencies is also similar. The anomalies of high fluid pressure at high frequencies due to the connectivity with spheres (Figure 5.3a-d) exhibit similar behavior as in the fraction of the torus models (Figure 5.2). The high pressure anomalies are also similar to those presented for the models with a crack connected to fractions of the torus (Figure 5.2).

The characteristic frequency shifts to lower values as the connected portion of the crack circumference reduces. This portion equals to the whole crack circumference for the Big torus model, reduces for the models with spherical pores and is the lowest for the 1 sphere model.

Table 5.3: Geometrical properties for the 1, 2, 4 spheres models and the Big torus model with crack aspect ratio $\alpha = 0.01$.

Geometrical parameter	1 sphere	2 spheres	4 spheres	Big torus
Flat cylinder (crack) radius, b	0.1 m	0.1 m	0.1 m	0.1 m
Flat cylinder (crack) thickness, h	0.002 m	0.002 m	0.002 m	0.002 m
Crack aspect ratio, $\alpha = h/(2b)$	0.01	0.01	0.01	0.01
Radius of sphere, $b/2$	0.05 m	0.05 m	0.05 m	0.05 m
The volume (crack+pore, interconnected)	$\approx 5.832 \times 10^{-4}$	≈ 0.0011	≈ 0.00214	≈ 0.00145
Total porosity	≈ 0.0182	≈ 0.0344	≈ 0.0669	≈ 0.0454
Crack porosity	≈ 0.002	≈ 0.002	≈ 0.002	≈ 0.002

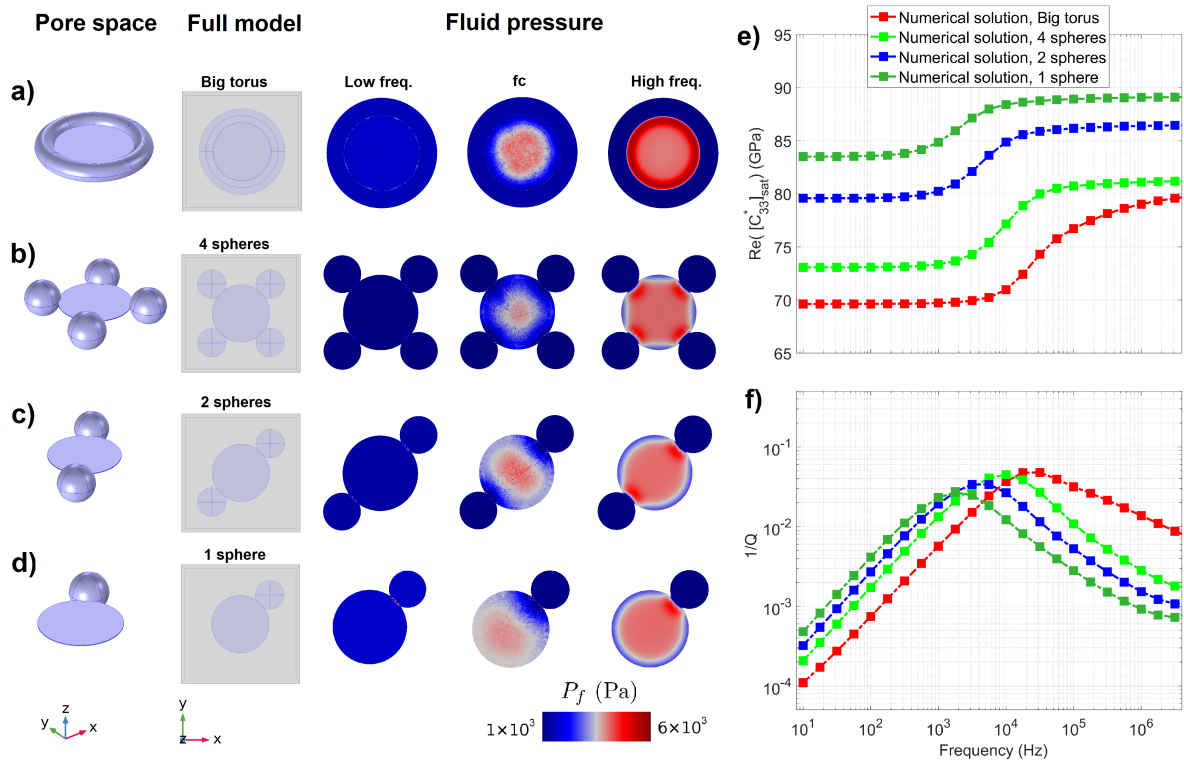


Figure 5.3: (a) the Big torus model, (b) 4 spheres model, (c) 2 spheres model, (d) 1 sphere model model. Results of numerical simulations for the Real part of the C_{33} component (e) and dimensionless attenuation for the C_{33} component (f). The crack aspect ratio $\alpha = 0.01$.

5.3 Analytical model

The present analytical model extends the analytical model presented in Part 1 (*Alkhimenkov and Quintal, 2021*) to the geometries involving partially connected stiff pores. The workflow is similar to Part 1, however, we provide more general approaches to calculate dry model compliances and the crack stiffness relaxation functions. For consistency, we present the workflow similar to that one from Part 1 (Figure 5.4).

- i) First, calculate (or measure) the moduli of the dry rock (step 1 in Figure 5.4). We need the moduli of the dry model with interconnected pore and crack, as well as, the moduli of the same model but with crack normal compliance equals to zero (or equals to a small number for the finite thickness crack).
- ii) At the second step, calculate the crack stiffness relaxation function due to squirt flow and use that expression as the frequency-dependent crack stiffness. As a result, we obtain the frequency-dependent moduli of the modified frame (the stiff pore is still dry).
- iii) At the last step, apply anisotropic Gassmann's equations (*Gassmann, 1951*) to calculate the moduli of the fully saturated model.

The methodologies to calculate the model compliances (step 1) and the crack stiffness relaxation function (step 2) are given below.

5.3.1 General expressions

The key result of Part 1 (*Alkhimenkov and Quintal, 2021*) is the general expression to calculate effective viscoelastic stiffness tensor for any geometry of the pore space using the property contribution tensors. The effective compliance matrix for the dry model represented in Figure 5.4a can be written as (in Voigt notation)

$$[S_{mn}^*]_{\text{dry}} = S_{mn}^g + [H_{mn}]_{\text{dry}}, \quad (5.1)$$

where S_{mn}^g is the compliance matrix of the solid grains, $[H_{mn}]_{\text{dry}}$ is the compliance contribution matrix of the dry pore space (a crack connected to a pore(s)). The effective compliance matrix for the modified frame can be calculated as

$$[S_{mn}^*(\omega)]^{\text{MF}} = S_{mn}^g + [H_{mn}^p]_{\text{dry}} + [H'_{mn}(\omega)]^{\text{MF}}, \quad (5.2)$$

where $[H_{mn}^p]_{\text{dry}}$ is the compliance contribution matrix of the stiff pore(s) and $[H'_{mn}(\omega)]^{\text{MF}}$ is the additional compliance contribution matrix due to the presence of a saturated crack connected to a dry pore(s), ω is the angular frequency; $[H'_{33}(\omega)]^{\text{MF}}$ is frequency-dependent component with the moduli of the crack stiffness relaxation (given below). Finally, the effective stiffness matrix for the saturated model is calculated as

$$[C_{mn}^*(\omega)]_{\text{sat}} = \left([S_{mn}^*(\omega)]^{\text{MF}} \right)^{-1} + [\text{fluid via Gassmann's equations}], \quad (5.3)$$

where $[\text{fluid via Gassmann's equations}]$ denotes the application of the anisotropic Gassmann's equations (*Gassmann, 1951*) to saturate a pore(s) with a fluid at each frequency.

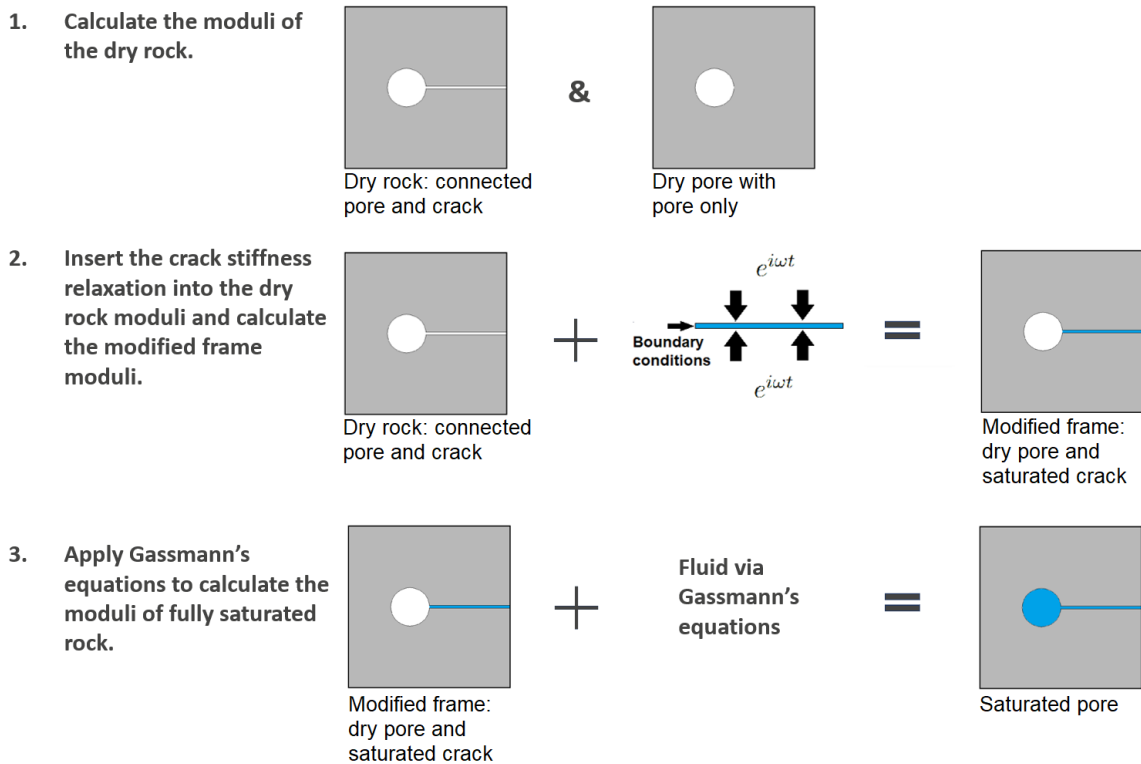


Figure 5.4: Sketch of the development of the present analytical model.

5.3.2 Step 1: Dry model compliances

Figure 5.5 shows three different geometries of the pore space: a crack connected to a torus (Figure 5.5a), a crack partially connected to a spherical pore (Figure 5.5b) and a crack with a pore in the center (“Saturn ring”). An analytical approach to calculate the effective compliance matrices of the mentioned above dry models is briefly explained below. We exploit the approach used in micromechanics to construct the property contribution matrix of complex geometries (e.g., intersecting cracks, inclusions of “irregular” shapes, chapters 4.3 and 4.4 in *Kachanov and Sevostianov (2018)*). The main idea is that by using three-dimensional numerical simulations for the complex pore space, we find the structure and the symmetry of the compliance contribution matrix, its principal directions and the key geometrical characteristics of the complex pore space which control the compliance of the model.

A crack connected to a torus

The method to calculate the compliance contribution matrices of a dry model with a crack connected to a torus (the same as in Figures 5.2f and 5.5a) is presented in *Alkhimenkov and Quintal (2021)*. The analytical approach to construct the property contribution matrix for this complex geometry provide us a very good approximation (validated against accurate numerical solutions). The disadvantage of this geometry is that this model is quite artificial; the components $[H_{33}]_{\text{dry}}$, $[H_{44}]_{\text{dry}}$ and $[H_{55}]_{\text{dry}}$ are controlled by the torus only, so the crack thickness doesn't affect the effective properties of the dry model (*Alkhimenkov and Quintal, 2021*). However, in real rocks crack density and crack thickness do affect the effective elastic moduli. That's why this widely used classical pore geometry for squirt flow should no be longer used.

A crack with a pore in the center

Another end-member is represented by a crack with a pore in the center (“Saturn ring”) geometry (Figure 5.5c). The analytical approach to construct the property contribution matrix for this geometry is given in *Kachanov and Sevostianov* (2018). In this configuration, the components $[H_{33}]_{\text{dry}}$, $[H_{44}]_{\text{dry}}$ and $[H_{55}]_{\text{dry}}$ are controlled by the crack only (if the crack radius is at least two times bigger than the radius of the sphere). Therefore, the compliance contribution matrix $[H_{mn}]_{\text{dry}}$ (expression 5.1) is calculated using the expressions for a spherical pore, except for the components $[H_{33}]_{\text{dry}}$, $[H_{44}]_{\text{dry}}$, $[H_{55}]_{\text{dry}}$. These components are calculated using the expressions for a crack (Figure 5.5c).

A crack partially connected to a (few) pore(s)

To date, there is no accurate approach to construct the compliance contribution matrices of a crack partially connected to a (few) pore(s) using analytical expressions (Figure 5.5b and Figure 5.3b-d). Here, we provide an approximate solution whose accuracy is lower compared to the two above mentioned geometries. Still, such an approximate solution should be used for the interconnected pore(s) and crack if no precise numerical solution is available.

Our approximate solution is simple, the property contribution matrix can be calculated using analytical expressions only. The general idea is the same as for the pore space geometry consisting of a crack connected to a torus (*Alkhimenkov and Quintal*, 2021). For the geometry presented in Figure 5.5b, the components $[H_{33}]_{\text{dry}}$, $[H_{44}]_{\text{dry}}$ and $[H_{55}]_{\text{dry}}$ are controlled simultaneously by the crack and the sphere. The compliance contribution matrix $[H_{mn}]_{\text{dry}}$ (expression 5.1) is calculated using the expressions for a spherical pore, except for the components $[H_{33}]_{\text{dry}}$, $[H_{44}]_{\text{dry}}$, $[H_{55}]_{\text{dry}}$. These components are calculated using the expressions for the extended crack (Figure 5.5c). The area of the projection of the crack partially connected to a pore on the XY-axis will define the area of the circular (penny-shaped) extended crack. The thickness of the extended crack can be the same as the thickness of the crack itself. However, if the area of the projection of the pore is comparable (or larger) to the area of the projection of the crack, then the thickness of the extended crack should be increased. For this case, the precise definition of the crack will be investigated in the future.

One can see that the extended crack radius (Figure 5.5c) is larger than the radius of the initial crack of the model. As a result, the compliance contribution matrix of a crack partially connected to a pore $[H_{mn}]_{\text{dry}}$ is constructed by using the obtained components of a pore $[H_{mn}^{\text{P}}]_{\text{dry}}$ and an extended crack $[H_{mn}^{\text{Ecr}}]_{\text{dry}}$:

$$[H_{mn}]_{\text{dry}} = \begin{bmatrix} [H_{11}^{\text{P}}]_{\text{dry}} & [H_{12}^{\text{P}}]_{\text{dry}} & [H_{13}^{\text{P}}]_{\text{dry}} & 0 & 0 & 0 \\ [H_{21}^{\text{P}}]_{\text{dry}} & [H_{22}^{\text{P}}]_{\text{dry}} & [H_{23}^{\text{P}}]_{\text{dry}} & 0 & 0 & 0 \\ [H_{31}^{\text{P}}]_{\text{dry}} & [H_{32}^{\text{P}}]_{\text{dry}} & [H_{33}^{\text{Ecr}}]_{\text{dry}} & 0 & 0 & 0 \\ 0 & 0 & 0 & [H_{44}^{\text{Ecr}}]_{\text{dry}} & 0 & 0 \\ 0 & 0 & 0 & 0 & [H_{55}^{\text{Ecr}}]_{\text{dry}} & 0 \\ 0 & 0 & 0 & 0 & 0 & [H_{66}^{\text{P}}]_{\text{dry}} \end{bmatrix}. \quad (5.4)$$

The compliance contribution matrix of the modified frame is

$$[H_{mn}(\omega)]^{\text{MF}} = \begin{bmatrix} [H_{11}^{\text{P}}]_{\text{dry}} & [H_{12}^{\text{P}}]_{\text{dry}} & [H_{13}^{\text{P}}]_{\text{dry}} & 0 & 0 & 0 \\ [H_{21}^{\text{P}}]_{\text{dry}} & [H_{22}^{\text{P}}]_{\text{dry}} & [H_{23}^{\text{P}}]_{\text{dry}} & 0 & 0 & 0 \\ [H_{31}^{\text{P}}]_{\text{dry}} & [H_{32}^{\text{P}}]_{\text{dry}} & [H_{33}^{\text{Ecr}}(\omega)]^{\text{MF}} & 0 & 0 & 0 \\ 0 & 0 & 0 & [H_{44}^{\text{Ecr}}]_{\text{dry}} & 0 & 0 \\ 0 & 0 & 0 & 0 & [H_{55}^{\text{Ecr}}]_{\text{dry}} & 0 \\ 0 & 0 & 0 & 0 & 0 & [H_{66}^{\text{P}}]_{\text{dry}} \end{bmatrix}, \quad (5.5)$$

where a new component $[H_{33}^{\text{Ecr}}(\omega)]^{\text{MF}}$ is introduced (analogous to the classical geometry presented in *Alkhimenkov and Quintal* (2021)). Fluid flow takes place in the crack in one plane, therefore, the relaxation of the crack compliance denoted by only the $[H_{33}^{\text{Ecr}}(\omega)]^{\text{MF}}$ component. The expression for the $[H_{33}^{\text{Ecr}}(\omega)]^{\text{MF}}$ is given below.

To separate the compliance contribution of a pore, which is a constant value across all frequencies, from the contribution of the extended crack compliance, which is frequency dependent, we introduce (Alkhimenkov and Quintal (2021)):

$$\left[H'_{mn}(\omega) \right]^{\text{MF}} = [H_{mn}(\omega)]^{\text{MF}} - [H_{mn}^{\text{tp}}]_{\text{dry}} = \begin{bmatrix} 0 & 0 & 0 & 0 & 0 & 0 \\ 0 & 0 & 0 & 0 & 0 & 0 \\ 0 & 0 & [H'_{33}(\omega)]^{\text{MF}} & 0 & 0 & 0 \\ 0 & 0 & 0 & [H'_{44}]_{\text{dry}}^{\text{MF}} & 0 & 0 \\ 0 & 0 & 0 & 0 & [H'_{55}]_{\text{dry}}^{\text{MF}} & 0 \\ 0 & 0 & 0 & 0 & 0 & 0 \end{bmatrix}. \quad (5.6)$$

The structure of the compliance contribution matrix (eq. 5.6) is the same as the compliance contribution matrix of a crack embedded into a homogeneous elastic material Schoenberg and Douma (1988); Schoenberg and Helbig (1997) (the crack compliance can be written in terms of normal and tangential compliances). However, the absolute values of its components are completely different compared to the values obtained for a crack embedded into a homogeneous elastic material (Alkhimenkov and Quintal, 2021). Note that

$$\lim_{\omega \rightarrow +0} [H'_{33}(\omega)]^{\text{MF}} = [H_{33}^{\text{Ecr}}]_{\text{dry}} - [H_{33}^{\text{P}}]_{\text{dry}} \equiv Z_n^{\text{Ap}}, \quad (5.7)$$

where for simplicity we introduce the apparent normal crack compliance Z_n^{Ap} . The apparent tangential crack compliance is $Z_t^{\text{Ap}} = [H'_{44}]_{\text{dry}}^{\text{MF}} \equiv [H'_{55}]_{\text{dry}}^{\text{MF}}$.

If there are several pores (as in Figure 5.3b-c), then the approach is the same. If the the area of the stiff pores projected into the XY-plane is comparable or bigger than the area of the initial crack, then the thickness of the extended crack can be increased to make the model softer in $[H_{33}]_{\text{dry}}$, $[H_{44}]_{\text{dry}}$, $[H_{55}]_{\text{dry}}$ components; the increase in the extended crack thickness can be significant. Here, the most important parameter is the fraction of the projected area of the stiff pores to the initial crack. The thickness of the extended crack is a function of this fraction; if the fraction is more than 1, then the thickness can be significantly increased.

Frequency-dependent crack stiffness

To derivation of the frequency-dependent normal component $[H'_{33}(\omega)]^{\text{MF}}$ of the modified frame contribution matrix is provided in Alkhimenkov and Quintal (2021) (Maple scrip is also provided to reproduce and extend the derivation). In this derivation, the anisotropic Gassmann's equations are used to calculate the moduli considering the crack saturated, given that the compliance contribution matrix of the thin crack is described by two parameters only (see expression 5.7). Here, we only report the resulting expression (Alkhimenkov and Quintal, 2021),

$$\left[H'_{33}(\omega) \right]^{\text{MF}} = \frac{(K_g - K_f^*(\omega)) \phi_c Z_n^{\text{Ap}}}{(K_g - K_f^*(\omega)) \phi_c + K_f^*(\omega) K_g Z_n^{\text{Ap}}}, \quad (5.8)$$

where ϕ_c is the compliant porosity (crack porosity), Z_n^{Ap} is the normal apparent compliance of the crack, $K_f^*(\omega)$ is the frequency-dependent fluid bulk modulus and K_g is the bulk modulus of the solid grains. The apparent tangential crack compliance is $Z_t^{\text{Ap}} = [H'_{44}]_{\text{dry}}^{\text{MF}} \equiv [H'_{55}]_{\text{dry}}^{\text{MF}}$. If the frequency of the applied strain to the walls of the model is low, then the crack is in a relaxed state and

$$\left[H'_{33}(0+) \right]^{\text{MF}} = Z_n^{\text{Ap}} \quad (5.9)$$

If the frequency of the applied strain to the walls of the model is high, then the crack is in an unrelaxed state and

$$\left[H'_{33}(+\infty) \right]^{\text{MF}} = 0 \quad (5.10)$$

The workflow to calculate analytically the effective elastic moduli of the interconnected pore space

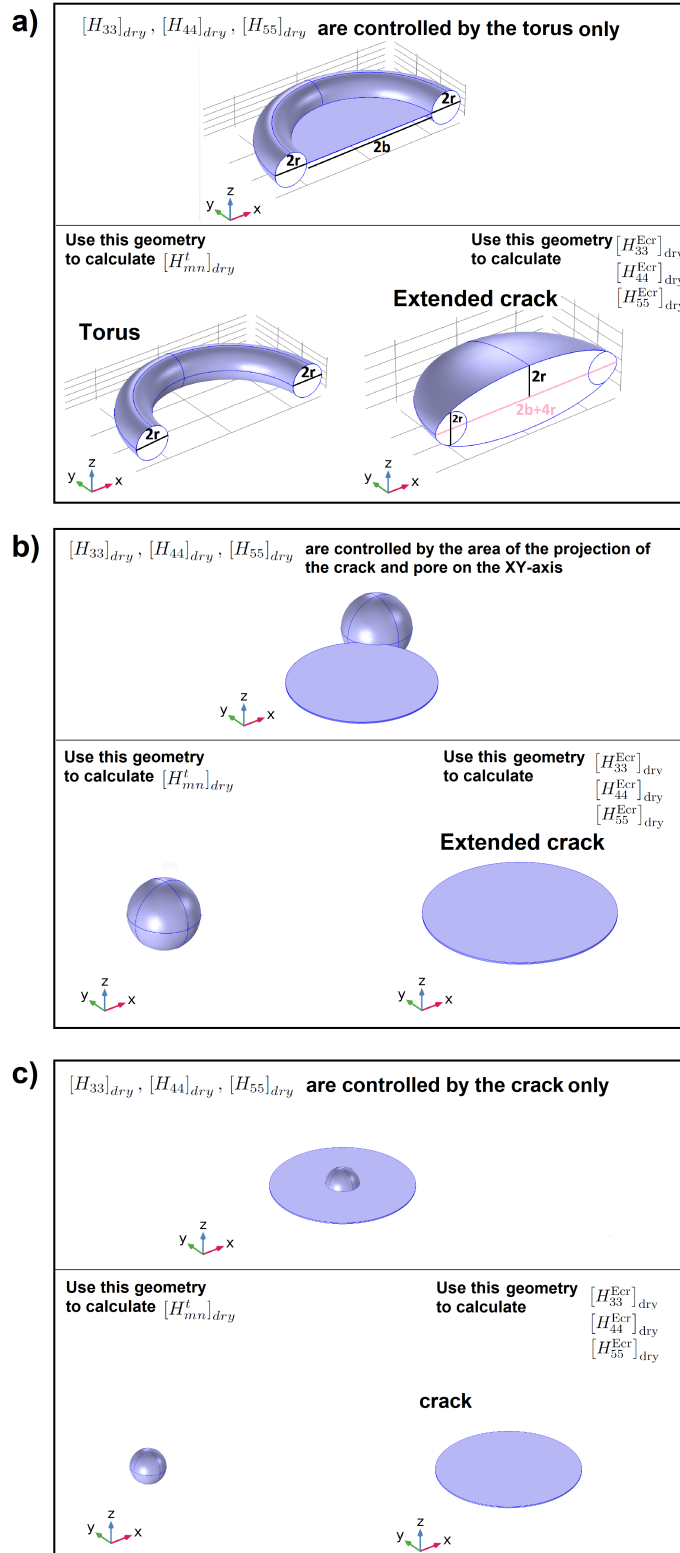


Figure 5.5: Sketch illustrating the workflow on calculating analytically the stiffness moduli for different configurations of interconnected isometric pores and cracks.

The full expression to calculate $K_f^*(\omega)$ is given in the next section.

Extension for cracks with finite thickness

Here we repeat the method presented by (Alkhimenkov and Quintal, 2021) to calculate the normal apparent crack compliance for a finite thickness crack. If the crack thickness is not so small (i.e., the aspect ratio is larger 0.0025) then the expression 5.8 is not equal to zero. A small non-zero value of Z_n^{fth} will be present,

$$\lim_{\omega \rightarrow +\infty} [H'_{33}(\omega)]^{MF} = [Z_n^{Ap}]^{fth}. \quad (5.11)$$

The normal apparent crack compliance becomes

$$[Z_n^{Ap}]^f = Z_n^{Ap} - [Z_n^{Ap}]^{fth}. \quad (5.12)$$

The only modification that is needed is a slight change in expression 5.8 by including the additional compliance $[Z_n^{Ap}]^{fth}$,

$$[H'_{33}]^{MF} = \frac{(K_g - K_f^*(\omega)) \phi_c [Z_n^{Ap}]^f}{(K_g - K_f^*(\omega)) \phi_c + K_f^*(\omega) K_g [Z_n^{Ap}]^f} + [Z_n^{Ap}]^{fth}. \quad (5.13)$$

5.3.3 Step 2: Relaxation of the crack stiffness

Fluid pressure diffusion behavior in the crack strongly depends on the portion of the crack circumference connected to the stiff pore as shown in Figures 5.2 and 5.3. Furthermore, high fluid pressure anomalies in the regions close to the connected stiff pores dramatically change the shape of the attenuation curve $1/Q$ (Figures 5.2h and 5.3f). The characteristic frequency is also different for different pore geometries even though the crack aspect ratio stays the same (Figures 5.2h and 5.3f). All these observations obtained from the three-dimensional numerical solutions allow us to revise the previous qualitative and quantitative description of the squirt flow physics. By analyzing the numerical results (Figures 5.2 and 5.3), we find that the characteristic frequency is different for radial and approximately one-dimensional fluid pressure diffusion. Then, we analyze analytical solutions for the fluid pressure considering radial and one-dimensional fluid pressure diffusion; we find out that the solutions for crack stiffness considering one-dimensional fluid pressure diffusion provide us an excellent approximation for pore space geometries presented in the present study. Below, we provide a new expression for the crack stiffness relaxation function. Only if the pore space geometry employs radial fluid pressure diffusion (Big torus and 8/9 torus geometries), expressions for radial fluid pressure diffusion should be used (they are presented in Appendix 5.7). We also revise the parameters which control the characteristic frequency of squirt flow.

Fluid pressure diffusion in a layer

For a one-dimensional configuration, we assume that fluid flow takes place in x - direction in an infinite-strip layer (i.e., infinite length in y - direction); l^{sq} and h^{sq} are the width and thickness of the layer, respectively. We set the following boundary conditions: the compression sinusoidal strain ϵ_c as a function of frequency is applied to the walls of the layer, zero fluid pressure is applied at the edge of the layer. The solution for the fluid pressure p in the layer is frequency dependent. The one-dimensional version of equation 23 in Alkhimenkov and Quintal (2021) for the fluid pressure can be written as

$$\frac{\partial^2 p}{\partial x^2} - k^2 p = -k^2 K_f \epsilon_c, \quad (5.14)$$

where

$$k = \frac{2}{h} \sqrt{3i\omega\eta / (K_f + \frac{4}{3}i\omega\eta)} \quad (5.15)$$

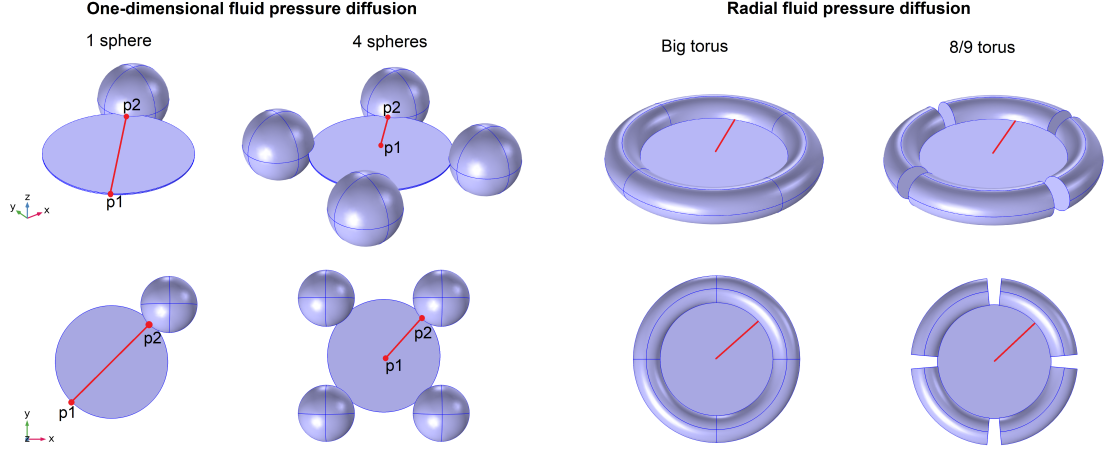


Figure 5.6: Sketch illustrating the definition of the squirt flow length l_{sq} for different geometries.

is a function of the rheology of the layer (e.g., *Tsai and Lee (1998)*), K_f is the fluid bulk modulus. For the derivation of the solution 5.14 with zero stress at the $x = l^{sq}$ boundary condition, we used elastic-viscoelastic correspondence principle (*Hashin, 1970*). A full derivation is given in a supplementary material (Maple script and a PDF with derivations). The resulting solution is

$$K_f^*(\omega) = 2i\omega\eta + (K_f - \frac{2}{3}i\omega\eta) \left[1 - \left(\frac{K_f - \frac{2}{3}i\omega\eta}{K_f + \frac{4}{3}i\omega\eta} \right) \frac{\tanh(\bar{k}_3)}{\bar{k}_3} \right], \quad (5.16)$$

where η is the fluid shear viscosity and

$$\bar{k}_3 = \frac{1}{\alpha} \sqrt{3i\omega\eta / (K_f + \frac{4}{3}i\omega\eta)}. \quad (5.17)$$

Note, that the solution 5.16 is the same as presented by *Tsai and Lee (1998)*.

The squirt flow aspect ratio, α^{sq}

The squirt flow length l^{sq} is the distance between the two points, p1 and p2; p1 is the most distant point (p1) in the crack from the pore(s), p2 is the point where crack is connected to a pore (see Figure 5.6). The squirt flow thickness h^{sq} is the crack aperture. For realistic cracks, the aperture varies due to asperities, then the minimum value of the aperture of the crack should be used (*Lissa et al., 2020*). Finally, the parameter controlling the characteristic frequency is the squirt flow aspect ratio α^{sq} ,

$$\alpha^{sq} = \frac{1}{2} \frac{h^{sq}}{l^{sq}}. \quad (5.18)$$

Figure 5.6 shows the definition of the squirt flow length parameter l_{sq} for different geometries. For 1 sphere and 4 sphere models, the expressions 5.16 and 5.8 for the crack stiffness relaxation should be used. Note, that the squirt flow length in the 1 sphere model is twice the squirt flow length in the 4 spheres model. For the Big torus or 8/9 torus models, the expression 5.23 and 5.8 should be used, since the fluid pressure diffusion is mainly radial. If the crack has finite thickness, then the expression 5.13 should be used instead of the expression 5.8.

5.3.4 Step 3: Stiffness of the fully saturated model

Once, the effective compliance matrix for the modified frame is calculated using the expression 5.2, we saturate the modified frame moduli with a fluid at each frequency using anisotropic Gassmann's equations (Gassmann, 1951) (see expression 5.3):

$$[C_{mn}^*(\omega)]_{\text{sat}} = \left([S_{mn}^*(\omega)]^{\text{MF}} \right)^{-1} + \alpha_m \alpha_n M, \quad (5.19)$$

$$\alpha_m = 1 - \left(\sum_{n=1}^3 C_{mn}^{\text{MF}} \right) / K_g / 3, \quad (5.20)$$

for $m = 1, 2, 3$ and $\alpha_4 = \alpha_5 = \alpha_6 = 0$, and where

$$M = \left(\phi / K_f + (1 - \phi) / K_g - K^* / K_g^2 \right)^{-1}, \quad (5.21)$$

$$K^* = \frac{1}{9} \sum_{m=1}^3 \sum_{n=1}^3 C_{mn}^{\text{MF}}(\omega), \quad (5.22)$$

where ϕ is the total porosity of the rock without the compliant porosity (which is neglected because it is usually two or more orders of magnitude lower than the stiff pore's porosity), K^* is the generalized bulk modulus of the modified frame and α_m is the Biot-Willis coefficient.

5.4 Validation: comparison against three-dimensional numerical solutions

Figure 5.7 shows results for the $[C_{33}^*(\omega)]_{\text{sat}}$ complex-valued component of the stiffness matrix the Big torus model, 1 sphere and 4 spheres models. Our analytical models are in good agreement with numerical solutions confirming that they can adequately describe the frequency-dependent stiffness and attenuation associated with squirt flow.

5.5 Discussion

Figure 5.8 shows results for the $[C_{33}^*(\omega)]_{\text{sat}}$ complex-valued component of the stiffness matrix the Big torus model, the Big torus plus the sphere in the center, and the crack with the sphere in the center. These results show that even a single crack interconnected to several pores can produce very smooth transition from low- to high-frequencies. Therefore, the usual belief that many cracks with a certain distribution of crack aspect ratios are needed to develop such a smooth transition is incorrect.

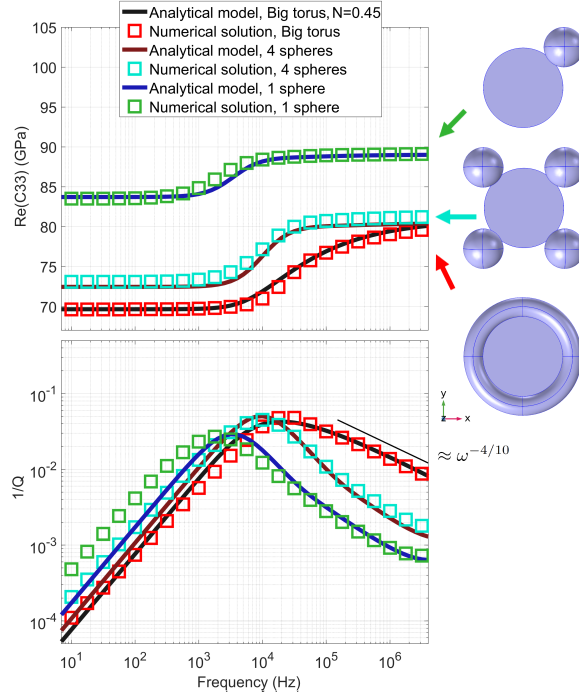


Figure 5.7: Numerical and analytical results for the Big torus, 4 spheres and 1 sphere models. The crack aspect ratio $\alpha = 0.01$: (a) Real part of the $[C_{33}^*(\omega)]_{\text{sat}}$ component and (b) dimensionless attenuation for the $[C_{33}^*(\omega)]_{\text{sat}}$ component. On the right, geometries of the pore-space are shown.

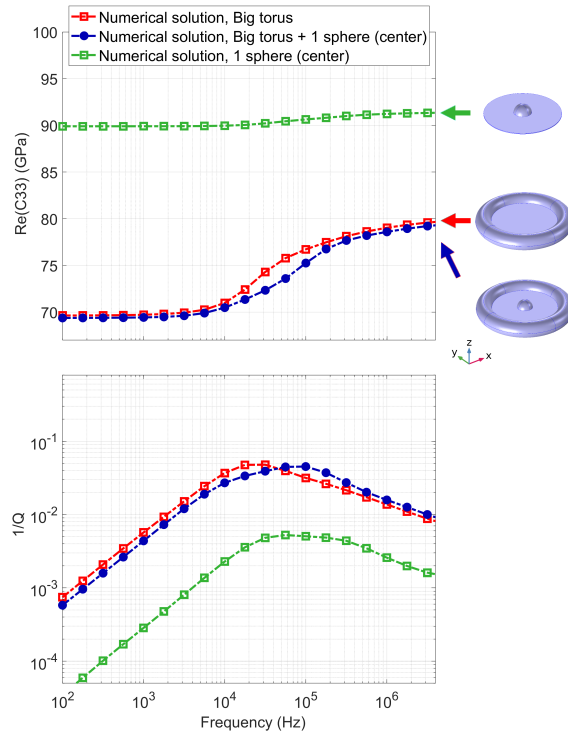


Figure 5.8: Numerical results for the Big torus model, the Big torus plus the sphere in the center, and the crack with the sphere in the center. The crack aspect ratio $\alpha = 0.01$: (a) Real part of the $[C_{33}^*(\omega)]_{\text{sat}}$ component and (b) dimensionless attenuation for the $[C_{33}^*(\omega)]_{\text{sat}}$ component. On the right, geometries of the pore-space are shown.

5.6 Conclusion

We have extended the analytical model for squirt flow associated seismic dispersion and attenuation presented in Part 1 to more complex geometries of the pore space, where the crack is partially connected to spherical pores. This geometry is much more closely representative of a rock pore space geometry than the classical geometry where the crack edge is fully connected to a toroidal pore. Our analytical model is in good agreement with accurate three-dimensional numerical simulations for a range of different geometries of the pore space. In our analytical model, we provide a general approach to calculate the elastic moduli of interconnected crack and pores. Even-though this approach is an approximation, the result is much better compared to the case where the inter-connectivity of cracks and pores is ignored in the calculation of the model compliances. We provide a good approximation for the relaxation of the crack stiffness due to fluid pressure diffusion, which makes our model accurate for the whole frequency band for different geometries. We showed that the crack aspect ratio does not control the characteristic frequency of squirt flow. Instead, we provide another parameter, squirt flow aspect ratio α^{sq} , which is a half of the ratio of the squirt flow thickness h^{sq} and the squirt flow length l^{sq} . If the crack aperture is constant, then the squirt flow thickness h^{sq} is equal to the crack thickness; if the crack aperture varies, then the squirt flow thickness h^{sq} is equal to the minimum aperture. The squirt flow length l^{sq} is the length between the point in the crack at the maximum distance from all pores and the point where the crack edge is connected to a pore.

5.7 Appendix A: Fluid pressure diffusion in a crack

Fluid pressure diffusion in a penny-shaped crack due to the applied strain to the walls of the crack is radial. For such a configuration the solutions are given by *Murphy et al.* (1986) for a boundary condition to the crack edge taking into account a finite volume of the pore and by *Chalhoub and Kelly* (1990); *Tsai and Lee* (1998) for zero fluid pressure boundary condition to the crack edge. However, if the sinusoidal strain is applied to the walls of the full model consisting of a crack connected to a torus and embedded into a solid material, the resulting fluid pressure diffusion in a crack is different due to presence of the torus (high pressure "ring anomaly" in Figure 5.2f). *Alkhimenkov and Quintal* (2021) proposed an approximation to the relaxation of the fluid pressure for the classical geometry by using the solution for a crack (*Murphy et al.*, 1986; *Chalhoub and Kelly*, 1990; *Tsai and Lee*, 1998) with a modified high-frequency asymptote. The present numerical analysis for a pore represented by fractions of a torus (Figure 5.2b-f) shows that the high high-frequency asymptote is different for models with different fractions of a torus. In the present study, we extend and improve the solution of *Alkhimenkov and Quintal* (2021) to capture the models having a crack connected to fractions of a torus (Figure 5.2b-f). We approximate the solution for crack stiffness relaxation via the frequency-dependent fluid bulk modulus $K_f^*(\omega)$ using the following branching function

$$K_f^*(\omega) = K_f - (K_f - y \cdot K_f^{LF}) / [1 - \zeta + \zeta(1 + i\omega\tau/\zeta^2)^N], \quad (5.23)$$

where $y = 0$ for the solution considering zero fluid pressure at the crack tip or $y = 1$ for the solution considering non-zero fluid pressure boundary condition at the crack tip. The parameter N denotes the slope of the high-frequency asymptote $1/Q$ of the fluid bulk $K_f^*(\omega)$ relaxation. If $N = 0.5$, then the expression 5.23 reduces to the expression 33 from *Alkhimenkov and Quintal* (2021), which is approximately valid for a toroidal pore. If $N \neq 0.5$, then the high-frequency asymptote of $K_f^*(\omega)$ relaxation is different; N is a function of the crack circumference connected to a (few) pore(s). A better result for a toroidal pore is achieved by taking $N = 0.45$, resulting in the slope of the $1/Q$ high-frequency asymptote of $\approx \omega^{-4/10}$. For 8/9 torus model, $N = 0.55$, resulting in the slope of the $1/Q$ high-frequency asymptote of $\approx \omega^{-4.5/10}$ (Figure 5.9). If $N > 0.55$, then the resulting slope is $\approx \omega^{-4.5/10}$. However, already for 6/9 torus model, the characteristic frequency shifts significantly and the expression 5.16 for a one-dimensional fluid pressure diffusion should be used.

We derived the expressions for ζ and τ analytically using the Maple symbolic environment. The resulting expressions are simple but cumbersome, they are given in a supplementary material (Matlab and Maple scripts,

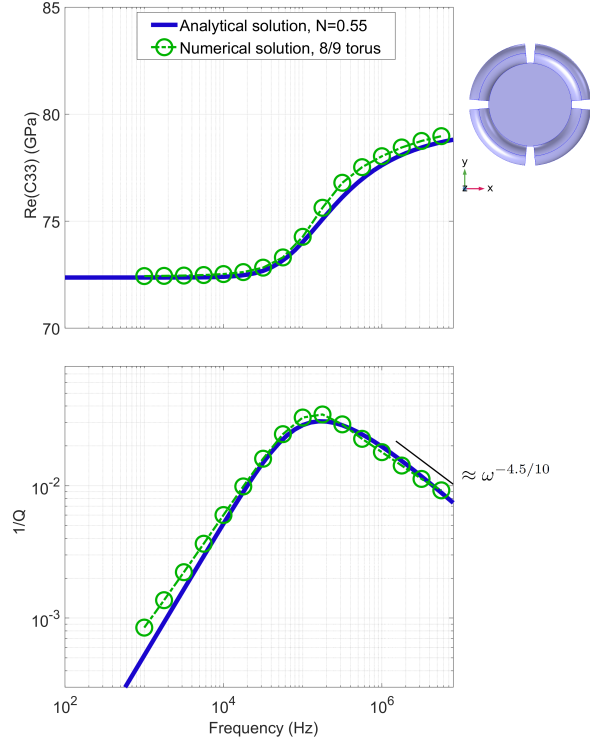


Figure 5.9: Numerical and analytical results for the 8/9 torus model: (a) Real part of the $[C_{33}^*(\omega)]_{\text{sat}}$ component and (b) dimensionless attenuation for the $[C_{33}^*(\omega)]_{\text{sat}}$ component. On the right, geometries of the pore-space are shown.

a PDF with a derivation). The characteristic frequency of $K_f^*(\omega)$ in the crack is

$$f_c^{\text{crack}} = \frac{4}{\sqrt{3}} \frac{\sqrt{K_f \cdot K_f^{LF}}}{\eta} \alpha^2. \quad (5.24)$$

The apparent fluid bulk modulus at low frequencies K_f^{LF} is

$$K_f^{LF} = \frac{V_{cr} K_f}{V_{cr} + V_{por}}. \quad (5.25)$$

A more accurate (and more cumbersome) expression for K_f^{LF} is also provided in supplementary material.

Chapter 6

Resolving wave propagation in anisotropic poroelastic media using graphical processing units (GPUs)

Yury Alkhimenkov, Ludovic Räss, Lyudmila Khakimova, Beatriz Quintal, Yury Podladchikov

Published¹ in *Journal of Geophysical Research: Solid Earth*.

¹Alkhimenkov, Y. et al. (2021). Resolving wave propagation in anisotropic poroelastic media using graphical processing units (GPUs). *Journal of Geophysical Research: Solid Earth*, e2020JB021175, doi:10.1029/2020JB021175

Abstract

Biot's equations describe the physics of hydro-mechanically coupled systems establishing the widely recognized theory of poroelasticity. This theory has a broad range of applications in Earth and biological sciences as well as in engineering. The numerical solution of Biot's equations is challenging because wave propagation and fluid pressure diffusion processes occur simultaneously but feature very different characteristic time scales. Analogous to geophysical data acquisition, high resolution and three dimensional numerical experiments lately re-defined state of the art. Tackling high spatial and temporal resolution requires a high-performance computing approach. We developed a multi-GPU numerical application to resolve the anisotropic elastodynamic Biot's equations that relies on a conservative numerical scheme to simulate, in a few seconds, wave fields for spatial domains involving more than 1.5 billion grid cells. We present a comprehensive dimensional analysis reducing the number of material parameters needed for the numerical experiments from ten to four. Furthermore, the dimensional analysis emphasizes the key material parameters governing the physics of wave propagation in poroelastic media. We perform a dispersion analysis as function of dimensionless parameters leading to simple and transparent dispersion relations. We then benchmark our numerical solution against an analytical plane wave solution. Finally, we present several numerical modeling experiments, including a three-dimensional simulation of fluid injection into a poroelastic medium. We provide the Matlab, symbolic Maple and GPU CUDA C routines to reproduce the main presented results. The high efficiency of our numerical implementation makes it readily usable to investigate three-dimensional and high-resolution scenarios of practical applications.

6.1 Introduction

Majority of the most powerful supercomputers on the world host hardware accelerators to sustain calculations at the petascale level and beyond. Graphical processing units (GPUs) are amongst widely employed hardware accelerators, initiating a revolution in high-performance computing (HPC) in the last decade. The three-dimensional calculations targeting billions of grid cells – technically impossible resolutions decades ago – became reality. This major breakthrough in HPC and supercomputing comes however with the cost of developing and re-engineering scientific codes to efficiently utilise the available computing power. Increasing the low-level parallelism is the key. In Earth sciences, HPC and GPU-accelerated applications target in particular forward and inverse seismic modeling and geodynamics – fields where high spatial and temporal resolutions as well as large spatial domains are required. We here develop a multi-GPU implementation for applications in seismic modeling in porous media.

Understanding seismic wave propagation in fluid-saturated porous media enables more accurate interpretation of seismic signals in Earth sciences. The two phase medium is represented by an elastic solid matrix (skeleton) saturated with a compressible viscous fluid. The dynamic response of such an isotropic two phase medium results in two longitudinal waves and one shear wave, as predicted by Frenkel (*Frenkel, 1944*) (see also *Pride and Garambois (2005)*). The wave of the first kind (fast wave) is a true longitudinal wave where the solid matrix motion and the fluid particle velocity are in-phase. The wave of the second kind (slow wave) is a highly attenuated wave where the solid matrix motion and the fluid particle velocity are out-of-phase. Depending on the medium's properties, the slow wave may propagate as a longitudinal wave, or it may diffuse and attenuate quickly. Maurice Anthony Biot performed systematic studies of solid-fluid deformation in porous media based on the Hamiltonian principle of least action. He first investigated a static loading known as the theory of consolidation (*Biot, 1941; Biot and Willis, 1957*). The mathematical description of the macroscopic coupled solid-fluid deformation in a porous medium is analogous to the theory of thermoelasticity (*Biot, 1941; Zimmerman, 2000*). Biot later developed the theory of poroelasticity or Biot's theory for wave propagation in fluid-saturated media (*Biot, 1956b,a*). Biot summarized these results in *Biot (1962a,b)* and provided a final set of unknown fields, parameters, as well as, a guidance to expand poroelasticity to include viscoelasticity and non-linear effects (*Biot, 1965*). Fluid flow in porous media in Biot's theory is assumed to be laminar, described by Darcy's law (*Biot, 1956b*), and is usually referred to as the low frequency Biot's theory. If the fluid flow is accelerated, viscous boundary layers form in the pores and a slight modification of Biot's equations is needed to account for this high frequency effect (*Biot, 1956a*). We focus in this study on the low frequency Biot's theory (*Biot, 1956b*). A detailed analysis of the coupled solid-fluid deformation in a porous media can be found in

various recent studies, e.g. *Bourbié et al.* (1987); *Wang* (2000); *Cheng* (2016). Approximations based on this theory are widely used in biology and medical imaging, and in Earth sciences (e.g., *Carcione* (2014)), they are used in seismic exploration, seismic monitoring of geological CO₂ sequestration and nuclear waste disposal, geothermal energy production and hydrogeology.

One of the main application of Biot's equations in Earth sciences is the estimation of seismic dispersion and attenuation in porous media due to wave-induced fluid flow. Several wave attenuation mechanisms related to fluid flow arise from Biot's theory (*Pride et al.*, 2004; *Müller et al.*, 2010). The first attenuation mechanism introduced by Biot is the global fluid flow, which occurs at the wavelength scale of a propagating wave. In this mechanism, the dissipation is caused by the relative fluid motion between the solid matrix and the fluid (*Biot*, 1956b). The second mechanism is the wave-induced fluid flow at the mesoscopic scale. This scale is defined as much larger than the sizes of individual pores but much smaller than the wavelength of a propagating wave (*White et al.*, 1975; *Pride et al.*, 2004). In this mechanism, the dissipation is caused due to fluid-pressure gradients arising between mesoscopic heterogeneities in the medium. For example, fluid-pressure gradients appear between highly permeable structures such as fractures and the embedding solid matrix of much lower permeability. Wave-induced fluid flow at microscopic scale also occurs and is referred to as squirt flow, in which fluid-pressure gradients take place between compliant and stiff pores (*Mavko and Nur*, 1975; *Dvorkin et al.*, 1995). Other mechanisms involve different kinds of wave scattering and wave mode conversions at interfaces. Possible non-linear viscous and plastic effects are small for most of the applications in applied seismic and are then neglected under the linear approximation assumption.

The aforementioned analytical approaches for wave-induced fluid flow at global and mesoscopic scales mainly exist for simple geometries. For more complex geometries, a numerical approach is needed to estimate seismic dispersion and attenuation. In principle, it can be done numerically in two ways. One approach relies on direct modeling of wave propagation in porous media and estimation of dispersion and attenuation of a propagating wavelets (*Masson et al.*, 2006; *Caspari et al.*, 2019). The other approach is based on a quasi-static numerical modeling and estimation of effective frequency-dependent elastic properties. The modeled frequency-dependent properties are used to retrieve dispersion and attenuation of seismic waves (*Masson and Pride*, 2007; *Rubino et al.*, 2009; *Quintal et al.*, 2011; *Hunziker et al.*, 2018).

During the last three decades a significant number of studies targeted numerical simulations of wave propagation in poroelastic media. A detailed review of early studies is given in *Carcione et al.* (2010). Different methods have been used, based on combined finite-volumes/differences on structured grids (*Zhu and McMechan*, 1991; *Dai et al.*, 1995; *Carcione and Quiroga-Goode*, 1995; *Özdenvar and McMechan*, 1997; *Zeng et al.*, 2001; *Masson et al.*, 2006; *Wenzlau and Müller*, 2009; *Chiavassa et al.*, 2010; *Chiavassa and Lombard*, 2011; *Blanc et al.*, 2013), pseudo-spectral methods (*Özdenvar and McMechan*, 1997), discontinuous Galerkin methods (*de la Puente et al.*, 2008; *Dupuy et al.*, 2011; *Ward et al.*, 2017; *Zhan et al.*, 2019; *Shukla et al.*, 2019, 2020), spectral element methods (*Morency and Tromp*, 2008), finite-volume methods (*Lemoine et al.*, 2013; *Lemoine*, 2016). Most of these studies implemented the corresponding equations as a first-order hyperbolic system and used explicit time integration schemes as it is convenient for the elastic wave propagation, except for (*Özdenvar and McMechan*, 1997; *Morency and Tromp*, 2008), where a second-order system was considered. *Moczo et al.* (2019) and *Gregor et al.* (2021) investigated the accuracy of the discrete characterization of material heterogeneities and subcell-resolution for the finite-difference modeling of Biot's equations.

A major challenge in the numerical modeling of Biot's equations relies in the treatment of the dissipation term in the equations of motions. This term is represented by a parabolic operator coupled to viscosity, permeability and density and affects the numerical stability of the entire system of equations. The diffusion process exhibit a much larger characteristic time scale then the wave propagation process, which makes Biot's equations "stiff", thus challenging to solve. A straightforward explicit time integration of a "stiff" system is possible but requires very small time steps and is computationally inefficient. Various studies discuss stability conditions in the scope of poroelastic wave propagation and report a series of issues (*Carcione and Quiroga-Goode*, 1995; *Masson et al.*, 2006; *Chiavassa and Lombard*, 2011). A more detailed discussion regarding the stability of discrete schemes of Biot's equations can be found in *Alkhimenkov et al.* (2020c).

We here propose a multi-GPU numerical implementation of the anisotropic elastodynamic Biot's equations building upon three key ideas: Concise numerical implementation, high numerical resolution and high computational efficiency. A concise numerical implementation means that we designed a simple and short numerical

code ensuring it is suitable for parallel GPU devices. We use a variant of a conservative staggered space-time grid discretization (Virieux, 1986), which is equivalent to a finite volume approach (Dormy and Tarantola, 1995). High numerical spatial resolution up to 6 billion grid cells permits us to resolve very complex geometries. High computational efficiency allows our numerical model to simulate, in a few seconds only, wave fields in domains involving over 1.5 billion grid cells. We further explore several aspects of Biot’s equations, namely, wave propagation in poroelastic isotropic and anisotropic media, fluid diffusion, dimensional and dispersion analyses and numerical stability. The resulting code is implemented in CUDA C, which is suitable for programmable Nvidia GPU devices. The choice of a rectangular grid is determined by the usage of GPUs, so that the numerical implementation is straightforward. We provide the Matlab, symbolic Maple and GPU CUDA C routines to reproduce the main presented results. These routines are available for download from Bitbucket at https://bitbucket.org/yalkhimenkov/fastbiot_gpu3d_v1.0 (last access: 8 February 2021). The routines archive (v1.0) (Alkhimenkov et al., 2021a) is available from a permanent DOI repository (Zenodo) at <http://doi.org/10.5281/zenodo.4519367> (last access: 8 February 2021).

The novelties of the present article are summarized as following:

1. We present a dimensional analysis, reducing the number of needed material parameters from ten to four.
2. We perform a dispersion analysis as a function of dimensionless parameters.
3. We achieve a close-to-ideal parallel efficiency (98% and 96%) on a weak scaling tests up to 128 GPUs and an effective memory throughput efficiency of 90% for the 3D anisotropic poroelastic wave propagation code.
4. We achieve a very fast execution time (seconds) using high-resolution models involving more than 1.5 billion grid cells.

6.2 Elastodynamic Biot’s equations in isotropic media

6.2.1 Constitutive equations

Table 6.1: List of Principal Notation

Symbol	Meaning	Unit
σ^s, σ^f	solid and fluid stress	Pa
p_s, p_f	solid and fluid pressure	Pa
τ^s, τ^f	solid and fluid stress deviator	Pa
v^s, v^f	solid and fluid particle velocity	m/s
ρ^s, ρ^f	solid and fluid density	kg/m ³
K_g, K_f	elastic solid and fluid bulk modulus	Pa
G_g, G	elastic solid and drained shear modulus	Pa
K_d, K_u	elastic drained and undrained bulk modulus	Pa
η	fluid shear viscosity	Pa·s
k	permeability	m ²
ϕ	porosity	-

We describe the elastodynamic Biot’s equations for an isotropic medium saturated with a single phase fluid. We use a classical velocity-stress formulation for the Biot’s equations. The equations describing a two phase continuum mainly differ from the single phase continuum formulation (see 6.8) by the presence of both solid

Table 6.2: Shorthand notations

Symbol	Meaning
\bar{p}	$= (1 - \phi)p_s + \phi p_f$, total pressure
$\bar{\sigma}$	total stress
$\bar{\tau}$	total stress deviator
q_i^D	$= \phi(v_i^f - v_i^s)$, Darcy's flux
ρ_t	$= (1 - \phi)\rho + \phi\rho$, total density
α	Biot-Willis coefficient
B	Skempton's coefficient
δ_{ij}	Kronecker delta

and fluid particle velocities and as well as both solid and fluid pressure fields. Furthermore, the scalar parameters linking stresses and particle velocities in the single phase continuum become a symmetric coefficient matrix in the two phase continuum. The set of equations describing a two phase continuum (solid and fluid) was formulated in the theory of poroelasticity (*Biot*, 1956b, 1962b). The symmetric coefficient matrix is positive definite, which directly follows from the elastic potential energy. Biot's equations can be written in a symmetric form by separating volumetric and deviatoric parts of the stress tensor. Lists of symbols are given in Tables 7.1 and 6.2. The constitutive equations are (*Biot*, 1962b; *Pride et al.*, 2004; *Wang*, 2000; *Yarushina and Podladchikov*, 2015)

$$\begin{pmatrix} \nabla_k v_k^s \\ \nabla_k q_k^D \end{pmatrix} = -\frac{1}{K_d} \begin{pmatrix} 1 & -\alpha \\ -\alpha & \frac{\alpha}{B} \end{pmatrix} \begin{pmatrix} \frac{\partial \bar{p}}{\partial t} \\ \frac{\partial p_f}{\partial t} \end{pmatrix} \quad (6.1)$$

and

$$\frac{\partial \bar{\tau}_{ij}}{\partial t} = 2G \left(\frac{1}{2} (\nabla_j v_i^s + \nabla_i v_j^s) - \frac{1}{3} (\nabla_k v_k^s) \delta_{ij} \right), \quad (6.2)$$

linking the stress-strain relations for the solid and fluid phases with the conservation of mass (equation (6.1)) and representing the deviatoric stress-strain relation for the solid phase (equation (6.2)). The constitutive equations (6.1)-(6.2) are written for the total pressure \bar{p} and fluid pressure p_f , as it was originally suggested in *Biot* (1962b). The porosity ϕ in Darcy's flux q_i^D is constant in time but can be different spatially throughout the model domain.

For an isotropic material saturated with a single fluid, in which the solid frame consists of a single isotropic mineral, the Biot-Willis coefficient is

$$\alpha = 1 - K_d / K_g = (1 - K_d / K_u) / B, \quad (6.3)$$

where K_u is the undrained bulk modulus

$$K_u = K_d + \alpha^2 M, \quad (6.4)$$

M is the fluid storage coefficient

$$M = \left(\phi / K_f + (1 - \phi) / K_g - K_d / K_g^2 \right)^{-1} \quad (6.5)$$

or

$$M = BK_u / \alpha, \quad (6.6)$$

and the Skempton's coefficient B reads

$$B = \frac{1/K_d - 1/K_g}{1/K_d - 1/K_g + \phi(1/K_f - 1/K_g)}. \quad (6.7)$$

6.2.2 Dynamic equations

The conservation of linear momentum (Newton's second law or dynamic equations) can be written in a symmetric form (Biot, 1962b; Pride *et al.*, 2004; Wang, 2000; Yarushina and Podladchikov, 2015)

$$\begin{pmatrix} \nabla_j (-\bar{p}\delta_{ij} + \bar{\tau}_{ij}) \\ \frac{\eta}{k} q_i^D + \nabla_i p_f \end{pmatrix} = \begin{pmatrix} \rho_t & -\rho_f \\ -\rho_f & \rho_a \end{pmatrix} \begin{pmatrix} \frac{\partial v_i^s}{\partial t} \\ \frac{\partial q_i^D}{\partial t} \end{pmatrix}, \quad (6.8)$$

where $\rho_a = \rho_f T/\phi$, T is the tortuosity and $i, j, k = \overline{1, \dots, 3}$. The off-diagonal parameter fluid density ρ_f can be considered as the added mass coefficient. Equation (6.8) is analogous to that of a single phase media (equation (6.70)), the only difference being the substitution of the scalar density by a coefficient matrix with same dimensions.

Equations (6.1)-(6.8) are the elastodynamic Biot's equations for an isotropic medium saturated with a single phase fluid. The experiments to obtain poroelastic parameters are given in 6.9. We emphasize that the matrices of coefficients in equations (6.1) and (6.8) are symmetric. This symmetry combined with the non-dimensional analysis make it possible to derive the dispersion relations in a simple explicit form using symbolic calculations (Maple).

6.3 Dimensional analysis of the elastodynamic Biot's equations

Dimensional analysis of PDEs unveils the impact of various physical parameters on the considered physical system. The original Biot's equations (6.1)-(6.8) contain many material parameters making it difficult to understand how they affect the response of a poroelastic continuum. For enhanced clarity, we present a dimensional analysis of the elastodynamic Biot's equations. This analysis reduces the number of material parameters from ten to four, isolating the governing independent physical quantities.

For conciseness, we present our physical system as a one dimensional example to express the total stress tensor as a combination of the volumetric and deviatoric stresses (the entire analysis can be applied to three-dimensional continuum)

$$\frac{\partial \bar{\sigma}}{\partial t} = -\frac{\partial \bar{p}}{\partial t} + \frac{\partial \bar{\tau}}{\partial t} \quad (6.9)$$

We introduce the compliance s_{11}^d [Pa^{-1}] and the total density ρ_t [kg/m^3] to express equations (6.1), (6.2) and (6.8) in a dimensionless form. Compliance s_{11}^d relates to the drained bulk modulus K_d and the shear modulus G

$$s_{11}^d = 1/(K_d + 4/3G), \quad (6.10)$$

which has dimensions of [Pa^{-1}]. We first extract s_{11}^d and ρ_t out of the parentheses in equations (6.1), (6.2) and (6.8) (leaving only dimensionless parameters inside). We reformulate the system using equation (6.9) as

$$s_{11}^d \begin{pmatrix} 1 & -\alpha \\ -\alpha & \alpha_a \end{pmatrix} \begin{pmatrix} -\frac{\partial \bar{\sigma}}{\partial t} \\ \frac{\partial p_f}{\partial t} \end{pmatrix} = -\begin{pmatrix} \frac{\partial v^s}{\partial x} \\ \frac{\partial q^D}{\partial x} \end{pmatrix} \quad (6.11)$$

and

$$\rho_t \begin{pmatrix} 1 & -\frac{\rho_f}{\rho_t} \\ -\frac{\rho_f}{\rho_t} & \frac{\rho_a}{\rho_t} \end{pmatrix} \begin{pmatrix} \frac{\partial v^s}{\partial t} \\ -\frac{\partial q^D}{\partial t} \end{pmatrix} = \begin{pmatrix} \frac{\partial \bar{\sigma}}{\partial x} \\ \frac{\eta}{k} q^D + \frac{\partial p_f}{\partial x} \end{pmatrix}, \quad (6.12)$$

where

$$\alpha_a = \frac{\alpha}{B} \left(1 + \frac{4/3G}{K_u} \right), \quad (6.13)$$

is a dimensionless parameter (the apparent Biot-Willis coefficient).

We then substitute

$$\bar{\sigma} \rightarrow \frac{1}{s_{11}^d} \tilde{\sigma}, \quad p_f \rightarrow \frac{1}{s_{11}^d} \tilde{p}_f, \quad (6.14)$$

$$v^s \rightarrow \frac{L_x^*}{\tau^*} \tilde{v}^s, \quad q^D \rightarrow \frac{L_x^*}{\tau^*} \tilde{q}^D, \quad (6.15)$$

$$x \rightarrow L_x^* \tilde{x}, \quad t \rightarrow \tau^* \tilde{t}, \quad (6.16)$$

where L_x^* [m] is the characteristic length, τ^* [s] is the characteristic time and the superscript \sim refers to the dimensionless quantities. The resulting system of equations reads

$$\begin{pmatrix} 1 & -\alpha \\ -\alpha & \alpha_a \end{pmatrix} \begin{pmatrix} -\frac{\partial \tilde{\sigma}}{\partial \tilde{t}} \\ \frac{\partial \tilde{p}_f}{\partial \tilde{t}} \end{pmatrix} = - \begin{pmatrix} \frac{\partial \tilde{v}^s}{\partial \tilde{x}} \\ \frac{\partial \tilde{q}^D}{\partial \tilde{x}} \end{pmatrix} \quad (6.17)$$

and

$$(I_1)^2 \begin{pmatrix} 1 & -\rho_{ft} \\ -\rho_{ft} & \rho_{at} \end{pmatrix} \begin{pmatrix} \frac{\partial \tilde{v}^s}{\partial \tilde{t}} \\ -\frac{\partial \tilde{q}^D}{\partial \tilde{t}} \end{pmatrix} = \begin{pmatrix} \frac{\partial \tilde{\sigma}}{\partial \tilde{x}} \\ I_2 \tilde{q}^D + \frac{\partial \tilde{p}_f}{\partial \tilde{x}} \end{pmatrix}, \quad (6.18)$$

where $\rho_{ft} \equiv \rho_f / \rho_t$, $\rho_{at} \equiv \rho_a / \rho_t$,

$$I_1 = \sqrt{\rho_t s_{11}^d} \frac{L_x^*}{\tau^*} \equiv \frac{1}{V_d} \frac{L_x^*}{\tau^*}, \quad (6.19)$$

$$V_d = \sqrt{\frac{1}{\rho_t s_{11}^d}} \quad (6.20)$$

and

$$I_2 = \frac{\eta s_{11}^d (L_x^*)^2}{k \tau^*} \equiv \frac{1}{D} \frac{(L_x^*)^2}{\tau^*}, \quad (6.21)$$

$$D = \frac{k}{\eta s_{11}^d}. \quad (6.22)$$

The four dimensionless parameters α , α_a , ρ_{ft} and ρ_{at} define the coupling between the solid and fluid phase. The two key dimensionless parameters I_1 , I_2 denote the ratio between advection and diffusion time scales and relate to hyperbolic (advection) and parabolic (diffusion) processes, respectively. The pore fluid pressure transport time scale

$$\tau_d^* = \frac{(L_x^*)^2}{D} \quad (6.23)$$

refers to the characteristic time scale of diffusive processes. The elastic travel time scale

$$\tau_a^* = \frac{L_x^*}{V_d} \quad (6.24)$$

refers to the characteristic time scale of advection processes. In order to further reduce the number of parameters, we set $I_1 = 1$. From equation (6.19), $L_x^* = \tau^* V_d$, therefore, equation (6.21) becomes

$$I_2 = \frac{\eta}{k\rho_t} \tau^*, \quad (6.25)$$

where τ^* is a free parameter. We further choose τ^* as

$$\tau^* = \left(\frac{\eta}{k\rho_t} \right)^{-1}. \quad (6.26)$$

Equation (6.25) becomes

$$I_2 = \frac{\eta}{k\rho_t} \tau^* = \frac{\eta}{k\rho_t} \left(\frac{\eta}{k\rho_t} \right)^{-1} \equiv 1 \quad (6.27)$$

Taking into account that $I_1 = 1$ and $I_2 = 1$, we reformulate equation (6.18) as

$$\begin{pmatrix} 1 & -\rho_{ft} \\ -\rho_{ft} & \rho_{at} \end{pmatrix} \begin{pmatrix} \frac{\partial \tilde{v}^s}{\partial \tilde{t}} \\ -\frac{\partial \tilde{q}^D}{\partial \tilde{t}} \end{pmatrix} = \begin{pmatrix} \frac{\partial \tilde{\sigma}}{\partial \tilde{x}} \\ \tilde{q}^D + \frac{\partial \tilde{p}_f}{\partial \tilde{x}} \end{pmatrix}. \quad (6.28)$$

Equations (6.17) and (6.28) are the dimensionless elastodynamic Biot's equations for an isotropic medium saturated with a single fluid featuring only four dimensionless parameters: α , α_a , ρ_{ft} and ρ_{at} .

6.3.1 Dispersion analysis of the elastodynamic Biot's equations

We perform dispersion analysis to understand the behavior of the dimensionless elastodynamic Biot's equations (6.17)-(6.18). For simplicity, we only consider longitudinal waves. A single harmonic plane wave solution is

$$W = A e^{-i(\omega t - kl)}, \quad (6.29)$$

where A is the amplitude, i is the imaginary unit, $\omega = 2\pi f$ is the real angular frequency (f is the frequency), k is the complex wave number and l is the propagation direction. This solution is substituted into the system (6.17)-(6.18), which gives

$$\begin{bmatrix} i\omega & i\omega\alpha & ik & 0 \\ -i\omega\alpha & -i\omega\alpha_a & 0 & ik \\ -ik & 0 & -i\omega(I_1)^2 & -i\omega(I_1)^2\rho_{ft} \\ 0 & -ik & i\omega(I_1)^2\rho_{ft} & i\omega(I_1)^2\rho_{at} - I_2 \end{bmatrix} \quad (6.30)$$

The dispersion relation for longitudinal waves is

$$k^4 - a_2k^2 + a_0 = 0, \quad (6.31)$$

where

$$a_2 = (1 + \rho_{at}\alpha_a - 2\rho_{ft}\alpha)(I_1)^2\omega^2 + i\omega\alpha_a I_2 \quad (6.32)$$

$$a_0 = (I_1)^4 (\rho_{ft}^2 - \rho_{at}) (\alpha^2 - \alpha_a) \omega^4 - i\omega^3 (\alpha^2 - \alpha_a) (I_1)^2 I_2 \quad (6.33)$$

Equation (6.31) is bi-quadratic with respect to k , the four roots ($\pm k_1$ and $\pm k_2$) are the complex functions of the non-dimensional angular frequency ω

$$k_{1,2} = \pm \sqrt{\frac{a_2 \mp \sqrt{a_2^2 - 4a_0}}{2}} \quad (6.34)$$

The non-dimensional fast and slow wave phase velocities are

$$\tilde{V}_1 = \omega/\text{Re}(k_1), \quad \tilde{V}_2 = \omega/\text{Re}(k_2) \quad (6.35)$$

The inverse quality factors are defined as

$$\frac{1}{Q_1} = \frac{\text{Im}(k_1^2)}{\text{Re}(k_1^2)}, \quad \frac{1}{Q_2} = \frac{\text{Im}(k_2^2)}{\text{Re}(k_2^2)}. \quad (6.36)$$

If $I_2 \equiv 0$, the fast and slow waves become the real and non-dispersive functions of the angular frequency ω . Since $I_2 \equiv 0$ eliminates \tilde{q}^D in (6.18), the system of equations (6.17)-(6.18) becomes fully hyperbolic without the diffusive term. I_2 and the Biot-Willis coefficients α and α_a control the imaginary part of the wave numbers $\pm k_1$ and $\pm k_2$; they thus control dispersion and attenuation of the coupled system of equations. Setting $\alpha_a \equiv 0$ and $(\alpha^2 - \alpha_a) \equiv 0$ provides an alternative way to achieve real roots in (6.34).

Setting $I_1 = 1$ and $I_2 = 1$ and using the characteristic length ($L_x^* = \tau^* V_d$) and time ($\tau^* = \eta/(k\rho_t)$) scales permits to further simplify the dispersion relations (6.31)-(6.33) to

$$k^4 + ((2\rho_{ft}\alpha - \rho_{at}\alpha_a - 1)\omega^2 - i\omega\alpha_a)k^2 + (\rho_{ft}^2 - \rho_{at})(\alpha^2 - \alpha_a)\omega^4 - i\omega^3(\alpha^2 - \alpha_a) = 0, \quad (6.37)$$

which results in a bi-quadratic equation with respect to k . The four roots ($\pm k_1$ and $\pm k_2$) are the complex functions of the angular frequency ω . The dispersion relation (6.37) is the most important result of the dimensional analysis and relates to the final set of non-dimensional elastodynamic Biot's equations (equations (6.17) and (6.28)).

Figure 6.1a shows the non-dimensional phase velocities and inverse quality factors based on the system of equations (6.17) and (6.28) for a homogeneous medium, which are typical for Biot's mechanism. The properties of the medium are given in Table 6.3. The non-dimensional phase velocity \tilde{V}_1 exhibits some dispersion (less than

Table 6.3: Poroelastic properties of carbonate.

Rock properties		Carbonate
with independent units		
K_d	(GPa)	26
$\eta_k = \eta/k$	(Pa·s/m ²)	$0.001/10^{-12} = 1 \cdot 10^9$
ρ_s	(kg/m ³)	2700
nondimensional		
ϕ		0.3
T		1.9
with dependent units		
G_d	(GPa)	$15/13 \cdot K_d$
K_f	(GPa)	$0.0865 \cdot K_d$
ρ_f	(kg/m ³)	$0.4 \cdot \rho_s$
K_s	(GPa)	$1.42 \cdot K_d$

10%) and attenuation. The non-dimensional phase velocity \tilde{V}_2 behaves as a diffusion mode at low frequencies, having zero velocity. At higher frequencies, \tilde{V}_2 behaves as a true propagating wave. The low frequency limit of \tilde{V}_1 corresponds to the non-dimensional undrained phase velocity \tilde{V}_1^{LF} ,

$$\tilde{V}_1^{LF} = \frac{1}{V_d} \sqrt{\frac{K_u + 4/3G_d}{\rho_t}}. \quad (6.38)$$

The high frequency limit of \tilde{V}_1 corresponds to the non-dimensional undrained phase velocity \tilde{V}_1^{HF} which is larger than \tilde{V}_1^{LF} . We calculate \tilde{V}_1^{HF} from the dispersion relations under the assumption of $\omega \rightarrow +\infty$. The explicit formula is given in the following section.

Multiplying non-dimensional phase velocities (\tilde{V}_1 and \tilde{V}_2) by the drained velocity V_d (equation (6.20)) permits to recover the dimensional form of the dispersion curves (Figure 6.1b). We retrieve the dimensional angular frequency $\omega^d = \omega \omega^*$, where ω is the non-dimensional angular frequency (the y -axis in Figure 6.1a) and ω^* is the transformation frequency

$$\omega^* = \frac{1}{\tau^*} \equiv \frac{\eta}{k\rho_t}. \quad (6.39)$$

We highlight that the introduced transformation frequency ω^* is similar to Biot's characteristic frequency

$$\omega_c = \frac{\eta\phi}{k\rho_f T}. \quad (6.40)$$

We detail a dimensional analysis where the transformation frequency coincides with Biot's characteristic frequency in 6.10.

Figure 6.2 illustrates the advantage of the non-dimensional equations over their dimensional analog. The inverse quality factor $1/Q_1$ for the non-dimensional elastodynamic Biot's equations (Figure 6.2b) collapsed into the one curve considering the dimensional equations (Figure 6.2a).

The roots k_1 and k_2 of the dispersion relation (6.37) are the functions of the four material parameters and the non-dimensional angular frequency ω , i.e. $k_1 = f(\alpha, \alpha_a, \rho_{ft}, \rho_{at})$ and $k_2 = f(\alpha, \alpha_a, \rho_{ft}, \rho_{at})$. Let us analyze the solutions (6.35) and (6.36) as a function of the material parameters and ω . The non-dimensional phase velocities (\tilde{V}_1 and \tilde{V}_2) and the corresponding quality factors ($1/Q_1$ and $1/Q_2$) as a function of the non-dimensional frequency ω and the Biot-Willis coefficient α are shown in Figure 6.3. According to (6.17), α controls the coupling between solid and fluid phases, low values of α (0 – 0.3) correspond to weak coupling and high values of α (0.7 – 1.0) correspond to strong coupling. We vary α in the range of [0.05, 0.95] while the other parameters remain the same. \tilde{V}_1 non-linearly depends on α in the whole frequency range, as α increases, \tilde{V}_1 also increases (Figure 6.3a). $1/Q_1$ linearly depends on α , as α increases, $1/Q_1$ only slightly decreases (Figure 6.3b). \tilde{V}_2

and $1/Q_2$ are almost independent of α (Figures 6.3c, 6.3d). At low frequencies, \tilde{V}_2 is almost zero and the quality factor $1/Q_2$ is very high (Figure 6.3c-d), which corresponds to the diffusive regime of \tilde{V}_2 . At high frequencies, \tilde{V}_2 is significant and the quality factor $1/Q_2$ is almost zero, which corresponds to the regime where the slow wave behaves as a true longitudinal wave. The characteristic frequency where the transition from the diffusive to propagation regimes occurs is not affected by α .

Figure 6.4 is similar to Figure 6.3 but instead of α , the variations of ρ_{ft} are shown. We vary ρ_{ft} in the range of $[0.1, \sqrt{\rho_{at}}]$ while the other parameters remain the same. The non-dimensional parameter ρ_{ft} controls the coupling between solid and fluid phases in the dynamic equations (6.18). \tilde{V}_1 and $1/Q_1$ non-linearly depend on ρ_{ft} (Figures 6.4a and 6.4b), while at low frequencies ($\omega \in [10^{-4}, 10^{-1}]$), \tilde{V}_1 is independent on ρ_{ft} (Figure 6.4a). \tilde{V}_2 and $1/Q_2$ are almost independent on ρ_{ft} in the whole frequency range (Figures 6.4c, 6.4d).

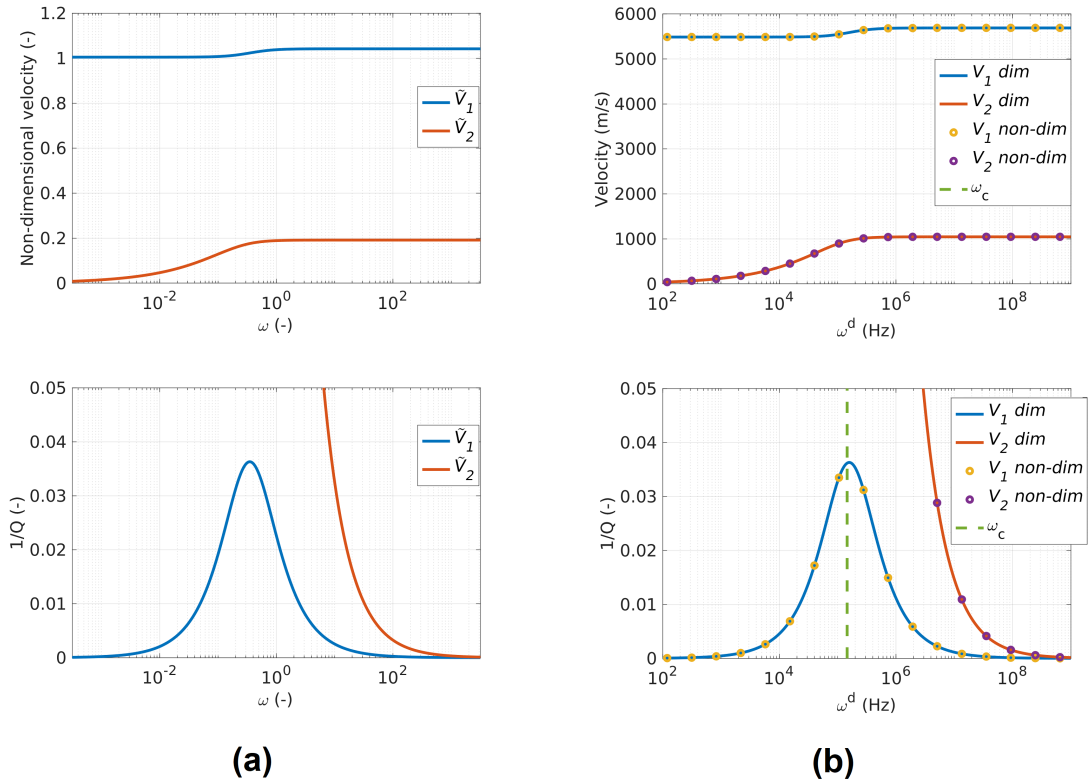


Figure 6.1: Phase velocities and the corresponding inverse quality factors $1/Q$ obtained via the dispersion analysis. (a) Dispersion relations for the non-dimensional elastodynamic Biot's equations, \tilde{V}_1 is the wave of the first kind (non-dimensional), \tilde{V}_2 is the wave of the second kind (non-dimensional). (b) Dispersion relations for the dimensional elastodynamic Biot's equations. V_1 dim and V_2 dim correspond to dimensional velocities, V_1 non-dim and V_2 non-dim correspond to non-dimensional velocities, which were re-scaled by the dimensional characteristic velocity V_d and the transformation frequency ω^* . ω_c is the Biot's characteristic frequency. The material parameters are those from Table 6.3.

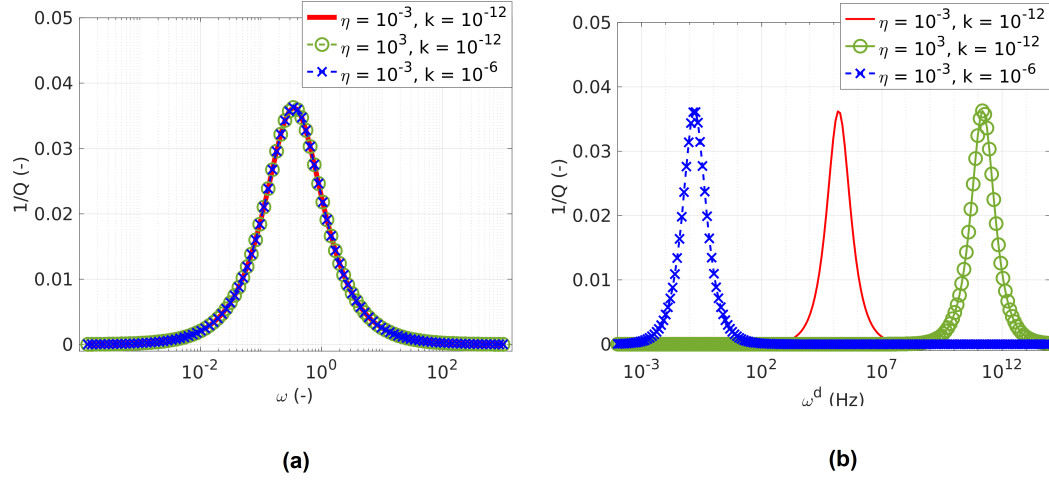


Figure 6.2: The inverse quality factors $1/Q$ of the wave of the first kind. (a) $1/Q$ for the non-dimensional elastodynamic Biot's equations having different viscosities and permeabilities, all collapsed into one curve. (b) $1/Q$ for the dimensional elastodynamic Biot's equations for the same data set of viscosities and permeabilities. The material parameters are those from Table 6.3, except for viscosities and permeabilities.

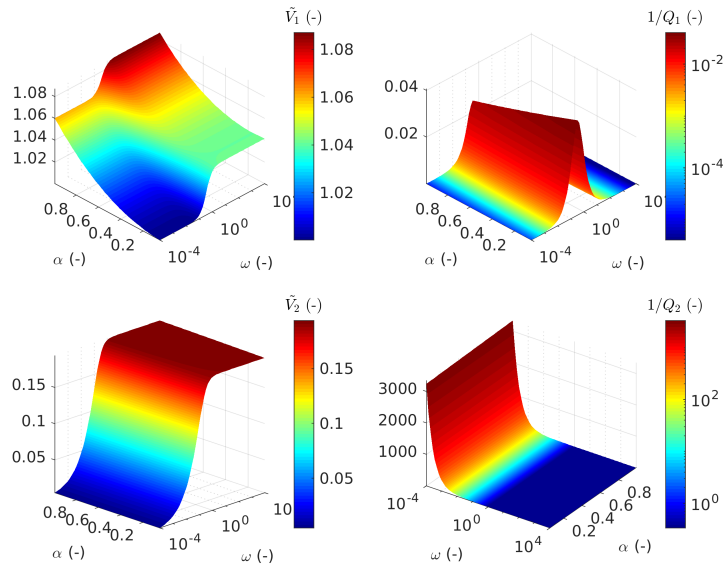


Figure 6.3: Non-dimensional phase velocities (\tilde{V}_1 and \tilde{V}_2) and the corresponding quality factors ($1/Q_1$ and $1/Q_2$) as a function of the non-dimensional Biot-Willis coefficient α and the non-dimensional angular frequency ω . The material parameters are those from Table 6.3.

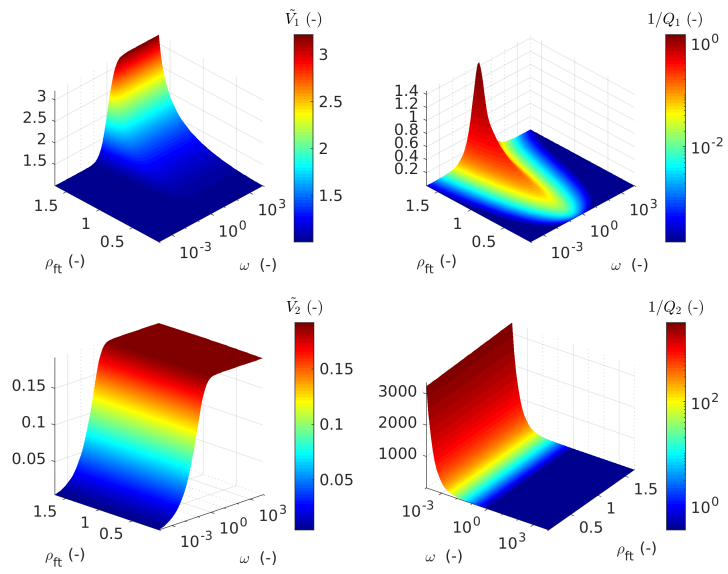


Figure 6.4: Non-dimensional phase velocities (\tilde{V}_1 and \tilde{V}_2) and the corresponding quality factors ($1/Q_1$ and $1/Q_2$) as a function of the non-dimensional parameter ρ_{ft} and the non-dimensional angular frequency ω . The material parameters are those from Table 6.3.

6.4 Numerical implementation of the elastodynamic Biot's equations

We solve the first order velocity-stress formulation of the elastodynamic Biot's equations (6.1)-(6.8) on a rectangular time-space grid. We base our approach on a conservative staggered space-time grid discretization (Virieux, 1986); for Darcy's flux, we use a semi-implicit discretization (Alkhimenkov et al., 2020c). A conservative staggered space-time grid discretization is equivalent to a finite volume approach (Dormy and Tarantola, 1995) (see also LeVeque (1992)). This approach follows from the early Marker and Cell (MAC) method which is a classical method in computational fluid dynamics (Harlow and Welch, 1965; McKee et al., 2008). Field variables are located either at the cell center or corners and fluxes are computed at the cell boundaries resulting in a conservative staggered grid formulation. Other similar methods were developed such as the standard staggered grid scheme (Virieux and Madariaga, 1982; Virieux, 1986; Levander, 1988), the rotated staggered grid scheme (Saenger et al., 2000) and the Lebedev scheme (Lebedev, 1964; Davydycheva et al., 2003; Lisitsa and Vishnevskiy, 2010). The elastodynamic Biot's equations using the standard staggered grid scheme were solved by Masson et al. (2006). Moczo et al. (2007) provides a review on staggered finite-difference methods for wave propagation in elastic media.

6.4.1 The first order elastodynamic Biot's equations with a volumetric-deviatoric split

Numerically solving the elastodynamic Biot's equations (6.1) and (6.8) requires the coefficient matrices in (6.1) and (6.8) to be inverted. This formulation leads to a system of equations describing poroelastic wave propagation in three-dimensional media and can be solved explicitly:

$$\begin{pmatrix} \frac{\partial \bar{p}}{\partial t} \\ \frac{\partial p_f}{\partial t} \end{pmatrix} = -K_u \begin{pmatrix} 1 & B \\ B & \frac{B}{\alpha} \end{pmatrix} \begin{pmatrix} \nabla_k v_k^s \\ \nabla_k q_k^D \end{pmatrix}, \quad (6.41)$$

$$\frac{\partial \bar{\tau}_{ij}}{\partial t} = 2G \left(\frac{1}{2} (\nabla_i v_j^s + \nabla_j v_i^s) - \frac{1}{3} (\nabla_k v_k^s) \delta_{ij} \right) \quad (6.42)$$

and

$$\begin{pmatrix} \frac{\partial v_i^s}{\partial t} \\ -\frac{\partial q_i^D}{\partial t} \end{pmatrix} = \frac{1}{\Theta} \begin{pmatrix} \rho_a & \rho_f \\ \rho_f & \rho_t \end{pmatrix} \begin{pmatrix} \nabla_j (-\bar{p} \delta_{ij} + \bar{\tau}_{ij}) \\ \frac{\eta_f}{k} q_i^D + \nabla_i p_f \end{pmatrix}, \quad (6.43)$$

where $\Theta = \rho_t \rho_a - \rho_f^2$. Note that the coefficient matrices in equations (7.94) and (7.95) are symmetric by analogy equations (6.1) and (6.8). Symmetry combined to non-dimensional analysis is a requirement that allows us to derive a time stepping condition in the explicit form.

6.4.2 Discretization

The numerical implementation consists of a time evolution operator to perform time steps within a time loop and space operators to relate fields at old and new times. We rely on a rectangular time-space grid. The time discretization is $t^l = l\Delta t$ and the spatial grid is $x_i = i\Delta x$, $y_j = j\Delta y$, $z_k = k\Delta z$. The particle velocity vector field and the Darcy's flux are defined at half-integer spatial nodes and integer time nodes:

$$(v_x^s)_{i+1/2,j,k}^l, (v_y^s)_{i,j+1/2,k}^l, (v_z^s)_{i,j,k+1/2}^l, (q_x^D)_{i+1/2,j,k}^l, (q_y^D)_{i,j+1/2,k}^l, (q_z^D)_{i,j,k+1/2}^l. \quad (6.44)$$

The total and fluid pressure scalar fields are defined at integer spatial nodes and half-integer time nodes: $(\bar{p})_{i,j,k}^{l+1/2}$, $(p_f)_{i,j,k}^{l+1/2}$. The stress deviator tensor fields are defined as $(\bar{\tau}_{xy})_{i+1/2,j+1/2,k}^{l+1/2}$, $(\bar{\tau}_{xz})_{i+1/2,j,k+1/2}^{l+1/2}$, $(\bar{\tau}_{yz})_{i,j+1/2,k+1/2}^{l+1/2}$. A

schematic representation of spatial positions is shown in Figure 6.5. The proposed discrete scheme is second order accurate in space and time. The material parameters are constant inside the finite volumes and may be discontinuous between them. The discrete operators for Biot's equations (7.94)-(7.95) are given in 6.12.

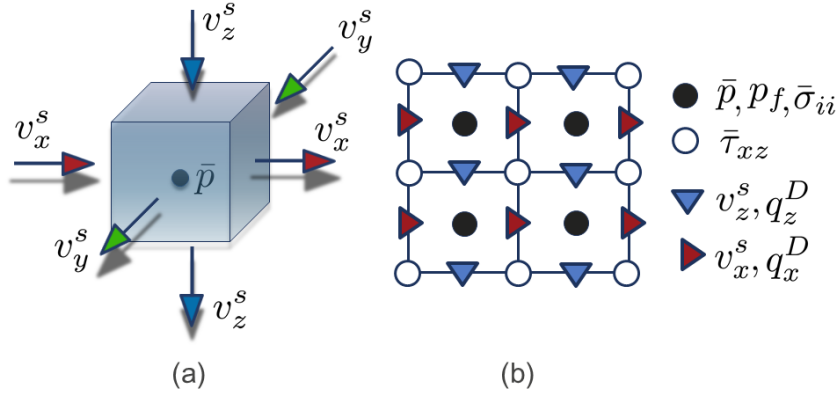


Figure 6.5: A sketch representing (a) the finite volume, where the solid particle velocities preserve mass balance and (b) the spatial positions of different fields in the X-Z plane. Darcy's fluxes obey the same behavior.

6.4.3 Stiffness of Biot's equations

Wave propagation and fluid pressure diffusion in poroelastic media occur simultaneously but feature very different time scales. This phenomenon is called stiffness of the Biot's equations (e.g., *Carcione and Quiroga-Goode* (1995)). Stiffness of an equation is a serious issue for numerical solutions because the discrete time step may drop to values hindering the numerical simulation to complete. A simple solution exist to circumvent this issue for Biot's equations (*Masson et al., 2006; Alkhimenkov et al., 2020c*), briefly reported here. The one-dimensional discrete version of (7.95) is

$$\begin{cases} -\frac{[q^D]_{i+1/2}^{l+1} - [q^D]_{i+1/2}^l}{\Delta t} = \frac{\rho_f}{\Theta} \frac{[\bar{\sigma}]_{i+1}^{l+1/2} - [\bar{\sigma}]_i^{l+1/2}}{\Delta x} + \frac{\rho_t}{\Theta} \left(\frac{[p_f]_{i+1}^{l+1/2} - [p_f]_i^{l+1/2}}{\Delta x} + \frac{\eta_f}{k} (\chi [q^D]_{i+1/2}^{l+1} + (1-\chi) [q^D]_{i+1/2}^l) \right) \\ \frac{[v^s]_{i+1/2}^{l+1} - [v^s]_{i+1/2}^l}{\Delta t} = \frac{\rho_a}{\Theta} \frac{[\bar{\sigma}]_{i+1}^{l+1/2} - [\bar{\sigma}]_i^{l+1/2}}{\Delta x} + \frac{\rho_f}{\Theta} \left(\frac{[p_f]_{i+1}^{l+1/2} - [p_f]_i^{l+1/2}}{\Delta x} + \frac{\eta_f}{k} (\chi [q^D]_{i+1/2}^{l+1} + (1-\chi) [q^D]_{i+1/2}^l) \right) \end{cases} \quad (6.45)$$

The weight parameter χ plays the key role in the numerical solution of Biot's equations. The case $\chi = 0$ corresponds to a fully explicit scheme; calculating $[q^D]^{l+1/2}$ (6.45) only requires $[q^D]^{l-1/2}$. In this case, the stable time step becomes very small due to the stiffness of Biot's equations. The opposite end-member $\chi = 1$ corresponds to an implicit scheme where the stiffness no longer affects the time step stability; calculating $[q^D]^{l+1/2}$ (6.45) requires $[q^D]^{l+1/2}$. Since Biot's equations do not contain spatial derivatives of the Darcy's flux q_x^D in (6.45), the implicit scheme $\chi = 1$ can be achieved in an iterative fashion (i.e., updates in the iteration loop are explicit). The one dimensional code for $\chi = 1/2$ is shown in Figure 6.7. The weight parameter χ plays the key role in the stability and convergence rate of the numerical scheme which is explored in the next section.

6.4.4 Von Neumann stability analysis

The von Neumann stability method analyzes a time evolution of a discrete numerical solution of a given PDE. The method provides the stability of linear schemes with constant coefficients. We here summarize the von Neumann stability analysis' main results (*Alkhimenkov et al., 2020c*) for Biot's poroelastic equations' discrete scheme (see also *Masson et al. (2006)*). For that let us introduce the matrices of coefficients

$$\zeta_{ij} = \begin{pmatrix} \zeta_{11} & \zeta_{12} \\ \zeta_{21} & \zeta_{22} \end{pmatrix} = \begin{pmatrix} K_u + 4/3G & \alpha M \\ \alpha M & M \end{pmatrix} \quad (6.46)$$

and

$$\varrho_{ij} = \begin{pmatrix} \varrho_{11} & \varrho_{12} \\ \varrho_{21} & \varrho_{22} \end{pmatrix} = \frac{1}{\Theta} \begin{pmatrix} \rho_a & \rho_f \\ \rho_f & \rho_t \end{pmatrix}, \quad (6.47)$$

the parameter Θ is already defined in (7.95). The determinants of these matrices are

$$\det(\zeta_{ij}) = \zeta_{11}\zeta_{22} - \zeta_{12}^2, \quad \det(\varrho_{ij}) = \varrho_{11}\varrho_{22} - \varrho_{12}^2, \quad (6.48)$$

and the Hadamard product (element-wise multiplication) of ζ_{ij} and ϱ_{ij} is

$$h_{ij} \equiv (\zeta \circ \varrho)_{ij} = \begin{pmatrix} \zeta_{11}\varrho_{11} & \zeta_{12}\varrho_{12} \\ \zeta_{21}\varrho_{21} & \zeta_{22}\varrho_{22} \end{pmatrix}. \quad (6.49)$$

The parameter A is defined as

$$A = h_{11} + h_{22} - 2h_{12} \quad (6.50)$$

By using (6.48) and (6.50), the fast wave phase velocity in the high-frequency limit V_1^{HF} can be calculated as

$$V_1^{HF} = \left(\frac{A - \sqrt{A^2 - 4\det(\zeta_{ij})\det(\varrho_{ij})}}{2\det(\zeta_{ij})\det(\varrho_{ij})} \right)^{-1/2}. \quad (6.51)$$

The matrices ζ_{ij} and ϱ_{ij} and $\eta_k \equiv \eta/k$ fully describe the dimensional elastodynamic Biot's equations (7.94)-(7.95). The main issue with the numerical modeling of the Biot's equations is the treatment of the parabolic operator in (7.110) and (6.121). If $\eta_k = 0$, then the system (7.94)-(7.95) corresponds to the two coupled hyperbolic equations, having two longitudinal waves. The stability analysis shows that the Courant-Friedrichs-Lewy (CFL) condition for such system is $\Delta t \leq \Delta x/V_1^{HF}$ (*Alkhimenkov et al., 2020c*), where V_1^{HF} is given by expression (6.51).

If $\eta_k \neq 0$ and $\chi = 0$, then the parabolic operator $\bar{D}_\chi[q_f^D]$ in (7.110) and (6.121) affects stability and the system of equations becomes stiff. If η_k reaches a certain value, the stable time step Δt dramatically decreases as a function of η_k (Figure 6.6a). The increase in porosity ϕ also reduces Δt but this reduction is small compared to the reduction due to the increase of η_k . However, for the $\chi = 1/2$ scheme or $\chi = 1$ scheme, the parameter η_k does not affect the the stable time step Δt (Figure 6.6b). In this case, the parabolic operator $\bar{D}_\chi[q_f^D]$ is calculated implicitly, thus, the CFL condition is not affected by η_k . The $\chi = 1/2$ or $\chi = 1$ schemes are stable in one space dimension under the CFL condition

$$\Delta t \leq \frac{\Delta x}{V_1^{HF}}, \quad (6.52)$$

where the expression for V_1^{HF} is given by equation (6.51), which is the same as for the inviscid case. The $\chi = 1/2$ scheme is more preferable than the $\chi = 1$ scheme, since the $\chi = 1/2$ scheme provides a second order accuracy, which is explored below.

For any considered above schemes, the matrices ζ_{ij} and ρ_{ij} must be positive definite as well in order to preserve hyperbolicity of the system (Alkhimenkov et al., 2020c). The positive definiteness of the matrix in equation (7.94) and ρ_{ij} also follows from physics, for example, from the classical irreversible thermodynamics (Jou et al., 2001; Yarushina and Podladchikov, 2015). Note, that the positive definiteness of the matrix in equation (7.94) is a more restrictive condition than the positive definiteness of ζ_{ij} (8.8) and are the same if the shear modulus G is zero.

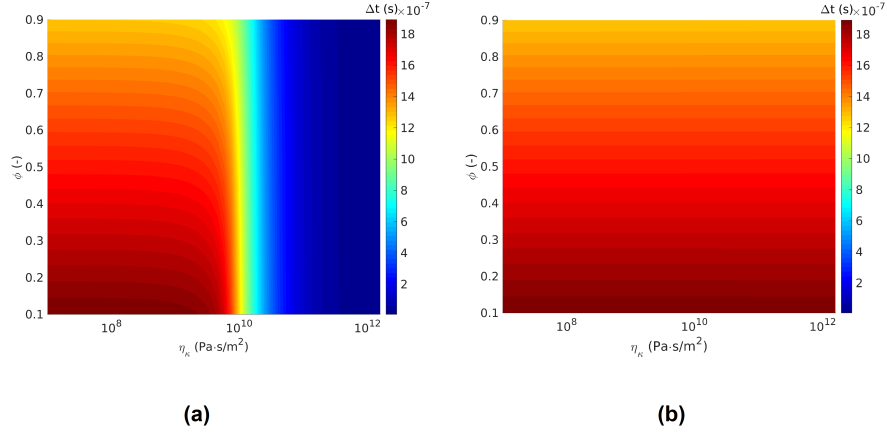


Figure 6.6: The von Neumann stability analysis for the elastodynamic Biot's equations (7.94)-(7.95) as a function of $\eta_k = \eta/k$ and porosity ϕ . Panel (a) corresponds to the $\chi = 0$ scheme and panel (b) corresponds to the $\chi = 1/2$ scheme. The stability of the $\chi = 1$ scheme is identical to that one of the $\chi = 1/2$ scheme. The material parameters are those from Table 6.3.

The extension of the CFL condition (6.52) to the two, three and n-dimensions is straightforward

$$\Delta t \leq \frac{1}{V_1^{HF} \sqrt{\sum_{i=1}^n \frac{1}{\Delta x_i^2}}}. \quad (6.53)$$

If $\Delta x_i = \Delta x$, then

$$\Delta t \leq \frac{\Delta x}{\sqrt{n} V_1^{HF}}. \quad (6.54)$$

The conditions (6.52)-(7.72) can be generalized to a fourth-order accurate in space, second-order accurate in time numerical scheme using the coefficients of the fourth-order approximation to the first derivative (Levander, 1988; Masson et al., 2006).

6.4.5 Sources, initial and boundary conditions

We initialize the majority of our simulations with a Gaussian perturbation,

$$F_G = A_0 e^{-(x/l_x)^2 - (y/l_y)^2 - (z/l_z)^2}, \quad (6.55)$$

where x , y and z are the arrays of spatial coordinates, l_x , l_y and l_z are the parameters controlling the shape (width) of the Gaussian and A_0 defines its amplitude. We set l_x , l_y and l_z as a certain fraction of the domain extend.

Depending on the model configuration, we implemented two types of sources in the right-hand side of the total pressure (isotropic media) or total stress (anisotropic media) equation (see 6.11 for the full set of equations). The first type of source is the Morlet wavelet

$$F_M(t) = \text{Re} \left[(\pi f_b)^{-1/2} e^{2\pi i f_c (t-t_0)} e^{-(t-t_0)^2 / f_b} \right] = (\pi f_b)^{-1/2} \cos(2\pi f_c (t-t_0)) e^{-(t-t_0)^2 / f_b} \quad (6.56)$$

and the second type of source is the Ricker wavelet

$$F_R(t) = (1 - 2(\pi(t-t_0)f_c)^2) e^{-\pi(t-t_0)f_c^2}, \quad (6.57)$$

where f_c is the the source peak frequency, t is time, t_0 is the wavelet delay and f_b is the time-decay parameter of the Morlet wavelet. The Morlet wavelet features a distinct narrow bandwidth in the frequency domain which significantly reduce the wavelet shape changes during the pulse propagation in a lossy medium. The disadvantage results in a significant time spread in time domain. We use reflecting boundary conditions in our simulations.

The one-dimensional time loop implementation of the proposed scheme (6.114)-(6.121) in MATLAB (R2018a) using the Gaussian initial condition (6.55) is shown in Figure 6.7.

```
Prf      = exp(-(x/lamx).^2); chi = 0.5;
for it = 1:nt
    stress_xx = stress_xx + ( zeta_11.*diff(Vx,1,1)/dx + zeta_12.*diff(Qx,1,1)/dx)*dt;
    Prf      = Prf      - ( zeta_21.*diff(Vx,1,1)/dx + zeta_22.*diff(Qx,1,1)/dx)*dt;
    Qx_old   = Qx;
    Qx(2:end-1) = (Qx(2:end-1)/dt - diff(stress_xx,1,1)/dx.*varrho_21 - (diff(Prf,1,1)/dx + ...
        (1-chi).*Qx(2:end-1) .*etaf_k).*varrho_22)./(1/dt + chi.*varrho_22.*etaf_k);
    Vx(2:end-1) = (Vx(2:end-1)/dt + diff(stress_xx,1,1)/dx.*varrho_11 + (diff(Prf,1,1)/dx + ...
        (chi.*Qx(2:end-1) + (1-chi).*Qx_old(2:end-1)).*etaf_k).*varrho_12)*dt;
end
```

Figure 6.7: The one dimensional code using the proposed scheme with $\chi = 1/2$ in MATLAB. The initial condition of the Gaussian form is set to the fluid pressure. zeta_{ij} are the matrix coefficients ζ_{ij} in equation (8.8), varrho_{ij} are the matrix coefficients ϱ_{ij} in equation (6.47), etaf_k corresponds to η/k , chi corresponds to χ , lamx stands for l_x , stress_xx stands for $\bar{\sigma}_{xx}$, Prf stands for p_f , Qx stands for q_x^D , Vx stands for v_x^s .

6.5 Multi-GPU implementation

Graphical processing units (GPUs) are many-core processors originally designed to refresh screen pixels at very high frame-rates for computer games. Nowadays, GPUs are widely used in high-resolution numerical modeling due to their ability to efficiently execute a large number of operations simultaneously. Several studies focused on the implementation of wave propagation solvers using GPUs (*Komatitsch et al., 2010; Michéa and Komatitsch, 2010; Mehra et al., 2012; Weiss and Shragge, 2013; Rubio et al., 2014*). The CUDA extension to the C language (*CUDA, 2020*) makes it possible to write C-style codes that are executed in parallel on GPUs. A brief description of the GPU architecture is given in 6.13.

6.5.1 Computing systems

We calculated our results on various computing systems depending mainly on the targeted numerical resolution. We performed most of our simulations on an Nvidia DGX-1 - like node hosting 8 Nvidia Tesla V100 Nvlink (32 GB) GPUs, 2 Intel Xeon Silver 4112 (2.6GHz) CPUs and 768 GB DDR4 RAM. The second computing system hosts a single Nvidia Tesla V100 PCIe (16 GB) GPU, 2 Intel XEON E5-2620V2 4112 (2.1GHz) CPUs and 64 GB DDR3 RAM. The third computing system is composed of 32 nodes, each featuring 4 Nvidia GeForce GTX Titan X Maxwell (12 GB) GPUs, 2 Intel XEON E5-2620V3 4112 (2.4GHz) CPUs and 128 GB DDR4 RAM.

6.5.2 Code implementation on a single GPU

The CUDA C code structure (Figure 6.8a) is similar to the MATLAB one (Figure 6.7). The time loop calls two kernels – or GPU functions – to sequentially update all stresses and the fluid pressure and then update the fluid and solid particle velocities. Darcy's fluxes q_x^D , q_y^D , q_z^D are time-dependent fields present in both equations (7.110) and (6.121) exhibiting history or time dependence that require them to be stored from previous iteration. We perform the update relying on a pointer swap at every iteration to prevent race conditions and to avoid copying the array itself, which would significantly deprecate the performance. To reduce redundant memory accesses, we locally precompute and store corresponding field variables. In the `compute_StressPrF()` kernel, we store the derivatives of the velocities v_i^s and Darcy fluxes q_i^D . In the `Update_QV()` kernel, we store derivatives of stresses $\bar{\sigma}_{ij}$ and fluid pressure p_f .

6.5.3 The multi-GPU code implementation

The single GPU code enables thousands of threads to simultaneously compute physics on every grid points of the computational domain in a shared (GPU) memory approach. To overcome the on-GPU DRAM memory limitation and leverage the simultaneous utilisation of multiple GPUs we implemented a distributed memory parallelisation using the message passing interface (MPI) standard. The parallelisation among multiple GPUs requires the exchange of the internal boundary values of the solid particle velocities v^s and the Darcy's fluxes q^D (represented by black lines in Figure 6.9). Global boundary conditions are applied if the local sub-domains coincide with the global domain boundaries. We rely on CUDA-aware non-blocking MPI messages for internal boundary condition updates among neighbouring GPUs. The CUDA-awareness implies that GPU device pointers can directly be exchanged with MPI bypassing a local CPU copy on both sender and receiver side.

We implemented an overlap among computation and MPI communication to avoid a drop in performance with an increase in the number of MPI processes (*Räss et al., 2019a*). Only minimal changes are required to implement this computation/communication overlap and fully hide the MPI boundary exchange latency (Figure 6.8b). We divided the local computational domain on each GPU in two parts, a boundary points region (1 in Figure 6.9) and an inner points region (2 in Figure 6.9). We then use CUDA Streams to perform an asynchronous kernel call in an iterative fashion using two distinct execution pipelines (*Räss et al., 2019a*). The first update kernel call computes the boundary flagged nodes only and executes on the high priority stream. Then, the MPI boundary updates starts on the same high priority stream (the `update_sides3` function). In the meanwhile, the update kernel call is executed a second time within the `istep` loop, now flagging and computing the remaining inner

points. A wise definition of the number of grid points to include (i.e. the boundary width) enables optimal performance results.

The Nvidia visual profiler (nvvp) is an informative tool to visualize the execution timeline of a GPU process (Figure 6.10). We compare multi-GPU codes without (Figure 6.10a) and with (Figure 6.10b) computation/communication overlap running on a 8 GPUs (information shown only for two GPUs). The visual timeline depicts the q^D and v^s boundary points update on the high priority CUDA stream 21 followed by the MPI message sending and receiving among GPUs (the time line is shown by red box in Figure 6.10b). During the same time, the q^D and v^s inner points update happens on the lower priority CUDA stream 22. The update kernel is executed two times (green boxes in Figure 6.10b). The cumulative time of the sequential executions is identical to the un-split execution time (Figures 6.10a-b).

a)

```

init<<<grid,block>>>(Prf, sigma_xx, sigma_yy, sigma_zz, Vx, Vy, Vz, ...);
cudaDeviceSynchronize();

for (it=0;it<nt;it++)
{
    compute_StressPrf<<<grid,block>>>(Prf, sigma_xx, sigma_yy, sigma_zz, ...);
    cudaDeviceSynchronize();

    swap(Qxold,Qx); swap(Qyold,Qy); swap(Qzold,Qz);
    cudaDeviceSynchronize();

    update_QV<<<grid,block>>>(Vx, Vy, Vz, Qxft, Qyft, Qzft, ...);
    cudaDeviceSynchronize();
}

```

b)

```

init<<<grid,block>>>(Prf, sigma_xx, sigma_yy, sigma_zz, Vx, Vy, Vz, ...);
cudaDeviceSynchronize();

for (it=0;it<nt;it++)
{
    compute_StressPrf<<<grid,block>>>(Prf, sigma_xx, sigma_yy, sigma_zz, ...);
    cudaDeviceSynchronize();

    swap(Qxold,Qx); swap(Qyold,Qy); swap(Qzold,Qz);
    cudaDeviceSynchronize();

    for (istep=0; istep<2; istep++)
    {
        update_QV<<<grid,block,0,streams[istep]>>>(Vx, Vy, Vz, Qxft, Qyft, Qzft, ...);
        update_sides3(Qx,nx+1,ny,nz, Qy,nx,ny+1,nz, Qz,nx,ny,nz+1)
        update_sides3(Vx,nx+1,ny,nz, Vy,nx,ny+1,nz, Vz,nx,ny,nz+1)
    }
    cudaDeviceSynchronize();
}

```

Figure 6.8: Time loop computations for (a) a single GPU CUDA C code and (b) a multi-GPUs CUDA C code implementation. `compute_StressPrf` corresponds to the update of all stresses $\bar{\sigma}_{ij}$ and fluid pressure p_f . `update_QV` corresponds to the update of velocities v_i^s and Darcy fluxes q_i^D . `swap(...)` stands for a pointer swap of Darcy's fluxes between old and new values.

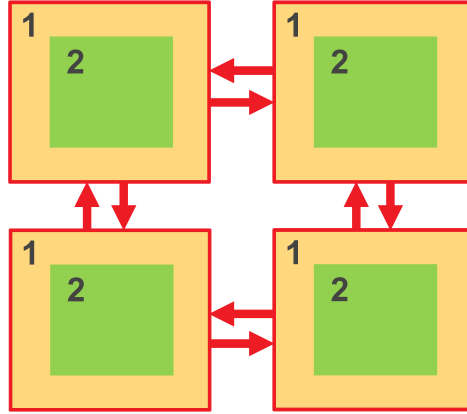


Figure 6.9: Schematic representation of a domain decomposition on four GPUs. First, the computation of the boundary points (1) of the local domains using streams is performed, then the computation of the inner points (2) of the local domains is carried out together with the non-blocking MPI messages to exchange the boundary values (represented by red boundary lines) among neighboring GPU units.

6.5.4 Performance benchmark

We assess the solver's performance and realize the weak scaling tests in a similar fashion as proposed by *Räss et al. (2019b)*; *Duretz et al. (2019a)*; *Räss et al. (2020)*. These studies highlight the memory-bounded nature (in opposition to compute-bounded) of a waste majority of PDE solver implementations nowadays on many-core (e.g., GPU) hardware; Memory transfers are limiting the performance of an application, while floating point (arithmetic) operations are not performance relevant. We therefore focus on the memory access efficiency in our numerical calculations. The effective memory throughput ($MTP_{\text{effective}}$) metric (*Omlin, 2016*; *Omlin et al., 2020*) evaluates how efficiently data is transferred between the memory and the computation units, in gigabytes per second (GB/s):

$$MTP_{\text{effective}} = \frac{n_x \times n_y \times n_z \times n_t \times n_{\text{IO}} \times n_p}{10^9 \times t_{n_t}}, \quad (6.58)$$

where n_x , n_y , n_z are the number of grid cells, n_t is the number of iterations, n_{IO} is the number of read and write memory accesses (the least value needed to solve the problem for the chosen numerical scheme), n_p is the floating-point arithmetic precision (either 4 or 8 bytes) and t_{n_t} is the time (in seconds) needed to perform the n_t iterations. The closer the value of $MTP_{\text{effective}}$ gets to the memory copy only value, the better the performance is. We carried out all the performance tests on the anisotropic Biot 3D implementation using the $\chi = 1/2$ scheme and scalar material properties (see 6.11 for the full set of equations). In that case $n_{\text{IO}} = 42$. We used a numerical spatial resolution of 576^3 grid cells on a Tesla V100 32GB Nvlink GPU, allocating 29 GB on-chip DRAM memory. We used a numerical spatial resolution of $511 \times 511 \times 127$ grid cells on the Titan X (Maxwell) 12GB GPU allocating 5 GB on-chip DRAM memory. The maximum global domain spatial resolution on 128 Titan X (Maxwell) 12GB GPUs involved 4.5 billion grid cells.

Benchmark results for a single GPU implementation

Figure 6.11 depicts the effective memory throughput (MTP) of the Biot 3D numerical application as a function of the number of threads per blocks in x-, y- and z- direction on a Tesla V100 32GB Nvlink GPU. The MTP_{ref} corresponds to the reference MTP, i.e. the best combination of threads per blocks (32, 2, 16) for a given resolution of 576^3 ; the MTP of all simulations ($MTP_{\text{effective}}$) are normalized by MTP_{ref} . The maximal performance drop from the reference MTP is about 17 %. It is interesting, that the (32, 2, 8) combination uses only 512 threads out of the 1024 available but shows almost the same performance as combinations involving 1024 threads. Good performance with under-utilization of the threads per block resources is known and may result by the increase in the number of concurrent blocks launched allowing for optimal scheduling.

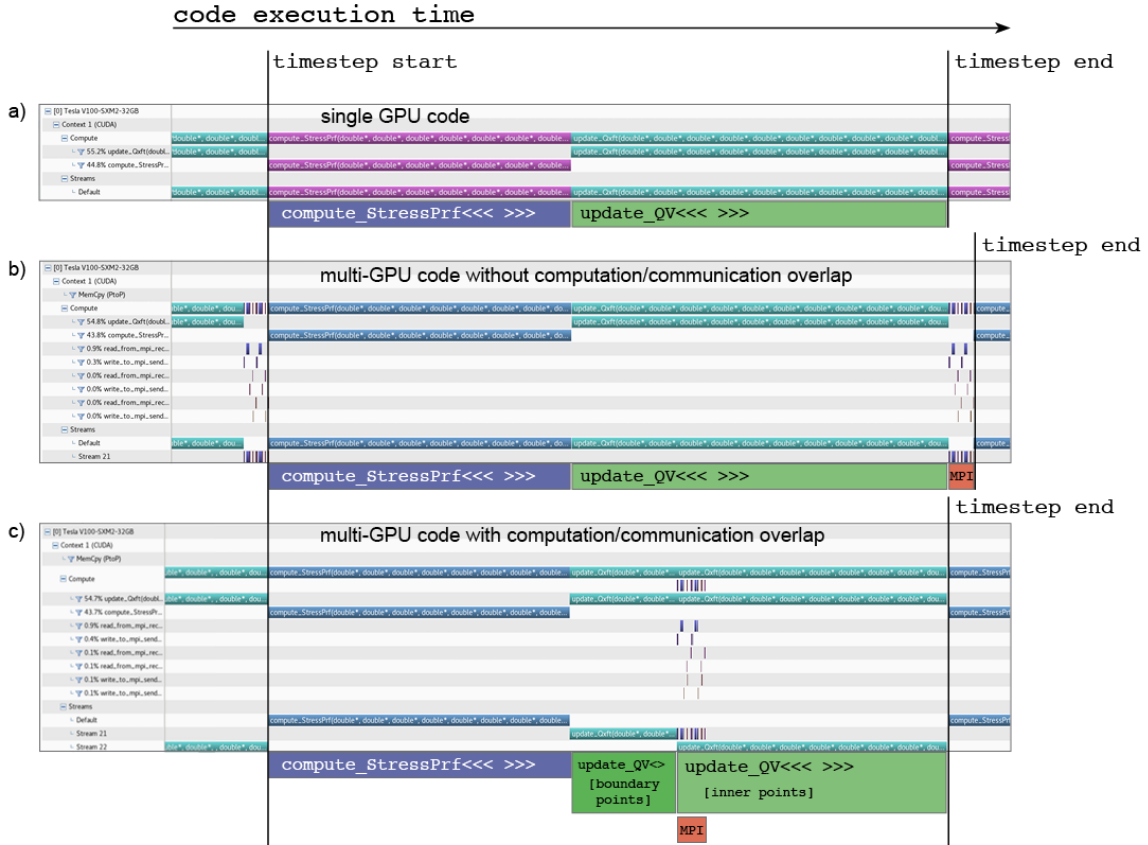


Figure 6.10: The Nvidia visual profiler (nvvp) output for various GPU code implementations: (a) single GPU (without computation/communication overlap), (b) multi-GPUs (without computation/communication overlap) and (c) multi-GPUs (with computation/communication overlap). All implementations share the same `compute_StressPrf` kernel. The `update_QV` kernel is (a) executed once per time step updating both boundary and inner points, (b) executed once per time step and followed by internal boundary exchange using MPI, (c) executed in a serial fashion, first updating the boundary points, then internal boundary exchange occurs using MPI while the inner points are asynchronously computed in the second call of the `update_QV` kernel. The computation/communication overlap referred to as computational split involves 48, 16 and 16 grid cells in x-, y- and z- directions, respectively.

Figure 6.12 shows memory access efficiency between the GPU global memory and the computation units as a function of on-chip RAM memory. Our 3D numerical application achieves on average 90% of the “ideal” memory copy only efficiency (copying two 3D arrays without performing any calculations, 740 GB/s) on a single Tesla V100 32 GB NVlink GPU. The average performance is 660 GB/s. A huge drop in the memory access performance at low on-chip RAM memory utilization reflects computations without enough data to saturate the memory bandwidth.

We additionally assessed the effective memory throughput of our 3D routine on a Tesla V100-SXM2 16 GB accessed on the Amazon Elastic Compute Cloud environment (Amazon EC2); our 3D routine performs on average at 740 GB/s (memory copy at 795 GB/s) validating the benchmark results obtained on our local GPU cluster. The discrepancy we observe may be caused by different versions of Nvidia drivers and compilers.

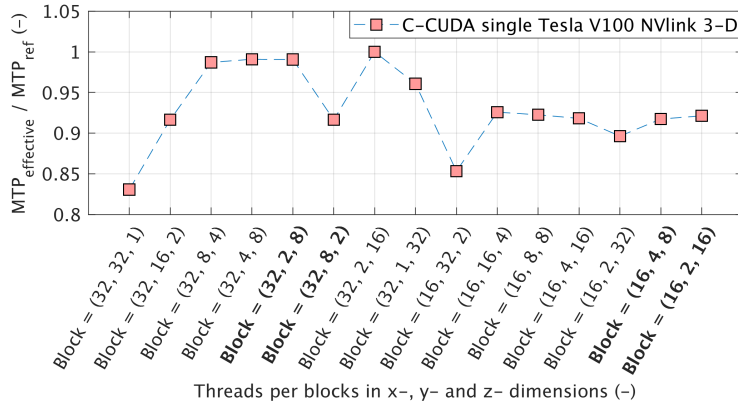


Figure 6.11: The effective memory throughput as a function of the number of threads per blocks (in x-, y- and z-direction). The MTP of all simulations ($MTP_{\text{effective}}$) are normalized by MTP_{ref} (corresponds to Block (32,2,16)). The bold color corresponds to thread-block combinations of 512 threads out of the 1024 available.

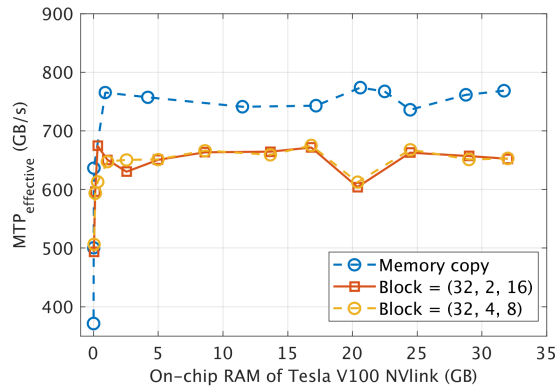


Figure 6.12: The memory access efficiently as a function of the allocated on-chip DRAM memory. The blue curve corresponds to the “ideal” memory copy efficiency (copying two 3D arrays without performing any calculations), red and yellow curves represent the memory copy efficiency involving all the physics, which is on average 90% of the “ideal” memory copy efficiency.

Benchmark results for a multi-GPU implementation

We further investigate the influence of the boundary width on the performance (Figure 6.13). The split among computation domains allowing for overlap of computation and communication affects the performance. Considering too few or too many boundary points hinders optimal kernel execution as too few resources may be used in the first or the second sequential call. The code execution on a single Tesla V100 GPU with boundary width ratios of 0.2-0.8 returns equivalent performance as the execution without the computational split. The performance of the code on 8 Tesla V100 GPUs including MPI communication shows a 2% performance drop compared to the single GPU process. We achieved the best performance using approximately a ratio of 0.3 between boundary and inner points. This splitting allows for enough data to keep all threads busy during the boundary point calculation (the first kernel execution) and provides sufficient time to hide the MPI message sent during the update of the inner points (the second kernel execution).

We performed a weak scaling test using the 1-8 Tesla V100 32 GB NVlink GPUs and the 1-128 Titan X 12 GB GPUs (Figure 6.14). The parallel efficiency of 1-8 GPUs is 98% and on average 96% on 16-128 Titan X GPUs with a standard deviation of 2%. A standard deviation was calculated as a result of ten simulations. We globally achieved a performance of about 5280 GB/s on 8 Tesla V100 32 GB NVlink GPUs. Such performance implies that only 95 seconds are needed to perform 1000 (double-precision) explicit time iterations of a model involving 1.5 billion grid cells (1152^3).

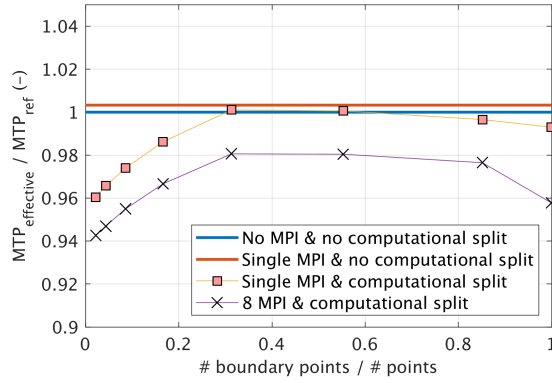


Figure 6.13: The impact of the boundary width on the memory access efficiency. All the performance results are normalized by MTP_{ref} of the non-MPI code implementation.

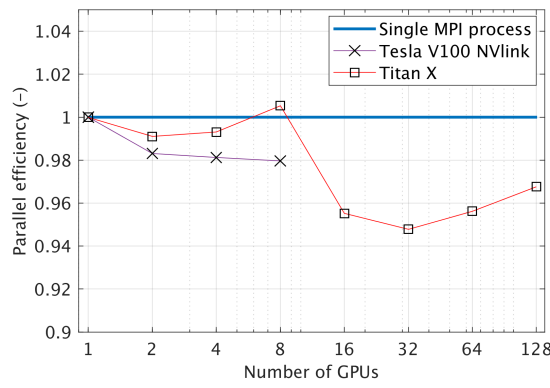


Figure 6.14: The MPI weak scaling tests of the anisotropic Biot 3D implementation. We show the parallel efficiency of the two Nvidia hardware accelerators, the 1-8 Tesla V100 32 GB NVlink GPUs (Volta) and the 1-128 Titan X 12 GB GPUs (Maxwell). All the performance results are normalized by the single-MPI code performance.

6.5.5 Validation of the numerical solver

Comparison against an analytical solution

We perform a direct comparison of our numerical solver against analytically derived non-dimensional phase velocities and the inverse quality factors of 1D Biot's equations in homogeneous poroelastic media. Biot's mechanism, often called global flow, is the unique cause leading to wave attenuation and velocity dispersion. We validated our numerical solver in 1D but the plane wave analysis is multidimensional as plane wave characteristics are identical in 1D, 2D and 3D. In the numerical simulation, we use the proposed scheme (6.114)-(6.121) with $\chi = 1/2$, the Morlet wavelet as a source function (6.56) and quantify velocity and the inverse of the quality factor of a propagating wavelet in the time domain. We obtain excellent agreement between numerical and analytical results (Figure 6.15).

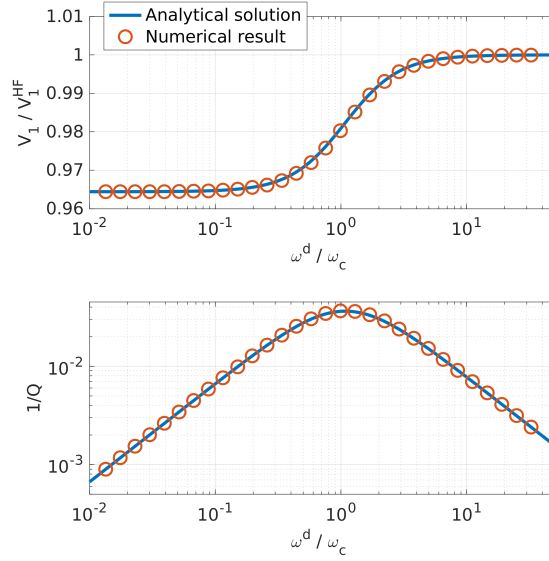


Figure 6.15: A comparison between numerically calculated dimensional phase velocities (up) and $1/Q$ (down) against an analytical solution of Biot's equations. Each red circle corresponds to a numerical simulation. The phase velocity V_1 is normalized by the velocity in the high frequency limit V_1^{HF} and the dimensional angular frequency ω^d is normalized against Biot's frequency ω_c . The material parameters are those from Table 6.3.

Convergence analysis

We performed a grid convergence analysis to validate the numerical implementation of the solver. We evaluate the magnitude of the phase velocity truncation errors (e_V) as functions of decreasing spatial discretization steps Δx . We calculate the truncation errors by subtracting numerically calculated fields from analytical fields and characterize the magnitude of the truncation errors by their L_1 norms, using the velocity estimation (Räss *et al.*, 2017)

$$e_V = \|V_a - V_n\|_1, \quad (6.59)$$

where V_a corresponds to the analytical velocity obtained via the dispersion analysis and V_n corresponds to the numerically estimated velocity.

Figure 6.16a shows the truncation error magnitudes of the estimated velocity in a lossless ($\eta/k = 0$) and lossy ($\eta/k \neq 0$) media using the $\chi = 1/2$ scheme (6.114)-(6.121). The source has the form of a Ricker wavelet (7.73) and the central frequency of the source corresponds to a very low frequency (much lower than the frequency of $1/Q$ maximum). Our numerical solutions for velocity exhibits second-order spatial and temporal accuracy. The truncation error magnitudes decrease by a factor k as the grid spacing is reduced by the same factor. We obtain similar results for a very high frequency source (much higher central frequency than the frequency of $1/Q$ maximum).

Figure 6.16b shows the truncation error magnitudes of the estimated velocity in a lossy medium for the scheme (6.114)-(6.121) with $\chi = 1/2$ and $\chi = 1.0$. Here, the central frequency of the source corresponds to the frequency of $1/Q$ maximum. In this analysis, we use the numerically estimated velocity of a very high resolution simulation. The $\chi = 1/2$ scheme exhibits second-order accuracy in space and in time. In contrast, the $\chi = 1.0$ scheme shows only about 1.8 order accuracy. Only the $\chi = 1/2$ scheme exhibits second-order spatial and temporal accuracy across all frequencies while the $\chi = 1.0$ scheme exhibit second-order spatial and temporal accuracy only at low or high frequencies where attenuation (and dispersion) is very low. For schemes with χ other than $1/2$ (we used $\chi = 0.6, 0.7, 0.8, 0.9$), tests show that the accuracy is lower than second-order. Therefore, the scheme with $\chi = 1/2$ is used for the numerical solution of Biot's equations in the rest of the manuscript.

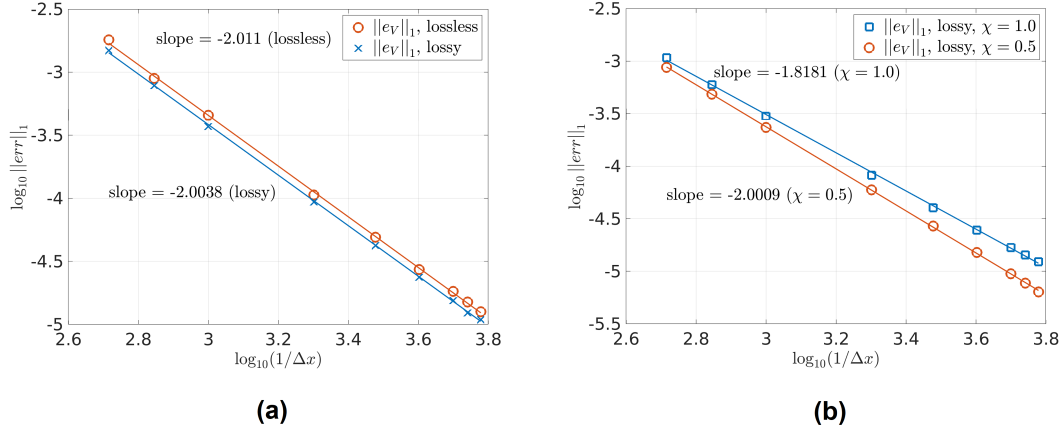


Figure 6.16: The truncation error magnitudes of the numerically estimated velocities. (a) the low frequency source and (b) f_c of the source is close to the frequency of $1/Q_1$ maximum. The material parameters are those from Table 6.3.

6.6 Numerical experiments

We here present a series of simulations based on Biot's equations in two and three dimensions. We discuss some basic aspects of poroelasticity, namely, wave propagation in homogeneous poro-acoustic and poro-elastic media, in isotropic and anisotropic poroelastic media and at low- and high- frequency regimes.

6.6.1 Wave propagation in 2D poroelastic media

Poro-acoustic and poro-elastic media

We examine the difference between poro-elastic and poro-acoustic wave propagation at low and high frequencies in two dimensions. The material properties are those of an isotropic sandstone (Table 6.4). For the poro-acoustic material, we set the shear modulus c_{55} to zero. A 2D square domain of $9.35\text{m} \times 9.35\text{m}$ is used. We define 32 threads per blocks in x - and z - directions with 128 blocks in x - and z - directions, which result in 4095×4095 grid resolution having $\approx 16 \cdot 10^6$ grid cells. We apply a Gaussian distribution (6.55) with $l_x = 0.08$, $l_y = 0.08$ and $A_0 = 1$ at the center of the model domain to the solid particle velocity (V_z) as an initial condition for the poro-acoustic and low frequency poro-elastic simulations. For the high frequency poro-elastic simulations we also apply the Gaussian distribution to the fluid pressure p_f .

Figure 6.17 shows the total pressure (\bar{p}) and solid particle velocity (V_x) fields for poro-acoustic and poro-elastic simulations. In total, 5000 time steps were performed and the total physical simulation time was approximately $t = 9 \cdot 10^{-4}$ seconds. The simulations were performed on a single Tesla V100 PCIe GPU. The running time was approximately 55 seconds for each simulation. For a performance comparison, a few simulations were executed on a single Tesla V100 Nvlink GPU, and the running time was approximately 51 seconds. Note, that the 2D codes performance is not optimized as it is done for 3D codes. For optimized 2D codes, the performance might be much higher. In the poro-acoustic simulations (Figure 6.17a-b), the initial condition corresponds to the low frequency regime and only the fast (longitudinal) wave V_1 can be observed. Also note that the 2D poro-acoustic medium can not unload the initial condition applied to the solid particle velocity field, which is represented by non-zero amplitudes at the center of the model (Figure 6.17b). In the poro-elastic simulations (Figure 6.17c-d), the initial condition corresponds to the low frequency regime and only two waves can be observed — the fast (longitudinal) wave V_1 and the shear wave V_s . In the poro-elastic simulations (Figure 6.17e-f), the initial condition of a Gaussian shape with $l_x = 8 \cdot 10^{-4}$ and $l_y = 8 \cdot 10^{-4}$ corresponds to the high frequency regime. Three waves can be clearly observed — the fast (longitudinal) wave V_1 , the shear wave V_s and the slow (longitudinal) wave V_2 (Figure 6.17e-f).

Table 6.4: Properties of anisotropic poroelastic rocks used for numerical simulations. VTI corresponds to a vertical transverse isotropic medium.

Rock properties		sandstone (VTI)	glass-epoxy (VTI)	sandstone (isotropic)
K_s	(GPa)	80	40	40
ρ_s	(kg/m ³)	2500	1815	2500
c_{11}	(GPa)	71.8	39.4	36
c_{12}	(GPa)	3.2	1.2	12
c_{13}	(GPa)	1.2	1.2	12
c_{33}	(GPa)	53.4	13.1	36
c_{55}	(GPa)	26.1	3.0	12
ϕ	(-)	0.2	0.2	0.2
k_1	(m ²)	$600 \cdot 10^{-15}$	$600 \cdot 10^{-15}$	$600 \cdot 10^{-15}$
k_3	(m ²)	$100 \cdot 10^{-15}$	$100 \cdot 10^{-15}$	$600 \cdot 10^{-15}$
T_1	(-)	2	2	2
T_3	(-)	3.6	3.6	3.6
K_f	(GPa)	2.5	2.5	2.5
ρ_f	(kg/m ³)	1040	1040	1040
η	(kg/m·s)	10^{-3}	10^{-3}	10^{-3}

Anisotropic poroelastic media

In this section, we reproduce similar two dimensional results shown in *de la Puente et al. (2008)*; *Lemoine et al. (2013)*, so the present simulations can be qualitatively compared to the previous works. The material properties of anisotropic rocks are similar to those of *de la Puente et al. (2008)*; *Lemoine et al. (2013)* (Table 6.4). We apply a Gaussian distribution to σ_{zz} and p_f with $l_x = 0.08$, $l_y = 0.08$ and $A_0 = 1$ to the center of the numerical model. Other parameters are the same as in the previous 2D simulations. The simulations were performed on a single Tesla V100 Nvlink GPU. The running time was approximately 51 seconds for both (glass-epoxy and sandstone-VTI) models, 5000 time steps were performed. The total physical simulation time was $t = 6.15 \cdot 10^{-04}$ seconds for the anisotropic sandstone and $t = 7.061 \cdot 10^{-04}$ seconds for the glass-epoxy model. The results of the solid-particle velocity fields V_x and V_z are shown in Figures 6.18 and 6.19. In analogy to *de la Puente et al. (2008)*; *Lemoine et al. (2013)*, we show numerical results for inviscid models ($\eta = 0$) and viscid models ($\eta \neq 0$). Simulations in inviscid media mimic the high frequency regime, therefore, fast, quasi-shear and slow waves can be observed (Figure 6.18a-b and Figure 6.19a-b). Simulations in viscid media correspond to the low frequency regime, therefore, only fast and quasi-shear waves are observed (Figure 6.18c-d and Figure 6.19c-d).

6.6.2 Wave propagation in 3D anisotropic poroelastic media

We simulate a wave propagating in 3D for the anisotropic poro-elastic material whose properties are of the glass-epoxy (Table 6.4), the properties in the x -direction are duplicated to the y -direction. The simulations were performed on eight Tesla V100 Nvlink GPUs. A three dimensional cubic domain of $9.35\text{m} \times 9.35\text{m} \times 9.35\text{m}$ is used. The total resolution is $1022 \times 1022 \times 1022$ grid cells in x -, y - and z - dimensions, respectively, which results in $\approx 1 \cdot 10^9$ grid cells. We apply a Gaussian distribution to the fluid pressure p_f (fluid injection) with $l_x = 0.18$, $l_y = 0.18$, $l_z = 0.18$ and $A_0 = 10^{10}$ at the center of the numerical model. The running time was approximately 73 seconds for all simulations, 1050 time steps were performed. The total physical simulation time was $6.8 \cdot 10^{-4}$ seconds. This model configuration corresponds to the low frequency regime.

Figure 6.20 shows the solid particle velocity field $V = V_x + V_y + V_z$. The velocity field is projected into several slices, also the isosurfaces of the wave amplitudes of $\pm 3 \cdot 10^{-3}$ are shown. Figure 6.21a shows the solid particle velocity field V_x for the same model (Figure 6.20) while Figure 6.21b shows V_x of the 100 times smaller model (the size is 0.0935^3m), which corresponds to the high frequency regime. The initial condition was scaled accordingly, $l_x = 0.018$, $l_y = 0.018$, $l_z = 0.018$ (A_0 is the same) and the total physical simulation time was also scaled to $6.8 \cdot 10^{-6}$ seconds. The behavior of fast and quasi-shear waves is similar in Figures 6.21a and 6.21b but the slow P-wave behavior is different. In Figure 6.21a, the slow P-wave degenerated into a diffusion mode representing viscous fluid flow in porous media while in Figure 6.21b the slow P-wave behaves as a true propagating wave.

6.7 Conclusions

We developed a multi-GPU solver for the anisotropic elastodynamic Biot's equations in 1D, 2D and 3D using the CUDA C programming language leveraging the parallel processing power of GPUs. We implement a simple approach to circumvent the stiffness of Biot's equations by using an implicit scheme for Darcy's flux while keeping explicit updates in the iteration loop. We achieve a close-to-ideal parallel efficiency (98% and 96%) on weak scaling tests up to 128 GPUs by overlapping MPI communication and computations. We also achieve an effective memory throughput of 90% of the memory copy throughput. Our multi-GPU implementation of Biot's equations permits to tackle high spatial resolution and exhibits fast execution times. We perform 1000 explicit time steps in 95 seconds for a model involving 1.5 billion grid cells (1152^3) on 8 Tesla V100 32GB Nvlink GPUs using double-precision arithmetics. We analyze the stability and accuracy of the three different numerical schemes and suggest the best out of three. We benchmark the numerical solver against an analytical solution of Biot's equations and present a comprehensive dimensional analysis of Biot's equations to reduce the number of material parameters from ten to four. Our numerical application to resolve Biot's equations enables practical applications in geophysics, engineering, biophysics and the further understanding the underlying hydro-mechanically coupled processes in 3D.

Acknowledgments

This research is funded by the Swiss National Science Foundation, project number 172691. Yury Alkhimenkov, Lyudmila Khakimova and Yury Y. Podladchikov gratefully acknowledge support from the Ministry of Science and Higher Education of the Russian Federation (project No. 075-15-2019-1890). Yury Alkhimenkov thanks Yder Masson for fruitful discussions regarding the stability of the discretized Biot's equations. Ludovic Räss thanks Samuel Omlin for fruitful discussions regarding the multi-GPU implementation. The authors thank Philippe Logean for technical support and the Swiss Geocomputing Centre for providing computational resources. No data were used in producing this manuscript. The routines to reproduce the main presented results are available for download from Bitbucket at https://bitbucket.org/yalkhimenkov/fastbiot_gpu3d_v1.0 (last access: 8 February 2021). The routines archive (v1.0) (Alkhimenkov *et al.*, 2021a) is available from a permanent DOI repository (Zenodo) at <http://doi.org/10.5281/zenodo.4519367> (last access: 8 February 2021).

Author contributions

YA: Conceptualization, Methodology, Software, Writing – Original Draft, Visualization, Investigation, Formal analysis, Project administration. **LR:** Methodology, Software, Visualization, Writing – review & editing. **LK:** Methodology, Software, Writing – review & editing. **BQ:** Conceptualization, Methodology, Writing – review & editing, Supervision. **YP:** Conceptualization, Methodology, Software, Writing – review & editing, Supervision.

Data Availability Statement

No data were used in producing this manuscript. The routines to reproduce the main presented results are available for download from Bitbucket at https://bitbucket.org/yalkhimenkov/fastbiot_gpu3d_v1.0 (last access: 8 February 2021). The routines archive (v1.0) (*Alkhimenkov et al., 2021a*) is available from a permanent DOI repository (Zenodo) at <http://doi.org/10.5281/zenodo.4519367> (last access: 8 February 2021).

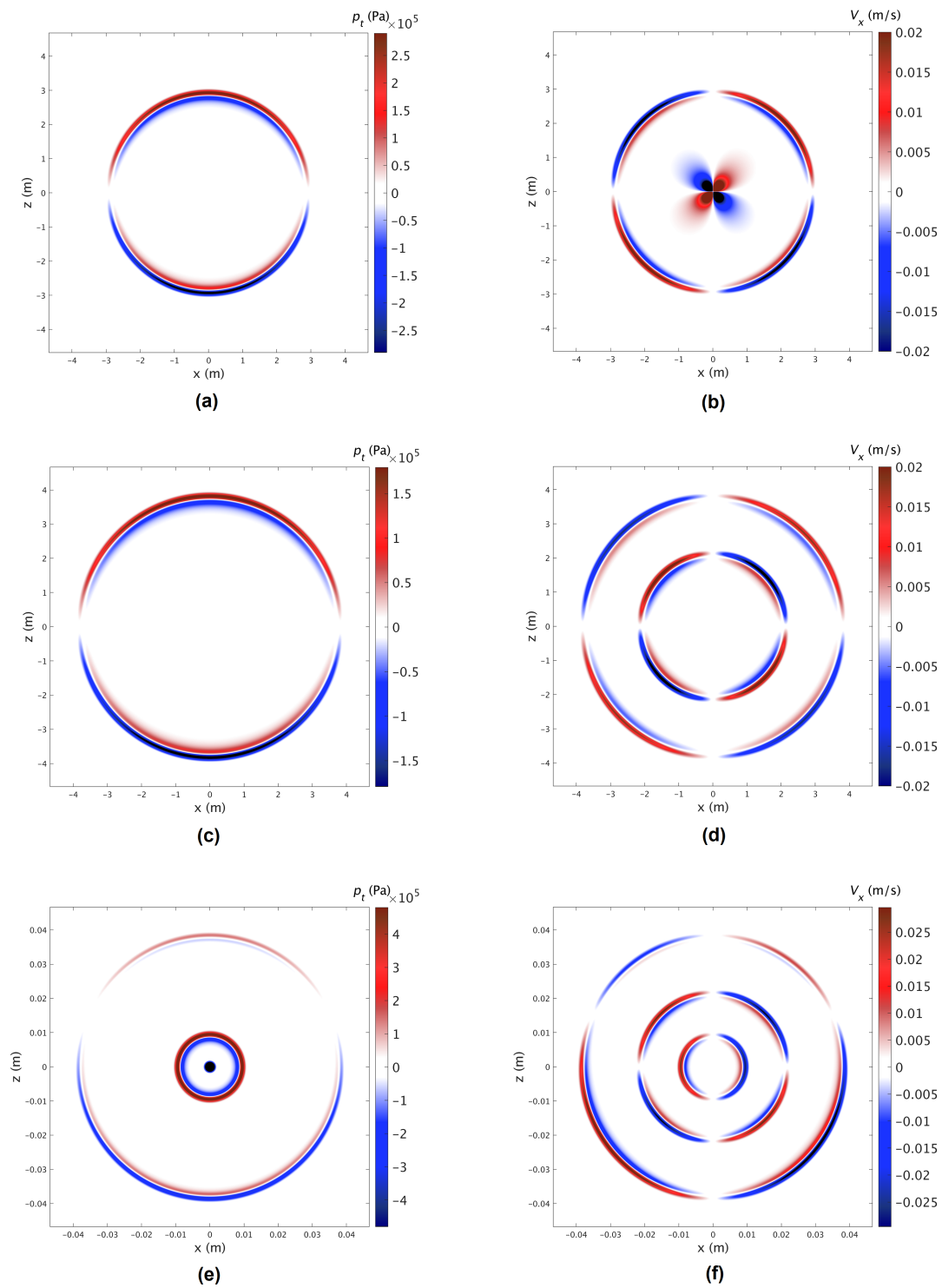


Figure 6.17: Numerical simulation of a propagating waves. (a), (c), (e) show the total pressure field \bar{p} , (v), (d), (f) show the particle-velocity field V_x . Plots (a) and (b) correspond to the poro-acoustic medium, (c) and (d) correspond to the poro-elastic medium (low frequency regime) and (e), (f) correspond to the poro-elastic medium (high frequency regime). The total physical simulation time is approximately $t = 9 \cdot 10^{-4}$ seconds. The material properties are those of an isotropic sandstone (Table 6.4).

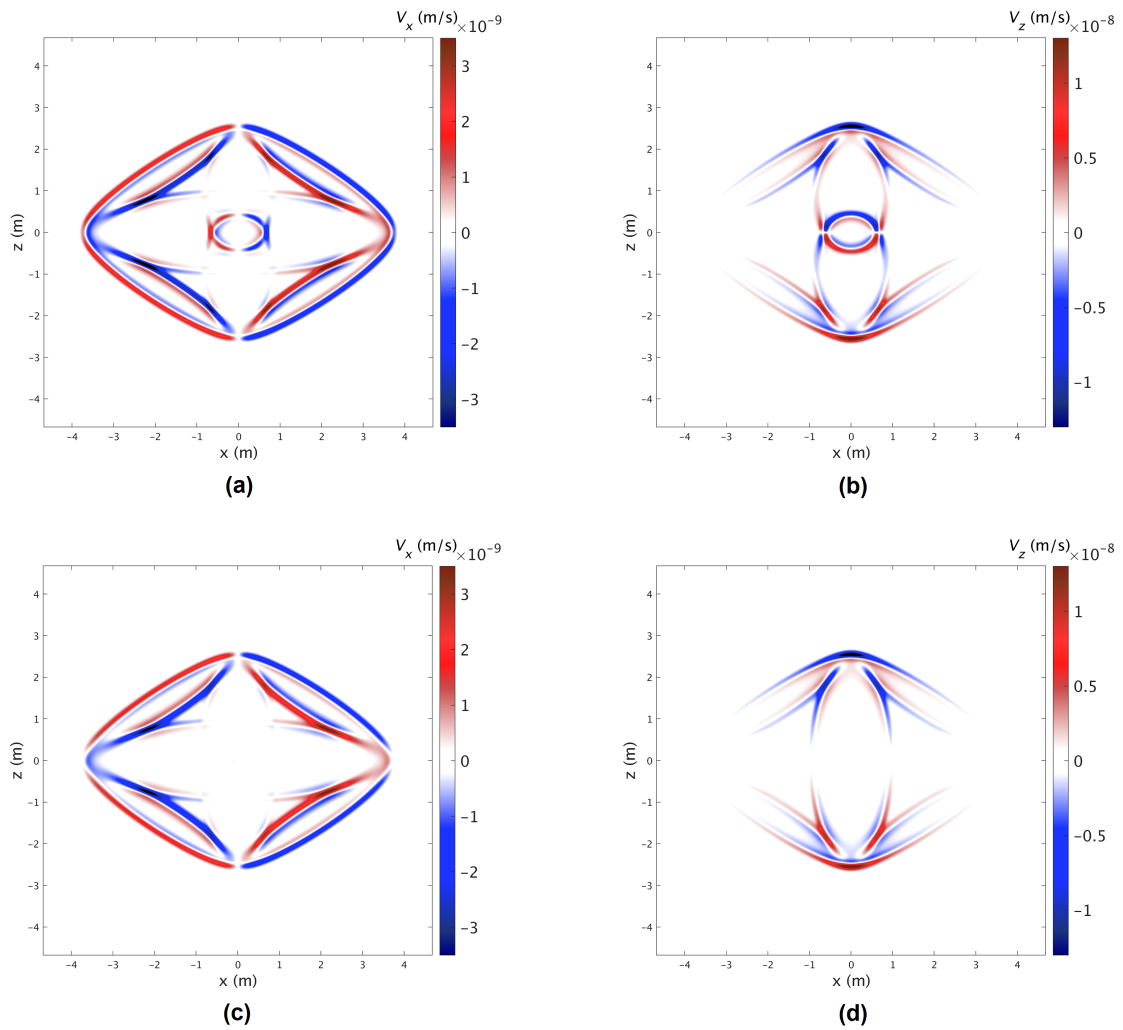


Figure 6.18: Snapshots showing particle-velocity fields V_x and V_z in the epoxy-glass medium (Table 6.4). Panels (a) and (b) correspond to the inviscid medium ($\eta = 0$), panels (c) and (d) correspond to the viscid medium ($\eta \neq 0$). The total physical simulation time is $t = 7.061 \cdot 10^{-04}$ seconds.

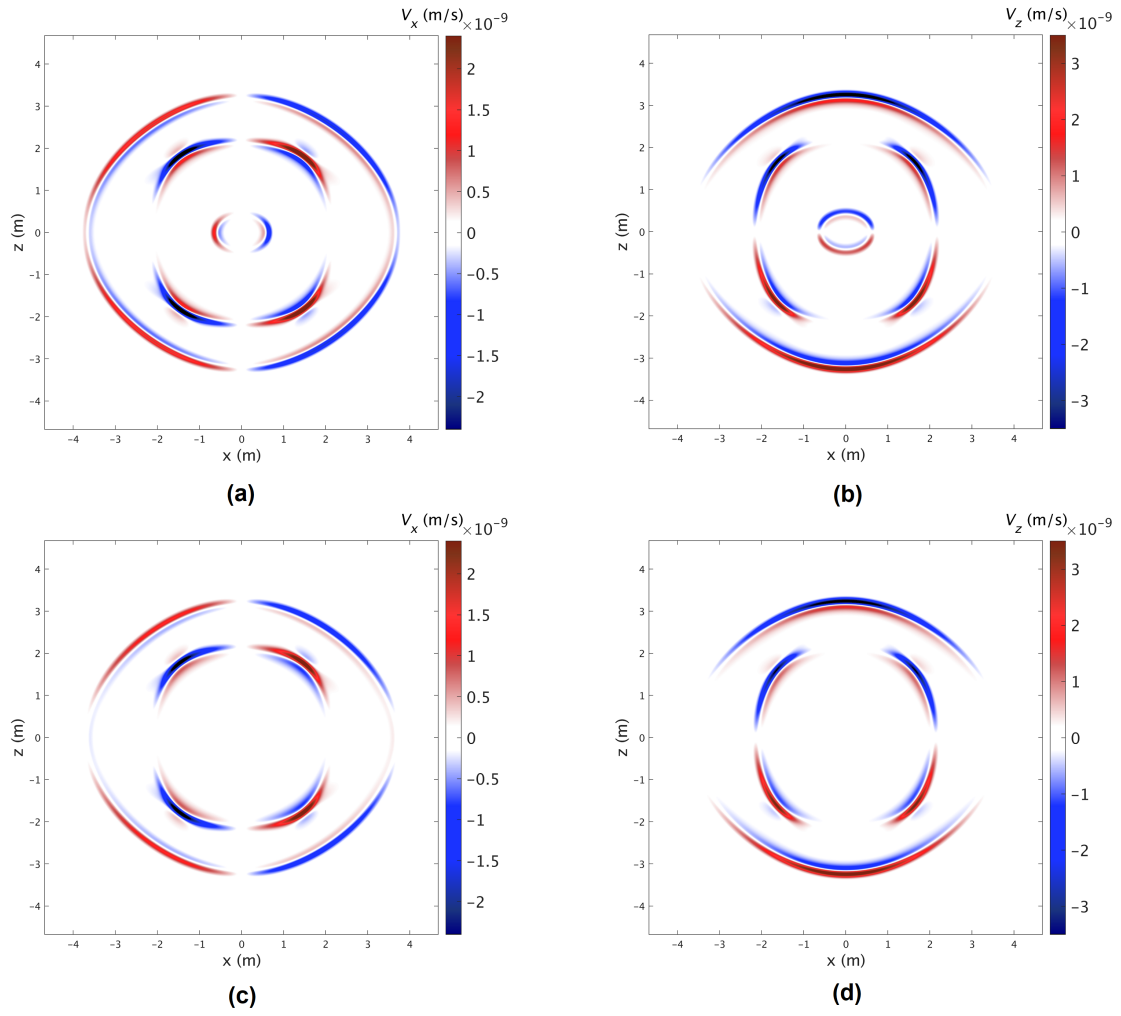


Figure 6.19: Snapshots showing particle-velocity fields V_x and V_z in the sandstone-VTI medium (Table 6.4). Panels (a) and (b) correspond to the inviscid medium ($\eta = 0$), panels (c) and (d) correspond to the viscid medium ($\eta \neq 0$). The total physical simulation time is $t = 6.15 \cdot 10^{-04}$ seconds.

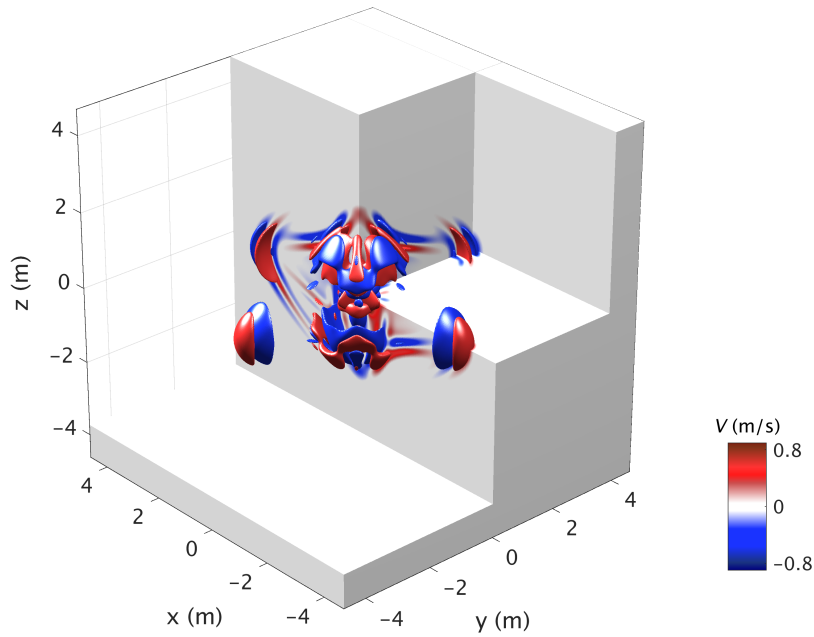


Figure 6.20: Snapshots showing the total solid particle velocity field $V = V_x + V_y + V_z$ in the medium having the properties of the glass-epoxy (Table 6.4). The velocity field is projected into $X - Z$ and $Y - Z$ slices. Red and blue isosurfaces denote the wave amplitudes of ± 0.4 . The anisotropic nature of the model is clearly visible due to the non-symmetric velocity field pattern. The total physical simulation time is $6.8 \cdot 10^{-4}$ seconds.

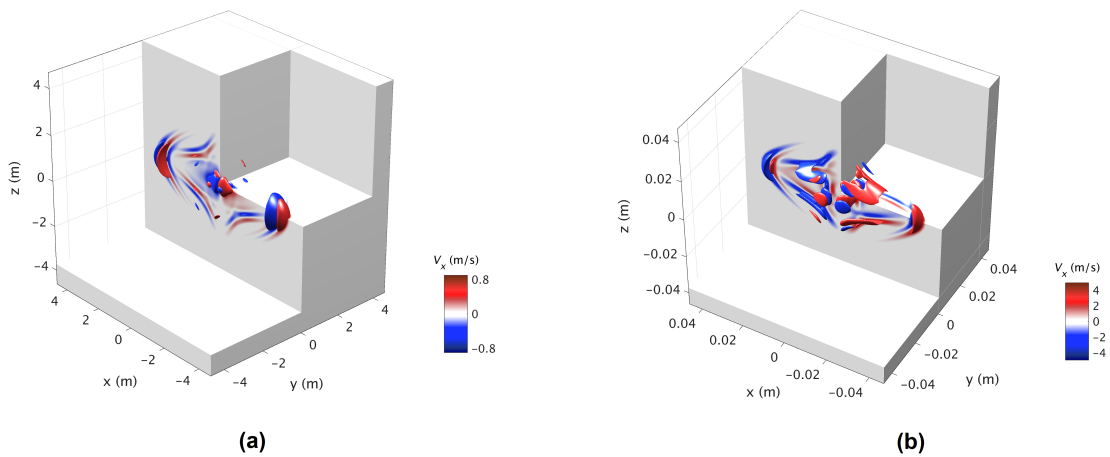


Figure 6.21: Snapshots showing the solid particle velocity field V_x in the medium having the properties of the glass-epoxy (Table 6.4). Panel (a) shows V_x of the same model as in Figure 6.20, red and blue isosurfaces denote the wave amplitudes of ± 0.4 , the total physical simulation time is $6.8 \cdot 10^{-4}$ seconds. Panel (b) shows V_x of the 100 times smaller model, which corresponds to the high frequency regime, The total physical simulation time is $6.8 \cdot 10^{-6}$ seconds. Red and blue isosurfaces denote the wave amplitudes of ± 3.0 .

6.8 Appendix A: Equations describing a single phase continuum material

6.8.1 Stress-strain relations

For a single phase linear elastic continuum material, the stress-strain relation (Hooke's Law) is

$$\boldsymbol{\sigma} = \mathbf{C} : \boldsymbol{\epsilon} \quad (6.60)$$

or using index (Einstein) notation

$$\sigma_{ij} = C_{ijkl} \epsilon_{kl}, \quad (6.61)$$

where $\boldsymbol{\sigma}$ is the second rank stress tensor, $\boldsymbol{\epsilon}$ is the second rank strain tensor, \mathbf{C} is the fourth rank stiffness tensor, $:$ denotes the double dot product and $i, j, k, l = \overline{1, \dots, 3}$. Bold symbols denote tensors and italic (non-bold) symbols denote tensor components. For small deformations, the strain tensor is defined as

$$\boldsymbol{\epsilon} = \frac{1}{2} (\nabla \otimes \mathbf{u} + (\nabla \otimes \mathbf{u})^T) \quad (6.62)$$

or

$$\epsilon_{kl} = \frac{1}{2} (\nabla_l u_k + \nabla_k u_l), \quad (6.63)$$

where \mathbf{u} is the displacement, \otimes denotes the tensor product, ∇ denotes the nabla operator and the superscript T corresponds to the transpose operator. For larger strains, an incremental formulation is preferable. Therefore, the relation between displacements and the time derivative of strain is

$$\frac{\partial \sigma_{ij}}{\partial t} = c_{ijkl} \frac{1}{2} (\nabla_l v_k^s + \nabla_k v_l^s), \quad (6.64)$$

where the particle velocity is defined as $v_i^s = \partial u_i / \partial t$. Note, that in the case of small linear deformations, the definition (6.60)-(6.63) coincides with the definition (6.64). For large deformations the definition (6.60)-(6.63) is not longer valid due to the absence of second-order terms of the finite strain tensor while the definition (6.64) still holds. In this article, we only use the incremental formulation (6.64). In isotropic media, the stress and strain tensors can be separated into volumetric and deviatoric parts. Equation (6.64) can be rewritten as

$$\frac{\partial \sigma_{ij}}{\partial t} = K \nabla_k v_k \delta_{ij} + 2G \left(\frac{1}{2} (\nabla_j v_i + \nabla_i v_j) - \frac{1}{3} \nabla_k v_k \delta_{ij} \right). \quad (6.65)$$

Equation (6.65) can be simplified, once pressure and deviatoric stresses are introduced,

$$\frac{\partial \sigma_{ij}}{\partial t} = - \frac{\partial p}{\partial t} \delta_{ij} + \frac{\partial \tau_{ij}}{\partial t}, \quad (6.66)$$

where pressure p is

$$\frac{\partial p}{\partial t} = -K \nabla_k v_k \quad (6.67)$$

and the deviatoric stress tensor τ_{ij} is expressed as

$$\frac{\partial \tau_{ij}}{\partial t} = 2G \left(\frac{1}{2} (\nabla_j v_i + \nabla_i v_j) - \frac{1}{3} \nabla_k v_k \delta_{ij} \right). \quad (6.68)$$

6.8.2 Dynamic equations

The conservation of linear momentum for a single phase material is

$$\rho \frac{\partial v_i}{\partial t} = \nabla_j \sigma_{ij}. \quad (6.69)$$

Equation (6.69) can also be called equation of motion or elastodynamic force balance law. By separating the stress tensor into deviatoric and volumetric parts, equation (6.69) can be written as

$$\rho \frac{\partial v_i}{\partial t} = \nabla_j (-p\delta_{ij} + \tau_{ij}) \quad (6.70)$$

In summary, the constitutive equations (6.67)-(6.68) and the conservation of linear momentum (6.70) fully describe the behavior of a single phase material. Depending on the initial conditions (or the source terms) and the material parameters, the response of a single phase material may include one fast (longitudinal) wave and one shear wave.

6.9 Appendix B: Poroelastic parameters

Three experiments permit to determine the poroelastic parameters required for Biot's equations (*Makhnenko and Podladchikov, 2018*). The drained bulk modulus K_d can be measured under drained experiments. In such experiments the pore fluid is allowed to leave the rock during loading and that pore fluid pressure is maintained at a constant level ($p_f = \text{const}$, see equation (6.1))

$$K_d = \frac{1}{\nabla_k v_k^s} \frac{\partial \bar{p}}{\partial t} \Big|_{(p_f = \text{const})} \quad (6.71)$$

The undrained bulk modulus K_u can be obtained under undrained experiments. In such experiments the fluid content inside the rock does not change during loading, meaning that fluid does not flow through the boundaries of the considered element ($\nabla_k q_k^D = 0$, see equation (6.1))

$$K_u = \frac{1}{\nabla_k v_k^s} \frac{\partial \bar{p}}{\partial t} \Big|_{(\nabla_k q_k^D = 0)} \quad (6.72)$$

The Biot-Willis parameter α can be obtained underunjacketed experiments, in which an increase in the total pressure \bar{p} is equal to the increase in fluid pressure p_f : ($d\bar{p} = dp_f$, see equation (6.1)). For more information about how to measure poroelastic constants in rock samples, we refer to *Zimmerman (1990)*.

6.10 Appendix C: An alternative dimensional analysis of Biot's equations

In (6.12), instead of the base quantity ρ_t , an alternative choice is possible, namely, ρ_a . In this case, equation (6.12) reads

$$\rho_a \begin{pmatrix} \frac{\rho_t}{\rho_a} & -\frac{\rho_f}{\rho_a} \\ -\frac{\rho_a}{\rho_t} & 1 \end{pmatrix} \begin{pmatrix} \frac{\partial v^s}{\partial t} \\ -\frac{\partial q^D}{\partial t} \end{pmatrix} = \begin{pmatrix} \frac{\partial \bar{\sigma}}{\partial x} \\ \frac{\eta}{k} q^D + \frac{\partial p_f}{\partial x} \end{pmatrix}, \quad (6.73)$$

where

$$\alpha_a = \frac{\alpha}{B} \left(1 + \frac{4/3G}{K_u} \right). \quad (6.74)$$

In the resulting system, equation (6.17) is still the same, while equation (6.18) becomes

$$(I_1)^2 \begin{pmatrix} \rho_{ta} & -\rho_{fa} \\ -\rho_{fa} & 1 \end{pmatrix} \begin{pmatrix} \frac{\partial \tilde{v}^s}{\partial \tilde{t}} \\ -\frac{\partial \tilde{q}^D}{\partial \tilde{t}} \end{pmatrix} = \begin{pmatrix} \frac{\partial \tilde{\sigma}}{\partial \tilde{x}} \\ I_2 \tilde{q}^D + \frac{\partial \tilde{p}_f}{\partial \tilde{x}} \end{pmatrix}, \quad (6.75)$$

where $\rho_{fa} \equiv \rho_f / \rho_a$, $\rho_{ta} \equiv \rho_t / \rho_a$,

$$I_1 = \sqrt{\rho_a s_{11}^d} \frac{L_x^*}{\tau^*}, \quad (6.76)$$

and

$$I_2 = \frac{\eta s_{11}^d (L_x^*)^2}{k \tau^*} \equiv \frac{1}{D} \frac{(L_x^*)^2}{\tau^*}, \quad (6.77)$$

$$D = \frac{k}{\eta s_{11}^d}. \quad (6.78)$$

The alternative four dimensionless parameters α , α_a , ρ_{fa} and ρ_{ta} now define the coupling between the solid and fluid phases. If we similarly set $I_1 = 1$, then $L_x^* = \tau^* / \sqrt{\rho_a s_{11}^d}$ and I_2 becomes

$$I_2 = \frac{\eta}{k \rho_a} \tau^*. \quad (6.79)$$

Thus, we choose the new τ^* as

$$\tau^* = \left(\frac{\eta}{k \rho_a} \right)^{-1} \equiv \left(\frac{\eta \phi}{k \rho_f T} \right)^{-1}, \quad (6.80)$$

we end up with $I_2 = 1$ and the transformation frequency now is equivalent to the Biot's characteristic frequency (6.40). Indeed, the dimensional angular frequency ω^d is calculated as $\omega^d = \omega \omega^*$, where ω is the non-dimensional angular frequency and ω^* is the transformation frequency (analogous to (6.39))

$$\omega^* = \frac{1}{\tau^*} \equiv \frac{\eta \phi}{k \rho_f T}, \quad (6.81)$$

which is exactly the Biot's characteristic frequency ω_c (6.40). This is the main advantage of the new dimensional analysis. The disadvantage is that the drained wave velocity V_d formula disappears in (6.76), which makes the interpretation of I_1 in terms of usual physical quantities less transparent. By using this new dimensional analysis, Figures 6.1-6.4 will remain almost the same with the only slight shift of the transition frequency closer to $\omega = 1$. This shift in ω is defined by the ratio between ρ_t and $(\rho_f T / \phi)$.

6.11 Appendix D: Elastodynamic Biot's equations for anisotropic media

6.11.1 Arbitrary anisotropic media

Elastodynamic Biot's equations in arbitrary anisotropic media can be written in the first order form. The stress-strain relations are

$$\frac{\partial \bar{\sigma}_{ij}}{\partial t} = c_{ijkl}^u \nabla_k v_l^s + \alpha_{ij} M \nabla_k q_k^D, \quad (6.82)$$

$$\frac{\partial p_f}{\partial t} = -M \left(\alpha_{ij} \nabla_i v_j^s + \nabla_m q_m^D \right), \quad (6.83)$$

where c_{ijkl}^u is the 4-th order undrained stiffness tensor and α_{ij} is the Biot-Willis parameter represented by a second order tensor. The conservation of linear momentum reads

$$\frac{\partial v_i^s}{\partial t} = \varrho_{11} \nabla_i \bar{\sigma}_{ij} + \varrho_{12} \left(\nabla_i p_f + \frac{\eta}{k_i} q_i^D \right), \quad (6.84)$$

$$\frac{\partial q_i^D}{\partial t} = -\varrho_{21} \nabla_i \bar{\sigma}_{ij} - \varrho_{22} \left(\nabla_i p_f + \frac{\eta}{k_i} q_i^D \right), \quad (6.85)$$

where

$$\varrho_{ij} = \begin{pmatrix} \varrho_{11} & \varrho_{12} \\ \varrho_{21} & \varrho_{22} \end{pmatrix} = \frac{1}{\Theta} \begin{pmatrix} \rho_a & \rho_f \\ \rho_f & \rho_t \end{pmatrix}, \quad (6.86)$$

$\Theta = \rho_t \rho_a - \rho_f^2$ and k_i denotes permeability in i - direction, respectively. In (6.82)-(6.86), ∂_t represents a time derivative, v_i and q_i^D are vector fields, σ_{ij} is a tensor field, p_f is a scalar field. All the material parameters, namely, c_{ijkl}^u , α_{ij} , M , ϱ_{ij} , η , k_i are constant in time but may vary in space.

6.11.2 Orthorhombic media

An orthorhombic medium is described by nine elastic components of the stiffness tensor. We use the shortened Voigt notation as a shortcut. The stress-strain relations are

$$\frac{\partial \bar{\sigma}_{xx}}{\partial t} = c_{11}^u \partial_x v_x^s + c_{12}^u \partial_y v_y^s + c_{13}^u \partial_z v_z^s + \alpha_1 M \left(\partial_x q_x^D + \partial_y q_y^D + \partial_z q_z^D \right), \quad (6.87)$$

$$\frac{\partial \bar{\sigma}_{yy}}{\partial t} = c_{12}^u \partial_x v_x^s + c_{22}^u \partial_y v_y^s + c_{23}^u \partial_z v_z^s + \alpha_2 M \left(\partial_x q_x^D + \partial_y q_y^D + \partial_z q_z^D \right), \quad (6.88)$$

$$\frac{\partial \bar{\sigma}_{zz}}{\partial t} = c_{13}^u \partial_x v_x^s + c_{23}^u \partial_y v_y^s + c_{33}^u \partial_z v_z^s + \alpha_3 M \left(\partial_x q_x^D + \partial_y q_y^D + \partial_z q_z^D \right), \quad (6.89)$$

$$\frac{\partial \bar{\sigma}_{yz}}{\partial t} = c_{44}^u \left(\partial_z v_y^s + \partial_y v_z^s \right), \quad (6.90)$$

$$\frac{\partial \bar{\sigma}_{xz}}{\partial t} = c_{55}^u \left(\partial_z v_x^s + \partial_x v_z^s \right), \quad (6.91)$$

$$\frac{\partial \bar{\sigma}_{xy}}{\partial t} = c_{66}^u \left(\partial_y v_x^s + \partial_x v_y^s \right), \quad (6.92)$$

$$\frac{\partial p_f}{\partial t} = -\alpha_1 M \partial_x v_x^s - \alpha_2 M \partial_y v_y^s - \alpha_3 M \partial_z v_z^s - M \left(\partial_x q_x^D + \partial_y q_y^D + \partial_z q_z^D \right), \quad (6.93)$$

∂_i represents a spatial derivative in i - direction. The relation between the drained stiffness matrix c_{ij} and the undrained stiffness matrix c_{ij}^u is

$$c_{ij}^u = c_{ij} + \alpha_i \alpha_j M, \quad (6.94)$$

where $\alpha_i = (\alpha_1, \alpha_2, \alpha_3, 0, 0, 0)$ and $\alpha_j = (\alpha_1, \alpha_2, \alpha_3, 0, 0, 0)^T$ are the Biot-Willis coefficients,

$$\alpha_i = 1 - \left(\sum_{j=1}^3 c_{ij} \right) / (3K_g), \quad (6.95)$$

for $i = 1, 2, 3$. For example,

$$\alpha_1 = 1 - \frac{c_{11} + c_{12} + c_{13}}{3K_g}, \quad (6.96)$$

$$\alpha_2 = 1 - \frac{c_{21} + c_{22} + c_{23}}{3K_g}, \quad (6.97)$$

$$\alpha_3 = 1 - \frac{c_{13} + c_{23} + c_{33}}{3K_g} \quad (6.98)$$

and M is the solid-fluid coupling modulus, defined as

$$M = \left(\phi / K_f + (1 - \phi) / K_g - K^* / K_g^2 \right)^{-1}, \quad (6.99)$$

$$K^* = \frac{1}{9} \sum_{i=1}^3 \sum_{j=1}^3 c_{ij} = [c_{11} + c_{22} + c_{33} + 2(c_{12} + c_{13} + c_{23})] / 9 \quad (6.100)$$

The modulus K^* is usually called the generalized bulk modulus, which, in fact, represents the Voigt average of the bulk modulus for an orthorhombic symmetry system. The conservation of linear momentum reads

$$\frac{\partial q_x^D}{\partial t} = \rho_{21} \left(-\partial_x \bar{\sigma}_{xx} - \partial_y \bar{\sigma}_{xy} - \partial_z \bar{\sigma}_{xz} \right) - \rho_{22} \left(\partial_x p_f + \frac{\eta}{k_1} q_x \right), \quad (6.101)$$

$$\frac{\partial q_y^D}{\partial t} = \varrho_{21} (-\partial_x \bar{\sigma}_{xy} - \partial_y \bar{\sigma}_{yy} - \partial_z \bar{\sigma}_{yz}) - \varrho_{22} \left(\partial_y p_f + \frac{\eta}{k_2} q_y \right), \quad (6.102)$$

$$\frac{\partial q_z^D}{\partial t} = \varrho_{21} (-\partial_x \bar{\sigma}_{xz} - \partial_y \bar{\sigma}_{yz} - \partial_z \bar{\sigma}_{zz}) - \varrho_{22} \left(\partial_z p_f + \frac{\eta}{k_3} q_z \right), \quad (6.103)$$

$$\frac{\partial v_x^s}{\partial t} = \varrho_{11} (\partial_x \bar{\sigma}_{xx} + \partial_y \bar{\sigma}_{xy} + \partial_z \bar{\sigma}_{xz}) + \varrho_{12} \left(\partial_x p_f + \frac{\eta}{k_1} q_x \right), \quad (6.104)$$

$$\frac{\partial v_y^s}{\partial t} = \varrho_{11} (\partial_x \bar{\sigma}_{xy} + \partial_y \bar{\sigma}_{yy} + \partial_z \bar{\sigma}_{yz}) + \varrho_{12} \left(\partial_y p_f + \frac{\eta}{k_2} q_y \right), \quad (6.105)$$

$$\frac{\partial v_z^s}{\partial t} = \varrho_{11} (\partial_x \bar{\sigma}_{xz} + \partial_y \bar{\sigma}_{yz} + \partial_z \bar{\sigma}_{zz}) + \varrho_{12} \left(\partial_z p_f + \frac{\eta}{k_3} q_z \right), \quad (6.106)$$

where ϱ_{ij} is given by (6.86).

6.12 Appendix E: Discretization of Biot's equations

For a given function $g_{i,j,k}^n = g(t^l, x_i, y_j, z_k)$, the following operators for the time evolution are introduced

$$D_t^1[g] = \frac{\partial g}{\partial t} = \frac{g_{i,j,k}^{l+1/2} - g_{i,j,k}^{l-1/2}}{\Delta t}, \quad (6.107)$$

$$D_t^2[g] = \frac{\partial g}{\partial t} = \frac{g_{i+1/2,j,k}^{l+1} - g_{i+1/2,j,k}^l}{\Delta t}, \quad (6.108)$$

$$\bar{D}_\chi[g] = \chi g_{i+1/2,j,k}^{l+1} + (1-\chi) g_{i+1/2,j,k}^l, \quad (6.109)$$

where $\chi \in [0; 1]$ is the weight parameter. The following operators for the spatial derivatives are introduced

$$D_x^1[g] = \frac{\partial g}{\partial x} = \frac{g_{i+1,j,k}^{l+1/2} - g_{i,j,k}^{l+1/2}}{\Delta x}, \quad D_y^1[g] = \frac{\partial g}{\partial y} = \frac{g_{i,j+1,k}^{l+1/2} - g_{i,j,k}^{l+1/2}}{\Delta y}, \quad D_z^1[g] = \frac{\partial g}{\partial z} = \frac{g_{i,j,k+1}^{l+1/2} - g_{i,j,k}^{l+1/2}}{\Delta z}, \quad (6.110)$$

$$D_x^2[g] = \frac{\partial g}{\partial x} = \frac{g_{i+1/2,j,k}^l - g_{i-1/2,j,k}^l}{\Delta x}, \quad D_y^2[g] = \frac{\partial g}{\partial y} = \frac{g_{i,j+1/2,k}^l - g_{i,j-1/2,k}^l}{\Delta y}, \quad D_z^2[g] = \frac{\partial g}{\partial z} = \frac{g_{i,j,k+1/2}^l - g_{i,j,k-1/2}^l}{\Delta z}, \quad (6.111)$$

The following averaging operators for the material parameters are introduced

$$([g]_1)_{i+1/2,j,k} = (g_{i,j,k} + g_{i+1,j,k})/2, \quad (6.112)$$

$$([g]_2)_{i+1/2,j+1/2,k} = 4(1/g_{i,j,k} + 1/g_{i+1,j,k} + 1/g_{i,j+1,k} + 1/g_{i+1,j+1,k})^{-1}. \quad (6.113)$$

For simplicity, equations only in x - direction are shown in the discrete form. A few additional operators are introduced

$$\nabla \cdot v^s = D_x^2[v_x^s] + D_y^2[v_y^s] + D_z^2[v_z^s], \quad \nabla \cdot q^D = D_x^2[q_x^D] + D_y^2[q_y^D] + D_z^2[q_z^D]. \quad (6.114)$$

The discretized system of equations is

$$D_t^1[\bar{p}] = -K_u \nabla \cdot v^s - K_u B \nabla \cdot q^D, \quad (6.115)$$

$$D_t^1[p_f] = -K_u B \nabla \cdot v^s - K_u B / \alpha \nabla \cdot q^D, \quad (6.116)$$

$$D_t^1[\bar{\tau}_{xx}] = 2G (D_x^2[v_x^s] - 1/3 \nabla \cdot v^s), \quad (6.117)$$

discretization of $\bar{\tau}_{yy}$ and $\bar{\tau}_{zz}$ is in analogy to that of $\bar{\tau}_{xx}$. The stress deviator tensor field is discretized as

$$D_t^1[\bar{\tau}_{xy}]_{i+1/2,j+1/2,k} = [G]_2 (D_x^2[v_y^s] + D_y^2[v_x^s]), \quad (6.118)$$

discretization of $\bar{\tau}_{xz}$ and $\bar{\tau}_{yz}$ is in analogy to that of $\bar{\tau}_{xy}$. The total stress tensor field $\nabla \cdot \bar{\sigma}_{xx}$ is

$$\nabla \cdot \bar{\sigma}_{xx} = D_x^1[\bar{\tau}_{xx}] - D_x^1[\bar{p}] + \frac{[\bar{\tau}_{xy}]_{i+1/2,j+1/2,k}^{l+1/2} - [\bar{\tau}_{xy}]_{i+1/2,j-1/2,k}^{l+1/2}}{\Delta y} + \frac{[\bar{\tau}_{xz}]_{i+1/2,j,k+1/2}^{l+1/2} - [\bar{\tau}_{xz}]_{i+1/2,j,k-1/2}^{l+1/2}}{\Delta z}. \quad (6.119)$$

The Darcy's flux and the particle velocity vector fields in the discrete form are

$$D_t^2[q_x^D] = \frac{1}{[\Theta]_1} \left(-[\rho_f]_1 \nabla \cdot \bar{\sigma}_{xx} - [\rho_t]_1 D_x^1[p_f] - [\rho_t]_1 \frac{[\eta_f]_1}{[k]_1} \bar{D}_\chi[q_f^D] \right), \quad (6.120)$$

$$D_t^2[v_x^s] = \frac{1}{[\Theta]_1} \left([\rho_a]_1 \nabla \cdot \bar{\sigma}_{xx} + [\rho_f]_1 D_x^1[p_f] + [\rho_f]_1 \frac{[\eta_f]_1}{[k]_1} \bar{D}_\chi[q_f^D] \right). \quad (6.121)$$

6.13 Appendix F: The GPU architecture

GPUs feature a hierarchic structure. The basic computational unit is the Thread. Threads are organized in Blocks of Threads that constitute the Grid. A GPU function (CUDA kernel) executes in as many concurrent instances as the total amount of Threads, i.e the Threads per Block times the amount of Blocks. We assign each data unit (grid cell) of our computational domain to a specific Thread; the identical numerical operation performed on each data unit (grid cell) will thus be executed simultaneously in the entire computational domain (Figure 6.22).

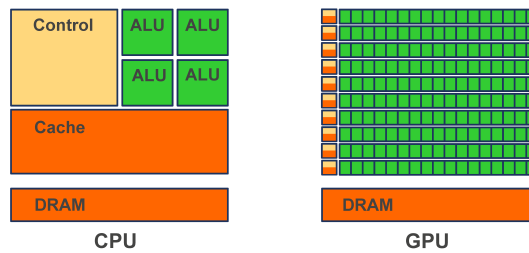


Figure 6.22: Schematic chip representation for both the central processing unit (CPU) and graphical processing unit (GPU) architectures. The GPU architecture consist of thousands of arithmetic and logical units (ALU). On the CPU, most of the on-chip space is devoted to controlling units and cache memory, while the number of ALUs is significantly reduced.

Chapter 7

Stability of discrete schemes of Biot's poroelastic equations

Yury Alkhimenkov, Lyudmila Khakimova and Yury Podladchikov

Published ¹ in *Geophysical Journal International*.

¹Alkhimenkov, Y. et al. (2021). Stability of discrete schemes of Biot's poroelastic equations. *Geophysical Journal International*, **225**(1), 354-377, doi:10.1093/gji/ggaa584

Abstract

The efficient and accurate numerical modeling of Biot's equations of poroelasticity requires the knowledge of the exact stability conditions for a given set of input parameters. Up to now, a numerical stability analysis of the discretised Biot's equations has been performed only for a few numerical schemes. We perform the von Neumann's stability analysis of the discretised Biot's equations. We use an explicit scheme for the wave propagation and different implicit and explicit schemes for the Darcy's flux. We derive the exact stability conditions for all the considered schemes. The obtained stability conditions for the discretised Biot's equations were verified numerically in one-, two- and three-dimensions. Additionally, we present the von Neumann's stability analysis of the discretised linear damped wave equation. We provide symbolic Maple scripts to obtain exact stability conditions for any given set of input material and numerical parameters.

7.1 Introduction

Poroelasticity is a well established discipline that describes the interaction between the deformation of an elastic porous solid and the fluid flow in a porous material. Poroelastic response of an isotropic two phase medium results in two longitudinal waves (*Frenkel*, 1944), the P-wave of the first kind (fast) and the P-wave of the second kind (slow), and in one shear wave. *Biot* (1941, 1956b,a, 1962a) established poroelasticity as a discipline, which includes static and dynamic responses of a porous material, the experiments to obtain the material parameters (*Biot and Willis*, 1957), the extensions to include viscoelasticity and non-linear behavior of a porous material (*Biot*, 1965). The theory of poroelasticity finds applications in many areas, including earth sciences, biology, medicine and others. In earth sciences, simplified models based on poroelasticity can be useful to induced seismicity, seismic exploration, hydrogeology, rock physics and others. Therefore, efficient and accurate numerical solutions of poroelastic equations are of great importance.

The simplest equation which describes the propagation of acoustic waves in a fluid flowing through a porous medium is called the linear damped wave equation (DWE) and is known far before the Biot's equations were introduced (*Pascal*, 1986). The DWE describes many physical systems. This equation initially was used in the description of the telegraph, today known as the telegraph equation (*Jordan and Puri*, 1999). The DWE also arises in the generalized (or hyperbolic) thermoelasticity (*Hetnarski and Ignaczak*, 1999). The numerical solutions of DWE were presented in different branches of mathematics and physics. DWE (as a hyperbolic conservation law with a stiff source term) was extensively studied by many authors (*Jin and Levermore*, 1996; *Pareschi and Russo*, 2005; *Boscarino and Russo*, 2013) and references therein. Many finite difference schemes were introduced, e.g. (*Mickens and Jordan*, 2004; *Mohanty*, 2004; *Macías-Díaz and Puri*, 2010; *Ding et al.*, 2012; *Najafi and Izadi*, 2014). The dynamic Biot's equations of poroelasticity are far more complicated than the DWE, and researchers used different numerical methods to solve them. A finite-differences/volumes on Cartesian space-time grids were the first numerical methods used to simulate poroelastic wave propagation (*Zhu and McMechan*, 1991; *Dai et al.*, 1995; *Carcione and Quiroga-Goode*, 1995; *Özdenvar and McMechan*, 1997; *Zeng et al.*, 2001; *Masson et al.*, 2006; *Wenzlau and Müller*, 2009; *Chiavassa et al.*, 2010; *Chiavassa and Lombard*, 2011). Other numerical solutions include pseudo-spectral methods (*Özdenvar and McMechan*, 1997), spectral element methods (*Morency and Tromp*, 2008), discontinuous Galerkin methods (*de la Puente et al.*, 2008; *Ward et al.*, 2017; *Zhan et al.*, 2019; *Shukla et al.*, 2020) and finite volume methods on unstructured grids (*Lemoine et al.*, 2013; *Lemoine*, 2016). Many studies have been performed for space-time finite element methods for hyperbolic (wave) and parabolic problems (*Schieweck*, 2010; *Köcher and Bause*, 2014; *Ernesti and Wieners*, 2019; *Bause et al.*, 2020) and the references therein. A splitting scheme has been investigated for the numerical approximation of simplified Biot's equations considering mixed hyperbolic-parabolic structure (*Bause et al.*, 2019). Despite the number of numerical studies, the precise stability conditions were determined only for a few numerical schemes. The first studies profited from approximate stability conditions or investigated a stable time step numerically. *Carcione and Quiroga-Goode* (1995) discussed the stability issues in explicit schemes for Biot's equation. *Masson et al.* (2006) investigated the stability condition of a particular numerical scheme for Biot's equations. *Chiavassa et al.* (2010) reported the exact limits of a stable time step for the explicit schemes. *O'Brien* (2010) explored the stability conditions of two numerical schemes for Biot's equations and found some inconsistencies in the previous studies. Nevertheless, there are no studies which explore the stability conditions of a range of implicit

and explicit schemes for Biot's equations of poroelasticity and provide closed form expressions to evaluate a stable time step for any given set of material and numerical parameters. An exact stability condition for the time step is the key parameter which helps to control the accuracy and computational efficiency of numerical solutions.

In this work, we perform a rigorous von Neumann's stability analysis of the discretised Biot's poroelastic equations. We use an explicit numerical scheme for the wave propagation (*Virieux and Madariaga, 1982; Virieux, 1986*) and three schemes (explicit, implicit-explicit and implicit) for the Darcy's flux. Momentum conservation is exact for the applied staggered scheme for the wave propagation, momentum conservation is also satisfied after the discretization. We also perform a rigorous von Neumann's stability analysis of the discretised DWE since they behave similarly to the original Biot's poroelastic equations and can help in understanding the stability of the latter. All our derivations are exact (if not mentioned otherwise) and were verified with the help of the symbolic math computing environment Maple 2019. Where it was possible, we provide the closed-form expressions for the stability conditions. Where it was not possible, we refer to the Maple script (supplementary material) where an exact stability condition can be calculated symbolically for any set of input material parameters. We also provide simple approximate expressions for the von Neumann's stability of the discretised Biot's poroelastic equations for all considered schemes. Furthermore, we discuss other implicit schemes which may provide different stability conditions for the DWE and Biot's equations. We have not used any specialized terminology from the numerical analysis, thus, this article is suitable for scientists across the disciplines.

The paper is organized as follows. In section 2, we briefly outline the theory of the von Neumann's stability analysis. In section 3, we perform the von Neumann's stability analysis of the discretised DWE. In section 4, we perform the von Neumann's stability analysis of the discretised Biot's equations of poroelasticity for different discretization schemes. In section 5, we summarize the results and compare them with previous studies.

7.2 Theory

The goal of a numerical solution of a partial differential equation (PDE) is to get the result, which is very close to the exact solution of the original "continuous" PDE. In order to achieve that, a desired PDE is discretized on a certain space and time mesh and, then, the discrete version of the PDE is solved on a computer. The validity of the obtained numerical solution can be evaluated using a very well established theory of numerical methods, well explained in many text books, for example, in *Hirsch (1988)*.

The basic idea of the numerical analysis is to evaluate several aspects of a discrete PDE (can be also called as a discretization scheme), namely, consistency, stability, convergence and accuracy. Consistency evaluates how well the discrete PDE approximates the exact (continuous) PDE. It can be done by analyzing the so-called truncation error, which roughly corresponds to a Taylor expansion of the discrete PDE and evaluation of the difference between the exact solution and the discrete solution. Stability evaluates the errors of the discrete PDE as it evolves in time. It can be done by calculating the evolution of all errors (decomposed into harmonics) made at one discrete time step. Evolution of all components must be bounded otherwise the errors will be amplified at each time step. Convergence states that the numerical solution approach the exact solution of the exact (continuous) PDE as space and time discretization tend to zero. The three definitions mentioned above are related via the Lax Equivalence Theorem. This theorem states that if the discretization scheme of a well-posed linear initial value problem is consistent and stable, the scheme is convergent. The accuracy of a discretization scheme defines how fast the numerical solution tends to the exact solution as space or time discretization are reduced by an order of magnitude. The accuracy can be, for example, second order in space and second order in time, meaning that if one refines the spatial and time discretization grids by one order of magnitude, the numerical solution will become closer to the exact solution by two orders of magnitude.

7.2.1 Basic theory for von Neumann stability analysis

Let us consider a 1D first order system of partial differential equations

$$\partial_t f(x, t) + A \partial_x f(x, t) = 0, \quad (7.1)$$

where A is a linear operator. For a numerical solution, a linear difference equation is needed. Let us use a rectangular time-space grid. The time is discretized as $t^l = l\Delta t$ and the spatial grid is discretized as $x_i = i\Delta x$. The PDE (7.1) can be written in a discrete form as

$$D_t f(x, t) + A D_x f(x, t) = 0, \quad (7.2)$$

where D_t and D_x are certain discrete time and space operators. The von Neumann's stability method analyzes a time evolution of a discrete numerical solution W_i^l of (7.2) in the space-temporal frequency domain. This method provides the stability of linear schemes with constant coefficients. A discrete plane wave harmonic is inserted into the discrete numerical solution, which is represented as

$$W_i^l = Q_j^l e^{Ik \cdot x_i} = Q_j^l e^{Ik \cdot i\Delta x} = Q_j^n e^{Ii\phi}, \quad (7.3)$$

where Q_j^l is the amplitude of the j harmonic of W_i , I is the imaginary unit, $k = k_j$ is the wave number, i is the mesh index and Δx is the mesh spacing, $\phi = i\Delta x$ is a phase angle. For a single harmonic wave $Q_j^l e^{Ii\phi}$, its time evolution is the same as for the full solution W_i^n . The stability criterion establishes a bound on the time evolution of any harmonic. The amplification factor is

$$F(\phi, \Delta t, \Delta x) = \frac{W^{l+1}}{W^l}. \quad (7.4)$$

For a single discrete equation, F is a scalar. For a system of discrete equations, F becomes a matrix. The von Neumann's necessary condition for stability assert that the spectral radius of the amplification matrix F must satisfy the following inequality

$$\lambda_\xi(F) \leq 1 + O(\Delta t), \quad (7.5)$$

where λ_ξ are the ξ eigenvalues of the amplification matrix F whose size is $\xi \times \xi$. Since, the stability condition depends on the spatial discretization Δx , the final analysis is performed using the inequality

$$\Delta t \leq \Delta x \cdot r, \quad (7.6)$$

where r is the parameter which controls what fraction of Δx must be used for stable Δt and corresponds to the most restrictive condition evaluated from (8.7). This stability condition (7.6) is known as the Courant-Friedrichs-Lewy (CFL) condition.

7.3 Discrete schemes of the linear damped wave equation

7.3.1 The damped linear wave equation

We consider the 1D scalar damped linear wave equation (DWE) as a first order hyperbolic system,

$$\begin{cases} \frac{1}{K} \partial_t p = -\partial_x q \\ \partial_t q = -\frac{1}{\rho} \partial_x p - \frac{1}{\tau} q, \end{cases} \quad (7.7)$$

where p is the pressure, q is the velocity, K is the bulk modulus, ρ is the density, τ is the relaxation time.

The PDE (8.1) represents the hyperbolic system with a “stiff” source term $1/\tau q$ in the right hand side (R.H.S) of (8.1)₂. The system (8.1) is called “stiff” if the two processes (advection and diffusion) have different characteristic time scales.

We introduce a dimensionless parameter ψ denoting the ratio of a characteristic time that wave travels $\tau_h = L^*/V$ (advection) over a characteristic relaxation time τ (diffusion)

$$\psi \equiv \frac{\tau}{\tau_h} = \frac{V\tau}{L^*}, \quad (7.8)$$

where L represents the characteristic length and V represents the wave velocity. If $\psi \ll 1$, the relaxation term is stiff (*Jin and Levermore, 1996*).

Let us introduce a discrete version of (8.1) where we use a classical conservative staggered space-time grid discretization (*Virieux, 1986*), which is equivalent to a finite volume approach (*Dormy and Tarantola, 1995*). The pressure p is defined at the center of a grid cell i and the velocity q is defined at the side of a grid cell $i \pm 1/2$ (q can be considered as a “flux” through the grid cell). The temporal discretization of p corresponds to the half integer nodes $l + 1/2$ and the temporal discretization of q corresponds to the node integers l . The explicit discretization of the system (8.1) is

$$\left\{ \begin{array}{l} \frac{1}{K} \frac{p_i^{l+1/2} - p_i^{l-1/2}}{\Delta t} = - \frac{q_{i+1/2}^l - q_{i-1/2}^l}{\Delta x} \\ q_{i+1/2}^{l+1} - q_{i+1/2}^l = - \frac{1}{\rho} \frac{p_{i+1}^{l+1/2} - p_i^{l+1/2}}{\Delta x} - \frac{1}{\tau} q_{i+1/2}^l. \end{array} \right. \quad (7.9)$$

The linear wave equation

If $1/\tau \equiv 0$, then the system (8.1) represents the wave equation and the von Neumann stability analysis for the discrete system (8.3) suggests that

$$\Delta t \leq \frac{\Delta x}{V}, \quad (7.10)$$

where $V = \sqrt{K/\rho}$ is the fast wave velocity.

The linear diffusion equation

The system (8.1) can also be treated as a diffusion equation. The discrete system for the diffusion equation can be derived from (8.3)

$$\left\{ \begin{array}{l} \frac{1}{K} \frac{p_i^{l+1/2} - p_i^{l-1/2}}{\Delta t} = - \frac{q_{i+1/2}^l - q_{i-1/2}^l}{\Delta x} \\ q_{i+1/2}^{l+1} = - \frac{\tau}{\rho} \frac{p_{i+1}^{l+1/2} - p_i^{l+1/2}}{\Delta x}, \end{array} \right. \quad (7.11)$$

where the only difference in (7.11) from (8.3) is the replacement of $q_{i+1/2}^l$ in (8.3) to $q_{i+1/2}^{l+1}$ in (7.11). The von Neumann stability analysis for the discrete system (7.11) suggests that

$$\Delta t \leq \frac{(\Delta x)^2}{2D}, \quad (7.12)$$

where $D = K\tau/\rho$ is the diffusivity.

The dimensionless damped linear wave equation

For further stability analysis we will rely on a dimensionless formulation. The following replacements to the original DWE (8.1) are done

$$p \longrightarrow K \tilde{p}, \quad q \longrightarrow \frac{L^*}{t^*} \tilde{q}, \quad x \longrightarrow L^* \tilde{x}, \quad t \longrightarrow t^* \tilde{t}, \quad (7.13)$$

where L^* [m] is the characteristic length, t^* [s] is the characteristic time and the variables with the symbol $\tilde{\cdot}$ on top correspond to the dimensionless quantities. We also set $L^* = V t^*$ and $t^* = \tau$. The dimensionless system (8.1) reads

$$\begin{cases} \partial_{\tilde{t}} \tilde{p} = -\partial_{\tilde{x}} \tilde{q} \\ \partial_{\tilde{t}} \tilde{q} = -\partial_{\tilde{x}} \tilde{p} - \tilde{q}. \end{cases} \quad (7.14)$$

Below, we will deal only with the dimensionless equations, and, for simplicity, we will omit the over-score tilde symbol $\tilde{\cdot}$ in the rest of the article (excluding appendices).

7.3.2 The discrete system of equations

Let us consider a more general discrete system than (8.3) where we will use the fact that there are no spatial derivatives of the field $q_{i+1/2}^l$ in R.H.S of (7.14)₂. Thus, $q_{i+1/2}^l$ can be replaced as a weighted average between the future $q_{i+1/2}^{l+1}$ and the past $q_{i+1/2}^l$ values,

$$\begin{cases} \frac{p_i^{l+1/2} - p_i^{l-1/2}}{\Delta t} = -\frac{q_{i+1/2}^l - q_{i-1/2}^l}{\Delta x} \\ \frac{q_{i+1/2}^{l+1} - q_{i+1/2}^l}{\Delta t} = -\frac{p_{i+1}^{l+1/2} - p_i^{l+1/2}}{\Delta x} - (\chi q_{i+1/2}^{l+1} + (1 - \chi) q_{i+1/2}^l). \end{cases} \quad (7.15)$$

If $\chi = 1/2$, the scheme (7.15) corresponds to an implicit-explicit scheme. If $\chi = 1$, the scheme (7.15) corresponds to an implicit scheme for q . The schemes with $\chi = 1/2$ and with $\chi = 1$, even though are implicit for q , can be executed fully explicitly. The consistency is shown in many studies, for example, in *Najafi and Izadi (2014)* and references therein. Our numerical tests show that all three schemes described above (explicit, implicit-explicit, implicit) under a sufficient resolution converge to the same numerical solution using homogeneous and heterogeneous material properties.

A typical behavior of the system (7.14) is shown in Figure 7.1. The wave propagation regime of DWE corresponds to a propagating wave (left and right going wavelets with the same velocities), which is equivalent to a standard wave equation (Figure 7.1a). The diffusion regime of DWE corresponds to a diffusion event, which is equivalent to the standard diffusion equation (Figure 7.1b).

7.3.3 The explicit scheme

Here, we explore the discrete system (7.15) with $\chi = 0$, which corresponds to the explicit scheme. The von Neumann stability analysis for this scheme suggests that

$$\Delta t \leq \Delta x \frac{-\Delta x + \sqrt{(\Delta x)^2 + 16}}{4}, \quad (7.16)$$

The behavior of this stability condition as a function of Δx is shown in Figure 7.2 (solid red curve). Let us analyze the result (7.16) in more detail.

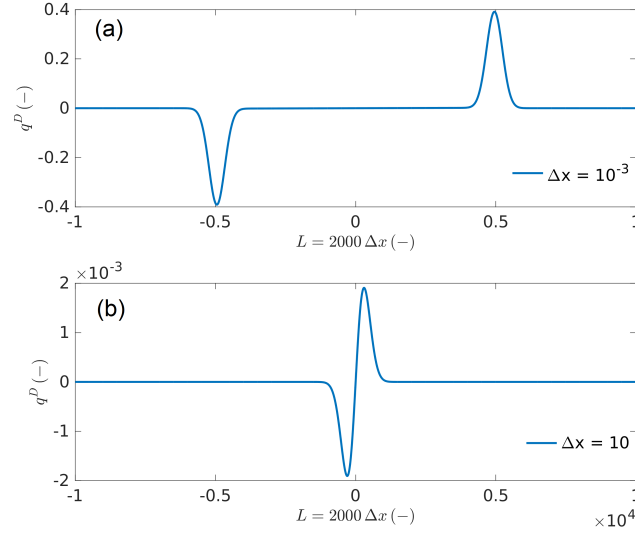


Figure 7.1: Snapshots of the velocity wave fields of DWE (7.14). Panel (a) shows one propagating wave, which corresponds to the wave propagation regime of DWE. Panel (b) shows a diffusive mode, which corresponds to the diffusive regime of DWE. We apply a Gaussian distribution to the pressure p at the center of the model as an initial condition.

Wave propagation regime of the damped linear wave equation

Lets us write a series expansion of the right hand side (R.H.S) of (7.16) of Δx , assuming $\Delta x \ll 1$,

$$\Delta x \frac{-\Delta x + \sqrt{(\Delta x)^2 + 16}}{4} = \Delta x - \frac{1}{4}(\Delta x)^2 + \frac{1}{32}(\Delta x)^3 + O((\Delta x)^5). \quad (7.17)$$

It can be seen form (7.17) that the limit of (7.17) as $\Delta x \rightarrow 0$ is

$$\lim_{\Delta x \rightarrow 0} \left(\Delta x \frac{-\Delta x + \sqrt{(\Delta x)^2 + 16}}{4} \right) = 0, \quad (7.18)$$

which corresponds to the hyperbolic limit. Indeed, taking into account (7.17), the inequality (7.16) can be written as

$$\Delta t \leq \Delta x, \quad (7.19)$$

which is valid when $\Delta x \ll 1$ (Figure 7.2, dashed green curve). This CFL condition is indeed corresponds to the CFL of the wave equation (7.10), because the velocity equals to 1. One can also take into account one more term in the series expansion (7.17) and the inequality (7.19) becomes

$$\Delta t \leq \Delta x - \frac{1}{4}(\Delta x)^2, \quad (7.20)$$

which is shown in Figure 7.2 (dotted blue curve).

Diffusive regime of the damped linear wave equation

Now we consider an opposite scenario. We write a series expansion of the R.H.S of (7.16) of $1/\Delta x$, assuming $1/\Delta x \ll 1$,

$$\Delta x \frac{-\Delta x + \sqrt{(\Delta x)^2 + 16}}{4} = 2 - \frac{8}{(\Delta x)^2} + \frac{64}{(\Delta x)^4} + O\left(\frac{1}{(\Delta x)^6}\right). \quad (7.21)$$

The limit of the right hand side of (7.21) as $\Delta x \rightarrow +\infty$ is

$$\lim_{\Delta x \rightarrow +\infty} \left(\Delta x \frac{-\Delta x + \sqrt{(\Delta x)^2 + 16}}{4} \right) = 2 \quad (7.22)$$

It is interesting that the R.H.S of (7.22) is finite. Thus, when $\Delta x \gg 1$, the stability conditions reads

$$\Delta t \leq 2, \quad (7.23)$$

which is a parabolic limit and is shown in Figure 7.2 (dashed light blue curve). One can also take into account one more term in the series expansion (7.21) and the inequality (7.23) becomes

$$\Delta t \leq 2 - \frac{8}{(\Delta x)^2}, \quad (7.24)$$

which is shown in Figure 7.2 (dotted black curve).

7.3.4 The implicit and implicit-explicit schemes

Let us now explore the implicit-explicit scheme ($\chi = 1/2$ in (7.15)). The von Neumann stability analysis for this scheme suggests that

$$\Delta t \leq \Delta x, \quad (7.25)$$

which is valid for any Δx (Figure 7.3, solid black curve). It means that the standard CFL for the wave equation (8.1) is valid in all regimes of the system (7.15).

Now, we analyze the implicit scheme ($\chi = 1$ in (7.15)). The von Neumann stability analysis for this scheme suggests that

$$\Delta t \leq \Delta x \left(\frac{\Delta x}{4} + \frac{\sqrt{(\Delta x)^2 + 16}}{4} \right), \quad (7.26)$$

which is shown in Figure 7.3 (solid blue curve). This CFL condition is equivalent to the CFL of the wave equation (8.1) for $\Delta x \ll 1$ (Figure 7.3, dashed green curve) and to the CFL of the diffusion equation (7.12) if $\Delta x \gg 1$ (Figure 7.3, dashed brown curve). For comparison, the CFL condition of the explicit scheme is also shown in Figure 7.3 (solid red curve), as well as, the parabolic limit (Figure 7.3, dashed light blue curve).

7.3.5 Summary to the CFL conditions of the linear damped wave equation

The general CFL condition of the linear damped wave equation can be written as a function of parameter χ , which defines the ratio between explicit and implicit schemes,

$$\Delta t \leq \Delta x \left(\frac{(2\chi - 1)}{4} \Delta x + \frac{\sqrt{16 + 4(\chi - \frac{1}{2})^2 (\Delta x)^2}}{4} \right). \quad (7.27)$$

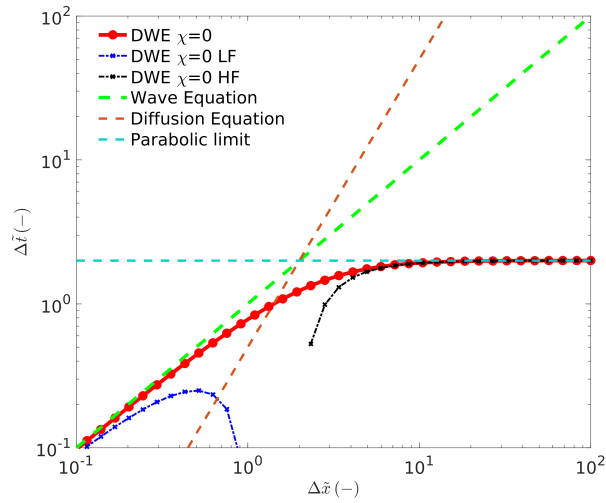


Figure 7.2: The CFL condition Δt as a function of Δx for the explicit scheme ($\chi = 0$) (red curve), its wave equation limit ($\Delta x \ll 1$) (blue curve), its parabolic limit (black curve), the standard wave equation (dashed green curve), the diffusive equation (dashed brown curve) and the parabolic limit (dashed light blue curve).

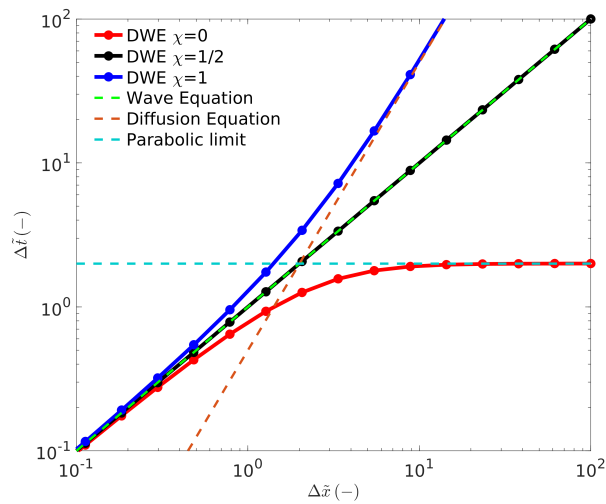


Figure 7.3: The CFL condition Δt as a function of Δx for the explicit scheme ($\chi = 0$) (red curve), the implicit-explicit scheme ($\chi = 0.5$) (black curve), the implicit scheme ($\chi = 1$) (blue curve), the standard wave equation (dashed green curve), the diffusive equation (dashed brown curve) and the parabolic limit (dashed light blue curve).

Table 7.1: List of Principal Notation

Symbol	Meaning	Unit
σ^s, σ^f	solid and fluid stresses	-
$\bar{\sigma}$	$= (1 - \phi)\sigma^s + \phi\sigma^f$, total stress	-
p_f	fluid pressure	-
v^s, v^f	solid and fluid velocities	-
q^D	$= \phi(v^f - v^s)$, Darcy's flux	-
$\bar{\alpha}, \bar{M}, \bar{\rho}_f, \bar{\rho}_t$	dimensionless material parameters specified in Appendix 7.10	-

The CFL condition (7.27) captures the CFL conditions for the three considered above schemes — explicit, implicit-explicit and implicit. To support the results presented above, we show the absolute values of the eigenvalues $\lambda_{1,2}$ of the amplification matrix F (8.6) for the three described above numerical schemes (Figure 7.4). We plot the eigenvalues $\lambda_{1,2}$ for two different values of Δx . $\Delta x = 10^2$ corresponds to the diffusive regime of DWE while $\Delta x = 10^{-1}$ corresponds to the wave propagation regime of DWE. In the explicit scheme, the eigenvalue λ_2 significantly reduces the stable Δt in the diffusive regime (Figure 7.4a, dashed red curve). In the implicit-explicit scheme, the eigenvalues $\lambda_{1,2}$ provide the same stability condition in the wave propagation and diffusive regimes (Figure 7.4b). In the implicit scheme, the eigenvalues $\lambda_{1,2}$ provide the CFL condition (7.25) in the wave propagation regime and the CFL condition (7.12) in the diffusive regime (Figure 7.4b, note a logarithmic scale of the x-axis). We also provide the von Neumann's stability analysis of the dimensional linear damped wave equation which can be found in Appendix 7.9. The corresponding Maple script for the derivation of the CFL conditions of DWE is provided as a supplementary material.

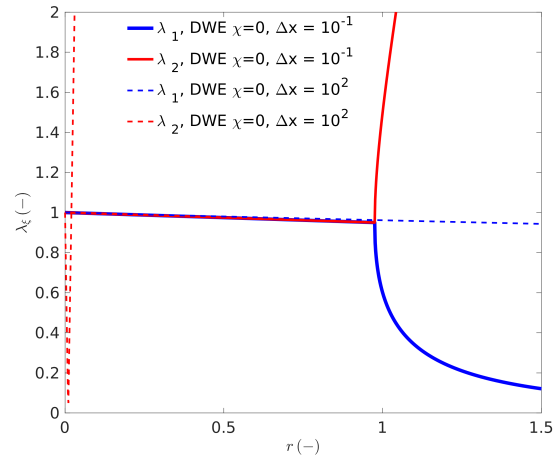
7.3.6 Back propagation of the damped linear wave equation

It is notable that the derived CFL conditions for the three schemes exhibit mirror symmetry along $\Delta t = 0$ (Figure 7.5). The CFL condition of the implicit-explicit scheme is exactly the same for positive and negative Δt (Figure 7.5, black curve). The CFL conditions of the explicit and implicit schemes are reciprocal (Figure 7.5, red and blue curves). One of the main properties of the wave equation is the ability to propagate forward and backward in time, which is due to the hyperbolicity of the system. DWE exhibits this property as long as the propagation regime dominates. If the diffusion regime dominates, the back propagation results in growing amplitudes at each time step, thus, the back propagation solution will never converge to the initial state. Remarkably, during the back propagation the numerical schemes remain stable under the negative CFL conditions in both wave propagation and diffusion regimes.

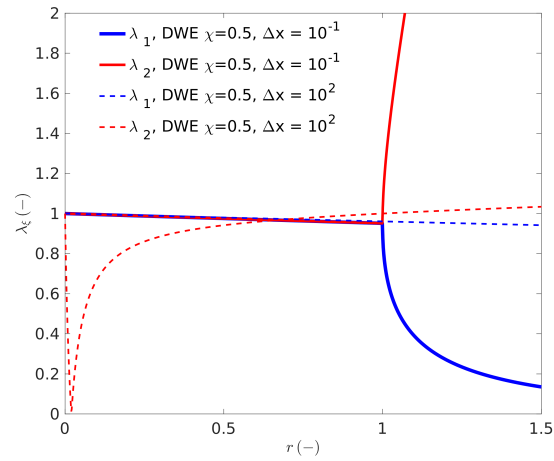
7.4 Discrete schemes of dimensionless Biot's poroelastic equations

The dimensionless Biot's poroelastic equations in 1D can be written as

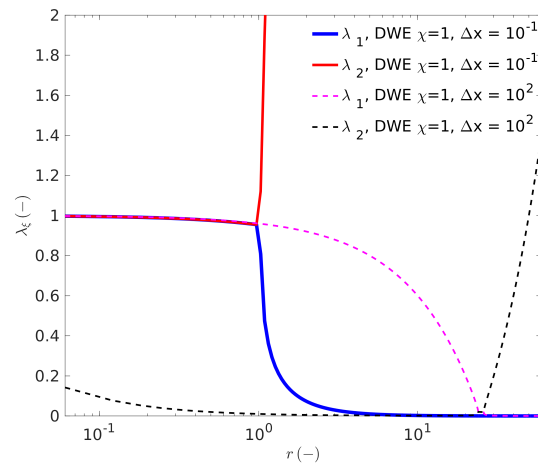
$$\begin{pmatrix} \frac{\partial \bar{\sigma}}{\partial t} \\ \frac{\partial p_f}{\partial t} \\ -\frac{\partial p_f}{\partial t} \end{pmatrix} = \zeta_{ij} \begin{pmatrix} \frac{\partial v^s}{\partial x} \\ \frac{\partial q^D}{\partial x} \end{pmatrix}, \quad (7.28)$$



(a)



(b)



(c)

Figure 7.4: The eigenvalues $\lambda_{1,2}$ of the amplification matrix F for the three discrete schemes as a function of r (7.6). (a) - explicit scheme ($\chi = 0$), (b) - implicit-explicit scheme ($\chi = 0.5$) and (c) implicit scheme ($\chi = 1$). The x -axis in panels (a) and (b) is linear while the x -axis in panel (c) is logarithmic.

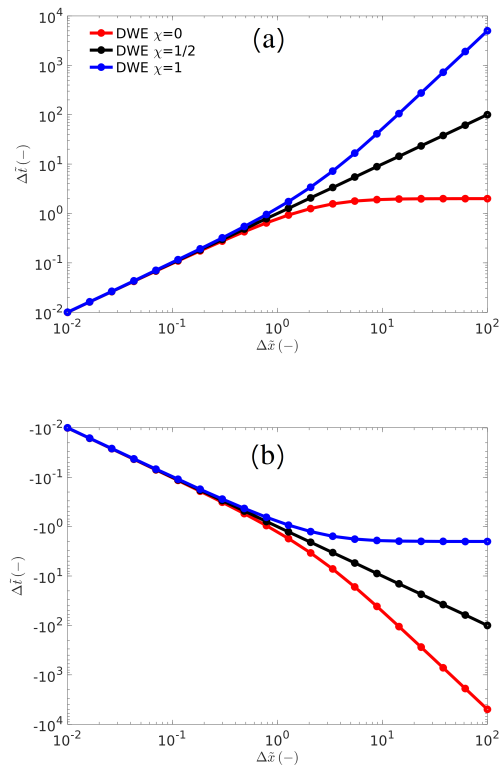


Figure 7.5: The CFL conditions of DWE for positive (a) and negative (b) Δt as a function of Δx for the three schemes — the explicit scheme ($\chi = 0$) (red curve), the implicit-explicit scheme ($\chi = 0.5$) (black curve), the implicit scheme ($\chi = 1$) (blue curve).

$$\begin{pmatrix} \frac{\partial v^s}{\partial t} \\ -\frac{\partial q^D}{\partial t} \end{pmatrix} = \varrho_{ij} \begin{pmatrix} \frac{\partial \bar{\sigma}}{\partial x} \\ q^D + \frac{\partial p_f}{\partial x} \end{pmatrix}, \quad (7.29)$$

where

$$\zeta_{ij} = \begin{pmatrix} 1 & \tilde{\alpha} \\ \tilde{\alpha} & \tilde{M} \end{pmatrix}, \quad \varrho_{ij} = \begin{pmatrix} 1 & \tilde{\varrho}_f \\ \tilde{\varrho}_f & \tilde{\varrho}_t \end{pmatrix}. \quad (7.30)$$

A detailed derivation of the dimensionless Biot's poroelastic equations (7.28)-(7.29) is given in Appendix 7.10. The list of notations is given in Table 7.1. The matrices of coefficients (7.30) define the material parameters and are positive definite and symmetric. The system (7.28)-(7.29) is called inviscid if q^D is not present in the R.H.S of (7.29). The inviscid system is hyperbolic and its solution results in propagating waves. If $\zeta_{ij} = a \cdot \varrho_{ij}$, where a is an arbitrary non-zero positive number, the solution of the inviscid system (7.28)-(7.29) results in one propagating wave (i.e. left and right going wavelets with the same velocities). If $\zeta_{ij} \neq a \cdot \varrho_{ij}$, then the solution of the inviscid system (7.28)-(7.29) results in two propagating waves with the two different velocities (i.e. two left and two right going wavelets).

If q^D is present in the R.H.S of (7.29), Biot's poroelastic equations (7.28)-(7.29) define the hyperbolic system with a stiff source term, represented by a parabolic operator. The behavior of such a dimensionless system of equations depends on Δx (i.e. depends on the spatial scale). If $\Delta x \ll 1$, the solution of the system (7.28)-(7.29) results in two propagating waves with the two different velocities (V_1^{HF} and V_2^{HF}) like in the case of an inviscid system (Figure 7.6a). The fastest P-wave is called the wave of the first kind (or fast P-wave) (*Biot*, 1956b) and the second wave is called the P-wave of the second kind (so-called slow P-wave). The superscript "HF" refers to the high frequency limit, since the velocities V_1^{HF} and V_2^{HF} correspond to the high frequency limit of the dimensional Biot's equations. The velocities V_1^{HF} and V_2^{HF} can be calculated as

$$V_1^{HF} = \left(\frac{-A + \sqrt{A^2 - 4\det(\zeta_{ij})\det(\varrho_{ij})}}{2\det(\zeta_{ij})\det(\varrho_{ij})} \right)^{-1/2} \quad (7.31)$$

and

$$V_2^{HF} = \left(\frac{-A - \sqrt{A^2 - 4\det(\zeta_{ij})\det(\varrho_{ij})}}{2\det(\zeta_{ij})\det(\varrho_{ij})} \right)^{-1/2}, \quad (7.32)$$

where the determinants are

$$\det(\zeta_{ij}) = \zeta_{11}\zeta_{22} - \zeta_{12}^2 \quad (7.33)$$

and

$$\det(\varrho_{ij}) = \varrho_{11}\varrho_{22} - \varrho_{12}^2. \quad (7.34)$$

The parameter A is defined as

$$A = \zeta_{11}\varrho_{11} + \zeta_{22}\varrho_{22} - 2\zeta_{12}\varrho_{12}. \quad (7.35)$$

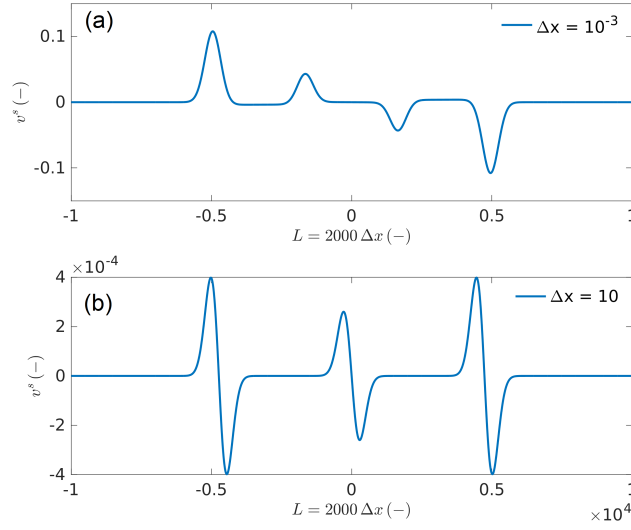


Figure 7.6: Snapshots of the solid velocity wavefields of the dimensionless Biot's poroelastic equations (7.28)-(7.29). Panel (a) shows two propagating waves V_1 and V_2 , which corresponds to the wave propagation regime for V_2 . Panel (b) shows one propagating wave V_1 and a diffusive mode, which corresponds to V_2 . The initial condition is given to the fluid pressure p_f of a Gaussian shape. The material parameters are $\zeta_{12} = 1/8$, $\zeta_{22} = 1/4$, $\rho_{12} = 1/4$, $\rho_{22} = 1/2$.

If $\Delta x \gg 1$, the solution of the system (7.28)-(7.29) results in one propagating P-wave with velocity V_1^{LF} (i.e. left and right going wavelets with the same velocities) and in a slow P-wave, which is degenerated into a diffusion mode (Figure 7.6b). The superscript "LF" refers to the low frequency limit, since the velocities V_1^{LF} and V_2^{LF} correspond to the low frequency limit of the dimensional Biot's equations. The velocity V_1^{LF} is lower than the velocity V_1^{HF} and can be calculated as

$$V_1^{LF} = \sqrt{\frac{\zeta_{11}}{\rho_{22}(\rho_{11}\rho_{22} - \rho_{12}^2)}}. \quad (7.36)$$

The discrete system of equations (7.28)-(7.29) can be written as

$$\begin{cases} \frac{(\bar{\sigma})_i^{l+1/2} - (\bar{\sigma})_i^{l-1/2}}{\Delta t} = \zeta_{11} \frac{(v^s)_{i+1/2}^l - (v^s)_{i-1/2}^l}{\Delta x} + \zeta_{12} \frac{(q^D)_{i+1/2}^l - (q^D)_{i-1/2}^l}{\Delta x} \\ -\frac{(p_f)_i^{l+1/2} - (p_f)_i^{l-1/2}}{\Delta t} = \zeta_{21} \frac{(v^s)_{i+1/2}^l - (v^s)_{i-1/2}^l}{\Delta x} + \zeta_{22} \frac{(q^D)_{i+1/2}^l - (q^D)_{i-1/2}^l}{\Delta x} \end{cases}, \quad (7.37)$$

$$\begin{cases} -\frac{(q^D)_{i+1/2}^{l+1} - (q^D)_{i+1/2}^l}{\Delta t} = \rho_{21} \frac{(\bar{\sigma})_{i+1}^{l+1/2} - (\bar{\sigma})_i^{l+1/2}}{\Delta x} + \rho_{22} \left(\frac{(p_f)_{i+1}^{l+1/2} - (p_f)_i^{l+1/2}}{\Delta x} + (\chi (q^D)_{i+1/2}^{l+1} + (1-\chi)(q^D)_{i+1/2}^l) \right) \\ \frac{(v^s)_{i+1/2}^{l+1} - (v^s)_{i+1/2}^l}{\Delta t} = \rho_{11} \frac{(\bar{\sigma})_{i+1}^{l+1/2} - (\bar{\sigma})_i^{l+1/2}}{\Delta x} + \rho_{12} \left(\frac{(p_f)_{i+1}^{l+1/2} - (p_f)_i^{l+1/2}}{\Delta x} + (\chi (q^D)_{i+1/2}^{l+1} + (1-\chi)(q^D)_{i+1/2}^l) \right) \end{cases}. \quad (7.38)$$

The discrete system (7.37)-(7.38) corresponds to the fully explicit scheme for the wave equations, but the scheme for the Darcy's flux can be different. If $\chi = 0$, the scheme for the Darcy's flux is explicit. If $\chi = 1/2$, the scheme for the Darcy's flux is implicit-explicit. If $\chi = 1$, the scheme for the Darcy's flux is implicit. In fact, the scheme (7.37)-(7.38) can be executed always explicitly for any scheme for the Darcy's flux (explicit or implicit-explicit)

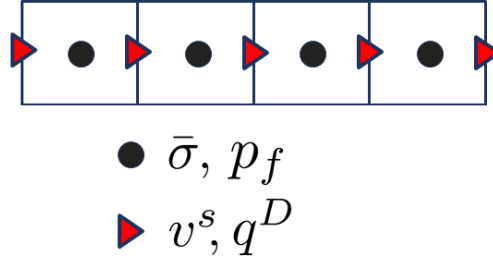


Figure 7.7: A sketch representing the spatial locations of the field variables of Biot's equations in a staggered mesh.

or implicit), since the the Darcy's flux q^D in the R.H.S of (7.29) does not have any spatial derivatives. Spatial locations of different fields in the mesh is shown in Figure 7.7.

We performed the stability analysis outlined in section 7.2 for the system (7.28)-(7.29). For the inviscid system (7.28)-(7.29), the CFL condition is

$$\Delta t \leq \frac{\Delta x}{V_1}, \quad (7.39)$$

where V_1 is the velocity of the fastest wave. This velocity V_1 is equivalent to the velocity of the system (7.28)-(7.29) (with the Darcy's flux in the R.H.S) V_1^{HF} ($\Delta x \ll 1$). In addition to the CFL condition (7.39), the matrices ζ_{ij} and ρ_{ij} must be positive definite, which follows from the energy laws and, independently, from the performed stability analysis. For the stability analysis of the original viscid Biot's poroelastic equations (7.28)-(7.29), let us consider the two examples.

7.4.1 Example 1

Let us set the dimensionless material parameters ζ_{ij} and ρ_{ij} as

$$\zeta_{ij} = \begin{pmatrix} 1 & 1/2 \\ 1/2 & 1 \end{pmatrix}, \quad \rho_{ij} = \begin{pmatrix} 1 & 1/2 \\ 1/2 & 1 \end{pmatrix}. \quad (7.40)$$

This set of parameters corresponds to a special condition when the velocities V_1 and V_2 are the same. The wave mode V_2 behaves as a propagating wave if $\Delta x \ll 1$ and as a diffusion mode if $\Delta x \gg 1$. The beauty of this example is that the CFL conditions for the considered above schemes can be derived fully analytically.

Explicit scheme for the Darcy's flux

We first consider the explicit scheme for the Darcy's flux ($\chi = 0$) for the system (7.37)-(7.38). The CFL condition can be derived by reproducing the workflow presented in section 7.2. The amplification matrix for this scheme is shown in Appendix 7.11. The CFL condition states that the eigenvalues of the amplification matrix F must satisfy the inequality (8.7), which can be represented as a solution of

$$\gamma = |\lambda_\xi(F)| - 1, \quad (7.41)$$

where λ_ξ are the ξ eigenvalues of the amplification matrix F and $\xi = \overline{1..4}$. The polynomial γ is of degree four and has four roots, $\gamma_{\overline{1..4}}$. The roots are

$$\gamma_{1,2} = \pm 1/V_1^{HF}, \quad \gamma_{3,4} = -\frac{\Delta x}{3} \pm \frac{\sqrt{(\Delta x)^2 + 12}}{3}, \quad (7.42)$$

where $V_1^{HF} = \sqrt{3}/2 \approx 0.866$. According to (7.6), the resulting CFL condition can be written as

$$\Delta t \leq \Delta x \min(\gamma_{\overline{1.4}}), \quad (7.43)$$

where the most restrictive condition $\gamma_{\overline{1.4}}$ must be chosen. The resulting constraints on Δt are

$$\Delta t \leq |\pm \Delta x / V_1^{HF}|, \quad (7.44)$$

$$\Delta t \leq \left| \Delta x \left(-\frac{\Delta x}{3} \pm \frac{\sqrt{(\Delta x)^2 + 12}}{3} \right) \right|, \quad (7.45)$$

It can be seen from (7.42)₁ and (7.44) that roots $\gamma_1 = -\gamma_2$ and $\gamma_{\overline{1.2}}$ represent the stability of the inviscid set of equations (7.39) (Figure 7.8, solid black curve). The most restrictive condition is represented by (7.45) with a plus sign, thus the CFL condition of the explicit scheme ($\chi = 0$) for Biot's equations (7.28)-(7.29) is represented by

$$\Delta t \leq \Delta x \left(-\frac{\Delta x}{3} + \frac{\sqrt{(\Delta x)^2 + 12}}{3} \right). \quad (7.46)$$

The CFL condition (7.46) is shown in Figure 7.8 (solid red curve). The hyperbolic limit ($\Delta x \ll 1$) of the CFL condition (7.46) is

$$\Delta t \leq \Delta x \frac{2}{\sqrt{3}} \approx \Delta x / 0.866. \quad (7.47)$$

The parabolic limit ($\Delta x \gg 1$) of (7.46) is

$$\Delta t \leq 2, \quad (7.48)$$

which is shown in Figure 7.8 (dashed light blue curve).

Implicit-explicit scheme for the Darcy's flux

We repeat the workflow presented in section 7.2 for the scheme (7.37)-(7.38) with $\chi = 1/2$ (implicit-explicit scheme for the Darcy's flux). The amplification matrix for this scheme is shown in Appendix 7.11. Again, the polynomial γ is of degree four and has four roots, $\gamma_{\overline{1.4}}$ (see (7.41)). The resulting CFL condition of the scheme with $\chi = 1/2$ for Biot's equations (7.28)-(7.29) can be written as

$$\Delta t \leq \Delta x / V_1^{HF}, \quad (7.49)$$

which is the most restrictive condition (Figure 7.8, solid black curve) and is the same as the CFL condition of the wave equation (7.10) (taking $V = V_1^{HF}$). In fact, the absolute values of all roots $\gamma_{\overline{1.4}}$ provide this stability condition.

Implicit scheme for the Darcy's flux

We repeat the workflow presented in section 7.2 for the scheme (7.37)-(7.38) with $\chi = 1$ (implicit scheme for the Darcy's flux). The amplification matrix for this scheme is shown in Appendix 7.11. The polynomial γ is of degree four and has four roots, $\gamma_{\overline{1.4}}$ (see (7.41)). The roots are

$$\gamma_{1,2} = \pm 1 / V_1^{HF}, \quad \gamma_{3,4} = \frac{\Delta x}{3} \pm \frac{\sqrt{(\Delta x)^2 + 12}}{3}, \quad (7.50)$$

where $V_1^{HF} = \sqrt{3}/2 \approx 0.866$. Note, that the only difference between (7.42) and (7.50) is the plus sign in (7.50) in front of $\Delta x/3$. The stability conditions arising from (7.50) with the help of (7.6) are

$$\Delta t \leq |\pm \Delta x / V_1^{HF}|, \quad (7.51)$$

Table 7.2: Summary of CFL conditions for different schemes in Example 1

Scheme for the Darcy's flux	explicit	implicit-explicit	implicit
Scheme for the wave propagation part	explicit	explicit	explicit
CFL condition	$\Delta t \leq \Delta x \left(-\frac{\Delta x}{3} + \frac{\sqrt{(\Delta x)^2 + 12}}{3} \right)$	$\Delta t \leq \frac{\Delta x}{V_1^{HF}}$	$\Delta t \leq \frac{\Delta x}{V_1^{HF}}$

$$\Delta t \leq \left| \Delta x \left(\frac{\Delta x}{3} \pm \frac{\sqrt{(\Delta x)^2 + 12}}{3} \right) \right|, \quad (7.52)$$

where $V_1^{HF} = \sqrt{3}/2 \approx 0.866$. The stability condition (7.51) (arising from $\gamma_{\overline{1,2}}$) is exactly the same as for the explicit and implicit-explicit schemes for the Darcy's flux. The stability condition (7.52) with a plus sign is shown in Figure 7.8 (solid dark blue curve). The most restrictive condition arising from (7.51)-(7.52) is

$$\Delta t \leq \Delta x / V_1^{HF}, \quad (7.53)$$

which is the same as the CFL condition of the wave equation (7.10) (taking $V = V_1^{HF}$).

The modified CFL condition of the DWE

Let us slightly modify the CFL condition of the linear damped wave equation (7.86) considering the explicit scheme ($\chi = 0$),

$$\Delta t \leq \Delta x \frac{\frac{1}{V_1^{HF}} \sqrt{(\Delta x)^2 \frac{1}{(V_1^{HF})^2} + 16 \frac{1}{\rho_{22}} + \frac{1}{(V_1^{HF})^2}}}{4 \frac{1}{\rho_{22}}}, \quad (7.54)$$

where for the wave velocity V in (7.86), the velocity of the first kind V_1^{HF} of Biot's equations (7.28)-(7.29) is used. In addition, the parabolic limit is modified by a factor $1/\rho_{22}$. The modified CFL condition of DWE with $\chi = 0$ (7.54) is shown in Figure 7.8 (dotted black curve), which is exactly equivalent to the CFL condition of Biot's equations for the explicit scheme for the Darcy's flux (7.46) (solid red curve in Figure 7.8).

The modified CFL condition of DWE with $\chi = 1/2$ (Figure 7.8, dotted red curve) is equivalent to the CFL of the wave equation (7.10) (taking $V = V_1^{HF}$). Thus, it is also equivalent to the CFL condition of Biot's equations for the implicit-explicit scheme for the Darcy's flux (7.53).

The modified CFL condition of DWE with $\chi = 1$ can be derived from (7.86) applying the the same changes as above (Figure 7.8, dotted green curve). This CFL condition is equivalent the CFL condition of Biot's equations arriving from the root γ_3 . Note, that the modified CFL condition of the DWE with $\chi = 1$ is always less restrictive than the stability condition of the wave equation (7.10) (using $V = V_1^{HF}$); thus, it does not have an effect in Biot's equations if the scheme for the hyperbolic part of Biot's equations is explicit.

The CFL condition of the diffusion equation (7.12) is shown in Figure 7.8 (dashed brown curve), where the diffusivity D is calculated according to

$$D = \zeta_{22} \left(1 - \frac{\zeta_{12}^2}{\zeta_{22}\zeta_{11}} \right). \quad (7.55)$$

This diffusivity coefficient defines the diffusion equation for the fluid pressure, which behaves exactly the same as the diffusive mode V_2 of Biot's equations (7.28)-(7.29) for $\Delta x \gg 1$. Note, the similarities between Figures 7.2 and 7.8. The summary of CFL conditions for different schemes in Example 1 is shown in Table 7.2.

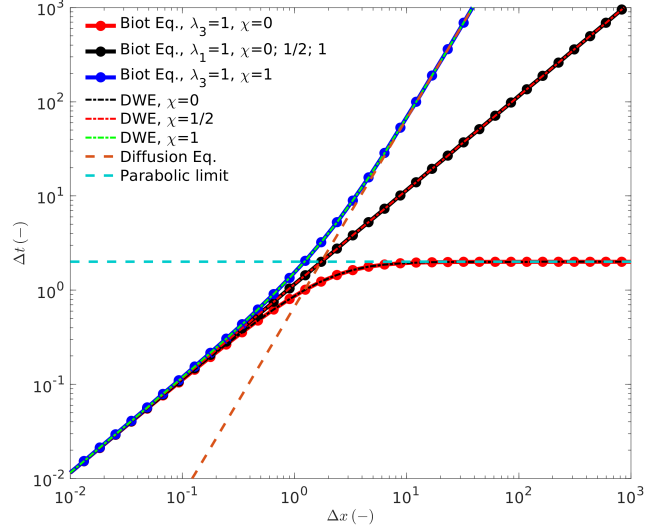


Figure 7.8: The restrictions on Δt arising from the roots $\gamma_{\overline{1.4}}$ as a function of Δx for Biot's and modified DWE equations considering explicit, implicit-explicit and implicit schemes for the Darcy's flux. $\lambda_1 = 1$ and $\lambda_3 = 1$ correspond to the positive roots.

7.4.2 Example 2

Let us set the dimensionless material parameters ζ_{ij} and ϱ_{ij} as

$$\zeta_{ij} = \begin{pmatrix} 1 & 1/8 \\ 1/8 & 1/4 \end{pmatrix}, \quad \varrho_{ij} = \begin{pmatrix} 1 & 1/4 \\ 1/4 & 1/2 \end{pmatrix} \quad (7.56)$$

This set of parameters corresponds to the different velocities V_1 and V_2 . In this example, the wave mode V_2 behaves as a propagating wave if $\Delta x \ll 1$ and as a diffusion mode if $\Delta x \gg 1$. The CFL condition can be written analytically as a root of a polynomial of degree four. The roots can be easily found numerically. We briefly repeat a similar workflow for this set of parameters as we performed in Example 1.

Explicit scheme for the Darcy's flux

We again first consider the explicit scheme ($\chi = 0$) for the Darcy's flux (7.28)-(7.29). For this scheme, the CFL condition can be written as

$$\Delta t \leq \Delta x \min |\gamma_\xi(z)|, \quad (7.57)$$

where γ_ξ are the four roots ($\xi = \overline{1.4}$) of the polynomial γ

$$\gamma(z) = 4(105z^4 + 56\Delta x z^3 - 68z^2 - 4\Delta x z + 4). \quad (7.58)$$

The roots of (7.58) obey a similar behavior as in Example 1, $\gamma_1 = -\gamma_2$ and $\gamma_{\overline{1.2}}$ represents the stability of the set of inviscid equations. The most restrictive condition is arriving from $\gamma_{3,4}$ (Figure 7.9, solid red curve). The hyperbolic limit ($\Delta x \ll 1$) of the CFL condition arriving from $\gamma_{1,2}$ is (here, we consider γ_1 , since it corresponds to the positive Δt)

$$\Delta t \leq \Delta x / V_1^{HF}, \quad (7.59)$$

where $V_1^{HF} \approx 0.977$ (Figure 7.9, solid black curve). The parabolic limit ($\Delta x \gg 1$) of the CFL condition arriving from $\gamma_{3,4}$ is (here, we consider γ_3 , since it corresponds to the positive Δt)

$$\Delta t \leq \frac{2}{\rho_{22}}. \quad (7.60)$$

The parabolic limit is shown in Figure 7.9 (dashed light blue curve). This limit ($\Delta x \gg 1$) of the CFL condition for Biot's equations was also determined by *Chiavassa et al.* (2010); *Chiavassa and Lombard* (2011) and used by *Blanc et al.* (2013).

Implicit-explicit scheme for the Darcy's flux

We repeat the same procedure for the scheme with $\chi = 1/2$. The roots of the polynomial γ are

$$\gamma_{1,2} = \pm 1/V_1^{HF}, \quad \gamma_{3,4} = \pm 1/V_2^{HF}, \quad (7.61)$$

where $V_1^{HF} \approx 0.977$, $V_2^{HF} \approx 0.328$. The roots $\gamma_{1,2}$ (7.61) are exactly the same as for the explicit scheme for the Darcy's flux (7.59). The roots $\gamma_{3,4}$ (7.61) are less restrictive as the roots $\gamma_{1,2}$. The most restrictive condition for this scheme is represented by $\gamma_{1,2}$ (7.61) (Figure 7.9, solid black curve)

$$\Delta t \leq \Delta x/V_1^{HF}, \quad (7.62)$$

which is the same as the CFL condition of the wave equation (7.10) (taking $V = V_1^{HF}$).

Implicit scheme for the Darcy's flux

The polynomial γ of the implicit scheme ($\chi = 1$) of Biot's equations (7.28)-(7.29) is

$$\gamma_\xi(z) = 4(105z^4 - 56\Delta x z^3 - 68z^2 + 4\Delta x z + 4). \quad (7.63)$$

The roots $\gamma_{1,2}$ are

$$\gamma_{1,2} = \pm 1/V_1^{HF}, \quad (7.64)$$

where $V_1^{HF} = \sqrt{3}/2 \approx 0.866$. The roots $\gamma_{1,2}$ (7.64) are exactly the same as for the explicit and implicit-explicit schemes for the Darcy's flux. The roots $\gamma_{3,4}$ (7.64) are calculated numerically and the associated restrictions on Δt are shown in Figure 7.9 (solid blue curve). The most restrictive condition for the implicit scheme is represented by the roots $\gamma_{1,2}$ (Figure 7.9, solid black curve)

$$\Delta t \leq \Delta x/V_1^{HF}, \quad (7.65)$$

which is the same as the CFL condition of the wave equation (7.10) (taking $V = V_1^{HF}$).

The modified CFL condition for the DWE

We use the same CFL stability condition (7.54) of DWE as we used in Example 1 for the explicit scheme ($\chi = 0$). The restriction on Δt from this condition is shown in Figure 7.9 (dotted black curve), which coincides with the exact CFL condition for Biot's equations (arriving from (7.58)) in the high and low frequency limits and slightly diverges in the intermediate regime $\Delta x \in [1, 10]$. Since it diverges to the smaller Δt , the condition of DWE always corresponds to the stable solution of Biot's equations (7.28)-(7.29).

The CFL conditions arising from (7.86) considering the implicit-explicit ($\chi = 1/2$) and implicit ($\chi = 1$) schemes are shown in Figure 7.9 (dotted red and solid green curves, respectively). The DWE CFL condition for the implicit-explicit scheme (7.54) is equivalent to the exact CFL conditions of Biot's equations for schemes with $\chi = 1/2$ and $\chi = 1$.

The DWE CFL (7.10) condition for the implicit scheme is very close to the exact one of Biot's equations with $\chi = 1$ arriving from the root γ_3 . This condition is always less restrictive than the CFL condition of the wave equation (7.10) (using $V = V_1^{HF}$); thus, does not take effect in Biot's equations if the scheme for the hyperbolic part of Biot's equations is explicit.

Table 7.3: Summary of CFL conditions for different schemes in Example 2

Scheme for the Darcy's flux	explicit	implicit-explicit	implicit
Scheme for the wave propagation part	explicit	explicit	explicit
CFL condition	Closed-form expression can be always calculated from the roots of (7.57). Limits: $\Delta t \leq \frac{\Delta x}{V_1^{HF}}$ for $\Delta x \ll 1$ $\Delta t \leq \frac{2}{\rho_{22}}$ for $\Delta x \gg 1$	$\Delta t \leq \frac{\Delta x}{V_1^{HF}}$	$\Delta t \leq \frac{\Delta x}{V_1^{HF}}$
Analytical expression for the CFL condition	Approximation by (7.54)	yes	yes

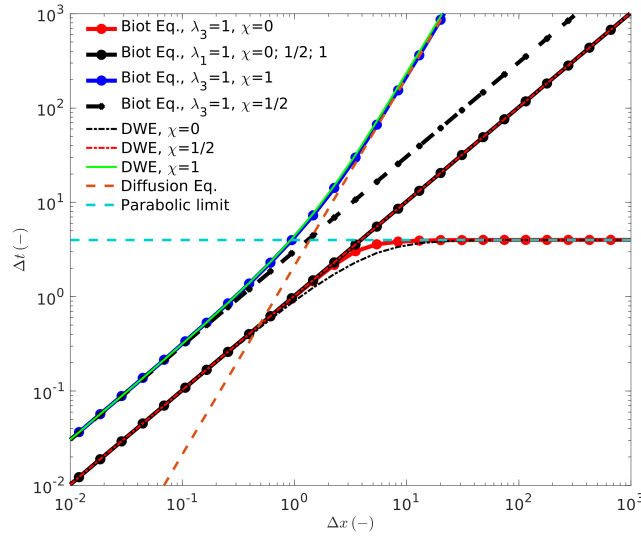


Figure 7.9: The restrictions on Δt arising from the roots $\gamma_{1..4}$ as a function of Δx for Biot's and DWE equations. $\lambda_1 = 1$ and $\lambda_3 = 1$ correspond to the positive roots of (7.57) for positive Δt .

The CFL condition of the diffusion equation (7.12) is shown in Figure 7.9 (dashed brown curve), where the diffusivity D is calculated according to (7.55). The CFL condition of the diffusion equation (7.12) is equivalent to the limit $\Delta x \gg 1$ of the CFL of Biot's equations with $\chi = 1$ arriving from the root γ_3 . Furthermore, the fluid pressure field predicted by the diffusion equation is equivalent to the fluid pressure field of Biot's equations (Figure 7.10). The summary of CFL conditions for different schemes for Biot's equations in Example 2 is shown in Table 7.3.

Back propagation of Biot's equations

The derived CFL conditions for the three schemes of Biot's equations exhibit mirror symmetry along $\Delta t = 0$, similarly to the DWE (Figure 7.5). The back propagation of Biot's equations fully depends on the behavior of the wave of the second kind. If V_2 is a propagating wave, the back propagation is possible. If V_2 is a diffusion process, the back propagation results in growing amplitudes of V_2 at each time step, thus, the back propagating solution will never converge to the initial state. Similarly to the DWE, the back propagation of Biot's equations is always stable and the physical correctness of the back propagation wavefields purely depends on V_2 .

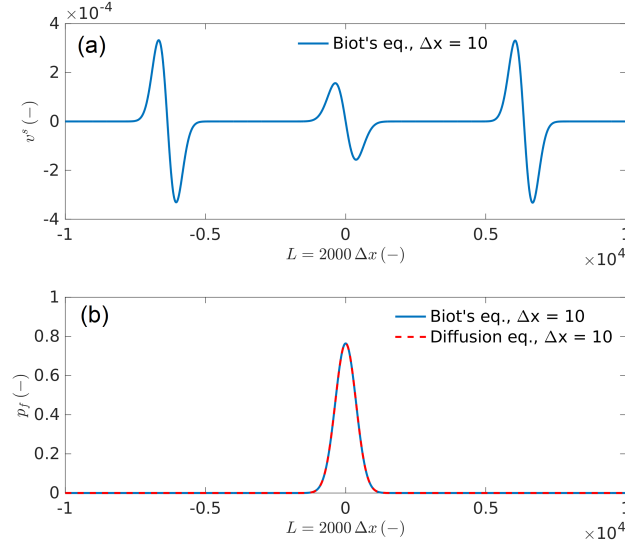


Figure 7.10: Snapshots of the solid velocity and fluid pressure wavefields of the dimensionless Biot's poroelastic equations (7.28)-(7.29) and for the diffusion equation. Panel (a) shows one propagating wave V_1 and a diffusive mode, which corresponds to V_2 . Panel (b) shows the fluid pressure field of Biot's equations (solid blue) and of the diffusion equation (dashed red). The initial condition is given to the fluid pressure p_f of a Gaussian shape. The material parameters are $\zeta_{12} = 1/8$, $\zeta_{22} = 1/4$, $\rho_{12} = 1/4$, $\rho_{22} = 1/2$.

7.5 Discrete schemes of dimensional Biot's poroelastic equations

The first order velocity-stress system of dimensional Biot's equations (*Biot*, 1962a) is given in Appendix 7.10 ((7.88)-(7.90)). The performed stability analysis for the dimensionless Biot's equations can be applied to the dimensional equations as well. For that, we introduce a set of dimensional material parameters $\hat{\zeta}$ and $\hat{\rho}$:

$$\hat{\zeta}_{ij} = \begin{pmatrix} K_u + 4/3G & \alpha M \\ \alpha M & M \end{pmatrix}, \quad \hat{\rho}_{ij} = \frac{1}{\Theta} \begin{pmatrix} \rho_a & \rho_f \\ \rho_f & \rho_t \end{pmatrix}. \quad (7.66)$$

We also need the determinants of those matrices

$$\det(\hat{\zeta}_{ij}) = \hat{\zeta}_{11}\hat{\zeta}_{22} - \hat{\zeta}_{12}^2, \quad \det(\hat{\rho}_{ij}) = \hat{\rho}_{11}\hat{\rho}_{22} - \hat{\rho}_{12}^2. \quad (7.67)$$

and the parameter \hat{A} ,

$$\hat{A} = \hat{\zeta}_{11}\hat{\rho}_{11} + \hat{\zeta}_{22}\hat{\rho}_{22} - 2\hat{\zeta}_{12}\hat{\rho}_{12}. \quad (7.68)$$

The dimensional velocity \hat{V}_1^{HF} can be calculated as

$$\hat{V}_1^{HF} = \left(\frac{-\hat{A} + \sqrt{\hat{A}^2 - 4\det(\hat{\zeta}_{ij})\det(\hat{\rho}_{ij})}}{2\det(\hat{\zeta}_{ij})\det(\hat{\rho}_{ij})} \right)^{-1/2}. \quad (7.69)$$

In the previous section, we studied the three schemes, namely, explicit ($\chi = 0$), implicit-explicit ($\chi = 1/2$) and implicit ($\chi = 1$) schemes for the Darcy's flux. The explicit scheme is not useful since it dramatically reduces the stable time step in the diffusive regime of the P-slow wave. The accuracy determines the choice between the implicit-explicit or implicit schemes for the Darcy's flux of Biot's equations. The implicit-explicit scheme is second order accurate in space and time. The implicit scheme provides slightly lower accuracy, around 1.8.

Table 7.4: Material parameters of a sandstone.

Symbol	Value	Unit
K_g	40	(GPa)
ρ_s	2500	(kg/m ³)
K_d	20	(GPa)
G	12	(GPa)
ϕ	0.2	(-)
κ	$600 \cdot 10^{-13}$	(m ²)
T	2	(-)
K_f	2.5	(GPa)
ρ_f	1000	(kg/m ³)
η	10^{-3}	(kg/m·s)
ω_c	$2 \cdot 10^4$	(Hz)
Δt_{st}^{1D}	$4.7045949598862 \cdot 10^{-6}$	(s)
Δt_{st}^{3D}	$1.0266267865612 \cdot 10^{-6}$	(s)

Therefore, the $\chi = 1/2$ scheme, described in section 4.2.2, is the most reasonable choice and the CFL condition for the dimensional case is determined as

$$\Delta t \leq \frac{\Delta x}{\hat{V}_1^{HF}}, \quad (7.70)$$

where \hat{V}_1^{HF} is given by (7.69). The extension to two, three and n-dimensions is straightforward

$$\Delta t \leq \frac{1}{\hat{V}_1^{HF} \sqrt{\sum_{i=1}^n \frac{1}{\Delta x_i^2}}}. \quad (7.71)$$

If $\Delta x_i = \Delta x$, then

$$\Delta t \leq \frac{\Delta x}{\sqrt{n} \hat{V}_1^{HF}}, \quad (7.72)$$

The conditions (7.70), (7.71), (7.72) can be generalized to a fourth-order accurate in space, second-order accurate in time discrete numerical scheme using the coefficients of the fourth-order approximation to the spatial derivatives (Levander, 1988; Masson et al., 2006).

There is also a criterion on the input material parameters. The stability analysis suggests that the matrices of material parameters $\hat{\zeta}$ and $\hat{\rho}$ (expression (7.66)) must be positive definite. It is notable that the condition on the matrix $\hat{\zeta}$ (eq. (7.66)) is less restrictive than the condition from the general principles of thermodynamic on the matrix in (7.88) (they are equivalent if the shear modulus is zero); thus, the most restrictive condition must be used. The positive definiteness of $\hat{\rho}$ suggests that all eigenvalues are positive.

Our stability analysis has been performed for homogeneous materials, but the results can be applied also for heterogeneous and anisotropic materials. If strong heterogeneities and anisotropies are present, the smallest time step should be used for numerical simulations. The smallest time step can be determined by calculating the time step for the most restrictive parameters presented in the model.

In some extreme scenarios, for example, if poroelastic media degenerates into acoustic media at some spatial location and the rest of the model domain is poroelastic, the smallest time step might be reduced by some factor otherwise numerical instabilities might appear at the interfaces. In this extreme case, numerical experiments are needed. Also, if poroelastic media degenerates into acoustic media the matrix $\hat{\zeta}$ (expression (7.66)) becomes singular (all components are the same) while the matrix $\hat{\rho}$ must be positive definite. In this case, poroelastic equations exactly reproduce acoustic wave propagation in a fluid.

7.5.1 Numerical examples

Let us test the derived above CFL conditions. We performed several 1D, 2D and 3D numerical simulations with different time steps. The source is the Ricker wavelet

$$F_R(t_m) = A_0(1 - 2(\pi(t_m - t_{m0})\Delta t_{st}f_c)^2) e^{-(\pi(t_m - t_{m0})\Delta t_{st}f_c)^2}, \quad (7.73)$$

where $A_0 = 1/\Delta t_{st}$ is the amplitude of the wavelet, Δt_{st} is the stable time step, $f_c = \omega_s/(2\pi)$ is the frequency of the source wavelet (ω_s is the angular frequency), t_m is the iteration number, t_{m0} is the wavelet delay (in iterations).

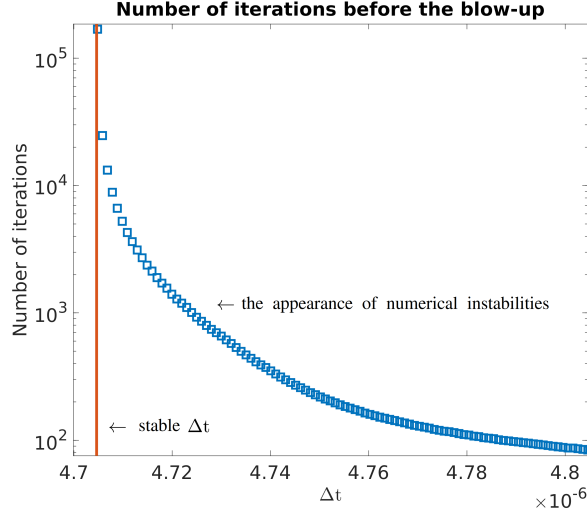


Figure 7.11: Number of iterations before the numerical instabilities appeared in the 1D numerical solution of Biot's equations. Each blue square corresponds to the numerical simulation. The material and numerical parameters are given in Table 7.4.

1D numerical experiment

First, we test the 1D CFL condition (7.70). We use a 1-D domain of 10m with $\Delta x^{1d} = 0.02$ m resulting in 500 grid cells. We apply the source (7.73) to the total stress $\bar{\sigma}$. The central frequency of the source wavelet is $f_c = 1 \cdot 10^4 / \pi$ Hz and the wavelet delay is $t_{m0} = 5 \cdot 10^{-4} / \Delta t_{st}^{1D}$. We perform a set of numerical simulations with different Δt using the parameters given in Table 7.4. For Δt derived by (7.70), the scheme is always stable (Figure 7.11, brown line). We increase the stable Δt by a small factor $l \cdot 2 \cdot 10^{-10}$ s, where $l \in [1, 500]$ m. The resulting set of different time steps Δt corresponds to the x-axis in Figure 7.11. A small increase of the stable Δt by $2 \cdot 10^{-10}$ s causes numerical instabilities of the numerical solution after 168603 time steps. A larger increase of the stable Δt causes numerical instabilities at significantly smaller time steps (blue squares in Figure 7.11).

In 2D or 3D numerical simulations of Biot's equations, the CFL condition is different from that one of the 1-D case. If the source (or the initial condition) is in the form of a plane wave and is aligned with the grid cells, then the 1D CFL condition is also valid in 2-D and 3-D. This is due to the fact that the plane wave is a multidimensional source and 1D, 2D and 3D simulations are similar. But once the wave propagation direction becomes different (for example, due to a reflection), the 1D CFL condition is not longer valid in 2D and 3D and the CFL condition (7.71) should be used.

3D numerical experiment

We simulate a wave propagating in 3D for the isotropic poro-elastic material whose properties are given in Table 7.4. We use the CFL condition (7.71). A 3D square domain of $10.2\text{m} \times 10.2\text{m} \times 10.2\text{m}$ is used. We set $\Delta x = 0.02\text{m}$, $\Delta y = 0.01\text{m}$ and $\Delta z = 0.005\text{m}$. The numerical model consists of $510 \times 1022 \times 2046$ grid cells in x -, y - and z -directions, respectively. The total number of grid cells is $\approx 1 \cdot 10^9$. We set a different number of grid cells in different directions for a more precise testing of the CFL condition (7.71) in 3D. The central frequency of the source wavelet is $f_c = 4 \cdot 10^3$ Hz and the wavelet delay is $t_{m0} = 3.3(3) \cdot 10^4$. The stable Δt is shown in Table 7.4 as Δt_{st}^{3D} . We multiplied Δt_{st}^{3D} by 0.99 and performed 850 time steps. The the solid velocity wave field V_x is shown in Figure 7.12, which obeys a perfect spherical behavior as expected. In another simulation, we multiplied Δt_{st}^{3D} by 1.01 and the simulation became unstable before 850 time steps.

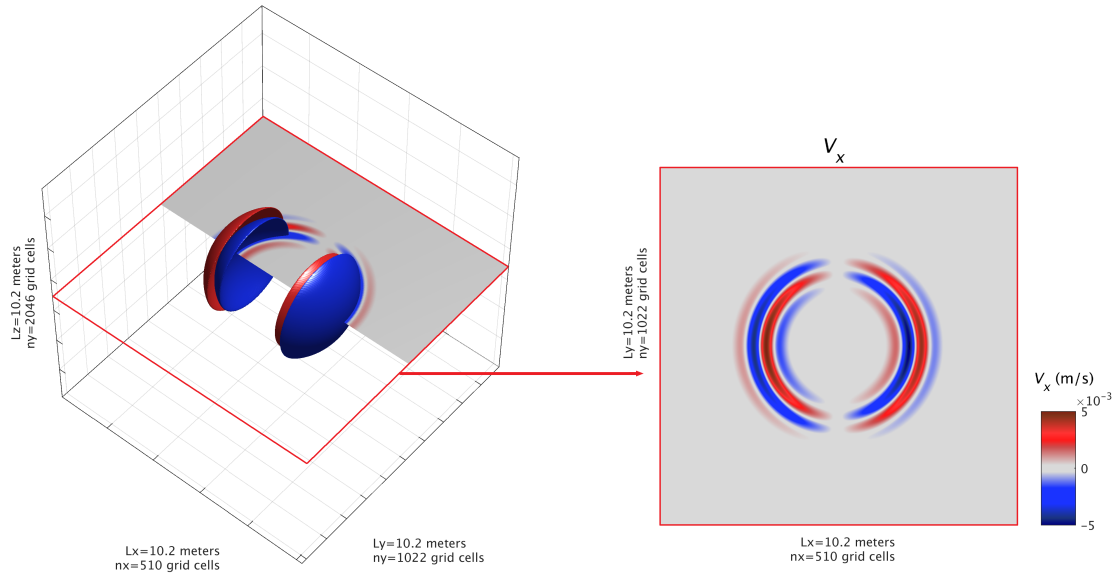


Figure 7.12: The the solid velocity wave field V_x after 850 time steps. The material and numerical parameters are given in Table 7.4.

7.6 Summary

We performed the von Neumann stability analysis of the elastodynamic Biot's equations (7.28)-(7.29). The characteristic times of the wave propagation (hyperbolic) and diffusion (parabolic) processes are different, thus, the system of equations exhibits a "stiff" behavior. The "stiffness" affects the CFL condition, which is derived for a discrete system of equations. In order to avoid very small time steps, different strategies are needed to discretize the hyperbolic and parabolic operators. We use the discrete scheme (7.37)-(7.38), which is explicit for the wave propagation part and varies for the diffusion process described by the Darcy's flux. The Darcy's flux is discretized using explicit, implicit-explicit and implicit schemes.

We provided the exact CFL conditions of Biot's equations, which are obtained by solving a polynomial of degree four. This polynomial exists for any set of input material and numerical parameters and can be derived analytically using the Maple script provided as supplementary material. Since, the scheme for the wave operator is explicit, the absolute values of the first two roots are determined by the fastest propagating wave. Thus, the CFL condition of Biot's equations is at least that one of the wave equation (7.10). The other two roots correspond to the wave of the second kind, which may behave as a propagating wave or as a diffusion process. The CFL condition arriving from the first two roots can be significantly affected by the CFL condition arriving from the third and fourth roots, depending of the scheme for the Darcy's flux.

If the scheme for the Darcy's flux is explicit, the CFL condition is highly affected. The time step might be very small in the diffusion regime of the slow P-wave V_2 and converges to the spectral radius of the parabolic operator (7.60). But the time step is not affected in the wave propagation regime of the slow P-wave V_2 (Figure 7.9, solid red curve).

If the scheme for the Darcy's flux is implicit-explicit or implicit, the CFL condition is not affected by the parabolic operator. In this case, the CFL condition of the wave equation (7.70) is valid (Figure 7.9, solid black curve). Note, that the CFL condition does not depend on viscosity and permeability of the medium. It is important to note that the fast wave velocity V_1 of Biot's equations (7.28)-(7.29) is different in wave propagation and diffusion regimes of the slow wave V_2 . The wave velocity in the CFL condition (7.10) must be chosen to that one of the high frequency limit V_1^{HF} (7.31) despite of the propagation or diffusive regime for V_2 for a given simulation. For example, if one solves numerically Biot's equations in the diffusive regime for V_2 (usually corresponds to low frequencies) and uses the CFL condition (7.10) with the current fastest velocity (7.36), the solution will explode. Thus, the CFL condition (7.70) with the velocity V_1^{HF} (7.31) always applies.

7.7 Discussion

In geophysics, explicit schemes for the wave simulations are very popular but also implicit schemes exist. If an implicit scheme for the wave operator of Biot's equations is used, the restriction on the time step arising from the wave equations vanishes. In this case, the time step will be determined by the scheme for the Darcy's flux. If the scheme for the Darcy's flux is also implicit, the scheme will be unconditionally stable and the time step will be determined by the accuracy and computational efficiency. If the scheme for the diffusion part is explicit, the time step will converge to the spectral radius of the parabolic operator (7.60) in the diffusive regime of the slow P-wave V_2 .

Another common approach to overcome the stiffness of PDEs is based on the operator splitting approach. The idea is that the system of PDEs is separated into the two parts. The first system contains only hyperbolic operators ("non stiff") and is solved using an explicit time integration. The second system contains parabolic operators ("stiff") and is solved independently from the first system at each time step. Operator splitting can be a first order Godunov-type, a second order, e.g., Strang splitting (Strang, 1968), or even higher order approaches exist. In the context of Biot's equations, some authors solve the stiff part analytically (Carcione and Quiroga-Goode, 1995; Chiavassa *et al.*, 2010; Chiavassa and Lombard, 2011). A detailed investigation of the operator splitting approach can be found in (Marchuk, 1975; LeVeque *et al.*, 2002). In order to converge to the original solution, the usual requirement to the operator splitting approach is that the solution of the system of PDEs is smooth (additionally, other requirements may be needed), which might not be always fulfilled in heterogeneous media. A proper usage of the operator splitting for a system of PDEs should be carefully investigated.

7.7.1 Comparison with previous works

Masson *et al.* (2006) studied the stability conditions of a $o(4,2)$ (4-th order in space and 2-nd order in time) numerical scheme for Biot's equations and used the implicit-explicit time integration for Darcy's flux. They derived the "analytical criterion", which coincides with our result (7.70) for the implicit-explicit scheme ($\chi = 1/2$). On the other hand, as an approximation Masson *et al.* (2006) pointed out that the classic Courant condition $\Delta t \leq 1/\hat{V}_1^{LF}$, where \hat{V}_1^{LF} is the undrained fast velocity (7.36), can be used. Note, that the velocity \hat{V}_1^{HF} is usually 10-20% higher than the \hat{V}_1^{LF} velocity, thus instead, the CFL condition (7.70) should be used. In addition, Masson *et al.* (2006) obtained the condition for material parameters (densities)

$$(1 + \Phi) \frac{T}{\phi} < \frac{\rho_f}{\rho}, \quad (7.74)$$

where Φ is a positive real dimensionless parameter related to the pore space structure (see Masson *et al.* (2006)). In the present notation, the condition (7.74) can be rewritten as

$$\rho_a \rho - \rho_f^2 > 0. \quad (7.75)$$

The condition (7.75) was also suggested by Carcione and Quiroga-Goode (1995); Wenzlau and Müller (2009). The condition (7.75) states that the determinant of the matrix \hat{q} (eq. (7.66)) is positive, which is equivalent to the statement that the matrix \hat{q}^{-1} is positive definite (assuming that the diagonal elements are positive).

Masson *et al.* (2006) and (Wenzlau and Müller, 2009) pointed out that the condition (7.74) is necessary but insufficient (see Figure 4 in Masson *et al.* (2006)). In other words, even if the inequality (7.74) (or (7.75)) is fulfilled, the scheme might not be stable and the stability depends on the viscosity and permeability. The von Neumann stability presented in this work does not support that. Our analytical derivations using Maple as well as numerical tests show that once the matrices of material parameters are positive definite (i.e. the condition (7.74) is fulfilled) and the CFL condition on the time step (7.70) (in 1D) is fulfilled — the $\chi = 1/2$ discrete scheme for the dynamic Biot's equations is stable. We have not discovered inconsistencies in the von Neumann stability analysis reported by O'Brien (2010).

7.8 Conclusions

We performed the von Neumann stability analyses of discrete schemes for the elastodynamic Biot's equations. The characteristic times of hyperbolic and parabolic processes are different thus the system of equations exhibits a "stiff" behavior. Such "stiffness" affects the stable time step. We use the explicit scheme for the wave propagation and apply different schemes for the Darcy's flux. If the scheme for the Darcy's flux is explicit, the stable time step becomes very small in the diffusion regime of the slow P-wave. If the scheme for the Darcy's flux is implicit-explicit or implicit, the stable time step is not affected. In this case, the Courant-Friedrichs-Lewy (CFL) condition of the discrete Biot's equations coincides with the CFL condition of the wave equation taking the highest fast P-wave velocity in the high frequency regime. All the analytical expressions derived for the discrete schemes were verified numerically in 1D, 2D and 3D.

Acknowledgments

Yury Alkhimenkov gratefully acknowledges support from the Swiss National Science Foundation, project number 172691. Yury Alkhimenkov, Lyudmila Khakimova and Yury Y. Podladchikov gratefully acknowledge support from the Russian Ministry of Science and Higher Education (project No. 075-15-2019-1890). Yury Alkhimenkov thanks Beatriz Quintal for many suggestions and comments which helped us to improve the quality of the manuscript. We thank Igor Morozov and an anonymous reviewer for many valuable suggestions and recommendations.

7.9 Appendix A: The dimensional damped linear wave equation

Explicit scheme for the Darcy's flux

The Von Neumann stability analysis for the discrete system (8.3) suggests that

$$\Delta t \leq \Delta x \frac{-\Delta x \rho + \sqrt{(\Delta x \rho)^2 + 16K\rho\tau^2}}{4K\tau}, \quad (7.76)$$

which is the exact CFL condition of the discrete scheme (8.3). Let us analyze the result (7.76).

Wave propagation regime of the explicit scheme

Lets us write a series expansion of the right hand side (R.H.S) of (7.76) assuming $\Delta x \rightarrow +0$ (equivalent to assuming $\tau \rightarrow +\infty$),

$$\Delta x \frac{-\Delta x \rho + \sqrt{(\Delta x \rho)^2 + 16K\rho\tau^2}}{4K\tau} = \frac{\sqrt{\rho}}{\sqrt{K}} \Delta x - \frac{1}{4} \frac{\rho}{K\tau} (\Delta x)^2 + \frac{1}{32} \frac{\sqrt{K}\rho}{K^2\tau^2} (\Delta x)^3 + O((\Delta x)^5). \quad (7.77)$$

It can be seen form (7.77) that the limit of the right hand side (R.H.S) of (7.76) as $\tau \rightarrow +\infty$ is

$$\lim_{\tau \rightarrow +\infty} \Delta x \frac{-\Delta x \rho + \sqrt{(\Delta x \rho)^2 + 16K\rho\tau^2}}{4K\tau} = \Delta x \frac{\sqrt{\rho}}{\sqrt{K}} \equiv \frac{\Delta x}{V}, \quad (7.78)$$

where $V = \sqrt{K/\rho}$. This CFL condition corresponds to the hyperbolic limit and is valid when $\tau \gg 1$. One can also take into account one more term in the series expansion (7.77) and the inequality (7.76) becomes

$$\Delta t \leq \frac{\Delta x}{V} - \frac{1}{4} \frac{1}{V^2\tau} (\Delta x)^2. \quad (7.79)$$

Diffusive regime of the explicit scheme

Now we consider an opposite scenario. We write a series expansion of the R.H.S of (7.76) assuming $\Delta x \rightarrow +\infty$ (equivalent to assuming $\tau \rightarrow +0$),

$$\Delta x \frac{-\Delta x \rho + \sqrt{(\Delta x \rho)^2 + 16K\rho\tau^2}}{4K\tau} = 2\tau - \frac{8K}{\rho(\Delta x)^2} \tau^3 + O\left(\frac{1}{(\Delta x)^4}\right). \quad (7.80)$$

It is interesting that the first term in the R.H.S of (7.80) does not depend on Δx . Thus, when $\tau \rightarrow +0$, the stability conditions reads

$$\Delta t \leq 2\tau, \quad (7.81)$$

which corresponds to the parabolic limit and is valid when $\tau \ll 1$. One can also take into account one more term in the series expansion (7.80) and the inequality (7.81) becomes

$$\Delta t \leq 2\tau - \frac{8K}{\rho(\Delta x)^2} \tau^3. \quad (7.82)$$

Implicit and implicit-explicit schemes for the Darcy's flux

The discrete system of (8.3) is written as

$$\begin{cases} \frac{1}{K} \frac{p_i^{l+1/2} - p_i^{l-1/2}}{\Delta t} = - \frac{q_{i+1/2}^l - q_{i-1/2}^l}{\Delta x} \\ \frac{q_{i+1/2}^{l+1} - q_{i+1/2}^l}{\Delta t} = - \frac{1}{\rho} \frac{p_{i+1}^{l+1/2} - p_i^{l+1/2}}{\Delta x} - \frac{1}{\tau} (\chi q_{i+1/2}^{l+1} + (1-\chi) q_{i+1/2}^l), \end{cases} \quad (7.83)$$

If $\chi = 1/2$, then (7.83) corresponds to the implicit-explicit scheme. The Von Neumann stability analysis for the discrete system (8.3) suggests that

$$\Delta t \leq \frac{\Delta x}{V}, \quad (7.84)$$

where $V = \sqrt{K/\rho}$ is the fast wave velocity.

If $\chi = 1$, then (7.83) corresponds to the implicit scheme for the Darcy's flux. The von Neumann stability analysis for this scheme suggests that

$$\Delta t \leq \Delta x \frac{\Delta x \rho + \sqrt{(\Delta x \rho)^2 + 16K\rho\tau^2}}{4K\tau}, \quad (7.85)$$

which is the exact CFL condition of the discrete scheme (7.83) with $\chi = 1$.

The general CFL condition of the dimensional linear damped wave equation (8.3) can be written as a function of the parameter χ , which defines the ratio of explicit to implicit schemes. For positive Δt , the CFL condition is

$$\Delta t \leq \Delta x \frac{\frac{1}{V} \sqrt{4(\chi - \frac{1}{2})^2 (\Delta x)^2 \frac{1}{V^2} + 16\tau^2} + 2(\chi - \frac{1}{2}) \frac{1}{V^2} \Delta x}{4\tau}, \quad (7.86)$$

for negative Δt , the CFL condition is

$$\Delta t \leq \Delta x \frac{-\frac{1}{V} \sqrt{4(\chi - \frac{1}{2})^2 (\Delta x)^2 \frac{1}{V^2} + 16\tau^2} + 2(\chi - \frac{1}{2}) \frac{1}{V^2} \Delta x}{4\tau}. \quad (7.87)$$

7.10 Appendix B: Dimensional analysis of the elastodynamic Biot's equations

The first order velocity-stress system of Biot's equations can be written as (Biot, 1962a)

$$\begin{pmatrix} \frac{\partial \bar{p}}{\partial t} \\ \frac{\partial p_f}{\partial t} \end{pmatrix} = - \begin{pmatrix} K_u & \alpha M \\ \alpha M & M \end{pmatrix} \begin{pmatrix} \nabla_k v_k^s \\ \nabla_k q_k^D \end{pmatrix}, \quad (7.88)$$

$$\frac{\partial \bar{\tau}_{ij}}{\partial t} = 2G \left(\frac{1}{2} (\nabla_i v_j^s + \nabla_j v_i^s) - \frac{1}{3} (\nabla_k v_k^s) \delta_{ij} \right) \quad (7.89)$$

and

$$\begin{pmatrix} \frac{\partial v_i^s}{\partial t} \\ -\frac{\partial q_i^D}{\partial t} \end{pmatrix} = \frac{1}{\Theta} \begin{pmatrix} \rho_a & \rho_f \\ \rho_f & \rho_t \end{pmatrix} \begin{pmatrix} \nabla_j (-\bar{p} \delta_{ij} + \bar{\tau}_{ij}) \\ \frac{\eta}{\kappa} q_i^D + \nabla_i p_f \end{pmatrix}, \quad (7.90)$$

Table 7.5: List of Principal Notation

Symbol	Meaning	Unit
σ^s, σ^f	solid and fluid stresses	Pa
τ^s, τ^f	solid and fluid stress deviators	Pa
\bar{p}, p_f	total and fluid pressures	Pa
v^s, v^f	solid and fluid velocities	m/s
ρ_s, ρ_f	solid and fluid densities	kg/m ³
K_g, K_f	elastic solid and fluid bulk moduli	Pa
G	elastic drained shear moduli	Pa
K_d, K_u	elastic drained and undrained bulk moduli	Pa
η	fluid shear viscosity	Pa·s
κ	permeability	m ²
ϕ	porosity	-
T	tortuosity	-
$\bar{\sigma}$	$= (1 - \phi)\sigma^s + \phi\sigma^f$, total stress	Pa
$\bar{\tau}$	$= (1 - \phi)\bar{\tau} + \phi\tau^f$, total stress deviator	Pa
q^D	$= \phi(v^f - v^s)$, Darcy's flux	m/s
ρ_t	$= (1 - \phi)\rho + \phi\rho$, total density	kg/m ³
α	Biot-Willis coefficient	-

where $\rho_a = \rho_f T / \phi$ and $\Theta = \rho_t \rho_a - \rho_f^2$. The list of field variables and material parameters is given in Table 7.5. From the general principles of thermodynamic, the matrices of coefficients in (7.88) and (7.90) must be positive definite. For an isotropic material saturated with a single fluid, in which the solid frame consists of a single isotropic mineral, the Biot-Willis coefficient is

$$\alpha = 1 - K_d / K_g \quad (7.91)$$

where K_u is the undrained bulk modulus

$$K_u = K_d + \alpha^2 M. \quad (7.92)$$

M is the fluid storage coefficient

$$M = \left(\phi / K_f + (1 - \phi) / K_g - K_d / K_g^2 \right)^{-1} \quad (7.93)$$

Dimensional analysis is a very powerful method to analyze PDEs and to understand how different physical parameters affect the physical system. For simplicity, a one dimensional example is considered, so the total stress tensor can be written instead of the volumetric and deviatoric stresses. The governing first order velocity-stress system of equations in one space dimension can be written as

$$\begin{pmatrix} \frac{\partial \bar{\sigma}}{\partial t} \\ \frac{\partial p_f}{\partial t} \end{pmatrix} = \begin{pmatrix} K_u + 4/3G & \alpha M \\ \alpha M & M \end{pmatrix} \begin{pmatrix} \frac{\partial v^s}{\partial x} \\ \frac{\partial q^D}{\partial x} \end{pmatrix}, \quad (7.94)$$

$$\begin{pmatrix} \frac{\partial v^s}{\partial t} \\ \frac{\partial q^D}{\partial t} \end{pmatrix} = \frac{1}{\Theta} \begin{pmatrix} \rho_a & \rho_f \\ \rho_f & \rho_t \end{pmatrix} \begin{pmatrix} \frac{\partial \bar{\sigma}}{\partial x} \\ \frac{\eta}{\kappa} q^D + \frac{\partial p_f}{\partial x} \end{pmatrix}, \quad (7.95)$$

By using the two base quantities — the stiffness c_{11}^u [Pa⁻¹] and total density ρ_t [kg/m³], equations (7.94) and (7.95) can be transformed into a dimensionless form. Let us define the undrained P-wave modulus as

$$c_{11}^u = (K_u + 4/3G), \quad (7.96)$$

which has dimensions of [Pa]. First, the two base quantities c_{11}^u and ρ_a are carried out of parentheses in equations (7.94) and (7.95), which can be rewritten as

$$\begin{pmatrix} \frac{\partial \bar{\sigma}}{\partial t} \\ \frac{\partial p_f}{\partial t} \end{pmatrix} = c_{11}^u \begin{pmatrix} 1 & \alpha M / c_{11}^u \\ \alpha M / c_{11}^u & M / c_{11}^u \end{pmatrix} \begin{pmatrix} \frac{\partial v^s}{\partial x} \\ \frac{\partial q^D}{\partial x} \end{pmatrix}, \quad (7.97)$$

$$\begin{pmatrix} \frac{\partial v^s}{\partial t} \\ \frac{\partial q^D}{\partial t} \end{pmatrix} = \tilde{\rho}_a \begin{pmatrix} 1 & \rho_f / \rho_a \\ \rho_f / \rho_a & \rho_t / \rho_a \end{pmatrix} \begin{pmatrix} \frac{\partial \bar{\sigma}}{\partial x} \\ \frac{\eta}{\kappa} q^D + \frac{\partial p_f}{\partial x} \end{pmatrix}, \quad (7.98)$$

where $\tilde{\rho}_a = \rho_a / \Theta$. Then, the following replacements are done

$$\bar{\sigma} \rightarrow c_{11}^u \tilde{\sigma}, \quad p_f \rightarrow c_{11}^u \tilde{p}_f, \quad (7.99)$$

$$v^s \rightarrow \frac{L_x^*}{\tau^*} \tilde{v}^s, \quad q^D \rightarrow \frac{L_x^*}{\tau^*} \tilde{q}^D, \quad (7.100)$$

$$x \rightarrow L_x^* \tilde{x}, \quad t \rightarrow \tau^* \tilde{t}, \quad (7.101)$$

where L_x^* [m] is the characteristic length and τ^* [s] is the characteristic time. The resulting system of equations is

$$\begin{pmatrix} \frac{\partial \tilde{\sigma}}{\partial \tilde{t}} \\ \frac{\partial \tilde{p}_f}{\partial \tilde{t}} \end{pmatrix} = \begin{pmatrix} 1 & \tilde{\alpha} \\ \tilde{\alpha} & \tilde{M} \end{pmatrix} \begin{pmatrix} \frac{\partial \tilde{v}^s}{\partial \tilde{x}} \\ \frac{\partial \tilde{q}^D}{\partial \tilde{x}} \end{pmatrix}, \quad (7.102)$$

$$(I_1)^2 \begin{pmatrix} \frac{\partial \tilde{v}^s}{\partial \tilde{t}} \\ -\frac{\partial \tilde{q}^D}{\partial \tilde{t}} \end{pmatrix} = \begin{pmatrix} 1 & \tilde{\rho}_f \\ \tilde{\rho}_f & \tilde{\rho}_t \end{pmatrix} \begin{pmatrix} \frac{\partial \tilde{\sigma}}{\partial \tilde{x}} \\ I_2 \tilde{q}^D + \frac{\partial \tilde{p}_f}{\partial \tilde{x}} \end{pmatrix}, \quad (7.103)$$

where $\tilde{\alpha} = \alpha M / c_{11}^u$, $\tilde{M} = M / c_{11}^u$, $\tilde{\rho}_f \equiv \rho_f / \rho_a$, $\tilde{\rho}_t \equiv \rho_t / \rho_a$,

$$I_1 = \sqrt{\frac{1}{\tilde{\rho}_a c_{11}^u} \frac{L_x^*}{\tau^*}}, \quad (7.104)$$

and

$$I_2 = \frac{\eta}{\kappa} \frac{1}{c_{11}^u} \frac{(L_x^*)^2}{\tau^*} \quad (7.105)$$

The four dimensionless parameters $\tilde{\alpha}$, \tilde{M} , $\tilde{\rho}_f$ and $\tilde{\rho}_t$ define the coupling between the solid and fluid phases. The two dimensionless parameters I_1 , I_2 are the key parameters denoting the ratio between the advection and diffusion time scales. The dimensionless quantities I_1 and I_2 are related to hyperbolic (advection) and parabolic (diffusion) processes, respectively. In order to further reduce the number of parameters, we set $I_1 = 1$. Thus, $L_x^* = \tau^* \sqrt{\tilde{\rho}_a c_{11}^u}$ and equation (7.105) becomes

$$I_2 = \frac{\eta}{\kappa} \tilde{\rho}_a \tau^*, \quad (7.106)$$

where τ^* is a free parameter. Let us choose τ^* as

$$\tau^* = \left(\frac{\eta}{\kappa} \tilde{\rho}_a \right)^{-1}. \quad (7.107)$$

Now, equation (7.106) becomes

$$I_2 \equiv \frac{\eta}{\kappa} \tilde{\rho}_a \tau^* = \frac{\eta}{\kappa} \tilde{\rho}_a \left(\frac{\eta}{\kappa} \tilde{\rho}_a \right)^{-1} \equiv 1 \quad (7.108)$$

Therefore, taking into account that $I_1 = 1$ and $I_2 = 1$, the system (7.102)-(7.103) can be rewritten as

$$\begin{pmatrix} \frac{\partial \tilde{\sigma}}{\partial \tilde{t}} \\ -\frac{\partial \tilde{p}_f}{\partial \tilde{t}} \end{pmatrix} = \begin{pmatrix} 1 & \tilde{\alpha} \\ \tilde{\alpha} & \tilde{M} \end{pmatrix} \begin{pmatrix} \frac{\partial \tilde{v}^s}{\partial \tilde{x}} \\ \frac{\partial \tilde{q}^D}{\partial \tilde{x}} \end{pmatrix}, \quad (7.109)$$

$$\begin{pmatrix} \frac{\partial \tilde{v}^s}{\partial \tilde{t}} \\ -\frac{\partial \tilde{q}^D}{\partial \tilde{t}} \end{pmatrix} = \begin{pmatrix} 1 & \tilde{\rho}_f \\ \tilde{\rho}_f & \tilde{\rho}_t \end{pmatrix} \begin{pmatrix} \frac{\partial \tilde{\sigma}}{\partial \tilde{x}} \\ \tilde{q}^D + \frac{\partial \tilde{p}_f}{\partial \tilde{x}} \end{pmatrix}, \quad (7.110)$$

The system of equations (7.109) and (7.110) defines the dimensionless elastodynamic Biot's equations for an isotropic medium saturated with a single fluid, where the only for dimensionless parameters are present ($\tilde{\alpha}$, \tilde{M} , $\tilde{\rho}_f$ and $\tilde{\rho}_t$). Note, that the presented dimensionless analysis is particularly useful for the stability analysis, since we have 1 in the main diagonals of (7.109) and (7.110). A much better dimensionless analysis can be performed by using the undrained P-wave modulus $c_{11}^d = (K_d + 4/3G)$ and ρ_t as two base quantities.

7.11 Appendix C: The amplification matrices for different schemes for Example 1

The amplification matrix F for the explicit scheme is

$$F = \begin{bmatrix} -3r^2 + 1 & 0 & 2Ir & Ir \\ 0 & -3r^2 + 1 & -Ir & 3/2 Ir^2 \Delta x - 2Ir \\ 2Ir & Ir & 1 & 1/2 \Delta x r \\ -Ir & -2Ir & 0 & -d x r + 1 \end{bmatrix}, \quad (7.111)$$

where $r = \Delta t \sin(1/2\omega)/\Delta x$. We add $\sin(1/2\omega)$ in order to avoid \cos and \sin functions in the resulting solutions. The stability of the explicit scheme is shown in section 7.4.1.

The amplification matrix F for the implicit-explicit scheme is

$$F = \begin{bmatrix} -3r^2 + 1 & 0 & 2Ir & Ir \\ 3/2 \frac{d x r^3}{\Delta x r + 2} & -1/2 \frac{-2\Delta x r + 12r^2 - 4}{\Delta x r + 2} & -1/2 \frac{2I\Delta x r^2 + 4Ir}{\Delta x r + 2} & -1/2 \frac{-2I\Delta x r^2 + 8Ir}{\Delta x r + 2} \\ 1/2 \frac{3I\Delta x r^2 + 8Ir}{\Delta x r + 2} & \frac{2Ir}{\Delta x r + 2} & 1/2 \frac{2\Delta x r + 4}{\Delta x r + 2} & \frac{\Delta x r}{\Delta x r + 2} \\ \frac{-2Ir}{\Delta x r + 2} & \frac{-4Ir}{\Delta x r + 2} & 0 & -\frac{\Delta x r - 2}{\Delta x r + 2} \end{bmatrix}, \quad (7.112)$$

where $r = \Delta t \sin(1/2\omega)/\Delta x$. The stability of the implicit-explicit scheme is shown in section 7.4.1.

The amplification matrix F for the implicit scheme is

$$F = \begin{bmatrix} -3r^2 + 1 & 0 & 2Ir & Ir \\ 3/2 \frac{\Delta x r^3}{\Delta x r + 1} & -1/2 \frac{-2\Delta x r + 6r^2 - 2}{\Delta x r + 1} & -1/2 \frac{2I\Delta x r^2 + 2Ir}{\Delta x r + 1} & -1/2 \frac{I\Delta x r^2 + 4Ir}{\Delta x r + 1} \\ 1/2 \frac{3I\Delta x r^2 + 4Ir}{\Delta x r + 1} & \frac{Ir}{\Delta x r + 1} & 1/2 \frac{2\Delta x r + 2}{\Delta x r + 1} & 1/2 \frac{\Delta x r}{\Delta x r + 1} \\ \frac{-Ir}{\Delta x r + 1} & \frac{-2Ir}{\Delta x r + 1} & 0 & (\Delta x r + 1)^{-1} \end{bmatrix}, \quad (7.113)$$

where $r = \Delta t \sin(1/2\omega)/\Delta x$. The stability of the implicit-explicit scheme is shown in section 7.4.1.

Chapter 8

Non-linear instabilities, strain localization and spontaneous earthquake nucleation

Yury Alkhimenkov and others

Abstract

Anthropogenic activities such as geothermal energy production, CO_2 sequestration, or fluid and wastewater injection share a common inconvenience: they may trigger earthquakes. For example, many seismic events were recorded during and after high-pressure fluid injection into the subsurface as part of a geothermal energy project, near Basel in Switzerland. The project had finally to be stopped after a major earthquake occurred. The Basel case is one project amongst others where inaccurate seismic risk hazard assessment resulted in hindering sustainable and economically profitable new energy projects. A similar outcome currently might lead the gas production from the Groningen field in the Netherlands to shut down in 2022 because of increasing seismic hazard and social impacts.

Understanding the physical processes governing induced seismicity has been a hot topic since the last decade. A lot of research has been done trying to explain the physics of seismic triggering events. However, the exact physics behind seismic events nucleation is still poorly understood. The main reasons for that are (i) oversimplified physics in analytical models and numerical simulations, which only describe a subset of the seismic cycle's features, (ii) mainly one- or two-dimensional modeling studies limited by the lack of computing power, (iii) lack of fully coupled physical models resolving fluid-solid interactions. These simple solutions result in (iv) very little predictive power of current models.

The theory of spontaneous earthquake nucleation is based on visco-plastic and elasto-plastic quasi-static solvers. We report here a matrix-free pseudo transient method to solve the non-linear physics of visco-plastic and elasto-plastic systems. By using spectral decomposition (i.e., Fourier analysis), the time evolution of the general damped wave equation is presented. Analytical formulas to evaluate the parameters corresponding to the fastest decay rate of the damped linear wave equation are given. The attractor of the damped linear wave equation corresponds to the steady-state solution. A simple explanation of the pseudo transient method is presented below. The double-damped wave equation is also analyzed below.

8.1 Introduction

Earthquakes are seismic events that are caused by natural processes in the Earth's subsurface (e.g. tectonic activity) and by anthropogenic activities (e.g. fluid injection). Natural processes include tectonic activity, seismicity accompanied by volcanic eruptions, seismicity, and rock failure due to accumulated stresses between and away from plate boundaries, faulting, and many others. Recently, human-made activities also resulted in earthquake triggering, such as CO_2 sequestration (to mitigate the negative impact of CO_2 on the climate change) reported by *Miller et al.* (2004); *Zoback and Gorelick* (2015), geothermal energy production (*Majer et al.*, 2007), water injection by oil and gas companies (*Suckale*, 2009), hydraulic fracturing (*Ellsworth*, 2013).

Earthquakes caused by fluid injection are usually of small magnitudes but sometimes they can be significant with magnitudes M_L 5.7 in 2011 and M_L 5.8 in 2016 (*Yeck et al.*, 2017; *Grigoli et al.*, 2018). Near Basel (Switzerland), more than 28 significant seismic events with a magnitude between 1.7 and 3.4 were recorded by the Swiss Seismological Service in 2006. Such significant seismic activity was the result of high-pressure fluid injection into a five-kilometer deep well (*Deichmann and Ernst*, 2009). Another example is the induced seismicity of the Groningen gas field caused by the production of gas which produced over 1000 earthquakes (*van Thienen-Visser and Breunese*, 2015; *Dost et al.*, 2017). The negative socio-economic impact in the Province of Groningen included building damage, reduced house prices, fear, and health issues (*Van der Voort and Vanclay*, 2015). Therefore, understanding the physics of induced seismicity and the mechanisms which may trigger seismic events is of high importance from scientific, social, safety, and climate control aspects.

First attempts to control the frequency and magnitude of fluid-induced seismicity were based on simple models considering simple failure condition linked to the fluid pressure and appearing seismic events on a contour map (*Raleigh et al.*, 1976). Other models are based on some empirical relations linking the occurrence and magnitude of seismic events with the amount of injected fluid (*McGarr*, 2014). All the models based on simple physics and/or empirical relations might work well for a particular field and mechanism but usually fail to adequately describe induced seismicity in other fields (*Alghannam and Juanes*, 2020). A broad range of field

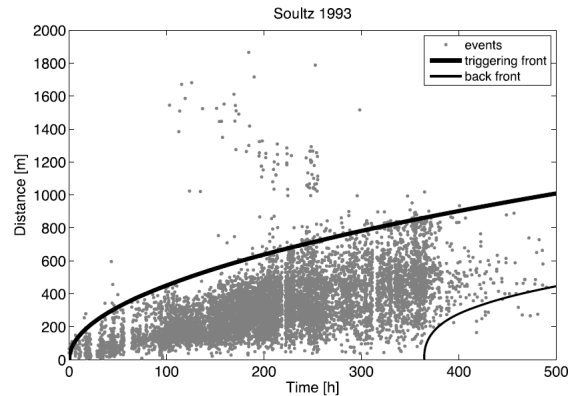


Figure 8.1: The triggering front of seismic events due to fluid injection at a borehole at Soulitz, France [from *Shapiro and Dinske* (2009)].

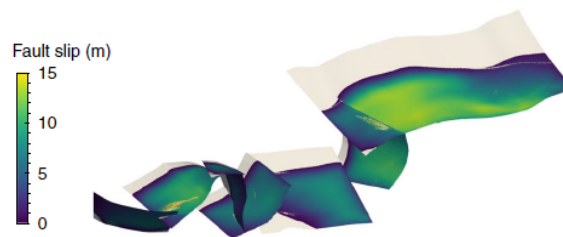


Figure 8.2: The dynamic rupture model: final slip magnitude [from *Ulrich et al.* (2019)].

observations suggest that many seismic events due to fluid injection can be described by the fluid-pressure front evolution with time (Figure 8.1) modeled by the non-linear diffusion equation (*Shapiro and Dinske*, 2009; *Shapiro*, 2015) but this concept does not take into account the physics of fault slip and fracture evolution. Laboratory experiments indeed confirmed that fluid injection may cause aseismic slip with many micro-seismic events (*Guglielmi et al.*, 2015).

Nowadays, several simplified analytical and numerical models exist to explain the earthquake triggering mechanism, foreshocks, and post-seismic events. The standard technique to reproduce many features of earthquake cycles is the concept of the rate-and-state fault friction (*Dieterich*, 1979; *Ruina*, 1983) which is an experimentally determined constitutive law. This concept is based on the assumption that the friction coefficient is a function of the slip rate and state variables. By setting the rate-and-state frictional behavior of a particular fault, some features of the seismic cycle can be reproduced (*Lapusta et al.*, 2000). The possibility of using complex 3-D faults was shown by *Wollherr et al.* (2018); *Ulrich et al.* (2019) who presented a dynamic rupture model of complex geometry (Figure 8.2). The brittle-ductile transition and localized frictional sliding on faults were analyzed by *Lavier et al.* (2021); *Allison and Dunham* (2021). Novel numerical approaches have been applied to model rate-and-state fault friction (*Hajarolasvadi and Elbanna*, 2017; *Erickson et al.*, 2017; *Abdelmeguid et al.*, 2019; *Almquist and Dunham*, 2021). *Brodsky et al.* (2020) studied the state of stress on the fault before, during, and after a major earthquake. *Erickson et al.* (2020) presented community code benchmarks of numerical simulations of sequences of earthquakes and aseismic slip. *Dal Zilio et al.* (2020) examined the scaling properties using dynamic simulations of frictional sliding.

Another approach is based on the modeling of elastic, viscous, elastoplastic, and viscoplastic rheologies of faults and surrounding regions (*Yin and Xie*, 2019). *Tong and Lavier* (2018) combined rate-and-state behavior at steady state to simulate earthquakes and plastic rheology to model permanent strain. *Torberntsson et al.* (2018) implemented poroelastic rheology and rate-and-state behavior to model earthquake sequences. *Nevitt et al.*

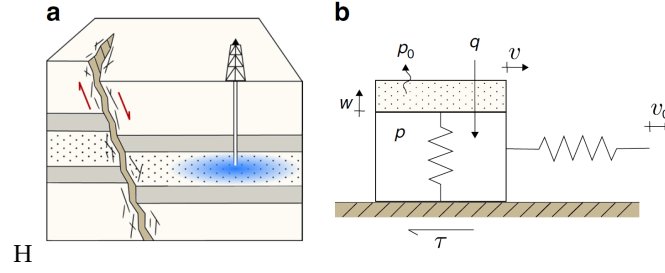


Figure 8.3: The conceptual model of fluid-induced seismicity mechanism. Panel (a) shows the reservoir surrounding the fault, panel (b) shows the poroelastic spring-poro-slider model of a fault [from *Alghannam and Juanes (2020)*].

(2020) showed that elastoplastic models likely provide the most reliable representations of subsurface fault behavior. Physically-driven simulations with coupled physics were presented by *Van Dinther et al. (2013a,b)*; *Preuss et al. (2020)*; *Petrini et al. (2020)*. Other approaches to model earthquake mechanics using coupled physics were presented by *Takeuchi and Fialko (2012)*; *Buijze et al. (2017)*; *Jin and Zoback (2018)*; *van Dinther et al. (2019)*; *Minakov and Yarushina (2021)*.

Fluid injection and pore pressure perturbations can trigger earthquakes, especially if the fluid encounters faults (*Miller et al., 2004*; *Maurer et al., 2020*; *Miller, 2020*; *Zhu et al., 2020*). Recently, a new model was developed based on spring-sliders (Figure 8.3) which combines poroelasticity with the rate-and-state friction technique (*Alghannam and Juanes, 2020*).

The current state of research in induced seismicity provides us with numerous field observations, detailed data sets, and statistical analyses of data. Nevertheless, there is a lack of high-resolution 3-D numerical modeling with fully coupled physics of fluid-solid interaction which I plan to address in in this chapter and subsequent work. Such modeling can help us to better understand how injection rate, fluid pressure diffusion, and its amplitude can trigger seismic events. Furthermore, the developed numerical algorithms can be used to study a particular field by using the corresponding rock properties and layers' geometries acquired from reflection seismic and well log data.

8.2 The pseudo-transient method

Pseudo-transient (PT) continuation is a physics-inspired iterative method that solves the steady-state problem by adding pseudotime derivative, through which the steady-state solution is progressively achieved via a pseudo-time stepping. In other words, the quasi-static solution is an attractor of the dynamic equation with a pseudotime derivative. This method is also known as the 2nd Richardson or relaxation method (*Frankel, 1950*).

8.2.1 The damped wave equation

For simplicity, we first consider the 1D scalar damped linear wave equation (DWE) as a first order hyperbolic system,

$$\begin{cases} \beta \partial_t p = -\partial_x v \\ \partial_t v = -\frac{1}{\rho} \partial_x p - \frac{1}{\tau_d} v, \end{cases} \quad (8.1)$$

where p is the pressure, v is the velocity, β is the compressibility (the bulk modulus is $K = 1/\beta$), ρ is the density, τ_d is the damping parameter. This system of equations can be represented by a single equation

$$\partial_t^2 v = \frac{1}{\beta\rho} \partial_x^2 v - \frac{1}{\tau_d} \partial_t v. \quad (8.2)$$

The solution of (8.1) (or equally 8.2) corresponds to propagating waves for $\tau_d \gg 1$ and to the diffusion process for $\tau_d \ll 1$. Let us find the optimal parameter τ_d , which corresponds to fastest decay of the velocity amplitudes v . This problem for DWE has been addressed by many researchers, e.g. *Benyamin et al. (2020)*; *Calder and Yezzi (2019)*. The discrete version of the system 8.1 can be written as

$$\begin{cases} \beta \frac{p_i^{l+1/2} - p_i^{l-1/2}}{\Delta t} = -\frac{v_{i+1/2}^l - v_{i-1/2}^l}{\Delta x} \\ \frac{v_{i+1/2}^{l+1} - v_{i+1/2}^l}{\Delta t} = -\frac{1}{\rho} \frac{p_{i+1}^{l+1/2} - p_i^{l+1/2}}{\Delta x} - \frac{1}{\tau_d} v_{i+1/2}^{l+1}, \end{cases} \quad (8.3)$$

where we use a conservative staggered space-time grid discretization. The pressure p is defined at the center of a grid cell i and the velocity v is defined at the side of a grid cell $i \pm 1/2$ (v can be considered as a "flux" through the grid cell). The temporal discretization of p corresponds to the half integer nodes $l + 1/2$ and the temporal discretization of q corresponds to the node integers l . The von Neumann stability analysis for this scheme *Alkhimenkov et al. (2020c)* suggests that

$$\Delta t \leq \Delta x \frac{\Delta x \rho + \sqrt{(\Delta x \rho)^2 + 16K\rho\tau_d^2}}{4K\tau_d}, \quad (8.4)$$

or a more restrictive condition can be used $\Delta t \leq \Delta x/V$, $V = \sqrt{K/\rho}$. The solution W of of the system (8.1) can be represented in the form

$$W(x, t) = Qe^{\lambda t} \sin\left(\frac{kx\pi}{L}\right), \quad (8.5)$$

where Q is the amplitude, k is the wave number, t is time, x is spatial coordinate and λ is the eigenvalue, L is the length of the one-dimensional domain. The solution of the form (8.5) of the system (8.1) leads to the two roots for λ ,

$$\lambda_{1,2} = -\left(\frac{Ld \mp \sqrt{-4(kV\Delta t\pi)^2 + (Ld)^2}}{2\Delta tL}\right). \quad (8.6)$$

where $d = \Delta t/\tau_d$, $V = \sqrt{K/\rho}$. The decay of the velocity amplitudes v per time step Δt obeys an exponential decay according to (8.6). The fastest decay can be achieved if the square root in (8.6) is equal to zero, giving

$$-4(kV\Delta t\pi)^2 + (Ld)^2 = 0. \quad (8.7)$$

The optimal damping parameter can be found from (8.7),

$$d_{opt} = \frac{2\pi V \Delta t k}{L}. \quad (8.8)$$

In other words, the optimal damping parameter should be efficient for the attenuation of all the waves presented in the numerical model. The largest wavelength within the model domain is represented by a single period of a sine function which corresponds to the wave number $k_1 = 1$. Let us consider a numerical experiment, a one-dimensional domain $L = 1$ (m) with the velocity $V = 1$ (m/s). The time step can be approximately written as $\Delta t = \Delta x/V$. The total number of grid cells is n_x , so $\Delta x = L/n_x$. The formula (8.8) can be rewritten as

$$d_{opt} = \frac{2\pi k}{n_x}, \quad (8.9)$$

According to (8.8) (or (8.9)), $d_{opt} \approx 0.0063$. We perform a numerical simulation for $nt = 8 \cdot n_x$ time steps for a set of different damping parameters d . The numerical result is compared with the analytical solution (8.6) (Figure 8.4). Both, the numerical and analytical solutions show that the expression (8.8) (or (8.9)) correspond to the optimal damping parameter d_{opt} .

8.2.2 The double damped wave equation

Now we consider the 1D scalar double damped linear wave equation (DDWE) as a first order hyperbolic system,

$$\begin{cases} \beta \partial_t p = -\partial_x v - \frac{1}{\eta} p \\ \rho \partial_t v = -\partial_x p - \frac{1}{k_{\eta f}} v, \end{cases} \quad (8.10)$$

The system (8.10) is different from the DWE (8.1) by the additional damping parameter η in (8.10)₁. This equations corresponds to

$$\beta \rho \partial_t^2 p = \partial_x^2 p - \left(\frac{\beta}{k_{\eta f}} + \frac{\rho}{\eta} \right) \partial_t p - \frac{1}{k_{\eta f} \eta} p. \quad (8.11)$$

Let us assume that in (8.10) all parameters are physical except for ρ , which represents the damping parameter. The task is to find the optimal parameters *rho*, which corresponds to fastest decay of the pressure amplitudes p . The discrete version of the system (8.10) can be written as

$$\begin{cases} \beta \frac{p_i^{l+1/2} - p_i^{l-1/2}}{\Delta t} = -\frac{v_{i+1/2}^l - v_{i-1/2}^l}{\Delta x} - \frac{1}{\eta} p_{i+1/2}^l \\ \rho \frac{v_{i+1/2}^{l+1} - v_{i+1/2}^l}{\Delta t} = -\frac{p_{i+1}^{l+1/2} - p_i^{l+1/2}}{\Delta x} - \frac{1}{k_{\eta f}} v_{i+1/2}^{l+1}, \end{cases} \quad (8.12)$$

where we use a conservative staggered space-time grid discretization. The solution W of of the system (8.10) can be represented in the same form as for DWE,

$$W(x, t) = Q e^{\lambda t} \sin\left(\frac{kx\pi}{L}\right), \quad (8.13)$$

where Q is the amplitude, k is the wave number, t is time, x is spatial coordinate and λ is the eigenvalue, L is the length of the one-dimensional domain. The solution of the form (8.13) of the system (8.10) leads to the two roots for λ ,

$$\lambda_{1,2} = -\frac{\mp \sqrt{(\rho_0 - 1)^2 L_{Lc}^2 - 4\pi^2 k^2 \rho_0 + L_{Lc}(\rho_0 + 1)}}{4\sqrt{\rho_0} n_x}, \quad (8.14)$$

where the following replacements are done: $\rho = \rho_0 \eta^2 \beta / L_c^2$, $L = L_{Lc} L_c$, $k_{\eta f} = L_c^2 / \eta$, $\Delta x = L_x / n_x$, $\Delta t = \Delta x / V$. We are looking for the optimal parameter ρ_0 , which corresponds to the fastest decay of the amplitudes of the system (8.10). The solution (8.14) gives the amplitudes of the propagating wavelets of the system (8.10), therefore, the optimal dumping parameter corresponds to the minimum of (8.14). Let us analyze the result (8.14). If $L_{Lc} = +\infty$, then the DDWE (8.10) degenerates into DWE (8.1) and the expression for the optimal parameter becomes

$$\lim_{L_{Lc} \rightarrow +\infty} \lambda_{1,2} = \frac{-1 - \rho_0 \pm \sqrt{(\rho_0 - 1)^2}}{4\sqrt{\rho_0}}. \quad (8.15)$$

The result (8.15) has a single minimum, while for $L_{Lc} \neq +\infty$, the solution (8.14) has two minimums (see Figure 8.4),

$$(\rho_0)_{1,2} = \frac{L_{Lc}^2 + 2\pi^2 k^2 \pm 2\sqrt{L_{Lc}^2 \pi^2 k^2 + \pi^4 k^4}}{L_{Lc}^2}. \quad (8.16)$$

We perform a numerical solution of the system (8.10) for a set of different damping parameters ρ_0 , the initial conditions are of the from (8.13). The numerical solution corresponds to propagating attenuating wavelets, the stop criteria for the simulation is when the amplitudes become less than 10^{-12} . The numerical result is

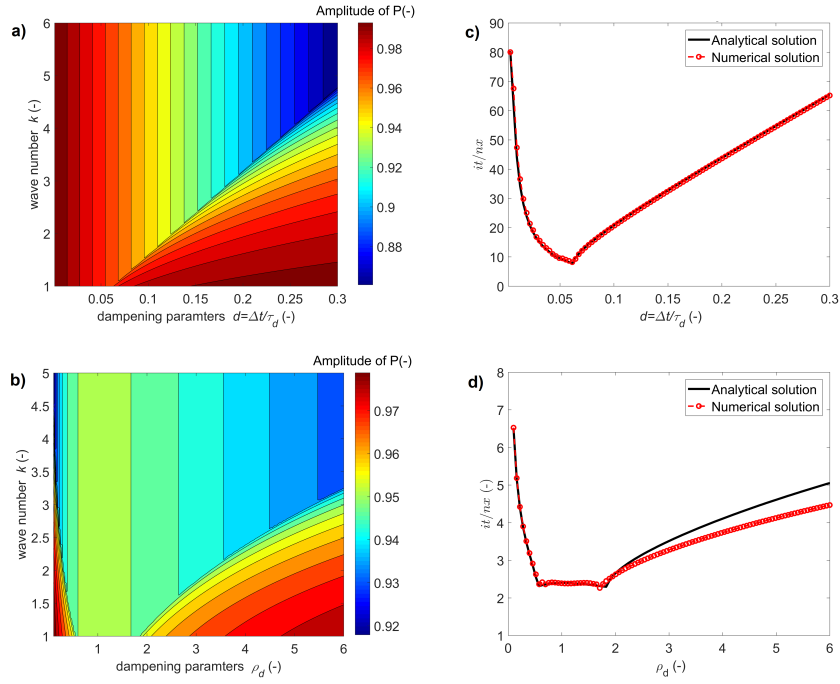


Figure 8.4: (a and b) The decay rate for residuals with different wavenumbers corresponding to different damping parameters for single (a) and double (b) damped wave equations. A total cell number of 100 is used for both cases. A larger absolute value of the decay rate ($\lambda \Delta t$) implies a faster the convergence process. (c and d). A comparison of the numerical and analytical processes via different damping parameters for single (c) and double (d) damped wave equations. An accuracy of 10^{-12} is used for both cases in terms of convergence criteria.

compared with the analytical solution (8.14) (Figure 8.4), where the two minimums are clearly observed with a plateau between them. The width of the plateau is controlled by L_{LC} , for large L_{LC} the plateau small, while for low L_{LC} , the plateau is wide (Figure 8.5). The intersection of the blue and red curves with zero are the roots, thus for $L_{LC} = 10$, the plateau is wider compared to the solution for $L_{LC} = 30$ (Figure 8.5).

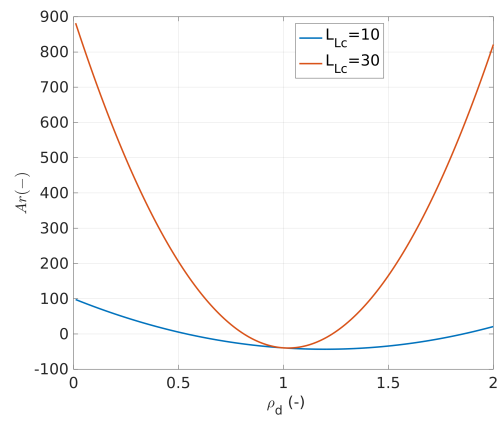


Figure 8.5: The solution (8.14) plotted for $L_{Lc} = 30$ and $L_{Lc} = 10$.

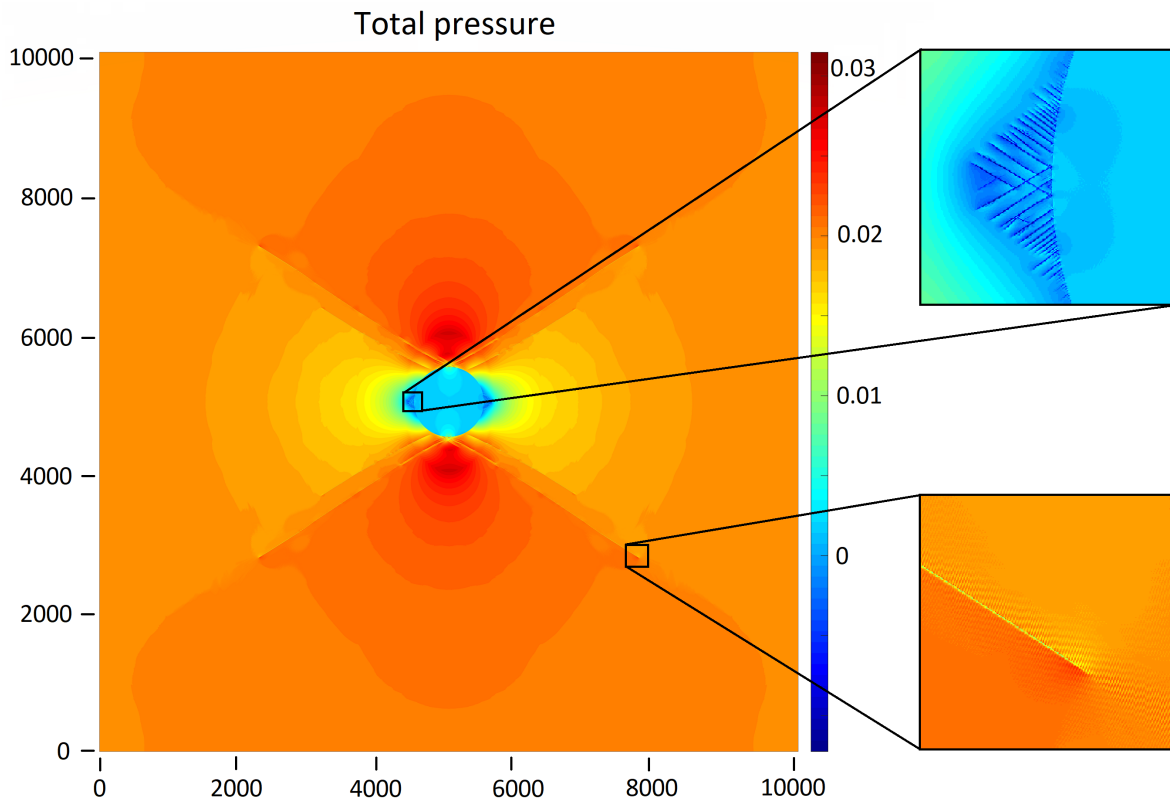


Figure 8.6: The strain localization of a poro-elasto-plastic medium under shear loading (total pressure). The resolution of the simulation is $10,000 \times 10,000 = 100,000,000$ grid cells.

8.3 Non-linear instabilities

8.3.1 Plasticity

The developed numerical tools for wave propagation (*Alkhimenkov et al., 2021b*) were extended to solve quasi-static problems via the so-called matrix-free approach. This approach recently gained new popularity because of its capability to solve problems of ultra-high resolution (more than 1 billion grid cells). I model the response of poro-elasto-plastic media under slow shear loading reflecting the quasi-static process and resulting into strain localization and multiple shear bands (Figure 8.7). Additional viscous terms are added to the poroelastic equations, which attenuate propagating waves to reach the attractor — quasi-static solution. The number of iterations needed to achieve the solution is proportional to nx , where nx is the number of grid cells in the x -direction.

The resolution of the simulation is $10,000 \times 10,000 = 100,000,000$ grid cells. Plasticity is implemented using the pressure-dependent Mohr-Coulomb law with a friction angle which is common for most of the rocks. Additionally, I show that the loading rate is of high importance. If the loading rate is fast then the fluid pressure diffusion does not equilibrate in the rock resulting into high variations of fluid pressures (*Alkhimenkov et al., 2021c*). If the loading rate is slow then the fluid pressure equilibrates throughout the model domain. Recent studies showed that fluid pressure behaves differently under different loading rates and can significantly change the effective stress and the resulting stability and failure (*Miller, 2020; Aben and Brantut, 2021*).

Fluid pressure fields for different viscosity / permeability.

Diagonal slice through the strain localization of fluid pressure. Shape is not mesh dependent.

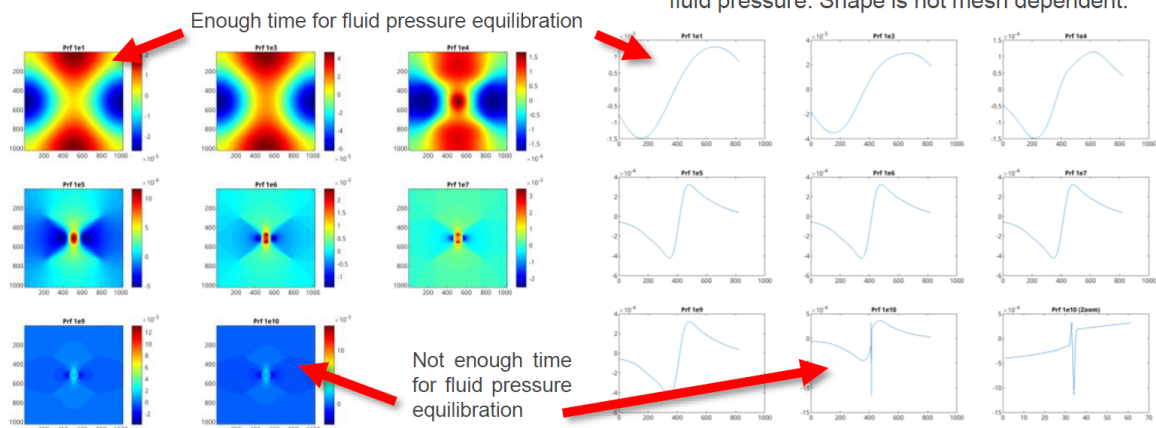


Figure 8.7: The fluid pressure snapshots of a poro-elasto-plastic medium under shear loading: 2-D fields (left) and 1-D diagonal cross sections (right).

8.3.2 The theory of spontaneous earthquake nucleation

The main outcome of this research is the new theory of earthquake nucleation (Figure 8.8). I use elasto-plastic rheology and slowly increase stress in the medium reflecting the stress increase due to tectonic forces in real rocks. The plasticity is implemented using a pressure-dependent Coulomb yield theory. At some point, the stress reaches the Coulomb yield surface and then local strain localizations start to develop, resulting in slowly developing fractal shear bands (Figure 8.8a and 8.8b). The evolution of the strain localizations is spontaneous and cannot be rigorously predicted. As time progresses, shear bands grow, and stress drops take place in the medium (Figure 8.8c). Such stress drops are caused by the instantaneous development of new shear bands (Figure 8.8a). As a result, the anti-symmetric source mechanism triggers seismic wave propagation (*Minakov and Yarushina, 2021*). We suggest that the (seismic) radiation pattern of the focal mechanism might be similar to a particular moment tensor source, typical for realistic earthquakes (*Tape and Tape, 2012*). Real earthquakes may also include more complicated processes with non-DC components which can be analysed with seismic full moment tensors (*Alvizuri et al., 2018*). Our new numerical algorithm simulates the quasi-static loading and wave propagation mechanics simultaneously and can be further extended to capture a more complex rheology. Follow up studies will be performed in 3D.

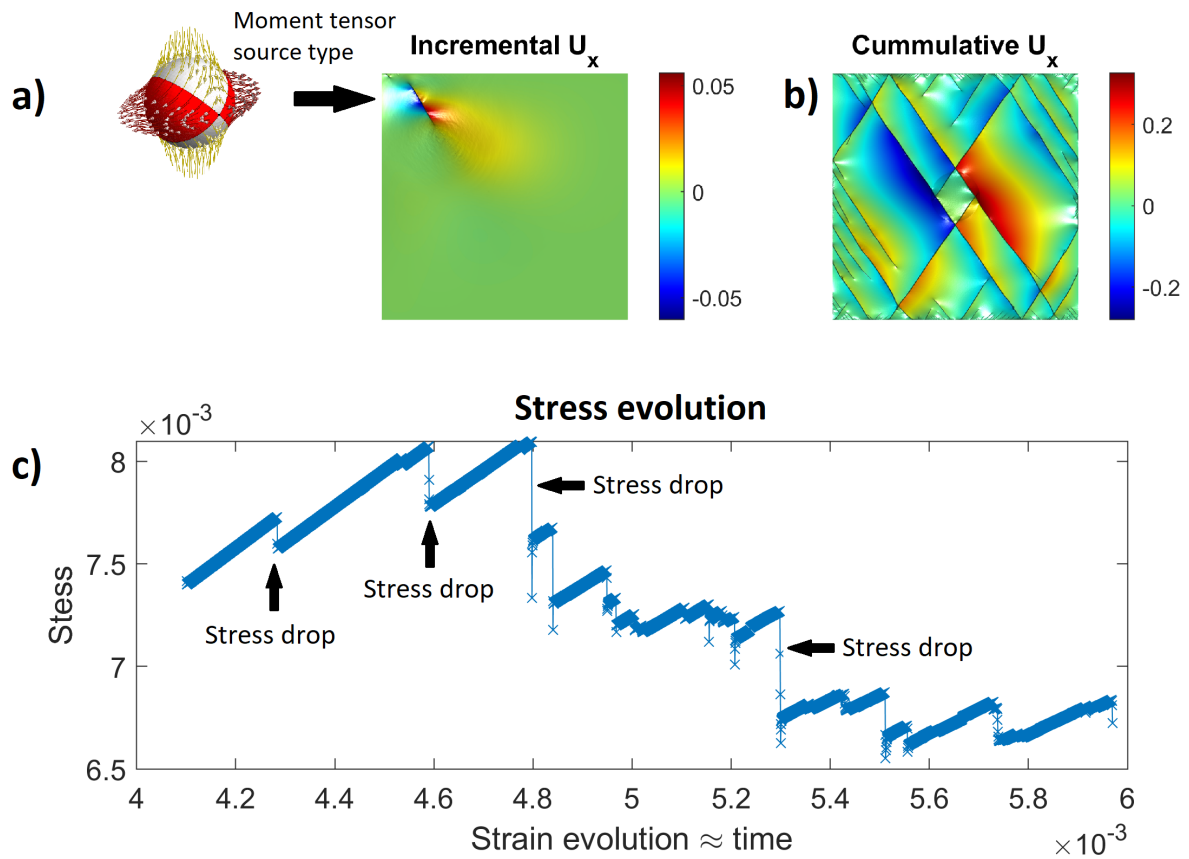


Figure 8.8: The conceptual model of the seismic event nucleation. Panel (a) shows the displacement field corresponding to a stress drop in the model representing the focal mechanism. Panel (b) shows the fractal shear bands developed during the evolution of the stress field. Panel (c) shown the stress evolution in the model as time evolves. The 3-D moment tensor source type figure (beach-ball) in panel (a) is grabbed from *Tape and Tape* (2012).

8.4 Conclusions

An efficient algorithm is presented to resolve quasi-static problems in ultra-high resolution. In the area of non-linear instabilities, a new theory of earthquake nucleation is presented. The simplest visco-plastic or elasto-plastic rheology allows us to model spontaneous earthquake nucleation. This new modeling approach is based on conservation laws without any experimentally derived constitutive relations.

Chapter 9

Perspectives

9.1 Conclusions

The contributions presented in this thesis are distributed across four different disciplines: micromechanics, geophysics, computational mechanics and computational poroelasticity, and the theory of non-linear instabilities. Many physical processes are coupled. Numerical and analytical models of such coupled physical systems require special treatment of the various couplings and concise numerical implementation.

In the areas of micromechanics and geophysics, the numerical study of seismic attenuation and dispersion in a fluid-saturated porous medium caused by squirt flow is performed. Based on this result, an accurate analytical model for seismic attenuation and dispersion is developed. The classical pore space geometry is used, a penny-shaped crack surrounded by a toroidal stiff pore. Additionally, the analytical model for a classical pore geometry is extended to more complex geometries of the pore space, where the crack edge is partially connected to multiple pores. This pore geometry is much more closely representative of a rock. The analytical models are compared against three-dimensional numerical solutions. The analytical and numerical results are in very good agreement for all considered relative sizes of pores and cracks. The key parameters of the pore space which control the characteristic frequency (at which the maximum of attenuation occurs) are re-defined. Closed-form analytical expressions to calculate the effective stiffness properties of a rock model whose pore space is described by a crack connected to a pore or multiple pores are also provided.

In the areas of computational mechanics and computational poroelasticity, a multi-graphical processing units (GPU) numerical solver is developed to resolve the anisotropic elastodynamic Biot's equations to simulate, in a few seconds, wave fields for spatial domains involving more than 4.5 billion grid cells. A comprehensive dimensional analysis is presented reducing the number of material parameters needed for the numerical experiments from ten to four. A dispersion analysis as a function of dimensionless parameters is performed leading to simple and transparent dispersion relations. Additionally, this research presents the results of the von Neumann stability analysis of the discretized Biot's equations and the discretized linear damped wave equation. The exact stability conditions for a number of implicit and explicit schemes are derived.

In the area of non-linear instabilities, a new theory of earthquake nucleation is presented and is based on the simplest visco-plastic or elasto-plastic rheology. This approach allows us to numerically model spontaneous earthquake nucleation and is based on conservation laws without any experimentally derived constitutive relations.

9.2 Outlook

Linear quasi-statics and dynamic phenomena

The next natural step in the area of quasi-static physics is the development of an analytical model for seismic attenuation and dispersion in an isotropic fluid-saturated porous medium caused by squirt flow. The next natural step in the area of wave phenomena is the development of high-performance computing applications for real fluid-saturated rocks.

High-performance computing approach

The next natural step in the area of high-performance computing is to continue the code development using the latest hardware accelerators, such as graphical processing units (GPU).

Non-linear instabilities and strain localization

The next natural step in the area of non-linear instabilities is the implementation of more complex physics and rheologies for spontaneous earthquake nucleation.

Bibliography

- Abdelmeguid, M., X. Ma, and A. Elbanna (2019), A novel hybrid finite element-spectral boundary integral scheme for modeling earthquake cycles: Application to rate and state faults with low-velocity zones, *Journal of Geophysical Research: Solid Earth*, 124(12), 12,854–12,881.
- Abe, K., K. Soga, and S. Bandara (2014), Material point method for coupled hydromechanical problems, *Journal of Geotechnical and Geoenvironmental Engineering*, 140(3), 04013,033.
- Aben, F. M., and N. Brantut (2021), Dilatancy stabilises shear failure in rock, *arXiv preprint arXiv:2101.10036*.
- Acosta, J. L. G., P. J. Vardon, G. Remmerswaal, and M. A. Hicks (2020), An investigation of stress inaccuracies and proposed solution in the material point method, *Computational Mechanics*, 65(2), 555–581.
- Ade, P. A., N. Aghanim, M. Arnaud, M. Ashdown, J. Aumont, C. Baccigalupi, A. Banday, R. Barreiro, J. Bartlett, N. Bartolo, et al. (2016), Planck 2015 results-xiii. cosmological parameters, *Astronomy & Astrophysics*, 594, A13.
- Adelinet, M., J. Fortin, Y. Guéguen, A. Schubnel, and L. Geoffroy (2010), Frequency and fluid effects on elastic properties of basalt: Experimental investigations, *Geophysical Research Letters*, 37(2).
- Alejano, L. R., and A. Bobet (2012), Drucker–prager criterion, *Rock Mechanics and Rock Engineering*, 45(6), 995–999, doi:10.1007/s00603-012-0278-2.
- Alghannam, M., and R. Juanes (2020), Understanding rate effects in injection-induced earthquakes, *Nature communications*, 11(1), 1–6.
- Alkhimenkov, Y., and I. Bayuk (2017), Unified effective medium theory for cracked porous rocks-theory and case study, in *79th EAGE Conference and Exhibition 2017*.
- Alkhimenkov, Y., and B. Quintal (2021), An accurate analytical model for squirt flow in anisotropic porous rocks — part 1: Classical geometry, *Geophysics*.
- Alkhimenkov, Y., E. Caspari, B. Gurevich, N. D. Barbosa, S. Glubokovskikh, J. Hunziker, and B. Quintal (2020a), Frequency-dependent attenuation and dispersion caused by squirt flow: Three-dimensional numerical study, *Geophysics*, 85(3), 1–71.
- Alkhimenkov, Y., E. Caspari, S. Lissa, and B. Quintal (2020b), Azimuth-, angle- and frequency-dependent seismic velocities of cracked rocks due to squirt flow, *Solid Earth*, 11(3), 855–871.
- Alkhimenkov, Y., L. Khakimova, and Y. Podladchikov (2020c), Stability of discrete schemes of biot’s poroelastic equations, *Geophysical Journal International*, doi:10.1093/gji/ggaa584, ggaa584.
- Alkhimenkov, Y., L. Räss, L. Khakimova, B. Quintal, and Y. Podladchikov (2021a), Fastbiot_gpu3d, doi:10.5281/zenodo.4519367.
- Alkhimenkov, Y., L. Räss, L. Khakimova, B. Quintal, and Y. Podladchikov (2021b), Resolving wave propagation in anisotropic poroelastic media using graphical processing units (gpus), *Journal of Geophysical Research: Solid Earth*, p. e2020JB021175.
- Alkhimenkov, Y., B. Quintal, and Y. Podladchikov (2021c), Fluid-total pressure partitioning in shear banding poro-visco-elasto-plastic media, in *EGU General Assembly Conference Abstracts*, pp. EGU21–15,459.
- Allison, K. L., and E. M. Dunham (2021), Influence of shear heating and thermomechanical coupling on earthquake sequences and the brittle-ductile transition, *Journal of Geophysical Research: Solid Earth*, 126(6), e2020JB021,394.

- Almqvist, M., and E. M. Dunham (2021), Elastic wave propagation in anisotropic solids using energy-stable finite differences with weakly enforced boundary and interface conditions, *Journal of Computational Physics*, 424, 109,842.
- Almqvist, B. S., and D. Mainprice (2017), Seismic properties and anisotropy of the continental crust: predictions based on mineral texture and rock microstructure, *Reviews of Geophysics*, 55(2), 367–433.
- Alvizuri, C., V. Silwal, L. Krischer, and C. Tape (2018), Estimation of full moment tensors, including uncertainties, for nuclear explosions, volcanic events, and earthquakes, *Journal of Geophysical Research: Solid Earth*, 123(6), 5099–5119.
- Amalokwu, K., A. I. Best, and M. Chapman (2016), Effects of aligned fractures on the response of velocity and attenuation ratios to water saturation variation: a laboratory study using synthetic sandstones, *Geophysical Prospecting*, 64(4), 942–957.
- Anderson Jr, C. E. (1987), An overview of the theory of hydrocodes, *International journal of impact engineering*, 5(1-4), 33–59.
- Andrä, H., N. Combaret, J. Dvorkin, E. Glatt, J. Han, M. Kabel, Y. Keehm, F. Krzikalla, M. Lee, C. Madonna, et al. (2013a), Digital rock physics benchmarks—part i: Imaging and segmentation, *Computers & Geosciences*, 50, 25–32.
- Andrä, H., N. Combaret, J. Dvorkin, E. Glatt, J. Han, M. Kabel, Y. Keehm, F. Krzikalla, M. Lee, C. Madonna, et al. (2013b), Digital rock physics benchmarks—part ii: Computing effective properties, *Computers & Geosciences*, 50, 33–43.
- Arena, A., C. D. Piane, and J. Sarout (2014), A new computational approach to cracks quantification from 2d image analysis: Application to micro-cracks description in rocks, *Comput. Geosci.*, 66, 106 – 120, doi: <https://doi.org/10.1016/j.cageo.2014.01.007>.
- Bakulin, A., V. Grechka, and I. Tsvankin (2000a), Estimation of fracture parameters from reflection seismic data part i: HTI model due to a single fracture set, *Geophysics*, 65(6), 1788–1802.
- Bakulin, A., V. Grechka, and I. Tsvankin (2000b), Estimation of fracture parameters from reflection seismic data part ii: Fractured models with orthorhombic symmetry, *Geophysics*, 65(6), 1803–1817.
- Bandara, S., and K. Soga (2015), Coupling of soil deformation and pore fluid flow using material point method, *Computers and geotechnics*, 63, 199–214.
- Bandara, S., A. Ferrari, and L. Laloui (2016), Modelling landslides in unsaturated slopes subjected to rainfall infiltration using material point method, *International Journal for Numerical and Analytical Methods in Geomechanics*, 40(9), 1358–1380.
- Barbosa, N. D., J. G. Rubino, E. Caspari, and K. Holliger (2017), Sensitivity of seismic attenuation and phase velocity to intrinsic background anisotropy in fractured porous rocks: A numerical study, *Journal of Geophysical Research: Solid Earth*, 122(10), 8181–8199.
- Bardenhagen, S., J. Brackbill, and D. Sulsky (2000), The material-point method for granular materials, *Computer methods in applied mechanics and engineering*, 187(3-4), 529–541.
- Bardenhagen, S. G., and E. M. Kober (2004), The generalized interpolation material point method, *Computer Modeling in Engineering and Sciences*, 5(6), 477–496.
- Baumgarten, A. S., and K. Kamrin (2019), A general fluid–sediment mixture model and constitutive theory validated in many flow regimes, *Journal of Fluid Mechanics*, 861, 721–764.
- Bause, M., J. W. Both, and F. A. Radu (2019), Iterative coupling for fully dynamic poroelasticity, *arXiv preprint arXiv:1912.05174*.
- Bause, M., U. Köcher, F. Radu, and F. Schieweck (2020), Post-processed galerkin approximation of improved order for wave equations, *Mathematics of Computation*, 89(322), 595–627.

- Bayuk, I. O., M. Ammerman, and E. M. Chesnokov (2007), Elastic moduli of anisotropic clay, *Geophysics*, 72(5), no. 5, D107–D117.
- Benyamin, M., J. Calder, G. Sundaramoorthi, and A. Yezzi (2020), Accelerated variational pdes for efficient solution of regularized inversion problems, *Journal of Mathematical Imaging and Vision*, 62(1), 10–36.
- Beran, M. J. (1968), Statistical continuum theories, *American Journal of Physics*, 36(10), 923–923, doi:10.1119/1.1974326.
- Berryman, J. G. (2007), Seismic waves in rocks with fluids and fractures, *Geophysical Journal International*, 171(2), 954–974.
- Best, A. I., J. Sothcott, and C. McCann (2007), A laboratory study of seismic velocity and attenuation anisotropy in near-surface sedimentary rocks, *Geophysical Prospecting*, 55(5), 609–625.
- Beuth, L., T. Benz, P. A. Vermeer, and Z. Więckowski (2008), Large deformation analysis using a quasi-static material point method, *Journal of Theoretical and Applied Mechanics*, 38(2), 45–60.
- Biot (1956a), Theory of propagation of elastic waves in a fluid-saturated porous solid. II. higher frequency range, *The Journal of the Acoustical Society of America*, 28(2), 179–191.
- Biot (1962a), Mechanics of deformation and acoustic propagation in porous media, *Journal of applied physics*, 33(4), 1482–1498.
- Biot (1965), *Mechanics of incremental deformations*, John Wiley & Sons.
- Biot, and D. Willis (1957), The elastic coefficients of the theory of consolidation, *J Appl Mech*, 15, 594–601.
- Biot, M. (1956b), Theory of propagation of elastic waves in a fluid-saturated porous solid. I. low-frequency range, *The Journal of the Acoustical Society of America*, 28(2), 168–178.
- Biot, M. A. (1941), General theory of three-dimensional consolidation, *Journal of applied physics*, 12(2), 155–164.
- Biot, M. A. (1962b), Generalized theory of acoustic propagation in porous dissipative media, *The Journal of the Acoustical Society of America*, 34(9A), 1254–1264.
- Bird, R. E., W. M. Coombs, and S. Giani (2017), Fast native-matlab stiffness assembly for sigp linear elasticity, *Computers & Mathematics with Applications*, 74(12), 3209–3230.
- Bisht, V., R. Salgado, and M. Prezzi (2021), Simulating penetration problems in incompressible materials using the material point method, *Computers and Geotechnics*, 133, 103,593, doi:https://doi.org/10.1016/j.compgeo.2020.103593.
- Blanc, E., G. Chiavassa, and B. Lombard (2013), A time-domain numerical modeling of two-dimensional wave propagation in porous media with frequency-dependent dynamic permeability, *The Journal of the Acoustical Society of America*, 134(6), 4610–4623.
- Borgomano, J. V., L. X. Pimienta, J. Fortin, and Y. Guéguen (2019), Seismic dispersion and attenuation in fluid-saturated carbonate rocks: Effect of microstructure and pressure, *Journal of Geophysical Research: Solid Earth*, 124(12), 12,498–12,522.
- Boscarino, S., and G. Russo (2013), Flux-explicit imex runge–kutta schemes for hyperbolic to parabolic relaxation problems, *SIAM Journal on Numerical Analysis*, 51(1), 163–190.
- Bourbié, T., O. Coussy, B. Zinszner, and M. C. Junger (1987), Acoustics of porous media.
- Brajanovski, M., B. Gurevich, and M. Schoenberg (2005), A model for p-wave attenuation and dispersion in a porous medium permeated by aligned fractures, *Geophysical Journal International*, 163(1), 372–384.
- Brodsky, E. E., J. J. Mori, L. Anderson, F. M. Chester, M. Conin, E. M. Dunham, N. Eguchi, P. M. Fulton, R. Hino, T. Hirose, et al. (2020), The state of stress on the fault before, during, and after a major earthquake, *Annual Review of Earth and Planetary Sciences*, 48, 49–74.

- Bui, H. H., R. Fukagawa, K. Sako, and S. Ohno (2008), Lagrangian meshfree particles method (sph) for large deformation and failure flows of geomaterial using elastic–plastic soil constitutive model, *International journal for numerical and analytical methods in geomechanics*, 32(12), 1537–1570.
- Buijze, L., P. A. Van Den Bogert, B. B. Wassing, B. Orlic, and J. Ten Veen (2017), Fault reactivation mechanisms and dynamic rupture modelling of depletion-induced seismic events in a rotliegend gas reservoir, *Netherlands Journal of Geosciences*, 96(5), s131–s148.
- Burghardt, J., R. Brannon, and J. Guilkey (2012), A nonlocal plasticity formulation for the material point method, *Computer Methods in Applied Mechanics and Engineering*, 225-228, 55–64, doi:<https://doi.org/10.1016/j.cma.2012.03.007>.
- Buzzi, O., D. M. Pedroso, and A. Giacomini (2008), Caveats on the implementation of the generalized material point method, *Computer Modeling in Engineering & Sciences*, 31(2), 85–106, doi:10.3970/cmcs.2008.031.085.
- Calder, J., and A. Yezzi (2019), Pde acceleration: a convergence rate analysis and applications to obstacle problems, *Research in the Mathematical Sciences*, 6(4), 1–30.
- Carcione, J., J. Santos, and S. Picotti (2011), Anisotropic poroelasticity and wave-induced fluid flow: harmonic finite-element simulations, *Geophysical Journal International*, 186(3), 1245–1254.
- Carcione, J. M. (2014), *Wave fields in real media: Wave propagation in anisotropic, anelastic, porous and electromagnetic media*, Elsevier.
- Carcione, J. M., and B. Gurevich (2011), Differential form and numerical implementation of biot’s poroelasticity equations with squirt dissipation, *Geophysics*, 76(6), N55–N64.
- Carcione, J. M., and G. Quiroga-Goode (1995), Some aspects of the physics and numerical modeling of biot compressional waves, *Journal of Computational Acoustics*, 3(04), 261–280.
- Carcione, J. M., C. Morency, and J. E. Santos (2010), Computational poroelasticity—a review, *Geophysics*, 75(5), 75A229–75A243.
- Carcione, J. M., B. Gurevich, J. E. Santos, and S. Picotti (2013), Angular and frequency-dependent wave velocity and attenuation in fractured porous media, *Pure and Applied Geophysics*, 170(11), 1673–1683.
- Caspari, E., B. Gurevich, and T. M. Müller (2013), Frequency-dependent effective hydraulic conductivity of strongly heterogeneous media, *Phys. Rev. E*, 88, 042,119, doi:10.1103/PhysRevE.88.042119.
- Caspari, E., M. Novikov, V. Lisitsa, N. D. Barbosa, B. Quintal, J. G. Rubino, and K. Holliger (2019), Attenuation mechanisms in fractured fluid-saturated porous rocks: a numerical modelling study, *Geophysical Prospecting*, 67(4), 935–955.
- Chalhoub, M. S., and J. M. Kelly (1990), Effect of bulk compressibility on the stiffness of cylindrical base isolation bearings, *International Journal of Solids and Structures*, 26(7), 743–760.
- Chalk, C. M., M. Pastor, J. Peakall, D. J. Borman, P. A. Sleight, W. Murphy, and R. Fuentes (2020), Stress-particle smoothed particle hydrodynamics: An application to the failure and post-failure behaviour of slopes, *Computer Methods in Applied Mechanics and Engineering*, 366, 113,034, doi:<https://doi.org/10.1016/j.cma.2020.113034>.
- Chapman, M. (2003), Frequency-dependent anisotropy due to meso-scale fractures in the presence of equant porosity, *Geophysical Prospecting*, 51(5), 369–379.
- Chapman, M., S. V. Zatsepin, and S. Crampin (2002), Derivation of a microstructural poroelastic model, *Geophysical Journal International*, 151(2), 427–451.
- Chapman, S., J. V. Borgomano, H. Yin, J. Fortin, and B. Quintal (2019), Forced oscillation measurements of seismic wave attenuation and stiffness moduli dispersion in glycerine-saturated berea sandstone, *Geophysical Prospecting*, 67(4), 956–968.
- Charlton, T., W. Coombs, and C. Augarde (2017), igimp: An implicit generalised interpolation material point method for large deformations, *Computers & Structures*, 190, 108–125.

- Charney, J. G., R. Fjörtoft, and J. Von Neumann (1950), Numerical integration of the barotropic vorticity equation, *Tellus*, 2(4), 237–254.
- Cheng, A. H.-D. (2016), *Poroelasticity*, vol. 877, Springer.
- Chiavassa, G., and B. Lombard (2011), Time domain numerical modeling of wave propagation in 2d heterogeneous porous media, *Journal of Computational Physics*, 230(13), 5288–5309.
- Chiavassa, G., B. Lombard, and J. Piraux (2010), Numerical modeling of 1d transient poroelastic waves in the low-frequency range, *Journal of Computational and Applied Mathematics*, 234(6), 1757–1765.
- Christakos, G. (1992), 2 - the spatial random field model, in *Random Field Models in Earth Sciences*, edited by G. Christakos, pp. 21–106, Academic Press, Boston, doi:<https://doi.org/10.1016/B978-0-12-174230-0.50007-X>.
- Collet, O., and B. Gurevich (2016), Frequency dependence of anisotropy in fluid saturated rocks—part i: aligned cracks case, *Geophysical Prospecting*, 64(4), 1067–1084.
- Coombs, W. M., and C. E. Augarde (2020), Ample: A material point learning environment, *Advances in Engineering Software*, 139, 102,748.
- Coombs, W. M., T. J. Charlton, M. Cortis, and C. E. Augarde (2018), Overcoming volumetric locking in material point methods, *Computer Methods in Applied Mechanics and Engineering*, 333, 1–21.
- Coombs, W. M., C. E. Augarde, A. J. Brennan, M. J. Brown, T. J. Charlton, J. A. Knappett, Y. G. Motlagh, and L. Wang (2020), On lagrangian mechanics and the implicit material point method for large deformation elasto-plasticity, *Computer Methods in Applied Mechanics and Engineering*, 358, 112,622.
- Cortis, M., W. Coombs, C. Augarde, M. Brown, A. Brennan, and S. Robinson (2018), Imposition of essential boundary conditions in the material point method, *International Journal for Numerical Methods in Engineering*, 113(1), 130–152.
- CUDA, C. (2020), Programming guide.
- Cuomo, S., P. Ghasemi, M. Martinelli, and M. Calvello (2019), Simulation of liquefaction and retrogressive slope failure in loose coarse-grained material, *International Journal of Geomechanics*, 19(10), 04019,116, doi:10.1061/(ASCE)GM.1943-5622.0001500.
- Dabrowski, M., M. Krotkiewski, and D. Schmid (2008), Milamin: Matlab-based finite element method solver for large problems, *Geochemistry, Geophysics, Geosystems*, 9(4).
- Dagan, G. (1982), Analysis of flow through heterogeneous random aquifers: 2. unsteady flow in confined formations, *Water Resources Research*, 18(5), 1571–1585, doi:10.1029/WR018i005p01571.
- Dai, N., A. Vafidis, and E. Kanasewich (1995), Wave propagation in heterogeneous, porous media: A velocity-stress, finite-difference method, *Geophysics*, 60(2), 327–340.
- Dal Zilio, L., N. Lapusta, and J.-P. Avouac (2020), Unraveling scaling properties of slow-slip events, *Geophysical Research Letters*, 47(10), e2020GL087,477.
- Das, V., T. Mukerji, and G. Mavko (2019), Numerical simulation of coupled fluid-solid interaction at the pore scale: A digital rock-physics technology, *Geophysics*, 84(4), no. 4, WA71–WA81.
- Davis, T. A. (2013), Suite sparse.
- Davydycheva, S., V. Druskin, and T. Habashy (2003), An efficient finite-difference scheme for electromagnetic logging in 3d anisotropic inhomogeneous media finite-difference scheme in anisotropic media, *Geophysics*, 68(5), 1525–1536.
- De Borst, R., M. A. Crisfield, J. J. C. Remmers, and C. V. Verhoosel (2012), *Nonlinear finite element analysis of solids and structures*, John Wiley & Sons.
- de Koster, P., R. Tielen, E. Wobbes, and M. Möller (2020), Extension of b-spline material point method for unstructured triangular grids using powell–sabin splines, *Computational Particle Mechanics*, pp. 1–16.

- de la Puente, J., M. Dumbser, M. Käser, and H. Igel (2008), Discontinuous galerkin methods for wave propagation in poroelastic media, *Geophysics*, 73(5), T77–T97.
- de Souza Neto, E. A., D. Peric, and D. R. Owen (2011), *Computational methods for plasticity: theory and applications*, John Wiley & Sons.
- de Vaucorbeil, A., V. Nguyen, and C. Hutchinson (2020), A total-lagrangian material point method for solid mechanics problems involving large deformations.
- Deichmann, N., and J. Ernst (2009), Earthquake focal mechanisms of the induced seismicity in 2006 and 2007 below basel (switzerland), *Swiss Journal of Geosciences*, 102(3), 457–466.
- Delle Piane, C., A. Arena, J. Sarout, L. Esteban, and E. Cazes (2015), Micro-crack enhanced permeability in tight rocks: An experimental and microstructural study, *Tectonophysics*, 665, 149 – 156, doi:<https://doi.org/10.1016/j.tecto.2015.10.001>.
- Dieterich, J. H. (1979), Modeling of rock friction: 1. experimental results and constitutive equations, *Journal of Geophysical Research: Solid Earth*, 84(B5), 2161–2168.
- Ding, H.-f., Y.-x. Zhang, J.-x. Cao, and J.-h. Tian (2012), A class of difference scheme for solving telegraph equation by new non-polynomial spline methods, *Applied Mathematics and Computation*, 218(9), 4671–4683.
- Dong, Y., and J. Grabe (2018), Large scale parallelisation of the material point method with multiple gpus, *Computers and Geotechnics*, 101, 149–158, doi:<https://doi.org/10.1016/j.compgeo.2018.04.001>.
- Dong, Y., D. Wang, and M. F. Randolph (2015), A gpu parallel computing strategy for the material point method, *Computers and Geotechnics*, 66, 31–38, doi:<https://doi.org/10.1016/j.compgeo.2015.01.009>.
- Dormy, E., and A. Tarantola (1995), Numerical simulation of elastic wave propagation using a finite volume method, *Journal of Geophysical Research: Solid Earth*, 100(B2), 2123–2133.
- Dost, B., E. Ruigrok, and J. Spetzler (2017), Development of seismicity and probabilistic hazard assessment for the groningen gas field, *Netherlands Journal of Geosciences*, 96(5), s235–s245.
- Duffy, T. S. (2018), Single-crystal elastic properties of minerals and related materials with cubic symmetry, *American Mineralogist: Journal of Earth and Planetary Materials*, 103(6), 977–988.
- Dunatunga, S., and K. Kamrin (2015), Continuum modelling and simulation of granular flows through their many phases, *Journal of Fluid Mechanics*, 779, 483–513.
- Dunatunga, S., and K. Kamrin (2017), Continuum modeling of projectile impact and penetration in dry granular media, *Journal of the Mechanics and Physics of Solids*, 100, 45–60.
- Dupuy, B., L. De Barros, S. Garambois, and J. Virieux (2011), Wave propagation in heterogeneous porous media formulated in the frequency-space domain using a discontinuous galerkin method, *Geophysics*, 76(4), N13–N28.
- Duretz, T., L. Räss, Y. Podladchikov, and S. Schmalholz (2019a), Resolving thermomechanical coupling in two and three dimensions: spontaneous strain localization owing to shear heating, *Geophysical Journal International*, 216(1), 365–379.
- Duretz, T., R. de Borst, and L. Le Pourhiet (2019b), Finite Thickness of Shear Bands in Frictional Viscoplasticity and Implications for Lithosphere Dynamics, *Geochemistry, Geophysics, Geosystems*, 20(11), 5598–5616, doi: <https://doi.org/10.1029/2019GC008531>.
- Dvorkin, J., and A. Nur (1993), Dynamic poroelasticity: A unified model with the squirt and the biot mechanisms, *Geophysics*, 58(4), 524–533.
- Dvorkin, J., G. Mavko, and A. Nur (1995), Squirt flow in fully saturated rocks, *Geophysics*, 60(1), 97–107.
- Dvorkin, J., N. Derzhi, E. Diaz, and Q. Fang (2011), Relevance of computational rock physics, *Geophysics*, 76(5), E141–E153, doi:10.1190/geo2010-0352.1.

- Ellsworth, W. L. (2013), Injection-induced earthquakes, *Science*, 341(6142).
- Erickson, B. A., E. M. Dunham, and A. Khosravifar (2017), A finite difference method for off-fault plasticity throughout the earthquake cycle, *Journal of the Mechanics and Physics of Solids*, 109, 50–77.
- Erickson, B. A., J. Jiang, M. Barall, N. Lapusta, E. M. Dunham, R. Harris, L. S. Abrahams, K. L. Allison, J.-P. Ampuero, S. Barbot, et al. (2020), The community code verification exercise for simulating sequences of earthquakes and aseismic slip (seas), *Seismological Research Letters*, 91(2A), 874–890.
- Ernesti, J., and C. Wieners (2019), A space-time discontinuous petrov–galerkin method for acoustic waves, *Space-Time Methods. Applications to Partial Differential Equations*, 25.
- Eshelby, J. D. (1957), The determination of the elastic field of an ellipsoidal inclusion, and related problems, *Proceedings of the royal society of London. Series A. Mathematical and physical sciences*, 241(1226), 376–396.
- Fedorov, F. I. (1968), *Theory of elastic waves in crystals*, Springer.
- Feng, J., B. Xiao, R. Zhou, W. Pan, and D. R. Clarke (2012), Anisotropic elastic and thermal properties of the double perovskite slab–rock salt layer $\text{Ln}_2\text{SrAl}_2\text{O}_7$ (Ln= La, Nd, Sm, Eu, Gd or Dy) natural superlattice structure, *Acta Materialia*, 60(8), 3380–3392.
- Fenton, G. A., and E. H. Vanmarcke (1990), Simulation of random fields via local average subdivision, *Journal of Engineering Mechanics*, 116(8), 1733–1749, doi:10.1061/(ASCE)0733-9399(1990)116:8(1733).
- Fern, J., A. Rohe, K. Soga, and E. Alonso (2019), *The material point method for geotechnical engineering: a practical guide*, CRC Press.
- Frankel, S. P. (1950), Convergence rates of iterative treatments of partial differential equations, *Mathematical Tables and Other Aids to Computation*, 4(30), 65–75.
- Frenkel, J. (1944), On the theory of seismic and seismoelectric phenomena in a moist soil, *Journal of Physics*, III(4), 230–241.
- Galavi, V., and H. F. Schweiger (2010), Nonlocal multilaminate model for strain softening analysis, *International Journal of Geomechanics*, 10(1), 30–44, doi:10.1061/(ASCE)1532-3641(2010)10:1(30).
- Galvin, R., and B. Gurevich (2009), Effective properties of a poroelastic medium containing a distribution of aligned cracks, *Journal of Geophysical Research: Solid Earth*, 114(B7).
- Gan, Y., Z. Sun, Z. Chen, X. Zhang, and Y. Liu (2018), Enhancement of the material point method using b-spline basis functions, *International Journal for numerical methods in engineering*, 113(3), 411–431.
- Gao, M., X. Wang, K. Wu, A. Pradhana, E. Sifakis, C. Yuksel, and C. Jiang (2018), Gpu optimization of material point methods, *ACM Trans. Graph.*, 37(6), doi:10.1145/3272127.3275044.
- Gassmann, F. (1951), Über die elastizität poröser medien, *Vierteljahrsschrift der Naturforschenden Gesellschaft in Zürich*, 96, 1–23.
- Gaume, J., T. Gast, J. Teran, A. van Herwijnen, and C. Jiang (2018), Dynamic anticrack propagation in snow, *Nature communications*, 9(1), 1–10.
- Gaume, J., A. van Herwijnen, T. Gast, J. Teran, and C. Jiang (2019), Investigating the release and flow of snow avalanches at the slope-scale using a unified model based on the material point method, *Cold Regions Science and Technology*, 168, 102,847.
- Glubokovskikh, S., B. Gurevich, and N. Saxena (2016), A dual-porosity scheme for fluid/solid substitution, *Geophysical Prospecting*, 64(4-Advances in Rock Physics), 1112–1121.
- González Acosta, J. L., X. Zheng, P. J. Vardon, M. A. Hicks, and F. Pisano (2019), On stress oscillation in mpm simulations involving one or two phases, in *Proceedings of the Second International Conference on the Material Point Method for Modelling Soil-Water-Structure Interaction*.

- González Acosta, J. L., P. J. Vardon, and M. A. Hicks (2021), Development of an implicit contact technique for the material point method, *Computers and Geotechnics*, 130, 103,859, doi:<https://doi.org/10.1016/j.compgeo.2020.103859>.
- Grab, M., B. Quintal, E. Caspari, H. Maurer, and S. Greenhalgh (2017), Numerical modeling of fluid effects on seismic properties of fractured magmatic geothermal reservoirs, *Solid Earth*, 8(1), 255–279.
- Gracia, F., P. Villard, and V. Richefeu (2019), Comparison of two numerical approaches (dem and mpm) applied to unsteady flow, *Computational Particle Mechanics*, 6(4), 591–609.
- Grechka, V., and M. Kachanov (2006), Effective elasticity of rocks with closely spaced and intersecting cracks, *Geophysics*, 71(3), D85–D91.
- Gregor, D., P. Moczo, J. Kristek, A. Mesgouez, G. Lefeuvre-Mesgouez, and M. Kristekova (2021), Subcell-resolution finite-difference modelling of seismic waves in biot and jkd poroelastic media, *Geophysical Journal International*, 224(2), 760–794.
- Grigoli, F., S. Cesca, A. P. Rinaldi, A. Manconi, J. A. Lopez-Comino, J. Clinton, R. Westaway, C. Cauzzi, T. Dahm, and S. Wiemer (2018), The november 2017 mw 5.5 pohang earthquake: A possible case of induced seismicity in south korea, *Science*, 360(6392), 1003–1006.
- Guéguen, Y., and J. Sarout (2009), Crack-induced anisotropy in crustal rocks: predicted dry and fluid-saturated thomsen's parameters, *Physics of the Earth and Planetary Interiors*, 172(1-2), 116–124.
- Guéguen, Y., and J. Sarout (2011), Characteristics of anisotropy and dispersion in cracked medium, *Tectonophysics*, 503(1-2), 165–172.
- Guglielmi, Y., F. Cappa, J.-P. Avouac, P. Henry, and D. Elsworth (2015), Seismicity triggered by fluid injection–induced aseismic slip, *Science*, 348(6240), 1224–1226.
- Guilkey, J. E., and J. A. Weiss (2003), Implicit time integration for the material point method: Quantitative and algorithmic comparisons with the finite element method, *International Journal for Numerical Methods in Engineering*, 57(9), 1323–1338.
- Guo, J., J. Germán Rubino, N. D. Barbosa, S. Glubokovskikh, and B. Gurevich (2017a), Seismic dispersion and attenuation in saturated porous rocks with aligned fractures of finite thickness: Theory and numerical simulations—part 1: P-wave perpendicular to the fracture plane, *Geophysics*, 83(1), no. 1, WA49–WA62.
- Guo, J., J. G. Rubino, S. Glubokovskikh, and B. Gurevich (2017b), Effects of fracture intersections on seismic dispersion: theoretical predictions versus numerical simulations, *Geophysical Prospecting*, 65(5), 1264–1276.
- Guo, J., J. G. Rubino, S. Glubokovskikh, and B. Gurevich (2018a), Dynamic seismic signatures of saturated porous rocks containing two orthogonal sets of fractures: theory versus numerical simulations, *Geophysical Journal International*, 213(2), 1244–1262.
- Guo, J., J. G. Rubino, N. D. Barbosa, S. Glubokovskikh, and B. Gurevich (2018b), Seismic dispersion and attenuation in saturated porous rocks with aligned fractures of finite thickness: Theory and numerical simulations ? part 1: P-wave perpendicular to the fracture plane, *Geophysics*, 83(1), WA49–WA62, doi: 10.1190/geo2017-0065.1.
- Gurevich, B. (2003), Elastic properties of saturated porous rocks with aligned fractures, *Journal of Applied Geophysics*, 54(3-4), 203–218.
- Gurevich, B., D. Makarynska, and M. Pervukhina (2009a), Ultrasonic moduli for fluid-saturated rocks: Mavko-jizba relations rederived and generalized, *Geophysics*, 74(4), no. 4, N25–N30.
- Gurevich, B., M. Brajanovski, R. J. Galvin, T. M. Müller, and J. Toms-Stewart (2009b), P-wave dispersion and attenuation in fractured and porous reservoirs—poroelasticity approach, *Geophysical Prospecting*, 57(2), 225–237.
- Gurevich, B., D. Makarynska, O. B. de Paula, and M. Pervukhina (2010), A simple model for squirt-flow dispersion and attenuation in fluid-saturated granular rocks, *Geophysics*, 75(6), no. 6, N109–N120.

- Hajarolasvadi, S., and A. E. Elbanna (2017), A new hybrid numerical scheme for modelling elastodynamics in unbounded media with near-source heterogeneities, *Geophysical Journal International*, 211(2), 851–864.
- Harlow, F. H., and J. E. Welch (1965), Numerical calculation of time-dependent viscous incompressible flow of fluid with free surface, *The physics of fluids*, 8(12), 2182–2189.
- Hashin, Z. (1970), Complex moduli of viscoelastic composites—i. general theory and application to particulate composites, *International Journal of Solids and Structures*, 6(5), 539–552.
- Hetnarski, R. B., and J. Ignaczak (1999), Generalized thermoelasticity, *Journal of Thermal Stresses*, 22(4-5), 451–476.
- Hirsch, C. (1988), Numerical computation of internal and external flows, volume 1: Fundamentals of numerical discretization, *John Wiley and Sons*, 9, 10.
- Holzzapfel, A. G. (2000), Nonlinear solid mechanics ii.
- Homel, M. A., R. M. Brannon, and J. Guilkey (2016), Controlling the onset of numerical fracture in parallelized implementations of the material point method (mpm) with convective particle domain interpolation (cpdi) domain scaling, *International Journal for Numerical Methods in Engineering*, 107(1), 31–48.
- Hu, Y., T.-M. Li, L. Anderson, J. Ragan-Kelley, and F. Durand (2019), Taichi: A language for high-performance computation on spatially sparse data structures, *ACM Trans. Graph.*, 38(6), doi:10.1145/3355089.3356506.
- Huang, P., S.-l. Li, H. Guo, and Z.-m. Hao (2015), Large deformation failure analysis of the soil slope based on the material point method, *computational Geosciences*, 19(4), 951–963.
- Hudson, J. A., and E. Liu (1999), Effective elastic properties of heavily faulted structures, *Geophysics*, 64(2), 479–485, doi:10.1190/1.1444553.
- Hughes, T. J. R. (1980), Generalization of selective integration procedures to anisotropic and nonlinear media, *International Journal for Numerical Methods in Engineering*, 15(9), 1413–1418, doi:https://doi.org/10.1002/nme.1620150914.
- Hungr, O., S. Leroueil, and L. Picarelli (2014), The varnes classification of landslide types, an update, *Landslides*, 11(2), 167–194, doi:10.1007/s10346-013-0436-y.
- Hunziker, J., M. Favino, E. Caspari, B. Quintal, J. G. Rubino, R. Krause, and K. Holliger (2018), Seismic attenuation and stiffness modulus dispersion in porous rocks containing stochastic fracture networks, *Journal of Geophysical Research: Solid Earth*, 123(1), 125–143.
- Iaconeta, I., A. Larese, R. Rossi, and Z. Guo (2017), Comparison of a material point method and a galerkin meshfree method for the simulation of cohesive–frictional materials, *Materials*, 10(10), 1150.
- Jaeger, J., N. G W Cook, and R. Zimmerman (2007), *Fundamental of Rock Mechanics*, doi:10.1017/CBO9780511735349.
- Jakobsen, M., and M. Chapman (2009), Unified theory of global flow and squirt flow in cracked porous media, *Geophysics*, 74(2), no. 2, WA65–WA76.
- Jänicke, R., B. Quintal, and H. Steeb (2015), Numerical homogenization of mesoscopic loss in poroelastic media, *Eur. J. Mech. A Solids*, 49, 382–395.
- Jassim, I., D. Stolle, and P. Vermeer (2013), Two-phase dynamic analysis by material point method, *International Journal for Numerical and Analytical Methods in Geomechanics*, 37(15), 2502–2522, doi:https://doi.org/10.1002/nag.2146.
- Jiang, H., and Y. Xie (2011), A note on the Mohr–Coulomb and Drucker–Prager strength criteria, *Mechanics Research Communications*, 38(4), 309–314, doi:https://doi.org/10.1016/j.mechrescom.2011.04.001.
- Jin, L., and M. D. Zoback (2018), Fully dynamic spontaneous rupture due to quasi-static pore pressure and poroelastic effects: An implicit nonlinear computational model of fluid-induced seismic events, *Journal of Geophysical Research: Solid Earth*, 123(11), 9430–9468.

- Jin, S., and C. D. Levermore (1996), Numerical schemes for hyperbolic conservation laws with stiff relaxation terms, *Journal of computational physics*, 126(2), 449–467.
- Johnson, D. L. (2001), Theory of frequency dependent acoustics in patchy-saturated porous media, *The Journal of the Acoustical Society of America*, 110(2), 682–694.
- Jones, T. D. (1986), Pore fluids and frequency-dependent wave propagation in rocks, *Geophysics*, 51(10), 1939–1953.
- Jordan, P., and A. Puri (1999), Digital signal propagation in dispersive media, *Journal of Applied Physics*, 85(3), 1273–1282.
- Jou, D., J. Casas-Vázquez, and G. Lebon (2001), *Extended irreversible thermodynamics, 3rd ed.*, 462 pp., Springer, Berlin.
- Kachanov, M. (1993), Elastic solids with many cracks and related problems, *Advances in applied mechanics*, 30, 259–445.
- Kachanov, M., and V. Mishakin (2019), On crack density, crack porosity, and the possibility to interrelate them, *International Journal of Engineering Science*, 142, 185 – 189, doi:<https://doi.org/10.1016/j.ijengsci.2019.06.010>.
- Kachanov, M., and I. Sevostianov (2018), *Micromechanics of materials, with applications*, Springer.
- Klimentos, T. (1995), Attenuation of p- and s-waves as a method of distinguishing gas and condensate from oil and water, *GEOPHYSICS*, 60(2), 447–458, doi:10.1190/1.1443782.
- Köcher, U., and M. Bause (2014), Variational space–time methods for the wave equation, *Journal of Scientific Computing*, 61(2), 424–453.
- Komatitsch, D., G. Erlebacher, D. Göddeke, and D. Michéa (2010), High-order finite-element seismic wave propagation modeling with mpi on a large gpu cluster, *Journal of computational physics*, 229(20), 7692–7714.
- Krabbenhof, K., M. R. Karim, A. V. Lyamin, and S. W. Sloan (2012), Associated computational plasticity schemes for nonassociated frictional materials, *International Journal for Numerical Methods in Engineering*, 90(9), 1089–1117, doi:<https://doi.org/10.1002/nme.3358>.
- Kube, C. M., and M. De Jong (2016), Elastic constants of polycrystals with generally anisotropic crystals, *Journal of Applied Physics*, 120(16), 165,105.
- Lakes, R. (2009), *Viscoelastic Materials*, Cambridge University Press, doi:10.1017/CBO9780511626722.
- Landau, L., and E. Lifshitz (1959a), *Course of theoretical physics. vol. 6: Fluid mechanics*, Pergamon Press, London.
- Landau, L. D., and E. M. Lifshitz (1959b), *Course of Theoretical Physics Vol 7: Theory and Elasticity*, Pergamon press.
- Lapusta, N., J. R. Rice, Y. Ben-Zion, and G. Zheng (2000), Elastodynamic analysis for slow tectonic loading with spontaneous rupture episodes on faults with rate-and state-dependent friction, *Journal of Geophysical Research: Solid Earth*, 105(B10), 23,765–23,789.
- Lavier, L. L., X. Tong, and J. Biemiller (2021), The mechanics of creep, slow slip events, and earthquakes in mixed brittle-ductile fault zones, *Journal of Geophysical Research: Solid Earth*, 126(2), e2020JB020,325.
- Leavy, R., J. Guilkey, B. Phung, A. Spear, and R. Brannon (2019), A convected-particle tetrahedron interpolation technique in the material-point method for the mesoscale modeling of ceramics, *Computational Mechanics*, 64(3), 563–583.
- Lebedev, V. I. (1964), Difference analogues of orthogonal decompositions, basic differential operators and some boundary problems of mathematical physics. i, *USSR Computational Mathematics and Mathematical Physics*, 4(3), 69–92.

- Lei, X., S. He, and L. Wu (2020), Stabilized generalized interpolation material point method for coupled hydro-mechanical problems, *Computational Particle Mechanics*, doi:10.1007/s40571-020-00365-y.
- Lemoine, G. I. (2016), Three-dimensional mapped-grid finite volume modeling of poroelastic-fluid wave propagation, *SIAM Journal on Scientific Computing*, 38(5), B808–B836.
- Lemoine, G. I., M. Y. Ou, and R. J. LeVeque (2013), High-resolution finite volume modeling of wave propagation in orthotropic poroelastic media, *SIAM Journal on Scientific Computing*, 35(1), B176–B206.
- Levander, A. R. (1988), Fourth-order finite-difference p-sv seismograms, *Geophysics*, 53(11), 1425–1436.
- LeVeque, R. J. (1992), *Numerical methods for conservation laws*, vol. 132, Springer.
- LeVeque, R. J., et al. (2002), *Finite volume methods for hyperbolic problems*, vol. 31, Cambridge university press.
- Lisitsa, V., and D. Vishnevskiy (2010), Lebedev scheme for the numerical simulation of wave propagation in 3d anisotropic elasticity, *Geophysical Prospecting*, 58(4), 619–635.
- Lissa, S., N. D. Barbosa, J. Rubino, and B. Quintal (2019), Seismic attenuation and dispersion in poroelastic media with fractures of variable aperture distributions, *Solid Earth*, 10(4), 1321–1336.
- Lissa, S., N. D. Barbosa, E. Caspari, Y. Alkhimenkov, and B. Quintal (2020), Squirt flow in cracks with rough walls, *Journal of Geophysical Research: Solid Earth*, 125(4), e2019JB019,235.
- Lissa, S., M. Ruf, H. Steeb, and B. Quintal (2021), Digital rock physics applied to squirt flow, *Geophysics*, 86(4), 1–40.
- Liu, X., Y. Wang, and D.-Q. Li (2019), Investigation of slope failure mode evolution during large deformation in spatially variable soils by random limit equilibrium and material point methods, *Computers and Geotechnics*, 111, 301–312.
- Liu, X., Y. Wang, and D.-Q. Li (2020), Numerical simulation of the 1995 rainfall-induced fei tsui road landslide in hong kong: new insights from hydro-mechanically coupled material point method, *Landslides*, 17(12), 2755–2775, doi:10.1007/s10346-020-01442-2.
- Macías-Díaz, J., and A. Puri (2010), A boundedness-preserving finite-difference scheme for a damped nonlinear wave equation, *Applied numerical mathematics*, 60(9), 934–948.
- Madonna, C., B. Quintal, M. Frehner, B. S. Almqvist, N. Tisato, M. Pistone, F. Marone, and E. H. Saenger (2013), Synchrotron-based x-ray tomographic microscopy for rock physics investigations, *Geophysics*, 78(1), D53–D64.
- Majer, E. L., R. Baria, M. Stark, S. Oates, J. Bommer, B. Smith, and H. Asanuma (2007), Induced seismicity associated with enhanced geothermal systems, *Geothermics*, 36(3), 185–222.
- Makhnenko, R. Y., and Y. Y. Podladchikov (2018), Experimental poroviscoelasticity of common sedimentary rocks, *Journal of Geophysical Research: Solid Earth*, 123(9), 7586–7603.
- Marchuk, G. I. (1975), *Methods of numerical mathematics*.
- Markov, A., S. Abaimov, I. Sevostianov, M. Kachanov, S. Kanaun, and I. Akhatov (2019), The effect of multiple contacts between crack faces on crack contribution to the effective elastic properties, *International Journal of Solids and Structures*, 163, 75–86.
- Masson, Y. J., and S. Pride (2014), On the correlation between material structure and seismic attenuation anisotropy in porous media, *Journal of Geophysical Research: Solid Earth*, 119(4), 2848–2870.
- Masson, Y. J., and S. R. Pride (2007), Poroelastic finite difference modeling of seismic attenuation and dispersion due to mesoscopic-scale heterogeneity, *Journal of Geophysical Research: Solid Earth*, 112(B3), B3204.
- Masson, Y. J., S. Pride, and K. Nihei (2006), Finite difference modeling of Biot's poroelastic equations at seismic frequencies, *Journal of Geophysical Research: Solid Earth*, 111(B10), B10,305.

- Mast, C., P. Mackenzie-Helnwein, P. Arduino, G. R. Miller, and W. Shin (2012), Mitigating kinematic locking in the material point method, *Journal of Computational Physics*, 231(16), 5351–5373.
- Maultzsch, S., M. Chapman, E. Liu, and X. Y. Li (2003), Modelling frequency-dependent seismic anisotropy in fluid-saturated rock with aligned fractures: implication of fracture size estimation from anisotropic measurements, *Geophysical Prospecting*, 51(5), 381–392.
- Maurer, J., E. M. Dunham, and P. Segall (2020), Role of fluid injection on earthquake size in dynamic rupture simulations on rough faults, *Geophysical Research Letters*, 47(13), e2020GL088377.
- Mavko, G., and D. Jizba (1991), Estimating grain-scale fluid effects on velocity dispersion in rocks, *Geophysics*, 56(12), 1940–1949.
- Mavko, G., and A. Nur (1975), Melt squirt in the asthenosphere, *Journal of Geophysical Research*, 80(11), 1444–1448.
- Mavko, G., T. Mukerji, and J. Dvorkin (2009), *The rock physics handbook: Tools for seismic analysis of porous media*, Cambridge university press.
- Mavko, G., T. Mukerji, and J. Dvorkin (2020), *The rock physics handbook*, Cambridge university press.
- Mayr, S. I., and H. Burkhardt (2006), Ultrasonic properties of sedimentary rocks: effect of pressure, saturation, frequency and microcracks, *Geophysical Journal International*, 164(1), 246–258.
- McGarr, A. (2014), Maximum magnitude earthquakes induced by fluid injection, *Journal of Geophysical Research: solid earth*, 119(2), 1008–1019.
- McKee, S., M. F. Tomé, V. G. Ferreira, J. A. Cuminato, A. Castelo, F. Sousa, and N. Mangiavacchi (2008), The mac method, *Computers & Fluids*, 37(8), 907–930.
- Mehra, R., N. Raghuvanshi, L. Savioja, M. C. Lin, and D. Manocha (2012), An efficient gpu-based time domain solver for the acoustic wave equation, *Applied Acoustics*, 73(2), 83–94.
- Metz, B., O. Davidson, H. de Coninck, M. Loos, and L. Meyer (2005), *Ippc special report on carbon dioxide capture and storage*, Cambridge University Press, p. 431.
- Michéa, D., and D. Komatitsch (2010), Accelerating a three-dimensional finite-difference wave propagation code using gpu graphics cards, *Geophysical Journal International*, 182(1), 389–402.
- Mickens, R. E., and P. Jordan (2004), A positivity-preserving nonstandard finite difference scheme for the damped wave equation, *Numerical Methods for Partial Differential Equations: An International Journal*, 20(5), 639–649.
- Mikhaltsevitch, V., M. Lebedev, and B. Gurevich (2015), A laboratory study of attenuation and dispersion effects in glycerol-saturated berea sandstone at seismic frequencies, in *SEG Technical Program Expanded Abstracts 2015*, pp. 3085–3089, Society of Exploration Geophysicists.
- Milani, M., J. G. Rubino, T. M. Müller, B. Quintal, E. Caspari, and K. Holliger (2016), Representative elementary volumes for evaluating effective seismic properties of heterogeneous poroelastic media, *Geophysics*, 81, D21–D33, doi:10.1190/GEO2015-0173.1.
- Miller, S. A. (2020), Aftershocks are fluid-driven and decay rates controlled by permeability dynamics, *Nature communications*, 11(1), 1–11.
- Miller, S. A., C. Collettini, L. Chiaraluce, M. Cocco, M. Barchi, and B. J. Kaus (2004), Aftershocks driven by a high-pressure co 2 source at depth, *Nature*, 427(6976), 724–727.
- Minakov, A., and V. Yarushina (2021), Elastoplastic source model for microseismicity and acoustic emission, *Geophysical Journal International*, 227(1), 33–53.
- Moczko, P., J. O. Robertsson, and L. Eisner (2007), The finite-difference time-domain method for modeling of seismic wave propagation, *Advances in geophysics*, 48, 421–516.

- Moczo, P., D. Gregor, J. Kristek, and J. de la Puente (2019), A discrete representation of material heterogeneity for the finite-difference modelling of seismic wave propagation in a poroelastic medium, *Geophysical Journal International*, 216(2), 1072–1099.
- Mohanty, R. (2004), An unconditionally stable difference scheme for the one-space-dimensional linear hyperbolic equation, *Applied Mathematics Letters*, 17(1), 101–105.
- Moler, C. (2000), Matlab incorporates lapack.
- Morency, C., and J. Tromp (2008), Spectral-element simulations of wave propagation in porous media, *Geophysical Journal International*, 175(1), 301–345.
- Mukerji, T., and G. Mavko (1994), Pore fluid effects on seismic velocity in anisotropic rocks, *Geophysics*, 59(2), 233–244.
- Müller, T., J. Toms-Stewart, and F. Wenzlau (2008), Velocity-saturation relation for partially saturated rocks with fractal pore fluid distribution, *Geophysical Research Letters*, 35(9).
- Müller, T. M., B. Gurevich, and M. Lebedev (2010), Seismic wave attenuation and dispersion resulting from wave-induced flow in porous rocks—a review, *Geophysics*, 75(5), no. 5, 75A147–75A164.
- Murphy, W. F., K. W. Winkler, and R. L. Kleinberg (1986), Acoustic relaxation in sedimentary rocks: Dependence on grain contacts and fluid saturation, *Geophysics*, 51(3), 757–766.
- Nairn, J. A. (2003), Material point method calculations with explicit cracks, *Computer Modeling in Engineering and Sciences*, 4(6), 649–664.
- Najafi, H. S., and F. Izadi (2014), Comparison of two finite-difference methods for solving the damped wave equation, *International Journal of Mathematical Engineering and Science*, pp. 35–49.
- Nemat-Nasser, S., and M. Hori (2013), *Micromechanics: overall properties of heterogeneous materials*, vol. 37, Elsevier.
- Nevitt, J. M., B. A. Brooks, R. D. Catchings, M. R. Goldman, T. L. Ericksen, and C. L. Glennie (2020), Mechanics of near-field deformation during co- and post-seismic shallow fault slip, *Scientific reports*, 10(1), 1–13.
- Nguyen, N. H. T., H. H. Bui, and G. D. Nguyen (2020), Effects of material properties on the mobility of granular flow, *Granular Matter*, 22(3), 59, doi:10.1007/s10035-020-01024-y.
- Ni, R., and X. Zhang (2020), A precise critical time step formula for the explicit material point method, *International Journal for Numerical Methods in Engineering*, 121(22), 4989–5016.
- Nolte, D. D., and L. J. Pyrak-Nolte (1991), Stratified continuum percolation: Scaling geometry of hierarchical cascades, *Phys. Rev. A*, 44, 6320 – 6333, doi:10.1103/PhysRevA.44.6320.
- Nvidia (2007), Cuda programming guide version 1.0.
- O’Brien, G. S. (2010), 3d rotated and standard staggered finite-difference solutions to biot’s poroelastic wave equations: Stability condition and dispersion analysis, *Geophysics*, 75(4), T111–T119.
- O’Connell, R., and B. Budiansky (1978), Measures of dissipation in viscoelastic media, *Geophysical Research Letters*, 5(1), 5–8.
- O’Connell, R. J., and B. Budiansky (1977), Viscoelastic properties of fluid-saturated cracked solids, *Journal of Geophysical Research*, 82(36), 5719–5735.
- Omlin, S. (2016), Development of massively parallel near peak performance solvers for three-dimensional geodynamic modelling, Ph.D. thesis, Université de Lausanne, Faculté des géosciences et de l’environnement.
- Omlin, S. (2017), Development of massively parallel near peak performance solvers for three-dimensional geodynamic modelling, Ph.D. thesis.

- Omlin, S., L. Räss, and Y. Y. Podladchikov (2018), Simulation of three-dimensional viscoelastic deformation coupled to porous fluid flow, *Tectonophysics*, 746, 695–701, doi:<https://doi.org/10.1016/j.tecto.2017.08.012>, understanding geological processes through modelling - A Memorial Volume honouring Evgenii Burov.
- Omlin, S., L. Räss, G. Kwasniewski, B. Malvoisin, S. Omlin, and Y. Podladchikov (2020), Solving nonlinear multi-physics on gpu supercomputers with julia, <https://developer.nvidia.com/gtc/2019/video/S9368>, *GTC Silicon Valley - 2019, 2019b*.
- O’Sullivan, S., R. E. Bird, W. M. Coombs, and S. Giani (2019), Rapid non-linear finite element analysis of continuous and discontinuous galerkin methods in matlab, *Computers & Mathematics with Applications*, 78(9), 3007–3026.
- Özdenvar, T., and G. A. McMechan (1997), Algorithms for staggered-grid computations for poroelastic, elastic, acoustic, and scalar wave equations, *Geophysical Prospecting*, 45(3), 403–420.
- Palmer, I., and M. Traviolia (1980), Attenuation by squirt flow in undersaturated gas sands, *Geophysics*, 45(12), 1780–1792.
- Pareschi, L., and G. Russo (2005), Implicit–explicit runge–kutta schemes and applications to hyperbolic systems with relaxation, *Journal of Scientific computing*, 25(1), 129–155.
- Pascal, H. (1986), Pressure wave propagation in a fluid flowing through a porous medium and problems related to interpretation of stoneley’s wave attenuation in acoustical well logging, *International journal of engineering science*, 24(9), 1553–1570.
- Pervukhina, M., B. Gurevich, D. N. Dewhurst, and A. F. Siggins (2010), Applicability of velocity–stress relationships based on the dual porosity concept to isotropic porous rocks, *Geophysical Journal International*, 181(3), 1473–1479.
- Petrini, C., T. Gerya, V. Yarushina, Y. van Dinther, J. Connolly, and C. Madonna (2020), Seismo-hydro-mechanical modelling of the seismic cycle: Methodology and implications for subduction zone seismicity, *Tectonophysics*, 791, 228,504.
- Pimienta, L., J. Fortin, and Y. Guéguen (2015a), Bulk modulus dispersion and attenuation in sandstones, *Geophysics*, 80(2), no. 2, D111–D127.
- Pimienta, L., J. Fortin, and Y. Guéguen (2015b), Experimental study of Young’s modulus dispersion and attenuation in fully saturated sandstones, *Geophysics*, 80(5), no. 5, L57–L72.
- Poincaré, H. (1885), Sur l’équilibre d’une masse fluide animée d’un mouvement de rotation, *Acta mathematica*, 7(1), 259–380.
- Poliakov, A. N., H. J. Herrmann, Y. Y. Podladchikov, and S. Roux (1994), Fractal plastic shear bands, *Fractals*, 2(04), 567–581.
- Preuss, S., J. P. Ampuero, T. Gerya, and Y. van Dinther (2020), Characteristics of earthquake ruptures and dynamic off-fault deformation on propagating faults, *Solid Earth*, 11(4), 1333–1360.
- Pride, S. R., and J. G. Berryman (2003a), Linear dynamics of double-porosity dual-permeability materials. i. governing equations and acoustic attenuation, *Physical Review E*, 68(3), 036,603.
- Pride, S. R., and J. G. Berryman (2003b), Linear dynamics of double-porosity dual-permeability materials. ii. fluid transport equations, *Physical Review E*, 68(3), 036,604.
- Pride, S. R., and S. Garambois (2005), Electro seismic wave theory of frenkel and more recent developments, *Journal of Engineering Mechanics*, 131(9), 898–907.
- Pride, S. R., F. D. Morgan, and A. F. Gangi (1993), Drag forces of porous-medium acoustics, *Physical review B*, 47(9), 4964.
- Pride, S. R., J. G. Berryman, and J. M. Harris (2004), Seismic attenuation due to wave-induced flow, *Journal of Geophysical Research: Solid Earth*, 109(B1), no. B1, B01,201.

- Pyrak-Nolte, L., L. Myer, N. Cook, and P. Witherspoon (1987), Hydraulic and mechanical properties of natural fractures in low-permeability rock.
- Quintal, B., H. Steeb, M. Frehner, and S. M. Schmalholz (2011), Quasi-static finite element modeling of seismic attenuation and dispersion due to wave-induced fluid flow in poroelastic media, *Journal of Geophysical Research: Solid Earth*, 116(B1).
- Quintal, B., R. Jänicke, J. G. Rubino, H. Steeb, and K. Holliger (2014), Sensitivity of s-wave attenuation to the connectivity of fractures in fluid-saturated rocks, *Geophysics*, 79(5), WB15–WB24.
- Quintal, B., J. G. Rubino, E. Caspari, and K. Holliger (2016), A simple hydromechanical approach for simulating squirt-type flow, *Geophysics*, 81(4), no. 4, D335–D344.
- Quintal, B., E. Caspari, K. Holliger, and H. Steeb (2019), Numerically quantifying energy loss caused by squirt flow, *Geophysical Prospecting*, 67(8), 2196–2212.
- Raleigh, C., J. Healy, and J. Bredehoeft (1976), An experiment in earthquake control at Rangely, Colorado, *Science*, 191(4233), 1230–1237.
- Ranganathan, S. I., and M. Ostojca-Starzewski (2008), Universal elastic anisotropy index, *Physical Review Letters*, 101(5), 055,504.
- Rapoport, M. B., L. I. Rapoport, and V. I. Ryjkov (2004), Direct detection of oil and gas fields based on seismic inelasticity effect, *The Leading Edge*, 23(3), 276–278, doi:10.1190/1.1690901.
- Räss, L., T. Duretz, Y. Y. Podladchikov, and S. M. Schmalholz (2017), M2di: Concise and efficient matlab 2-ds tokens solvers using the finite difference method, *Geochemistry, Geophysics, Geosystems*, 18(2), 755–768.
- Räss, L., N. S. C. Simon, and Y. Y. Podladchikov (2018), Spontaneous formation of fluid escape pipes from subsurface reservoirs, *Scientific Reports*, 8(1), 11,116, doi:10.1038/s41598-018-29485-5.
- Räss, L., S. Omlin, and Y. Podladchikov (2019a), Resolving spontaneous nonlinear multi-physics flow localization in 3-d: Tackling hardware limit, <https://developer.nvidia.com/gtc/2019/video/S9368>, *GTC Silicon Valley - 2019, 2019b*.
- Räss, L., T. Duretz, and Y. Podladchikov (2019b), Resolving hydromechanical coupling in two and three dimensions: spontaneous channelling of porous fluids owing to decompaction weakening, *Geophysical Journal International*, 218(3), 1591–1616.
- Räss, L., A. Licul, F. Herman, Y. Y. Podladchikov, and J. Suckale (2020), Modelling thermomechanical ice deformation using an implicit pseudo-transient method (fastice v1. 0) based on graphical processing units (gpu), *Geoscientific Model Development*, 13(3), 955–976.
- Ravindran, P., L. Fast, P. A. Korzhavyi, B. Johansson, J. Wills, and O. Eriksson (1998), Density functional theory for calculation of elastic properties of orthorhombic crystals: Application to tisi 2, *Journal of Applied Physics*, 84(9), 4891–4904.
- Remmerswaal, G., P. J. Vardon, and M. A. Hicks (2021), Evaluating residual dyke resistance using the random material point method, *Computers and Geotechnics*, 133, 104,034, doi:https://doi.org/10.1016/j.compgeo.2021.104034.
- Räss, L., D. Kolyukhin, and A. Minakov (2019), Efficient parallel random field generator for large 3-d geophysical problems, *Computers & Geosciences*, 131, 158–169, doi:https://doi.org/10.1016/j.cageo.2019.06.007.
- Rubino, J., E. Caspari, T. M. Müller, and K. Holliger (2017), Fracture connectivity can reduce the velocity anisotropy of seismic waves, *Geophysical Journal International*, 210(1), 223–227.
- Rubino, J., J. Germán, L. Guarracino, T. M. Müller, and K. Holliger (2013), Do seismic waves sense fracture connectivity?, *Geophysical Research Letters*, 40(4), 692–696.
- Rubino, J. G., C. L. Ravazzoli, and J. E. Santos (2009), Equivalent viscoelastic solids for heterogeneous fluid-saturated porous rocks, *Geophysics*, 74(1), N1–N13.

- Rubino, J. G., T. M. Müller, L. Guarracino, M. Milani, and K. Holliger (2014), Seismoacoustic signatures of fracture connectivity, *Journal of Geophysical Research: Solid Earth*, 119(3), 2252–2271.
- Rubino, J. g., E. Caspari, T. M. Müller, M. Milani, N. D. Barbosa, and K. Holliger (2016), Numerical upscaling in 2-d heterogeneous poroelastic rocks: Anisotropic attenuation and dispersion of seismic waves, *J. Geophys. Res.*, 121(9), 6698–6721.
- Rubio, E., M. Hanzich, A. Farrés, J. De La Puente, and J. M. Cella (2014), Finite-difference staggered grids in gpus for anisotropic elastic wave propagation simulation, *Computers & geosciences*, 70, 181–189.
- Rudnicki, J. W., and J. Rice (1975), Conditions for the localization of deformation in pressure-sensitive dilatant materials, *Journal of the Mechanics and Physics of Solids*, 23(6), 371–394.
- Ruina, A. (1983), Slip instability and state variable friction laws, *Journal of Geophysical Research: Solid Earth*, 88(B12), 10,359–10,370.
- Sadeghirad, A., R. M. Brannon, and J. Burghardt (2011), A convected particle domain interpolation technique to extend applicability of the material point method for problems involving massive deformations, *International Journal for numerical methods in Engineering*, 86(12), 1435–1456.
- Sadeghirad, A., R. Brannon, and J. Guilkey (2013), Second-order convected particle domain interpolation (cpdi2) with enrichment for weak discontinuities at material interfaces, *International Journal for numerical methods in Engineering*, 95(11), 928–952.
- Saenger, E. H., N. Gold, and S. A. Shapiro (2000), Modeling the propagation of elastic waves using a modified finite-difference grid, *Wave motion*, 31(1), 77–92.
- Saenger, E. H., O. S. Krüger, and S. A. Shapiro (2004), Effective elastic properties of randomly fractured soils: 3d numerical experiments, *Geophysical Prospecting*, 52(3), 183–195.
- Saenger, E. H., F. Enzmann, Y. Keehm, and H. Steeb (2011), Digital rock physics: Effect of fluid viscosity on effective elastic properties, *Journal of Applied Geophysics*, 74(4), 236 – 241, doi:<https://doi.org/10.1016/j.jappgeo.2011.06.001>.
- Saenger, E. H., M. Lebedev, D. Uribe, M. Osorno, S. Vialle, M. Duda, S. Iglauer, and H. Steeb (2016), Analysis of high-resolution x-ray computed tomography images of bentheim sandstone under elevated confining pressures, *Geophysical Prospecting*, 64(4), 848–859, doi:10.1111/1365-2478.12400.
- Sanchez-Vila, X., A. Guadagnini, and J. Carrera (2006), Representative hydraulic conductivities in saturated groundwater flow, *Reviews of Geophysics*, 44(3), doi:10.1029/2005RG000169.
- Saxena, N., and G. Mavko (2016), Estimating elastic moduli of rocks from thin sections: Digital rock study of 3d properties from 2d images, *Computers & geosciences*, 88, 9–21.
- Sayers, C., and M. Kachanov (1995), Microcrack-induced elastic wave anisotropy of brittle rocks, *Journal of Geophysical Research: Solid Earth*, 100(B3), 4149–4156.
- Sayers, C. M. (2002), Stress-dependent elastic anisotropy of sandstones, *Geophysical prospecting*, 50(1), 85–95.
- Schenk, O., and K. Gärtner (2004), Solving unsymmetric sparse systems of linear equations with pardiso, *Future Generation Computer Systems*, 20(3), 475–487.
- Schieweck, F. (2010), A-stable discontinuous galerkin–petrov time discretization of higher order, *Journal of Numerical Mathematics*, 18(1), 25–57.
- Schoenberg, M., and J. Douma (1988), Elastic wave propagation in media with parallel fractures and aligned cracks¹, *Geophysical prospecting*, 36(6), 571–590.
- Schoenberg, M., and K. Helbig (1997), Orthorhombic media: Modeling elastic wave behavior in a vertically fractured earth, *Geophysics*, 62(6), 1954–1974.
- Schoenberg, M., and C. M. Sayers (1995), Seismic anisotropy of fractured rock, *Geophysics*, 60(1), 204–211.

- Sevostianov, I., and M. Kachanov (1999), Compliance tensors of ellipsoidal inclusions, *International Journal of Fracture*, 96(1), 3–7.
- Shapiro, S. A. (2003), Elastic piezosensitivity of porous and fractured rocks, *Geophysics*, 68(2), 482–486, doi: 10.1190/1.1567215.
- Shapiro, S. A. (2015), *Fluid-induced seismicity*, Cambridge University Press.
- Shapiro, S. A., and C. Dinske (2009), Fluid-induced seismicity: Pressure diffusion and hydraulic fracturing, *Geophysical Prospecting*, 57(2), 301–310.
- Shukla, K., J. S. Hesthaven, J. M. Carcione, R. Ye, J. de la Puente, and P. Jaiswal (2019), A nodal discontinuous galerkin finite element method for the poroelastic wave equation, *Computational Geosciences*, 23(3), 595–615.
- Shukla, K., J. Chan, V. Maarten, and P. Jaiswal (2020), A weight-adjusted discontinuous galerkin method for the poroelastic wave equation: penalty fluxes and micro-heterogeneities, *Journal of Computational Physics*, 403, 109,061.
- Silliman, S. E. (1989), An interpretation of the difference between aperture estimates derived from hydraulic and tracer tests in a single fracture, *Water Resources Research*, 25(10), 2275–2283, doi:10.1029/WR025i10p02275.
- Simpson, G. (2017), *Practical finite element modeling in earth science using matlab*, Wiley Online Library.
- Sinaie, S., V. P. Nguyen, C. T. Nguyen, and S. Bordas (2017), Programming the material point method in julia, *Advances in Engineering Software*, 105, 17–29.
- Solazzi, S. G., J. G. Rubino, T. M. Müller, M. Milani, L. Guarracino, and K. Holliger (2016), An energy-based approach to estimate seismic attenuation due to wave-induced fluid flow in heterogeneous poroelastic media, *Geophys. J. Int.*, 207(2), 823–832.
- Solazzi, S. G., S. Lissa, J. G. Rubino, and K. Holliger (2021), Squirt flow in partially saturated cracks: a simple analytical model, *Geophysical Journal International*, 227(1), 680–692.
- Steffen, M., R. M. Kirby, and M. Berzins (2008a), Analysis and reduction of quadrature errors in the material point method (mpm), *International journal for numerical methods in engineering*, 76(6), 922–948.
- Steffen, M., P. Wallstedt, J. Guilkey, R. Kirby, and M. Berzins (2008b), Examination and analysis of implementation choices within the material point method (mpm), *Computer Modeling in Engineering and Sciences*, 31(2), 107–127.
- Stomakhin, A., C. Schroeder, L. Chai, J. Teran, and A. Selle (2013), A material point method for snow simulation, *ACM Transactions on Graphics (TOG)*, 32(4), 1–10.
- Strang, G. (1968), On the construction and comparison of difference schemes, *SIAM journal on numerical analysis*, 5(3), 506–517.
- Subramaniyan, S., B. Quintal, C. Madonna, and E. H. Saenger (2015), Laboratory-based seismic attenuation in fontainebleau sandstone: Evidence of squirt flow, *Journal of Geophysical Research: Solid Earth*, 120(11), 7526–7535.
- Suckale, J. (2009), Induced seismicity in hydrocarbon fields, in *Advances in geophysics*, vol. 51, pp. 55–106, Elsevier.
- Sulem, J., and I. Vardoulakis (1995), *Bifurcation analysis in geomechanics*, CRC Press.
- Sulsky, D., Z. Chen, and H. L. Schreyer (1994), A particle method for history-dependent materials, *Computer methods in applied mechanics and engineering*, 118(1-2), 179–196.
- Sulsky, D., S.-J. Zhou, and H. L. Schreyer (1995), Application of a particle-in-cell method to solid mechanics, *Computer physics communications*, 87(1-2), 236–252.
- Takeuchi, C. S., and Y. Fialko (2012), Dynamic models of interseismic deformation and stress transfer from plate motion to continental transform faults, *Journal of Geophysical Research: Solid Earth*, 117(B5).

- Tape, W., and C. Tape (2012), A geometric setting for moment tensors, *Geophysical Journal International*, 190(1), 476–498.
- Tester, J. W., B. J. Anderson, A. S. Batchelor, D. D. Blackwell, R. DiPippo, E. M. Drake, J. Garnish, B. Livesay, M. C. Moore, K. Nichols, S. Petty, M. Nafi Toksoz, R. W. Veatch, R. Baria, C. Augustine, E. Murphy, P. Negraru, and M. Richards (2007), Impact of enhanced geothermal systems on us energy supply in the twenty-first century, *Philosophical Transactions of the Royal Society A: Mathematical, Physical and Engineering Sciences*, 365(1853), 1057–1094, doi:10.1098/rsta.2006.1964.
- Thomsen, L. (1986), Weak elastic anisotropy, *Geophysics*, 51(10), 1954–1966.
- Tillotson, P., J. Sothcott, A. I. Best, M. Chapman, and X.-Y. Li (2012), Experimental verification of the fracture density and shear-wave splitting relationship using synthetic silica cemented sandstones with a controlled fracture geometry, *Geophysical Prospecting*, 60(3), 516–525.
- Tillotson, P., M. Chapman, J. Sothcott, A. I. Best, and X.-Y. Li (2014), Pore fluid viscosity effects on p-and s-wave anisotropy in synthetic silica-cemented sandstone with aligned fractures, *Geophysical Prospecting*, 62(6), 1238–1252.
- Tong, X., and L. L. Lavier (2018), Simulation of slip transients and earthquakes in finite thickness shear zones with a plastic formulation, *Nature communications*, 9(1), 1–8.
- Torberntsson, K., V. Stiernström, K. Mattsson, and E. M. Dunham (2018), A finite difference method for earthquake sequences in poroelastic solids, *Computational Geosciences*, 22(5), 1351–1370.
- Tran, Q.-A., and W. Sołowski (2019), Generalized interpolation material point method modelling of large deformation problems including strain-rate effects—application to penetration and progressive failure problems, *Computers and Geotechnics*, 106, 249–265.
- Trofimov, A., B. Drach, M. Kachanov, and I. Sevostianov (2017), Effect of a partial contact between the crack faces on its contribution to overall material compliance and resistivity, *International Journal of Solids and Structures*, 108, 289–297.
- Tsai, H.-C., and C.-C. Lee (1998), Compressive stiffness of elastic layers bonded between rigid plates, *International Journal of Solids and Structures*, 35(23), 3053–3069.
- Tsvankin, I. (1997), Anisotropic parameters and p-wave velocity for orthorhombic media, *Geophysics*, 62(4), 1292–1309.
- Tsvankin, I. (2012), *Seismic signatures and analysis of reflection data in anisotropic media*, Society of Exploration Geophysicists.
- Tsvankin, I., and V. Grechka (2011), *Seismology of azimuthally anisotropic media and seismic fracture characterization*, Society of Exploration Geophysicists.
- Ulrich, T., A.-A. Gabriel, J.-P. Ampuero, and W. Xu (2019), Dynamic viability of the 2016 mw 7.8 kaikōura earthquake cascade on weak crustal faults, *Nature communications*, 10(1), 1–16.
- Van der Voort, N., and F. Vanclay (2015), Social impacts of earthquakes caused by gas extraction in the province of groningen, the netherlands, *Environmental Impact Assessment Review*, 50, 1–15.
- Van Dinther, Y., T. Gerya, L. Dalguer, P. M. Mai, G. Morra, and D. Giardini (2013a), The seismic cycle at subduction thrusts: Insights from seismo-thermo-mechanical models, *Journal of Geophysical Research: Solid Earth*, 118(12), 6183–6202.
- Van Dinther, Y., T. Gerya, L. A. Dalguer, F. Corbi, F. Funiciello, and P. M. Mai (2013b), The seismic cycle at subduction thrusts: 2. dynamic implications of geodynamic simulations validated with laboratory models, *Journal of Geophysical Research: Solid Earth*, 118(4), 1502–1525.
- van Dinther, Y., H. R. Künsch, and A. Fichtner (2019), Ensemble data assimilation for earthquake sequences: probabilistic estimation and forecasting of fault stresses, *Geophysical Journal International*, 217(3), 1453–1478.

- van Thienen-Visser, K., and J. Breunese (2015), Induced seismicity of the groningen gas field: History and recent developments, *The Leading Edge*, 34(6), 664–671.
- Vardon, P. J., B. Wang, and M. A. Hicks (2017), Slope failure simulations with mpm, *Journal of Hydrodynamics*, 29(3), 445–451.
- Varnes, D. J. (1958), Landslide types and processes, *Landslides and engineering practice*, 24, 20–47.
- Varnes, D. J. (1978), Slope movement types and processes, in *Special Report 176: Landslides: Analysis and Control*, edited by R. L. Schuster and R. J. Krizek, pp. 11–33, Transportation and Road Research Board, National Academy of Science, Washington D.C.
- Vermeer, P. A., and R. De Borst (1984), Non-associated plasticity for soils, concrete and rock, *HERON*, 29 (3), 1984.
- Vieira, R. T., D. de Bortoli, M. V. de Carvalho, and F. A. Pires (2019), The role of elastic anisotropy on the macroscopic constitutive response and yield onset of cubic oligo- and polycrystals, *International Journal of Plasticity*.
- Virieux, J. (1986), P-sv wave propagation in heterogeneous media: Velocity-stress finite-difference method, *Geophysics*, 51(4), 889–901.
- Virieux, J., and R. Madariaga (1982), Dynamic faulting studied by a finite difference method, *Bulletin of the Seismological Society of America*, 72(2), 345–369.
- Wallstedt, P. C., and J. Guilkey (2008), An evaluation of explicit time integration schemes for use with the generalized interpolation material point method, *Journal of Computational Physics*, 227(22), 9628–9642.
- Walsh, J. (1965), The effect of cracks on the compressibility of rock, *Journal of Geophysical Research*, 70(2), 381–389.
- Wang, B., P. J. Vardon, M. A. Hicks, and Z. Chen (2016a), Development of an implicit material point method for geotechnical applications, *Computers and Geotechnics*, 71, 159–167.
- Wang, B., M. Hicks, and P. Vardon (2016b), Slope failure analysis using the random material point method, *Géotechnique Letters*, 6(2), 113–118.
- Wang, B., P. Vardon, and M. Hicks (2016c), Investigation of retrogressive and progressive slope failure mechanisms using the material point method, *Computers and Geotechnics*, 78, 88–98.
- Wang, H. F. (2000), *Theory of linear poroelasticity with applications to geomechanics and hydrogeology*, Princeton University Press.
- Wang, L., W. M. Coombs, C. E. Augarde, M. Cortis, T. Charlton, M. Brown, J. Knappett, A. Brennan, C. Davidson, D. Richards, et al. (2019), On the use of domain-based material point methods for problems involving large distortion, *Computer Methods in Applied Mechanics and Engineering*, 355, 1003–1025.
- Wang, X., Y. Qiu, S. R. Slattery, Y. Fang, M. Li, S.-C. Zhu, Y. Zhu, M. Tang, D. Manocha, and C. Jiang (2020), A massively parallel and scalable multi-gpu material point method, *ACM Trans. Graph.*, 39(4), doi:10.1145/3386569.3392442.
- Ward, N. D., T. Lähivaara, and S. Eveson (2017), A discontinuous galerkin method for poroelastic wave propagation: The two-dimensional case, *Journal of Computational Physics*, 350, 690–727.
- Weiss, R. M., and J. Shragge (2013), Solving 3d anisotropic elastic wave equations on parallel gpu devices, *Geophysics*, 78(2), F7–F15.
- Wenzlau, E., and T. M. Müller (2009), Finite-difference modeling of wave propagation and diffusion in poroelastic media, *Geophysics*, 74(4), T55–T66.
- White, J. (1975), Computed seismic speeds and attenuation in rocks with partial gas saturation, *Geophysics*, 40(2), 224–232.

- White, J. E., N. Mihailova, and F. Lyakhovitsky (1975), Low-frequency seismic waves in fluid-saturated layered rocks, *The Journal of the Acoustical Society of America*, 57(S1), no. S1, S30–S30.
- Więckowski, Z. (2004), The material point method in large strain engineering problems, *Computer methods in applied mechanics and engineering*, 193(39–41), 4417–4438.
- Wilson, P., R. Wüchner, and D. Fernando (2021), Distillation of the material point method cell crossing error leading to a novel quadrature-based c0 remedy, *International Journal for Numerical Methods in Engineering*, 122(6), 1513–1537, doi:<https://doi.org/10.1002/nme.6588>.
- Wollherr, S., A.-A. Gabriel, and C. Uphoff (2018), Off-fault plasticity in three-dimensional dynamic rupture simulations using a modal discontinuous galerkin method on unstructured meshes: implementation, verification and application, *Geophysical Journal International*, 214(3), 1556–1584.
- Wyser, E., Y. Alkhimenkov, M. Jaboyedoff, and Y. Y. Podladchikov (2020a), A fast and efficient matlab-based mpm solver: fmpmm-solver v1. 1, *Geoscientific Model Development*, 13(12), 6265–6284.
- Wyser, E., Y. Alkhimenkov, M. Jayboyedoff, and Y. Podladchikov (2020b), fmpmm-solver, doi:10.5281/zenodo.4068585.
- Wyser, E., Y. Alkhimenkov, M. Jaboyedoff, and Y. Y. Podladchikov (2020c), fmpmm-solver, doi:10.5281/zenodo.4068585.
- Wyser, E., Y. Alkhimenkov, M. Jaboyedoff, and Y. Y. Podladchikov (2021a), An explicit gpu-based material point method solver for elastoplastic problems (ep2-3de v1. 0), *Geoscientific Model Development Discussions*, pp. 1–39.
- Wyser, E., Y. Alkhimenkov, M. Jaboyedoff, and Y. Y. Podladchikov (2021b), ep2-3de v1.0, doi:10.5281/zenodo.5600373.
- Xu, S. (1998), Modelling the effect of fluid communication on velocities in anisotropic porous rocks, *International Journal of Solids and Structures*, 35(34–35), 4685–4707.
- Yabuno, H. (2021), *Linear and Nonlinear Instabilities in Mechanical Systems: Analysis, Control and Application*, John Wiley & Sons.
- Yan, H., B. Dupuy, A. Romdhane, and B. Arntsen (2019), CO2 saturation estimates at Sleipner (North Sea) from seismic tomography and rock physics inversion, *Geophysical Prospecting*, 67(4), 1055–1071.
- Yarushina, V. M., and Y. Y. Podladchikov (2015), (de) compaction of porous viscoelastoplastic media: Model formulation, *Journal of Geophysical Research: Solid Earth*, 120(6), 4146–4170.
- Yeck, W. L., G. P. Hayes, D. E. McNamara, J. L. Rubinstein, W. D. Barnhart, P. S. Earle, and H. M. Benz (2017), Oklahoma experiences largest earthquake during ongoing regional wastewater injection hazard mitigation efforts, *Geophysical Research Letters*, 44(2), 711–717.
- Yin, A., and Z. Xie (2019), Anisotropic viscoplasticity explains slow-slip m0-t scaling at convergent plate margins, *Tectonophysics*, 751, 229–244.
- Ying, C., K. Zhang, Z.-N. Wang, S. Siddiqua, G. M. H. Makeen, and L. Wang (2021), Analysis of the run-out processes of the xinlu village landslide using the generalized interpolation material point method, *Landslides*, 18(4), 1519–1529, doi:10.1007/s10346-020-01581-6.
- York, A. R., D. Sulsky, and H. L. Schreyer (1999), The material point method for simulation of thin membranes, *International journal for numerical methods in engineering*, 44(10), 1429–1456.
- Zeng, Y., J. He, and Q. Liu (2001), The application of the perfectly matched layer in numerical modeling of wave propagation in poroelastic media, *Geophysics*, 66(4), 1258–1266.
- Zhan, Q., M. Zhuang, Y. Fang, Y. Hu, Y. Mao, W.-F. Huang, R. Zhang, D. Wang, and Q. H. Liu (2019), Full-anisotropic poroelastic wave modeling: A discontinuous galerkin algorithm with a generalized wave impedance, *Computer Methods in Applied Mechanics and Engineering*, 346, 288–311.

- Zhang, W., Z. hao Zhong, C. Peng, W. hai Yuan, and W. Wu (2021), Gpu-accelerated smoothed particle finite element method for large deformation analysis in geomechanics, *Computers and Geotechnics*, 129, 103,856, doi:<https://doi.org/10.1016/j.compgeo.2020.103856>.
- Zhang, X., Z. Chen, and Y. Liu (2016), *The material point method: a continuum-based particle method for extreme loading cases*, Academic Press.
- Zhang, Y., and M. N. Toksöz (2012), Computation of dynamic seismic responses to viscous fluid of digitized three-dimensional berea sandstones with a coupled finite-difference method, *The Journal of the Acoustical Society of America*, 132(2), 630–640.
- Zhang, Y., L. Song, M. Deffenbaugh, and M. N. Toksöz (2010), A finite difference method for a coupled model of wave propagation in poroelastic materials, *The Journal of the Acoustical Society of America*, 127(5), 2847–2855.
- Zhu, W., K. L. Allison, E. M. Dunham, and Y. Yang (2020), Fault valving and pore pressure evolution in simulations of earthquake sequences and aseismic slip, *Nature communications*, 11(1), 1–11.
- Zhu, X., and G. McMechan (1991), Numerical simulation of seismic responses of poroelastic reservoirs using biot theory, *Geophysics*, 56(3), 328–339.
- Zimmerman (2000), Coupling in poroelasticity and thermoelasticity, *International Journal of Rock Mechanics and Mining Sciences*, 37(1-2), 79–87.
- Zimmerman, R., and I. Main (2004), Hydromechanical behavior of fractured rocks, *InGeo*, 89, 363–422.
- Zimmerman, R. W. (1990), *Compressibility of sandstones*, Elsevier.
- Zoback, M. D., and S. M. Gorelick (2015), To prevent earthquake triggering, pressure changes due to co2 injection need to be limited, *Proceedings of the National Academy of Sciences*, 112(33), E4510–E4510.
- Zuo, Z., S. Gong, and G. Xie (2020), Numerical simulation of granular mixing in a rotary drum using a generalized interpolation material point method, *Asia-Pacific Journal of Chemical Engineering*, 15(2), e2426, doi:<https://doi.org/10.1002/apj.2426>, e2426 APJ-19-0407.R1.

Appendix A

Appendix A: S squirt flow in cracks with rough walls

Simón Lissa, Nicolás D. Barbosa, Eva Caspari, Yury Alkhimenkov, and Beatriz Quintal

Published ¹ in *Journal of Geophysical Research: Solid Earth*.

¹Lissa, S., et al. (2020). S squirt flow in cracks with rough walls. *Journal of Geophysical Research: Solid Earth*, 125, e2019JB019235, , doi:10.1029/2019JB019235.

Abstract

We explore the impact of roughness in crack walls on the P-wave modulus dispersion and attenuation caused by squirt flow. For that, we numerically simulate oscillatory relaxation tests on models having interconnected cracks with both simple and intricate aperture distributions. Their viscoelastic responses are compared with those of models containing planar cracks but having the same hydraulic aperture as the rough wall cracks. In the absence of contact areas between crack walls, we found that three apertures affect the P-wave modulus dispersion and attenuation: the arithmetic mean, minimum and hydraulic apertures. We show that the arithmetic mean of the crack apertures controls the effective P-wave modulus at the low- and high-frequency limits, thus representing the mechanical aperture. The minimum aperture of the cracks tends to dominate the energy dissipation process, and consequently, the characteristic frequency. An increase in the confining pressure is emulated by uniformly reducing the crack apertures, which allows for the occurrence of contact areas. The contact area density and distribution play a dominant role in the stiffness of the model and, in this scenario, the arithmetic mean is not representative of the mechanical aperture. On the other hand, for a low percentage of minimum aperture or in presence of contact areas, the hydraulic aperture tends to control the characteristic frequency. Analysing the local energy dissipation, we can more specifically visualise that a different aperture controls the energy dissipation process at each frequency, which means that a frequency-dependent hydraulic aperture might describe the squirt flow process in cracks with rough walls.

A.1 Introduction

The indirect geophysical characterisation of fluid-saturated rocks in subsurface has a fundamental role in several activities, such as the monitoring of radioactive waste disposal and of geological CO₂ sequestration, the exploration and production of geothermal energy and hydrocarbons, among others (*Klimentos, 1995; Rapoport et al., 2004; Metz et al., 2005; Tester et al., 2007*). In particular, rock pores such as micro-cracks are very important in this scenario since they can modify significantly the hydraulic and mechanical properties of fluid-saturated rocks. Seismic methods are widely used for rock characterisation given that seismic waves are strongly affected by the presence of fluid in the rock pores as well as by the characteristics of the pore space including pore volume, compliance, distribution, and connectivity. Frequently, the porosity of rocks is split into the contributions of stiff and compliant porosities *Müller et al. (2010)*. Pores having spherical geometries constitute the stiff porosity often referred to as the equant porosity. Compliant porosity is represented by pores of very low aspect ratio such as micro-cracks and grain contacts which can be observed, for example, in micro-CT images (e.g., *Madonna et al., 2013*). When a seismic wave propagates through a medium containing fluid saturated connected pores with different compliances, it can be significantly attenuated and dispersed due to squirt flow at the pore scale *O'Connell and Budiansky (1977); Murphy et al. (1986); Mavko and Jizba (1991); Dvorkin et al. (1995); Gurevich et al. (2010)*. In this scenario, the seismically induced pressure gradients between connected pores of dissimilar compliance are equilibrated through a fluid pressure diffusion (FPD) process. The consequent friction between particles of the viscous fluid dissipates energy. Squirt flow evidence at seismic and sonic frequencies were shown in laboratory experiments in which glycerine-saturated samples of Fontainebleau and Berea sandstones, as well as of limestones, were submitted to forced oscillations by *Subramaniyan et al. (2015); Borgomano et al. (2019); Chapman et al. (2019)*.

A variety of analytical squirt flow models considering different geometries of pore shapes and cracks has been developed (e.g., *O'Connell and Budiansky, 1977; Mavko and Jizba, 1991; Dvorkin et al., 1995; Chapman et al., 2002; Pride et al., 2004; Gurevich et al., 2010*). *Alkhimenkov et al. (2020a)* presented a comparison between numerical results and an analytical model for squirt flow. In general, accepted analytical models should reproduce the equations of *Gassmann (1951)* in the low frequency limit *Chapman et al. (2002)*. The reason is that at the relaxed state for undrained boundary conditions (low-frequency limit), the time of a half period of a passing wave allows for fluid pressure to equilibrate through FPD. At the unrelaxed state (high-frequency limit), the fluid pressure has no time to equilibrate during a half period of a passing wave and the elastic properties of the saturated material are predicted by the formulation of *Mavko and Jizba (1991)*, which assumes that no FPD occurs during the passage of the wave. At intermediate frequencies, FPD occurs inside the cracks during the passage of the wave and part of its energy is dissipated. Nevertheless, all analytical solutions assume smooth

walls for the cracks despite the fact that crack walls in rocks have been observed to present complex profiles including wall roughness and contact areas, irregular shapes, among others (e.g., *Pyrak-Nolte et al.*, 1987; *Jaeger et al.*, 2007). In view of this limitation, numerical analyses are the most adequate tools to quantitatively explore the impact of roughness in the crack walls on squirt flow and the resulting effective moduli dispersion and attenuation.

Digital rock physics (DRP) is a technique that consists of imaging (micro-CT) and digitising the pore space, as well as, the mineral rock matrix and using numerical simulations to obtain effective rock properties, such as, elastic moduli, permeability, electrical conductivity, among others. DRP has been frequently performed with the objective of reproducing experimental measurements (e.g., *Saenger et al.*, 2011; *Dvorkin et al.*, 2011; *Saenger et al.*, 2016). In the particular case of elastic moduli, results obtained using DRP methods are in general not able to reproduce the corresponding laboratory observations. This is usually attributed to either the dimension of micro-cracks being below the rock image resolution *Zhang and Toksöz* (2012); *Madonna et al.* (2013); *Das et al.* (2019), or to the filters and interpreter-dependent cut-offs applied during the segmentation process *Arena et al.* (2014). In any case, the roughness of crack walls tends to be largely underestimated during the digitalisation process. To date, the effects of underestimating or completely neglecting the roughness of crack wall remains unexplored. Recent attempts to account for these effects include the work of *Quintal et al.* (2019), which considered 2-D cracks having walls with asperities producing narrow throats, and showed that a shift of the attenuation peak to lower frequencies occurs due to the change of the aperture associated with the introduced asperities. This result points to the importance of quantifying the effects of crack asperities on squirt flow and the associated seismic response.

This work focus on studying the effects of crack roughness on squirt flow in terms of the effective P-wave modulus dispersion and attenuation of a rock model. For that, we numerically perform quasi-static, oscillatory relaxation tests following the numerical scheme proposed by *Quintal et al.* (2016, 2019). This approach employs the quasi-static, linearised Navier-Stokes equations to describe the fluid physics within the pore space coupled with the linear elasticity equations for the solid elastic material (grains) embedding the pore space. We consider 3D models having two hydraulically interconnected micro-cracks with rough walls. In such models, cracks are perpendicularly orientated and allowing for one of them to be highly compressed during the oscillatory tests (i.e., representing the compliant porosity of the model) and the other remains nearly unaffected by the compression (i.e., representing the stiff porosity of the model). First, we consider cracks with a binary distribution of apertures (i.e., crack aperture is allowed to have only two possible values). We then extend the analysis to crack models having more intricate distributions of the crack aperture *Nolte and Pyrak-Nolte* (1991). Finally, we investigate the expected changes due to an increase in the confining pressure emulated by reducing the crack apertures and allowing for the occurrence of contact areas. We provide a comprehensive analysis of the role played by the geometrical aperture distribution as well as by the hydraulic aperture of the cracks in the numerically obtained effective moduli and attenuation.

A.2 Methodology

A.2.1 Mathematical formulation

We quantify the effective P-wave modulus dispersion and attenuation due to squirt flow in cracked media. For that, we numerically apply quasi-static, oscillatory displacements on a model of cracked material. We follow the numerical approach of *Quintal et al.* (2016, 2019), which couples the elasticity equations for the solid background (representing the rock grains) with the quasi-static, linearised Navier-Stokes equations for the laminar flow of a viscous fluid in the cracks. We neglect inertial terms, which is valid considering that wavelengths are much bigger than the size of analysed numerical models. Viscous friction between fluid particles inside the cracks due to FPD is the only possible cause for energy dissipation. Additionally, in Appendix A we calculate the reduced Reynolds number *Zimmerman and Main* (2004) and verify the validity of employing the linearised Navier-Stokes equations for the fluid flow inside the cracks induced by oscillatory displacements.

We solve the conservation of momentum equation, which, neglecting inertial terms, reduces to

$$\nabla \cdot \boldsymbol{\sigma} = 0, \quad (\text{A.1})$$

where $\boldsymbol{\sigma}$ is the total stress tensor, considering a generalised constitutive equation, whose components in the frequency domain Quintal *et al.* (2019) are

$$\sigma_{kl} = 2\mu\epsilon_{kl} + \lambda e\delta_{kl} + 2i\omega\eta\epsilon_{kl} - \frac{2}{3}i\omega\eta e\delta_{kl}, \quad (\text{A.2})$$

where ϵ_{kl} are the components of the strain tensor, e is the cubical dilatation given by the trace of the strain tensor, δ_{kl} is the Kronecker delta, $\lambda = K - \frac{2}{3}\mu$ is the Lamé parameter written in terms of the bulk K and the shear μ moduli, η is the shear viscosity, ω is the angular frequency and i is the imaginary unit.

Eq. 2 is valid for the whole model since it is reduced to Hooke's law in the solid elastic background by setting the shear viscosity η to zero,

$$\sigma_{kl} = 2\mu\epsilon_{kl} + \lambda e\delta_{kl}, \quad (\text{A.3})$$

and, inside the cracks Eq. 2 is reduced to

$$\sigma_{kl} = Ke\delta_{kl} + 2i\omega\eta\epsilon_{kl} - \frac{2}{3}i\omega\eta e\delta_{kl}, \quad (\text{A.4})$$

because the shear modulus μ is zero in the fluid (e.g., Table A.1). Combining Eqs. 1 and 4 yields the quasi-static, linearised Navier-Stokes equations, which describe a Newtonian flow inside the cracks.

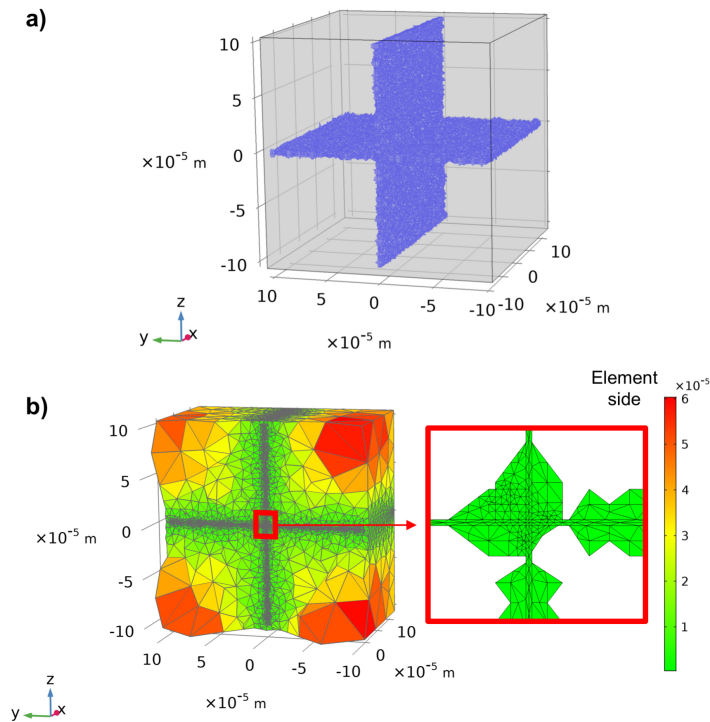


Figure A.1: a) Numerical model consisting of two perpendicular and hydraulically interconnected cracks of $200 \times 200 \times h \mu\text{m}^3$ embedded in a cubic non-porous solid elastic background of $210 \times 210 \times 210 \mu\text{m}^3$. b) Mesh of the numerical model coloured according to the side length of each tetrahedral element. The inset of panel b shows the meshing inside the cracks only.

Table A.1: Material properties of the models.

Properties	Solid	Fluid
Bulk modulus \mathcal{K} [GPa]	35	4.35
Shear modulus μ [GPa]	40	0
Fluid viscosity η [Pa · s]	0	1

A.2.2 Numerical upscaling

Our numerical models consist of two perpendicular cracks, that intersect each other at their centres, embedded in a solid elastic background representing the rock grains (Figure A.1a). These models are a representative elementary volume (REV) of periodic media consisting of a repetition of these fundamental blocks (Appendix B). We consider cracks having a length of $200 \mu\text{m}$ and, depending on the model, the apertures (h) varying from 0.3 to $2.7 \mu\text{m}$ (in the case of planar cracks that would be equivalent to aspect ratios that vary from 0.0015 to 0.0135). The REV is a cube of $210 \mu\text{m}$ side. These models build up media having porosities from 0.2% to 2% . We have chosen the approximate crack dimensions based on the statistical analysis of thermally cracked rock samples described by *Delle Piane et al.* (2015). We employ material properties of quartz for the grains *Mavko et al.* (2009) and of glycerin for the fluid filling the cracks (Table A.1), as commonly used in forced-oscillations laboratory experiments so that the frequencies at which maximal squirt flow effects are expected fall within the seismic frequency range. In order to study the role played by the roughness of the cracks on the squirt flow mechanism, the aperture distribution of the cracks has been generated following the approach introduced by *Nolte and Pyrak-Nolte* (1991). The full workflow for the model generation is described by *Lissa et al.* (2019).

To calculate the P-wave modulus dispersion and attenuation, we solve equations 1 and 2 using a finite element direct solver from COMSOL Multiphysics. The numerical models are discretised in tetrahedral elements with side length represented by the colour bar in Figure A.1b. The smallest elements are located inside the cracks, where energy dissipation occurs. The number of tetrahedral elements depends on the model. The number increases due to an increase in the wall roughness or due to a decrease in the aperture. This is because the mesh elements increase their size from the crack to the grains and, consequently, a smaller aperture, as well as a rough wall, require smaller element sizes. In general, the total number of elements is around $1'000'000$ for the cracks and $1'000'000$ for the grains. We numerically perform quasi-static relaxation tests by applying an oscillatory displacement at the top boundary of the models. Additionally, normal solid displacements are set to zero on the lateral and bottom boundaries of the models. Assuming an incident wavelength much bigger than the REV size, the effective P-wave modulus (H) in the vertical direction (z) and corresponding attenuation (Q^{-1}) are obtained by volumetrically averaging the vertical component of the stress and strain fields in the entire spatial domain *O'Connell and Budiansky* (1978):

$$H(\omega) = \frac{\langle \sigma_{zz}(\omega) \rangle}{\langle \epsilon_{zz}(\omega) \rangle}, \quad (\text{A.5})$$

$$Q^{-1}(\omega) = \frac{\langle \text{Im}[H(\omega)] \rangle}{\langle \text{Re}[H(\omega)] \rangle}, \quad (\text{A.6})$$

where $\langle \sigma_{zz}(\omega) \rangle$ and $\langle \epsilon_{zz}(\omega) \rangle$ represent the volumetric averages of σ_{zz} and ϵ_{zz} for each frequency *Lakes* (2009); *Jänicke et al.* (2015) and *Re* and *Im* correspond to the real and imaginary parts of a complex number.

Given that the crack tips in our numerical models are close to the model boundaries, elastic interaction effects between the cracks are expected to occur, which are accounted for in our numerical approach *Guo et al.* (2018b). Nevertheless, in some cases, the stress and strain fields in the sample and those imposed at the boundaries may not be compatible with the assumed periodicity, which is manifested as disturbed fields at the boundaries. We

performed a test for assessing possible undesired boundary effects *Milani et al. (2016)*. The test consists on comparing the effective P-wave modulus response of our model, or the repeating unity cell, with that of a model formed by an assembly of 4 identical repeating unity cells. The results, which are reported in Appendix B, show that there are no boundary artefacts affecting the numerical results.

A.2.3 Local energy dissipation

For a better understanding on how the energy dissipation occurs in the interconnected cracks, we calculated the local contribution $1/q_n$ to the total attenuation $1/Q$ from each element Ω_n of our 3D model as function of frequency as follows *Solazzi et al. (2016)*; *O'Connell and Budiansky (1978)*:

$$\frac{1}{q_n(\omega)} = \frac{\langle \Delta P_n(\omega) \rangle / \delta_n^3}{2\omega \langle W(\omega) \rangle}, \quad (\text{A.7})$$

where $\langle \Delta P_n(\omega) \rangle$ and $\langle W(\omega) \rangle$ are the average power dissipated per cycle in harmonic loading from each considered element of volume δ_n^3 and the average strain energy per cycle in the whole domain, respectively, given by *Quintal et al. (2019)*

$$\begin{aligned} \langle \Delta P_n(\omega) \rangle = 2\eta Re [& \dot{\epsilon}_{xx} \dot{\epsilon}_{xx}^* + \dot{\epsilon}_{yy} \dot{\epsilon}_{yy}^* + \dot{\epsilon}_{zz} \dot{\epsilon}_{zz}^* + \dot{\epsilon}_{xy} \dot{\epsilon}_{xy}^* + \dot{\epsilon}_{xz} \dot{\epsilon}_{xz}^* + \dot{\epsilon}_{yz} \dot{\epsilon}_{yz}^* \\ & - \frac{1}{3} (\dot{\epsilon}_{xx} + \dot{\epsilon}_{yy} + \dot{\epsilon}_{zz}) (\dot{\epsilon}_{xx} + \dot{\epsilon}_{yy} + \dot{\epsilon}_{zz})^*]_n \delta_n^3, \quad (\text{A.8}) \end{aligned}$$

and

$$\langle W(\omega) \rangle = \sum_{\Omega} \frac{1}{4} Re [\sigma_{xx} \dot{\epsilon}_{xx}^* + \sigma_{yy} \dot{\epsilon}_{yy}^* + \sigma_{zz} \dot{\epsilon}_{zz}^* + \sigma_{xy} \dot{\epsilon}_{xy}^* + \sigma_{xz} \dot{\epsilon}_{xz}^* + \sigma_{yz} \dot{\epsilon}_{yz}^*]_n \delta_n^3, \quad (\text{A.9})$$

where a dot on top of a variable implies the multiplication of the variable by $i\omega$ and the symbol * denotes the complex conjugate of the variable. The total attenuation can be obtained as the sum in the whole model of the local contribution $1/q_n$ weighted by each element volume, that is,

$$\frac{1}{Q(\omega)} = \sum_{\Omega} \frac{1}{q_n(\omega)} \delta_n^3. \quad (\text{A.10})$$

A.3 Results

We estimate the effective P-wave modulus dispersion and attenuation caused by squirt-flow between hydraulically interconnected cracks by numerically applying quasi-static, oscillatory relaxation tests to models such as the one shown in Figure A.1a. The squirt flow process is usually described as the compression of a compliant pore or crack which is connected to a stiffer one. In our models we consider vertical oscillatory compression emulating the deformation caused by a P-wave with vertical (z) incidence and a wavelength much bigger than the model. Consequently, the horizontal crack behaves as the compliant pore while the vertical one, which remains nearly undeformed, behaves as the stiff pore. We first consider a simple crack walls roughness which corresponds to a binary distribution of apertures in the cracks and, then, we extend the analysis to more complex roughness of the crack walls by considering fully variable apertures. In both cases, the cracks are completely open (i.e., no contact areas). We also compute the hydraulic apertures of the crack models according to the workflow described in Appendix C. The P-wave modulus and attenuation for planar cracks having such hydraulic apertures are compared with that of the binary and fully variable aperture crack models to help understanding the effects of rough crack walls. Finally, we emulate an increase in the confining pressure on certain models by applying a uniform reduction of the crack apertures which, in turn, creates contact areas.

A.3.1 Cracks with binary aperture distribution

First, we consider aperture distributions with only two possible aperture values. Figure A.2 shows a model of interconnected cracks having a minimum aperture, a maximum aperture and no intermediate ones, here referred to as a binary model. The cracks are embedded in a non-porous elastic solid cube as shown in Figure A.1a. We consider six different binary aperture distributions, which are illustrated in Figure A.3. Additionally, the cracks are symmetrical with respect to their central plane. In those models, the percentages of the crack having the minimum aperture of $0.3 \mu\text{m}$ are 2.5%, 5%, 7.5%, 10%, 20% and 50%, while the rest of the crack has the maximum aperture of $2.7 \mu\text{m}$. This means that cracks with 100% and 0% of minimum aperture h_{min} are planar cracks (i.e., have constant aperture) with apertures of $0.3 \mu\text{m}$ and $2.7 \mu\text{m}$, respectively.

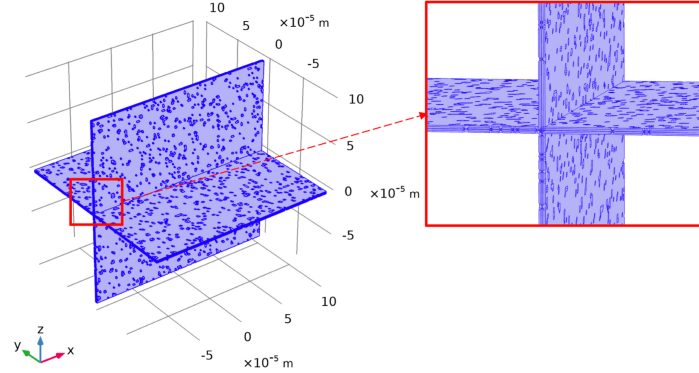


Figure A.2: Example of one model having two hydraulically interconnected cracks with a binary aperture distribution, i.e., only two apertures of $h_{min} = 0.3 \mu\text{m}$ (5% of crack area) and of $h_{max} = 2.7 \mu\text{m}$ (95% of crack area) are present. The distribution of the minimum aperture zones is uncorrelated.

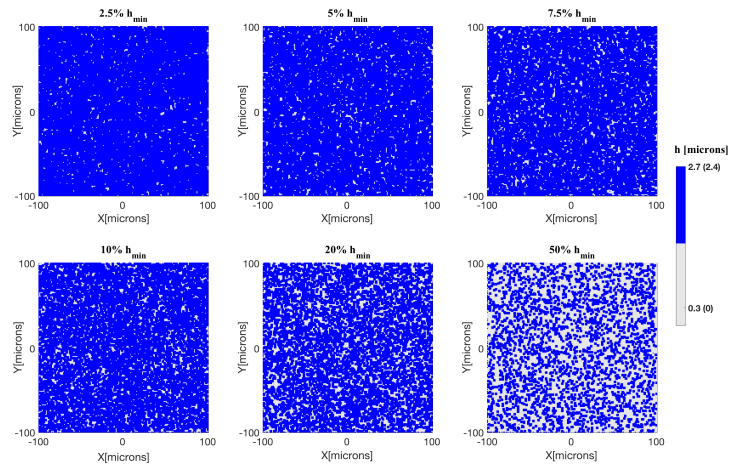


Figure A.3: Aperture distributions employed in the model of Figure A.2 containing two identical and perpendicular cracks with binary apertures: $h_{min} = 0.3 \mu\text{m}$ (varying from 2.5% to 50% of crack areas) and $h_{max} = 2.7 \mu\text{m}$ (for the remaining percentage of crack wall areas). In addition, the apertures between parenthesis correspond to the crack conditions after an increase of the confining pressure described in Section 3.3.

The P-wave modulus and corresponding attenuation in the vertical direction for the binary models, with aperture distributions shown in Figure A.3, are plotted in Figure A.4. The compression of the horizontal crack, due to the vertical deformation, generates a fluid pressure gradient between the highly compressed horizontal crack and the nearly undeformed vertical one. As a consequence, FPD occurs and energy is dissipated due to

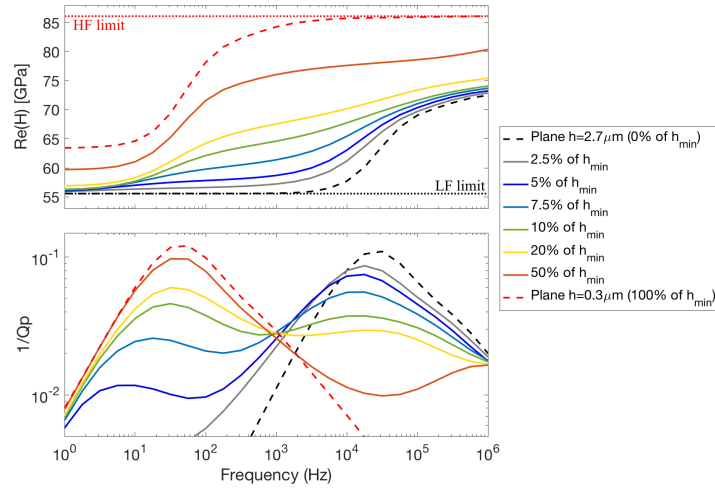


Figure A.4: Real part of the P-wave modulus $\text{Re}(H)$ and attenuation $1/Q_p$ as functions of frequency for the interconnected cracks presented in Figure A.3 and for pairs of interconnected planar cracks with aperture of 0.3 or 2.7 μm . In addition, P-wave modulus at low- and high-frequency limits following *Gassmann* (1951) and *Mavko and Jizba* (1991) approaches, respectively, are shown in dotted lines for the planar crack models having 0.3 μm (red dotted lines) and 2.7 μm (black dotted lines) of aperture.

friction between layers of the viscous fluid. For validation of our numerical simulations, we obtained the low- (LF) and high-frequency (HF) limits following the approaches of *Gassmann* (1951) and *Mavko and Jizba* (1991), respectively. In the first case, we numerically compute the anisotropic dry stiffness matrix from 6 relaxation test by extending the 2-D methodology of *Rubino et al.* (2016) to 3-D for the planar crack model having 2.7 μm of aperture and under dry conditions. Then, using Gassmann's equations, we calculate the saturated stiffness matrix (P-wave modulus with vertical incidence obtained from this analysis is shown as dotted black line). At the LF limit, the P-wave modulus depends on the porosity of the rock and, thus, it changes with the percentage of h_{min} . For the HF limit, we consider no hydraulic communication between cracks. For that, we employ a boundary condition within the cracks that restricts the fluid flow to zero between cracks. The numerically obtained P-wave modulus in the vertical direction for the saturated planar crack model having 0.3 μm of aperture is shown as red dotted line. The increase in the percentage of h_{min} in the crack aperture distributions, increases the P-wave modulus at the LF and HF limits, stiffening the models due to the reduction in the crack volume.

Considering now the attenuation responses, we observe in Figure A.4 (bottom) that the binary models having 5% to 20% of h_{min} exhibit two attenuation peaks at characteristic frequencies f_{c1} close to 10 Hz and f_{c2} close to 10^4 Hz. Based on theoretical solutions for the squirt flow characteristic frequency of the form $f_c \sim \frac{\kappa}{\eta} \left(\frac{h}{L}\right)^3$ (e.g., *Gurevich et al.*, 2010), the two attenuation peaks suggests that there are two characteristic aspect ratios or apertures playing a role in the energy dissipation. The characteristic frequency f_{c2} is located near to that observed for 0% of h_{min} (i.e., $h=2.7 \mu\text{m}$), while f_{c1} is closer to the characteristic frequency observed for 100% of h_{min} . The magnitude of the high-frequency attenuation peak decreases and the one of the low-frequency peak increases as the percentage of h_{min} in the crack aperture increases. Moreover, the transition between dominating peaks occurs for a percentage of h_{min} as low as 10%.

To gain a better understanding of where the energy dissipation occurs we apply the methodology described in Section 2.3. Figure A.5 shows the local contribution $1/q_n$ (Eq. 7) to the total attenuation $1/Q_p$ in horizontal slices within the horizontal crack for the model having 5% of the h_{min} at the frequencies $f_{c1}=10$ Hz and $f_{c2}=10^4$ Hz. The colour-bar range is fixed equally for both considered frequencies in order to clearly represent the magnitude differences. The colour plots correspond to two horizontal slices (xy -planes) at $z=0 \mu\text{m}$ (top) and $z=1.05 \mu\text{m}$ (middle). Despite the fact that $1/q_n$ is maximal in the cracks intersection for both frequencies, they present a minor contribution to the overall dissipation. At the bottom, the sum of the $1/q_n$ over each horizontal slice within the crack is plotted for both frequencies. In agreement with the attenuation curve in Figure A.4 (blue solid line), the local contribution $1/q_n$ corresponding to f_{c2} presents the highest magnitudes. Important

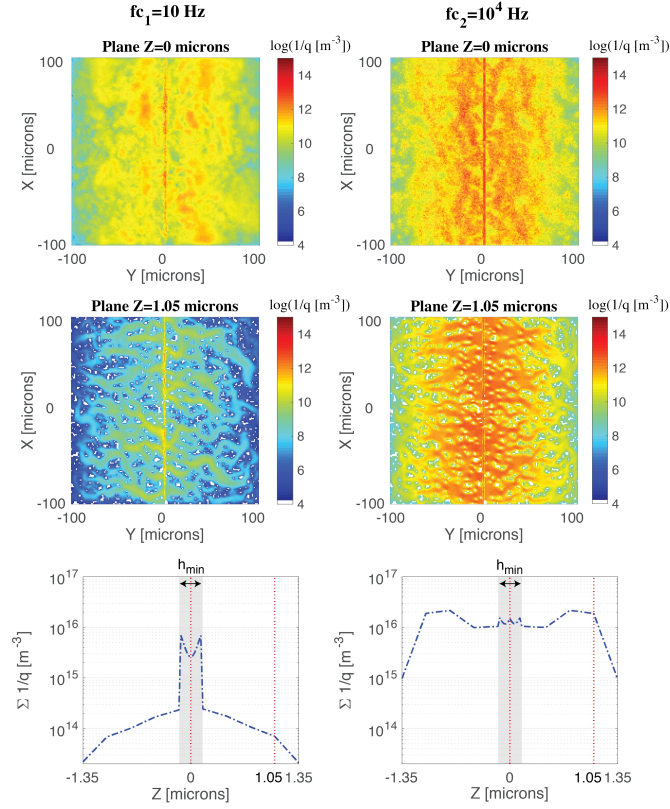


Figure A.5: Local contribution $1/q_n$ (Eq. 7) to the total attenuation $1/Q$ at $f_{c1} = 10$ Hz (left) and $f_{c2} = 10^4$ Hz (right) in two horizontal slices (xy -planes), at $z=0$ μm (top) and $z=1.05$ μm (middle), for the binary model of Figure A.3 having 5% of h_{min} . At the bottom, the sum of the $1/q_n$ for each horizontal slice within the crack is plotted for both frequencies.

differences regarding where energy is being dissipated can be observed for the two frequencies. Although energy dissipation is reasonably similar in the middle plane ($z=0$ μm) for both frequencies, there is a significant difference between them in the plane outside the aperture h_{min} , closer to the walls of the cracks ($z=1.05$ μm). Furthermore, dissipation is much more concentrated within $abs(z) < h_{min}$ at f_{c1} than at f_{c2} . From the sum of $1/q_n$ over each horizontal slice within the cracks (bottom), we observe for f_{c1} high concentration of energy dissipation within the minimum aperture (h_{min}) for the whole horizontal crack. Consequently, for the binary models (Figure A.4) the attenuation at f_{c1} is controlled by the minimum aperture while at f_{c2} the attenuation is controlled by a bigger aperture.

To better illustrate where energy dissipation occurs at each frequency within a crack for the model having 5% of the h_{min} , we calculate the sum of the local contribution to the attenuation in the horizontal crack as a function of z (vertical coordinate) at six frequencies (Figure A.6, top). The area under each curve after multiplying each $1/q_n$ by their element volume (i.e., δ_n^3) represents the contribution of the energy dissipation inside the horizontal crack to the total attenuation for the considered frequencies. Energy dissipation outside the minimum aperture, increases from low- to high-frequency until reaching its maximum at $f_{c2} = 10^4$ Hz. Although energy dissipation for $f = 10$ Hz is lowest outside h_{min} , inside the minimum aperture it reaches higher magnitudes similar to the other considered frequencies. Figure A.6 (bottom) shows the contribution to the total attenuation ($1/Qp$) taking place inside the minimum aperture (blue circles) as well as the total attenuation (green solid line) for the model having 5% of h_{min} . The excellent match between the curves at the low frequency peak confirms that the minimum aperture (h_{min}) has predominant control over attenuation at f_{c1} .

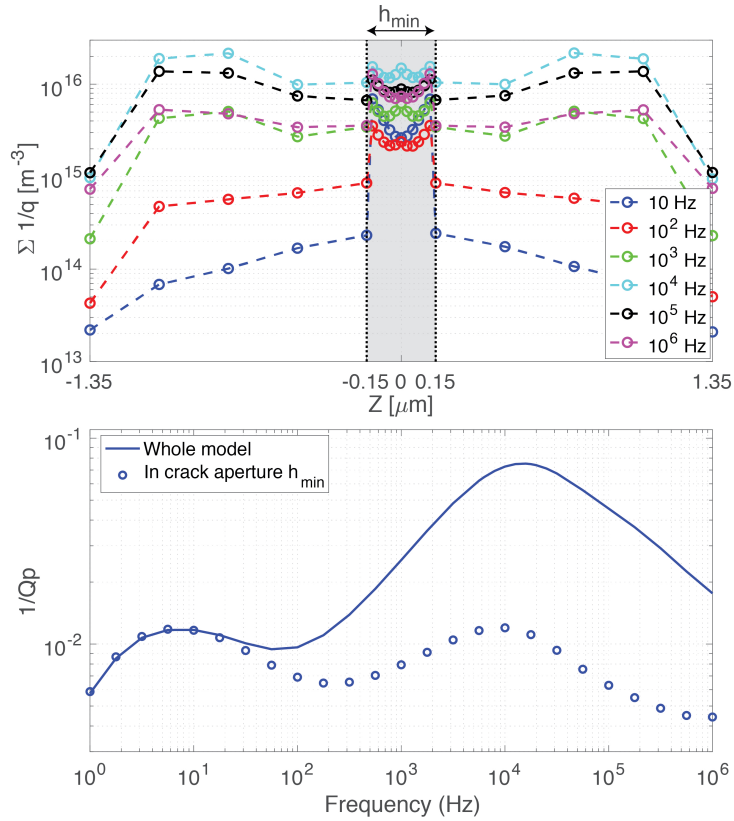


Figure A.6: Sum of the local attenuation contribution $1/q_n$ for each horizontal slice within the horizontal crack at six frequencies (top) and the total attenuation (blue solid line) with the volumetric integration of $1/q_n$ only inside aperture h_{min} (blue circles) as a function of frequency (bottom) for the binary model having 5% of h_{min} .

Effect of hydraulic apertures

Relating the hydraulic behaviour of a cracked-model with its P-wave modulus dispersion and attenuation requires quantifying the hydraulic transmissivity of the crack which is controlled by its aperture distribution. Even though the hydraulic transmissivity of the media considered in this work is zero, since the cracks are not in contact with the REV boundaries, the local transmissivity within each crack governs squirt flow between the connected cracks. We then focus on the fluid flow behaviour of each crack (the horizontal and vertical cracks are equal in our models). We use the numerical methodology described in Appendix C to obtain the hydraulic apertures for some of the binary models shown in Figure A.3.

Figure A.7 (top) shows the calculated arithmetic and harmonic mean of apertures, and hydraulic apertures for the binary models having from 5% to 70% of h_{min} in their aperture distributions. In agreement with *Beran* (1968); *Silliman* (1989); *Zimmerman and Main* (2004), our results for the hydraulic aperture are bounded by the arithmetic $\langle h^3 \rangle$ and harmonic $\langle h^{-3} \rangle^{-1}$ means. Most importantly, the hydraulic aperture takes values similar to the harmonic mean and much closer to h_{min} even though h_{min} represents less than 50% of the crack. Figure A.7 (bottom) shows the total attenuation magnitudes for the binary models at the two discussed characteristic frequencies, as function of h_{min} percentage. The attenuation at f_{c1} is higher than at f_{c2} already from 10% of h_{min} and from 50% it is close to the maximum value possible (that for the plane crack with 100% of h_{min} , Figure A.4). Thus, for these models, both the hydraulic aperture and the characteristic frequency of the maximum attenuation are predominantly governed by the minimum aperture once it exceeds 50%.

Figure A.8 shows the P-wave modulus dispersion and attenuation of the three binary models having 5%, 10% and 50% of h_{min} , together with that of three models having cracks with a constant aperture equal to the corresponding hydraulic apertures. The match between the dominating characteristic frequency (f_{c2}) of the binary model with 5% of h_{min} (blue curves) and that one of a model with planar cracks whose aperture is equal

to the hydraulic aperture indicates that the latter controls the main attenuation peak caused by squirt-flow in this model. When there is not a clear dominating attenuation peak, such as, for 10% of h_{min} (green curves), the f_c of the planar model having the hydraulic aperture is still located close to f_{c2} . The f_c of the binary model having 50% of h_{min} , on the other hand, matches the f_{c1} corresponding to an aperture of 100% of h_{min} or $h = 0.3 \mu\text{m}$ (shown in Figure A.4). Meanwhile, the planar model having the hydraulic aperture of the model with 50% of h_{min} predicts a characteristic frequency located one order of magnitude higher than that of the corresponding binary model. Which emphasizes that it is the h_{min} , and not the hydraulic aperture, the one controlling the energy dissipation process for this model.

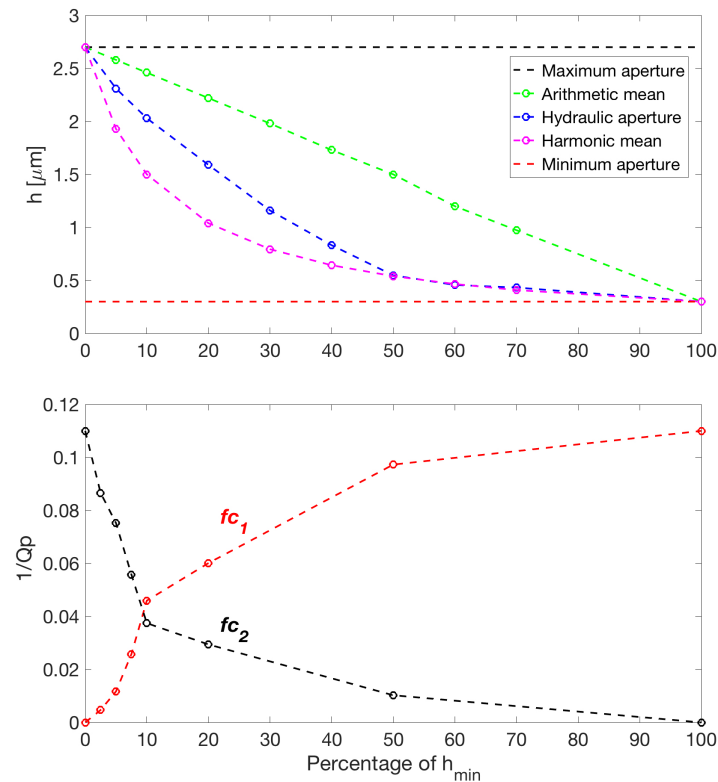


Figure A.7: Arithmetic mean, harmonic mean and hydraulic apertures for binary model having from 5% to 70% of h_{min} in their apertures. Also $h_{min}=0.3 \mu\text{m}$ and $h_{max}=2.7 \mu\text{m}$ are plotted in dashed lines for reference (top). Seismic attenuation ($1/Qp$) for the binary models of Figure A.3 at the characteristic frequencies as functions of h_{min} (bottom).

A.3.2 Cracks with more intricate rough walls

The analysis presented in Section 3.1 deals with simple models to understand the effects that cracks with rough walls have on squirt flow. However, their abrupt changes in aperture are expected to unrealistically enhance the influence of the aperture variation. In this section we consider more realistic aperture distributions (Figure A.9), but still considering symmetric rough walls. The two numerical models A and B have cracks with fully variable apertures, with 20% of $h_{min} = 0.3 \mu\text{m}$ and equal arithmetic mean aperture $h_{mean} = 2.7 \mu\text{m}$. Model A presents a regular distribution of zones having apertures equal to h_{min} (white zones), which we refer to as uncorrelated distribution, while Model B has the zones with h_{min} gathered in broader areas, i.e., correlated distribution. To quantify the amount of variation of their apertures, we compute the standard deviation (std). Model B has a higher standard deviation ($std_B=2.55 \mu\text{m}$) than Model A ($std_A=1.9 \mu\text{m}$). Figure A.10 (top) shows the real part of the P-wave modulus and attenuation for both models. For comparison, the same curves of planar crack models having crack apertures equal to h_{min} and h_{mean} are also included. The P-wave modulus

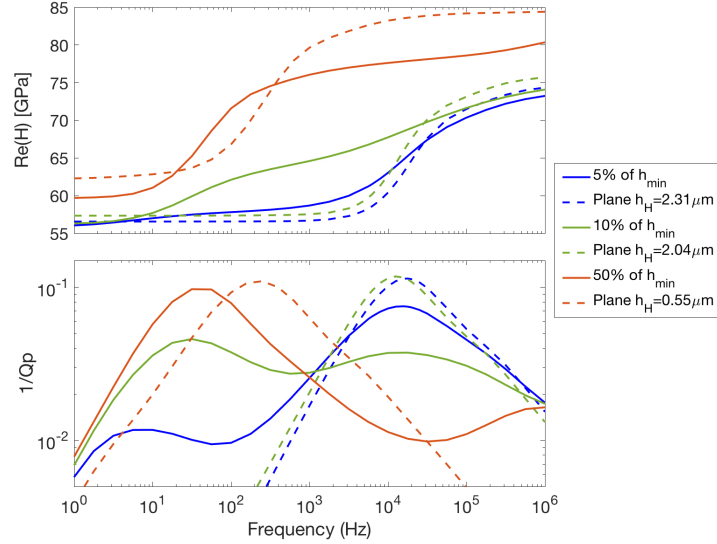


Figure A.8: Real part of the P-wave modulus and attenuation for binary models having 5%, 10% and 50% of h_{min} (solid lines) and the ones corresponding to planar crack models having their equivalent hydraulic apertures, that is $h_H=2.31 \mu\text{m}$, $h_H=2.04 \mu\text{m}$ and $h_H=0.55 \mu\text{m}$, respectively (dashed lines).

Table A.2: Apertures for crack models presented in Figure A.9

Model	Minimum	Arithmetic mean	Hydraulic
A	$h_{min} = 0.3 \mu\text{m}$	$h_{mean} = 2.7 \mu\text{m}$	$h_H = 1.31 \mu\text{m}$
B	$h_{min} = 0.3 \mu\text{m}$	$h_{mean} = 2.7 \mu\text{m}$	$h_{Hx} = 1.28 \mu\text{m}$; $h_{Hy} = 1.92 \mu\text{m}$

at the LF and HF limits of both models tend to converge to that of the planar crack model having the same mean aperture h_{mean} (black dashed curve). Due to the absence of contact areas, the crack density (given by the number of cracks and their surface in a certain volume) controls the stiffness of the models *Kachanov and Mishakin* (2019). The crack density is high and equal in all our models, which means that the difference in their stiffness is controlled by the difference in the crack volumes of the models. Moreover, provided that all models have the same area in the xy -plane ($200 \times 200 \mu\text{m}^2$), the arithmetic mean of the apertures is the only geometrical parameter controlling the crack volumes. Therefore, we refer to the aperture controlling the elastic response of the fracture (h_{mean}) as the mechanical aperture. Interestingly, Model A has a clearly defined dominating attenuation peak in the considered frequency range while Model B presents a broader attenuation curve. This is explained by the fact that Model B has a higher standard deviation of the crack aperture than Model A, which implies that more crack apertures are playing a role in the attenuation response. Figure A.10 also shows the P-wave modulus dispersion and attenuation of planar crack models having the hydraulic apertures of Model A and B (A.2). The characteristic frequency of the planar crack model with aperture h_H in y -direction, which is the same as the fluid flow in the oscillatory test for Model B, matches the frequency range corresponding to the maximum attenuation for Model B. On the other hand, the characteristic frequency of Model A, which is dominated by h_{min} , is significantly lower than the one associated with the planar crack model with aperture h_H . This means that the distribution of zones having apertures equal to h_{min} (i.e., correlated or uncorrelated) also plays a role in the characteristic frequency.

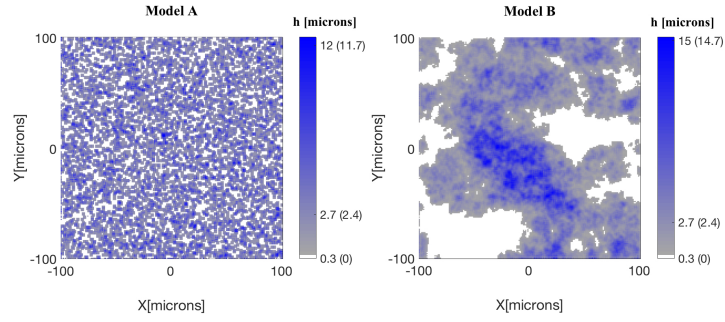


Figure A.9: Aperture of cracks having rough walls with uncorrelated (Model A) and correlated (Model B) distributions of zones of minimum aperture $h_{min} = 0.3 \mu\text{m}$ (white zones). In addition, the apertures between parenthesis correspond to the crack conditions after an uniform reduction in the apertures that emulates an increase of the confining pressure.

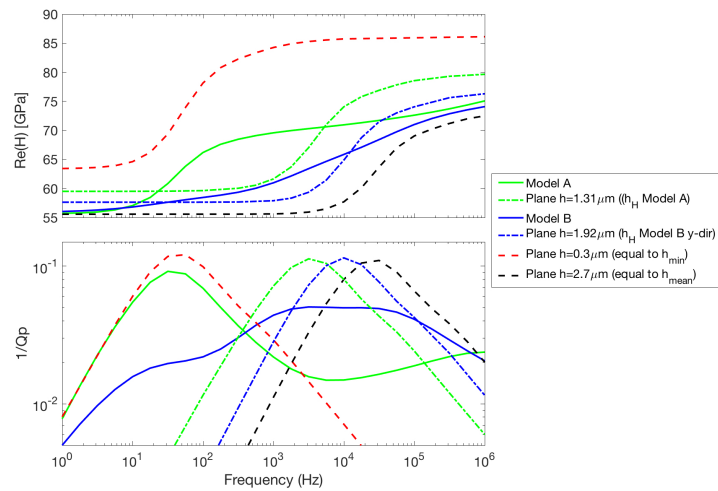


Figure A.10: Real part of the P-wave modulus and attenuation as functions of frequency for the interconnected cracks presented in Figure A.9 and for interconnected planar cracks having the minimum, the mechanical and the hydraulic apertures of the Models A and B.

A.3.3 Cracks with contact areas

Laboratory measurements of seismic attenuation on fluid-saturated rock samples are usually obtained under variable confining pressure at ranges affecting the rocks in subsurface (e.g., *Subramaniyan et al.*, 2015; *Chapman et al.*, 2019). The increase of confining pressure on cracked rock samples produces the occurrence of contact areas between crack walls or compliant pores, which in turns increases the overall stiffness of the rock *Shapiro* (2003). For analysing the corresponding effects on squirt-flow, we emulate an increase in confining pressure by introducing an uniform reduction in the crack apertures.

We first consider the binary uncorrelated crack models of Figure A.3 having 5% and 10% of $h_{min}=0.3 \mu\text{m}$ and we apply a uniform reduction of $0.3 \mu\text{m}$. This yields a reduction of the maximum aperture from 2.7 to $2.4 \mu\text{m}$ and the occurrence of 5% and 10% of contact area density (CAD), respectively (apertures in brackets in the colour bar of Figure A.3). We numerically estimate the hydraulic apertures of those models following the methodology outlined in Appendix C (Table A.3). Figure A.11 shows the P-wave modulus dispersion and attenuation for the considered models with and without contact areas, emulating their opening state before and after an increase in the confining pressure, as well as the response of planar crack models having the hydraulic aperture of the models with contact areas. The increase in the confining pressure produces a stiffening of the cracks, as seen from the overall reduction of P-wave modulus dispersion and attenuation. As expected, such effects are larger for the model with 10% of CAD due to the further reduction in pore space. In addition, the low-frequency

Table A.3: Apertures for crack binary models with contact areas

Model	Minimum	Maximum	Arithmetic Mean	Hydraulic
5% CAD	$h_{min} = 0 \mu\text{m}$	$h_{max} = 2.4 \mu\text{m}$	$h_{mean} = 2.28 \mu\text{m}$	$h_H = 2.12 \mu\text{m}$
10% CAD	$h_{min} = 0 \mu\text{m}$	$h_{max} = 2.4 \mu\text{m}$	$h_{mean} = 2.16 \mu\text{m}$	$h_H = 1.85 \mu\text{m}$

attenuation peak vanishes due to the closure of the minimum aperture. The characteristic frequencies of the planar crack models with the corresponding hydraulic apertures are in qualitative agreement with that of the models with contact areas. Nevertheless, significant discrepancies between their attenuation magnitude can be observed, which emphasises the necessity of employing three apertures to describe the squirt flow process: the mechanical aperture governing the P-wave magnitude at the frequency limits (we showed that it is the mean aperture in absence of contact areas), and the minimum and hydraulic apertures having control on the characteristic frequencies of the attenuation curve. In presence of contact areas (i.e., $h_{min}=0 \mu\text{m}$), only the mechanical and hydraulic apertures control the squirt flow effects.

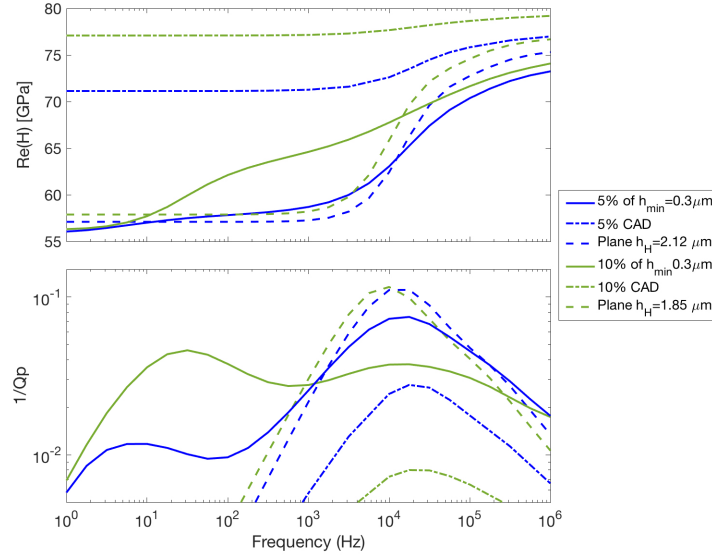


Figure A.11: Real part of the P-wave modulus and attenuation as functions of frequency for the interconnected cracks presented in Figure A.3 having 5% and 10% of contact area density (CAD) and for interconnected planar cracks having their equivalent hydraulic apertures. Same curves of those models with binary aperture before the emulated confining pressure increment are also included.

We extended the analysis of contact area effects to the models with fully variable apertures presented in Figure A.9. A uniform reduction in their apertures of $0.3 \mu\text{m}$ closes the cracks in the areas with previous apertures of h_{min} and equally reduces the rest of their aperture. Therefore, both models have 20% of contact area density after an increase in the confining pressures. Table A.4 shows their relevant apertures and Figure A.12 presents their P-wave modulus dispersion and attenuation. The responses from planar crack models having their hydraulic aperture as well as models from Figure A.9 without contact areas are also included in the analysis. From the analysis of Figure A.10, we know that the attenuation of Model A occurs mostly at low-frequencies, being governed by the minimum aperture. Given that the increase in the confining pressure closes the minimum aperture, Figure A.12 shows that Model A with contact areas presents negligible P-wave modulus dispersion and attenuation. For the same reason, the emulated increase in the confining pressure in Model B concentrates most of the remaining attenuation at high-frequencies. Comparison between Model B with contact areas and that of

Table A.4: Apertures for crack models with contact areas presented in Figure A.9

Model	Minimum	Arithmetic Mean	Hydraulic
A with CA	$h_{min} = 0 \mu\text{m}$	$h_{mean} = 2.4 \mu\text{m}$	$h_H = 1.11 \mu\text{m}$
B with CA	$h_{min} = 0 \mu\text{m}$	$h_{mean} = 2.4 \mu\text{m}$	$h_{Hy} = 1.5 \mu\text{m}$

the planar cracks having its hydraulic aperture h_H present relatively large discrepancies on their attenuation and P-wave modulus magnitudes.

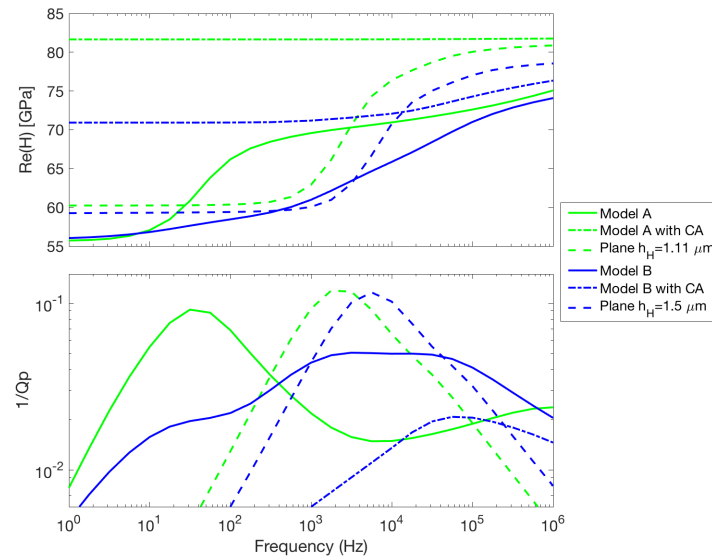


Figure A.12: Real part of the P-wave modulus and attenuation as functions of frequency for the interconnected cracks presented in Figure A.9 having 20% of contact areas and for interconnected plane cracks having their hydraulic apertures. Same curves of Models A and B before the emulated confining pressure increment are also included.

A.4 Discussion

The aim of the present contribution was to analyse the effects that the roughness of the crack walls has on the P-wave modulus dispersion and attenuation caused by squirt flow and to investigate whether there are certain crack apertures that could be used to interpret this physical process. The considered numerical models are in the micro-scale, or pore scale. We followed the proposed hydromechanical approach of *Quintal et al.* (2016, 2019) coupling the equations of an elastic background, and fluid filled cracks described by the quasi-static, linearised Navier-Stokes (LNS) equations. *Quintal et al.* (2016) showed an equivalency between the results based on the LNS and poroelastic Biot's equations at the mesoscale. Therefore, it is expected that similar results as those observed for micro cracks in this study hold for mesoscale fractures exhibiting rough walls.

The roughness in the crack walls considered in our first models was not allowed to produce contact areas. Such constrain implies that the volume of the cracks controls the P-wave modulus values at the LF and HF limits. Therefore, the P-wave modulus of the models with rough cracks (Models A and B) converge to those of a model with planar cracks having their mean aperture at the LF and HF limits. This means that the mechanical aperture

is represented by the arithmetic mean aperture without influence of the wall roughness. The inclusion of contact areas increases the model stiffness and, then, contact areas density and distribution start playing a role on the effective response of the models (e.g., *Hudson and Liu, 1999*). By analysing the attenuation curves, we observed that the occurrence of contact areas significantly reduces the attenuation magnitude and that their stiffening effects are higher for Model A, which has an uncorrelated aperture distribution, than for Model B which has a correlated one. For Model B, the aperture reduction giving rise to contact areas resulted in significant changes in the P-wave modulus dispersion and attenuation. On the other hand, since the attenuation for Model A was dominated by the minimum aperture, the aperture reduction caused the magnitude of attenuation to be reduced to negligible levels.

Our results show that rock image simplifications or errors commonly associated with DRP methods can significantly affect the calculations of the P-wave modulus dispersion and attenuation as well as the hydraulic transmissivity of cracks. For the analysed binary models, for example, we observed that a minor change in the percentage of h_{min} (from 5% to 20%) can shift the attenuation peak from 10^4 Hz to 10 Hz. In addition, we show that the characteristic frequency is not controlled by the arithmetic mean aperture of the cracks having rough walls. This relevant observation must be considered when crack apertures are estimated from the characteristic frequency, for example, in laboratory experiments. Effects of roughness of crack walls, as well as the contact area distribution, need to be accounted for when comparing certain experimental measurements with DRP estimations.

In analytical solutions for computing seismic attenuation and moduli dispersion due to squirt-flow, the characteristic frequency corresponding to the attenuation peak is related to the cubic of an aperture h (among other parameters), which is the aperture of a crack with smooth parallel walls (e.g., *Gurevich et al., 2010*). Based on those analytical solutions, the characteristic frequencies of all the planar crack models considered in this work can be approximated as $f_c \sim \frac{1}{2} \frac{K_S}{\eta} \left(\frac{h}{L}\right)^3$, where K_S is the bulk modulus of the solid (i.e., rock grains), η the fluid viscosity, h the aperture of the cracks and L is the diameter of a penny-shape crack having the same surface as our rectangular cracks (i.e., $L=226 \mu\text{m}$). Our work showed that the characteristic frequency of cracks with rough walls is mostly related to the minimum aperture h_{min} and/or the hydraulic aperture h_H depending on the percentage of h_{min} present in the crack and on the presence of contact areas. Moreover, we showed that each aperture present in the crack aperture distribution makes a contribution to the attenuation curve. In other words, there is a different aperture dominating the attenuation at each frequency. Therefore, assuming a link between aperture and the fluid flow at a given frequency, a frequency-dependent hydraulic aperture could be considered for squirt flow. At the mesoscale, a frequency-dependent hydraulic conductivity for transient (oscillatory) flow is not a new concept (e.g., *Dagan, 1982; Sanchez-Vila et al., 2006; Caspari et al., 2013*). However, the numerically estimated hydraulic apertures of our work consider a stationary fluid flow inside the rough cracks. Since the P-wave modulus dispersion and attenuation respond to a frequency dependent phenomenon, the comparison between both approaches might not be completely fair. Nevertheless, our work highlights the importance of analysing the relation between the frequency dependent attenuation caused by squirt flow and the hydraulic aperture of the cracks.

A.5 Conclusions

We studied the effects that roughness in the crack walls have on squirt-flow by numerically simulating oscillatory relaxation tests on models containing interconnected cracks. Their effects were analysed in terms of the effective P-wave modulus dispersion and attenuation. We first considered models having cracks with wall roughness described as binary aperture distributions, which allowed for the occurrence of only two apertures: h_{min} and h_{max} . In a step towards more complex models, we analysed the effects of two models with fully variable aperture of the cracks between h_{min} and h_{max} having correlated and uncorrelated distributions of h_{min} zones. At last, we emulated an increase in the confining pressure on those models by reducing the crack apertures, which allowed for the occurrence of contact areas. Additionally, we interpreted our results using a numerically estimated hydraulic aperture h_H of the considered rough cracks.

We observed that in absence of contact areas the arithmetic mean aperture of the cracks controls the stiffness of the models (P-wave modulus) at the high- and low-frequency limits. In addition, visualising the local contribution to the total attenuation curve, we observed that at each frequency a different aperture controls

the energy dissipation process caused by squirt flow. This means that the higher the standard deviation of the aperture distribution is, the broader the attenuation curve will be. Moreover, we identified two main apertures controlling the peak frequencies of the attenuation curve. Predominantly, the minimum aperture h_{min} tends to govern the energy dissipation process, but in presence of contact areas or with significantly small percentage of h_{min} , the hydraulic aperture h_H might control the characteristic frequency.

A.6 Acknowledgments

This research has been supported by the Swiss National Science Foundation (grant no. 172691). We thank Holger Steeb for insightful discussions and Santiago G. Solazzi and J. Germán Rubino for useful suggestions. The data for this paper are available online (at <http://doi.org/10.5281/zenodo.3573817>).

A.7 Appendix

A.7.1 Reduced Reynolds number

We calculated the reduced Reynolds number *Zimmerman and Main* (2004)

$$Re^* = \frac{\rho U h}{\eta \Lambda}, \quad (\text{A.11})$$

that is the product of the traditional Reynolds number and the geometric parameter $\frac{h}{\Lambda}$, where ρ and η are the bulk density and viscosity of the fluid, U is the average velocity in the main flow direction, h is the mean crack aperture and Λ is the mean distance between asperities of the walls of the cracks.

According with *Zimmerman and Main* (2004), the condition for the inertia forces to be negligible compared with the viscous forces is that $Re^* \ll 1$. An upper limit for Re^* for the cases considered in our study corresponds to the binary model having 50% of h_{min} as it is the one having the minimum $\Lambda=0.01 \mu\text{m}$. As U increases with the frequency, we compute Re^* for the maximum considered frequency (i.e., 10^6 Hz of the oscillatory displacement). For the described case and a strain on the model of 10^{-5} (similar to the ones impose in laboratory experiments), we obtained $U \approx 5 \times 10^{-5}$ and $Re^* \approx 1 \times 10^{-5}$, which comfortably satisfy the condition for the inertia forces to be negligible compared with the viscous forces.

A.7.2 REV boundary effects

Given the dimensions of the numerical model used for our analysis, we followed the methodology employed by *Milani et al.* (2016) to verify the absence of boundary effects affecting the results. For that, we consider our REV (Figure A.1) to be a repeating unit cell (RUC) and created a model consisting of four RUCs as shown in Figure A.13. Following the methodology presented in Section 2 we calculate the P-wave modulus and the attenuation for models consisting of one and four RUCs having planar crack with an aperture of $2.7 \mu\text{m}$. The choice of such an aperture is based on the fact that this model is the most compliant from all the considered models in this work and, consequently, the most likely to present boundary effects as shown by *Milani et al.* (2016). In addition, the configuration of the composited RUCs model looks for maximise boundary effects given that the distance between the vertical cracks of two consecutive RUCs is minimal.

Figure A.14 shows a negligible discrepancy between numerical results for the models composed by one and four RUCs. These results validate the consideration of all the numerical models presented in this work as REV. Moreover, it verifies the fact that no considerable boundary effects are affecting the presented results.

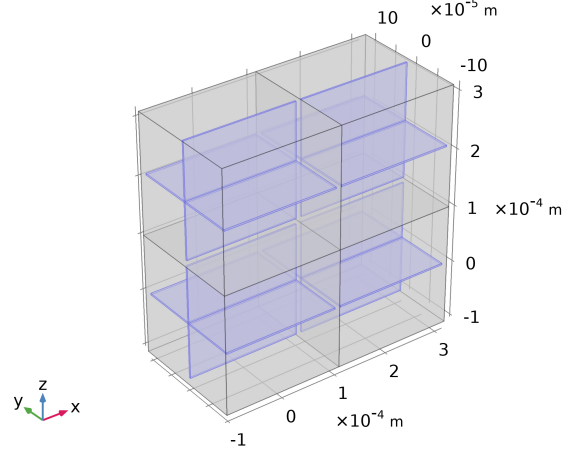


Figure A.13: Model composed by four RUCs as the one presented in Figure A.1 having two planar cracks with $2.7 \mu\text{m}$ of aperture.

A.7.3 Hydraulic aperture

As part of our analysis, we compute the effective hydraulic aperture of the different cracks considered in this work. This allows us to interpret the seismic responses in terms of hydraulic properties of the cracks. We combine the cubic law and Darcy's law to obtain the hydraulic aperture (h_H) of our crack models *Jaeger et al.* (2007),

$$h_H^3 = -\frac{Q_y 12\eta}{w \nabla p_y} \quad (\text{A.12})$$

where Q_y and ∇p_y are the volumetric flux and the fluid pressure gradient for the horizontal crack, respectively, in the fluid flow direction (i.e., y -direction) and w is the crack length in the horizontal direction normal to the fluid flow (i.e., x -direction). To obtain Q_y , we solve Stokes equations (neglecting inertial terms), using the finite element software COMSOL Multiphysics, for laminar incompressible flow within a horizontal crack. This test is performed in time domain and the fluid flow is stationary. The numerical estimation of the hydraulic aperture of a crack is obtained by applying a constant fluid pressure gradient ∇p_y between two opposite boundaries of a single crack. We measure Q_y at the crack boundary having the lowest fluid pressure. Unlike the numerical test previously described, there is no solid deformation in this test. Additionally, no slip boundary conditions are applied to the crack walls. Finally, we use Eq. C1 to obtain the crack hydraulic aperture.

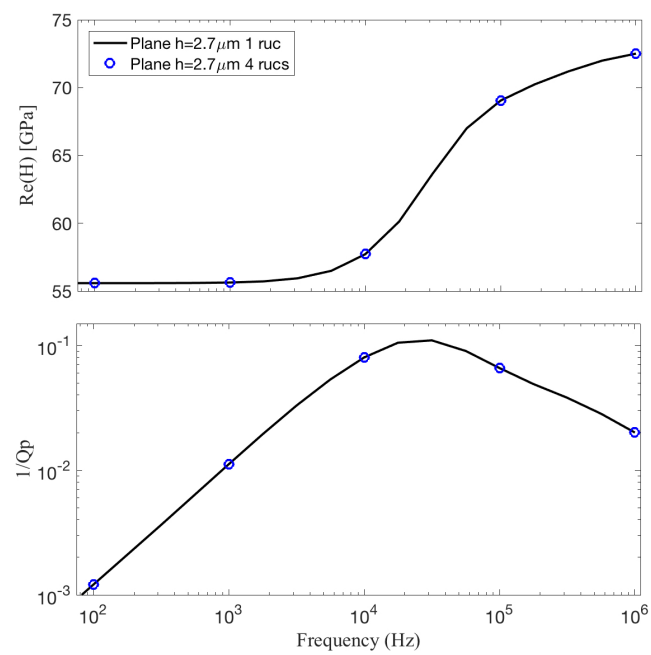


Figure A.14: Real part of the P-wave modulus $\text{Re}(H)$ and attenuation $1/Q_p$ as functions of frequency for two models composed by one and four RUCs (as the one presented in Figure A.13) having planar cracks with $2.7\ \mu\text{m}$ of aperture.

Appendix B

Appendix B: Fast and efficient MATLAB-based MPM solver (fMPMM-solver v1.1)

Emmanuel Wyser, Yury Alkhimenkov, Michel Jaboyedoff and Yury Podladchikov

Published ¹ in *Geoscientific Model Development*.

¹Wyser, E., et al. (2020). Fast and efficient MATLAB-based MPM solver (fMPMM-solver v1.1). *Geoscientific Model Development*, **13**(12), 6265-6284, doi:10.5194/gmd-13-6265-2020.

Abstract

We present an efficient MATLAB-based implementation of the material point method (MPM) and its most recent variants. MPM has gained popularity over the last decade, especially for problems in solid mechanics in which large deformations are involved, i.e., cantilever beam problems, granular collapses, and even large-scale snow avalanches. Although its numerical accuracy is lower than that of the widely accepted finite element method (FEM), MPM has been proven useful in overcoming some of the limitations of FEM, such as excessive mesh distortions. We demonstrate that MATLAB is an efficient high-level language for MPM implementations that solve elasto-dynamic and elasto-plastic problems. We accelerate the MATLAB-based implementation of MPM method by using the numerical techniques recently developed for FEM optimization in MATLAB. These techniques include vectorisation, the usage of native MATLAB functions, the maintenance of optimal RAM-to-cache communication, and others. We validate our in-house code with classical MPM benchmarks including i) the elastic collapse under self-weight of a column, ii) the elastic cantilever beam problem, and iii) existing experimental and numerical results, i.e., granular collapses and slumping mechanics respectively. We report a performance gain by a factor of 28 for a vectorised code compared to a classical iterative version. The computational performance of the solver is at least 2.8 times greater than those of previously reported MPM implementations in Julia under a similar computational architecture.

B.1 Introduction

The material point method (MPM), developed in the 1990s (*Sulsky et al.*, 1994), is an extension of a particle-in-cell (PIC) method to solve solid mechanics problems involving massive deformations. It is an alternative to Lagrangian approaches (updated Lagrangian finite element method) that is well suited to problems with large deformations involved in geomechanics, granular mechanics or even snow avalanche mechanics. *Vardon et al.* (2017); *Wang et al.* (2016a) investigated elasto-plastic problems of strain localization of slumping processes relying on an explicit or implicit MPM formulation. Similarly, *Bandara et al.* (2016); *Bandara and Soga* (2015); *Abe et al.* (2014) proposed a poro-elasto-plastic MPM formulation to study levee failures induced by pore pressure increases. Additionally, *Baumgarten and Kamrin* (2019); *Dunatunga and Kamrin* (2017, 2015); *Więckowski* (2004) proposed a general numerical framework of granular mechanics, i.e., silo discharge or granular collapses. More recently, *Gaume et al.* (2019, 2018) proposed a unified numerical model in the finite deformation framework to study the whole process, i.e., from failure to propagation, of slab avalanche releases.

The core idea of MPM is to discretize a continuum with material points carrying state variables (e.g., mass, stress, and velocity). The latter are mapped (accumulated) to the nodes of a regular or irregular background FE mesh, on which an Eulerian solution to the momentum balance equation is explicitly advanced forward in time. Nodal solutions are then mapped back to the material points, and the mesh can be discarded. The mapping from material points to nodes is ensured using the standard FE hat function that spans over an entire element (*Bardenhagen and Kober*, 2004). This avoids a common flaw of FEM, which is an excessive mesh distortion. We will refer to this first variant as the standard material point method (sMPM).

MATLAB[®] allows a rapid code prototyping but, at the expense of significantly lower computational performances than compiled language. An efficient MATLAB implementation of FEM called MILAMIN (Million a Minute) was proposed by *Dabrowski et al.* (2008) that was capable of solving two-dimensional linear problems with one million unknowns in one minute on a modern computer with a reasonable architecture. The efficiency of the algorithm lies on a combined use of vectorised calculations with a technique called blocking. MATLAB uses the Linear Algebra PACKages (LAPACK), written in Fortran, to perform mathematical operations by calling Basic Linear Algebra Subroutines (BLAS, *Moler* 2000). The latter results in an overhead each time a BLAS call is made. Hence, mathematical operations over a large number of small matrices should be avoided and, operations on fewer and larger matrices preferred. This is a typical bottleneck in FEM when local stiffness matrices are assembled during the integration point loop within the global stiffness matrix. *Dabrowski et al.* (2008) proposed an algorithm, in which a loop reordering is combined with operations on blocks of elements to address this bottleneck. However, data required for a calculation within a block should entirely reside in the CPUs cache. Otherwise, an additional time is spent on the RAM-to-cache communication and the performance

decreases. Therefore, an optimal block size exists and, is solely defined by the CPU architecture. This technique of vectorisation combined with blocking significantly increases the performance.

More recently, *Bird et al.* (2017) extended the vectorised and blocked algorithm presented by *Dabrowski et al.* (2008) to the calculation of the global stiffness matrix for Discontinuous Galerkin FEM considering linear elastic problems using only native MATLAB functions. Indeed, the optimisation strategy chosen by *Dabrowski et al.* (2008) also relied on non-native MATLAB functions, e.g., `sparse2` of the SuiteSparse package (*Davis*, 2013). In particular, *Bird et al.* (2017) showed the importance of storing vectors in a column-major form during calculation. Mathematical operations are performed in MATLAB by calling LAPACK, written in FORTRAN, in which arrays are stored in column-major order form. Hence, element-wise multiplication of arrays in column-major form is significantly faster and thus, vectors in column-major form are recommended, whenever possible. *Bird et al.* (2017) concluded that vectorisation alone results in a performance increase between 13.7 and 23 times, while blocking only improved vectorisation by an additional 1.8 times. *O'Sullivan et al.* (2019) recently extended the works of *Bird et al.* (2017); *Dabrowski et al.* (2008) to optimised elasto-plastic codes for Continuous Galerkin (CG) or Discontinuous Galerkin (DG) methods. In particular, they proposed an efficient native MATLAB function, i.e., `accumarray()`, to efficiently assemble the internal force vector. Such function constructs an array by accumulation. More generally, *O'Sullivan et al.* (2019) reported a performance gain of x25.7 when using an optimised CG code instead of an equivalent non-optimised code.

Since MPM and FEM share common grounds, we aim at increasing the performances of MATLAB up to what was reported by *Sinaie et al.* (2017) using Julia language environment. In principal, Julia is significantly faster than MATLAB for a MPM implementation. We combine the most recent and accurate versions of MPM: the explicit generalized interpolation material point method (GIMPM, *Bardenhagen and Kober* 2004) and the explicit convected particle domain interpolation with second-order quadrilateral domains (CPDI2q and CPDI, *Sadeghirad et al.* 2013, 2011) variants with some of the numerical techniques developed during the last decade of FEM optimisation in MATLAB. These techniques include the use of `accumarray()`, optimal RAM-to-cache communication, minimum BLAS calls and the use of native MATLAB functions. We did not consider the blocking technique initially proposed by *Dabrowski et al.* (2008) since an explicit formulation in MPM excludes the global stiffness matrix assembly procedure. The performance gain mainly comes from the vectorisation of the algorithm, whereas blocking has a less significant impact over the performance gain, as stated by *Bird et al.* (2017). The vectorisation of MATLAB functions is also crucial for a straight transpose of the solver to a more efficient language, such as the C-CUDA language, which allows the parallel execution of computational kernels of graphics processing units (GPUs).

In this contribution, we present an implementation of an efficiently vectorised explicit MPM solver (fMPMM-solver, which v1.1 is available for download from Bitbucket at: <https://bitbucket.org/ewyser/fmpmm-solver/src/master/>), taking advantage of vectorisation capabilities of MATLAB[®]. We extensively use native functions of MATLAB[®] such as `repmat()`, `reshape()`, `sum()` or `accumarray()`. We validate our in-house code with classical MPM benchmarks including i) the elastic collapse under self-weight of a column, ii) the elastic cantilever beam problem, and iii) existing experimental results, i.e., granular collapses and slumping mechanics. We demonstrate the computational efficiency of a vectorised implementation over an iterative one for the case of an elasto-plastic collapse of a column. We compare the performances of Julia and MATLAB language environments for the collision of two elastic discs problem.

B.2 Overview of the Material Point Method (MPM)

B.2.1 A Material Point Method implementation

The material point method (MPM), originally proposed by *Sulsky et al.* (1995, 1994) in an explicit formulation, is an extension of the particle-in-cell (PIC) method. The key idea is to solve the weak form of the momentum balance equation on a FE mesh while state variables (e.g., stress, velocity or mass) are stored at Lagrangian points discretizing the continuum, i.e., the material points, which can move according to the deformation of the grid (*Dunatunga and Kamrin*, 2017). MPM could be regarded as a finite element solver in which integration points (material points) are allowed to move (*Guilkey and Weiss*, 2003) and are thus not always located at

the Gauss-Legendre location within an element, resulting in higher quadrature errors and poorer integration estimates, especially when using low-order basis functions (Steffen *et al.*, 2008a,b).

A typical calculation cycle (see Fig. B.1) consists of the three following steps (Wang *et al.*, 2016b):

1. A Mapping phase, during which properties of the material point (mass, momentum or stress) are mapped to the nodes.
2. An updated-Lagrangian FEM (UL-FEM) phase, during which the momentum equations are solved on the nodes of the background mesh and, the solution is explicitly advanced forward in time.
3. A Convection phase, during which i) the nodal solutions are interpolated back to the material points, and ii) the properties of the material point are updated.

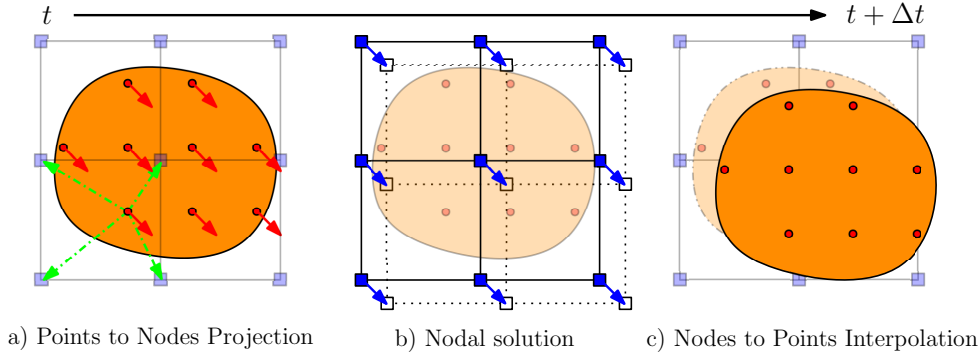


Figure B.1: Typical calculation cycle of a MPM solver for a homogeneous velocity field, inspired by *Dunatunga and Kamrin* (2017). a) The continuum (orange) is discretized into a set of Lagrangian material points (red dots), at which state variables or properties (e.g., mass, stress, and velocity) are defined. The latter are mapped to an Eulerian finite element mesh made of nodes (blue square). b) Momentum equations are solved at the nodes and, the solution is explicitly advanced forward in time. c) The nodal solutions are interpolated back to the material points and, their properties are updated.

Since the 1990's, several variants were introduced to resolve a number of numerical issues. The generalized interpolation material point method (GIMPM) was first presented by *Bardenhagen and Kober* (2004). They proposed a generalization of the basis and gradient functions that were convoluted with a characteristic domain function of the material point. A major flaw in sMPM is the lack of continuity of the gradient basis function, resulting in spurious oscillations of internal forces as soon as a material point crosses an element boundary while entering into its neighbour. This is referred to as cell-crossing instabilities due to the C_0 continuity of the gradient basis functions used in sMPM. Such issue is minimized by the GIMPM variant (*Acosta et al.*, 2020).

GIMPM is categorized as a domain-based material point method, unlike the later development of the B-spline material point method (BSMPM, e.g. *de Koster et al.* 2020; *Gan et al.* 2018; *Gaume et al.* 2018; *Stomakhin et al.* 2013) which cures cell-crossing instabilities using B-spline functions as basis functions. Whereas in sMPM only nodes belonging to an element contribute to a given material point, GIMPM requires an extended nodal connectivity, i.e., the nodes of the element enclosing the material point and the nodes belonging to the adjacent elements (see Fig. B.2). More recently, the convected particle domain interpolation (CPDI and its most recent development CPDI2q) has been proposed by *Sadeghirad et al.* (2013, 2011).

We choose the explicit GIMPM variant with the modified update stress last scheme (MUSL, see *Nairn* (2003); *Bardenhagen et al.* (2000) for a detailed discussion), i.e., the stress of material point is updated after the nodal solutions are obtained. The updated momentum of the material point is then mapped back a second time to the nodes in order to obtain an updated nodal velocity, further used to calculate derivative terms such as strains or the deformation gradient of the material point. The explicit formulation also implies the well-known restriction on the time step, which is limited by the Courant-Friedrich-Lewy (CFL) condition to ensure numerical stability.

Additionally, we implemented a CPDI/CPDI2q version (in an explicit and quasi-static implicit formulation) of the solver. However, in this paper, we do not present the theoretical background of the CPDI variant nor

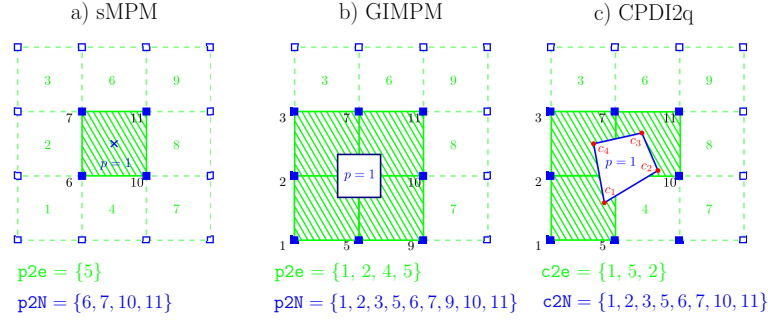


Figure B.2: Nodal connectivities of a) standard MPM, b) GIMPM and c) CPDI2q variants. The material point's location is marked by the blue cross. Note that for sMPM (and similarly BSMPPM) the particle domain does not exist, unlike GIMPM or CPDI2q (the blue square enclosing the material point). Nodes associated with the material point are denoted by filled blue squares, and the element number appears in green in the centre of the element. For sMPM and GIMPM, the connectivity array between the material point and the element is $p2e$ and, the array between the material point and its associated nodes is $p2N$. For CPDI2q, the connectivity array between the corners (filled red circles) of the quadrilateral domain of the material point and the element is $c2e$ and, the array between the corners and their associated nodes is $c2N$.

the implicit implementation of a MPM-based solver. Therefore, interested readers are referred to the original contributions of *Sadeghirad et al. (2013, 2011)* and *Acosta et al. (2020)*; *Charlton et al. (2017)*; *Iaconeta et al. (2017)*; *Beuth et al. (2008)*; *Guilkey and Weiss (2003)*, respectively. Regarding the quasi-static implicit implementation, we strongly adapted our vectorisation strategy to some aspects of the numerical implementation proposed by *Coombs and Augarde (2020)* in the MATLAB code AMPLE v1.0. However, we did not consider blocking, because our main concern for performance is on the explicit implementation.

B.2.2 Domain-based material point method variants

Domain-based material point method variants could be treated as two distinct groups:

- The material point's domain is a square for which the deformation is always aligned with the mesh axis, i.e., a non-deforming domain uGIMPM (*Bardenhagen and Kober, 2004*) or, a deforming domain cpGIMPM (*Wallstedt and Guilkey, 2008*), the latter being usually related to a measure of the deformation, e.g., the determinant of the deformation gradient.
- The material point's domain is either a deforming parallelogram for which its dimensions are specified by two vectors, i.e., CPDI (*Sadeghirad et al., 2011*), or a deforming quadrilateral solely defined by its corners, i.e., CPDI2q (*Sadeghirad et al., 2013*). However, the deformation is not necessarily aligned with the mesh anymore.

We first focus on the different domain updating methods for GIMPM. Four domain updating methods exists: i) the domain is not updated, ii) the deformation of the domain is proportional to the determinant of the deformation gradient $\det(F_{ij})$ (*Bardenhagen and Kober, 2004*), iii) the domain lengths l_p are updated accordingly to the principal component of the deformation gradient F_{ii} (*Sadeghirad et al., 2011*) or, iv) are updated with the principal component of the stretch part of the deformation gradient U_{ii} (*Charlton et al., 2017*). *Coombs et al. (2020)* highlighted the suitability of generalised interpolation domain updating methods accordingly to distinct deformation modes. Four different deformation modes were considered by *Coombs et al. (2020)*: simple stretch, hydrostatic compression/extension, simple shear and, pure rotation. *Coombs et al. (2020)* concluded the following:

- Not updating the domain is not suitable for simple stretch and hydrostatic compression/extension.
- A domain update based on $\det(F_{ij})$ will results in an artificial contraction/expansion of the domain for simple stretch.
- The domain will vanish with increasing rotation when using F_{ii} .
- The domain volume will change under isochoric deformation when using U_{ii} .

Consequently, *Coombs et al. (2020)* proposed a hybrid domain update inspired by CPDI2q approaches: the corners of the material point domain are updated accordingly to the nodal deformation but, the midpoints of the domain limits are used to update domain lengths l_p to maintain a rectangular domain. Even though *Coombs et al. (2020)* reported an excellent numerical stability, the drawback is to compute specific basis functions between nodes and material point's corners, which has an additional computational cost. Hence, we did not selected this approach in this contribution.

Regarding the recent CPDI/CPDI2q, *Wang et al. (2019)* investigated the numerical stability under stretch, shear and torsional deformation modes. CPDI2q was found to be erroneous in some case, especially when torsion mode is involved, due to distortion of the domain. In contrast, CPDI and even sMPM performed better in modelling torsional deformations. Even though CPDI2q can exactly represent the deformed domain (*Sadeghirad et al., 2013*), care must be taken when dealing with very large distortion, especially when the material has yielded, which is common in geotechnical engineering (*Wang et al., 2019*).

Consequently, the domain-based method as well as the domain updating method should be carefully chosen accordingly to the deformation mode expected for a given case. The latter will be always specify in the following and, the domain update method will be clearly stated.

B.3 MATLAB-based MPM implementation

B.3.1 Rate formulation and elasto-plasticity

The large deformation framework in a linear elastic continuum requires an appropriate stress-strain formulation. One approach is based on the finite deformation framework, which relies on a linear relationship between elastic logarithmic strains and Kirchoff stresses (*Coombs et al., 2020; Gaume et al., 2018; Charlton et al., 2017*). In this study, we adopt another approach, namely, a rate dependent formulation using the Jaumann stress rate (e.g. *Huang et al. 2015; Bandara et al. 2016; Wang et al. 2016a,c*). This formulation provides an objective (invariant by rotation or frame-indifferent) stress rate measure (*de Souza Neto et al., 2011*) and is simple to implement. The Jaumann rate of the Cauchy stress is defined as

$$\frac{\mathcal{D}\sigma_{ij}}{\mathcal{D}t} = \frac{1}{2}C_{ijkl} \left(\frac{\partial v_l}{\partial x_k} + \frac{\partial v_k}{\partial x_l} \right), \quad (\text{B.1})$$

where C_{ijkl} is the fourth rank tangent stiffness tensor and v_k is the velocity. Thus, the Jaumann stress derivative can be written as

$$\frac{\mathcal{D}\sigma_{ij}}{\mathcal{D}t} = \frac{D\sigma_{ij}}{Dt} - \sigma_{ik}\omega_{jk} - \sigma_{jk}\omega_{ik}, \quad (\text{B.2})$$

where $\omega_{ij} = (\partial_i v_j - \partial_j v_i)/2$ is the vorticity tensor and $D\sigma_{ij}/Dt$ denotes the material derivative

$$\frac{D\sigma_{ij}}{Dt} = \frac{\partial \sigma_{ij}}{\partial t} + v_k \frac{\partial \sigma_{ij}}{\partial x_k}. \quad (\text{B.3})$$

Plastic deformation is modelled with a pressure dependent Mohr-Coulomb law with non-associated plastic flow, i.e., both the dilatancy angle ψ and the volumetric plastic strain ϵ_v^p are null (*Vermeer and De Borst, 1984*). We have adopted the approach of *Simpson (2017)* for a two dimensional linear elastic, perfectly plastic (elasto-plasticity) continuum because of its simplicity and its ease of implementation. The yield function is defined as

$$f = \tau + \sigma \sin \phi - c \cos \phi, \quad (\text{B.4})$$

where c is the cohesion and ϕ the angle of internal friction,

$$\sigma = (\sigma_{xx} + \sigma_{yy})/2, \quad (\text{B.5})$$

and

$$\tau = \sqrt{(\sigma_{xx} - \sigma_{yy})^2/4 + \sigma_{xy}^2}. \quad (\text{B.6})$$

The elastic state is defined when $f < 0$. However when $f > 0$, plastic state is declared and stresses must be corrected (or scaled) to satisfy the condition $f = 0$, since $f > 0$ is an inadmissible state. *Simpson (2017)* proposed the following simple algorithm to return stresses to the yield surface,

$$\sigma_{xx}^* = \sigma + (\sigma_{xx} - \sigma_{yy})\beta/2, \quad (\text{B.7})$$

$$\sigma_{yy}^* = \sigma - (\sigma_{xx} - \sigma_{yy})\beta/2, \quad (\text{B.8})$$

$$\sigma_{xy}^* = \sigma_{xy}\beta, \quad (\text{B.9})$$

where $\beta = (|c \cos \phi - \sigma \sin \phi|)/\tau$, and σ_{xx}^* , σ_{yy}^* and σ_{xy}^* are the corrected stresses, i.e., $f = 0$.

A similar approach is used to return stresses when considering a non-associated Drucker-Prager plasticity (see *Huang et al. (2015)* for a detailed description of the procedure). In addition, their approach allows also to model associated plastic flows, i.e., $\psi > 0$ and $e_v^p \neq 0$.

B.3.2 Structure of the MPM solver

The solver procedure is shown in Fig. B.3. In the `main.m` script, both functions `mpSetup.m` and `meSetup.m`, respectively, define the geometry and related quantities such as the nodal connectivity (or element topology) array, e.g., the `e2N` array. The latter stores the nodes associated with a given element. As such, a material point p located in an element e can immediately identify which nodes n it is associated with.

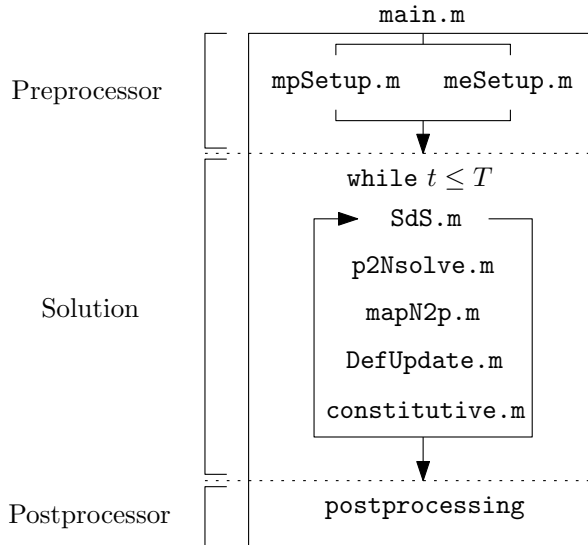


Figure B.3: Workflow of the explicit GIMP solver and the calls to functions within a calculation cycle. The role of each function is described in the text.

After initialization, a while loop solves the elasto-dynamic (or elasto-plastic) problem until a time criterion T is reached. This time criterion could be restricted to the time needed for the system to reach an equilibrium, or if the global kinetic energy of the system has reached a threshold.

At the beginning of each cycle, a connectivity array $p2e$ between the material points and their respective element (a material point can only reside in a single element) is constructed. Since i) the nodes associated with the elements and ii) the elements enclosing the material points are known, it is possible to obtain the connectivity array $p2N$ between the material points and their associated nodes, e.g., $p2N=e2N(p2e, :)$ in a MATLAB syntax (see Fig. B.2 for an example of these connectivity arrays). This array is of dimension (n_p, n_n) , with n_p the total number of material points, n_n the total number of nodes associated with an element (16 in two-dimensional problems) and $n_{i,j}$ the node number where i corresponds to the material point and j corresponds to its j -th associated nodes, which results in the following:

$$p2N = \begin{pmatrix} n_{1,1} & \cdots & n_{1,n_n} \\ \vdots & \ddots & \vdots \\ n_{n_p,1} & \cdots & n_{n_p,n_n} \end{pmatrix}. \quad (\text{B.10})$$

The following functions are called successively during one calculation cycle:

1. `SdS.m` calculates the basis functions, derivatives and, assembles the strain-displacement matrix for each material points.
2. `p2Nsolve.m` projects the quantities of the material point (e.g., mass and momentum) to the associated nodes, solves the equations of motion and sets boundary conditions.
3. `mapN2p.m` interpolates nodal solutions (acceleration and velocity) to the material points with a double mapping procedure (see *Zhang et al. (2016)* or *Nairn (2003)* for a clear discussion of USE, USL and MUSL algorithms).
4. `DefUpdate.m` updates incremental strains and deformation-related quantities (e.g., the volume of the material point or the domain half-length) at the level of the material point based on the remapping of the updated material point momentum.
5. `constitutive.m` calls two functions to solve for the constitutive elasto-plastic relation, i.e.,
 - (a) `elastic.m`, which predicts an incremental objective stress assuming a purely elastic step, further corrected by
 - (b) `plastic.m`, which corrects the trial stress by a plastic correction if the material has yielded.

When a time criterion is met, the calculation cycle stops and further post-processing tasks (visualization, data exportation) can be performed.

The numerical simulations are conducted using MATLAB[®] R2018a within a Windows 7 64-bit environment on an Intel Core i7-4790 (4th generation CPU with 4 physical cores of base frequency at 3.60 GHz up to a maximum turbo frequency of 4.00 GHz) with 4×256 kB L2 cache and 16 GB DDR3 RAM (clock speed 800 MHz).

B.3.3 Vectorisation

Basis functions and derivatives

The GIMPM basis function (*Coombs et al., 2018; Steffen et al., 2008a; Bardenhagen and Kober, 2004*) results from the convolution of a characteristic particle function χ_p (i.e., the material point spatial extent or domain) with

the standard basis function $N_n(x)$ of the mesh, which results in:

$$S_n(x_p) = \begin{cases} 1 - (4x^2 + l_p^2)/(4hl_p) & \text{if } |x| < l_p/2 \\ 1 - |x|/h & \text{if } l_p/2 \leq |x| < h - l_p/2 \\ (h + l_p/2 - |x|)^2 / (2hl_p) & \text{if } h - l_p/2 \leq |x| < h + l_p/2 \\ 0 & \text{otherwise,} \end{cases} \quad (\text{B.11})$$

with l_p the length of the material point domain, h the mesh spacing, $x = x_p - x_n$ where x_p is the coordinate of a material point and x_n the coordinate of its associated node n . The basis function of a node n with its material point p is constructed for a two-dimensional model, as follows:

$$S_n(\mathbf{x}_p) = S_n(x_p)S_n(y_p), \quad (\text{B.12})$$

for which the derivative is defined as:

$$\nabla S_n(\mathbf{x}_p) = (\partial_x S_n(x_p)S_n(y_p), S_n(x_p)\partial_y S_n(y_p)). \quad (\text{B.13})$$

Similar to the FEM, the strain-displacement matrix \mathbf{B} consists of the derivatives of the basis function and is assigned to each material point, which results in the following:

$$\mathbf{B}(\mathbf{x}_p) = \begin{pmatrix} \partial_x S_1 & 0 & \cdots & \partial_x S_{n_n} & 0 \\ 0 & \partial_y S_1 & \cdots & 0 & \partial_y S_{n_n} \\ \partial_y S_1 & \partial_x S_1 & \cdots & \partial_y S_{n_n} & \partial_x S_{n_n} \end{pmatrix}, \quad (\text{B.14})$$

where n_n is the total number of associated nodes to an element e , in which a material point p resides.

The algorithm outlined in Fig. B.4 (the function `[mpD] = SdS(meD, mpD, p2N)` called at the beginning of each cycle, see Fig. B.4) represents the vectorised solution of the computation of basis functions and their derivatives.

Coordinates of the material points `mpD.x(: , 1:2)` are first replicated and then subtracted by their associated nodes coordinates, e.g., `meD.x(p2N)` and `meD.y(p2N)` respectively (Lines 3 or 5 in Fig. B.4). This yields the array `D` with the same dimension of `p2N`. This array of distance between the points and their associated nodes is sent as an input to the nested function `[N, dN] = NdN(D, h, lp)`, which computes 1D basis function and its derivative through matrix element-wise operations (operator `.*`) (either in Line 4 for x coordinates or Line 6 for y coordinates in Fig. B.4).

Given the piece-wise Eq. C.42, three logical arrays (`c1`, `c2` and `c3`) are defined (Lines 21-24 in Fig. B.4), whose elements are either 1 (the condition is true) or 0 (the condition is false). Three arrays of basis functions are calculated (`N1`, `N2` and `N3`, Lines 26-28) according to Eq. C.43. The array of basis functions `N` is obtained through a summation of the element-wise multiplications of these temporary arrays with their corresponding logical arrays (Line 29 in Fig. B.4). The same holds true for the calculation of the gradient basis function (Lines 31-34 in Fig. B.4). It is faster to use logical arrays as multipliers of precomputed basis function arrays rather than using these in a conditional indexing statement, e.g., `N(c2==1) = 1-abs(dX(c2==1))./h`. The performance gain is significant between the two approaches, i.e., an intrinsic 30 % gain over the wall-clock time of the basis functions and derivatives calculation. We observe an invariance of such gain with respect to the initial number of material point per element or to the mesh resolution.


```

1 function [mpD] = SdS(meD,mpD,p2N)
2 %% COMPUTE (X,Y)-BASIS FUNCTION
3 D = (repmat(mpD.x(:,1),1,meD.nNe) - meD.x(p2N));%
4 [Sx,dSx] = NdN(D,meD.h(1),repmat(mpD.1(:,1),1,meD.nNe));%
5 D = (repmat(mpD.x(:,2),1,meD.nNe) - meD.y(p2N));%
6 [Sy,dSy] = NdN(D,meD.h(2),repmat(mpD.1(:,2),1,meD.nNe));%
7 %% CONVOLUTION OF BASIS FUNCTIONS
8 mpD.S = Sx.* Sy ;%
9 mpD.dSx = dSx.* Sy ;%
10 mpD.dSy = Sx.* dSy ;%
11 %% B MATRIX ASSEMBLY
12 iDx = 1:meD.DoF:meD.nDoF(1)-1 ;%
13 iDy = iDx+1 ;%
14 mpD.B(1,iDx,:) = mpD.dSx' ;%
15 mpD.B(2,iDy,:) = mpD.dSy' ;%
16 mpD.B(3,iDx,:) = mpD.dSy' ;%
17 mpD.B(3,iDy,:) = mpD.dSx' ;%
18 end
19 function [N,dN]=NdN(dX,h,lp)
20 %% COMPUTE BASIS FUNCTIONS
21 lp = 2*lp ;%
22 c1 = (abs(dX)<(0.5*lp)) ;%
23 c2 = ((abs(dX)>=(0.5*lp)) & (abs(dX)<(h-0.5*lp))) ;%
24 c3 = ((abs(dX)>=(h-0.5*lp)) & (abs(dX)<(h+0.5*lp))) ;%
25 % BASIS FUNCTION
26 N1 = 1-((4*dX.^2+lp.^2)./(4*h.*lp)) ;%
27 N2 = 1-(abs(dX)./h) ;%
28 N3 = ((h+0.5*lp-abs(dX)).^2)./(2*h.*lp) ;%
29 N = c1.*N1+c2.*N2+c3.*N3 ;%
30 % BASIS FUNCTION GRADIENT
31 dN1= -(8*dX)./(4*h.*lp) ;%
32 dN2= sign(dX).*(-1/h) ;%
33 dN3=-sign(dX).*(h+0.5*lp-abs(dX))./(h*lp) ;%
34 dN = c1.*dN1+c2.*dN2+c3.*dN3 ;%
35 end

```

Figure B.4: Code Fragment 1 shows the vectorised solution to the calculation of the basis functions and their derivatives within `SdS.m`. Table B.3 lists the variables used.

Integration of internal forces

Another computationally expensive operation for MATLAB[®] is the mapping (or accumulation) of the material point contributions to their associated nodes. It is performed by the function `p2Nsolve.m` in the workflow of the solver.

The standard calculations for the material point contributions to the lumped mass m_n , the momentum \mathbf{p}_n , the external \mathbf{f}_n^e and internal \mathbf{f}_n^i forces are given by:

$$m_n = \sum_{p \in n} S_n(\mathbf{x}_p) m_p, \quad (\text{B.15})$$

$$\mathbf{p}_n = \sum_{p \in n} S_n(\mathbf{x}_p) m_p \mathbf{v}_p, \quad (\text{B.16})$$

$$\mathbf{f}_n^e = \sum_{p \in n} S_n(\mathbf{x}_p) m_p \mathbf{b}_p, \quad (\text{B.17})$$

$$\mathbf{f}_n^i = \sum_{p \in n} v_p \mathbf{B}^T(\mathbf{x}_p) \boldsymbol{\sigma}_p, \quad (\text{B.18})$$

with m_p the material point mass, \mathbf{v}_p the material point velocity, \mathbf{b}_p the body force applied to the material point and $\boldsymbol{\sigma}_p$ the material point Cauchy stress tensor in the Voigt notation.

Once the mapping phase is achieved, the equations of motions are explicitly solved forward in time on the mesh. Nodal accelerations \mathbf{a}_n and velocities \mathbf{v}_n are given by:

$$\mathbf{a}_n^{t+\Delta t} = m_n^{-1} (\mathbf{f}_n^e - \mathbf{f}_n^i), \quad (\text{B.19})$$

$$\mathbf{v}_n^{t+\Delta t} = m_n^{-1} \mathbf{p}_n + \Delta t \mathbf{a}_n^{t+\Delta t}. \quad (\text{B.20})$$

Finally, boundary conditions are applied to the nodes that belong to the boundaries.

```

1 function [meD] = p2Nsolve(meD,mpD,g,dt,l2g,p2N,bc)
2 %% INITIALIZATION
3 % NODAL VECTOR INITIALIZATION
4 meD.m(:) = 0.0 ; meD.mr(:) = 0.0 ; meD.f(:) = 0.0 ; meD.d(:) = 0.0 ;%
5 meD.a(:) = 0.0 ; meD.p(:) = 0.0 ; meD.v(:) = 0.0 ; meD.u(:) = 0.0 ;%
6 %% CONTRIBUTION TO NODES
7 % PREPROCESSING
8 m = reshape( mpD.S.*repmat(mpD.m,1,meD.nNe) ,mpD.n*meD.nNe ,1) ;%
9 p = reshape([mpD.S.*repmat(mpD.p(:,1),1,meD.nNe);...
10 mpD.S.*repmat(mpD.p(:,2),1,meD.nNe)],mpD.n*meD.nDoF(1),1) ;%
11 f = reshape([mpD.S.*0.0 ;...
12 mpD.S.*repmat(mpD.m,1,meD.nNe).*-g ],mpD.n*meD.nDoF(1),1) ;%
13 fi = squeeze(sum(mpD.B.*repmat(reshape(mpD.s,size(mpD.s,1),1,mpD.n)...
14 ,1,meD.nDoF(1)),1)).*repmat(mpD.V',meD.nDoF(1),1) ;%
15 % CONTRIBUTION FROM p TO N
16 meD.m = accumarray(p2N(:),m,[meD.nN 1]) ;%
17 meD.p = accumarray(l2g(:),p,[meD.nDoF(2) 1]) ;%
18 meD.f = accumarray(l2g(:),f,[meD.nDoF(2) 1]) ;%
19 for n = 1:meD.nNe
20 l = [(meD.DoF*p2N(:,n)-1);(meD.DoF*p2N(:,n))] ;%
21 meD.f = meD.f - accumarray(1,[fi(n*meD.DoF-1,:);...
22 fi(n*meD.DoF ,:)]',[meD.nDoF(2) 1]) ;%
23 end %
24 %% SOLVE EXPLICIT MOMENTUM BALANCE EQUATION
25 % UPDATE GLOBAL NODAL INFORMATIONS
26 iDx = 1:meD.DoF:meD.nDoF(2)-1 ;%
27 iDy = iDx+1 ;%
28 % COMPUTE GLOBAL NODAL FORCE
29 meD.d(iDx) = sqrt(meD.f(iDx).^2+meD.f(iDy).^2) ;%
30 meD.d(iDy) = meD.d(iDx) ;%
31 meD.f = meD.f - meD.vd*meD.d.*sign(meD.p) ;%
32 % UPDATE GLOBAL NODAL MOMENTUM
33 meD.p = meD.p + dt*meD.f ;%
34 % COMPUTE GLOBAL NODAL ACCELERATION AND VELOCITY
35 meD.mr = reshape(repmat(meD.m',meD.DoF,1),meD.nDoF(2),1) ;%
36 iD = meD.mr==0 ;%
37 meD.a = meD.f./meD.mr ;%
38 meD.v = meD.p./meD.mr ;%
39 meD.a(iD) = 0.0 ;%
40 meD.v(iD) = 0.0 ;%
41 % BOUNDARY CONDITIONS: FIX DIRICHLET BOUNDARY CONDITIONS
42 meD.a(bc.x(:,1))=bc.x(:,2) ;%
43 meD.a(bc.y(:,1))=bc.y(:,2) ;%
44 meD.v(bc.x(:,1))=bc.x(:,2) ;%
45 meD.v(bc.y(:,1))=bc.y(:,2) ;%
46 end

```

Figure B.5: Code Fragment 2 shows the vectorised solution to the nodal projection of material point quantities (e.g., mass and momentum) within the local function `p2Nsolve.m`. The core of the vectorization process is the extensive use of the built-in function of MATLAB[®] `accumarray()`, for which we detail the main features in the text. Table B.3 lists the variables used.

The vectorised solution comes from the use of the built-in function `accumarray()` of MATLAB[®] combined with `reshape()` and `repmat()`. The core of the vectorization is to use `p2N` as a vector (i.e., flattening the array `p2N(:)` results in a row vector) of subscripts with `accumarray`, which accumulates material point contributions (e.g., mass or momentum) that share the same node.

In the function `p2Nsolve` (Code Fragment 2 shown in Fig. B.5), the first step is to initialize nodal vectors (mass, momentum, forces, etc.) to zero (Lines 4-5 in Fig. B.5). Then, temporary vectors (`m`, `p`, `f` and `fi`) of material point contributions (namely, mass, momentum, and external and internal forces) are generated (Lines 10-17 in Fig. B.5). The accumulation (nodal summation) is performed (Lines 19-26 in Fig. B.5) using either the flattened `p2n(:)` or `l2g(:)` (e.g., the global indices of nodes) as the vector of subscripts. Note that for the accumulation of material point contributions of internal forces, a short for-loop iterates over the associated node (e.g., from 1 to `meD.nNe`) of every material point to accumulate their respective contributions.

To calculate the temporary vector of internal forces (`fi` at Lines 15-17 in Fig. B.5), the first step consists of the matrix multiplication of the strain-displacement matrix `mpD.B` with the material point stress vector `mpD.s`. The vectorised solution is given by i) element-wise multiplications of `mpD.B` with a replication of the transposed stress vector `repmat(reshape(mpD.s, size(mpD.s, 1), 1, mpD.n), 1, meD.nDoF(1))`, whose result is then ii) summed by means of the built-in function `sum()` along the columns and, finally multiplied by a replicated transpose of the material point volume vector, e.g., `repmat(mpD.V', meD.nDoF(1), 1)`.

To illustrate the numerical efficiency of the vectorised multiplication between a matrix and a vector, we have developed an iterative and vectorised solution of $\mathbf{B}(\mathbf{x}_p)^T \boldsymbol{\sigma}_p$ with an increasing n_p and considering single (4 bytes) and double (8 bytes) arithmetic precision. The wall-clock time increases with n_p with a sharp transition for the vectorised solution around $n_p \approx 1000$, as showed in Fig B.6a. The mathematical operation requires more memory than available in the L2 cache (1024 kB under the CPU architecture used), which inhibits cache reuse (Dabrowski *et al.*, 2008). A peak performance of at least 1000 Mflops, showed in Fig. B.6b, is achieved when $n_p = 1327$ or $n_p = 2654$ for simple or double arithmetic precision respectively, i.e., it corresponds exactly to 1024 kB for both precisions. Beyond, the performance dramatically drops to approximately the half of the peak value. This drop is even more severe for a double arithmetic precision.

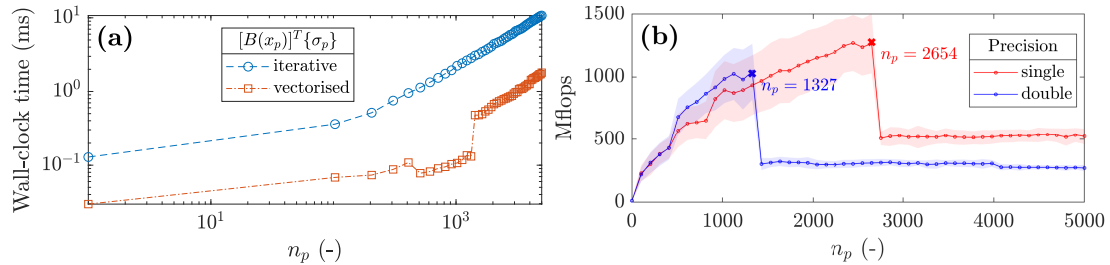


Figure B.6: a) Wall-clock time to solve for a matrix multiplication between a multidimensional array and a vector with an increasing number of the third dimension with a double arithmetic precision and, b) number of floating point operations per second (flops) for single and double arithmetic precisions. The continuous line represents the averages value whereas the shaded area denotes the standard deviation.

Update of material point properties

Finally, we propose a vectorisation of the function `mapN2p.m` that i) interpolates updated nodal solutions to the material points (velocities and coordinates) and ii) the double mapping (DM or MUSL) procedure (see *Fern et al.* 2019). The material point velocity \mathbf{v}_p is defined as an interpolation of the solution of the updated nodal accelerations, given by:

$$\mathbf{v}_p^{t+\Delta t} = \mathbf{v}_p^t + \Delta t \sum_{n=1}^{n_n} S_n(\mathbf{x}_p) \mathbf{a}_n^{t+\Delta t}. \quad (\text{B.21})$$

The material point updated momentum is found by $\mathbf{p}_p^{t+\Delta t} = m_p \mathbf{v}_p^{t+\Delta t}$. The double mapping procedure of the nodal velocity \mathbf{v}_n consists of the remapping of the updated material point momentum on the mesh, divided by the nodal mass, given as:

$$\mathbf{v}_n^{t+\Delta t} = m_n^{-1} \sum_{p \in n} S_n(\mathbf{x}_p) \mathbf{p}_p^{t+\Delta t}, \quad (\text{B.22})$$

and for which boundary conditions are enforced. Finally, the material point coordinates are updated based on the following:

$$\mathbf{x}_p^{t+\Delta t} = \mathbf{x}_p^t + \Delta t \sum_{n=1}^{n_n} S_n(\mathbf{x}_p) \mathbf{v}_n^{t+\Delta t}. \quad (\text{B.23})$$

To solve for the interpolation of updated nodal solutions to the material points, we rely on a combination of element-wise matrix multiplication between the array of basis functions `mpD.S` with the global vectors through a transform of the `p2N` array, i.e., `iDx=meD.DoF*p2N-1` and `iDy=iDx+1` (Lines 3-4 in Code Fragment 3 in Fig. B.7), which are used to access to `x` and `y` components of global vectors.

When accessing global nodal vectors by means of `iDx` and `iDy`, the resulting arrays are naturally of the same size as `p2N` and are therefore dimension-compatible with `mpD.S`. For instance, a summation along the columns (e.g., the associated nodes of material points) of an element-wise multiplication of `mpD.S` with `meD.a(iDx)` results in an interpolation of the `x`-component of the global acceleration vector to the material points.

This procedure is used for the velocity update (Line 6 in Fig. B.7) and for the material point coordinate update (Line 10 in Fig. B.7). A remapping of the nodal momentum is carried out (Lines 12 to 16 in Fig. B.7), which allows calculating the updated nodal incremental displacements (Line 17 in Fig. B.7). Finally, boundary conditions of nodal incremental displacements are enforced (Lines 21-22 in Fig. B.7).

```

1 function [meD,mpD] = mapN2p(meD,mpD,dt,l2g,p2N,bc)
2 %% INTERPOLATE SOLUTIONS N to p
3 iDx = meD.DoF*p2N-1 ;%
4 iDy = iDx+1 ;%
5 % VELOCITY UPDATE
6 mpD.v = mpD.v+dt*[sum(mpD.S.*meD.a(iDx),2) sum(mpD.S.*meD.a(iDy),2)] ;%
7 % MOMENTUM UPDATE
8 mpD.p = mpD.v.*repmat(mpD.m,1,meD.DoF) ;%
9 %% UPDATE NODAL MOMENTUM WITH UPDATED MP MOMENTUM (MUSL OR DOUBLE MAPPING)
10 meD.p(:) = 0.0 ;%
11 p = reshape([mpD.S.*repmat(mpD.p(:,1),1,meD.nNe) ;...
12 mpD.S.*repmat(mpD.p(:,2),1,meD.nNe)],...
13 mpD.n*meD.nDoF(1),1) ;%
14 meD.p = accumarray(l2g(:),p,[meD.nDoF(2) 1]) ;%
15 meD.u = dt*(meD.p./meD.mr) ;%
16 iD = meD.mr==0 ;%
17 meD.u(iD) = 0.0 ;%
18 %% BOUNDARY CONDITIONS: FIX DIRICHLET BOUNDARY CONDITIONS
19 meD.u(bc.x(:,1))=bc.x(:,2) ;%
20 meD.u(bc.y(:,1))=bc.y(:,2) ;%
21 %% UPDATE COORDINATE AND DISPLACEMENT
22 mpD.x = mpD.x+[sum(mpD.S.*meD.u(iDx),2) sum(mpD.S.*meD.u(iDy),2)] ;%
23 mpD.u = mpD.u+[sum(mpD.S.*meD.u(iDx),2) sum(mpD.S.*meD.u(iDy),2)] ;%
24 end

```

Figure B.7: Code Fragment 3 shows the vectorised solution for the interpolation of nodal solutions to material points with a double mapping procedure (or MUSL) within the function `mapN2p.m`.

B.3.4 Initial settings and adaptive time step

Regarding the initial setting of the background mesh of the demonstration cases further presented, we select a uniform mesh and a regular distribution of material points within the initially populated elements of the mesh. Each element is evenly filled with 4 material points, e.g., $n_{pe} = 2^2$, unless otherwise stated.

In this contribution, Dirichlet boundary conditions are resolved directly on the background mesh, as in the standard finite element method. This implies that boundary conditions are resolved only in contiguous regions between the mesh and the material points. Deviating from this contiguity or having the mesh not aligned with the coordinate system requires specific treatments for boundary conditions (Cortis *et al.*, 2018). Furthermore, we ignore the external tractions as their implementation is complex.

As explicit time integration is only conditionally stable, any explicit formulation requires a small time step Δt to ensure numerical stability (Ni and Zhang, 2020), e.g., smaller than a critical value defined by the Courant-Friedrich-Lewy (CFL) condition. Hence, we employ an adaptive time step (de Vaucorbeil *et al.*, 2020), which considers the velocity of the material points. The first step is to compute the maximum wave speed of the material using (Zhang *et al.*, 2016; Anderson Jr, 1987)

$$(c_x, c_y) = \left(\max_p (V + |(v_x)_p|), \max_p (V + |(v_y)_p|) \right), \quad (\text{B.24})$$

where the wave speed is $V = ((K + 4G/3)/\rho)^{\frac{1}{2}}$, K and G are the bulk and shear moduli respectively, ρ is the material density, $(v_x)_p$ and $(v_y)_p$ are the material point velocity components. Δt is then restricted by the CFL condition as followed:

$$\Delta t = \alpha \min \left(\frac{h_x}{c_x}, \frac{h_y}{c_y} \right), \quad (\text{B.25})$$

where $\alpha \in [0; 1]$ is the time step multiplier, and h_x and h_y are the mesh spacings.

B.4 Results

In this section, we first demonstrate our MATLAB-based MPM solver to be efficient in reproducing results from other studies, i.e., the compaction of an elastic column (Coombs *et al.*, 2020) (e.g., quasi-static analysis), the cantilever beam problem (Sadeghirad *et al.*, 2011) (e.g., large elastic deformation) and an application to landslide dynamics (Huang *et al.*, 2015) (e.g., elasto-plastic behaviour). Then, we present both the efficiency and the numerical performances for a selected case, e.g., the elasto-plastic collapse. We conclude and compare the performances of the solver with respect to the specific case of an impact of two elastic disks previously implemented in a Julia language environment by (Sinaie *et al.*, 2017).

Regarding the performance analysis, we investigate the performance gain of the vectorised solver considering a double arithmetic precision with respect to the total number of material point because of the following reasons: i) the mesh resolution, i.e., the total number of elements n_{el} , influences the wall-clock time of the solver by reducing the time step due to the CFL condition hence increasing the total number of iterations. In addition, ii) the total number of material points n_p increases the number of operations per cycle due to an increase of the size of matrices, i.e., the size of the strain-displacement matrix depends on n_p and not on n_{el} . Hence, n_p consistently influences the performance of the solver whereas n_{el} determines the wall-clock time of the solver. The performance of the solver is addressed through both the number of floating point operations per second (flops), and by the average number of iteration per second (it/s). The number of floating point operations per second was manually estimated for each function of the solver.

B.4.1 Validation of the solver and numerical efficiency

Convergence: elastic compaction under self-weight of a column

Following the convergence analysis proposed by *Coombs and Augarde* (2020); *Wang et al.* (2019); *Charlton et al.* (2017), we analyse an elastic column of an initial height $l_0 = 10$ m subjected to an external load (e.g. the gravity). We selected the cpGIMP variant with a domain update based on the diagonal components of the deformation gradient. *Coombs et al.* (2020) showed that such domain update is well suited for hydrostatic compression problems. We also selected the CPDI2q variant as a reference, because of its superior convergence accuracy for such problem compared to GIMP (Coombs et al., 2020).

The initial geometry is shown in Fig. B.8. The background mesh is made of a bi-linear four-noded quadrilaterals, and roller boundary conditions are applied on the base and the sides of the column, initially populated by 4 material points per element. The column is 1 element wide and n elements tall and, the number of element in the vertical direction is increased from 1 to a maximum of 1280 elements. The time step is adaptive and we selected a time step multiplier of $\alpha = 0.5$, e.g., minimal and maximal time step values of $\Delta t_{\min} = 3.1 \cdot 10^{-4}$ s and $\Delta t_{\max} = 3.8 \cdot 10^{-4}$ s respectively for the finest mesh of 1280 elements.

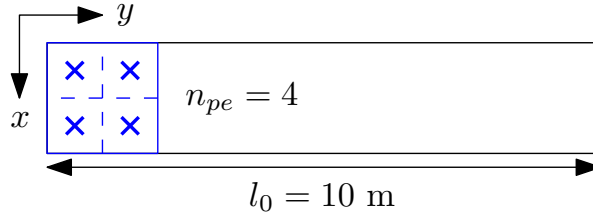


Figure B.8: Initial geometry of the column.

To consistently apply the external load for the explicit solver, we follow the recommendation of *Bardenhagen and Kober* (2004), i.e., a quasi-static solution (given an explicit integration scheme is chosen) is obtained if the total simulation time is equal to 40 elastic wave transit times. The material has a Young's modulus $E = 1 \cdot 10^4$ Pa and a Poisson's ratio $\nu = 0$ with a density $\rho = 80 \text{ kg m}^{-3}$. The gravity g is increased from 0 to its final value, i.e., $g = 9.81 \text{ m s}^{-2}$. We performed additional implicit quasi-static simulations (named iCPDI2q) in order to consistently discuss the results with respect to what was reported in *Coombs and Augarde* (2020). The external force is consistently applied over 50 equal load steps. The vertical normal stress is given by the analytical solution (*Coombs and Augarde*, 2020) $\sigma_{yy}(y_0) = \rho g(l_0 - y_0)$, where l_0 is the initial height of the column and y_0 is the initial position of a point within the column.

The error between the analytical and numerical solutions is as follows:

$$\text{error} = \sum_{p=1}^{n_p} \frac{\|(\sigma_{yy})_p - \sigma_{yy}(y_p)\|(V_0)_p}{(\rho g l_0) V_0}, \quad (\text{B.26})$$

where $(\sigma_{yy})_p$ is the stress along the y -axis of a material point p (Fig. B.8) of an initial volume $(V_0)_p$ and V_0 is the initial volume of the column, i.e., $V_0 = \sum_{p=1}^{n_p} (V_0)_p$.

The convergence toward a quasi-static solution is shown in Fig. B.9 (a). It is quadratic for both cpGIMP and CPDI2q, but contrary to *Coombs et al.* (2020); *Coombs and Augarde* (2020) who reported a full convergence, it stops at error $\approx 2 \cdot 10^{-6}$ for the explicit implementation. This was already outlined by *Bardenhagen and Kober* (2004) as a saturation of the error caused by resolving the dynamic stress wave propagation, which is inherent to any explicit scheme. Hence, a static solution could never be achieved because, unlike quasi-static implicit methods, the elastic waves propagate indefinitely and the static equilibrium is never resolved. This is consistent when compared to the iCPDI2q solution we implemented, whose behaviour is still converging below the limit error $\approx 2 \cdot 10^{-6}$ reached by the explicit solver. However, the convergence rate of the implicit algorithm decreases as the mesh resolution increases. We did not investigate this since our focus is on the explicit implementation. The vertical stresses of material points are in good agreements with the analytical solution (see Fig. B.9 b)).

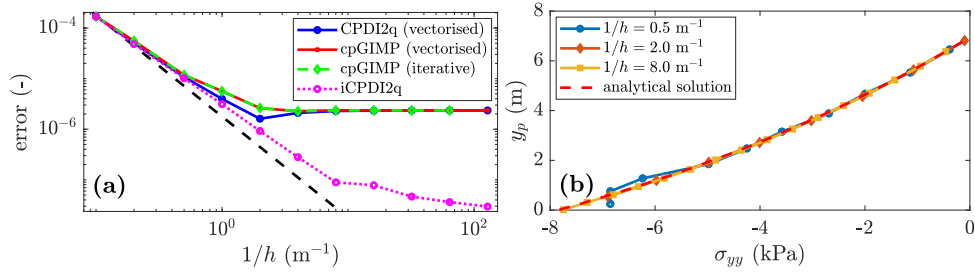


Figure B.9: a) Convergence of the error: a limit is reached at error $\approx 2 \cdot 10^{-6}$ for the explicit solver, whereas the quasi-static solution still converges. This was already demonstrated in *Bardenhagen and Kober (2004)* as an error saturation due to the explicit scheme, i.e., the equilibrium is never resolved. b) The stress σ_{yy} along the y -axis predicted at the deformed position y_p by the CPDI2q variant is in good agreements with the analytical solution for a refined mesh.

Some oscillations are observed for a coarse mesh resolution but these rapidly decrease as the mesh resolution increases.

We finally report the wall-clock time for the cpGIMPM (iterative), cpGIMPM (vectorised) and the CPDI2q (vectorised) variants. As claimed by *Sadeghirad et al. (2013, 2011)*, the CPDI2q variant induces no significant computational cost compared to the cpGIMPM variant. However, the absolute value between vectorised and iterative implementations is significant. For $n_p = 2560$, the vectorised solution completed in 1161 s whereas the iterative solution completed in 52'856 s. The vectorised implementation is roughly 50 times faster than the iterative implementation.

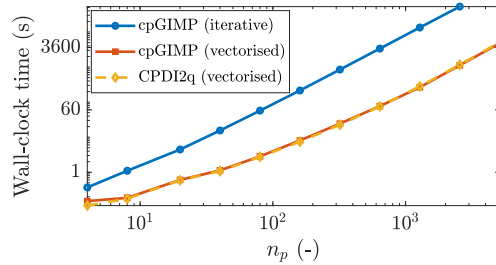


Figure B.10: Wall-clock time for cpGIMPM (vectorised and iterative solutions) and the CPDI2q solution with respect to the total number of material points n_p . There is no significant differences between CPDI2q and cpGIMPM variants regarding the wall-clock time. The iterative implementation is also much slower than the vectorised implementation.

Large deformation: the elastic cantilever beam problem

The cantilever beam problem (*Sinaie et al., 2017; Sadeghirad et al., 2011*) is the second benchmark which demonstrates the robustness of the MPM solver. Two MPM variants are implemented, namely, i) the contiguous GIMPM (cpGIMPM) which relies on the stretch part of the deformation gradient (see *Charlton et al. 2017*) to update the particle domain since large rotations are expected during the deformation of the beam, and ii) the convected particle domain interpolation (CPDI, *Leavy et al. 2019; Sadeghirad et al. 2011*). We selected the CPDI variant since it is more suitable to large torsional deformation modes (*Coombs et al., 2020*) than the CPDI2q variant. Two constitutive elastic models are selected, i.e., neo-Hookean *Guilkey and Weiss (2003)* or linear elastic *York et al. (1999)* solids. For consistency, we use the same physical quantities as in *Sadeghirad et al. (2011)*, i.e., an elastic modulus $E = 10^6$ Pa, a Poisson's ratio $\nu = 0.3$, a density $\rho = 1050$ kg/m³, the gravity $g = 10.0$ m/s and a real-time simulation $t = 3$ s with no damping forces introduced.

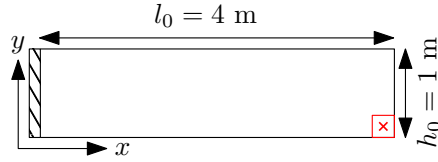


Figure B.11: Initial geometry for the cantilever beam problem; the free end material point appears in red where a red cross marks its centre.

The beam geometry is depicted in Fig. B.11 and is discretized by 64 four-noded quadrilaterals, each of them initially populated by 9 material points (e.g., $n_p = 576$) with a adaptive time step determined by the CFL condition, i.e., the time step multiplier is $alpha = 0.1$, which yields minimal and maximal time step values of $\Delta t_{\min} = 5.7 \cdot 10^{-4}$ s and $\Delta t_{\max} = 6.9 \cdot 10^{-4}$ s respectively. The large deformation is initiated by suddenly applying the gravity at the beginning of the simulation, i.e., $t = 0$ s.

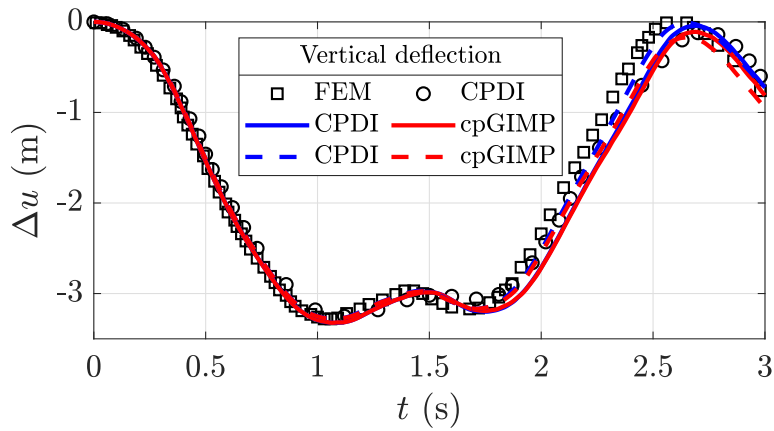


Figure B.12: Vertical deflection Δu for the cantilever beam problem. The black markers denote the solutions of *Sadeghirad et al. (2011)* (circles for CPDI and squares for FEM). The line colour indicates the MPM variant (blue for CPDI and red for cpGIMP), solid lines refer to a linear elastic solid, whereas dashed lines refer to a neo-Hookean solid. Δu corresponds to the vertical displacement of the bottom material point at the free end of the beam (the red cross in Fig. B.11).

As indicated in *Sadeghirad et al. (2011)*, the cpGIMPM simulation failed when using the diagonal components of the deformation gradient to update the material point domain, i.e., the domain vanishes under large rotations as stated in (*Coombs et al., 2020*). However and as expected, the cpGIMPM simulation succeeded when using the diagonal terms of the stretch part of the deformation gradient, as proposed by *Coombs et al. (2020)*; *Charlton et al. (2017)*. The numerical solutions, obtained by the latter cpGIMPM and CPDI, to the vertical deflection Δu of the material point at the bottom free end of the beam (e.g., the red cross in Fig. B.11) are shown in Fig. B.12. Some comparative results reported by *Sadeghirad et al. (2011)* are depicted by black markers (squares for the FEM solution and circles for the CPDI solution), whereas the results of the solver are depicted by lines.

The local minimal and the minimal and maximal values (in timing and magnitude) are in agreement with the FEM solution of *Sadeghirad et al. (2011)*. The elastic response is in agreement with the CPDI results reported by *Sadeghirad et al. (2011)* but, it differs in timing with respect to the FEM solution. This confirms our numerical implementation of CPDI when compared to the one proposed by *Sadeghirad et al. (2011)*. In addition, the elastic response does not substantially differ from a linear elastic solid to a neo-Hookean one. It demonstrates the incremental implementation of the MPM solver to be relevant in capturing large elastic deformations for the cantilever beam problem.

Figure B.13 shows the finite deformation of the material point domain, i.e., a) or c), and, the vertical Cauchy stress field, i.e., b) or d), for CPDI and cpGIMPM. The stress oscillations due to the cell-crossing error are

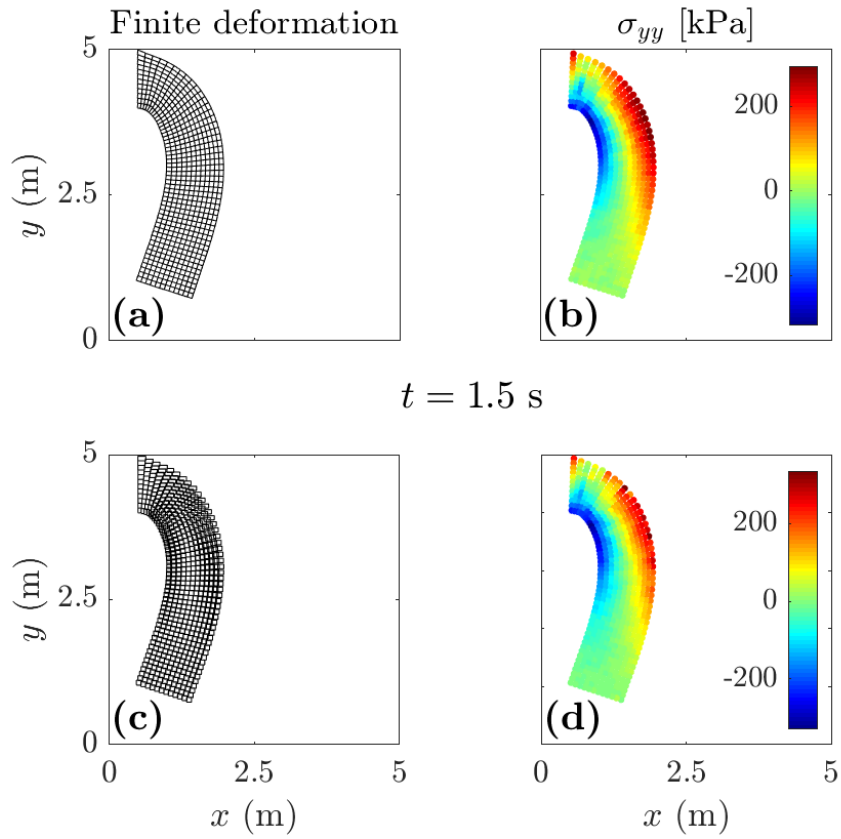


Figure B.13: Finite deformation of the material point domain and vertical Cauchy stress σ_{yy} for CPDI, i.e., a) & b), and for cpGIMPM, i.e., c) & d). The CPDI variant gives a better and contiguous description of the material point's domain and a slightly smoother stress field, compared to the cpGIMPM variant, which is based on the stretch part of the deformation gradient.

partially cured when using a domain-based variant compared to the standard MPM. However, spurious vertical stresses are more developed in Fig. B.13 (d) compared to Fig. B.13 (b) where the vertical stress field appears even smoother. Both CPDI and cpGIMPM give a decent representation of the actual geometry of the deformed beam.

We also report a quite significant difference in execution time between the CPDI variant compared to the CPDI2q and cpGIMPM variants, i.e., CPDI executes in an average 280.54 it/s whereas both CPDI2q and cpGIMPM execute in an average 301.42 it/s and an average 299.33 it/s, respectively.

Application: the elasto-plastic slumping dynamics

We present an application of the MPM solver (vectorised and iterative version) to the case of landslide mechanics. We selected the domain-based CDPI variant since it performs better than the CPDI2q variant in modelling torsional and stretch deformation modes (Wang *et al.*, 2019) coupled to an elasto-plastic constitutive model based on a non-associated Mohr-Coulomb (M-C) plasticity (Simpson, 2017). We i) analyse the geometrical features of the slump and, ii) compare the results (the geometry and the failure surface) to the numerical simulation of Huang *et al.* (2015), which is based on a Drucker-Prager model with tension cut-off (D-P).

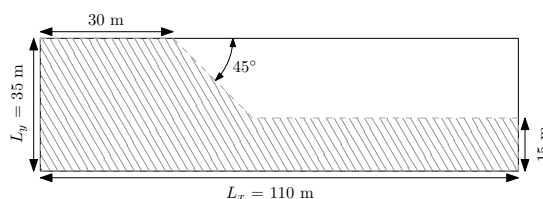


Figure B.14: Initial geometry for the slump problem from Huang *et al.* (2015). Roller boundary conditions are imposed on the left and right of the domain while a no-slip condition is enforced at the base of the material.

The geometry of the problem is shown in Fig. B.14, the soil material is discretized by 110×35 elements with $n_{pe} = 9$, resulting in $n_p = 21'840$ material points. A uniform mesh spacing $h_{x,y} = 1$ m is used and, rollers are imposed at the left and right domain limits while a no-slip condition is enforced at the base of the material. We closely follow the numerical procedure proposed in Huang *et al.* (2015), i.e., no local damping is introduced in the equation of motion and the gravity is suddenly applied at the beginning of the simulation. As in Huang *et al.* (2015), we consider an elasto-plastic cohesive material of density $\rho = 2100 \text{ kg}\cdot\text{m}^3$, with an elastic modulus $E = 70 \text{ MPa}$ and a Poisson's ratio $\nu = 0.3$. The cohesion is $c = 10 \text{ Pa}$, the internal friction angle is $\phi = 20^\circ$ with no dilatancy, i.e., the dilatancy angle is $\psi = 0$. The total simulation time is 7.22 s and, we select a time step multiplier $\alpha = 0.5$. The adaptive time steps (considering the elastic properties and the mesh spacings $h_{x,y} = 1$ m) yield minimal and maximal values $\Delta t_{\min} = 2.3 \cdot 10^{-3} \text{ s}$ and $\Delta t_{\max} = 2.4 \cdot 10^{-3} \text{ s}$ respectively.

The numerical solution to the elasto-plastic problem is shown in Fig. B.15. An intense shear zone, highlighted by the second invariant of the accumulated plastic strain ϵ_{II} , develops at the toe of the slope as soon as the material yields and propagates backwards to the top of the material. It results in a rotational slump. The failure surface is in good agreement with the solution reported by Huang *et al.* (2015) (continuous and discontinuous red lines in Fig. B.15) but, we also observe differences, i.e., the crest of the slope is lower compared to the original work of Huang *et al.* (2015). This may be explained by the problem of spurious material separation when using sMPM or GIMPM (Sadeghirad *et al.*, 2011), the latter being overcome with the CPDI variant, i.e., the crest of the slope experiences considerable stretch deformation modes. Despite some differences, our numerical results appear coherent with those reported by Huang *et al.* (2015).

The vectorised and iterative solutions are resolved within approximately 630 s (a wall-clock time of ≈ 10 min. and an average 4.20 it/s) and 14'868 s (a wall-clock time of ≈ 4.1 hrs. and an average 0.21 it/s) respectively. This corresponds to a performance gain of 23.6. The performance gain is significant between an iterative and a vectorised solver for this problem.

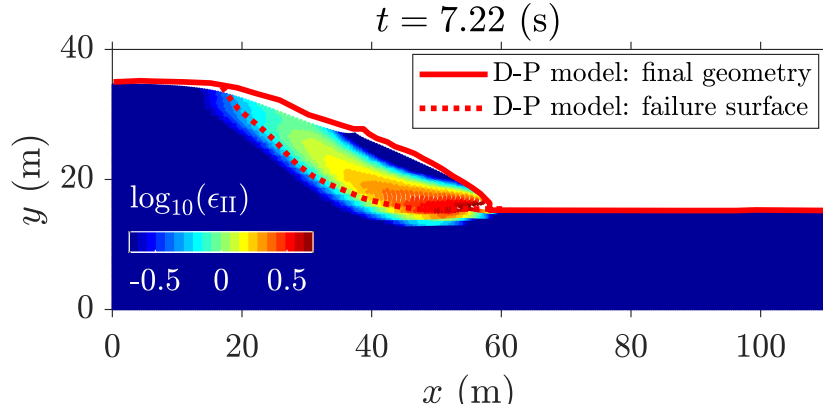


Figure B.15: MPM solution to the elasto-plastic slump. The red lines indicate the numerical solution of *Huang et al. (2015)* and, the coloured points indicate the second invariant of the accumulated plastic strain ϵ_{II} obtained by the CPDI solver. An intense shear zone progressively develops backwards from the toe of the slope, resulting in a circular failure mode.

B.4.2 Computational performance

Iterative and vectorised elasto-plastic collapses

We evaluate the computational performance of the solver, using the MATLAB version R2018a on an Intel Core i7-4790, with a benchmark based on the elasto-plastic collapse of the aluminium-bar assemblage, for which numerical and experimental results were initially reported by *Bui et al. (2008)* and *Huang et al. (2015)* respectively.

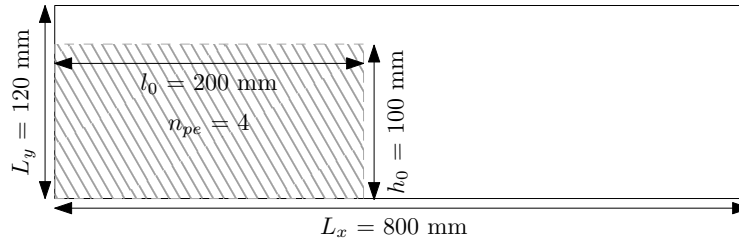


Figure B.16: Initial geometry for the elasto-plastic collapse (*Huang et al., 2015*). Roller boundaries are imposed on the left and right boundaries of the computational domain while a no-slip condition is enforced at the bottom of the domain. The aluminium-bar assemblage has dimensions of $l_0 \times h_0$ and is discretized by $n_{pe} = 4$ material points per initially populated element.

We vary the number of elements of the background mesh, which results in a variety of different regular mesh spacings $h_{x,y}$. The number of elements along the x- and y- directions are $n_{el,x} = [10, 20, 40, 80, 160, 320, 640]$ and $n_{el,y} = [1, 2, 5, 11, 23, 47, 95]$ respectively. The number of material points per element is kept constant, i.e., $n_{pe} = 4$, and this yields a total number of material points $n_p = [10, 50, 200, 800, 3'200, 12'800, 51'200]$. The initial geometry and boundary conditions used for this problem are depicted in Fig. B.16. The total simulation time is 1.0 s and, the time step multiplier is $\alpha = 0.5$. Accordingly to *Huang et al. (2015)*, the gravity $g = 9.81 \text{ m}\cdot\text{s}^{-2}$ is applied to the assemblage and, no damping is introduced. We consider a non-cohesive granular material (*Huang et al., 2015*) of density $\rho = 2650 \text{ kg}\cdot\text{m}^{-3}$, with a bulk modulus $K = 0.7 \text{ MPa}$ and a Poisson's ratio $\nu = 0.3$. The cohesion is $c = 0 \text{ Pa}$, the internal friction angle is $\phi = 19.8^\circ$ and there is no dilatancy, i.e., $\psi = 0$.

We conducted preliminary investigations using either uGIMPM or cpGIMPM variants, the latter with a domain update based either on the determinant of the deformation gradient or on the diagonal components of the stretch part of the deformation gradient. We concluded the uGIMPM was the most reliable, even though its suitability is restricted to both simple shear and pure rotation deformation modes (*Coombs et al., 2020*).

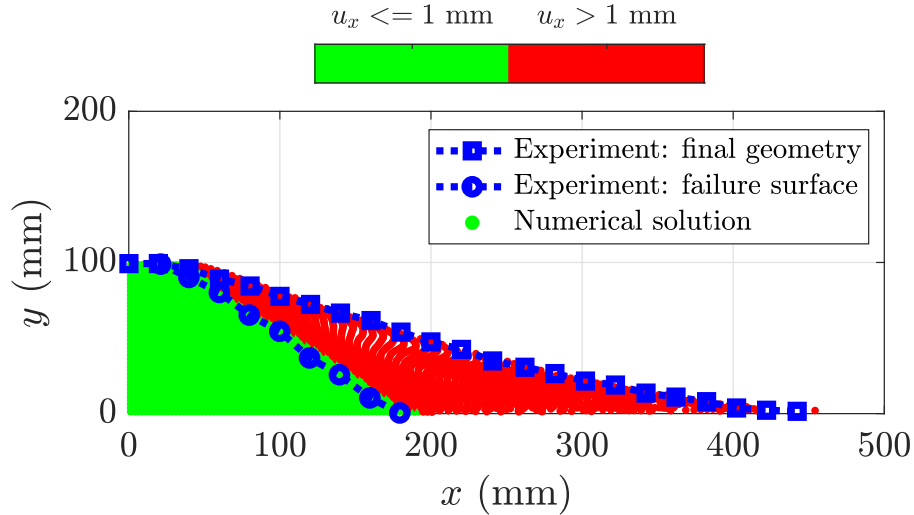


Figure B.17: Final geometry of the collapse: in the intact region (horizontal displacement $u_x < 1$ mm), the material points are coloured in green, whereas in the deformed region (horizontal displacement $u_x > 1$ mm), they are coloured in red and indicate plastic deformations of the initial mass. The transition between the deformed and undeformed region marks the failure surface of the material. Experimental results of (Bui *et al.*, 2008) are depicted by the blue dotted lines. The computational domain is discretized by a background mesh made of 320×48 quadrilateral elements with $n_p = 4$ per initially populated element, i.e., a total $n_p = 12'800$ material points discretize the aluminium assemblage.

We observe a good agreement between the numerical simulation and the experiments (see Fig. B.17), considering either the final surface (blue square dotted line) or the failure surface (blue circle dotted line). The repose angle in the numerical simulation is approximately 13° , which is in agreement with the experimental data reported by Bui *et al.* (2008), e.g., they reported a final angle of 14° .

The vectorised and iterative solutions (for a total of $n_p = 12'800$ material points) are resolved within approximately 1595 s (a wall-clock time of ≈ 0.5 hrs. and an average 10.98 it/s) and 43'861 s (a wall-clock time of ≈ 12 hrs. and an average 0.38 it/s) respectively. This corresponds to a performance gain of 28.24 for a vectorised code over an iterative code to solve this elasto-plastic problem.

The performance of the solver is demonstrated in Fig. B.18. A peak performance of ≈ 900 Mflops is reached, as soon as n_p exceeds 1000 material points and, a residual performance of ≈ 600 Mflops is further resolved (for $n_p \approx 50'000$ material points). Every functions provide an even and fair contribution on the overall performance, except the function `constitutive.m` for which the performance appears delayed or shifted. First of all, this function treats the elasto-plastic constitutive relation, in which the dimensions of the matrices are smaller when compared to the other functions. Hence, the amount of floating point operations per second is lower compared to other functions, e.g., `p2Nsolve.m`. This results in less performance for an equivalent number of material points. It also requires a greater number of material points to increase the dimensions of the matrices in order to exceed the L2 cache maximum capacity.

This considerations provide a better understanding of the performance gain of the vectorised solver showed in Fig. B.19: the gain increases and then, reaches a plateau and ultimately, decreases to a residual gain. This is directly related to the peak and the residual performances of the solver showed in Fig. B.18.

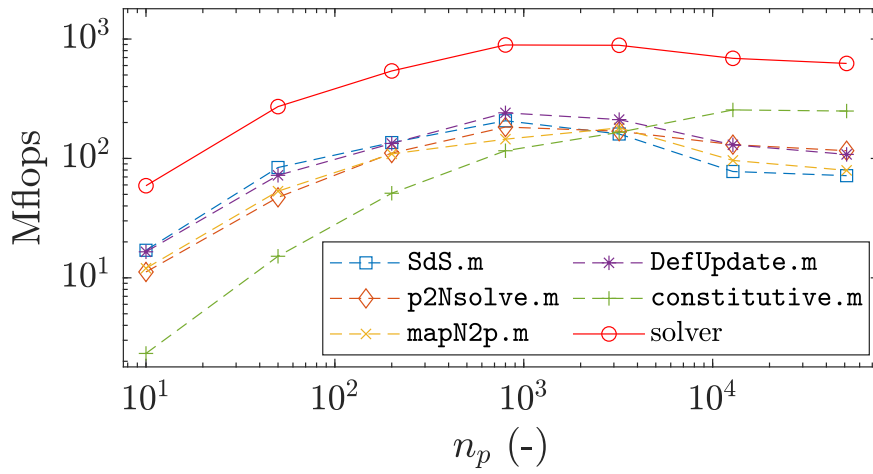


Figure B.18: Number of floating point operation per seconds (flops) with respect to the total number of material point n_p for the vectorised implementation. The discontinuous lines refer to the functions of the solver, whereas the continuous line refer to the solver. A peak performance of 900 Mflops is reached by the solver for $n_p > 1000$ and, a residual performance of 600 Mflops is further resolved for an increasing n_p .

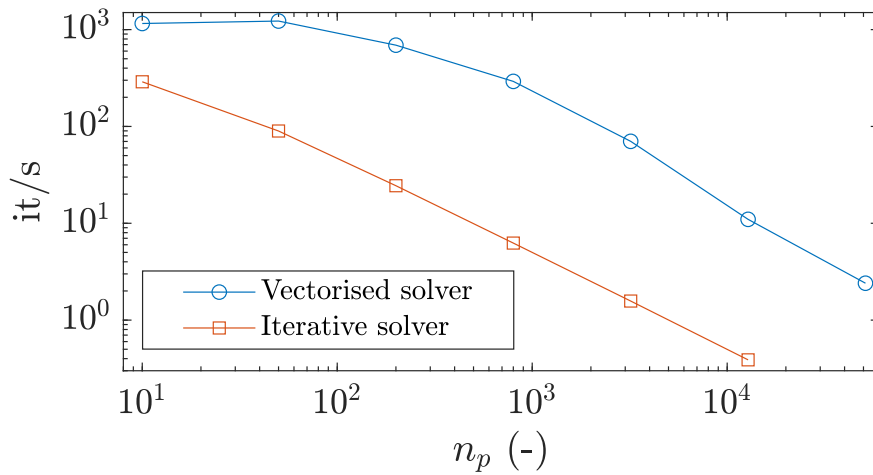


Figure B.19: Number of iterations per second with respect to the total number of material point n_p . The greatest performance gain is reached around $n_p = 1000$, which is related to the peak performance of the solver (see Fig. B.18). The gains corresponding to the peak and residual performances are 46 and 28 respectively.

Comparison between Julia and MATLAB

We compare the computational efficiency of the vectorised CPDI2q MATLAB implementation and the computational efficiency reported by *Sinaie et al. (2017)* of a Julia-based implementation of the collision of two elastic disks problem. However, we note a difference between the actual implementation and the one used by *Sinaie et al. (2017)*; the latter is based on a USL variant with a cut-off algorithm, whereas the present implementation relies on the MUSL (or double mapping) procedure, which necessitates a double mapping procedure. The initial geometry and parameters are the same as those used in *Sinaie et al. (2017)*. However, the time step is adaptive and, we select a time step multiplier $\alpha = 0.5$. Given the variety of mesh resolution, we do not present minimal and maximal time step values.

Our CPDI2q implementation, in MATLAB R2018a, is, at least, 2.8 times faster than the Julia implementation proposed by *Sinaie et al. (2017)* for similar hardware (see Table B.1). *Sinaie et al. (2017)* completed the analysis with an Intel Core i7-6700 (4 cores with a base frequency of 3.40 GHz up to a turbo frequency of 4.00 GHz) with 16 GB RAM, whereas we used an Intel Core i7-4790 with similar specifications (see Section B.2). However, the performance ratio between MATLAB and Julia seems to decrease as the mesh resolution increases.

Table B.1: Efficiency comparison of the Julia implementation of *Sinaie et al. (2017)*, and the MATLAB-based implementation for the two elastic disk impact problems.

mesh	n_{pe}	n_p	Its/s		
			Julia	MATLAB	Gain
20×20	2^2	416	132.80	450.27	3.40
20×20	4^2	1'624	33.37	118.45	3.54
40×40	2^2	1'624	26.45	115.59	4.37
80×80	4^2	25'784	1.82	5.21	2.86

B.5 Discussion

In this contribution, a fast and efficient explicit MPM solver is proposed that considers two variants (e.g., the uGIMPM/cpGIMPM and the CPDI/CPDI2q variants).

Regarding the compression of the elastic column, we report a good agreement of the numerical solver with previous explicit MPM implementations, such as *Bardenhagen and Kober (2004)*. The same flaw of an explicit scheme is also experienced by the solver, i.e., a saturation of the error due to the specific usage of an explicit scheme that resolves the wave propagation, thus preventing any static equilibrium to be reached. This confirms that our implementation is consistent with previous MPM implementations. However, the implicit implementation suffers from a decrease of the convergence rate for a fine mesh resolution. Further work would be needed to investigate this decrease of convergence rate. This case also demonstrated that cpGIMPM and CPDI variants have a similar computational cost and, this confirms the suitability of cpGIMPM with respect to CPDI, as previously mentioned by *Coombs et al. (2020)*; *Charlton et al. (2017)*.

For the cantilever beam, we report a good agreement of the solver with the results of *Sadeghirad et al. (2011)*, i.e., we report the vertical deflection of the beam to be very close in both magnitude and timing (for the CPDI variant) to the FEM solution. However, we also report a slower execution time for the CPDI variant when compared to both cpGIMPM and CPDI2q variants.

The elasto-plastic slump also demonstrates the solver to be efficient in capturing complex dynamics in the field of geomechanics. The CDPI solution showed that the algorithm proposed by *Simpson (2017)* to return stresses when the material yields is well suited to the slumping dynamics. However and as mentioned by *Simpson (2017)*, such return mapping is only valid under the assumption of a non-associated plasticity with no volumetric plastic strain. This particular case of isochoric plastic deformations rises the issue of volumetric locking. In the actual implementation, no regularization techniques are considered. As a result, the pressure field experience severe locking for isochoric plastic deformations. One way to overcome locking phenomenon would be to implement the regularization technique initially proposed by *Coombs et al. (2018)* for quasi-static sMPM and GIMPM implementations.

Regarding the elasto-plastic collapse, the numerical results demonstrate the solver to be in agreement with both previous experimental and numerical results (*Huang et al., 2015; Bui et al., 2008*). This confirms the ability of the solver to address elasto-plastic problems. However, the choice of whether to update or not the material point domain remains critical. Such question remains open and would require a more thorough investigation of the suitability of each of these domain updating variants. Nevertheless, the uGIMPM variant is a good candidate since, i) it is able to reproduce the experimental results of *Bui et al. (2008)* and, ii) it ensures numerical stability. However, one has to keep in mind its limited range of suitability regarding the deformation modes involved. If a cpGIMPM is selected, the splitting algorithm proposed in *Gracia et al. (2019); Homel et al. (2016)* could be implemented to mitigate the amount of distortion experienced by the material point domains during deformation. We did not select the domain updating method based on the corners of the domain as suggested in *Coombs et al. (2020)*. This is because such domain updating method necessitates to calculate additional shape functions between the corners of the domain of the material point with their associated nodes. This results in an additional computational cost. Nevertheless, such variant is of interest and should be addressed as well when the computational performances are not the main concern.

The computational performance comes from the combined use of the connectivity array `p2N` with the built-in function `accumarray()` to i) accumulate material point contributions to their associated nodes or, ii) to interpolate the updated nodal solutions to the associated material points. When a residual performance is resolved, an overall performance gain (e.g., the amount of it/s) of 28 is reported. As an example, the functions `p2nsolve.m` and `mapN2p.m` are 24 and 22 times faster than an iterative algorithm when the residual performance is achieved. The overall performance gain is in agreement to other vectorised FEM codes, i.e., *O'Sullivan et al. (2019)* reported an overall gain of 25.7 for a optimised continuous Galerkin finite element code.

An iterative implementation would require multiple nested for-loops and a larger number of operations on smaller matrices, which increase the number of BLAS calls, thus inducing significant BLAS overheads and decreasing the overall performance of the solver. This is limited by a vectorised code structure. However and as showed by the matrix multiplication problem, the L2 cache reuse is the limiting factor and, it ultimately affects the peak performance of the solver due to these numerous RAM-to-cache communications for larger matrices. Such problem is serious and, its influence is demonstrated by the delayed response in terms of performance for the function `constitutive.m`. However, we also have to mention that the overall residual performance was resolved only for a limited total number of material points. The performance drop of the function `constitutive.m` has never been achieved. Consequently, we suspect an additional decrease of overall performances of the solver for larger problems.

The overall performance achieved by the solver is higher than expected and, is even higher with respect to what was reported by *Sinaie et al. (2017)*. We demonstrate that MATLAB is even more efficient than Julia, i.e., a minimum 2.86 performance gain achieved compared to a similar Julia CPDI2q implementation. This confirms the efficiency of MATLAB for solid mechanics problems, provided a reasonable amount of time is spent on the vectorisation of the algorithm.

B.6 Conclusions

We have demonstrated the capability of MATLAB as an efficient language in regard to a material point method (MPM) implementation in an explicit formulation when bottleneck operations (e.g., calculations of the shape function or material point contributions) are properly vectorised. The computational performances of MATLAB are even higher than those previously reported for a similar CPDI2q implementation in Julia, provided that built-in functions such as `accumarray()` are used. However, the numerical efficiency naturally decreases with the level of complexity of the chosen MPM variant (sMPM, GIMPM or CPDI/CPDI2q).

The vectorisation activities we performed provide a fast and efficient MATLAB-based MPM solver. Such vectorised code could be transposed to a more efficient language, such as the C-CUDA language, that is known to efficiently take advantage of vectorised operations.

As a final word, a future implementation of a poro-elasto-plastic mechanical solver could be applied to complex geomechanical problems such as landslide dynamics while benefiting from a faster numerical implementation in C-CUDA, thus resolving high three-dimensional resolutions in a decent and affordable amount of time.

Code availability

The fMPMM-solver developed in this study is licensed under the GPLv3 free software licence. The latest version of the code is available for download from Bitbucket at: <https://bitbucket.org/ewyser/fmpmm-solver/src/master/> (last access: October 6, 2020). The fMPMM-solver archive (v1.0 and v1.1) is available from a permanent DOI repository (Zenodo) at: <https://doi.org/10.5281/zenodo.4068585> (Wyser *et al.*, 2020b). The fMPMM-solver software includes the reproducible codes used for this study.

Acknowledgments

Yury Alkhimenkov gratefully acknowledges the support from the Swiss National Science Foundation (grant no. 172691). Yury Alkhimenkov and Yury Y. Podladchikov gratefully acknowledge support from the Russian Ministry of Science and Higher Education (project No. 075-15-2019-1890). The authors gratefully thank Johan Gaume for his comments that contributed to improve the overall quality of the manuscript.

Author contribution

EW wrote the original manuscript and developed, together with YP, the first version of the solver (fMPMM-solver, v1.0). YA provided technical supports, assisted EW in the revision of the latest version of the solver (v1.1) and corrected specific parts of the solver. EW and YA wrote together the revised version of the manuscript. MJ and YP supervised the early stages of the study and provided guidance. All authors have reviewed and approved the final version of the paper.

B.7 Appendix A: Acronyms

Table B.2: Acronyms used throughout the manuscript

PIC	P article- i n- C ell
FLIP	F Luid I mplicit P article
FEM	F inite E lement M ethod
sMPM	s tandard M aterial P oint M ethod
GIMPM	G eneralized M aterial P oint M ethod
uGIMPM	u ndeformed G eneralized M aterial P oint M ethod
cpGIMPM	cp ontiguous p article G eneralized M aterial P oint M ethod
CPDI	C onvected P article D omain I nterpolation
CPDI2q	C onvected P article D omain I nterpolation 2 nd order q uadrilateral

B.8 Appendix B: fMPMM-solver Variables

Table B.3: Variables of the structure arrays for the mesh `meD` and the material point `mpD` used in Code Fragment 1 & 2 shown in Figs. B.4 & B.5. `nDF` stores the local and global number of degrees of freedom, i.e., $\text{nDF} = [\text{nNe}, \text{nN} * \text{DoF}]$. The constant `nstr` is the number of stress components, according to the standard definition of the Cauchy stress tensor using the Voigt notation, e.g., $\boldsymbol{\sigma}_p = (\sigma_{xx}, \sigma_{yy}, \sigma_{xy})$.

Variable	Description	Dimension	
	<code>nNe</code> nodes per element	(1)	
	<code>nN</code> number of nodes	(1)	
	<code>DoF</code> degree of freedom	(1)	
	<code>nDF</code> number of DoF	(1, 2)	
<code>meD.</code>	<code>h</code> mesh spacing	(1, DoF)	
	<code>x</code> node coordinates	(nN, 1)	
	<code>y</code> node coordinates	(nN, 1)	
	<code>m</code> nodal mass	(nN, 1)	
	<code>p</code> nodal momentum	(nDF(2), 1)	
	<code>f</code> nodal force	(nDF(2), 1)	
		<code>n</code> number of points	(1)
		<code>l</code> domain half-length	(np, DoF)
	<code>V</code> volume	(np, 1)	
	<code>m</code> mass	(np, 1)	
	<code>x</code> point coordinates	(np, DoF)	
<code>mpD.</code>	<code>p</code> momentum	(np, DoF)	
	<code>s</code> stress	(np, nstr)	
	<code>S</code> basis function	(np, nNe)	
	<code>dSx</code> derivative in x	(np, nNe)	
	<code>dSy</code> derivative in y	(np, nNe)	
		<code>B</code> B matrix	(nstr, nDF(1), np)

Appendix C

Appendix C: An explicit GPU-based material point method solver for elastoplastic problems (ep2-3De v1.0)

Emmanuel Wyser, Yury Alkhimenkov, Michel Jaboyedoff and Yury Podladchikov

Accepted for publication ¹ in *Geoscientific Model Development*.

¹Wyser, E., et al. (2021). An explicit GPU-based material point method solver for elastoplastic problems (ep2-3De v1.0). *Geoscientific Model Development*, doi:10.5194/gmd-2021-200.

Abstract

We propose an explicit GPU-based solver within the material point method (MPM) framework using graphics processing units (GPUs) to resolve elastoplastic problems under two- and three-dimensional configurations (i.e., granular collapses and slumping mechanics). Modern GPU architectures, including Ampere, Turing and Volta, provide a computational framework that is well suited to the locality of the material point method in view of high-performance computing. For intense and nonlocal computational aspects (i.e., the back-and-forth mapping between the nodes of the background mesh and the material points), we use straightforward atomic operations (the scattering paradigm). We select the generalized interpolation material point method (GIMPMP) to resolve the cell-crossing error, which typically arises in the original MPM, because of the C_0 continuity of the linear basis function. We validate our GPU-based in-house solver by comparing numerical results for granular collapses with the available experimental data sets. Good agreement is found between the numerical results and experimental results for the free surface and failure surface. We further evaluate the performance of our GPU-based implementation for the three-dimensional elastoplastic slumping mechanics problem. We report i) a maximum performance gain of x200 between a CPU- and a single GPU-based implementation, provided that ii) the hardware limit (i.e., the peak memory bandwidth) of the device is reached. Furthermore, our multi-GPU implementation can resolve models with nearly a billion material points. We finally showcase an application to slumping mechanics and demonstrate the importance of a three-dimensional configuration coupled with heterogeneous properties to resolve complex material behavior.

C.1 Introduction

Graphics processing units, or GPUs, have revolutionized the entire field of high-performance computing (HPC) in the last decade. GPUs are many-core processors that were originally developed by the gaming industry in the mid-1990s to accelerate graphics and video rendering. Currently, GPUs are widely employed hardware accelerators used in various applications, including artificial intelligence (AI) and machine learning. GPUs are also increasingly used for high-performance scientific computing (see *Dong et al.* 2015; *Omlin et al.* 2018; *Räss et al.* 2018; *Zhang et al.* 2021; *Alkhimenkov et al.* 2021b). The majority of the scientific algorithms on many-core (e.g., GPU) hardware accelerators are memory-bounded, meaning that data transferring (reading and writing) limits the performance of a solver. This is in contrast to the recent compute-bounded algorithms, where arithmetic floating point calculations are the main limiting factor in solver performance. This GPU supercomputing breakthrough requires re-engineering existing scientific codes or developing new algorithmic structures to efficiently take advantage of the intrinsic low-level parallelism of GPUs.

The material point method (MPM) was first proposed by *Sulsky et al.* (1994) and was further advanced by the generalized interpolation material point method (GIMPMP) by *Bardenhagen and Kober* (2004). It can be think of as a finite element method (FEM) in which a) integration points (i.e., material points) move and b) convey state variables, e.g., stress and strain components. The continuum is discretized by material points. The nodal momentum equations are solved on a background mesh and nodal basis functions provide a mapping framework between the mesh and the material points to transfer either the updated nodal solution or material point properties. The background mesh is reset and actually never deforms. It has been widely used for large deformation geomechanical problems such as retrogressive failure, coupled hydromechanical landslides or granular collapses (*Tran and Sołowski*, 2019; *Bandara and Soga*, 2015; *Dunatunga and Kamrin*, 2015).

From a computational point a view, it is critical for MPM to be able to simulate large-scale problems in both two- and three-dimensional configurations. From this perspective, a few researchers have exploited parallel computing using a single or multiple GPU strategy (*Dong et al.*, 2015; *Dong and Grabe*, 2018) to efficiently implement an explicit GIMPMP for two-dimensional configurations. More recently, some researchers in the graphics community presented a similar implementation (*Gao et al.*, 2018; *Hu et al.*, 2019; *Wang et al.*, 2020) for three-dimensional configurations. One of the most computationally expensive operations in MPM is mapping between material points and their associated nodes, which is supported by basis functions. When implementing a GPU, the two most common approaches are *gathering* and *scattering*. The former gathers the material point's state variables (i.e., mass, velocity component or stresses) to the nodes, whereas the latter scatters (i.e., distributes) the material point's state variables to their associated nodes. This leads to write

conflicts, as several threads are writing into the same memory location at the same time. *Gao et al. (2018)* demonstrated the superiority of *scattering* over *gathering*, provided that the write conflicts are handled without atomic operations. *Gao et al. (2018)* proposed parallel scattering that results in a performance of an order of magnitude higher than that of a naive atomic implementation. Recently, *Wang et al. (2020)* proposed an Array of Structures of Arrays (AoSoA) as an efficient layout. It is largely responsible for CPU or GPU performances, as it dictates the memory access pattern by ensuring coalesced memory accesses (*Wang et al., 2020*).

We propose an explicit GIMP implementation in a three-dimensional configuration on a single and multiple GPUs (ep2-3De v1.0), taking advantage of the efficient vectorized algorithmic structure of the MPM solver proposed by *Wyser et al. (2020a)*. Our GPU-based solver relies on built-in functions of atomic operations for the mapping between material points and their associated nodes (i.e., scattering). For large-scale simulations, the main hardware limit is the GPU on-chip memory, which was well documented by *Dong and Grabe (2018)*. To resolve the GPU on-chip memory limitation, we rely on a distributed memory parallelization using the message passing interface (MPI) standard. The multi-GPU implementation can resolve models with nearly a billion material points. The GPU solver ep2-3De v1.0² combines MATLAB for pre- and postprocessing activities with the massive power of the most recent GPU architectures available (Ampere, Turing and Tesla architectures). This approach allows the user to easily set the problem's geometry and initialize the material points as well as their state variables. Everything needed is then passed to the GPU, which further performs the computations. We propose a formal framework to evaluate the performance of our GPU-based implementation based on the metric for memory-bounded codes, i.e., the effective memory throughput (*Omlin, 2017*). Since the memory wall has been reached, the memory bandwidth becomes the limiting factor for performance. In addition, it is an easily comparable metric. Similarly, we also report the average number of iterations per second for the same reason: it indicates a relative performance, and it does not depend on material properties (e.g., bulk or shear moduli). We also implement the solver ep2-3De v1.0 under a single-CPU architecture to provide a reference baseline for the performance evaluation of the GPU-based implementation. For the validation of our solver, we simulate the granular collapse problem in a three-dimensional configuration and compare the result against the well-known experimental results of *Bui et al. (2008)*.

C.2 Numerical implementation

In this section, we briefly describe the governing equations implemented in the MPM solver. We use a linear elastoplastic rheology. Large deformations are carried out via a rate-dependent formulation with the Jaumann stress rate.

C.2.1 Governing equations

The conservation of linear momentum is given by (using the Einstein summation convention)

$$\rho \frac{\partial v_k}{\partial t} = \frac{\partial \sigma_{kl}}{\partial x_l} + \rho g_k, \quad (\text{C.1})$$

where σ_{kl} is the Cauchy stress tensor, $v_k = \partial u_k / \partial t$ is the velocity, u_k is the displacement, g_k is the body force, and $k, l = \overline{1..3}$. The conservation of angular momentum is given by $\sigma_{kl} = \sigma_{lk}$. Dirichlet and Neumann boundary conditions are

$$u_k = \bar{u}_k \quad \text{on} \quad \partial\Omega_u, \quad (\text{C.2})$$

$$\sigma_{kl} n_l = \bar{\tau}_k \quad \text{on} \quad \partial\Omega_\tau, \quad (\text{C.3})$$

where \bar{u}_k and $\bar{\tau}_k$ are prescribed displacements, and n_k is a unit normal vector pointing outward from the boundary $\partial\Omega$ of the domain Ω . Following the standard FEM procedure, we use the updated Lagrangian framework; thus, the weak form of Eq. C.1 is written in the current spatial configuration. The weak form of

²The routines of the ep2-3De v1.0 solver are available for download from GitHub at: <https://github.com/ewyser/ep2-3De> (last access: October 26, 2021). The routines archive (v1.0) (*Wyser et al., 2021b*) is available from a permanent DOI repository (Zenodo) at <https://doi.org/10.5281/zenodo.5600373> (last access: October 26, 2021).

Eq. C.1 can be obtained by multiplying it with a test function ϕ and then applying integration by parts and divergence theorem, leading to

$$\int_{\Omega} \phi \rho a_k d\Omega = \int_{\Omega} \phi \rho g_k d\Omega - \int_{\Omega} \frac{\partial \phi}{\partial x_l} \sigma_{kl} d\Omega + \int_{\partial\Omega_{\tau}} \phi \bar{\tau}_k dS, \quad (\text{C.4})$$

where $\partial v_k / \partial t = a_k$ is the acceleration, ϕ is any test function that vanishes on $\partial\Omega_u$, and $\bar{\tau}_k$ is the external traction applied on the boundary $\partial\Omega$, $k = \overline{1..3}$. However, in our MPM implementation, tractions on the boundary are not used. Eq. C.4 can be solved using a finite element approach leading to the following compact form:

$$[M_{ij} a_j]_k = [f_i^{\text{ext}} - f_i^{\text{int}}]_k, \quad (\text{C.5})$$

where $M_{ij} = \sum_{p=1}^{n_p} m_p \phi_i(\mathbf{x}_p) \phi_j(\mathbf{x}_p)$ is the consistent mass matrix with $\phi_i(\mathbf{x}_p)$ being the basis function between node i and material point p . This work adopts a lumped mass matrix, i.e., $m_i \equiv M_{ii} = \sum_{p=1}^{n_p} m_p \phi_i(\mathbf{x}_p)$, to avoid an expensive matrix inversion (Sulsky *et al.*, 1994; Bardenhagen and Kober, 2004; Acosta *et al.*, 2020). The external $f_{k,n}^{\text{ext}}$ and internal $f_{k,n}^{\text{int}}$ forces at node n are then defined by

$$f_{k,n}^{\text{ext}} = \sum_{p=1}^{n_p} m_p \phi_n(\mathbf{x}_p) g_k, \quad (\text{C.6})$$

$$f_{k,n}^{\text{int}} = \sum_{p=1}^{n_p} v_p \frac{\partial \phi_n}{\partial x_l}(\mathbf{x}_p) \sigma_{kl,p}, \quad (\text{C.7})$$

where m_p is the material point's mass, v_p is the material point's volume and $\sigma_{kl,p}$ is the material point's Cauchy stress tensor. Solving Eq. C.5 for the acceleration $a_{k,n}$, the updated velocity is obtained via a forward-Euler scheme,

$$v_{k,n}^{t+\Delta t} = v_{k,n}^t + \Delta t a_{k,n}, \quad (\text{C.8})$$

where the velocity is given by $v_{k,n}^t = m_n^{-1} \sum_{p=1}^{n_p} \phi_n(\mathbf{x}_p) m_p v_{k,p}$ and $v_{k,p}$ is the material point's velocity. Boundary conditions are enforced on the boundary nodes. The material point velocity $v_{k,p}$ and coordinates $x_{k,p}$ are defined by mapping (i.e., an interpolation) between the updated solution on the mesh and the material points, i.e.,

$$v_{k,p}^{t+\Delta t} = v_{k,p}^t + \Delta t \sum_{n=1}^{n_n} \phi_n(\mathbf{x}_p) a_{k,n}, \quad (\text{C.9})$$

$$x_{k,p}^{t+\Delta t} = x_{k,p}^t + \Delta t \sum_{n=1}^{n_n} \phi_n(\mathbf{x}_p) v_{k,n}^{t+\Delta t}, \quad (\text{C.10})$$

where n_n is the number of associated nodes n to a material point p . The remaining tasks are i) to update the material point volume and ii) to solve for the constitutive stress-strain relationship.

C.2.2 Rate formulation

The large deformation framework necessitates a suitable stress-strain formulation. Some studies prefer the finite deformation framework and employ a linear relationship between Kirchhoff stresses and logarithmic strains (Charlton *et al.*, 2017; Gaume *et al.*, 2018; Coombs *et al.*, 2020). In the present work, we adopt a rate-dependent framework by applying the Jaumann rate (e.g., Huang *et al.* 2015; Wang *et al.* 2016a,c; Bandara *et al.* 2016), which yields an objective stress rate measure.

The Jaumann rate of the Cauchy stress is given by

$$\frac{\mathcal{D}\sigma_{ij}}{\mathcal{D}t} = C_{ijkl} \frac{1}{2} \left(\frac{\partial v_l}{\partial x_k} + \frac{\partial v_k}{\partial x_l} \right), \quad (\text{C.11})$$

where C_{ijkl} is the 4th rank tangent stiffness tensor. Thus, the Jaumann stress derivative may be written as

$$\frac{\mathcal{D}\sigma_{ij}}{\mathcal{D}t} = \frac{D\sigma_{ij}}{Dt} - \sigma_{ik}\dot{\omega}_{jk} - \sigma_{jk}\dot{\omega}_{ik}, \quad (\text{C.12})$$

where $\omega_{ij} = (\partial_i v_j - \partial_j v_i)/2$ is the vorticity tensor, $D\sigma_{ij}/Dt$ corresponds to the material derivative

$$\frac{D\sigma_{ij}}{Dt} = \frac{\partial\sigma_{ij}}{\partial t} + v_k \frac{\partial\sigma_{ij}}{\partial x_k}. \quad (\text{C.13})$$

By rearranging the Jaumann stress derivative in Eq. C.12, we obtain

$$\frac{\partial\sigma_{ij}}{\partial t} = \frac{\mathcal{D}\sigma_{ij}}{\mathcal{D}t} + \overbrace{\sigma_{ik}\dot{\omega}_{jk} + \sigma_{jk}\dot{\omega}_{ik}}^{\sigma_{ij}^{\mathcal{R}}}, \quad (\text{C.14})$$

where $\sigma_{ij}^{\mathcal{R}}$ represents the rotation of the Cauchy stress tensor, which satisfies the stress objectivity for the rate-dependent formulation.

Let us expand $\sigma_{ij}^{\mathcal{R}}$ in Eq. C.14 using identities $\sigma_{ij} = \sigma_{ji}$, $\dot{\omega}_{ij} = -\dot{\omega}_{ji}$ and $\dot{\omega}_{kk} = 0$. The Cauchy stress tensor is written using the so-called Voigt notation (as a vector $\boldsymbol{\sigma} = \{\sigma_{xx}, \sigma_{yy}, \sigma_{zz}, \sigma_{xy}, \sigma_{yz}, \sigma_{xz}\}$). After expanding, collecting and rearranging terms, the objective stress terms $\sigma_{ij}^{\mathcal{R}}$ for a three-dimensional configuration are

$$\sigma_{xx}^{\mathcal{R}} = 2(\sigma_{xy}\dot{\omega}_{xy} + \sigma_{xz}\dot{\omega}_{xz}), \quad (\text{C.15})$$

$$\sigma_{yy}^{\mathcal{R}} = -2(\sigma_{xy}\dot{\omega}_{xy} - \sigma_{yz}\dot{\omega}_{yz}), \quad (\text{C.16})$$

$$\sigma_{zz}^{\mathcal{R}} = -2(\sigma_{xz}\dot{\omega}_{xz} + \sigma_{yz}\dot{\omega}_{yz}), \quad (\text{C.17})$$

$$\sigma_{xy}^{\mathcal{R}} = \dot{\omega}_{xy}(\sigma_{yy} - \sigma_{xx}) + \sigma_{yz}\dot{\omega}_{xz} + \sigma_{xz}\dot{\omega}_{yz}, \quad (\text{C.18})$$

$$\sigma_{yz}^{\mathcal{R}} = \dot{\omega}_{yz}(\sigma_{zz} - \sigma_{yy}) - \sigma_{xy}\dot{\omega}_{xz} - \sigma_{xz}\dot{\omega}_{xy}, \quad (\text{C.19})$$

$$\sigma_{xz}^{\mathcal{R}} = \dot{\omega}_{xz}(\sigma_{zz} - \sigma_{xx}) + \sigma_{yz}\dot{\omega}_{xy} - \sigma_{xy}\dot{\omega}_{yz}, \quad (\text{C.20})$$

and, for a two-dimensional configuration assuming plane strain conditions, Eqs. C.15, C.16 and C.18 reduce to

$$\sigma_{xx}^{\mathcal{R}} = 2\sigma_{xy}\dot{\omega}_{xy}, \quad (\text{C.21})$$

$$\sigma_{yy}^{\mathcal{R}} = -2\sigma_{xy}\dot{\omega}_{xy}, \quad (\text{C.22})$$

$$\sigma_{xy}^{\mathcal{R}} = \dot{\omega}_{xy}(\sigma_{yy} - \sigma_{xx}). \quad (\text{C.23})$$

C.2.3 Elastoplastic deformation

A nonassociated Drucker-Prager model (D-P model) with a tension cutoff is used in this study, similar to *Huang et al. (2015)*; *Liu et al. (2020)*; *Nguyen et al. (2020)*; *Zuo et al. (2020)*, because of its straightforward implementation within explicit numerical solvers. The D-P model has been established as an approximation of the Mohr-Coulomb (M-C) model (*Krabbenhoft et al., 2012*; *Alejano and Bobet, 2012*), i.e., a conical yield surface that approximates the M-C yield surface in the principal stress space. The former can be adjusted by parameters, so it passes either through the outer or inner edges of the M-C yield surface (*Jiang and Xie, 2011*; *De Borst et al., 2012*).

The D-P yield function f (see Fig. C.1) is typically defined in terms of invariants; The first invariant of the Cauchy stress tensor $I_1 = \sigma_{kk}$, and the second invariant $J_2 = \frac{1}{2}\tau_{ij}\tau_{ji}$ of its deviatoric part τ_{ij} , where the deviatoric part of the Cauchy stress is $\tau_{ij} = \sigma_{ij} + \delta_{ij}p$ with the pressure $p = -\frac{1}{3}\sigma_{kk}$. The D-P yield surface is made of two

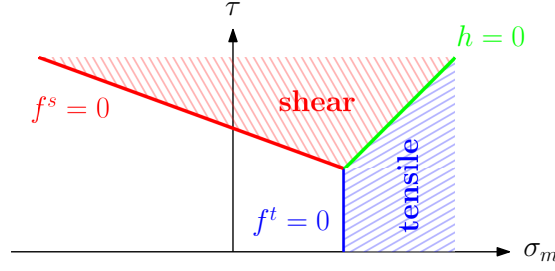


Figure C.1: Drucker-Prager yield surface in the $(\sigma_m - \tau)$ space. The yield surface is made of a shear line segment (in red) and a tensile line segment (in blue).

surfaces (i.e., representing shear and tensile yield criteria), delimited by

$$f^s(\sigma_m, \tau) = \tau + q_\phi \sigma_m - k_\phi, \quad (\text{C.24})$$

$$f^t(\sigma_m) = \sigma_m - \sigma^t, \quad (\text{C.25})$$

where $\tau = \sqrt{J_2}$ is the effective shear stress, $\sigma_m = -p$ is the mean stress, q_ϕ and k_ϕ are the material parameters defined by ϕ as the internal friction angle, σ^t is the tensile strength and c is the cohesion. Cohesion varies with the accumulated plastic strain $\bar{\epsilon}_p$ when considering a strain softening material, i.e., $c = f(\bar{\epsilon}_p)$. These two surfaces define two plastic regions (see Fig. C.1) corresponding to either the shear or tensile failure mode. We use a nonassociated plastic flow law for shear and tensile failures; thus, the plastic potential function g is written as

$$g^s(\sigma_m, \tau) = \tau + q_\psi \sigma_m, \quad (\text{C.26})$$

$$g^t(\sigma_m) = \sigma_m, \quad (\text{C.27})$$

where q_ψ is a material parameter estimated with the dilation angle ψ .

The line segment $h(\sigma_m, \tau) = 0$ represents the diagonal line between $f^s(\sigma_m, \tau) = 0$ and $f^t(\sigma_m, \tau) = 0$ in the (σ_m, τ) plane, i.e., h is the boundary between shear and tensile failure modes. The function $h(\sigma_m, \tau)$ is given by

$$h(\sigma_m, \tau) = \tau - \tau^P - \alpha^P (\sigma_m - \sigma^t), \quad (\text{C.28})$$

with the constants $\tau^P = k_\phi - q_\phi \sigma^t$ and $\alpha^P = (1 - q_\phi^2)^{1/2} - q_\phi^2$. We consider an inner adjustment of the D-P yield surface with respect to the M-C yield surface, and the model parameter used in Eqs. C.24 & C.26 are given by

$$q_\phi = \frac{6 \sin \phi}{\sqrt{3}(3 + \sin \phi)}, \quad (\text{C.29})$$

$$q_\psi = \frac{6 \sin \psi}{\sqrt{3}(3 + \sin \psi)}, \quad (\text{C.30})$$

$$k_\phi = \frac{6c \cos \phi}{\sqrt{3}(3 + \sin \phi)}. \quad (\text{C.31})$$

In the following, we briefly detail the return mapping strategy used to return the trial Cauchy stress σ_{ij}^{tr} (i.e., assuming pure elastic deformation only) onto the yield surfaces considering $\psi = 0$. A complete description of such return mapping can be found in *Huang et al. (2015)*. Shear failure is declared when i) $f^s(\sigma_m^{tr}, \tau^{tr}) > 0$ and $\sigma_m^{tr} < \sigma^t$ or if ii) $h(\sigma_m^{tr}, \tau^{tr}) > 0$ and $\sigma_m^{tr} \geq \sigma^t$. The corrected Cauchy stress tensor now reads

$$\sigma_{ij}^{t+\Delta t} = \tau_{ij}^{tr} \left(\frac{k_\phi - q_\phi \sigma_m^{tr}}{\tau^{tr}} \right) + \sigma_m^{tr} \delta_{ij}, \quad (\text{C.32})$$

with δ the Kronecker tensor. Tensile failure is declared when $h(\sigma^{tr}, \tau^{tr}) \leq 0$ and $\sigma_m^{tr} \geq \sigma^t$. The corrected Cauchy stress tensor reads as

$$\sigma_{ij}^{t+\Delta t} = \sigma_{ij}^{tr} + (\sigma^t - \sigma_m^{tr})\delta_{ij}. \quad (\text{C.33})$$

C.3 GIMPM implementation under a GPU architecture

We propose an explicit generalized interpolation material point method (GIMPM) implementation (Dong and Grabe, 2018; Wang et al., 2020) in a three-dimensional configuration on a GPU, taking advantage of the efficient vectorized algorithmic structure (Wyser et al., 2020a,c). We select explicit GIMPM implementation, which is valid for a variety of problems compared to other latest variants (Wang et al., 2019; Coombs et al., 2020), i.e., CPDI or CPDI2q. Additionally, we use a double-mapping approach (MUSL, see Nairn 2003; Buzzi et al. 2008), which consists of updating the stress at the end of the time step. We implement the following domain-update methods: a) no update of the material point domain, further labelled uGIMPM, and b) a domain update controlled by the determinant of the deformation gradient, i.e., $\det(F_{ij})$, further labelled cpGIMPM. These domain-update methods are commonly used in the literature (Baumgarten and Kamrin, 2019; Tran and Solowski, 2019). The limitation of the two methods is that they are not ideally suited for specific tests: simple stretching and compression modes (Coombs et al., 2020).

C.3.1 Implementation on a graphical processing unit (GPU)

Graphical processing units (GPUs) are many-core processors originally designed to refresh screen pixels (e.g., for computer games) independently. A schematic representation of the main architecture differences between a CPU and a GPU is depicted in Fig. C.2. On the GPU chip, most of the physical space is dedicated to arithmetic logical units, whereas on a CPU, most of the physical space is dedicated to chip host scheduling and control microsystems. GPUs feature many more cores, a lower thread-scheduling cost and a higher memory bandwidth than CPUs. The programming model is based on a parallel principle called single instruction - multiple data (or SIMD), i.e., every single instruction is executed on different data. GPUs feature a hierarchical structure. The lowest computational unit is the thread. Threads are organized into blocks of threads, the whole constituting a hierarchical grid of blocks of threads. A GPU typically launches thousands of threads, which execute the same instruction in parallel, thus achieving massive parallelism. Additionally, the most recent GPUs offer a high throughput (close to a TB per second peak memory throughput).

Currently, most of the algorithms are memory-bounded, meaning that memory transfers limit the performance, in contrast to computer-bounded algorithms, where floating point (arithmetic) operations limit the performance. Thus, for an efficient implementation of an algorithm, one must consider a) limiting the memory transfers to the bare minimum and b) avoiding complex data structures (Räss et al., 2019b) to benefit from the high throughput capabilities of GPUs. The ability of a GPU is particularly well suited to efficiently execute a large number of local operations in parallel, i.e., single instruction, multiple data (SIMD) programming. In the case of a GIMPM implementation, this includes the calculation of shape functions and the update of various quantities at the material point level (i.e., stresses, domain lengths, material point volumes, etc.). Below, we present key aspects of our GPU-based implementation using the Computed Unified Device Architecture (CUDA C) language of the Nvidia Corporation, which is a syntax extension of the C programming language.

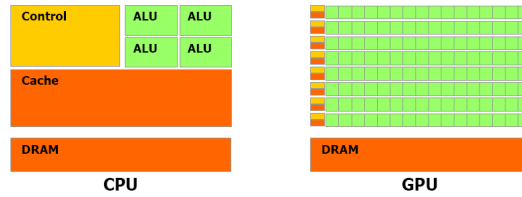


Figure C.2: Schematic chip representation for both the central processing unit (CPU) and the graphical processing unit (GPU) architecture (Nvidia, 2007). The latter is made of thousands of arithmetic logical units (ALUs). The CPU architecture is primarily dedicated to controlling units and cache memory, and the physical space allowed for ALUs is considerably reduced compared to a GPU architecture.

C.3.2 The multi-GPU code implementation

One of the major limitation of a single GPU implementation is the on-chip memory. It is then essential to overcome this limit in order to resolve larger computational domain with a greater amount of material points. We address this concern by implementing a distributed memory parallelisation using the message passing interface (MPI) standard. However, we limit our implementation efforts by considering 1) a one-dimensional GPU topology, 2) no computation/communication overlaps, and 3) only mesh-related quantities are shared amongst GPUs, i.e., the material points are not transferred between GPUs during a simulation. We also selected a non-adaptive time step to avoid the collection of the material point's velocities located in different GPUs at the beginning of each calculation cycle.

Algorithm workflow

In our implementation, MATLAB acts as an architect (see Fig. C.3). It 1) defines the problem geometry (i.e., the background mesh, material point locations and related quantities, etc.), which can be tedious to initialize in a CUDA C environment. It also calls an external MATLAB script, which compiles the necessary source codes, i.e., `gpu.cu` or `cpu.cu`. It further 2) calls either a CUDA C or plain C executable, i.e., `gpu.exe` or `cpu.exe`, within a Windows OS to solve for the numerical problem and finally 3) imports the results of calculations for further postprocessing tasks.

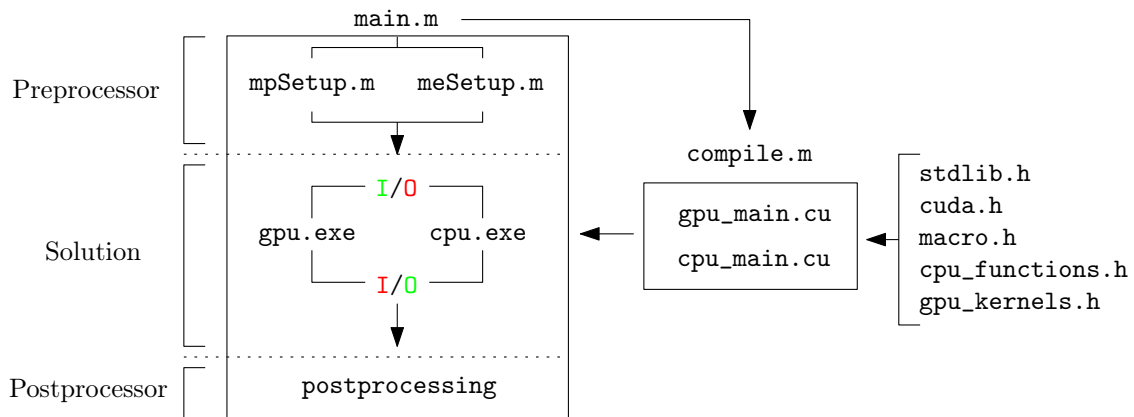


Figure C.3: Multifunctional workflow: 1) usage of MATLAB for data initialization, compilation and postprocessing activities and 2) system calls to a performant compiled language such as C (CPU-based) and CUDA C (GPU-based) for heavy calculations. Here, I/O stands for input/output, and the colouring (red or green) specifies which one is active, i.e., `I/O` means data only are transferred to the GPU (or CPU) for further calculation activities.

This is a powerful combination between a high-level language such as MATLAB and a performant low-level language such as CUDA C or plain C. It is also easy to invoke system commands directly via MATLAB, i.e., to compile source codes and/or run executables using the built-in command `system('...')`. We focus on OS-free scripting in MATLAB using a built-in command (i.e., `isunix` or `ispc`) to ensure that it performs well under all operating system (OS) architectures. In addition, such a workflow can be easily extended to other high-level languages such as Python.

Kernels and launch configuration

We briefly describe our GPU-based implementation (`gpu_main.cu`) while focusing mainly on the computational aspects of the implementation. Implementation of an explicit GIMP solver into the CUDA C language requires dispatching computational activities into several kernels, i.e., similar to classic functions for a serial implementation in the C language. Each kernel is operated by the GPU only, and kernel launch configuration parameters must be defined for its proper execution. Among them, one must define the number of active threads per block (i.e., the block size) and the number of blocks (i.e., the grid size). A typical kernel is executed N times in parallel by N distinct threads organized into blocks of threads, i.e., a grid of blocks of threads. The principal hardware limitation is the total number of threads within a block: it cannot exceed 1024 threads per block. One must ensure that the maximal size of a block is lower than or equal to this limit.

The computational activities are handled by multiple GPU kernels; 11 kernels are successively launched over a computational cycle. An overall description is given in Fig. C.4. A `while` loop is used to perform the computational cycles, and an MPM step is solved at every cycle. n_{IO} (i.e., the number of accesses to the GPU global memory) is reported in Fig. C.4 for each kernel and is estimated by a careful examination of relevant operations within the kernels. Note that all calculations are performed on the GPU, except the calculation of the adaptive time step, which is serially executed by the CPU.

In our GPU-based implementation, we define two distinct types of kernel launch parameters: 1) those used for mapping between material points and background nodes (i.e., accumulations and projections between material points with their associated nodes and back and forth) and 2) those used for local calculation at the material point or node level (i.e., update of material point stresses or the solution to the momentum balance equations on the Eulerian background mesh). We use regular background mesh because it is straightforward to find the material point's location. However, computing a material point's location using an irregular background mesh is more complicated.

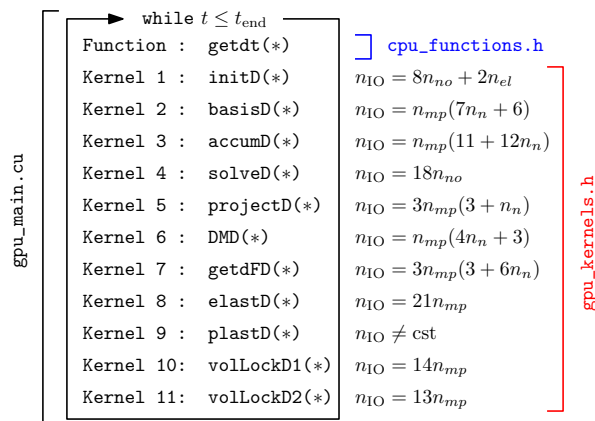


Figure C.4: Specific workflow for the source code running of the GPU, t_{end} is a user-defined time that controls the total time of the simulation, and the operator `*` stands for the pointer object, as in the C language. It should be noted that a vast majority of operations within kernels are performed on pointers.

Adaptative time step

An adaptive time step is implemented. For three-dimensional configurations, the maximum elastic wave speed of the material (Anderson Jr, 1987; Zhang et al., 2016) reads as

$$(c_x, c_y, c_z) = c_{el} + \left(\max_p(|v_{x,p}|), \max_p(|v_{y,p}|), \max_p(|v_{z,p}|) \right), \quad (\text{C.34})$$

where $c_{el} = ((K + 4G/3)/\rho)^{\frac{1}{2}}$ is the elastic wave speed of the material, K and G are the bulk and shear moduli, respectively, ρ is the material density, and $v_{x,p}$, $v_{y,p}$ and $v_{z,p}$ are the material point velocity components. The time step Δt is then restricted by the CFL condition,

$$\Delta t = \alpha \min \left(\frac{\Delta x}{c_x}, \frac{\Delta y}{c_y}, \frac{\Delta z}{c_z} \right), \quad (\text{C.35})$$

where $\alpha \in [0; 1]$ is the time step multiplier, and Δx , Δy , and Δz are the background mesh resolutions.

This requires evaluation of the maximum velocity of all material points at the beginning of each calculation cycle. We choose to sequentially find the maximum velocity using the CPU instead of a parallel implementation on the GPU. This results in systematic memory transfers between the GPU global memory and the random access memory (RAM) of the CPU. However, we report a low performance loss due to these transfers, i.e., a maximal loss of 2-5 % in performance, which is acceptable.

Back-and-forth mapping between material points and their associated nodes

The GPU-based algorithm relies heavily on the use of arrays `p2e` and `e2n` (Wyser et al., 2020a). Elements are numbered with an increasing index. Associated nodes are also numbered in a similar manner. The array `e2n` of dimension $n_{el} \times n_n$, where n_{el} is the total number of nodes and n_n is the number of nodes associated with an element e , describes the topological relation between the elements and the nodes of the mesh. Similarly, the array `p2e` describes the topological relation between the material points and the element in which they are located. These two arrays provide an intuitive definition of the relations between i) the material points and the nodes they are associated with (i.e., `p2n`) and ii) the element and their nodes (i.e., `e2n`). Then, it is a computationally straightforward process to identify which nodes n are associated with a material point p , which is occupying an element e .

The GPU-based implementation relies on the built-in function `atomicAdd()` in CUDA C. It performs atomic operations, which avoid the data race of multiple threads, from the same or different blocks to update the same memory location. Atomic operations are extensively used to calculate internal and external force contributions (Eqs. C.6 & C.7), as well as the lumped mass matrix, and to update the material point's properties such as velocities and coordinates (Eqs. C.9 & C.10). Dong et al. (2015); Wang et al. (2020) reported (for older GPU architectures such as Pascal or Kepler) that atomic scattering can be significantly slower compared to an optimized parallel implementation. However, atomic operations are a) intuitive to both understand and implement, and b) they avoid a complex data layout, such as recently proposed in Wang et al. (2020). The use of built-in atomic operations considerably reduces programming efforts.

Treatment of volumetric locking for low-order elements

When low-order elements are used in a GIMP formulation, volumetric locking arises and results in spurious oscillations of the stress field (Jassim et al., 2013; Coombs et al., 2018; González Acosta et al., 2019; González Acosta et al., 2021). We implement a simple procedure to mitigate volumetric locking when considering near-incompressible behaviour for ischoric plastic flows. Cuomo et al. (2019); Lei et al. (2020) introduced an element-based averaging method, following Mast et al. (2012). Selected material point properties are reconstructed based on an average value calculated at the element's centre at the end of a time step. However, we propose averaging only the volumetric part of the stress tensor, i.e., the pressure $p = -\frac{1}{3}\sigma_{kk}$, while its deviatoric part $\tau_{ij} = \sigma_{ij} - p\delta_{ij}$ remains unchanged. We believe our approach is conceptually similar to the

B-bar technique (Hughes, 1980; Bisht et al., 2021). This results in the following:

$$p_e = \frac{\sum_{p \in e} v_p p_p}{\sum_{p \in e} v_p}, \quad (\text{C.36})$$

where v_p is the material point's volume. This gives a constant distribution of the pressure field over an element because of its zero-order reconstruction (Lei et al., 2020). The Cauchy stress tensor $\sigma_{ij,p}$ of a material point p occupying an element e is corrected as

$$\sigma_{ij,p} = \tau_{ij,p} + \delta_{ij}(p_e)_p, \quad (\text{C.37})$$

where δ_{ij} is the Kronecker delta and $(p_e)_p$ is the averaged pressure within an element e and assigned to a material point p .

C.3.3 Available computational resources

The CPU- and GPU-based simulations are performed on a modern workstation running on a Windows 10 operating system with the latest CUDA version v11.2. The CPU is an Intel Core i9-10900K with 10 physical cores of base clock speed (or frequency) of 3.70 GHz, which can rise up to a maximum clock speed of 5.30 GHz, supported with 64 GB DDR4 RAM. It hosts a consumer electronics Nvidia RTX 3090 GPU (the latest Ampere architecture) with 82 streaming multiprocessors (SM units) with a base frequency of 1.40 GHz. This results in 10490 CUDA cores that are supported with an on-chip memory of 24 GB GDDR6 (i.e., the GPU global memory). Other GPUs installed on older desktops are also used to compare their respective GPU performances, i.e., an RTX 2080 ti (workstation) and a GTX 1650 (laptop), both running on a Windows 10 operating system. Additional simulations were also ran on a workstation equipped with the latest Nvidia A100 GPU at the Lomonosov Moscow State University.

Furthermore, GPU-based simulations are also performed on the Octopus GPU supercomputer at the Swiss Geocomputing Centre, University of Lausanne, Switzerland. In particular, the GPU-based simulations are run on the Volta node, hosting an Nvidia Tesla V100 (Volta architecture) 16 GB, supported by an Intel(R) Xeon(R) E5-2620 v2 (Haswell) @ 2.1 GHz CPU. The latest CUDA version installed is v11.0, and the supercomputer Octopus is operated under a CentOS 6.9. environment. To summarize the computational resources in use, Table C.2 presents the main characteristics of the GPUs used in this study.

Table C.1: List of the graphical processing units (GPUs) used throughout this study. We also report the peak memory throughput, i.e., MTP_{peak} , measured thanks to the routine `bandwidthTest.cu` provided by Nvidia alongside with the CUDA toolkit. When compared with the effective memory throughput MTP_{eff} , one can estimate the possible gain of an additional optimization of the algorithm. This is particularly useful when estimating the level of optimization of a GPU-based implementation.

GPU	Architecture	SM count	On-chip memory [GB]	MTP_{peak} [$\text{GB}\cdot\text{s}^{-1}$]
A100	Ampere	108	40	1127.1
RTX 3090	Ampere	82	24	774.1
RTX 2080 ti	Turing	68	11	513.1
GTX 1650	Turing	14	4	168.7
V100	Volta	80	16	732.6

The multi-GPU simulations are run on the two different systems. The first one is an Nvidia DGX-1 - like node hosting 8 Nvidia Tesla V100 Nvlink (32 GB) GPUs, 2 Intel Xeon Silver 4112 (2.6 GHz) CPUs. The second one is composed of 32 nodes, each featuring 4 Nvidia GeForce GTX Titan X Maxwell (12 GB) GPUs, 2 Intel XEON E5-2620V3 4112 (2.4 GHz) CPUs. To summarize the computational resources in use, Table C.2 presents the main characteristics of the GPUs used in this study.

Table C.2: List of the graphical processing units (GPUs) used for multi-GPU simulations.

GPU	Architecture	On-chip memory [GB]
8×V100	Volta	8×32
128×GTX Titan X	Maxwell	128×12

C.3.4 Measuring computational performance on a GPU

Omlin (2017); Räss *et al.* (2019b); Räss *et al.* (2019); Alkhimenkov *et al.* (2021b) demonstrated that a pertinent metric to quantify the performance of memory-bounded algorithms is the effective memory throughput, i.e., MTP_{eff} in $\text{GB}\cdot\text{s}^{-1}$. It quantifies the efficiency of data transfers between the global memory (i.e., the on-chip memory of the GPU) and the arithmetic logical units (ALUs) of the GPU. To determine the effective memory throughput, one must estimate (or quantify) the overall set of memory operations (read-and-write or read only), i.e., n_{IO} , which are needed to resolve a given problem. Consequently, we carefully estimate the minimum number of memory operations while considering a GIMPM-based implementation. This results in the following effective memory throughput:

$$MTP_{\text{eff}} = \frac{n_{\text{iter}} \times n_{\text{IO}} \times n_{\text{p}}}{1024^3 \times t_{\text{GPU}}} [\text{GB}\cdot\text{s}^{-1}], \quad (\text{C.38})$$

where n_{p} is the arithmetic precision (i.e., single-precision floating-point format FP32 or double-precision floating-point format FP64) and t_{GPU} is the wall-clock time in seconds to complete the n_{iter} iterations to solve for the numerical problem. For three-dimensional problems, we estimate the minimal number of memory operations for an explicit GIMP implementation as

$$n_{\text{IO}} = 2n_{mp}(43 + 22n_n) + 26n_{no} + 2n_{el}, \quad (\text{C.39})$$

where n_{mp} is the number of material points, n_n is the number of associated nodes for an element (i.e., $n_n = 16$ in 2D and $n_n = 64$ in 3D), n_{no} is the number of nodes, and n_{el} is the number of elements. Additionally, we also report the count of calculation cycles per second of the GPU, i.e., $\text{it}\cdot\text{s}^{-1}$ as well as the wall-clock time. These two metrics give an intuitive sense of the time-to-solution, which is convenient for potential application purposes.

C.4 Results

In this section, we present two numerical models using the solver ep2-3De v1.0, namely,

1. Model 1, the granular collapse, which serves as
 - (a) a validation benchmark against the results of the widely-accepted experiment of *Bui et al.* (2008) under a three-dimensional configuration
 - (b) a demonstration of the influence of the mesh resolution on plastic strain localization under a plane strain configuration
2. Model 2, the three-dimensional earth slump (*Varnes, 1958, 1978*), which serves as

- (a) an evaluation of the relative performances of a single and multi GPU- and CPU-based implementations of the solver ep2-3De v1.0 considering a variety of recent GPU architectures
- (b) a showcase of a potential application of the solver ep2-3De v1.0 for an elastoplastic problem considering different isotropic peak cohesion fields (homogeneous and heterogeneous)

C.4.1 Model 1

Settings for Models 1a & 1b

We investigate the granular collapse of an aluminium-bar assemblage (Bui *et al.*, 2008) under three-dimensional or plane strain configurations. The geometry of the problem is shown in Fig. C.5, and its variables are summarized in Table C.3 for both three-dimensional and plane strain configurations. Note that for Model 1a, we use the same number of elements along the x -direction $n_{el,x} = 80$ as in Huang *et al.* (2015). As a direct comparison for Model 1b under a plane strain configuration, Huang *et al.* (2015) used $n_{el} = 15360$, $\Delta x = \Delta z = 2.5$ mm and $n_{mp} = 25600$.

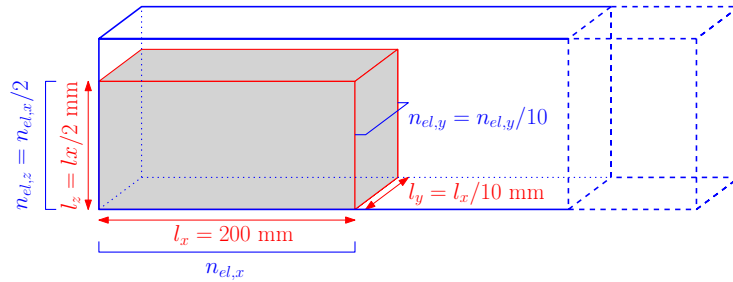


Figure C.5: Initial configuration for the granular collapse numerical model. The blue surrounding frame depicts the computational domain, i.e., the background Eulerian mesh, and the red volume is the granular material, which is discretized by 8 material points. The total number of background elements n_{el} depends on the number of elements in the x - direction $n_{el,x}$ used to discretize the granular material.

We consider a noncohesive granular material of density $\rho = 2650 \text{ kg}\cdot\text{m}^{-3}$, with a bulk modulus $K = 0.7 \text{ MPa}$ and a Poisson's ratio $\nu = 0.3$, as in Huang *et al.* (2015). The cohesion is $c = 0 \text{ Pa}$, the internal friction angle is $\phi = 19.8^\circ$ with a dilatancy angle $\psi = 0$ according to Bui *et al.* (2008). However, the density and stiffness properties have negligible effects on the granular flow dynamics, as reported by Nguyen *et al.* (2020). We introduce local damping D (see Wang *et al.* 2016c) to resolve numerical results that are compatible with the experimental results of Bui *et al.* (2008). We find that $D = 0.025$ results in the most compatible dynamics. The reasons for the introduction of local damping can be found in Appendix C.9. Fully fixed boundary conditions (i.e., no slip) are enforced at the bottom and rollers on the sidewalls. The total simulation time is 1.0 s, considering a the time step multiplier $\alpha = 0.5$.

Table C.3: Parameters used in Models 1 a & b for the granular collapse. $n_{el,i}$ is the number of elements to discretize the granular material along the i -th direction, n_{el} and n_{no} are the total number of elements and nodes of the background mesh, n_{pe} is the number of material points per element and n_{mp} is the total number of material points. Note that the mesh resolution is $\Delta x = \Delta y = \Delta z = 2.5$ mm.

Experiment	$n_{el,x}$	$n_{el,y}$	$n_{el,z}$	n_{el}	n_{no}	n_{pe}	n_{mp}	Δx [mm]
1a	80	20	40	342144	365625	8	512000	2.5
1b	640	-	240	833300	836190	4	819200	0.3

Model 1a: the three-dimensional granular collapse

To validate the numerical implementation under a GPU architecture, we first compare it against the well-known granular collapse experiments initially performed by *Bui et al. (2008)*. Here, we present and compare numerical results without focusing on the performance of the GPU-based implementation. All the simulations are performed on a consumer electronics RTX 3090 GPU with double-arithmetic precision (i.e., $n_p = 8$ bytes).

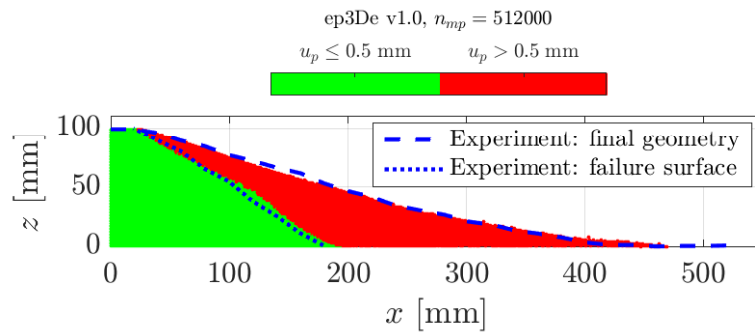


Figure C.6: Final geometry of the granular collapse for three-dimensional configuration of our GPU-based explicit GIMPM implementation ep3De v1.0. The green region (i.e., the intact region) is defined by the L_2 -norm of the material point displacement $u_p = \|\mathbf{u}_p\|_2 \leq 0.5$ mm, whereas the red region (i.e., the deformed region) is defined by $u_p = \|\mathbf{u}_p\|_2 > 0.5$ mm. The experiment of *Bui et al. (2008)* is indicated by the blue dashed line (i.e., the free surface) and the blue dotted line (i.e., the failure surface).

The results from the numerical simulation under a three-dimensional configuration are shown in Fig. C.6. A direct and visual comparison demonstrates excellent agreement between the numerical solver and the experiments of *Bui et al. (2008)*. We observe a slightly lower run-out distance, but the overall geometry of both the failure surface and the free surface is very close to the experimental data. We also report an angle of repose of $\approx 13^\circ$. This value is also consistent with the value reported by *Bui et al. (2008)*, i.e., 14° . The good agreement between the numerical results and the experimental work of *Bui et al. (2008)* demonstrates that the solver ep2-3De v1.0 is suitable to simulate large deformation elastoplastic problems such as granular collapses.

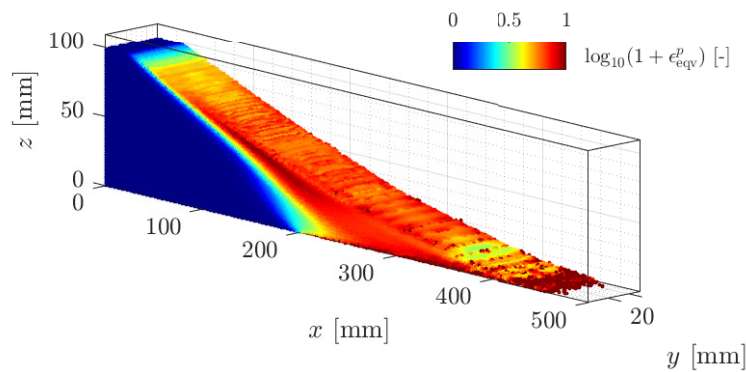


Figure C.7: Equivalent plastic strain ϵ_{eqv}^p for the final configuration of the granular collapse. The principal feature of a granular collapse can be observed, i.e., a backward propagation of plastic deformation along a principal failure surface.

The equivalent accumulated plastic strain ϵ_{eqv}^p is shown in Fig. C.7. We observe a coherent deformation of the granular material with a large shear zone that propagates backward from the base of the material to the top of the granular material. The mobilized granular material flows along a principal failure surface. However, the

overall deformation pattern is rather coarse, i.e., fine structures or local shear bands are not yet observed, even though slight deformation heterogeneities can be observed. This coarse behaviour of shear banding is also consistent with previous studies (see *Huang et al. 2015*; *Chalk et al. 2020*; *Zhang et al. 2021*). This is mainly due to the background mesh resolution used in the numerical simulation. We further investigate shear banding using a higher background mesh resolution under a plane strain configuration in Model 1b.

Model 1b: the plane strain granular collapse

We investigate granular collapse under a plane strain configuration, as this allows an increase in the number of elements, resulting in an even finer background mesh (see Table C.3). For Model 1a, the numerical solution is in agreement with the experimental work of *Bui et al. (2008)* regarding either the free surface or the failure surface (see Fig. C.8). This demonstrates that both the three-dimensional and plane strain configurations are in agreement with each other. However, we observe a lower run-out for the granular collapse under a plane strain configuration.

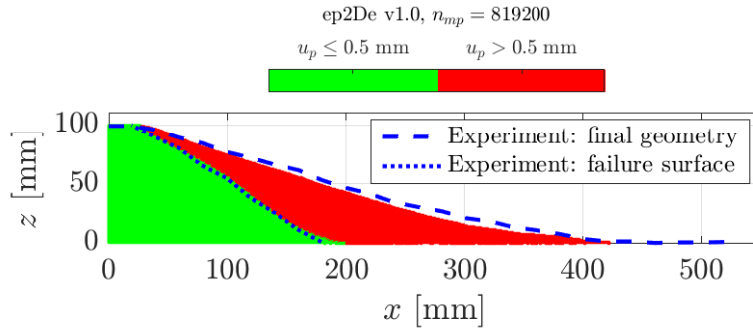


Figure C.8: Final geometry of the granular collapse for the plane-strain configuration for our GPU-based explicit GIMP implementation ep2De v1.0. The numerical solution and the experimental results are in good agreement. Some differences are more pronounced when compared with the numerical results obtained under a three-dimensional configuration.

An interesting feature of granular collapse is the equivalent accumulated plastic strain (see Figs. C.9 and C.10 a) and b)). The GPU-based implementation allows to increase both the background mesh resolution and the total number of material points. This results in finer plastic strain localizations, as demonstrated in Fig. C.10 a) by the various shear bands and their complex interactions during collapse. Such detailed shear bands are almost impossible to obtain at lower resolutions, which demonstrates the importance of a GPU-based implementation to overcome the hardware limitation of a CPU-based implementation, i.e., mainly longer wall-clock times.

Furthermore, Figs. C.10 a) and b) demonstrate the influence of the mesh resolution over shear banding: the finer the background mesh, the thinner the shear bands. This is significant since it shows that the dynamics of shallower granular avalanches appears more complex for higher resolutions.

C.4.2 Model 2

Settings for Models 2a & 2b

Here, we select a cohesive elastoplastic isotropic material (i.e., a homogeneous or heterogeneous peak cohesion field) with no dilatancy behaviour. It is modelled with a pressure-sensitive Drucker-Prager model with linear strain-softening behaviour. It is well known that the numerical solutions (as in FEM) are mesh-dependent when considering the strain-softening behaviour of the material. We did not implement techniques to address this issue, but the use of nonlocal plasticity (*Galavi and Schweiger, 2010*; *Burghardt et al., 2012*) or viscoplastic formulations (*Duretz et al., 2019b*) are possible ways to address this specific task.

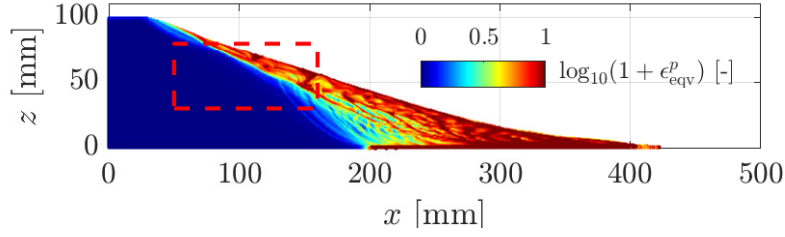


Figure C.9: Equivalent plastic strain ϵ_{eqv}^p for the final configuration of the granular collapse. The dashed red rectangle denotes the location of the zoomed-in region in Fig. C.10 (a). One can observe more complex plastic strain localizations compared to the numerical results obtained in Fig. C.7 for a three-dimensional configuration with a coarser background mesh resolution.

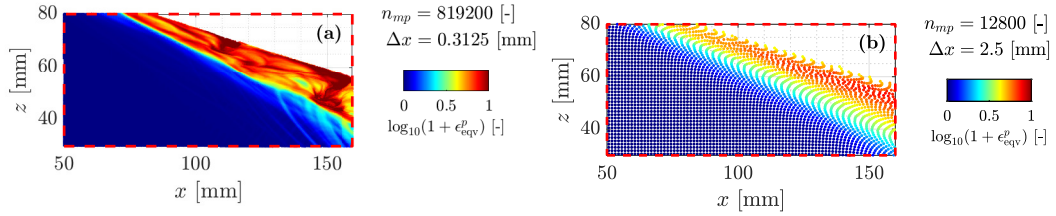


Figure C.10: (a) ϵ_{eqv}^p for the zoomed-in area in Fig. C.9. A shallow granular flow clearly appears, as suggested by the higher values of ϵ_{eqv}^p . This supports evidence of shallower granular avalanches during collapses. Deeper structures, which result in lower accumulated plastic strains, probably highlight slower deformation modes along well-defined and persistent shear bands. (b) ϵ_{eqv}^p for a coarser background mesh resolution, which demonstrates the influence of the mesh resolution over shear bands.

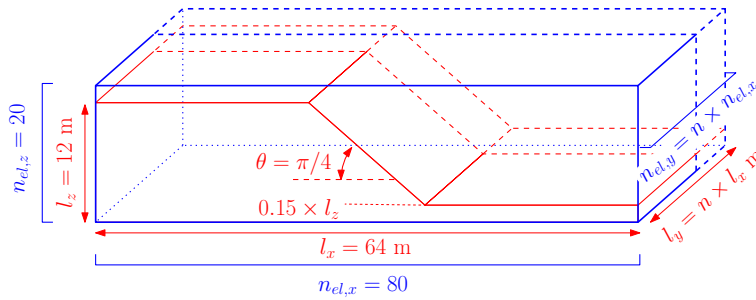


Figure C.11: Geometry for the earth slump. The number of elements in the y -direction $n_{el,y}$ and the width of the problem l_y are variable. This allows us to increase (or decrease) the number of both elements and material points without decreasing the mesh resolution. The parameter n controls the dimension of the domain and the number of elements along the y -direction. The wall-clock time depends only on the total number of elements, nodes and material points and is not influenced by the mesh resolution.

We have chosen an arbitrary geometry (see Fig. C.11 and Table C.5), which represents an idealized three-dimensional setting, to observe elastoplastic *slumps* (i.e., earth slumps according to the original classification proposed by *Varnes* 1958, 1978), which are now classified as rotational slides in the recent update of the *Varnes* classification proposed by *Hungr et al.* (2014). The geometrical setting differs from the one typically used in the literature, as in *Zhang et al.* (2021). However, it promotes the compression of the toe, which is an expected feature we want to reproduce. The size of the physical domain $l_z \times l_x \times l_y$ is, at most, 12 m \times 64 m \times 1024 m for Model 2a, whereas it is 12 m \times 64 m \times 16 m for Model 2b.

We assume this setting features the principal first-order characteristics of a typical rotational earth slump (*Varnes*, 1958, 1978), i.e., a complex zone of scarps (minor and major) delimiting a crown-like structure, followed by a transition (or depletion) zone in which the material flows homogeneously along internal shear zones due to severe plastic strain localizations and, finally, a compression (or accumulation) zone resulting in complex thrusting at the toe of the slump. Because of the nature of the boundary condition at the bottom of the material (i.e., free-slip), an additional horizontal sliding component is introduced within the rotational part of the displacement. This results in stronger deformations, which we want to highlight. However, the bottom boundary condition influences the shear band propagation and the overall behaviour by introducing a stronger horizontal component in the motion.

Table C.4: Material properties shared by both Models 2a & 2b.

Parameter	Symbol	Value	Unit
Density	ρ	2700	kg·m ⁻³
Poisson's ratio	ν	0.3	-
Elastic modulus	E	1	MPa
Softening modulus	H	50	kPa
Friction angles	$\phi / \phi_{\text{weak}}$	20 / 7.5	°

We select material properties (i.e., bulk and shear moduli K and G , friction angle ϕ and peak and residual cohesions c_{peak} and c_{res}) that result in severe deformation processes and strain localizations. The material properties are presented in Table C.4. They are close to the values commonly used in the literature (*Wang et al.*, 2016c,b; *Bandara et al.*, 2016; *Zhang et al.*, 2021). To increase deformations even more, we also introduce a weak layer of thickness $0.3 \times l_z$ m at the base of the material with a lower friction angle ϕ_{weak} . A time step multiplier $\alpha = 0.5$ is selected, i.e., $\Delta t_{\text{min}} = 1.56 \cdot 10^{-2}$ s is obtained over the whole simulation according to the CFL condition for both Models 2a & 2b. As in *Zhang et al.* (2021), elastic loading dynamic relaxation is applied for a period of $t = 8$ s (i.e., Models 2a & 2b), and the elastoplastic behaviour is activated for an additional 7 s, resulting in a total simulation time $t = 15$ s (i.e., Model 2b only).

Gaussian random fields (see Appendix C.8) are used to initialize the peak cohesion field c_{peak} , which is parametrized by an average cohesion \bar{c}_{peak} and its standard deviation σ (see Table C.5) along with the residual cohesion $c_{\text{res}} = c_{\text{peak}}/4$. This allows us to account for heterogeneities within the material, which lead to complex and heterogeneous displacement fields. We first perform preliminary simulations with a constant cohesion field and notice a homogenous solution of the displacement field along the y -direction. Using Gaussian fields allows us to mitigate this homogeneity.

Free-slip boundary conditions are applied on the sides and the bottom of the computational domain; only the normal component to the boundary is constrained, while the two others are free. Finally, and as suggested in *Wang et al.* (2016c) for landslide applications, we introduce local damping, i.e., $D = 0.1$.

Table C.5: Geometrical and material properties for Models 2a & 2b. The correlation length vector is $\boldsymbol{\lambda} = (\lambda_x, \lambda_y, \lambda_z) = (2.5, 2.5, 2.5)$ m for both Gaussian and exponential isotropic covariance functions. The grid spacing is always constant in Models 2a & 2b, i.e., $\Delta z = \Delta y = \Delta x = 0.8$ m

Model	$n_{el,y}$ [-]	n_{mp} [-]	Δx [m]	\bar{c}_{peak} [kPa]	σ [kPa]
2a	$\in [1; 1280]$	$\leq 3.2 \cdot 10^6$	0.8	20	0
2b	20	$\approx 10^5$	0.8	20	0 / 5

Model 2a: single GPU performances

Here, we investigate the computational performances of the solver ep2-3De v1.0 under a three-dimensional configuration on a variety of GPUs with recent architectures: Ampere, Turing and Volta. Furthermore, we restrict our performance analysis only for the elastic loading phase (i.e., 8 s of simulation) because it is more complex to determine the exact number of material points that are yielding during each computational cycle (see Fig. C.4) and to infer the exact effective memory throughput.

All the numerical simulations are performed on the computational resources and GPU hardware presented in Table C.2 under double-arithmetic precision (i.e., $n_p = 8$ bytes in Eq. C.38). As a reference baseline, we use the performance obtained for a CPU-based single-threaded implementation of ep2-3De v1.0 on an i9-10900K CPU (e.g., latest Intel CPU chip). However, this is not representative of a highly optimized multithreaded implementation under a CPU architecture.

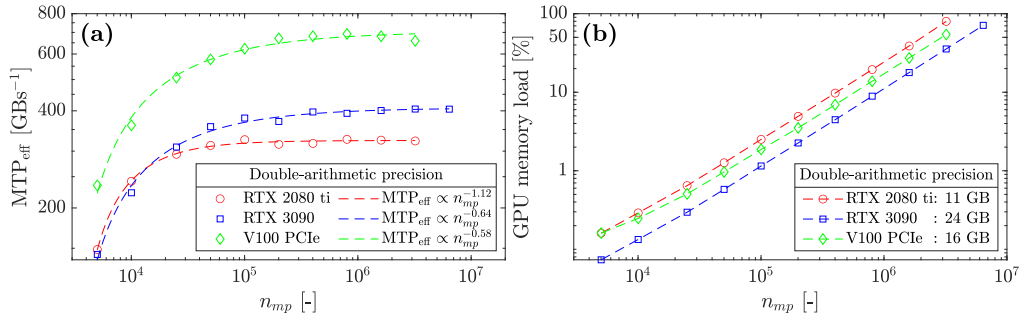


Figure C.12: a) Effective memory throughput MTP_{eff} of the solver ep2-3De v1.0 for double-arithmetic precision. One can see the on-chip memory limit, as both the RTX 2080 ti and V100 cannot resolve the same number of material points as the RTX 3090. b) GPU on-chip memory load increases with the number of material points n_{mp} , which demonstrates, as expected, one of the GPU’s hardware limits.

We report the effective memory throughput MTP_{eff} of the solver ep2-3De v1.0 on various GPUs and CPUs (see Fig. C.12). An increase in the effective memory throughput is observed as the number of material points increases. All GPUs reach a maximum effective throughput, but the Tesla V100 scores a maximum effective throughput of $\approx 650 GB \cdot s^{-1}$. This corresponds to 88 % of its peak throughput (for the GPU’s hardware limit, see Table C.2). We report a similar observation for the RTX 2080 ti, $MTP_{eff} \approx 320 GB \cdot s^{-1}$ corresponding to 62 % of its hardware limit. RTX 3090 and GTX 1650 reach $MTP_{eff} \approx 405 GB \cdot s^{-1}$ and $MTP_{eff} \approx 75 GB \cdot s^{-1}$, respectively, which correspond to 52 % and 44 % of their respective hardware limits. Finally, we report a memory throughput of at least $MTP_{eff} \approx 5 GB \cdot s^{-1}$ for the i9-10900K CPU (10 % of its hardware limit).

The overall results suggest, as in *Räss et al.* (2019), that most recent GPUs, such as the data-centre Tesla V100 (Volta), offer significant performances compared to entry-level consumer electronics GPUs, such as the GTX 1650. In terms of absolute performance, the more recent the GPU is, the higher its performance. A demonstration is given by the absolute effective throughput between the RTX 2080 ti and the RTX 3090: The latter achieves an additional 20 % throughput compared to the former. We highly suspect the hardware itself to

be the main reason for this. We further investigate the performances of the most recent data-centre GPU, i.e., the A100 (Ampere architecture), with its predecessor the V100 (Tesla architecture). The A100 reaches $\approx 1100 \text{ GB}\cdot\text{s}^{-1}$, which yields a performance gain of $1.6\times$ with respect to the Tesla V100. When compared to the maximum effective memory throughput in Table C.2, this correspond to 97 % of the hardware limit.

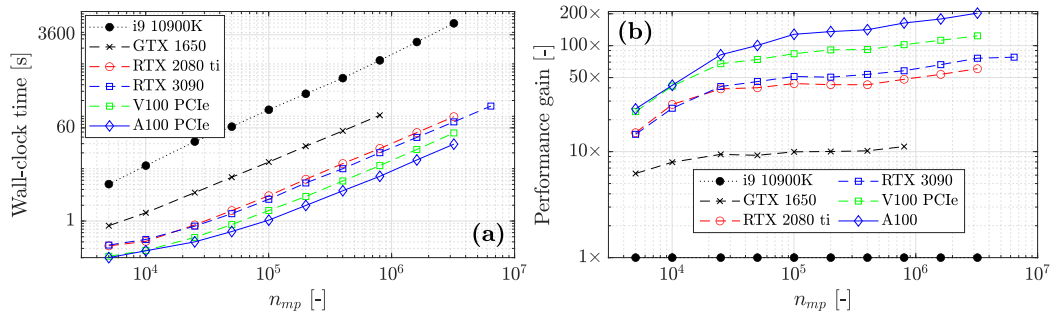


Figure C.13: a) Wall-clock time reported for various computing architectures (GPUs and CPU). The differences in the maximal number of material points n_{mp} are due to the on-chip memory limit. A significant difference in terms of wall-clock time is observed between the CPU and GPUs, even for the low-entry consumer electronic GTX 1650, i.e., a performance gain of $\approx 10\times$. b) Performance gains of GPUs relative to the CPU, i.e., $1\times$ as a baseline. We add the CPU and the GTX 1650 wall-clock time for an easier comparison.

Finally, we report the wall-clock time for various computing architectures (see Fig. C.13a). As expected by the maximum effective memory throughput, A100 delivers the fastest solution, regardless of the number of material points n_{mp} . The A100 GPU resolves a geometry of $n_{mp} \approx 3.2 \cdot 10^6$ in less than a minute (29 seconds), whereas the i9-10900K CPU resolves the same problem in more than an hour (5949 seconds). This corresponds to a $200\times$ performance gain ($123\times$ performance gain for the V100, see Fig. C.13b) compared to the CPU-based implementation of ep2-3De v1.0. The RTX 2080 ti and the RTX 3090 reach a $60\times$ and $77\times$ performance gain, respectively. However, the entry-level GTX 1650 is only ten times faster than i9-10900 K. As already shown in Fig. C.12a, these performance gains are only expected when the different GPUs reach their maximum effective memory throughput. In terms of runtime, the performance gain (Fig. C.13b) is in agreement with the memory throughputs reported in Fig. C.12a.

Model 2a: multi-GPU performances

To avoid frequent material point's transfers amongst the GPUs, we consider an overlap of 8 elements between neighbouring meshes, i.e., 9 nodes. This results in a one-dimensional GPU topology, for which both material points and meshes are distributed along the y -direction of the global computational domain (see Figs. C.11 & C.14). Arranging GPUs along this direction allows to overcome the need to transfer material points amongst GPUs, provided that the material point's displacement is not greater than the buffer zone, i.e., the element overlap. The evaluation of the multi-GPU implementation is based on the Model 2a, with slight modifications, i.e., the number of element along the y -direction is largely increased. The size of the physical domain $l_z \times l_x \times l_y$ is, at most, $12 \text{ m} \times 64 \text{ m} \times (64 \times 2048) \text{ m}$.

We consider two distributed computing systems for parallel GPU computation, using up to 8 Tesla V100 (Volta architecture) or 128 Geforce GTX Titan X (Maxwell architecture). All numerical simulations are performed using a single-arithmetic precision (i.e., $n_p = 4$ bytes). This allows to increase the maximum number of material points and mesh dimensions. In addition, our GPU implementation relies on the usage of the built-in function `atomi cAdd()`. It does not support the double-precision floating-point format FP64 for GPUs with compute capabilities lower than 6.0, i.e., the Maxwell architecture amongst others. Note that, unlike the Tesla V100, the Geforce GTX Titan X only delivers an effective memory throughput of $\text{MTP}_{\text{eff}} \approx 100 \text{ GB}\cdot\text{s}^{-1}$. This corresponds to 38 % of its hardware limit. This was already reported by *Räss et al.* (2019b); *Alkhimenkov et al.* (2021b) and, it could be attributed to its older Maxwell architecture (*Gao et al.*, 2018). This performance drop is even more severe, mainly due to the use of built-in functions like `atomi cAdd()`.

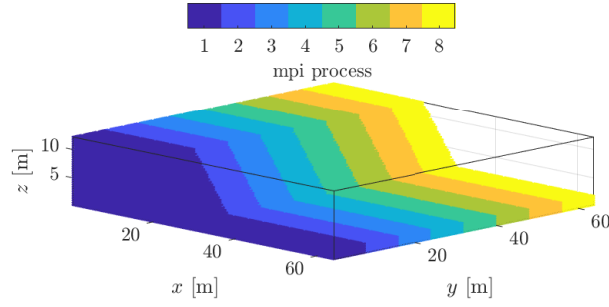


Figure C.14: Domain partition of the material points amongst 8 GPUs. Combined with an overlap of 8 elements along the y -direction, material points can moderately move while still residing within the same GPU during the whole simulation.

We first performed parallel simulations with a moderate number of GPUs, up to 8 Tesla V100 NVlink (32 GB). The respective wall-clock times are reported in Fig. C.15. We report a wall-clock time of ≈ 110 s for $n_{mp} \approx 10^8$. If n_{mp} is increased by a factor 2, 4 or 8, the wall-clock time is roughly similar to the baseline, i.e., $n_{GPU} = 1$. The effective memory throughput MTP_{eff} is shown in Figure C.16 (the total sum of MTP_{eff} across all the GPUs). Based on the memory throughput of 1 GPU, an estimation of a perfect weak scaling is possible. For 8 GPUs, an ideal weak scaling corresponds to $MTP_{\text{eff}} = 4824 \text{ GBs}^{-1}$, whereas we report $MTP_{\text{eff}} = 4538 \text{ GBs}^{-1}$. This gives a parallel efficiency of $\approx 94\%$ and, an effective speed-up of $7.5\times$. Similar observations are made for $n_{GPU} = 2$ and $n_{GPU} = 4$.

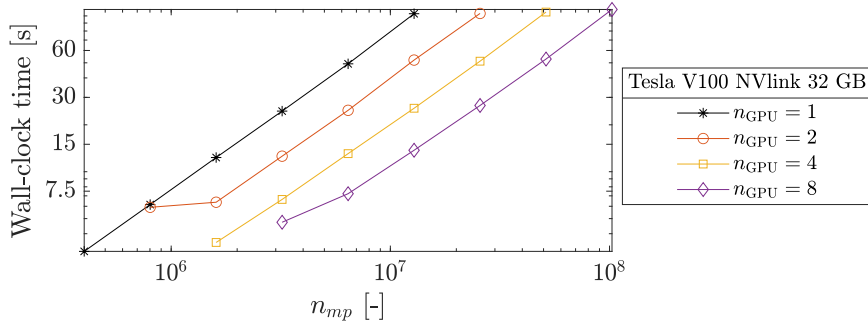


Figure C.15: Wall-clock time for 1, 2, 4 and 8 Tesla V100 GPUs.

We investigate a parallel GPU computing using up to 128 Geforce GTX Titan X. This allows to address even larger geometries, as showed in Figure C.17 where the geometry of nearly $n_{mp} \approx 9.75 \cdot 10^8$ is resolved in less than 8 minutes. For parallel computing up to 64 GPUs, the wall-clock time evolution is smooth. For 128 GPUs, the wall-clock time is chaotic for fewer material points whereas it stabilizes as the number of material points increases. We suspect the absence of computation/communication overlaps to be the main reason of this erratic behaviour. The communication between many GPUs requires careful synchronization between GPUs which can be hidden under computation/communication overlap (Räss *et al.*, 2019b; Alkhimenkov *et al.*, 2021b). The total size of the overlap is constant, regardless of the y -dimension. As the number of material points increases, the time spent on computation becomes larger compared to the time spent on exchanges between GPUs and the wall-clock time stabilizes. The effective memory throughput MTP_{eff} is shown in Figure C.18. An ideal weak

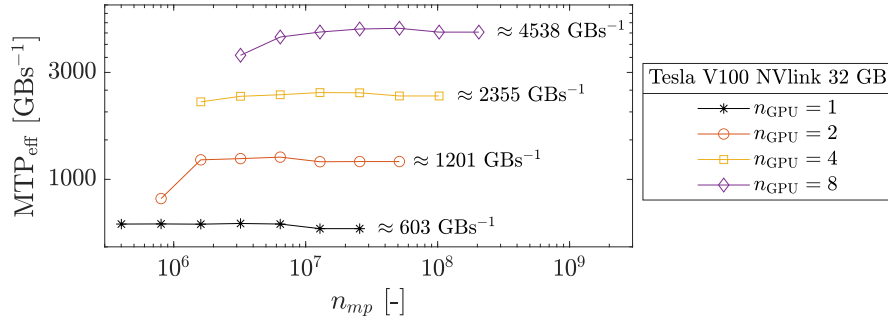


Figure C.16: Sum across the GPUs involved of the MTP_{eff} . We roughly report a weak scaling between the number of GPUs and the overall effective memory throughput.

scaling corresponds to the effective memory throughput $MTP_{\text{eff}} = 12800 \text{ GBs}^{-1}$ for 128 GPUs, whereas we report only $MTP_{\text{eff}} = 11326 \text{ GBs}^{-1}$. This gives a parallel efficiency of $\approx 90\%$ and, an effective speed-up of $\approx 113\times$.

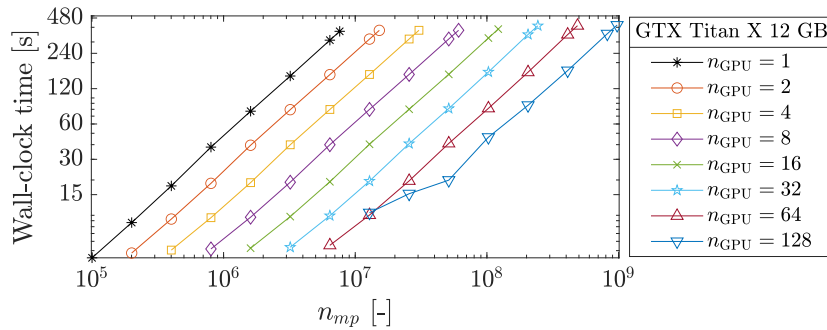


Figure C.17: Wall-clock time reported for up to 128 Geforce GTX Titan X GPUs and up to $n_{mp} \approx 9.75 \cdot 10^8$.

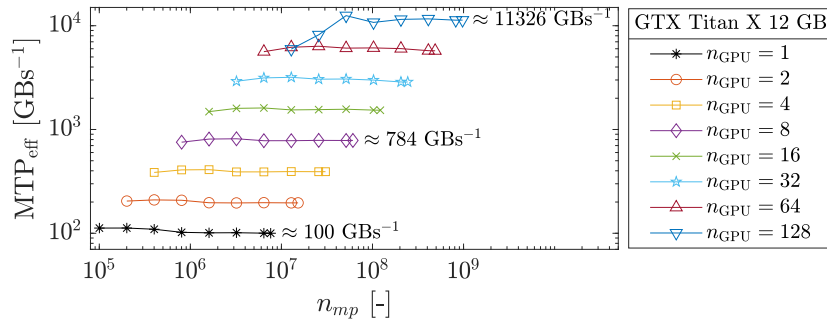


Figure C.18: MTP_{eff} sum across the GPUs involved.

C.4.3 Model 2b: homogeneous and heterogeneous slumps

As a final experiment, we show the results of the ep2-3De v1.0 solver for a slump with homogeneous or heterogeneous cohesion fields. In this numerical model, we only show the displacement field at the end of the numerical simulation at $t = 15$ s. The interested reader is referred to Appendix C.10 for an overview of the temporal evolution of the equivalent plastic strain ϵ_{eqv} for the slump under the three settings of the peak cohesion field. All the numerical simulations are run on a laptop equipped with GTX 1650; $t_{\text{GPU}} \approx 30$ s with the settings presented in Table C.5. In the following, we present the main results for the three peak cohesion fields, and we discuss the main characteristics obtained for typical slumping mechanics.

Homogeneous peak cohesion field The homogeneous solution gives preliminarily interesting results (see Fig. C.19). The first-order characteristics of a slump can be observed, even though their magnitude is relatively fair compared to the real slump. The most striking feature is the development of one major shear zone, along which the material flows (i.e., depletion) towards the toe of the slump, resulting in a compression zone (i.e., thrusting and folding deformations). The crown-like structure develops linearly along the y -direction and is highly localized at the surface of the slump (at $x \approx 20$ m in Fig. C.19). However, the material flows homogeneously along the x -direction (see the vertical profile in Fig. C.19), as shown by the displacement field. The lateral variation of the displacement field (along the y -direction) is almost nonexistent, which is mainly due to the spatial homogeneity of the peak cohesion field.

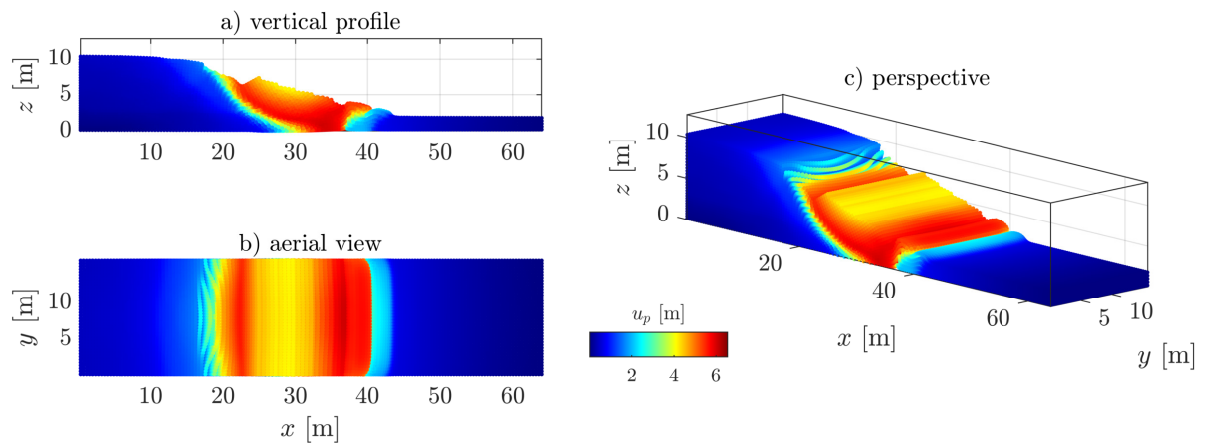


Figure C.19: Displacement field obtained after $t = 15$ s for a homogeneous peak cohesion field. One can see an overall homogenous displacement field with some of the first-order characteristics of a slump, i.e., a rotational displacement with a compression zone at the toe, a transition zone delimited by one principal shear zone and a major scarp at the top of the material.

Isotropic Gaussian covariance Considering heterogeneities with a Gaussian covariance function for the cohesion field, the displacement field starts to resolve a differential behaviour (see Fig. C.20). Higher and/or weaker values of the peak cohesion field yield lower and/or greater displacements. This is obvious, especially in the transition zone where this differential is observable. In addition, the compression zone also starts to resolve spatial variations due to weaker and stronger cohesion values.

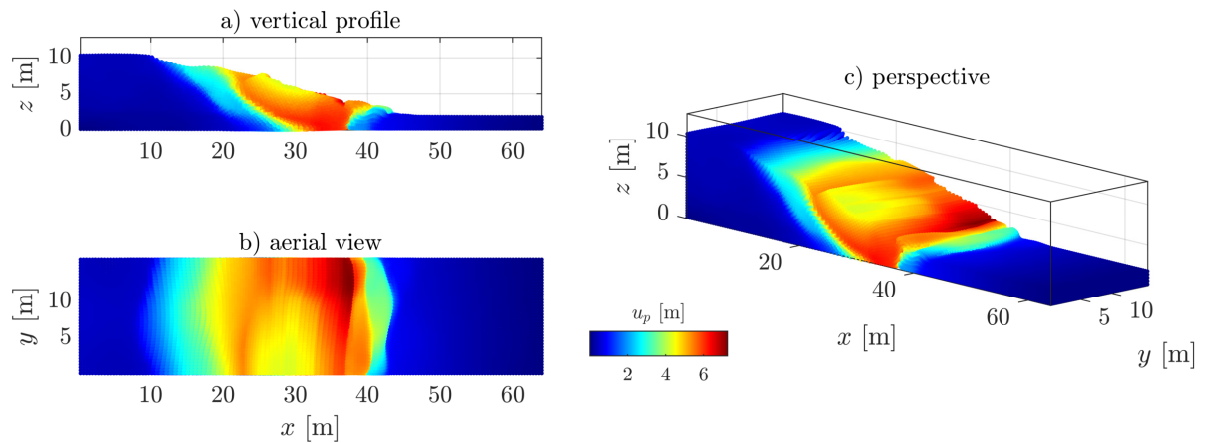


Figure C.20: Displacement field obtained after $t = 15$ s for a heterogeneous peak cohesion field with a Gaussian covariance function.

A striking difference is the shear zone itself (see Fig. C.27): the shear zone exhibits a more complex spatial pattern, whereas only one major shear zone is observed in Fig. C.27. Retrogressive shear banding appears during the time evolution of the slump, which suggests the development of a secondary shear zone within the slump. Moreover, the crown-like structure is now curved and not linear along the y -direction. Its spatial extent is more important and is not as localized as in the homogeneous case. Nevertheless, a more complex arrangement of major and minor scarps within the crown-like structure has not yet been observed. Such a structure is more evident if one observes the accumulated equivalent plastic strain ϵ_{eqv}^p in Fig. C.27 in Appendix C.10.

The high magnitude of the displacement field in the areas $x \in [20; 40]$ m and $y \geq 8$ m is due to a weaker zone in the peak cohesion field (see Fig. C.27). This shows a strong influence of the heterogeneous peak cohesion field on the final displacement field. A lower shear strength of the material yields faster strain-softening behaviour, promoting a faster response of shear banding.

Isotropic exponential covariance Shear banding activities become even more complex when an exponential covariance function is used, relative to Fig. C.19 and even with Fig. C.20 to some extent. The spatial distribution of the peak cohesion (see Fig. C.28) resolves finer heterogeneities with a smaller length scale compared to when Gaussian covariance is used. Principal differences are observed at the top and toe of the slump, where the crown-like structure turns into a complex zone made of minor and major scarps (see Fig. C.21). The displacement field becomes highly heterogeneous, particularly at the toe and the top of the slump. However, it is also more homogeneous when compared with Fig. C.20, particularly in $x \in [25; 35]$. The difference is evident between Figs. C.22 & C.20 at this particular location.

The difference between the Gaussian and exponential covariance of the peak cohesion suggests the following. Heterogeneous displacement fields could be influenced by larger and/or coarser fluctuations of the shear strength within the material. By extrapolation, this could imply that the magnitude of the heterogeneity might be related to the fluctuation scales of the peak cohesion field. Locally rather homogeneous fluctuations of the peak cohesion (i.e., Gaussian covariance) seem to promote an increasingly heterogeneous displacement field at the surface. The characteristic length scale of spatial fluctuations could have important implications for highly

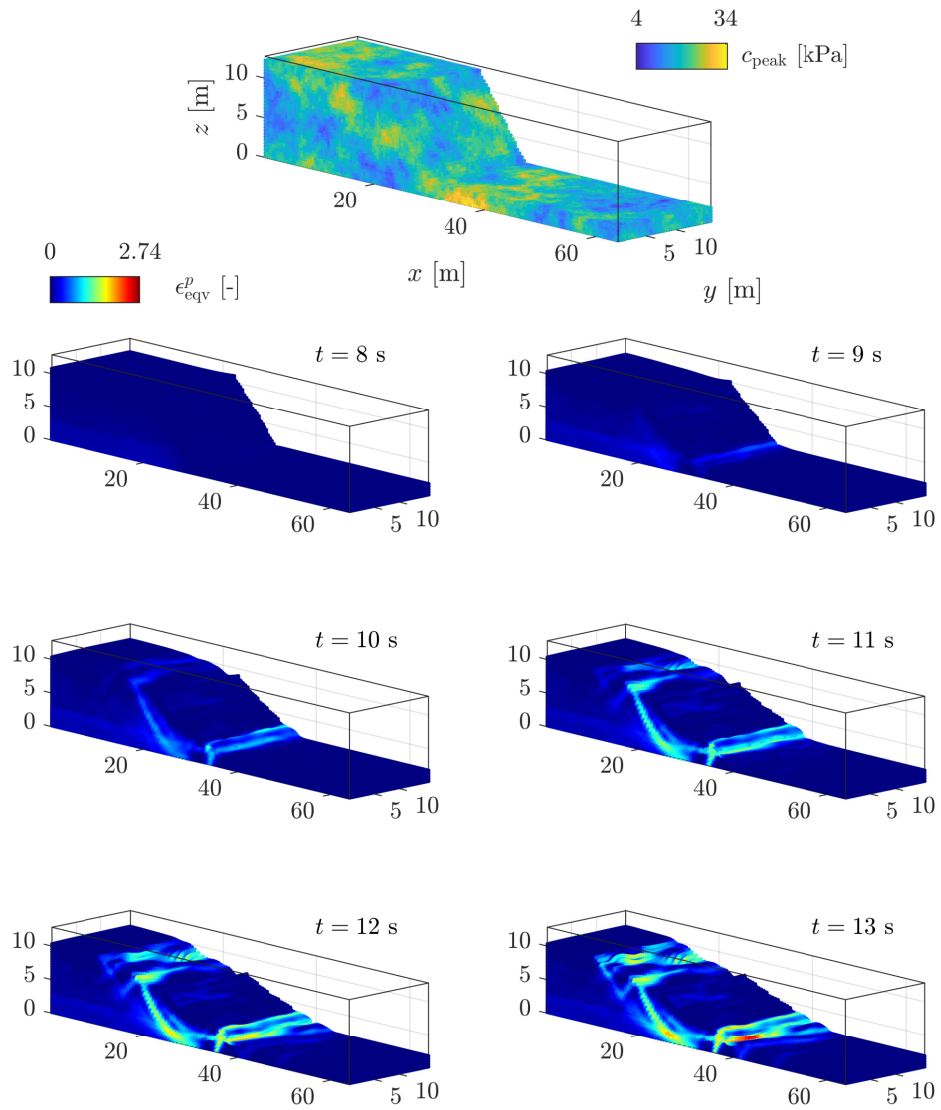


Figure C.21: Heterogeneous cohesion field with an exponential covariance function: time evolution of the equivalent plastic strain ϵ_{eqv}^p . Similar to Fig. C.27, heterogeneous behaviour is observed. However, the exponential covariance function results in an even more complex pattern of strain localization, i.e., minor and major scarps develop at the top. The crown-like structure of the slump becomes even more heterogeneous.

heterogeneous displacements within landslides. The same assumption could hold for understanding the more complex crown-like structure of slumps (see Fig. C.28)

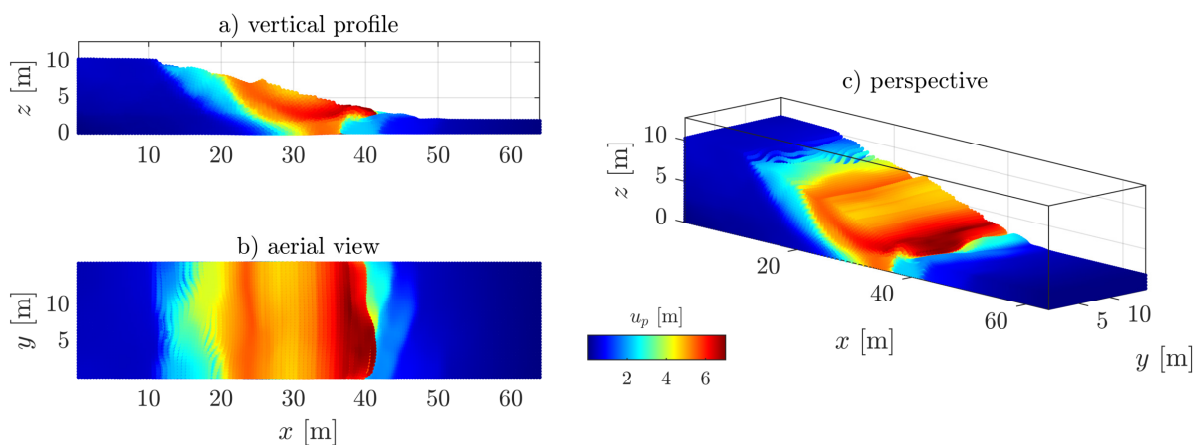


Figure C.22: Displacement field obtained after $t = 15$ s for a heterogeneous peak cohesion field with an exponential covariance function.

C.5 Discussion

C.5.1 GIMPM suitability

We investigated granular collapses in both three-dimensional and plane strain configurations. Our numerical results demonstrated the suitability of GIMPM to correctly reproduce experimental granular collapses. They also demonstrated that the results did not significantly differ between these two spatial configurations and that both approaches give similar numerical solutions.

C.5.2 Collapse limitation

For Model 1a, the principal hardware limit is the on-chip memory of the GPU. Even though RTX3090 is supported by 24 GB DDR4, it is physically impossible to achieve the resolution used for plane strain granular collapse. This would require more than 24 GB of on-chip memory. Model 1b demonstrated the importance of the background mesh resolution over strain localization. Using a higher numerical resolution (i.e., finer background mesh) allows full resolution plastic strain localization. Similarly, future additional development efforts towards MPI implementation could resolve highly detailed three-dimensional granular collapse simulations in the future. This will definitely benefit future studies on complex strain localization.

The wall-clock time for Model 1b is $t_{\text{GPU}} = 1470.5$ s (25 min), and the number of iterations per second is $85.5 \text{ it}\cdot\text{s}^{-1}$ for $n_{mp} = 819200$. As a preliminary example, the same numerical model was performed by Wyser *et al.* (2020a), who reported $19.98 \text{ it}\cdot\text{s}^{-1}$ for $n_{mp} = 12800$. Proportionally, this corresponds to a performance gain factor of 275 for the GPU-based implementation (ep2-3De v1.0) over the MATLAB-based implementation (fMPMM-solver v1.1) (Wyser *et al.*, 2020a).

C.5.3 Performance

The performance analysis we carried out in Model 2a demonstrated that even though the algorithm heavily relies on atomic operations to accumulate material point quantities on the nodes, the effective memory throughput reaches 88 % at most (for Tesla V100). We expected a much lower throughput due to the use of these atomic operations, since they are likely known to undermine the computational performances of an implementation under previous GPU architectures (e.g., Kepler) (Dong *et al.*, 2015; Dong and Grabe, 2018; Gao *et al.*, 2018). Our actual understanding (at least for a GPU-based implementation of GIMPM) is that the latest GPU architecture (Ampere and Turing) is now efficient when dealing with atomic operations and that the need to use a complex data layout for scattering is not as important as before. Furthermore, we identify the memory throughput as the main bottleneck: an additional 12 % performance improvement on the V100 before reaching the hardware limit of the memory bandwidth. The A100 shows that the solver reaches the hardware limit with an effective memory throughput which is very close (i.e., 97 %) to the actual maximum memory throughput. Similarly, the true limiting factor of the single GPU implementation is the hardware limit of the GPU on-chip memory.

The multi-GPU implementation resolves the on-chip memory limitation problem. Our multi-GPU implementation is particularly well-suited to resolve highly-detailed three-dimensional shear-banding. We also reported decent wall-clock times (less than 8 minutes) for simulations with nearly a billion material points. However, investigating high-resolution three-dimensional granular collapses is not possible under the assumptions made, because of small displacement required along the y -direction. This is incompatible with three-dimensional granular collapses. Hence, this motivates future deeper investigations toward a more versatile multi-GPU implementation. In addition, we report a slight drop of the parallel efficiency, as the number of GPUs increases. Future works should be directed toward a parallel strategy that hides communication latency, as proposed in Räss *et al.* (2019b, 2020); Alkhimenkov *et al.* (2021b). This will allow us to achieve an optimal parallel efficiency of 95-98 % of the weak scaling tests involving up to 128 GPUs.

C.5.4 Slumping mechanics

We show the application of the GIMPM solver ep2-3De v1.0 for slumping mechanics. We have presented various slump results and demonstrated the significant influence of heterogeneities within the peak cohesion field over the displacement field or the equivalent plastic strain. However, we have arbitrarily selected values that resulted in severe deformations of the material, which we wanted to highlight to demonstrate the potential of the solver. Further efforts should now be oriented towards numerical models that are closer to real and well-documented cases, such as in Tran and Sołowski (2019); Ying *et al.* (2021). Despite the simplifications we made, we have reported three-dimensional simulations that resolve all the first-order characteristics of slumps, including complex major and minor scarps, different shear zones of various activities and a complex arrangement within the compression zone. The use of three-dimensional GIMPM implementation under a GPU architecture will highly benefit future studies in the field, allowing faster and detailed numerical simulations of heterogeneous and complex strain localization problems.

C.5.5 Local damping coefficient

Due to our explicit formulation, a damping relaxation term should be introduced to mitigate dynamic wave propagations (Wang *et al.*, 2016a). In this work, we selected damping values that were either commonly accepted (e.g., $D = 0.1$ for slumps) or that were better resolving experimental results (e.g., $D = 0.025$ for granular collapses). Future investigations should specifically address the influence of damping terms on the material's behavior.

C.5.6 Code portability

Our numerical models showed the efficient computing capabilities of modern GPUs under the latest Nvidia GPU architectures. An important concern is the code portability. CUDA C is only applicable for Nvidia's GPUs and is not yet compatible with other corporation's GPUs, such as AMD (ATI Technologies). As such, an extension of the ep2-3De v1.0 solver towards an OpenCL-based implementation would ensure better code portability in the future.

C.6 Conclusions

We developed ep2-3De v1.0, an explicit GPU-based implementation of the generalized interpolation material point method that exploits the capabilities of the most recent GPU architectures (Ampere, Turing and Volta). We achieved fast execution times on a single GPU with a scattering approach that relies on extensive usage of atomic operations. We report, at most, an effective memory bandwidth of 88 % relative to the maximal hardware capabilities of the GPUs. We achieve, at most, a performance gain of 200× on a single GPU compared to a single-threaded CPU-based implementation of the solver. On entry-level customer electronics GPUs, we report a performance gain of $\approx 10\times$. Our multi-GPU implementation permits to resolve geometries with almost a billion material points and demonstrates fast execution times. We achieve a parallel efficiency of $\approx 94\%$ on weak scaling tests for 8 GPUs and $\approx 90\%$ for 128 GPUs. We also report that the memory bandwidth is the main limiting performance factor. We validated our solver against the well-known experimental results of the granular collapse problem in a three-dimensional configuration. We show applications of the solver to model slumping mechanics in three-dimensional configurations considering different material heterogeneities.

Code availability

The solver ep2-3De v1.0 developed in this study is licenced under the GPLv3 free software licence. The solver ep2-3De v1.0³ archive (v1.0) is available from a permanent DOI repository (Zenodo) at: <https://doi.org/10.5281/zenodo.5600373> (Wyser *et al.*, 2021b).

Acknowledgments

Yury Alkhimenkov gratefully acknowledges support from the Swiss National Science Foundation (grant no. 172691). Yury Alkhimenkov and Yury Y. Podladchikov gratefully acknowledge support from the Russian Ministry of Science and Higher Education (project No. 075-15-2019-1890).

Author contribution

EW and YA wrote the original manuscript and developed the first version the ep2-3De v1.0 solver. MJ and YP supervised the early stages of the study and provided guidance. All authors have reviewed and approved the final version of the paper.

³The latest version of the code is available for download from GitHub at: <https://github.com/ewyser/ep2-3De> (last access: October 26, 2021).

C.7 Appendix A: GIMPM basis functions and derivatives

One of the most important problems of any sMPM formulation is the cell-crossing instability (or error, see *Steffen et al.* 2008a; *Wilson et al.* 2021). As material points move through the mesh, they cross element boundaries. The discontinuous gradient due to the C_0 continuity of the basis functions results in spurious oscillations of the stress field and internal forces (*Acosta et al.*, 2020; *González Acosta et al.*, 2019; *Bardenhagen and Kober*, 2004) when material points cross element boundaries.

To solve for this instability, *Bardenhagen and Kober* (2004) introduced the generalized interpolation material point method (GIMPM). Whereas the material point is treated as a point in sMPM, *Bardenhagen and Kober* (2004) assigned a *spatial extent* or a *domain* to the material point. Alternative basis functions are constructed, i.e., to consider the material point domain, as follows:

$$\phi_{np} \equiv \phi_n(\mathbf{x}_p) = \frac{1}{v_p} \int_{\Omega_p \subset \Omega} \chi_p(\mathbf{x}) N_n(\mathbf{x}) d\Omega, \quad (\text{C.40})$$

where v_p is the material point volume, Ω_p denotes the material point domain, $\chi_p(\mathbf{x})$ is the *particle characteristic function*, $N_n(\mathbf{x})$ is the basis function (or shape function) for the mapping between the material point p and its associated nodes n , and $\mathbf{x} = \mathbf{x}_p - \mathbf{x}_n$ are the local coordinates between node n and material point p .

The particle characteristic function must satisfy the partition of unity property, i.e., $\sum_p \chi_p(\mathbf{x}) = 1$ (*Bardenhagen and Kober*, 2004). The simplest particle characteristic function is given by the hat function, i.e.,

$$\chi_p(\mathbf{x}) = \begin{cases} 1, & \text{if } \mathbf{x} \in \Omega_p, \\ 0 & \text{otherwise.} \end{cases} \quad (\text{C.41})$$

The GIMPM basis functions and derivatives are constructed analytically (*Coombs et al.*, 2020; *Charlton et al.*, 2017) in one dimension from a convolution of the standard finite element basis functions and the material point characteristic function (*Steffen et al.*, 2008a), i.e.,

$$\phi_n(x_p) = \begin{cases} 1 - (4x^2 + l_p^2)/(4hl_p) & \text{if } |x| < l_p/2 \\ 1 - |x|/h & \text{if } l_p/2 \leq |x| < h - l_p/2 \\ (h + l_p/2 - |x|)^2 / (2hl_p) & \text{if } h - l_p/2 \leq |x| < h + l_p/2 \\ 0 & \text{otherwise,} \end{cases} \quad (\text{C.42})$$

where l_p is the length of the material point domain, h is the mesh resolution, and $x = x_p - x_n$, where x_p is the coordinate of a material point and x_n is the coordinate of its associated node n . The two-dimensional basis function of a node n with its material point p is constructed as

$$\phi_{np} \equiv \phi_n(\mathbf{x}_p) = \phi_n(x_p)\phi_n(y_p), \quad (\text{C.43})$$

for which the gradient is defined as

$$\nabla \phi_{np} \equiv \nabla \phi_n(\mathbf{x}_p) = (\partial_x \phi_n(x_p)\phi_n(y_p), \phi_n(x_p)\partial_y \phi_n(y_p)). \quad (\text{C.44})$$

C.8 Appendix B: Gaussian random cohesion fields

In Earth Sciences, random fields (*Christakos*, 1992) are numerically generated predictions of a geophysical property (i.e., rock- or soil-related properties) with probabilistic spatial variability. These predictions are based on i) an assumed probability density function, i.e., characterized by a mean value μ with a standard deviation σ , and ii) an assumed spatial correlation function, characterised by fluctuation scales in a vector format, i.e., $\boldsymbol{\lambda} = (\lambda_x, \lambda_y, \lambda_z)$. In regard to numerical modelling, the principal requirement is that both small and large scales are simultaneously resolved over the computational mesh to ensure physically meaningful solutions.

Recently, *Räss et al.* (2019) presented an efficient implementation based on a spectral representation of Gaussian random fields for geophysical applications using either Gaussian or exponential covariance functions. The numerical codes, named GRFS, were made available by *Räss et al.* (2019) in both native MATLAB and CUDA C languages⁴. However, a sufficiently large number of harmonics should be used to obtain convergent Gaussian random fields, as stated in *Räss et al.* (2019).

Similar to the random material point method (RMPM, see *Wang et al.* 2016b; *Liu et al.* 2019; *Remmerswaal et al.* 2021) initially proposed by *Fenton and Vanmarcke* (1990) to generate RFs for a finite element mesh (RFEM), we combined this approach with the codes proposed by *Räss et al.* (2019) to generate an isotropic peak cohesion field to demonstrate its influence on the mechanical behaviour.

C.9 Appendix C: Volumetric locking and damping corrections

In *Huang et al.* (2015), no volumetric locking mitigation strategy was introduced, even though tough low-order elements were used. This should promote volumetric locking and an overall stiffer response of the granular material. In addition, *Huang et al.* (2015) used the standard (or original) material point method (instead of the generalized interpolation material point method), which is well known to introduce spurious oscillations of internal forces (*Acosta et al.*, 2020).

When implementing the proposed volumetric locking mitigation strategy, we observed a) larger deformations of the granular material with a stronger vertical compaction (i.e., stronger vertical displacement) and b) slightly longer run-out distances when compared to the experimental data. The softer mechanical response of the granular material had to be compensated somehow, which can be achieved by the introduction of a small local damping parameter.

We reproduced the numerical setting used in *Huang et al.* (2015) with the same mesh resolution, i.e., $\Delta x = \Delta y = 2.5$ mm, and a similar number of material points $n_{mp} = 28800$ with an initial number of material points per initially filled element $n_{pe} = 9$. The material parameters used for this preliminary investigation are presented in §C.4.1.

Figure C.23 a) & b) shows the major differences between either a locking-free or a locking-prone solution and the experimental results. As mentioned before, a slightly longer run-out distance is obtained for the locking-free solution. As a result, the numerical prediction given by the locking-free solution of the free surface is underestimated. However, the most noticeable difference is the failure surface. Whereas the failure surface predicted by the locking-prone solution fits with the experiment of *Bui et al.* (2008), it diverges for a locking-free solution. In particular, the onset of the failure surface at the top of the material is underestimated by the locking-free solution compared to the experimental results. This is due to the softer response of the granular material when volumetric locking is mitigated, which promotes greater vertical compaction and stronger run-out distance at the same time.

Even though the introduction of local damping better resolves the experimental results, one can argue that the locking-free solution without the introduction of local damping still agrees with the experiment of *Bui et al.* (2008). The overall response of the numerical granular collapse is still very close to the actual physical

⁴The routines GRFS are available at <https://bitbucket.org/lraess/grfs/src/master/>

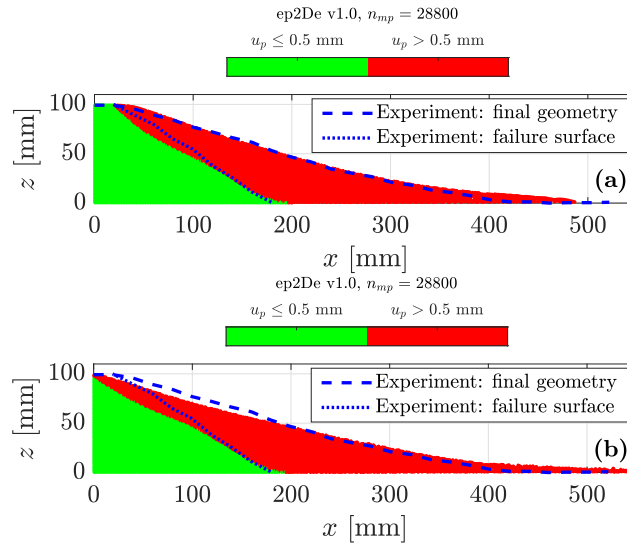


Figure C.23: a) Numerical solution without any volumetric locking strategy and b) numerical solution with the proposed volumetric locking strategy. For both cases, no damping is introduced.

experiment, and the differences between the numerical and experimental results can still be considered acceptable.

We further present additional three-dimensional results for Model 2b for a homogeneous cohesion field (see Figs. C.24 and C.25). Three-dimensional simulations of cohesive material better illustrate the influence of volumetric locking. Figure C.25 demonstrates that a significantly smoother pressure field is resolved with the proposed method.

In addition, the pressure field is certainly smoothed, but it does not significantly differ from the original pressure field (in locations where locking is minimum). Volumetric locking is particularly highlighted within shear bands due to isochoric plastic flows, resulting in significant stress oscillations.

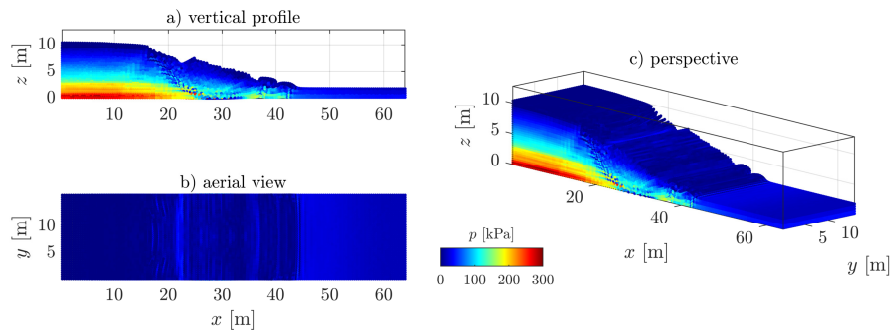


Figure C.24: Non-smooth pressure field due to volumetric locking. The typical check-board pattern of volumetric locking can be observed where the material has yielded, i.e., the shear band.

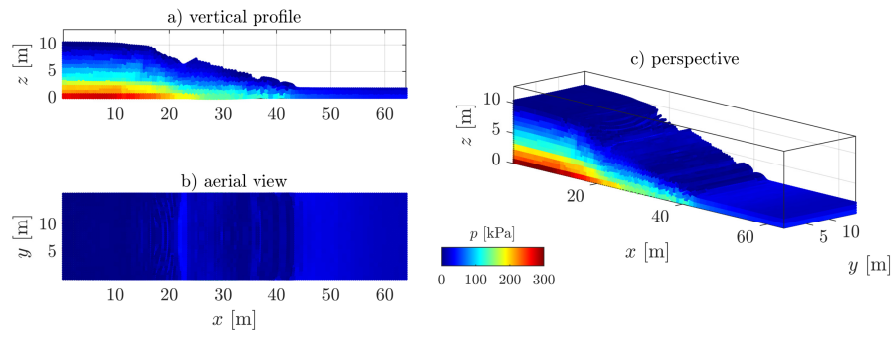


Figure C.25: Smoother pressure field when volumetric locking is mitigated with the proposed solution.

C.10 Appendix E: Heterogeneities for the peak cohesion field

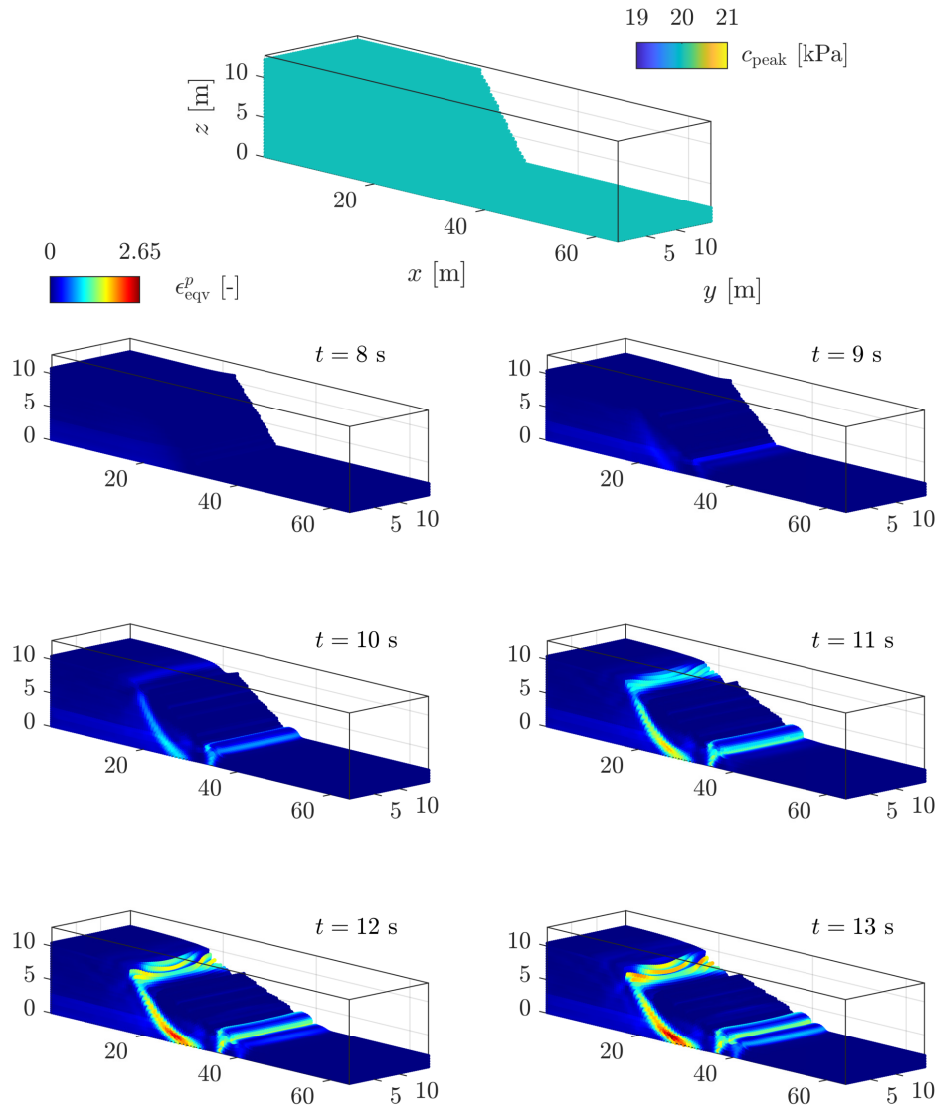


Figure C.26: Homogeneous cohesion field: time evolution of the equivalent plastic strain ϵ_{eqv}^p . Its evolution is rather homogeneous, and the overall plastic behaviour is free of any heterogeneities. Some of the first-order characteristics are observed, i.e., a principal shear zone and a compression zone at the toe of the slump.

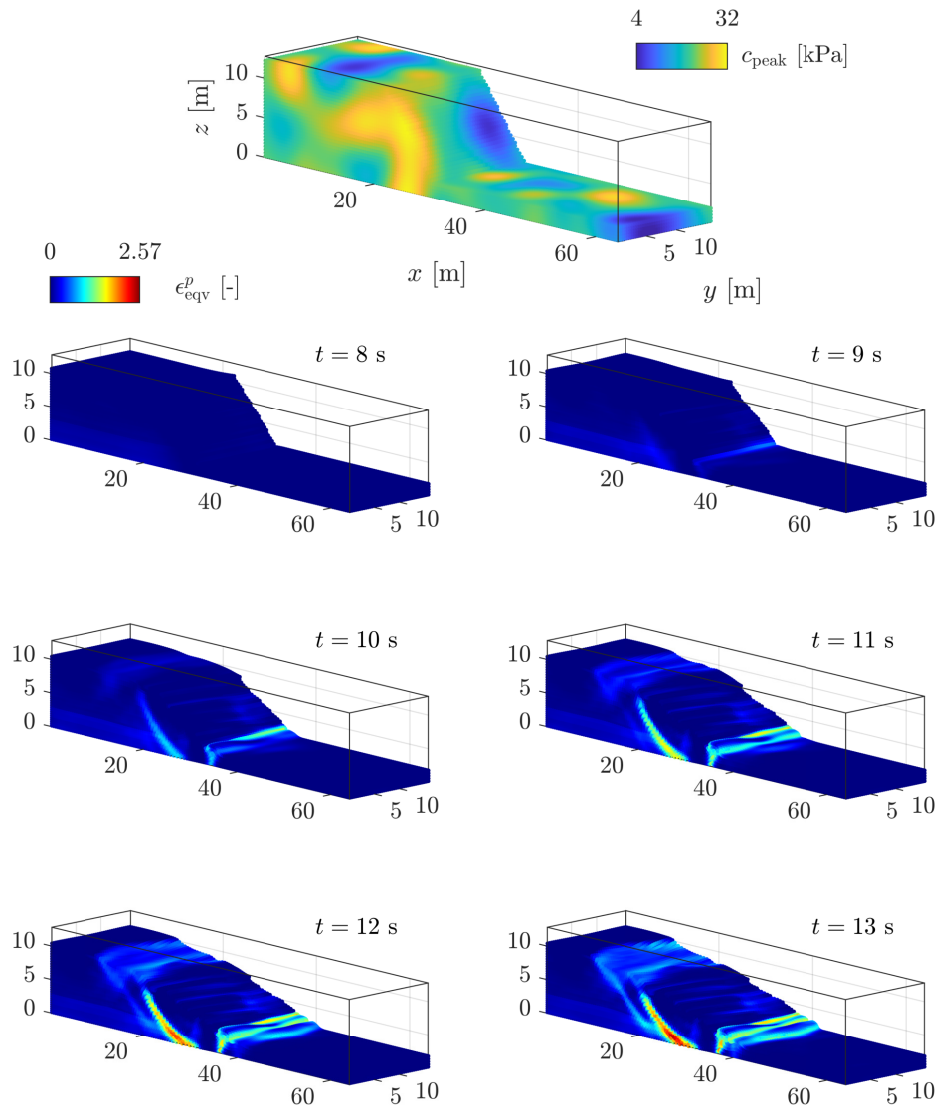


Figure C.27: Heterogeneous cohesion field with a Gaussian covariance function: time evolution of the equivalent plastic strain ϵ_{eqv}^p . Unlike Fig. C.26, heterogeneous behaviour is observed, i.e., the appearance of a second shear zone highlights a more complex deformation pattern. Moreover, a crown-like structure starts to develop at the top of the material, where an initial weak zone is located.

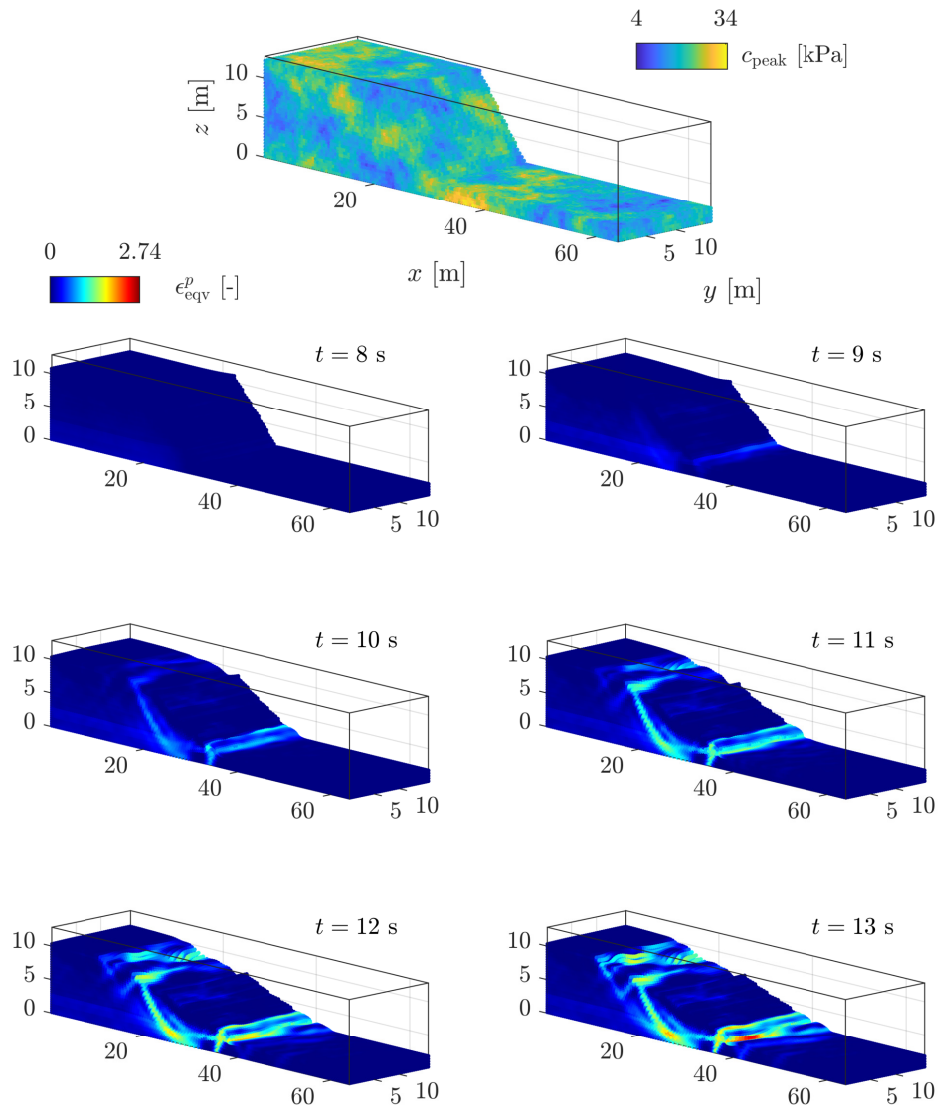


Figure C.28: Heterogeneous cohesion field with an exponential covariance function: time evolution of the equivalent plastic strain ϵ_{eqv}^p . Similar to Fig. C.27, heterogeneous behaviour is observed. However, the exponential covariance function results in an even more complex pattern of strain localization, i.e., minor and major scarps develop at the top. The crown-like structure of the slump becomes even more heterogeneous.